INTELLIGENT TECHNOLOGIES IN LOGISTICS AND MECHATRONICS SYSTEMS
ITELMS'2013

PROCEEDINGS OF THE 8TH INTERNATIONAL CONFERENCE

EDITED BY Z. BAZARAS AND V. KLEIZA

May 23-24, 2013
Panevėžys, Lithuania

CONFERENCE IS ORGANIZED BY

Kaunas University of Technology Panevezys Institute
Panevezys Technology and Science Park
Intelligent Transport Systems, Poland
Tallinn University of Technology
Riga Technical University

The proceedings of the 8th International Conference INTELLIGENT TECHNOLOGIES IN LOGISTICS AND MECHATRONICS SYSTEMS contain selected papers.

All papers were reviewed.

The style and language of authors were not corrected. Only minor editorial corrections have been carried out by the Publisher.

CONFERENCE SCIENTIFIC COMMITTEE

CHAIRMAN
Prof. Z. Bazaras, Kaunas University of Technology, Lithuania

SCIENTIFIC SECRETARY
Prof. V. Kleiza, Kaunas University of Technology, Lithuania

MEMBERS
Dr. G. Badenes, Institute of Photonic Sciences, Spain
Prof. P. Balckars, Riga Technical University, Latvia
Prof. J. Bareišis, Kaunas University of Technology, Lithuania
Prof. P. T. Castro, Porto University, Portugal
Prof. J. Furch, Brno University of Defence, Czech Republic
Dr. V. Hutsaylyuk, Military University of Technology, Poland
Prof. I. Karabegović, Bosnia and Herzegovina
Prof. A. Levchenkov, Riga Technical University, Latvia
Dr. M. Litwin, Intelligent Transport Systems**,** Poland
Prof. V. Ostasevicius, Lithuania
Prof. L. Ribickis, Riga Technical University, Latvia
Prof. M. Sitarz, Silezian Technical University, TRANSMEC, Poland
Prof. A. Sladkowsky, Silezian Technical University, Poland
Prof. D. Sprečić, Bosnia and Herzegovina
Dr. Ch. Tatkeu, Transport Electronics and Signal Processing Laboratory, France
Prof. V. Tilipalov, Kaliningrad State Technical University, Russia
Prof. B. Timofeev, St. Petersburg State Polytechnic Institute, Russia
Dr. D. Vinnikov, Tallinn University of Technology, Estonia
Prof. J. Sapragonas, Kaunas University of Technology, Lithuania

LOCAL ORGANIZING COMMITTEE
R. Bukėnas
V. Narbutas
E. Patapienė
Dr. D. Susnienė
Dr. A. Tautkus
Dr. D. Vaičiulis

8th International Conference
"INTELLIGENT TECHNOLOGIES IN LOGISTICS AND MECHATRONICS SYSTEMS"

Klaipedos str. 3, Panevezys LT-35209, Lithuania
http://en.ktu.lt/content/research/conferences-2013

PREFACE

The first (2006) and second International Workshops "Intelligent Technologies in Logistics and Mechatronics Systems ITELMS" were held at Riga Technical University. The 3rd international workshop ITELMS'2008 was held at Kaunas University of Technology Panevezys Institute on 22 – 23 May, 2008. The international conferences ITELMS'2009 – ITELMS'2013 traditionally takes place at Kaunas University of Technology Panevezys Institute.

The aims of the Conference are to share the latest topical information on the issues of intelligent technologies in logistics and mechatronics Systems. The papers in the Proceedings presented the following areas:

- Intelligent Logistics Systems
- Multi Criteria Decision Making
- Composites in Infrastructures
- Automotive Transport
- Intelligent applications of solid state physics
- Intelligent Mechatronics Systems
- Mechanisms of Transport Means and their Diagnostics
- Railway Transport
- Transport Technologies
- Modern Building Technologies
- Sensors and Sensing Phenomena

In the invitations to Conference, sent year before the Conference starts, the instructions how to prepare reports and manuscripts provided as well as the deadlines for the reports are indicated.

A primary goal of Conference is to present the highest quality research results. A key element in attiring goal is the evolution and selection procedure developed by the Conference Scientific Committee.

All papers presented in Conference and published in Proceedings undergo this procedure. Instruction for submitting proposals, including requirements and deadlines, are published in "Call for Papers" in the http://en.ktu.lt/content/research/conferences-2013. Paper proposals must contain sufficient information for a trough review. All submissions to determine topic areas are directed to appropriate Topic Coordinators. The Topic Coordinators review the submissions much them to the expertise according to the interests and forward them to selected reviewers. At least two reviewers examine each submission in details.

Selection of papers for the Conference is highly competitive, so authors should assure their submissions to meet all Conference Scientific Committee's requirements and to be of the highest possible quality.

All Conference participants prepare manuscripts according to the requirements that make our Proceedings to be valuable recourse of new information which allows evaluating investigations of the scientists from different countries.

Prof. Z. Bazaras
Prof. V. Kleiza

Contents

General Programme Schedule

**International Conference
Intelligent Technologies in Logistics and
Mechatronics Systems**

ITELMS'2013

23-24 May 2013, Panevezys, Lithuania

THURSDAY, MAY 23

12:00   REGISTRATION, WELCOME, RECEPTION (Klaipedos Str. 3, Panevezys)

OPENING OF THE CONFERENCE

14:00   **Z. Bazaras** (Director of KTU Panevezys Institute)
Greetings from vice minister **R. Vaitkus** (Ministry of Education and Science of the Republic of Lithuania)

PLENARY SESSION
(Conference hall, Klaipedos Str. 3, Panevezys)
The conference hall is well provided for PowerPoint Viewer 2007 presentations
Moderator **Z. Bazaras**

14:15   **I. Alps, M. Gorobetz, A. Levchenkov** (*Latvia*)
Experiments Results Using the Method of Statistical Estimation of the Hypothesis for Latvian Railway

14:30   **J. Tilindis, V. Kleiza** (*Lithuania*)
Manufacturing cost forecasting based on learning curve models

14:45   CONFERENCE PHOTO SESSION

MODERN BUILDING TECHNOLOGIES
(Conference hall, Klaipedos Str. 3, Panevezys)
Moderators: **O. Purvinis, V. Kleiza**

15:00   **P. Tint, A. Traumann, D. Karai, K. Oha, T. Koppel, V. Pille, V. R. Tuulik, V. Tuulik, K. Meigas** (*Estonia*)
The Computer Workers' Working Conditions Influencing the Health in Modern Buildings

15:10   **B. Nasilowska, T. Slezak, L. Sniezek, J. Torzewski** (*Poland*)
Mechanical Properties of LaserWelded Joints in the Difficult-to-Weld Steels

15:20   **P. Tint, T. Koppel** (*Estonia*)
Natural Daylight in Office Workplaces

15:30   **E. Shatkovskis, V. Zagadskij, R. Mitkevicius, J. Stupakova** (*Lithuania*)
Characteristics and Performance of the Silicon Solar Cells Improved by Complex Porous Silicon Structure

15:40   **T. Koppel, P. Tint** (*Estonia*)
Office Workers with Better Lighting Conditions Suffer Less Health Symptoms

MILITARY TECHNOLOGIES
(Workshop room 4, Klaipedos Str. 3, Panevezys)
Moderators: **O. Purvinis, V. Kleiza**

15:00   **L. Baliulyte, J. Tamulienė** (*Lithuania*)
Theoretical Investigation of the Asparagine Molecule Fragmentation by Low Energy Electrons

15:10   **S. Konopka, M. J. Lopatka, M. Przybysz** (*Poland*)
Kinematic Discrepancy of Hydrostatic Drive of Unmanned Ground Vehicle

15:20   **J. Furch** (*Czech Republic*)
Suggestion of a Inventory Control Model Used in the Army

15:30   **V. Neumann** (*Czech Republic*)
Vehicle Moving Evaluation with Simulating Technologies Support

15:40   **A. Pincevicius, S. Bekesiene** (*Lithuania*)
The Features of the Small Arms Usage

COMPOSITES AND INFRASTRUCTURES
(Workshop room 7, Klaipedos Str. 3, Panevezys)
Moderators: **O. Purvinis, V. Kleiza**

15:00   **V. Hutsaylyuk, H. Sulym, I. Turchyn, I. Pasternak** (*Poland*)
Dissipative Structures Modeling in the Aluminium Alloy: An Energy Approach

15:10   **N. Partaukas, J. Bareisis** (*Lithuania*)
The Stress State in Two−Layer Pipes Subjected to Internal Pressure

15:20   **Sniezek, I. Szachogluchowicz, K. Gocman** (*Poland*)
The Mechanical Properties of Composites AA2519-Ti6Al4V Obtained by Detonation Method

15:30   **I. Szachogluchowicz, L. Sniezek, K. Gocman** (*Poland*)
Ti6Al4V Produced by Explosive Welding Method

15:40   **Z. Bazaras, B. Timofeev, N. Vasileva** (*Lithuania*, *Russia*)
Thermo-Stable Steels Welded Joints Microstructure and Properties of the Heat-Affected Zone Metal

15:50   **R. Jackuviene, R. Karpavicius, V. Kleiza** (*Lithuania*)
Introduction of Investigation of Implementation Possibilities of LEAN Manufacturing System in Metal Processing Industry Using Statistical Methods

16:00   **M. Gecas, V. Lukosevicius, Z. Bazaras** (*Lithuania*)
Research of contact stresses in crossing

16:10   **S. Konopka, P. Krogul, M. J. Lopatka** (*Poland*)
Simulation Research of Hydrostatic Power System Control of Engineer Robot Manipulator

16:20   **D. Vaičiulis** (*Lithuania*)
Determination of Stress Strain State in Two-Layer Pipe Subjected to Hydrostatic Pressure at Plane Strain Condition under Elastic Loading

TRANSPORT SYSTEMS
(Workshop room 4, Klaipedos Str. 3, Panevezys)
Moderators: **O. Purvinis, V. Kleiza**

15:00   **A. Bartnicki, M. J. Lopatka, T. Muszyński, M. B. Jaskołowski** (*Poland*)
The Researches of Stability Evaluation Articulated Loader while Working on Slope

15:10   **L. Pelenyte-Vysniauskiene, A. Bartulis, T. Šilinskas** (*Lithuania*)
Benefits of Eco-driving Case Study

15:20   **K. Videikis, L. Pelenyte-Vysniauskiene** (*Lithuania*)
Automatic Brake System (ABS) Performance Study

15:30   **A. Mor-Yaroslavtsev, A. Levchenkov** (*Latvia*)
Testing the Immune Algorithms for Electrical Transport using the Mathematical Methods

15:40   **A. Potapov, M. Gorobetz, A. Levchenkov** (*Latvia*)
Development of Neural-network Based Control Algorithm for Train Adaptive and Smooth Braking System

15:50   **A. Tautkus, D. Misevičienė** (*Lithuania*)
Vehicle Stability under Crosswinds

SENSORS AND SENSING PHENOMENA
(Workshop room 6, Klaipedos Str. 3, Panevezys)
Moderators: **D. Viržonis, V. Kleiza**

15:00   **D. Barauskas, D. Virzonis** (*Lithuania*)
Atmosphere Pressure Tracking for CMUT Operating Point Adjustment

15:10 **A. Jukna, J. Gradauskas, J. Sulcas, A. Suziedelis, V. Nargeliene, A. Abrutis, V. Lisauskas, K.Sliuziene** (*Lithuania*)
Electric Properties of Asymmetrically Narrowed Superconducting Detectors

15:20 **I. Morkvenaite-Vilkonciene, A. Ramanavicius, I. Astrauskaite** (*Lithuania*)
Characterization of Biosensors by Scanning Electrochemical Microscopy

15:30 **G. Vanagas, D. Virzonis** (*Lithuania*)
CMUT Resonance Measurements Applied for Material Properties Analysis

15:40 **E. Sapeliauskas, D. Virzonis** (*Lithuania*)
Advances of Ultrasonic Sensing in Microchannels

15:50 **A. Vasiliauskas, A. Ciegis** (*Lithuania*)
Piezoresistive Properties of Diamond Like Carbon Films

16:00 **T. Jukna, M. Mikolajunas, R. Kaliasas, A. Bartulis** (*Lithuania*)
Fabrication of Diffraction Gratings using Electron Beam Lithography and their Transfer to a Quartz Substrate

16:10 **R. Kaliasas, L. Jakucionis, T. Jukna** (*Lithuania*)
Identifying Electropolishing Parameters for Aluminium Surface Treatment in AAO Processes

16:20 **I. Grybas, D. Jucius, A. Lazauskas, V. Grigaliūnas, M. Mikolajūnas** (*Lithuania*)
Polymer Scales for Precise Measurement System

16:30 **I. Morkvenaite-Vilkonciene, A. Ramanavicius, P. Genys** (*Lithuania*)
Scanning Electrochemical Microscopy for Characterization of Diffusion Processes

INTELLIGENT MECHATRONICS SYSTEMS
(Workshop room 2, Klaipedos Str. 3, Panevezys)
Moderators: **D. Viržonis, V. Kleiza**

15:00 **A. Baskys, V. Bleizgys, M. Sapurov, R. Zubavicius** (*Lithuania*)
AC Induction Motor Speed Stabilization Technique Based on Amplitude Control

15:10 **A. Cesnulevicius, A. Bartulis, O. Fiodorova, V. Sinkevicius, A. Tautkus** (*Lithuania*)
Orientation in Urban and Semi-Urban Environment Using Segmentation of Homogeneous Regions

15:20 **A. Platakis, A. Baskys** (*Lithuania*)
Active Harmonic Compensation with Grid-Connected Photovoltaic Inverter

15:30 **A. Typiak** (*Poland*)
Ladar-Aided Navigation System for Unmanned Ground Vehicles

15:30 **V. Skopis, I. Uteshevs** (*Latvia*)
Perspective Methods for Adaptive Sensor System for Control of Automatized Industrial Processes

17:00 DISCUSSION
(Conference hall, Klaipedos Str. 3, Panevezys)

FRIDAY, MAY 24

MODERN BUILDING TECHNOLOGIES
(Workshop room 2, Klaipedos Str. 3, Panevezys)
Moderator: **V. Kleiza**

10:00 **S. Susinskas, A. Stasiskis, R. Baltusnikiene** (*Lithuania*)
Technology of Pile-columns with Reinforced Concrete Ring Installation

10:10 **S. Susinskas, A. Stasiskis, R. Baltusnikiene** (*Lithuania*)
The Comparison of Pile-columns with Reinforced Concrete Ring and Steel Ring Installation

10:20 **R. Baltusnikiene, S. Susinskas, A. Stasiskis** (*Lithuania*)
Modern Automated Designing Systems

10:30 **R. Baltusnikiene, S. Susinskas, A. Stasiskis** (*Lithuania*)
Single-Family Residential Building Standard Design (Walls, Floor) Multiple Criteria Analysis

10:40 **D. Aviza, J. Kaupiene, A. Stasiskis, L. Cerniauskaite** (*Lithuania*)
Prediction and Evaluation of Public Building Heat Loss

INTELLIGENT MECHATRONICS SYSTEMS
(Workshop room 6, Klaipedos Str. 3, Panevezys)
Moderator: **O. Purvinis**

10:00 **R. Bayir, A. E. Cosgun** (*Turkey*)
Design of Control System for a Quadrotor Flight Vehicle

10:10 **R. Bayır, H. Demir** (*Turkey*)
Comparison of PID and Fuzzy Controller in the Cascade Tank System

10:20 **H. Demir, H. M. Ertunc** (*Turkey*)
Control of Cascade Tank System using Types of Fuzzy Logic

10:30 **A. Dabrowska, A. Typiak, R. Typiak** (*Poland*)
Universal Robotic Control Station for a Grouping of Unmanned Engineering Machines

10:40 **S. Konopka, P. Sprawka, T. Muszynski, K. Spadlo** (*Poland*)
Investigating Resistance of Turn Six-Wheel Skid-Steer Vehicle

TRANSPORT SYSTEMS
(Conference hall, Klaipedos Str. 3, Panevezys)
Moderators: **O. Purvinis, V. Kleiza**

10:00 **S. Kairienė, A. Dėmenienė, R. Laurikietytė** (*Lithuania*)
Analysis of Freight Transport in Lithuania

10:10 **V. Spangelevicius, V. Lukosevicius, V. Dzerkelis** (*Lithuania*)
Optimization of sports car body

10:20 **P. Stodola, J. Stodola** (*Czech Republic*)
Tools and Processes for Affordable Machines

10:30 **H. Amirian, A. Pezouvanis, B. Mason, K. M. Ebrahimi** (*England*)
Rotary Compact Power Pack for Series Hybrid Electric Vehicle

10:40 **M. J. Lopatka** (*Poland*)
Influence of Power Steering System on Directional Stability of Articulated Wheel Loader

12:40 **S. Konopka, M. J. Lopatka, M. Przybysz** (*Poland*)
Kinematic Discrepancy of Hydrostatic Drive of Unmanned Ground Vehicle

12:50 **I. Alps, M. Gorobetz, A. Levchenkov** (*Latvia*)
Evaluation of the Intelligent Electrical Transport Control Systems Computer Experiments Results Using the Method of Statistical Estimation of the Hypothesis

MULTI CRITERIA DECISION MAKING
(Workshop room 4, Klaipedos Str. 3, Panevezys)
Moderators: **O. Purvinis, V. Kleiza**

10:00 **R. Mazgelis, S. Bekesiene** (*Lithuania*)
Sustainability of Government Debt in the Baltic States

10:10 **S. Bekesiene** (*Lithuania*)
Leadership Styles in the Military

10:20 **S. Kairienė, A. Dėmenienė, R. Laurikietytė** (*Lithuania*)
Open Source Software usage Analysis in the Baltic Countries

13:00 DISCUSSION
(Conference hall, Klaipedos Str. 3, Panevezys)

Prediction and Evaluation of Public Building Heat Loss

D. Aviža*, **, J. Kaupienė*, A. Stasiškis*, L. Černiauskaitė*

*Department of Civil Engineering, Faculty of Technologies, Kaunas University of Technologies, Panevezys Institute, S. Daukanto st. 12-138, LT-35212 Panevezys, Lithuania, E-mail: stk@ktu.lt
**Department of Construction Technology and Management, Faculty of Civil Engineering, Vilnius Gediminas Technical University, Sauletekio ave. 11, LT-10223 Vilnius, Lithuania, E-mail: donatas.aviza@dok.vgtu.lt

Abstract

The increasing energy consumption promotes to search for effective heat loss detection and mitigation measures. By refurbishing buildings qualitatively and comprehensively, the consumption of heating energy can fall twice. It is appropriate to make an energetic certification and thermo graphic study of the building before its renovation. The article deals with selected three-story building with a basement, which is educational destination. Its thermo visual analysis is made, the defects are identified, and energy costs are estimated at present and after renovation.

KEY WORDS: *heat loss, public buildings, partitions, energy certification, thermo vision.*

1. Introduction

Until 1990 in Lithuania were built brick, reinforced concrete panel and monolithic reinforced concrete buildings. The houses built on this period characterized by a large thermal conductance of partitions and technically obsolete and inefficient heating systems. These homes consume two times more heating than the new construction apartment. It is known that houses are getting older and is not eternal, that the price of energy is constantly increasing and for Lithuania, who importees almost all of the energy resources, it is very important to reduce the energy consumption.

The main disadvantages of these homes are the cracking of the internal or external wall and a heat loss. A heat loss which is made through the partitions of such buildings consists of: flat roofs – 25% through external walls – 29% through basement spans – 20% through the floor above the ground – 4% through the windows – 22% [1]. A huge scathe of heat losses is made by building walls and flat roofs. Before restoration of buildings, it is necessary to audit energy efficiency and estimate the strategy of the renovation. The audit has to be commenced from collecting data about thermal and energy economy of the building. The data also have to comprise the thermal – technical characteristics of the walls, windows, doors and etc. Therefore, the external heated surfaces of the building are measured, the general area of the windows is calculated taking into consideration the composition of all the external insulations, their thermal resistance is also calculated. What is more, the data about the building engineering systems, the devices, using energy, the heating system, the actual and nominal power of the boiler and the installing scheme of hot water are also collected. When the supply system of hot water is centralized, other supplemented calculations are then made. Finally, it is necessary to analyze the microclimate of the internal lodgings.

The most popular method of building energy audit is thermal filming [3]. Using this method it is possible to check the thermal protection of the building qualitatively. The thermo vision is used for this process. The standing place of the thermo vision camera is chosen in the way that the surface of the analyzed object could be seen properly. The chosen filming points are foreseen in the construction plan. The object is photographed, the defects of external surfaces and insulation constructions are registered, also, the areas, where the closer definition of the data is required. During the process of this filming the registration of the meteorological conditions also takes place: the temperature of the weather is measured, as well, the wind direction and its speed. Measurements are also taken in the internal lodgings: the temperature, humidity and movement have to be taken. After this, the thermal resistance of the insulating constructions is defined and the density of the heat flows moving through the constructions

2. Energetic certification of buildings

Certification of the energy efficiency of the building – is the regulated process, where the consumption of the energy in the building is defined, building energy efficiency is estimated, defining the class of the energy efficiency of the building and, finally, the certificate of the energy efficiency of the building is given.

Certification of the energy efficiency of the building is necessary to estimate the energy efficiency of the building or its part in order to reckon the building to certain class of energy efficiency. The certification and estimation of the energy efficiency of the building is done calculating heat losses through the walls, roof, ceilings, windows, doors, heat small bridges, heat in draught from outside, internal heat dispersal, energy consumption for electricity, hot water heating and ventilation.

Energy efficiency certification should inform building owners and users about energy efficiency of buildings what, firstly, means heating expenditure and would promote people to improve energy efficiency and, therefore, would reduce the amount of carbon dioxide into the atmosphere.

The class of the energy efficiency of new buildings (building parts) till 1January, 2014 has to be not lower than C (the requirements for the energy efficiency classes are presented in table 1). Reconstructed, renewed (modernized) or repaired buildings (their parts), when reconstruction, renewal (modernization) or repair price make up more than 25 percent of the building value, excluding the plot on which the building stands, the class of the energy efficiency has to be not lower than D (till 1January, 2014). Requirements for the energy efficiency class for sale and rented houses (building parts) are not appointed.

Requirements for the energy efficiency of buildings:

- having completed the construction of new buildings (their parts);
- having completed the reconstruction, renewal (modernization) or capital repair of buildings (their parts), when the price of reconstruction, renewal (modernization) or capital repair improving insulating and (or) physical and energy properties of engineering systems make up more than 25 percent of the building value, excluding the plot on which the building stands;
- selling or renting buildings and (or) their parts (flats or lodgings of other purpose);
- larger than 500 square meters (since 9 July, 2015 – larger than 250 square meters) of useful internal space of hotels, administrative buildings, commercial, catering, transport, culture, science, sports, curing and leisure buildings.

Table 1

Requirements for D, C, B, A, A+ and A++ energy efficiency buildings [2]

The class of energy efficiency of the buildings	Requirements for the respective energy utility in class buildings
Buildings of D class	1. The value of the energy efficiency ratio C_1 of a building must meet the requirements of the regulation
	2. Building envelope calculation of specific heat loss should not be higher than the reference building envelope own specific heat loss: $H_{env} \leq H_{env.R}$
Buildings of C and D classes	1. The values of energy efficiency indicators C_1 and C_2 of the buildings should meet the requirements of the regulation
	2. Calculation, specific heat loss of a building partitions should not be greater than the regulatory own specific heat loss: $H_{env} \leq H_{env.N}$
Buildings of A class	1. The values of energy efficiency indicators C_1 and C_2 of the buildings should meet the requirements of the regulation
	2. Calculation, specific heat loss of a building partitions should not be greater than the regulatory own specific heat loss: $H_{env} \leq H_{env.(A)}$
	3. Tightness of the building must comply with requirements of Regulation Part XXVII Chapter
	4. If the building is equipped with mechanical ventilation with heat recovery system exchanger efficiency should not be less than 0.65, and the exchanger fan the amount of electricity used shall not be greater than 0.75 Wh/m³
Buildings of A+ class	1. The values of energy efficiency indicators C_1 and C_2 of the buildings should meet the requirements of the regulation
	2. Calculation, specific heat loss of a building partitions should not be greater than the regulatory own specific heat loss: $H_{env} \leq H_{env.(A+)}$
	3. Tightness of the building must comply with requirements of Regulation Part XXVII Chapter
	4. If the building is equipped with mechanical ventilation with heat recovery system exchanger efficiency should not be less than 0.80 and the exchanger fan the amount of electricity used shall not be greater than 0.55 Wh/m³
Buildings of A++ class	1. The values of energy efficiency indicators C_1 and C_2 of the buildings should meet the requirements of the regulation
	2. Calculation, specific heat loss of a building partitions should not be greater than the regulatory own specific heat loss $H_{env} \leq H_{env.(A++)}$
	3. Tightness of the building must comply with requirements of Regulation Part XXVII Chapter
	4. If the building is equipped with mechanical ventilation with heat recovery system exchanger efficiency should not be less than 0.90, and the exchanger fan the amount of electricity used shall not be greater than 0.45 Wh/m³
	5. The energy consumption from renewable sources in the building should meet the requirements of this Regulation

Requirements for the energy efficiency of buildings are established:

- for the buildings of cultural heritage if, following the requirements, their appearance and particular properties change undesirably;
- for prayer houses and other religious buildings;
- for temporary buildings (no longer than 2 years);
- for rest, garden purpose buildings, which are used no longer than 4 months a year;
- for separate buildings, where the useful space is not larger than 50 square meters;
- for production, agricultural, warehouse and industrial buildings using not much energy;
- for not heated buildings.

The method of building certification is to calculate the consumption of energy in the building and also to estimate the energy efficiency [2]. The class of energy efficiency is defined according to the building indicators of their value: insulating calculated losses; building tightness, mechanical ventilation with recuperation system technical indicators; the value of building energy consumption efficiency indicator C_1, defining the primary nonrenewable energy consumption for heating, ventilation, cooling and lightning; the value of the building energy consumption efficiency indicator C_2, defining the primary nonrenewable energy consumption to prepare hot water; a part of consumed energy from renewable resources.

The value of building energy efficiency criteria C_1 should be calculated as follows:

$$\text{if} - \frac{\sum_{m=1}^{12} Q_{PRn.H,m} + Q_{PRn.E}^{I}}{\sum_{m=1}^{12} Q_{N.PRn.H,m} + \sum_{m=1}^{12}(Q_{N.E.\lg,m} \cdot f_{N.PRn.E})} \leq 1 \tag{1}$$

$$\text{then} \quad C_1 = \frac{\sum_{m=1}^{12} Q_{PRn.H,m} + Q_{PRn.E}^{I}}{\sum_{m=1}^{12} Q_{N.PRn.H,m} + \sum_{m=1}^{12}(Q_{N.E.\lg,m} \cdot f_{N.PRn.E})} \; ; \tag{2}$$

$$\text{if} - \frac{\sum_{m=1}^{12} Q_{PRn.H,m} + Q_{PRn.E}^{I}}{\sum_{m=1}^{12} Q_{R.PRn.H,m} + \sum_{m=1}^{12}(Q_{R.E.\lg,m} \cdot f_{R.PRn.E})} \geq 1 \tag{3}$$

$$\text{then} \quad C_1 = 1 + \frac{\sum_{m=1}^{12} Q_{PRn.H,m} + Q_{PRn.E}^{I}}{\sum_{m=1}^{12} Q_{R.PRn.H,m} + \sum_{m=1}^{12}(Q_{R.E.\lg,m} \cdot f_{R.PRn.E})} \; ; \tag{4}$$

$$\text{in other cases} \quad C_1 = 1 + \frac{\sum_{m=1}^{12} Q_{PRn.H,m} + Q_{PRn.E}^{I} - \sum_{m=1}^{12} Q_{N.PRn.H,m}}{\sum_{m=1}^{12} Q_{R.PRn.H,m} - \sum_{m=1}^{12} Q_{N.PRn.H,m}} \tag{5}$$

where: $Q_{N.PRn.H,m}$ – normative $Q_{N.PRn.H,m}$ (kWh/(m²·month)), non-renewable, primary energy consumptions of building heating of every month "m"; $Q_{R.PRn.H,m}$ – reference $Q_{R.PRn.H,m}$ (kWh/(m²·month)), non-renewable primary energy consumptions for heating buildings of every month "m"; $Q_{N.E.\lg,m}$, $Q_{R.E.\lg,m}$, $f_{N.PRn.E}$, $f_{R.PRn.E}$ – regulatory $Q_{N.E.\lg,m}$ (kWh/(m²·month)), reference (kWh/(m²·m month)) electricity consumptions of every month for heated premises lighting; $f_{N.PRn.E}$ – regulatory non-renewable primary energy factor for energy of electricity; $f_{R.PRn.E}$ – reference non-renewable primary energy factor for electricity; $Q_{PRn.E}^{I}$ is calculated like this:

$$Q_{PRn.E}^{I} = (\sum_{m=1}^{12} Q_{E.\lg,m} + \sum_{m=1}^{12} Q_{E.vent,m} + \sum_{m=1}^{12} Q_{C.E,m} - \sum_{m=1}^{12} Q_{E.SK+WE+HE,m}) \cdot f_{PRn.E} + \sum_{m=1}^{12} Q_{PRn.E.SK+WE+HE,m} \tag{6}$$

and

if $Q_{PRn.E}^{I} < 0$, then we should know that $Q_{PRn.E}^{I} = 0$;

where: $Q_{E.\lg,m}$ – computational $Q_{E.\lg,m}$ (kWh/(m²·month)) power consumptions for heated premises lighting of every month "m"; $Q_{E.vent,m}$ – monthly, calculating electric power consumptions of a building heating per unit area $Q_{E.vent,m}$, (kWh/(m²·month)) of a building mechanical ventilation system ventilators of every month "m"; $Q_{C.E,m}$ – computational

consumptions of electricity to cool the building $Q_{C.E,m}$ (kWh/(m²·month)) of every month "m"; $Q_{E.SK+WE+HE,m}$ – the total consumption of electric power in a building $Q_{E.SK+WE+HE,m,x}$ (kWh/(m²·month)), which is made by Solar collectors, wind power stations and hydro electricity generation every month "m"; $Q_{PRn.E.SK+WE+HE,m}$ – calculated, non-renewable, monthly primary energy consumption of building hot water preparation system is $Q_{PRn.E.SK+WE+HE,m,x}$ (kWh/(m²·month)); $f_{PRn.E}$ – the factor of primary energy for electricity.

The value of energy efficiency indicator C_2 of a building should be calculated as follows:

$$C_2 = \sum_{m=1}^{12} Q_{PRn.hw,m} \Big/ \sum_{m=1}^{12} Q_{N.PRn.hw,m} \tag{7}$$

where: $Q_{N.PRn.hw,m}$ – regulatory $Q_{N.PRn.hw,m}$ (kWh/(m²·month)), non-renewable primary energy consumptions to prepare hot water of every month "m"; $Q_{PRn.hw,m}$ – monthly energy consumption for electric appliances from solar, wind and hydro non-renewable primary energy $Q_{PRn.hw,m}$ (kWh/(m²·month)).

The relevant values of the efficiency indicators shall meet the following requirements: A++ class: $C_1 < 0.25$ and $C_2 \le 0.70$; A+ class: $0.25 \le C_1 < 0.375$ and $C_2 \le 0.80$; A class: $0.375 \le C_1 < 0.5$ and $C_2 \le 0.85$; B class: $0.5 \le C_1 < 1$ and $C_2 \le 0.99$; C class: $1 \le C_1 < 1.5$ and $C_2 \le 0.99$; D class: $1.5 \le C_1 < 2$; E class: $2 \le C_1 < 2.5$; F class: $2.5 \le C_1 < 3$; G class: $C_1 \ge 3$.

E, F and G energy efficiency class buildings must comply with the set requirements for a value of the energy efficiency rate C1 of a building.

D, C, B, A, A+ and A++ the energy efficiency class buildings are appointed if these buildings meet all the requirements listed in Table 1.

3. Calculations and measurements

The technical specifications for the calculations of a chosen building (a part of technology faculty building) are contained in the tables 2, 3 and 4.

Table 2

The specifications of educational use part of the building partitions

No.	The name of partitions	Area, m²	The coefficient of heat transfer U, W/(m²·K)	
			Before reconstruction	After reconstruction
1.	Walls – the masonry of silicate bricks 510 mm + (20 cm Rockwool + reinforced plaster)	867.09	1.27	0.19
2.	Roof – holly g/b panel + existing roof structure + (20 cm Rockwool + waterproofing)	514.91	0.95	0.14
3.	The floor on the primer 10 cm of concrete	442.92	0.88	0.88
4.	The windows, PVC	473.81	1.7	1.7
5.	The doors, armored	4.49	2.2	2.2

Table 3

The specifications of educational use part of the building linear thermal bridges

No.	The characterization of linear thermal bridge	The length of linear thermal bridge $l_{y.e}$, m	The value of linear thermal bridge heat transfer coefficient Y, W/(m·K)	
			Before reconstruction	After reconstruction
1.	Between the building foundation and exterior walls	95.93	0.6	0.3
2.	Between the walls and the roof	121.76	0.7	0.1
3.	Around the openings in windows in walls (masonry – window)	687.44	0.35	0.35
4.	Around the openings in windows in walls (r/c – window)	258.72	1	0.65
5.	Around the exterior entrance door openings in the walls (masonry – doors)	4.36	0.35	0.35
6.	Around the exterior entrance door openings in the walls (r/c – doors)	4.12	1	0.65
7.	The outer corner of facade	43.31	-0.1	-0.1
8.	The internal corner of facade	22.14	0.15	0.05

Table 4

The data of educational use part of the building engineering systems

No.	Name	Information
1.	Useful floor area of the building, which is equipped with a natural ventilation system $A_{n.v.}$, m^2	1698.29
2.	The characterization of heating system control devices. The devices of heating system control	Control devices are installed so that they do not cover the whole building heating control; 0.9;
3.	The characterization of heat source. The efficiency of the heat source.	Heat networks, automatic control; 1.0
4.	The description of water heating system. The efficiency of the water heating system $h_{h.w}$.	Substation of the building + automatic control; 0.95;

The thermography measurements of a building were accomplished. In the received thermo photos, which are supplied in a table 5, see:

- the photo, "a" shows the temperature differences at the junction of building and land surface;
- photos "b" and "c" show the defective areas of individual walls.

The calculated building energy consumptions are shown in Table 6.

Table 5

The thermo photos of a building

a)		

Object Parameter	Value
Max	6.1°C
S0	0.7°C
Min	-11.6°C
R1:AvgTemp	0.4°C
R1:MaxTemp	0.5°C
R1:MinTemp	0.2°C
L1:AvgTemp	1.3°C
L1:MaxTemp	5.8°C
L1:MinTemp	-2.8°C
L2:AvgTemp	1.9°C
L2:MaxTemp	6.0°C
L2:MinTemp	-2.3°C

b)		

Object Parameter	Value
Max	6.9°C
S0	4.5°C
Min	-11.2°C
R1:AvgTemp	4.8°C
R1:MaxTemp	6.5°C
R1:MinTemp	3.7°C

c)		

Object Parameter	Value
Max	6.2°C
S0	-0.5°C
Min	-30.9°C
R1:AvgTemp	3.6°C
R1:MaxTemp	4.7°C
R1:MinTemp	3.0°C
R2:AvgTemp	3.6°C
R2:MaxTemp	4.7°C
R2:MinTemp	1.8°C
R3:AvgTemp	1.3°C
R3:MaxTemp	2.6°C
R3:MinTemp	0.3°C

Table 6

The results of educational use part of the building energy consumptions calculation

No.	The characterization of the energy consumption	Computational energy consumptions per square meter of building floor space per year, kWh/(m²·year)	
		Before reconstruction	After reconstruction
1.	Heat loss through the walls of a building	66.42	9.94
2.	Heat loss through the roof of a building	29.50	4.35
3.	Heat loss through the basement walls which adjacent to the primer	8.01	8.01
4.	Heat loss through the Windows of a building	47.93	47.93
5.	Heat loss through the doors of external entrance, except for the loss which is caused by door opening	0.6	0.6
6.	Heat loss through the linear thermal bridges of a building	39.01	27.18
7.	Heat loss because of the external entrance door opening	2.19	2.19
8.	The energy consumption of the building ventilation	24.04	24.04
9.	Heat loss because of the overworked infiltration of outside air	31.51	31.51
10.	Heat inflow into the building from the outside	-33.88	-33.88
11.	Internal heat emission in the building	-43.12	-43.12
12.	Electricity consumptions in the building	9.00	9.00
13.	The energy consumptions to prepare hot water	10.53	10.53
14.	Energy consumption for the heating of a building	197.71	98.46
15.	Total energy consumptions of the building	217.24	117.98
16.	A class of a building energy efficiency	D	C

4. Conclusions

1. The defective building areas, bridges of cold, thermal insulation descent zones were identified using thermography analysis. The temperature of defective wall zones differ 4-8°C from the base temperature.
2. The energy efficiency class of the building will change from "D" to "C" increasing insulation (by 20 cm of rock wool) of building walls and roof, and the reducing of linear thermal bridges a negative impact on energy consumption.
3. It is predicted that summary energy consumption will be reduced by almost half – 45.69% (from 217.24 to 117.98 kWh/(m²·year)) after the building reconstruction.

References

1. **V. Babrauskas, V. Stankevičius**. Pastatų atitvarų šiluminė fizika.-Kaunas: Technologija, 2000-286 p.
2. STR 2.01.09:2012 „Pastatų energinis naudingumas. Energinio naudingumo sertifikavimas". Vilnius, 2012
3. **J. Pikutis, V. Stankevičius**. Pastatų atitvarų renovacija. Vilnius: Statybos literatūra, 1999-136 p.
4. **E. K. Zavadskas, A. Kaklauskas**. Pastatų sistemotechninis įvertinimas.- Vilnius: Technika, 1996-296 p.

Theoretical investigation of the asparagine monohydrate molecule fragmentation by low energy electrons

L. Baliulytė*, J. Tamulienė**

***Vilnius University, Faculty of Natural Sciences, M.K. Ciurlionio st. 21/27, LT-03101 Vilnius, Lithuania, E-mail: Laura.Baliulyte@gf.stud.vu.lt*
****Vilnius University, Institute of Theoretical Physics and Astronomy, A. Gostauto 12, LT-01108 Vilnius, Lithuania, E-mail: Jelena.Tamuliene@tfai.vu.lt*

Abstract

Fragmentation of the most stable isomer of the asparagine monohydrate molecule due to the low-energy electron impact has been studied theoretically using the density functional theoretical approach. A special attention has been paid to the energy characteristics of the ionic fragment yield. The formation of the several fragments is described.
KEY WORDS: a*sparagine monohydrate, fragmentation, low energy electrons.*

1. Introduction

The studies of damages in biological molecules, amino acids included, resulting from the influence of ionizing radiation are very important. The majority of the above damages are not usually due to the primary high-energy radiation but results from the effect of the secondary low-energy charged particles produced in the course of ionization. Kinetic energy of some of secondary electrons is sufficient to induce electron impact ionization and dissociative electron impact ionization. These reactions are responsible for the formation of positive / negative ions and neutral fragments [1].

Asparagine plays an important role in the biosynthesis of proteins and is also essential to maintain balance in the central nervous system [2]. We investigate fragmentation of the one form of the asparagine monohydrate that is the most stable according to our studies (Fig. 1).
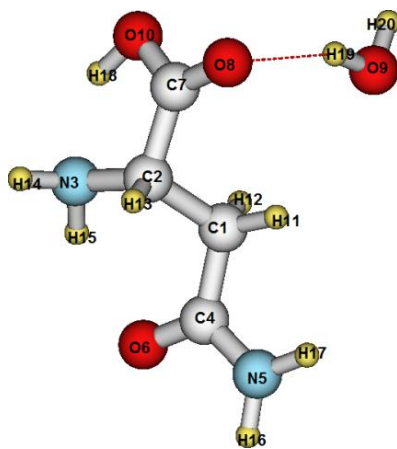
Fig. 1. View of the asparagine monohydrate

In the study we made presumption that the processes of the hydrogen migration and dehydration are not occurred during the low electron impact. It allow us foresee are the above processes realised and how often during the impact of the asparagine monohydrate by low energy electrons.

2. Theoretical investigation

The structure of the asparagine monohydrate molecule and its fragment energies of appearance have been studied using the generalized gradient approximation for the exchange–correlation potential in the density functional theory (DFT) as it is described by the Becke's three-parameter hybrid functional, using the non-local correlation provided by Lee, Yang and Parr. The DFT method is commonly referred to as B3LYP [3] – a representative standard DFT method. The cc-pVTZ basis set has been used as well [4]. There were investigated several structures of the asparagine monohydrate molecules in order to obtain the most stable position of water in respect of asparagine. The fragmentation of the stablest molecule by low electron impact was investigated. In order to model the fragmentation processes, the possible positive, negative and neutral fragments both with and without geometry optimization have been

analyzed to predict the influence of dissociation energy on the fragmentation processes. The GAMESS program packages have been applied here [6].

The peaks with $m = 18, 28, 44$ and 87 Th are the most noticeable in the asparagine mass-spectrum. Notable that the mass spectra of the asparagine monohydrate molecule was not found, however in [5] the fragments formed are listened. Aiming to identify the above fragments and found ways of their formation we calculated the appearance energies of the fragments with certain mass. The appearance energy E_{ap} was calculated as:

$$E_{ap} = |E_{asp}| - |\Sigma(E_i)| \qquad (1)$$

where E_{asp} is the total energy of the neutral asparagine molecule, while E_i is the total energy of all fragments produced.

This calculation does not take into account the activation energy of the molecular ion fragmentation, but comparison of the energy appearance of the fragments with similar mass allow us to find the energetically more probable reaction of the fragmentation.

According to our calculations, the $m = 18$ Th fragment is H_2O that may be produced according to the pathways:

$$C_4H_8N_2O_3 \bullet H_2O + e \rightarrow \begin{cases} H_2O^+ + C_4H_8N_2O_3^- + e & (2) \\ H_2O^+ + C_4H_8N_2O_3^+ + 3e & (3) \\ H_2O^+ + C_4H_8N_2O_3^0 + 2e & (4) \end{cases}$$

Calculated appearance energies (in eV) before and after optimization for the H_2O and $C_4H_8N_2O_3$ fragments are listed in Table 1.

Table 1

Calculated appearance energies (in eV) before and after optimization for the
H_2O and $C_4H_8N_2O_3$ fragments formed from the asparagine monohydrate

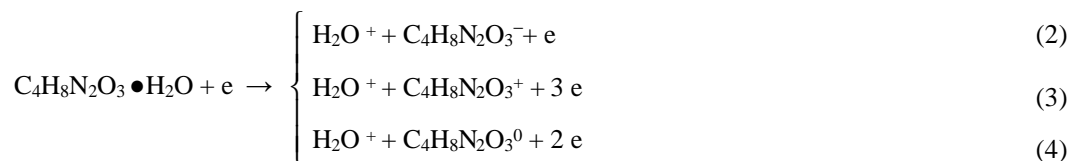| H_2O (m=18 Th) charge	$C_4H_8N_2O_3$ ($m = 132$ Th) charge	Asparagine molecule geometry not changed*	Asparagine molecule geometry changed**
1	−1	14.45	13.69
1	1	22.57	20.89
1	0	13.28	12.84

* "Asparagine molecule geometry not changed" means that the single point energy calculation of the fragments, taking into account the geometry of the certain part of the asparagine monohydrate molecule, was performed;

** "Asparagine molecule geometry changed" indicates that the equilibrium geometry structure of the asparagine monohydrate molecule fragments is investigated.

The results of the appearance energy studies indicate the pathway (4) to be the most energetically favorable (Table 1). The H_2O dissociation during asparagine monohydrate fragmentation is the most probable processes that requires $0.86 - 0.42$ eV only because 12.42 eV is necessary to remove an electron from the water molecule. We established also that water isn't formed from the asparagine monohydrate molecule as results of the destruction of the ($C_4H_8N_2O_3$).

According to our theoretical investigation $m = 28$ Th fragment is CH_2N. This fragment may be produced according to the pathways:

$$C_4H_8N_2O_3 \bullet H_2O + e \rightarrow \begin{cases} CH_2N^+ + (C_3H_6NO_3 \bullet H_2O)^- + e & (5) \\ CH_2N^+ + (C_3H_6NO_3 \bullet H_2O)^+ + 3e & (6) \\ CH_2N^+ + (C_3H_6NO_3 \bullet H_2O)^0 + 2e & (7) \end{cases}$$

Calculated appearance energies for the CH_2N and $C_3H_6NO_3 \bullet H_2O$ fragments formed are listed in Table 2.

Table 2

Calculated appearance energies (in eV) before and after optimization for the
CH_2N and $C_3H_6NO_3 \bullet H_2O$ fragments formed from the asparagine monohydrate

CH_2N ($m = 28$ Th) charge	$C_3H_6NO_3 \bullet H_2O$ charge	Asparagine molecule geometry not changed*	Asparagine molecule geometry changed**
1	−1	19.17	10.99
1	1	28.27	23.89
1	0	20.03	13.86

*, ** – see explanatory notes in Table 1.

According to our results obtained the process corresponding to a pathway (5) is more energetically favorable than (5) and (6).

We predict mass $m = 44$ Th fragment is CH_2ON. The CH_2ON fragment may be produced according to the following pathways:

$$C_4H_8N_2O_3 \bullet H_2O + e \rightarrow \begin{cases} CH_2ON^+ + (C_3H_6NO_3 \bullet H_2O)^- + e & (8) \\ CH_2ON^+ + (C_3H_6NO_3 \bullet H_2O)^+ + 3\,e & (9) \\ CH_2ON^+ + (C_3H_6NO_3 \bullet H_2O)^0 + 2\,e & (10) \end{cases}$$

Calculated appearance energies for the CH_2ON and $C_3H_6NO_3 \bullet H_2O$ fragments formed are listed in Table 3.

Table 3

Calculated appearance energies (in eV) before and after optimization for the
CH_2ON and $C_3H_6NO_3 \bullet H_2O$ fragments formed from the asparagine monohydrate

CH_2ON ($m = 44$ Th) charge	$C_3H_6NO_3 \bullet H_2O$ charge	Asparagine molecule geometry not changed*	Asparagine molecule geometry changed**
1	−1	9.45	4.51
1	1	16.06	11.70
1	0	13.41	9.97

*, ** – see explanatory notes in Table 1.

Comparison of the appearance energies of the CH_2ON fragment allows us to conclude the (8) fragmentation pathway as the most probable energetically. On the other hand the fragment with mass $m = 44$ Th may appeared due to dissociation $C_4H_8N_2O_3$, i.e. the processes may occured:

$$C_4H_8N_2O_3 + e \rightarrow CH_2ON^+ + (C_3H_6NO_3)^- + e \qquad (11)$$

However, this dissociation required larger energy than that of the pathway (8) (Table 4). The energy of the formation of the $C_4H_8N_2O_3$ cation must be accounted too. Thus, this dissotiation is less possible.

Table 4

Calculated appearance energies (in eV) before and after optimization for the
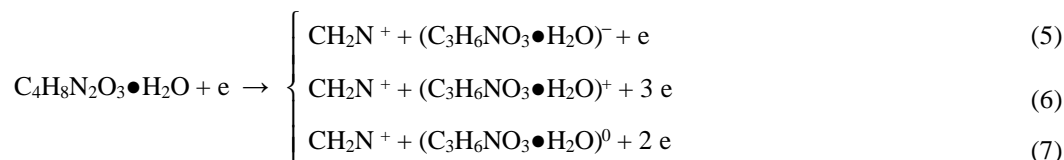CH_2ON and $C_3H_6NO_3$ fragments formed from the asparagine monohydrate

CH_2ON ($m = 44$ Th) charge	$C_3H_6NO_3$ charge	Asparagine molecule geometry not changed*	Asparagine molecule geometry changed**
1	1	13.49	10.53

*, ** – see explanatory notes in Table 1.

We also have checked the possibility of formation of the CO_2^+ fragment with mass 44 Th. This fragment can be produced only during reactions:

$$C_4H_8N_2O_3 \bullet H_2O + e \rightarrow \begin{cases} CO_2^+ + (C_3H_8N_2O \bullet H_2O)^- + e & (12) \\ CO_2^+ + (C_3H_8N_2O \bullet H_2O)^+ + 3\,e & (13) \\ CO_2^+ + (C_3H_8N_2O \bullet H_2O)^0 + 2\,e & (14) \end{cases}$$

However, the problem occurred with convergence of the $C_3H_8N_2O \bullet H_2O$ fragment. It indicates indirectly that other proceses (as example the migration of the hydrogen atom) must be investigated too. Thus, we may conclude what the pathway is more probable and which fragment with mass $m = 44$ Th is formed when additional investigations would performed. On the other hand, it is necessary to pay attention that the apperance energy of the fragment is smaller than other fragments under investigations. It allows us to predict the high yield of the fragments with $m = 44$ Th and, as consequence, intensive line in the mass spectrum (electron ionization) of the asparagine monohydrate based on the comparison of the appearance energy of the different mass fragments.

In this research we determined that mass $m = 87$ Th cation is $C_3ON_2H_7$ and can be produced according to the following pathways:

$$C_4H_8N_2O_3 \bullet H_2O + e \rightarrow \begin{cases} C_3ON_2H_7^+ + (CHO_2 \bullet H_2O)^- + e & (15) \\ C_3ON_2H_7^+ + (CHO_2 \bullet H_2O)^+ + 3\,e & (16) \\ C_3ON_2H_7^+ + (CHO_2 \bullet H_2O)^0 + 2\,e & (17) \end{cases}$$
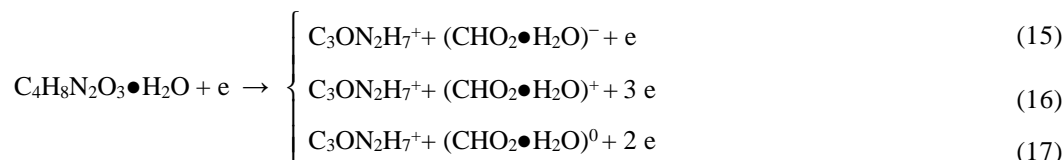
Calculated appearance energies (in eV) before and after optimization for the $C_3ON_2H_7$ and $CHO_2 \bullet H_2O$ fragments formed from the asparagine monohydrate are listed in Table 5.
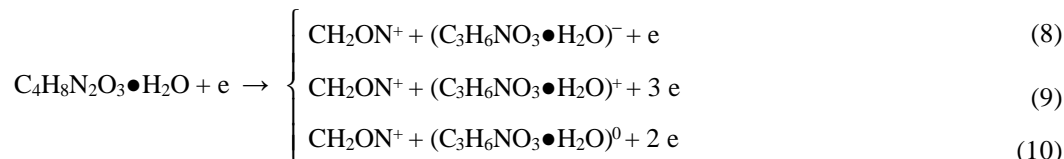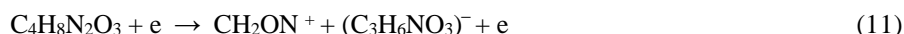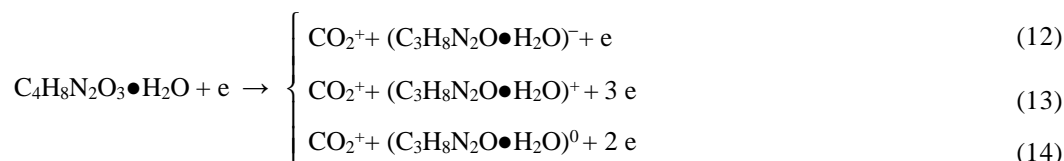
Table 5

Calculated appearance energies (in eV) before and after optimization for the
CH_2ON and $C_3H_6NO_3 \bullet H_2O$ fragments formed from the asparagine monohydrate

$C_3ON_2H_7$ ($m = 87$ Th) charge	$CHO_2 \bullet H_2O$ charge	Asparagine molecule geometry not changed*	Asparagine molecule geometry changed**
1	−1	13.18	9.75
1	1	21.67	17.10
1	0	16.29	13.20

*, ** – see explanatory notes in Table 1.

According to our results obtained the process corresponding to a pathway (15) is more energetically favorable than (16) and (17) (Table 5).

3. Conclusions

Calculated appearance energies for the fragments with $m = 18$, 28, 44 and 87 Th allows us to identified the fragment and found the most probable energetically pathway. According to our research, fragment with mass 18 Th is water, fragment with mass $m = 28$ Th is CH_2N and fragment with mass 87 Th is $C_3ON_2H_7$. Additional investigations could be performed to identify fragment with mass 44 Th that may be CH_2ON or CO_2. However, the comparison of the appearance energies of the fragments investigated allows one to predict the high yield of the fragments with $m = 44$ Th and, as consequence, intensive line in the mass spectrum (electron ionization) of the asparagine monohydrate molecule.

References

1. **Cristoni S., Bernardi L. R.** Mass. Spectr. Rev., 22 (2003), p. 369.
2. **John F. Valliere-Douglass, Catherine M. Eakin, Alison Wallace, Randal R. Ketchem, Wesley Wang, Michael J. Treuheit** and **Alain Balland.** Glutamine-linked and Non-consensus Asparagine-linked Oligosaccharides Present in Human Recombinant Antibodies Define Novel Protein Glycosylation Motifs. *J Biol Chem.* 285(2010), pp.16012-16022.
3. **Becke A. D.** J. Chem. Phys., 98 (1993), p. 5648.
4. **Kendall R. A., Dunning Jr. T. H., Harrison R. J.** Electron affinities of the first-row atoms revisited. Systematic basis sets and wave functions. J. Chem. Phys., 96 (1992), pp. 6796–6806.
5. **Vukstich V. S., Romanova L. G.** and **Snegursky A. V.** Determination of the Atomic Composition of Isobaric Ionsin the Mass Spectrometric Study of the L-Asparagine Monohydrate. *Tech Phys Lett.* 38 (2012), pp. 347-350.
6. **M. W. Schmidt, Baldrige K. K., Boatz J. A., Elbert S. T., Gordon M. S., Jensen J. H., Koseki S., Matsunaga N., Nguyen K. A., Su S. J., Windus T. L., Dupuis M.** and **Montgomery J. A.** J. Comp. Chem. 14 (1993) 1347.

Proceedings of 8th International Conference ITELMS'2013

Modern Automated Designing Systems

R. Baltušnikienė*, S. Sušinskas*, A. Stasiškis*

*Kaunas University of Technology, Daukanto str. 12, 35212, Panevėžys, Lithuania, E-mail: stk@ktu.lt

Abstract

Foreign experience in a virtual building design is reviewed, where all graphical objects are volumetric bodies, they are managed parametrically and they are intelligent i.e. each object "knows" about themselves not only quantitative information (length, area, volume, etc.) but also qualitative information (material, composition), it can also preserve its history and even "recognize" its creator.
KEY WORDS: *building information modelling, database, multi-criteria, virtual design.*

1. Introduction

While designing a project an architect, a constructor or an engineer has to deal with lots of problems: how to create a competitive, artistic and high quality project in a short term. A project which could ensure a choice of rational and effective structural solutions while realizing the concept of architectural form and space, which could let evaluate actual consumption of time and resources as accurate as possible, which could help avoid mistakes and inaccuracies and ensure quick and smooth process of construction [8, 14].

Even today some big companies still use "paper and pencil" technology, which must be replaced by modern computer aided design facilities if a company wants to remain competitive. Modern designing is impossible without a computer.

Additionally to automatizing of just the designing, computer software also allows to automate preparation of documentation, specifications, estimates and reports. It is possible to automatize about 60-70% of the whole planning process.

Modern automatized or computer design [9] is a whole scientific branch which is based on object modelling methodology [2, 3, 6, 7]: from an idea to the real object. Based on this methodology a term "computer design" involves whole sequence of actions. The sequence begins with creating a virtual model of the analysed object (a detail, a building, an engineering system) by describing its physical parameters and conditions of its links with other objects. Later, when life-like conditions are created, the analysis of model behaviour is performed, various simulations of influences (static and dynamic loads, variations of temperature and humidity, internal pressure) are described and results are analysed (reactions, deformed state, stresses). Based on this analysis, structural solutions are considered and correction of the project is performed. Then these results are given in a standard technical documentation form [10]: drawings are generated, components and elements are detailed, estimates and specifications are made [13, 15, 16]. All in all modern computer technologies allow us to simulate life-like conditions and act with the model like with the material object while it is just in project designing state [14].

2. 3D building model

Modern computer designing technology generally replaces traditional designing concept by transferring drawing methods from 2D to 3D interface which involves:
- Geometric model of an object;
- Its physical properties;
- Functional properties of the model's components.
    Consolidates all the parts of the project:
- architectural-structural;
- engineering networks;
- building environment and city plan;
- estimates;
- construction management technologies and etc.

A 3D building model acts as a synchronized graphical and digital database. The data is collected coherently when creating the model of the building in all states of the process also ensuring coordination of all project parts and synchronization of all the designing processes. Documentation in level of technical or working project is generated from the model. [14].
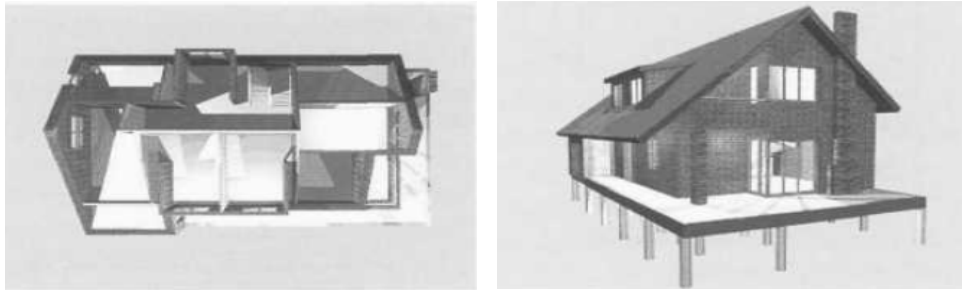
Fig. 1.   In modern automatized design systems construction elements of building are graphically modelled as volume containing elements but from the standpoint of contained information – as "intellectual elements" [1]

Instead of the term CAD (*Computer Aided Design*) another term BIM (*Building Information Modelling*) is used more usually. Its concept is to [5, 9, 11]:

- Ensure integrated management of graphical and informational data streams while combining virtual graphics (CAD) [101] with data streams (DB) and descriptions of the processes in united software interface;
- Create the unified strategy which includes design of the building, construction process of the building and exploitation management of the building, based on computerized object and its construction modelling technologies while ensuring the cycle of building's engineering support;
- Unite different actions to one-piece processes

It is suggested to use the PLM (Product Lifecycle Management) or so called 4D conception to define theoretical parameter values as accurate as possible and reduce errors [4].

For example, **Bentley BIM** (Building Information Modelling) conception includes all the parts of the project. It allows to collect all the information about the object in a digital 3D model and to work the model like with a material object. When we link the 3D model of a building with calculations of resources demand, timetables and alternate comparison, we receive a 3D model projected in time – a 4D conception.

3. Virtual design of a building

In the webpage www.navigram.com [22] a Dutch company offers an interactive 3D design technology. It is possible to plan rooms, furniture, lightning, to choose materials and colours using a simple interface. Bellow there are 4 visualization styles made using the "Navigram planner" software (Fig. 2 – 5):
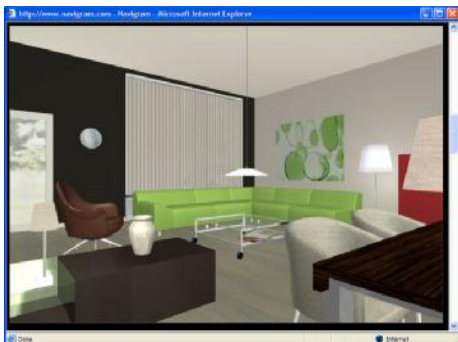
Fig. 2.   "Navigram planner" 1st style
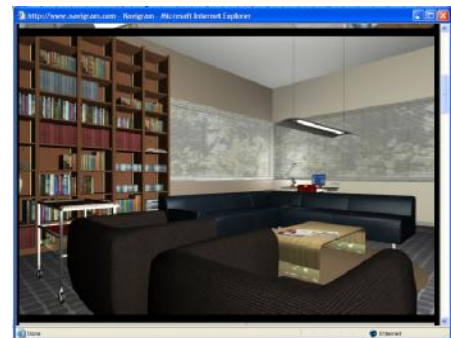
Fig. 3.   "Navigram planner" 2nd style
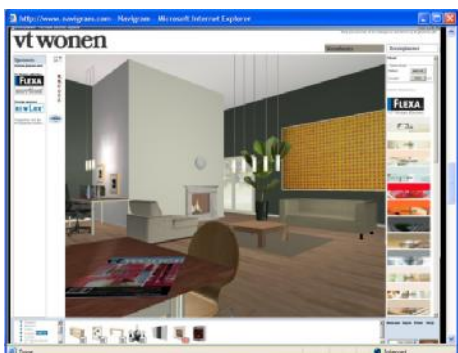
Fig. 4.   "Navigram planner" 3rd style
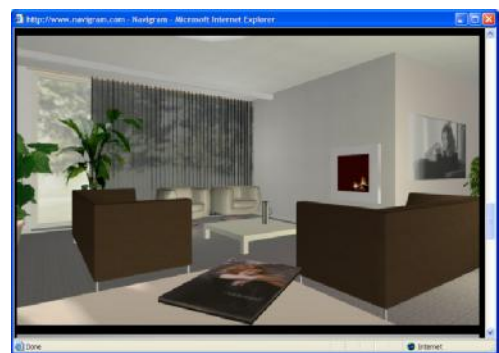
Fig. 5.   "Navigram planner" 4th style

In this webpage you can choose these online modules:
1. "To Navigram Room Planner".
2. "To Imagegallery".
3. "To VTwonen Room Planner (Dutch)".
4. "To Online Productplanner".
5. "Online House planner".
6. "To Online Virtual Plan".

The module "Room planner" allows to use planning in 2D and 3D interfaces. You can switch between these interfaces at any moment. A realistic view can be generated without any additional software.

Fig. 6.   3D perspective view

In the module "Virtual Plan" you can walk in 3D virtual area of one-flat dwelling-houses. When the wanted package (with a garage, balcony, etc.) of the house is chosen, a program automatically calculates the estimates. Whole project can be transferred to a planning system and all required building materials can be ordered online. A virtual town is given in a Fig. 7.

Fig. 7.   Virtual housing development

A customer can plan the house in a virtual space himself. It is possible to tune the lightning, plumbing, colours of walls and other elements. For such works the module "VTwonen Room Planner (Dutch)" is suitable. It is in Dutch language only. An example of lighting adjustments is given in Fig. 8.
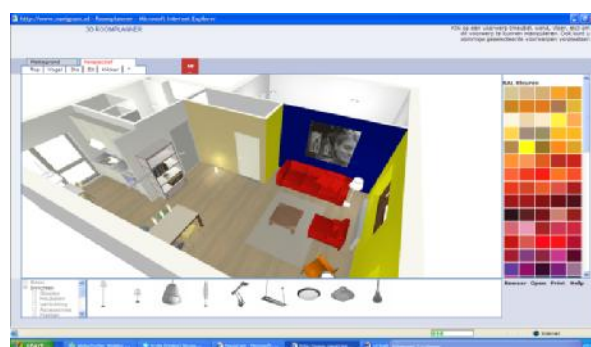
Fig. 8.   Modelling of lightning

The Dutch national housing agency is executing the project which allows customers to satisfy their individual needs using a 3D building model (Fig. 9).

Fig. 9.   Direct abilities of a customer when using a 3D building module [21]

The customer can use these potentials when using a 3D model:

Basic model:
a) visualisation;
b) photographs;
c) video;
d) virtual environment;
e) a digital model of the town;
f) environmental analysis;
g) results of the analysis;
h) customer support and help.

Individual potentials model:
a) Modelling of the internal climate;
b) Modelling of a fire situation;
c) Modelling of energy consumption;
d) Acoustic modelling;
e) Determination of the most economic offer;
f) Faster preparation of building documents;
g) Choice of quality materials;
Better quality of the final building.

4. Decision support systems

In developed world countries economic, technic and technologic environment forces traditional designing systems to transform into electronic systems and use online decision support (SPS) (SPS).

The decision support system is an information system which collects data and knowledge from various sources, processes it by using various mathematic and logic models, provides information necessary to analyse possible decision alternatives and to accept final decision.

The decision support system is made of several components: data (databases and database management system), models (model bases and management system), user-friendly interface and e-mail management system (Table 1) [12, 20].

Table 1

Components of the decision support system

MANDATORY			4.
1.	2.	3	
DATA	MODELS	USER INTERFACE	E-MAIL

Data is a vital component of the decision support system. The more data is collected, the more accurate decision can be made [23, 19]. Decision support systems can also be applied on 4D conception ("SAS" project [23]).

When a user uses decision support systems, analyses alternative decisions and makes best final decisions, not only time is saved but also new opportunities are employed. The object can be inspected in 3D, alternative variants can be analysed as a complex.

Data which is necessary to make decisions can be given in digital, graphical (drawings, schemes, diagrams), equational, audio, photo, video or other forms. These data forms give complex information about an object. For example, cost, height of a building, number of rooms can be expressed in digital form although the view of the building and its environment is best given in visual form such as pictures or video.

In a decision support database data can be stored together and linked. Databases describing the object can be in different places, also online. When the user makes a request, decision support system can give information about the object prepared in different aspects. For such operations database management systems are necessary. They allow the user to manipulate with lots of data without programming skills. Database management system also facilitates linking between different data sources. [12, 19, 20].
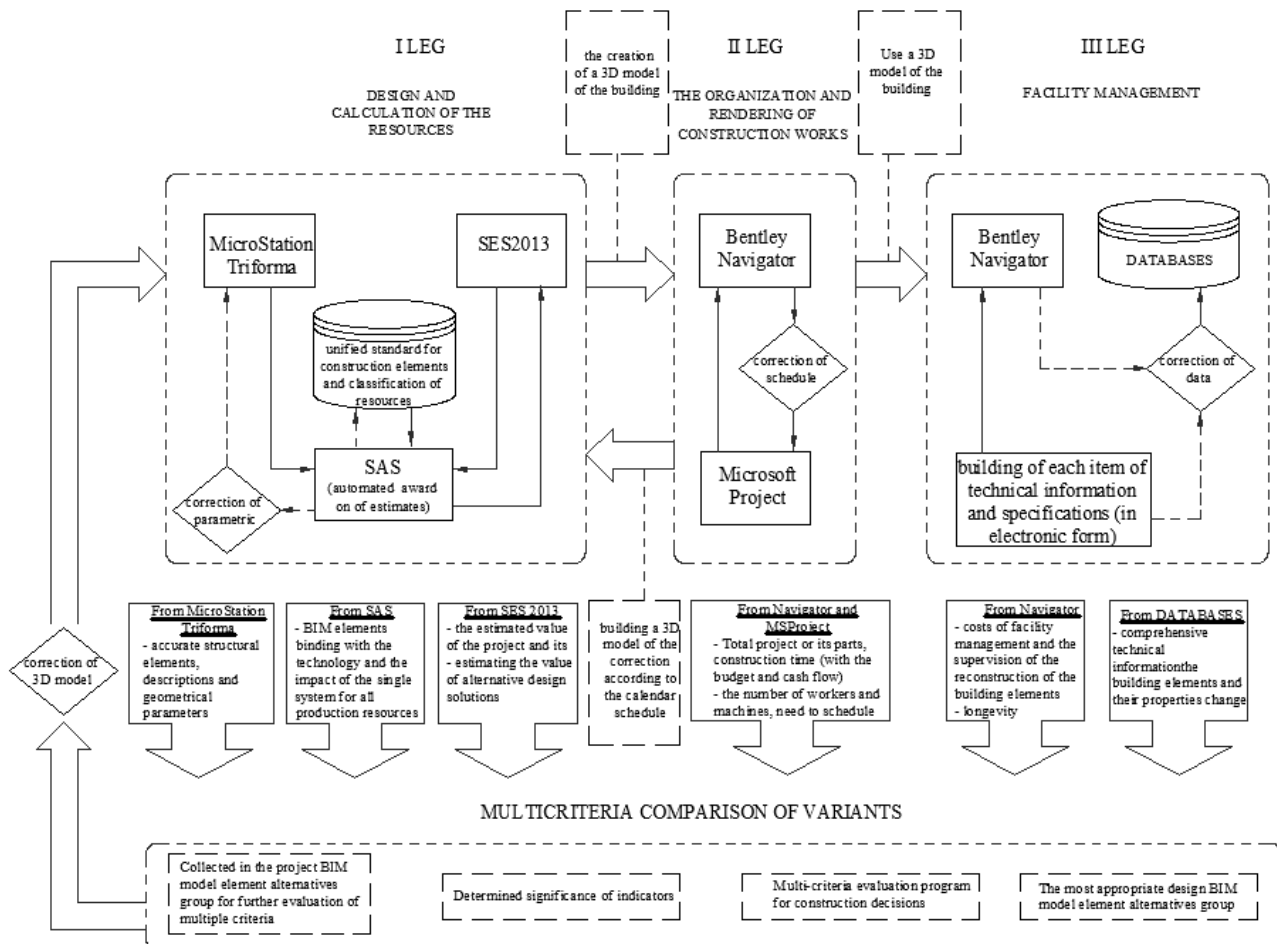
Fig. 10. Application of The decision support system in construction management and 4D conception (project "AS")

5. Databases

There are several conceptions of databases.

The first conception identifies DB as stored data. Database examples: project catalogue, typical constructions catalogue and etc. DB – a set of data linked and stored together. Stored in this way data matches with a model of a real world which is intended to automatize. The data is usually used by several users. DB user can be not only a user but also an application.

Data descriptions and their associations are of two types: logical and physical. Physical data description gives physical ways of data storage in external memory. Logical data description is dedicated to DB users. Data structures and their associations can be very different in physical and logical description.

To describe logic data these terms are usually used: data element (field), data group, record, file, databases.

Properties, common for all the data stored in databases: integrity, excessity, uncontradictionarity, safety, independence.

Data, stored in DB must be protected from any modifications or destruction. Every DB user has well-defined rights to the data.

Data independence means that data management applications are not affected by modifications of data storage or organisation ways. Physical and logical data organisation can be modified.

Usefulness of data is connected straight with how data affects making of decisions. Usefulness of data is analysed [12] and given in table 2.

The second DB conception identifies DB as a set of data processing programs. Such software is called the database management system (DBMS). DBMS has software appliances to administrate, use, install and describe data. DBMS also acts as an interface between data and the user. The user uses DBMS to manage data in the DB.

The third DB conception is the widest: it includes systemic and technological aspects. DB – a system of mathematic, linguistic, programmed, technical and organisational appliances which centralises collection and usage of the needed data [17].

Characteristics of usefulness of data

1. OPERATIVITY	Shows how the moment of receiving of the information match the moment of its usage in making decisions.
2. DETALISATION	Data in the base can be arranged as a tree to make usage of the data easy and time saving for every user to analyse, detail and aggregate it.
3. CLARITY	Data in DB must be given clearly without alternative meanings to make interpretation of data clear and uniform. Electronic dictionaries can be useful.
4. PARTICULARITY	Data in the database must describe the analysed object from every aspect.
5. COMPARABILITY	Effectiveness of every project can be evaluated only by comparing it with similar projects. Information about alternative projects stored in DB must be compared
6. RELIABILITY	Reliability is determined by faultless performance of technical.
7. DIGITAL PRESENTATION OF THE INFO	Necessary information is rational to give in digital form. It is easier to perform calculations and associate it with other data.
8. SUITABILITY OF THE PRESENTATION	Information in a database can be presented in many ways. The most effective presentation for the exact project must be used.
9. RELATION BETWEEN COST AND USEFULNESS	DB must include data which could buy off after their usage in making decisions.

Next to traditional resources (capital, land, buildings, finances, materials), data has become a very important resource. This resource is managed by databases and informational systems. Connection between database and a construction project is given in Fig. 11.
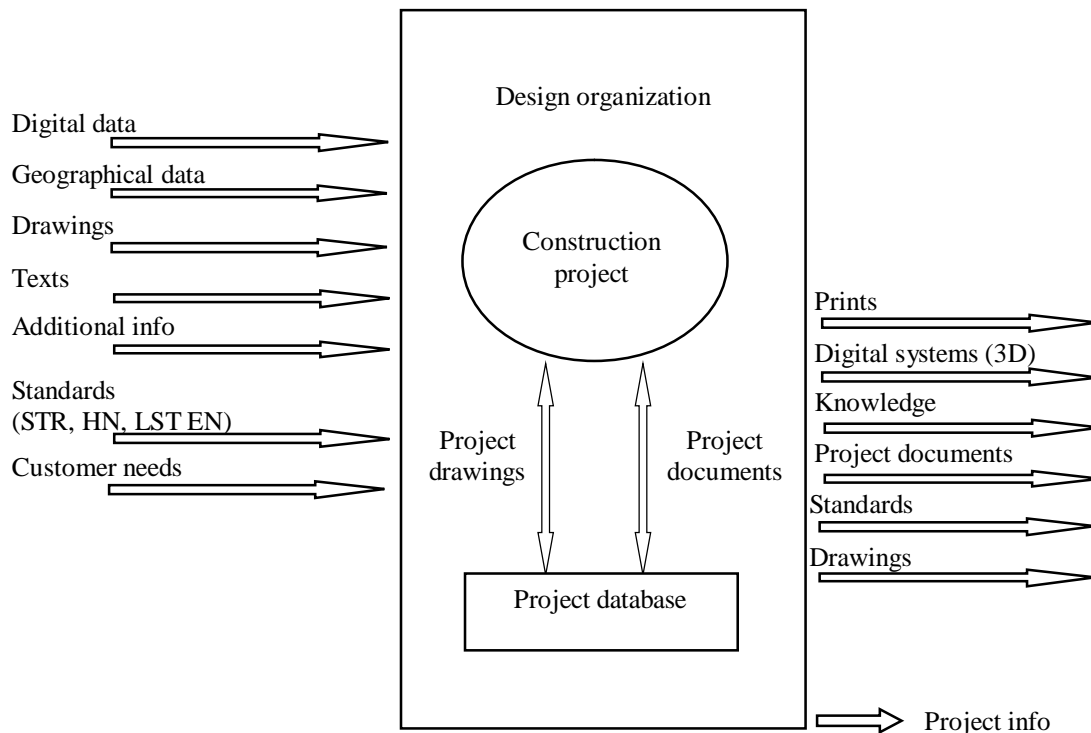
Fig. 11. Connection between database and a construction project

Information exchange principles scheme between database, customer and designer considering historical stages of development is given in the fig.12

Building organisations, to create effective conditions for operation of whole building industry branch, must receive accurate, clear, reliable and comprehensive information: from law, standard building documents, to recommendations, scientific researches and technical analyses. Streams of information grows more and more as time goes by, but terms to make decisions get shorter [18].
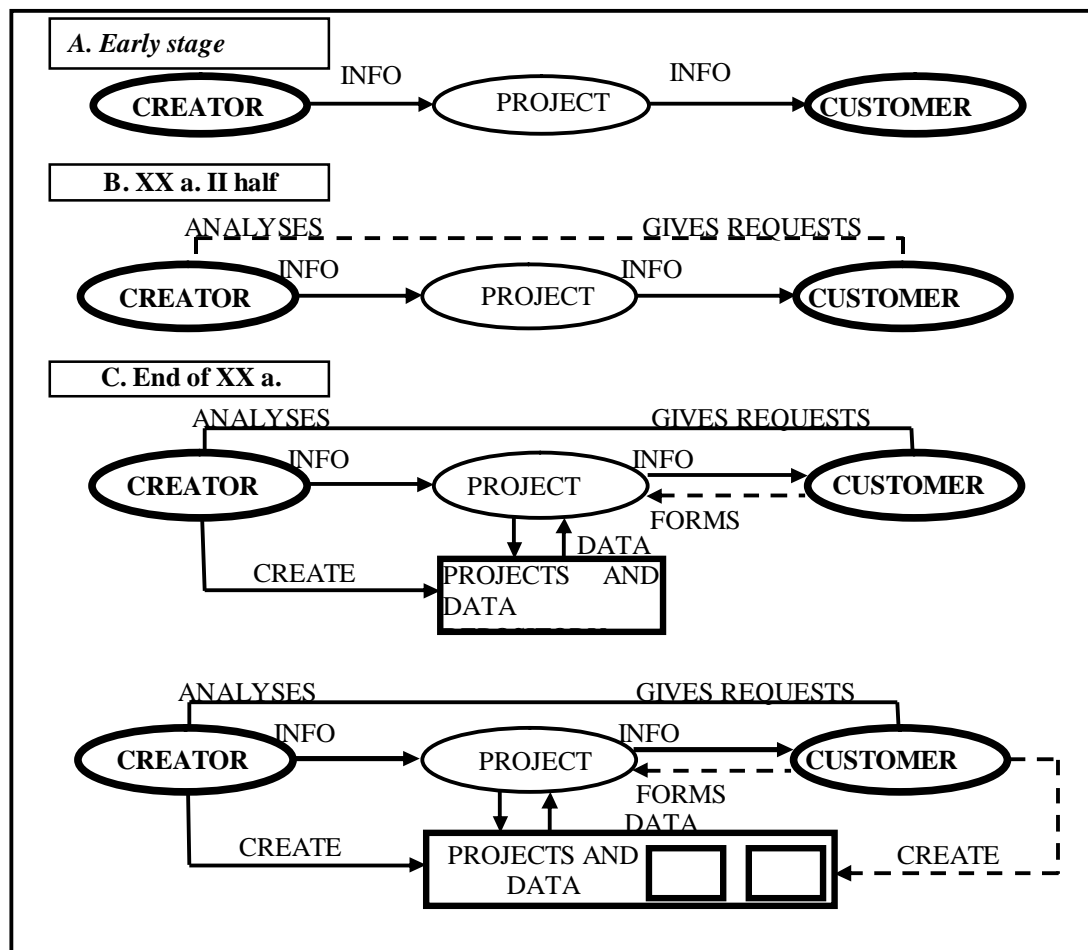
Fig. 12. Development of projects and databases

4. Conclusions

Modern computer-aided design technology essentially replaces the traditional design concept, moving from manual creation of drawings in 2D to a static 3D graphical-informational model. It is suggested to use the product's life-time management (PLM) also known as the 4D concept in the design field.

Acknowledgements

References

1. **Alkass S. T., Farnaz S., Osama M.** Computer-Aided Site Layout Planning // Journal Construction Engineering and Management, Volume 132, Issue 2, February 2006, pp. 143-151.
2. **Austin S., Baldwin A., Li B., Waskett P.** Analytical design planning technique: a model of the detailed building design process. Design Studies, Vol 20, No 3, 1999, pp. 279-296.
3. **Brown F. E., Cooper G. S., Ford S., Aouad G., Brandon P., Child T., Kirkham J. A., Oxman R., Young B.** An integrated approach to CAD: modelling concepts in building design and construction. Design Studies, Vol 16, No 3, 1995, pp. 327-347.
4. **Dawood N., Sriprasert E., Mallasi Z., Hobbs B.** 4D visualisation development: real life case studies, Agger K (ed.); Distributing knowledge in building; Arhus, June 12 - 14, Denmark, 2002.
5. **Donath D., Loemker T. M., Richter K.** Plausibility in the planning process—reason and confidence in the computeraided design and planning of buildings. Automation in Construction, Vol 13, No 2, 2004, pp. 159-166.
6. **Ekholm A., Fridqvist S.** A concept of space for building classification, product modelling, and design. Automation in Construction, Vol 9, No 3, 2000, pp. 315-328.

7. **Ford S., Aouad G., Kirkham J., Brandon P., Brown F., Child T., Cooper G., Oxman R., Young B.** An information engineering approach to modelling building design. Automation in Construction, Vol 4, No 1, 1995, pp. 5-15.

8. **Ford S., Aouad G., Brandon P., Brown F., Child T., Cooper G., Kirkham J., Oxman R., Young B.** The object oriented modelling of building design concepts. Building and Environment. Vol 29, No 4, 1994, pp. 411-419.

9. **Gabbar H. A., Aoyama A., Naka Y.** Model-based computeraided design environment for operational design. Computers & Industrial Engineering, In Press, Available online 5 2004.

10. **Garner B., Raban R.** Context management in modeling information systems (IS). Information and Software Technology, Vol 41, No 14, 1999, pp. 957-961.

11. **Hoekstra J.** Big Buzz for BIM. Architecture, Vol 92, No 7, 2003, pp. 79-82.

12. **Kaklauskas A., Zavadskas E. K.** Internetinė sprendimų parama. Monografija. V.: Technika, 2002. 292 p.

13. **Narmontas D., Popovas V.** Development of integrated design and analysis systems. The problems of Structural Engineering, Klaipeda 2000, pp. 112-113 (in Lithuanian).

14. **Popovas V., Jarmolajevas A., Grigorjeva T.** Automated design systems today. New Construction magazine (Nauja statyba), No 6, 2003, p. 26-29, No. 7, 2003, pp. 40-41 (in Lithuanian).

15. **Popovas V.** Trends of contemporary CAD systems development. Abstracts of the conference "Building structures: development and strengthening", held on December 3 d. 1999 m., Vilnius, Technika, p. 78-83 fin Lithuanian).

16. **Sacks R., Eastmanand C. M., Lee G.** Parametric 3D modeling in building construction with examples from precast concrete. Automation in Construction, In Press, Corrected Proof, Available online 27 January 2004.

17. **Sekliuckis V.** ir kt. Informacijos sistemos ir duomenų bazės. Kaunas: Technologija, 2004. – 338 p.

18. **Vanier D. J., Mellon B. S., Thomas R. Worling.** Management of Construction Information Technology // Management of Information Technology for Construction. Proceedings of the First International Conference on the Management of Information Technology for Construction. World Scientific Publishing Co. Pte. Ltd., 1993. – 602 p.

19. **Zavadskas E. K., Kaklauskas A., Banaitienė N.** Pastato gyvavimo proceso daugiakriterinė analizė. Monografija. V.: Technika, 2001. – 380 p.

20. **Zavadskas E. K., Simanauskas L., Kaklauskas A.** Sprendimų paramos sistemos statyboje. Monografija. V.: Technika, 1999. – 236 p.

21. National Agency for Enterprise and Construction. http://www.naec.dk/.

22. Navigram. Interactive 3D design solutions for the furniture and real estate market. http://www.navigram.com.

23. Šiuolaikinės automatizuotos projektavimo sistemos. http://www.inre.lt/download/publikacijos/statyba_06_03.pdf.

Single-Family Residential Building Standard Design (Walls, Floor) Multiple Criteria Analysis

R. Baltušnikienė*, S. Sušinskas*, A. Stasiškis*

*Kaunas University of Technology, Daukanto str. 12, 35212, Panevėžys, Lithuania, E-mail: stk@ktu.lt

Abstract

This article analyzes two multicriteria analysis methods of the typical wall and floor structures of a building. These methods analyzed in the article are: complex proportional assessment and the degree of performance and market valuation. Once the commercial offers degree of efficiency is determined, we can see which offer is the most effective.
KEY WORDS: *multiple criteria analysis, method, walls, floor, decision support systems, single family residential building.*

1. Introduction

According to the virtual home concept, and automated location of the building, it is proposed to create a newly constructed single family residential building construction standard database. Centralized database composed of five separate part of the building above ground structures [1] variant design matrix roof, walls, floors, windows and doors (Fig. 1).
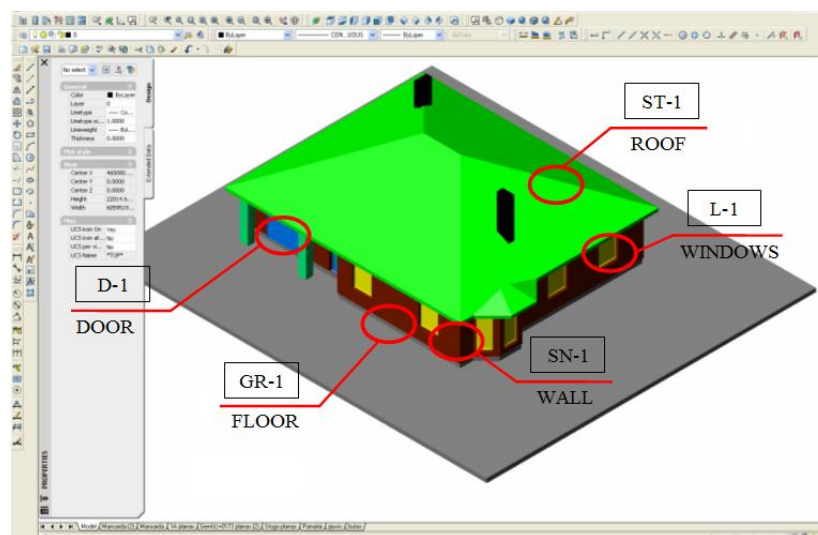
Fig. 1. Typical design of single family residential building superstructure

Specific calculations and structured decision-making matrix for typical walls and floors construction are performed for separate Lithuanian cities. Two multi-criteria analysis methods – complex proportional assessment and degree of utility and market valuation – will be examined further.

2. Newly constructed single-family residential building standard design (floors, walls) analysis based on multi-criteria complex proportional evaluation method

Prioritizing and significance of options of multi-criteria complex proportional evaluation method directly and in proportion depends on system of criteria describing alternatives, the criteria meanings and values of significances. Experts assess the system of criteria and compute the criteria meanings and original significances.

The prioritizing and significance of examining alternatives is calculated in four steps [2, 3].

Step 1. The rated normalized decision matrix D is formed. The purpose of this step is to find the normalized and assessed dimensions. Then it is possible to compare all different indicators of measurement units. In the following formula is applied:

$$d_{ij} = \frac{x_{ij} \cdot q_i}{\sum\limits_{j=1}^{n} x_{ij}} \qquad (1)$$

where: $i = \overline{1, m}$; $j = \overline{1, n}$; $x_{ij} - i$ is meaning of criteria in j version of the decision; m is the number of criteria; n is the number of comparative versions; q_i is the significance of criteria.

For example:

$$d_{11} = \frac{0.321\times \ldots}{191.74 + 201.42 + 188.56 + 167.34 + 168.90 + 174.67 + 163.51 + 147.92 +}$$

$$\ldots \frac{\times 191.74}{+ 161.51 + 134.52 + 156.01 + 147.86 + 163.17 + 153.83 + 160.44 + 145.58} = 0.0234$$

$$d_{12} = \frac{0.321\times \ldots}{191.74 + 201.42 + 188.56 + 167.34 + 168.90 + 174.67 + 163.51 + 147.92 +}$$

$$\ldots \frac{\times 201.42}{+ 161.51 + 134.52 + 156.01 + 147.86 + 163.17 + 153.83 + 160.44 + 145.58} = 0.0246$$

$$d_{21} = \frac{0.116 \cdot 5.25}{5.25 + 5.44 + 5.43 + 5.01 + 5.02 + 5.15 + 5.16 + 4.72 + 4.19 + 3.79 + 4.19 + 4.19 + 4.04 + 4.04 + 4.15 + 4.04} = 0.00831$$

and etc.

The sum of non dimensional meanings d_{ij} of every criteria x is always equal to the significance of this criteria q_i:

$$q_i = \sum\limits_{j=1}^{n} d_{ij} \qquad (2)$$

The meaning of the significance of criteria q_i apportioned to all alternatives versions a_j, according to their meanings x_{ij}.

For example:

$$q_1 = 0.0234 + 0.0246 + 0.0230 + 0.0204 + 0.0206 + 0.0213 + 0.0200 + 0.0181 +$$
$$+ 0.0197 + 0.0164 + 0.0191 + 0.0181 + 0.0199 + 0.0188 + 0.0196 + 0.0178 = 0.3210$$

$$q_2 = 0.0083 + 0.0085 + 0.0085 + 0.0079 + 0.0079 + 0.0081 + 0.0081 + 0.0074 +$$
$$+ 0.0066 + 0.0060 + 0.0066 + 0.0066 + 0.0063 + 0.0063 + 0.0065 + 0.0063 = 0.1160$$

$$q_3 = 0.0067 + 0.0067 + 0.0067 + 0.0067 + 0.0067 + 0.0067 + 0.0067 + 0.0067 +$$
$$+ 0.0064 + 0.0064 + 0.0064 + 0.0064 + 0.0074 + 0.0074 + 0.0074 + 0.0074 = 0.1090$$

and etc.

Step 2. The amounts of normalized minimizated S_{-j} and maximinazed S_{+j} indicators describing version j is computed. They are calculated according to the formula:

$$S_{+j} = \sum\limits_{i=1}^{m} d_{+ij} \qquad \text{and} \qquad S_{-j} = \sum\limits_{i=1}^{m} d_{-ij} \qquad (3)$$

The dimensions S_{+j} and S_{-j} expresses the level of purposes that achieve interested groups in every alternative wall unit.

For example:

$$S_{+1} = 0.0076 + 0.0005 + 0.0023 + 0.0034 = 0.0138$$

$$S_{+2} = 0.0077 + 0.0012 + 0.0023 + 0.0034 = 0.0147$$

$$S_{-1} = 0.0234 + 0.0083 + 0.0067 + 0.0027 + 0.0016 + 0.0007 + 0.0128 + 0.0005 + 0.0004 + 0.0006 = 0.0576$$

and etc.

The amounts of all alternative "pluses" S_{+j} and "minuses" S_{-j} of wall unit are always accordingly equal to all amounts of minimizated and maximinazed criteria significances in any case:

$$S_+ = \sum_{j=1}^{n} S_{+j} = \sum_{i=1}^{m} \sum_{j=1}^{n} d_{+ij} \quad \text{and} \quad S_- = \sum_{j=1}^{n} S_{-j} = \sum_{i=1}^{m} \sum_{j=1}^{n} d_{-ij} \tag{4}$$

So it is possible to verify the correctness of calculations again.
For example:

$$S_+ = 0.0138 + 0.0147 + 0.0130 + 0.0108 + 0.0138 + 0.0147 + 0.0130 + 0.0108 +$$
$$+ 0.0138 + 0.0147 + 0.0130 + 0.0108 + 0.0138 + 0.0147 + 0.0130 + 0.0108 = 0.2090$$

$$S_- = 0.0576 + 0.0532 + 0.0558 + 0.466 + 0.0546 + 0.0497 + 0.0525 + 0.0439 +$$
$$+ 0.0511 + 0.0413 + 0.0487 + 0.0419 + 0.0532 + 0.0462 + 0.0513 + 0.0433 = 0.7910$$

and etc.

Step 3. The relative significance (efficiency) of comparative versions is assessed on the basis of positive "pluses" S_{+j} and negative "minuses" S_{-j} features describing them. The relative significance (efficiency) Q_j of every wall unit a_j is assessed according to the formula:

$$Q_j = S_{+j} + \frac{S_{-min} \sum_{j=1}^{n} S_{-j}}{S_{-j} \sum_{j=1}^{n} \frac{S_{-min}}{S_{-j}}} \tag{5}$$

For example:

$$Q_1 = 0.0138 + \frac{0.0413(0.0576 + 0.0532 + 0.0558 + 0.0466 + 0.0546 + 0.0497 + 0.0525 + 0.0439 + \cdots}{0.0576\left(\dfrac{0.0413}{0.0576} + \dfrac{0.0413}{0.0532} + \dfrac{0.0413}{0.05558} + \dfrac{0.0413}{0.0466} + \dfrac{0.0413}{0.0546} + \dfrac{0.0413}{0.0497} + \dfrac{0.0413}{0.0525} + \dfrac{0.0413}{0.0439} + \right.}$$

$$\cdots \frac{+ 0.0511 + 0.0413 + 0.0487 + 0.0419 + 0.0532 + 0.0462 + 0.0513 + 0.0433)}{\left. + \dfrac{0.0413}{0.0511} + \dfrac{0.0413}{0.0413} + \dfrac{0.0413}{0.0487} + \dfrac{0.0413}{0.0419} + \dfrac{0.0413}{0.0532} + \dfrac{0.0413}{0.0462} + \dfrac{0.0413}{0.0513} + \dfrac{0.0413}{0.0433} \right)} = 0.0558$$

$$Q_2 = 0.0147 + \frac{0.0413 \cdot 0.7910}{0.0532 \cdot 13.5092} = 0.0601$$

and etc.

Step 4. The prioritizing of the wall unit is assessed. The greater Q_j, the greater efficiency of the wall unit.

We can conclude that according to the method described previously it is simple to assess and after that to select the most rational walls. Moreover generalized (reduced) criteria Q_j, formed according to the method, directly and proportionally depends on the relative influence of comparable criteria meanings x_{ij} and significances q_i.

Table 1

The results of multi-criteria analysis of wall constructions commercial offers

The quantitative information describing commercial offers									
Examined criteria	*	Significance	Measurement units	Examined commercial offers					
				1	2	...	j	...	n
X_1	$\check{z}_1$	q_1	m_1	d_{11}	d_{12}	...	d_{1j}	...	d_{1n}
X_2	$\check{z}_2$	q_2	m_2	d_{21}	d_{22}	...	d_{2j}	...	d_{2n}
X_3	$\check{z}_3$	q_3	m_3	d_{31}	d_{32}	...	d_{3j}	...	d_{3n}
...	...	...	...	...	...	...	...	...	...
X_i	$\check{z}_i$	q_i	m_i	d_{i1}	d_{i2}	...	d_{ij}	...	d_{in}
...	...	...	...	...	...	...	...	...	...
X_m	$\check{z}_m$	q_m	m_m	d_{m1}	d_{m2}	...	d_{mj}	...	d_{mn}
The sum S_{+j} of maximinized normalized rating indicators				S_{+1}	S_{+2}	...	S_{+j}	...	S_{+n}
The sum S_{-j} of minimized normalized rating indicators				S_{-1}	S_{-2}	...	S_{-j}	...	S_{-n}
The significance of alternative of commercial offers				Q_1	Q_2	...	Q_j	...	Q_n
The prioritization of alternative of commercial offers				P_1	P_2	...	P_j	...	P_n

* – the sign + (−) shows that accordingly the greater (lower) meaning of criteria more corresponds the requirements of customer.

Table 2

The results of multi-criteria analysis of typical floor structures

Nr.	Examined criteria	The measurement units of criteria	*	The significance of criteria	GR-1	GR-2	GR-3	GR-4	GR-5	GR-6	GR-7	GR-8	GR-9	GR-10	GR-11	GR-12
1	Topcoat's resistance to wear, scratching	class	+	0.0436	0.0022	0.0016	0.0005	0.0016	0.0022	0.0027	0.0022	0.0016	0.0005	0.0016	0.0022	0.0027
2	The performance of topcoat	scores	+	0.0340	0.0014	0.0013	0.0016	0.0013	0.0013	0.0016	0.0014	0.0013	0.0016	0.0013	0.0013	0.0016
3	Healthiness	scores	+	0.0900	0.0036	0.0040	0.0032	0.0040	0.0040	0.0036	0.0036	0.0040	0.0032	0.0040	0.0040	0.0036
4	Aestheticity	scores	+	0.0450	0.0017	0.0019	0.0017	0.0021	0.0021	0.0019	0.0017	0.0019	0.0017	0.0021	0.0021	0.0019
5	Resistivity of topcoat's deck	$m^2 K/W$	+	0.0032	0.0001	0.0001	0.0002	0.0002	0.0003	0.0001	0.0000	0.0001	0.0001	0.0001	0.0003	0.0000
6	Thermal transmis. coeff. of thermal insulation	$W/m^2 K$	–	0.1960	0.0086	0.0086	0.0086	0.0086	0.0086	0.0086	0.0080	0.0080	0.0080	0.0080	0.0080	0.0080
7	The thickness of thermal insulation	m	–	0.0014	0.0001	0.0001	0.0001	0.0001	0.0001	0.0001	0.0001	0.0001	0.0001	0.0001	0.0000	0.0001
8	Long-term water absorption, (W_{lp})	%	–	0.0072	0.0006	0.0006	0.0006	0.0006	0.0006	0.0006	0.0001	0.0001	0.0001	0.0001	0.0001	0.0001
9	Flammability classification	Euroclass	–	0.0130	0.0002	0.0002	0.0002	0.0002	0.0002	0.0002	0.0007	0.0007	0.0007	0.0007	0.0007	0.0007
10	The compressive strength, (σ_m)	kPa	+	0.0015	0.0000	0.0000	0.0000	0.0000	0.0000	0.0000	0.0001	0.0001	0.0001	0.0001	0.0001	0.0001
11	Density	kg/m^3	+	0.0060	0.0005	0.0005	0.0005	0.0005	0.0005	0.0005	0.0001	0.0001	0.0001	0.0001	0.0001	0.0001
12	Junction resistivity	$m^2 K/W$	+	0.0180	0.0008	0.0008	0.0008	0.0008	0.0008	0.0008	0.0008	0.0008	0.0008	0.0008	0.0008	0.0008
13	Junction 1 m^2 price	LT/m^2	–	0.3115	0.0101	0.0131	0.0108	0.0126	0.0132	0.0138	0.0099	0.0129	0.0106	0.0124	0.0130	0.0137
14	1 m^2 installation time	human hour	–	0.1976	0.0063	0.0059	0.0067	0.0085	0.0086	0.0116	0.0063	0.0059	0.0067	0.0085	0.0086	0.0116
15	Calc. thermal trans-mission coeff. of floor on ground, U_{fg}	$w/(m^2 K)$	–	0.0050	0.0002	0.0002	0.0002	0.0002	0.0002	0.0002	0.0002	0.0002	0.0002	0.0002	0.0002	0.0002
16	Internal specific heat loss, H_{pi}	W/K	–	0.0050	0.0002	0.0002	0.0002	0.0002	0.0002	0.0002	0.0002	0.0002	0.0002	0.0002	0.0002	0.0002
17	External specific heat loss, H_{pe}	W/K	–	0.0050	0.0002	0.0002	0.0002	0.0002	0.0002	0.0002	0.0002	0.0002	0.0002	0.0002	0.0002	0.0002
18	Calc. heat flow average, Φ_{fg}	W	–	0.0050	0.0002	0.0002	0.0002	0.0002	0.0002	0.0002	0.0002	0.0002	0.0002	0.0002	0.0002	0.0002
19	Calc. loss through the floor, Q_{fg}	$\dfrac{kWh}{m^2 \cdot years}$	–	0.0050	0.0002	0.0002	0.0002	0.0002	0.0002	0.0002	0.0002	0.0002	0.0002	0.0002	0.0002	0.0002
20	Totals included financial losses through the floor	$\dfrac{Lt}{m^2 \cdot years}$	–	0.0070	0.0003	0.0003	0.0003	0.0003	0.0003	0.0003	0.0003	0.0003	0.0003	0.0003	0.0003	0.0003
	The sum of maximizing normalized evaluations indicators, S_{+j}				0.0103	0.0102	0.0085	0.0105	0.0112	0.0112	0.0099	0.0099	0.0081	0.0101	0.0109	0.0108
	The sum of minimizing normalized evaluations indicators, S_{+j}				0.0272	0.0298	0.0283	0.0319	0.0326	0.0362	0.0264	0.029	0.0275	0.0311	0.0317	0.0355
	The significance of commercial offer, Q_j				0.0465	0.0433	0.0433	0.0414	0.0414	0.0384	0.0472	0.0439	0.044	0.0418	0.042	0.0386
	The efficiency degree of commercial offer, N_j				99%	92%	92%	88%	88%	81%	100%	93%	93%	89%	89%	82%
	The priority of commercial offers				2	6	7	13	14	21	1	5	4	12	11	20
	Price of construction, Lt/m^2				128.66	167.01	137.48	160.36	169.12	176.82	126.23	164.61	135.12	158.00	166.30	174.38
	Comparative price, Lt/m^2				128.66	167.01	137.48	159.66	168.38	163.14	126.23	164.61	135.12	158.00	166.30	162.70

Nr.	Examined criteria	The measurement units of criteria	*	The significance of criteria	GR-13	GR-14	GR-15	GR-16	GR-17	GR-18	GR-19	GR-20	GR-21	GR-22	GR-23	GR-24
1	Topcoat's resistance to wear, scratching	class	+	0.0436	0.0022	0.0016	0.0005	0.0016	0.0022	0.0027	0.0022	0.0016	0.0005	0.0016	0.0022	0.0027
2	The performance of topcoat	scores	+	0.0340	0.0014	0.0013	0.0016	0.0013	0.0013	0.0016	0.0014	0.0013	0.0016	0.0013	0.0013	0.0016
3	Healthiness	scores	+	0.0900	0.0036	0.0040	0.0032	0.0040	0.0040	0.0036	0.0036	0.0040	0.0032	0.0040	0.0040	0.0036

Nr.	Examined criteria	The measurement units of criteria	*	The significance of criteria	GR-13	GR-14	GR-15	GR-16	GR-17	GR-18	GR-19	GR-20	GR-21	GR-22	GR-23	GR-24
4	Aestheticity	scores	+	0.0450	0.0017	0.0019	0.0017	0.0021	0.0021	0.0019	0.0017	0.0019	0.0017	0.0021	0.0021	0.0019
5	Resistivity of topcoat's deck	m²K/W	+	0.0032	0.0001	0.0001	0.0002	0.0002	0.0003	0.0001	0.0000	0.0001	0.0001	0.0001	0.0003	0.0000
6	Thermal transmis. coeff. of thermal insulation	W/m²K	–	0.1960	0.0086	0.0086	0.0086	0.0086	0.0086	0.0086	0.0074	0.0074	0.0074	0.0074	0.0074	0.0074
7	The thickness of thermal insulation	m	–	0.0014	0.0001	0.0001	0.0001	0.0001	0.0001	0.0001	0.0000	0.0000	0.0000	0.0000	0.0000	0.0000
8	Long-term water absorption, (W_{lp})	%	–	0.0072	0.0005	0.0005	0.0005	0.0005	0.0005	0.0005	0.0000	0.0000	0.0000	0.0000	0.0000	0.0000
9	Flammability classification	Euroclass	–	0.0130	0.0005	0.0005	0.0005	0.0005	0.0005	0.0005	0.0007	0.0007	0.0007	0.0007	0.0007	0.0007
10	The compressive strength, (σ_m)	kPa	+	0.0015	0.0000	0.0000	0.0000	0.0000	0.0000	0.0000	0.0000	0.0002	0.0002	0.0002	0.0002	0.0002
11	Density	kg/m³	+	0.0060	0.0002	0.0002	0.0002	0.0002	0.0002	0.0002	0.0002	0.0002	0.0002	0.0002	0.0002	0.0002
12	Junction resistivity	m²K/W	+	0.0180	0.0008	0.0008	0.0008	0.0008	0.0008	0.0008	0.0008	0.0008	0.0008	0.0008	0.0008	0.0008
13	Junction 1 m² price	LT/m²	–	0.3115	0.0115	0.0145	0.0127	0.0144	0.0130	0.0157	0.0119	0.0148	0.0125	0.0143	0.0147	0.0156
14	1 m² installation time	human hour	–	0.1976	0.0074	0.0070	0.0082	0.0099	0.0100	0.0122	0.0063	0.0059	0.0067	0.0085	0.0086	0.0116
15	Calc. thermal transmission coeff. of floor on ground, U_{fg}	w/(m²K)	–	0.0050	0.0002	0.0002	0.0002	0.0002	0.0002	0.0002	0.0002	0.0002	0.0002	0.0002	0.0002	0.0002
16	Internal specific heat loss, H_{pi}	W/K	–	0.0050	0.0002	0.0002	0.0002	0.0002	0.0002	0.0002	0.0002	0.0002	0.0002	0.0002	0.0002	0.0002
17	External specific heat loss, H_{pe}	W/K	–	0.0050	0.0002	0.0002	0.0002	0.0002	0.0002	0.0002	0.0002	0.0002	0.0002	0.0002	0.0002	0.0002
18	Calc. heat flow average, Φ_{fg}	W	–	0.0050	0.0002	0.0002	0.0002	0.0002	0.0002	0.0002	0.0002	0.0002	0.0002	0.0002	0.0002	0.0002
19	Calc. loss through the floor, Q_{fg}	$\frac{kWh}{m^2 \cdot years}$	–	0.0050	0.0002	0.0002	0.0002	0.0002	0.0002	0.0002	0.0002	0.0002	0.0002	0.0002	0.0002	0.0002
20	Totals included financial losses through the floor	$\frac{Lt}{m^2 \cdot years}$	–	0.0070	0.0003	0.0003	0.0003	0.0003	0.0003	0.0003	0.0003	0.0003	0.0003	0.0003	0.0003	0.0003
	The sum of maximizing normalized evaluations indicators, S_{+j}				0.01	0.0099	0.0082	0.0102	0.0109	0.0109	0.0099	0.0101	0.0083	0.0103	0.0111	0.011
	The sum of minimizing normalized evaluations indicators, S_{+j}				0.0299	0.0325	0.0319	0.0353	0.034	0.0389	0.0276	0.0301	0.0286	0.0322	0.0327	0.0366
	The significance of commercial offer, Q_j				0.043	0.0402	0.0391	0.0381	0.0399	0.0362	0.0456	0.0429	0.0428	0.0409	0.0413	0.0379
	The efficiency degree of commercial offer, N_j				91%	85%	83%	81%	85%	77%	97%	91%	91%	87%	88%	80%
	The priority of commercial offers				8	17	19	22	18	24	3	9	10	16	15	23
	Price of construction, Lt/m²				146.84	185.24	161.59	184.47	166.01	200.49	151.47	189.38	159.23	182.11	187.81	199.62
	Comparative price, Lt/m²				146.84	178.64	152.46	170.19	160.09	159.49	151.47	189.38	159.23	179.42	186.99	182.09

Table 3

The results of multi-criteria analysis of typical walls structures

Nr.	Examined criteria	The measurement units of criteria	*	The significance of criteria	SN-1	SN-2	SN-3	SN-4	SN-5	SN-6	SN-7	SN-8
1	Price	Lt/m²	–	0.3210	0.0232	0.0243	0.0228	0.0202	0.0204	0.0211	0.0198	0.0179
2	Installation time	human, hour	–	0.1160	0.0083	0.0085	0.0085	0.0079	0.0079	0.0081	0.0081	0.0074
3	Thermal transmission coefficient of thermal insulation	W/m²K	–	0.1090	0.0067	0.0067	0.0067	0.0067	0.0067	0.0067	0.0067	0.0067
4	The thickness of thermal insulation	m	–	0.0430	0.0028	0.0031	0.0030	0.0023	0.0030	0.0031	0.0031	0.0025
5	Thermal transmission coefficient of masonry blocks	W/m²K	–	0.0390	0.0016	0.0047	0.0029	0.0010	0.0016	0.0029	0.0029	0.0010

Continuation of Table 3

Nr.	Examined criteria	The measurement units of criteria	*	The significance of criteria	SN-1	SN-2	SN-3	SN-4	SN-5	SN-6	SN-7	SN-8
6	Block thickness	m	–	0.0100	0.0006	0.0006	0.0006	0.0006	0.0006	0.0006	0.0006	0.0006
7	Parameter R_w of sound isolation Block sound	dB	+	0.1150	0.0076	0.0078	0.0075	0.0060	0.0076	0.0075	0.0075	0.0060
8	Healthiness	scores	–	0.1280	0.0122	0.0030	0.0091	0.0061	0.0122	0.0091	0.0091	0.0061
9	The compressive strength of masonry blocks	MPa	+	0.0110	0.0005	0.0012	0.0009	0.0002	0.0005	0.0009	0.0009	0.0002
10	Block resistance to cold	cycles	+	0.0280	0.0024	0.0024	0.0012	0.0012	0.0024	0.0012	0.0012	0.0012
11	Weight of block	kg/m²	–	0.0090	0.0005	0.0010	0.0006	0.0003	0.0005	0.0006	0.0006	0.0003
12	Junction resistivity	m²K/W	+	0.0550	0.0034	0.0034	0.0034	0.0034	0.0034	0.0034	0.0034	0.0034
13	Calc. loss through the walls, Q_w	$\frac{kWh}{m^2 \cdot years}$	–	0.0070	0.0004	0.0004	0.0004	0.0004	0.0004	0.0004	0.0004	0.0004
14	Totals included financial losses through the walls	$\frac{Lt}{m^2 \cdot years}$	–	0.0090	0.0006	0.0006	0.0006	0.0006	0.0006	0.0006	0.0006	0.0006
The sum of maximizing normalized evaluations indicators, S_{+j}					0.0139	0.0148	0.013	0.0108	0.0139	0.013	0.013	0.0108
The sum of minimizing normalized evaluations indicators, S_{+j}					0.0569	0.0529	0.0552	0.0461	0.0539	0.0532	0.0519	0.0435
The significance of commercial offer, Q_j					0.0563	0.0604	0.0567	0.0632	0.0587	0.0584	0.0595	0.0663
The efficiency degree of commercial offer, N_j					77%	83%	77%	86%	80%	80%	81%	91%
The priority of commercial offers					16	9	15	6	12	14	11	5
Price of construction, Lt/m²					191.74	201.42	188.56	167.34	168.90	174.67	163.51	147.92
Comparative price, Lt/m²					174.87	196.59	171.97	167.34	159.44	164.89	156.10	147.92

Nr.	Examined criteria	The measurement units of criteria	*	The significance of criteria	SN-9	SN-10	SN-11	SN-12	SN-13	SN-14	SN-15	SN-16
1	Price	Lt/m²	–	0.3210	0.0231	0.0163	0.0188	0.0179	0.0197	0.0186	0.0194	0.0176
2	Installation time	human, hour	–	0.1160	0.0066	0.0060	0.0066	0.0066	0.0063	0.0063	0.0065	0.0063
3	Thermal transmission coefficient of thermal insulation	W/m²K	–	0.1090	0.0064	0.0064	0.0064	0.0064	0.0074	0.0074	0.0074	0.0074
4	The thickness of thermal insulation	m	–	0.0430	0.0020	0.0023	0.0021	0.0015	0.0030	0.0035	0.0033	0.0025
5	Thermal transmission coefficient of masonry blocks	W/m²K	–	0.0390	0.0016	0.0047	0.0029	0.0010	0.0016	0.0047	0.0029	0.0010
6	Block thickness	m	–	0.0100	0.0006	0.0006	0.0006	0.0006	0.0006	0.0006	0.0006	0.0006
7	Parameter R_w of sound isolation Block sound	dB	+	0.1150	0.0076	0.0078	0.0075	0.0060	0.0076	0.0078	0.0075	0.0060
8	Healthiness	scores	–	0.1280	0.0122	0.0030	0.0091	0.0061	0.0122	0.0030	0.0091	0.0061
9	The compressive strength of masonry blocks	MPa	+	0.0110	0.0005	0.0012	0.0009	0.0002	0.0005	0.0012	0.0009	0.0002
10	Block resistance to cold	cycles	+	0.0280	0.0024	0.0024	0.0012	0.0012	0.0024	0.0024	0.0012	0.0012
11	Weight of block	kg/m²	–	0.0090	0.0005	0.0010	0.0006	0.0003	0.0005	0.0010	0.0006	0.0003
12	Junction resistivity	m²K/W	+	0.0550	0.0034	0.0034	0.0034	0.0034	0.0034	0.0034	0.0034	0.0034
13	Calc. loss through the walls, Q_w	$\frac{kWh}{m^2 \cdot years}$	–	0.0070	0.0004	0.0004	0.0004	0.0004	0.0004	0.0004	0.0004	0.0004
14	Totals included financial losses through the walls	$\frac{Lt}{m^2 \cdot years}$	–	0.0090	0.0006	0.0006	0.0006	0.0006	0.0006	0.0006	0.0006	0.0006
The sum of maximizing normalized evaluations indicators, S_{+j}					0.0139	0.0148	0.013	0.0108	0.0139	0.0148	0.013	0.0108
The sum of minimizing normalized evaluations indicators, S_{+j}					0.054	0.0413	0.0481	0.0414	0.0523	0.0461	0.0508	0.0428
The significance of commercial offer, Q_j					0.0586	0.0732	0.0632	0.0691	0.0601	0.0672	0.0605	0.0672
The efficiency degree of commercial offer, N_j					80%	100%	86%	94%	82%	92%	83%	92%
The priority of commercial offers					13	1	7	2	10	3	8	4
Price of construction, Lt/m²					191.51	134.52	156.01	147.86	163.17	153.83	160.44	145.58
Comparative price, Lt/m²					180.79	134.52	156.01	147.86	157.51	153.83	156.59	145.58

3. The multi-criteria market value and efficiency level of comercial offers for installation of tipical construction identification method

According the methods of multi-criteria analysis the commercial offers rate considering the prices of sold comparative constructional details commercial offers, market, quantitative and qualitative factors of examined commercial offers. To describe quantitatively the examined commercial offers, according mentioned factors, the system of criteria is formed and meanings of criteria and significances are calculated. According to formed system of criteria and meanings of criteria and significances is determined the market value of the measured object.

The significance Q_j of commercial offer a_j shows the level of purposes and needs which achieved interested groups. Always the significance Q_{max} of the most effective commercial offer will be largest. The significances of all others commercial offers are smaller than už Q_{max}. However practically not the significance and prioritization of commercial offers more interest customers, but what is the utility of commercial offers degree and what is the result to their market value. In other words the commercial offer, which best meet their needs and objectives at least cost and the least violate other interested groups needs and goals, customers interest most. A commercial offer utility degree and market value terms are used to express the assessment results.

In order to accurately assess the commercial offers good and bad qualities, to compare them with the interested groups needs and objectives and to match all this with prices, it is necessary to determine the level of usefulness of commercial offers and evaluative commercial offer market value. It goes without saying that, for example, construction from materials of very good quality indicators and which has good performance, and good other features can be costly.

The level of efficiency of commercial offers depends directly on the system of criteria, meanings and significances. If under one commercial offer the best price is secured, under another – best performance, and the same significance after the multi-criteria assessment is received, then issue commercial offers performance degrees are the same. If the significance of commercial offer is increasing (decreasing), then the efficiency of commercial offer is increasing (decreasing) too. The level of efficiency of commercial offer is compared with the most rational offer. In this case, all obtaining the commercial offers performance degrees will be from 0 (worst option) till 100% (best option). It will be easier to visually assess the performance of commercial offers.

In order to determine which price of evaluative commercial offer it will be equally competitive in the market, comprehensive assessment of the commercial offers all the positive and negative characteristics, it has been proposed the multi-criteria commercial offers utility degree and market value method.

The performance degrees of the commercial offers and the evaluative commercial offer's market value shall be determined in seven steps [2, 3].

Step 1. Quotation a_j utility grade N_j is determined by the following formula:

$$N_j = (Q_j : Q_{max}) \cdot 100\% \tag{6}$$

here Q_j and Q_{max} – units significances, determined by the formula.

For example, the degree of efficiency of wall installation commercial offers is calculated as follows:

$$N_1 = (Q_1 : Q_{max}) \cdot 100\% = (0.0601 : 0.0732) \cdot 100\% = 82\%$$

$$N_2 = (Q_2 : Q_{max}) \cdot 100\% = (0.0563 : 0.0732) \cdot 100\% = 77\%, \text{ etc.}$$

The degree of efficiency N_j of commercial offers a_j expresses the level of achievement of the objectives of interested groups of this commercial offer. It is more and more significant the objectives achieved, the greater the degree of efficiency of the quotation.

With reference to the quotation can be set up and based on the degree of utility of the assessee's quotation of market value.

Step 2. The degree of effectiveness E_{ji} of the amount of money invested in the commercial offer a_j is calculated. It shows how many percent better (worse) to invest the money to the commercial offer a_j, compared with the commercial offer a_i. The E_{ji} is determined by comparing the performance of the commercial offers degrees:

$$E_{ji} = N_j - N_i \tag{7}$$

For example, the degree of efficiency of wall installation commercial offers is calculated as follows:

$$E_{11} = N_1 - N_1 = 82.094 - 82.094 = 0.000$$

$$E_{12} = N_1 - N_2 = 82.094 - 76.937 = -5.863, \text{ etc.}$$

The results obtained are presented in the form of the matrix, which shows differences in the performance of commercial proposals. The floor and wall constructions are examined further (Tables 6-8).

Step 3. The average deviation k_j of the degree of efficiency N_j of commercial offer a_j is calculated, in relation to the others $(n - 1)$ commercial offers:

$$k_x = \sum_{i=1}^{n} E_{ji} : (n-1) \tag{8}$$

Table 4

The calculation of the average deviation of utility-grade of design and value of the proposed

The number of alternative	The difference of utility of examined options compared to the others, %					The average deviation k_x of the degree of efficiency N_x of alternative a_x, %	The value of the proposed alternative
1	0	E_{12}	E_{13}	...	E_{1m}	k_1	V_1
2	E_{21}	0	E_{23}	...	E_{2m}	k_2	V_2
3	E_{31}	E_{32}	0	...	E_{3m}	k_3	V_3
...	...	...	...	...	...	...	...
j	E_{j1}	E_{j2}	E_{j3}	...	E_{jm}	k_j	V_j
...	...	...	...	...	...	...	...
n	E_{n1}	E_{n2}	E_{n3}	...	0	k_n	V_n

Table 5

The calculation of the average deviation of utility-grade of walls design and value of the proposed

The number of alternative	The difference of utility of examined options compared to the others, %						The current price, Lt/m²	The average deviation k_x of the degree of efficiency N_x of alternative a_x, % The value of the alternative, Lt/m²	The difference from alternative	Lt/m²
	1	2	3	4	...	m				
1	0	E_{12}	E_{13}	E_{14}	...	E_{1m}	191.74	-9.747	173.05	-18.69
2	E_{21}	0	E_{23}	E_{24}	...	E_{2m}	201.42	-3.493	194.39	-7.04
3	E_{31}	E_{32}	0	E_{34}	...	E_{3m}	188.56	-8.994	171.60	-16.96
4	E_{41}	E_{42}	E_{43}	0	...	E_{4m}	167.34	0.302	167.84	0.51
5	E_{51}	E_{52}	E_{53}	E_{54}	...	E_{5m}	168.90	-6.364	158.15	-10.75
6	E_{61}	E_{62}	E_{63}	E_{64}	...	E_{6m}	174.67	1.268	176.88	2.21
7	E_{71}	E_{72}	E_{73}	E_{74}	...	E_{7m}	163.51	-4.972	155.38	-8.13
8	E_{81}	E_{82}	E_{83}	E_{84}	...	E_{8m}	147.92	4.985	155.29	7.37
9	E_{91}	E_{92}	E_{93}	E_{94}	...	E_{9m}	161.51	-1.996	158.29	-3.22
10	E_{101}	E_{102}	E_{103}	E_{104}	...	E_{10m}	134.52	15.607	155.52	51.00
11	E_{111}	E_{112}	E_{113}	E_{114}	...	E_{11m}	156.01	0.161	156.26	0.25
12	E_{121}	E_{122}	E_{123}	E_{124}	...	E_{12m}	147.56	8.892	161.01	13.15
13	E_{131}	E_{132}	E_{133}	E_{134}	...	E_{13m}	163.17	-4.659	155.56	-7.60
14	E_{141}	E_{142}	E_{143}	E_{144}	...	E_{14m}	153.83	6.522	163.86	10.03
15	E_{151}	E_{152}	E_{153}	E_{154}	...	E_{15m}	160.44	-3.521	154.80	-5.65
16	E_{161}	E_{162}	E_{163}	E_{164}	...	0	145.58	6.009	154.33	8.75

Table 6

The calculation of the average deviation of utility-grade of ground design and value of the proposed

The number of alternative	The difference of utility of examined options compared to the others, %						The current price, Lt/m²	The average deviation k_x of the degree of efficiency N_x of alternative a_x, % The value of the alternative, Lt/m²	The difference from alternative	Lt/m²
	1	2	3	4	...	m				
1	0	E_{12}	E_{13}	E_{14}	...	E_{1m}	128.66	10.530	142.21	13.55
2	E_{21}	0	E_{23}	E_{24}	...	E_{2m}	167.01	3.393	172.68	5.67
3	E_{31}	E_{32}	0	E_{34}	...	E_{3m}	137.48	3.457	142.23	4.75
4	E_{41}	E_{42}	E_{43}	0	...	E_{4m}	160.36	-0.704	159.23	-1.13
5	E_{51}	E_{52}	E_{53}	E_{54}	...	E_{5m}	169.12	-0.854	167.68	-1.44
6	E_{61}	E_{62}	E_{63}	E_{64}	...	E_{6m}	176.82	-7.454	163.64	-13.18
7	E_{71}	E_{72}	E_{73}	E_{74}	...	E_{7m}	126.23	12.291	141.74	15.51
8	E_{81}	E_{82}	E_{83}	E_{84}	...	E_{8m}	164.61	4.676	172.31	7.70
9	E_{91}	E_{92}	E_{93}	E_{94}	...	E_{9m}	135.12	4.985	141.86	6.74
10	E_{101}	E_{102}	E_{103}	E_{104}	...	E_{10m}	158.00	0.281	158.44	0.44
11	E_{111}	E_{112}	E_{113}	E_{114}	...	E_{11m}	166.30	0.282	166.77	0.47
12	E_{121}	E_{122}	E_{123}	E_{124}	...	E_{12m}	174.38	-6.920	162.31	-12.07
13	E_{131}	E_{132}	E_{133}	E_{134}	...	E_{13m}	146.84	3.099	151.39	4.55
14	E_{141}	E_{142}	E_{143}	E_{144}	...	E_{14m}	185.24	-2.943	179.79	-5.45
15	E_{151}	E_{152}	E_{153}	E_{154}	...	E_{15m}	161.59	-5.319	152.99	-8.59
16	E_{161}	E_{162}	E_{163}	E_{164}	...	E_{16m}	184.47	-7.838	170.01	-14.46
17	E_{171}	E_{172}	E_{173}	E_{174}	...	E_{17m}	166.01	-0.611	165.00	-1.01
18	E_{181}	E_{182}	E_{183}	E_{184}	...	E_{18m}	200.49	-11.95	176.54	-23.95
19	E_{191}	E_{192}	E_{193}	E_{194}	...	E_{19m}	151.47	8.609	164.51	13.04

Continuation of Table 6

The number of alternative	The difference of utility of examined options compared to the others, %						The current price, Lt/m²	The average deviation k_x of the degree of efficiency N_x of alternative a_x, %	The difference from alternative	Lt/m²
	1	2	3	4	…	m		The value of the alternative, Lt/m²		
20	E_{201}	E_{202}	E_{203}	E_{204}	…	E_{20m}	189.38	2.165	193.48	4.10
21	E_{211}	E_{212}	E_{213}	E_{214}	…	E_{21m}	159.23	2.275	162.85	3.62
22	E_{221}	E_{222}	E_{223}	E_{224}	…	E_{22m}	182.11	-1.741	178.94	-3.17
23	E_{231}	E_{232}	E_{233}	E_{234}	…	E_{23m}	187.81	-1.216	185.53	-2.28
24	E_{241}	E_{242}	E_{243}	E_{244}	…	0	199.62	-8.495	182.66	-16.96

For example, the average deviation of commercial offer of walls constructions:

$$k_1 = \frac{\sum_{i=1}^{n} E_{1i}}{(16-1)} = \frac{-146.204}{15} = -9.747$$

$$k_2 = \frac{\sum_{i=1}^{n} E_{2i}}{(16-1)} = \frac{-52.392}{15} = -3.493$$

$$k_3 = \frac{\sum_{i=1}^{n} E_{3i}}{(16-1)} = \frac{-134.911}{15} = -8.994, \text{ etc.}$$

Step 4. The preparation of the decision making matrix grouped by multi-criteria analyses of commercial offers for installation of typical constructions. The market value of evaluated commercial offer is calculated on the basis of the aggregated block diagram, which is shown in Fig. 2.

A grouped decision making matrix is formed at first (Table 9), in which the assessment of the comparative prices of commercial offers and commercial value of the proposal is first criteria. You need to set the market value $(X_{11} - X_R)$ of evaluated commercial offer a_1 in this matrix. Other comparative commercial offers $(a_2 - a_n)$ were chosen by customer and their prices jų $(x_{12} - x_{ln})$ are known. Also all other meanings and significances of criteria, describing commercial offers, are known (Table 1).

On the basis of grouped decision making matrix (Table 9) and (6)-(8) formulas, the calculations are carried out.

Step 5. The revised value x_{11-p} of evaluated commercial offer a_1 is calculated:

$$x_{11-p} = x_{11} \cdot (1 + k_1 : 100) \tag{9}$$
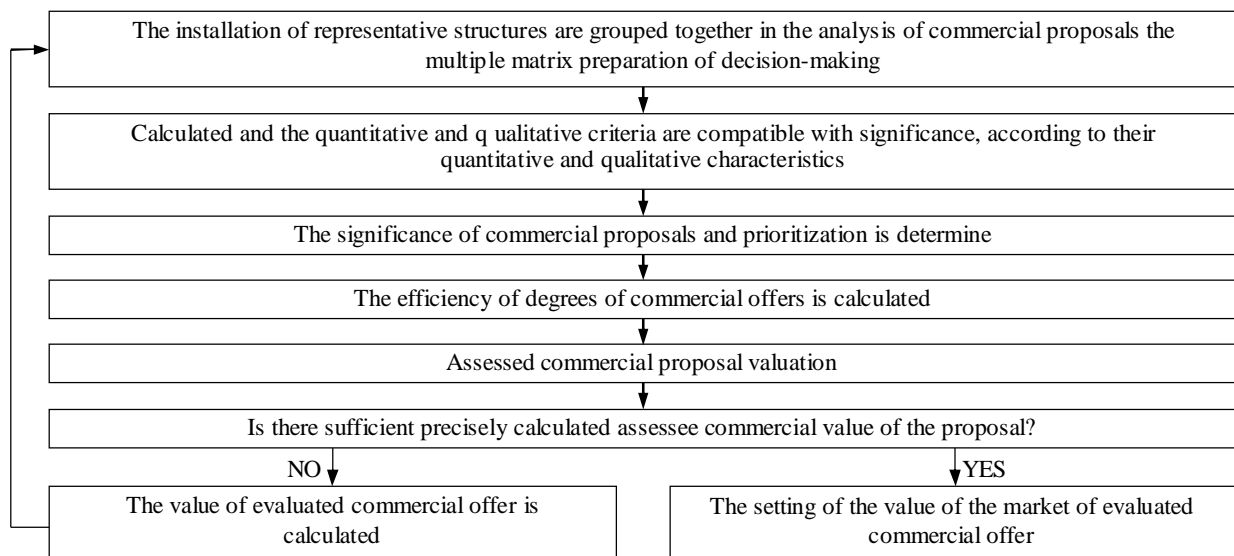
Fig. 2. The aggregated block diagram of the calculation of the market value of commercial offer submitted for installation of typical constructions

Table 7

The decision making matrix grouped by multi-criteria analyses of commercial offers for installation of typical constructions

Criteria, which describe examined constructions	*	Signifi-cances	Units of measure ment	The assessee and the comparative commercial offers					
				a_1	a_2	...	a_j	...	a_n
1. The value of evaluated commercial offer a_1 and actual prices of commercial offers $(a_2 - a_n)$ Quantitative criteria	$\check{z}_1$	q_1	m_1	x_{11}	x_{12}	...	x_{1j}	...	x_{1n}
	$\check{z}_2$	q_2	m_2	x_{21}	x_{22}	...	x_{2j}	...	x_{2n}
	...	...	...	...	...	...	...	...	...
	$\check{z}_i$	q_i	m_i	x_{i1}	x_{i2}	...	x_{ij}	...	x_{in}
	...	...	...	...	...	...	...	...	...
	$\check{z}_t$	q_t	m_t	x_{t1}	x_{t2}	...	x_{tj}	...	x_{tn}
Qualitative criteria	$\check{z}_{t+1}$	q_{t+1}	m_{t+1}	x_{t+11}	x_{t+12}	...	x_{t+1j}	...	x_{t+1n}
	$\check{z}_{t+2}$	q_{t+2}	m_{t+2}	x_{t+21}	x_{t+22}	...	x_{t+2j}	...	x_{t+2n}
	...	...	...	...	...	...	...	...	...
	$\check{z}_i$	q_i	m_i	x_{i1}	x_{i2}	...	x_{ij}	...	x_{in}
	...	...	...	...	...	...	...	...	...
	$\check{z}_m$	q_m	m_m	x_{m1}	x_{m2}	...	x_{mj}	...	x_{mn}

$*$ – The sign $\check{z}_i$ $(+ (-))$ shows that accordingly the greater (lower) meaning of criteria more corresponds the requirements of customer.

Step 6. Whether the revised value x_{11-p} of evaluated commercial offer a_1 is calculated exactly is determined:

$$|k_1| < s \qquad (10)$$

here s is percentage of the accuracy, in which we want to calculate the market value x_{11-R} of evaluated commercial offer a_1.

Step 7. The market value x_{11-R} of evaluated commercial offer a_1 is calculated. If the inequality (10) is satisfied, then the market value of evaluated commercial offer shall be determined as follows:

$$x_{11-R} = x_{11-p} \qquad (11)$$

If the inequality (10) is not satisfied, then the market value of evaluated commercial offer isn't calculated sufficiently precise and we need to continue the proximity cycle. In this case the revised value $x_{11} = x_{11-p}$ of evaluated commercial offer is inserted in the decision making matrix grouped by multi-criteria analyses of commercial offers for renovation and all calculations are repeated according formulas till the inequality (10) will be satisfied [2, 4].

4. Conclusions

In order to determine in which market value x_{11-R} the evaluated commercial offer a_1 would be equally competitive in the market compared to the customer's selected offers $(a_2 - a_n)$, comprehensive assessment of all of them positive and negative characteristics the multi-criteria market value and efficiency level of commercial offers identification method have been offered.

Under this method the degrees of efficiency of examined commercial offers and the market value of evaluated commercial offer directly and in proportion depend on the system of criteria, meanings of criteria and value of significances. After the performance the degree to which objects can be seen, what is the degree of efficiency of the projects and the cost ratio, i.e., where the money were used more effectively. See clearly where more worthwhile to invest the money and what their investment performance.

Acknowledgements

References

1. **Ražaitis V.** Pastatų konstravimo pagrindai. - Vilnius: Dailės akdemijos leidykla, 2004. – 328 p.
2. **Zavadskas E. K., Kaklauskas A., Banaitienė N.** Pastato gyvavimo proceso daugiakriterinė analizė. Monografija. V.: Technika, 2001. – 380 p.
3. **Zavadskas E. K., Simanauskas L., Kaklauskas A.** Sprendimų paramos sistemos statyboje. Monografija. V.: Technika, 1999. – 236 p.
4. **Kaklauskas A., Zavadskas E. K.** Internetinė sprendimų parama. Monografija. V.: Technika, 2002. – 292 p.

Atmosphere Pressure Tracking for CMUT Operating Point Adjustment

D. Barauskas, D. Viržonis

Kaunas University of Technology, S. Daukanto g. 12, 35212, Panevėžys, Lithuania, E-mail: DovydasBar@gmail.com

Abstract

Analysis of the capacitive micromachined ultrasound transducer (CMUT) membrane displacement due the ambient pressure was made. Finite element simulation was taken to find the displacement function of the membrane under changing ambient pressure conditions. Then the displacement function was passed to the parallel plate model in the Matlab/Simulink environment to determine the bias voltage values, which are producing equivalent displacement function. This pressure to voltage substitution technique was used to mimic the pressure difference acting over the membrane and to relate the effective collapse voltage to the pressure difference. This relationship will be implemented to the automatic loopback control of the bias voltage, while the pressure acting on the CMUT membrane is tracked by the ambient pressure senor.

KEY WORDS: *atmosphere pressure, capacitive micromachined ultrasonic transducer, pressure sensor.*

1. Introduction

Capacitive micromachined ultrasonic transducer (CMUT) is a device mostly used for ultrasound applications [1-3]. Fig. 1 shows the main parts of the transducer. CMUTs offer various advantages over piezoelectric transducers, such as wide bandwidth, comparatively easy integration with electronic circuits and well established fabrication processes.
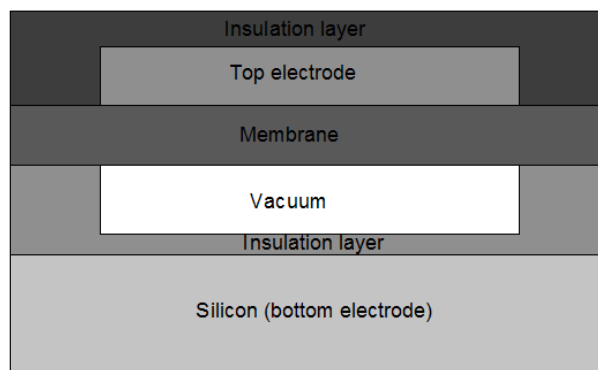
Fig. 1. CMUT cell cross section view (not to scale)
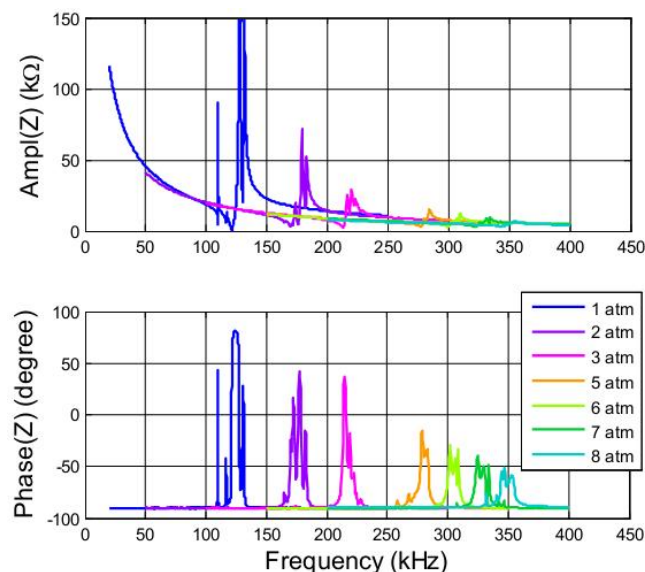
Fig. 2. Direct comparison of electrical impedance between measurements and FEA harmonic analysis [5]

CMUT technology has a wide variety of applications [4], one of them include pressure sensing, because CMUT operating point greatly depends on the atmosphere pressure acting on the membrane, inducing vacuum gap changes. This can become the source of the measurement errors if CMUT is used as a sensor or deviation from the optimum performance, when operated in imaging applications. Fig. 2 illustrates the sensitivity of a transducer to the ambient pressure with significant resonance frequency and electromechanical impedance amplitude and phase changes when the ambient pressure changes from 1 to 8 atmospheres [5]. If the ambient pressure change is a disturbance, not the measurand, CMUT operating point must be adjusted to keep the performance of the sensor/transducer intact.

2. Simulation methods and models

The sequence of the computation steps (shown in Fig. 3) was used to relate the pressure difference acting on the membrane to the operating point voltage of CMUT. Initially, the finite element analysis (FEA) software available from SolidWorks (Waltham, MA) was used to build a finite element model. It was used to determine the displacement function of the membrane to find the effective gap change Δg. Then obtained displacement function was transferred to the Simulink model to find the equivalent voltage function U_g, which would introduce the same deflection function and corresponding vacuum gap change as in the case of the pressure P. The voltage function was then used to simulate the pressure-induced deflection. An additive operator was used to superimpose said voltage function with the voltage applied to the CMUT input to mimic the deflection of the membrane for variable ambient pressure. Finally, using the results and Matlab Simulink model with added equivalent voltage function, we found the collapse voltage, U_{col}, of the transducer for different ambient pressures, giving us the function of the optimal bias voltages $U_{op} = 0.8 U_{col}$. This function obtained at the end of the computation path is to be used for the automatic control of the bias voltage in respect of the variable ambient pressure.
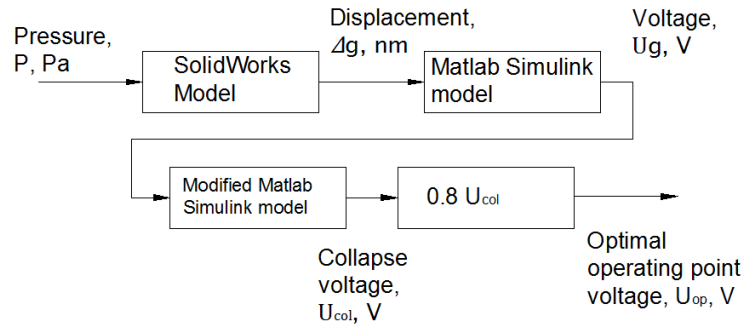
Fig. 3. CMUT operating point modeling stages

A model of capacitive micromachined ultrasound transducer membrane is created with SolidWorks software using Finite Element Method (FEM) [6]. In this model the membrane is a 1 µm thick round plate made of polycrystalline silicon with a diameter of 40 µm. Using SolidWorks simulation non-linear study tools the material properties are specified as such: Elastic modulus $1.48 \cdot 10^{11} \text{N/m}^2$; Poisson's Ratio – 0.1773; Mass density – 2329 kg/m^3. The model type is set to linear elastic isotropic assuming that material is polycrystalline silicon. As shown in the Fig. 4, the membrane is perimeter-clamped by adding fixtures using simulation tools provided. Then external load is applied as a uniformly distributed pressure normal to the surface of the membrane. Further, the model is divided into finite elements by using auto mesh tools and adjusting mesh density and mesh parameters such as global size of the elements and tolerance of the elements. Finally, nonlinear static computation is done and displacement function is acquired relating the membrane's effective displacement (equivalent to the parallel plate displacement) over the pressure applied, Fig. 6a.

The displacement function from the previous computation step was taken to the input of Matlab-Simulink model (Fig. 5) and corresponding voltage function V_{atm} was found by selecting the voltage value to match one of the model outputs, vacuum gap g, to the corresponding displacement value form the pressure-displacement function.
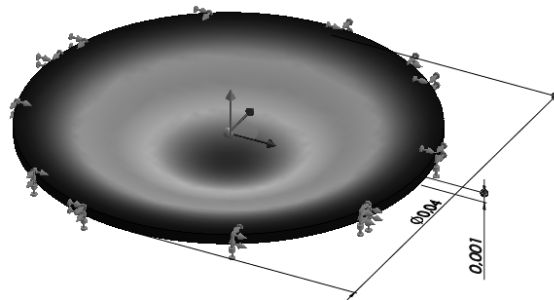
Fig. 4. SolidWorks model of CMUT membrane

Fig. 5 shows the Matlab-Simulink model of capacitive micromachined ultrasound transducer membrane approximated by the parallel plate. It is based on three state equations for parallel-plate electrostatic actuator [7]:

$$\dot{x}_1 = \frac{1}{R}\left(V_{in} - \frac{x_1\,x_2}{e\,A}\right)$$
$$\dot{x}_2 = x_3 \qquad (1)$$
$$\dot{x}_3 = -\frac{1}{m}\left(\frac{x_1^2}{2\,e\,A} + k\,(x_2 - g_0) + b\,x_3\right)$$

where: x_1 is the capacitor charge; x_2 is the capacitor gap; x_3 is the velocity of the moveable plate; e is the permittivity of the air; A is the plate area; g_0 is the at-rest gap; R is the source resistance of the time-dependent V_{in} voltage source.
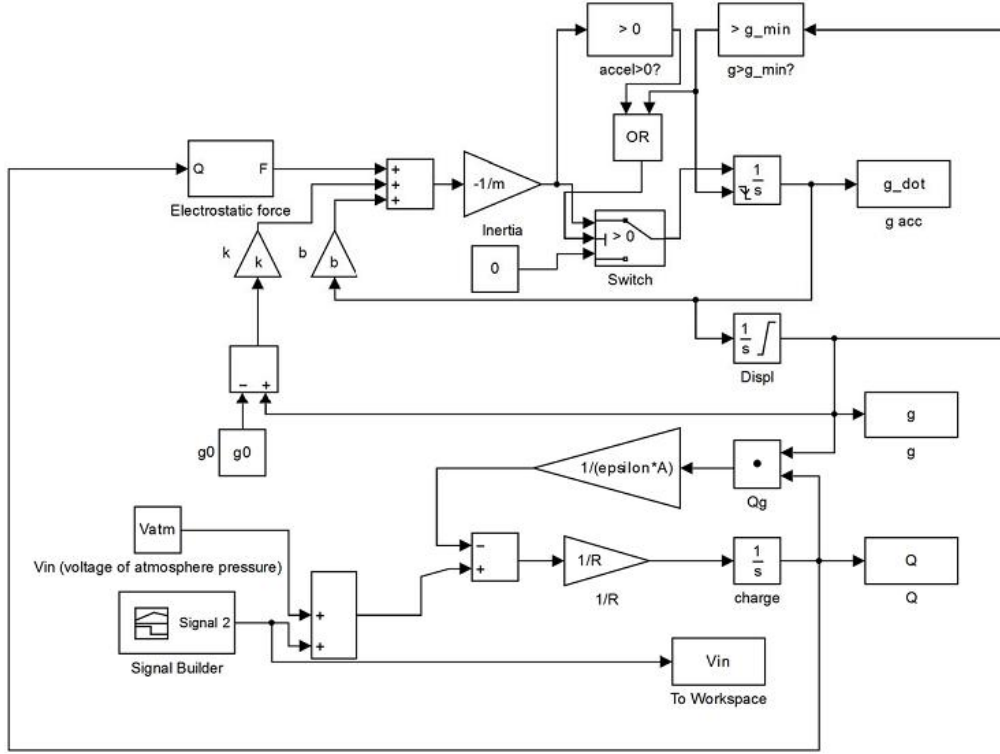
Fig. 5. Simulink implementation of state equations for the parallel-plate electrostatic actuator [7]

This model uses three integrators, one integrates acceleration to find velocity, another integrates velocity to find position and last one integrates current to find charge. The electrostatic-force block is a Simulink function that can perform nonlinear operations. The input in this case is charge Q [5].

The definition of the parameters and the values used for the simulations are given in Table 1.

Table 1

Parameters used in the modeling of electrostatic actuator

Parameter	Symbol	Value
Area	A	$1.256 \cdot 10^{-9}$
Permittivity	ε	$8.85 \cdot 10^{-12}$
Initial gap	g_0	$1.5 \cdot 10^{-7}$
Minimum gap	g_{min}	$1 \cdot 10^{-10}$
Mass	m	$2.92 \cdot 10^{-12}$
Damping constant	b	$4 \cdot 10^{-5}$
Spring constant	k	$1.92 \cdot 10^{4}$
Resistance	R	1000

The outside pressure was mimicked in the simulation as an additive voltage, V_{atm}, which was equivalently related to the pressure difference. Finally, a collapse voltage was found for each pressure difference value using the

modified Simulink model with additional constant block, V_{atm}. The best operating point voltage value for CMUT is determined when transducer is working in the range of 80% to 90% of collapse voltage, U_{col}.

3. Results

The functions found as a result of the simulation are shown in Fig. 6b. Only the lower range (10 to 170 kPa) of the pressures was used to find the voltage and displacement functions since CMUT enters to the collapse regime when the pressure difference is greater than 170 kPa. This can be seen in the diagram as a breakpoint at 163 – 167 kPa. One can also note that within this range the displacement function is quite close to linear. Fig. 6a show the displacement function of CMUT membrane at the greater range of the pressure difference (0.1 to 8.0 MPa), and here the non-linear character of the displacement is obvious, reaching more than 1 µm at 8.0 MPa. This corresponds to the well known plate theory, which tells that displacement nonlinearities appear only when the displacement reaches half value of the plate thickness.

a   b
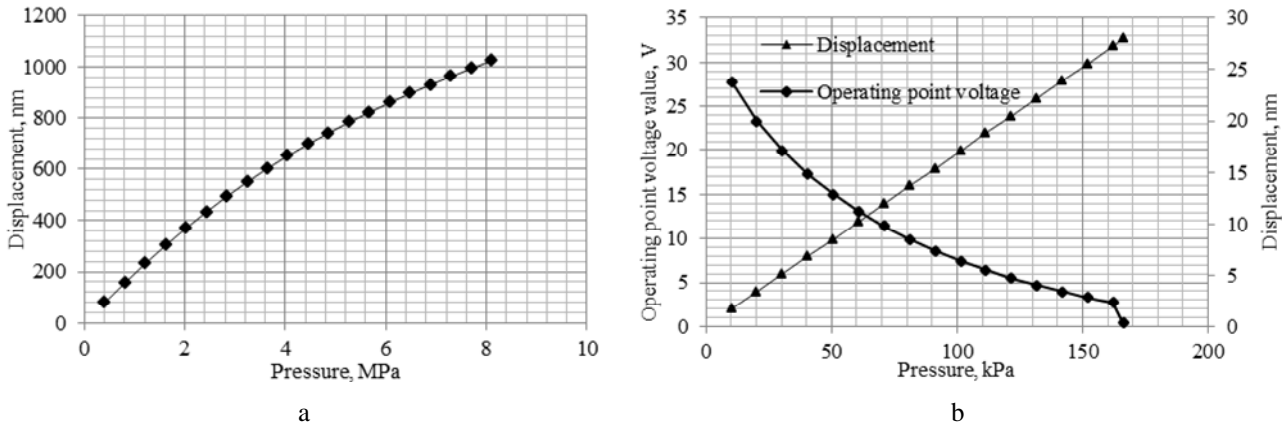
Fig. 6. a – membrane's displacement based on the pressure applied with non-linearities; b – FEM and Matlab Simulink results illustrated on one graph. FEM results show the displacement increase when more pressure is applied, Simulink results show the operating point voltage value change due to pressure applied

Since displacement function is linear to the pressure difference acting on the membrane within the reasonable range of CMUT working regime, only the non-linear relationship between the pressure and collapse voltage can be taken in to account when designing the automatic control of the bias voltage.

4. Conclusions

The non-linear simulation approach which was taken during this work led us to the conclusion that within reasonable CMUT operation range the pressure-displacement function of the membrane is nearly linear. This fact leads to the simplification of the bias voltage control law, which is to be designed. Also we found out the displacement and voltage functions, which both will be used during the controller design.

References

1. **Haller M. I.** and **Khuri-Yakub B. T.** A surface micromachined electrostatic ultrasonic air transducer. IEEE Trans. Ultrason., Ferroelect., Freq. Contr., vol. 43, pp. 1–6, Jan. 1996.
2. **Soh H. T., Ladabaum I., Atalar A., Quate C. F.** and **Khuri-Yakub B. T.** Silicon micromachined ultrasonic immersion transducers. Appl. Phys. Lett., vol. 69, pp. 3674–3676, Dec. 1996.
3. **Morkvenaite-Vilkonciene I., Virzonis D., Vanagas G., Krikscikas V.** Operating point of Capacitive Micromachined Ultrasonic Transducers with Sub-structural Elements. Elektronika ir Elektrotechnika Vol 18, No 9 (2012), pp. 43-46.
4. **Oralkan O., Ergun A. S., Johnson J. A., Karaman M., Demirci U., Kaviani K., Lee T. H., Khuri-Yakub B. T., Ginzton E.L.** Capacitive Micromachined Ultrasonic Transducers: Next-Generation Arrays For Acoustic Imaging? Laboratory and Center for Integrated Systems, Stanford University, Stanford, CA 94305-4070, USA.
5. **Ho M. -C., Kupnik M., Park K. K., Eckhoff K.** and **Khuri-Yakub B. T.** Wide pressure range operation of air-coupled CMUTs. Proc. IEEE Ultrasonics Symposium, pp. 93-96, 2012.
6. **Yaralioglu G. G., Ergun A. S.** and **Khuri-Yakub B. T.** Finite-element analysis of capacitive micromachined ultrasonic transducers. IEEE Trans. Ultrason., Ferroelect., Freq. Contr., vol. 52, no. 12, pp. 2185-2198, Dec. 2005.
7. **Senturia S. D.** Microsystem Design. 2002 Kluwer Academic Publishers, New York, Boston, Dirdrecht, London, Moscow, pp. 689, eBook ISBN: 0-306-47601-0, Print ISBN: 0-7923-7246-8.

Proceedings of 8th International Conference ITELMS'2013

The Researches of Stability Evaluation Articulated Loader while Working on Slopes

A. Bartnicki*, M. J. Łopatka**, T. Muszyński***, M. B. Jaskółowski****

Military University of Technology, gen. S. Kaliskiego str, 2, 00-908 Warsaw, Poland, E-mail:abartnicki@wat.edu.pl
**Military University of Technology, gen. S. Kaliskiego str, 2, 00-908 Warsaw, Poland, E-mail:mlopatka@wat.edu.pl*
***Military University of Technology, gen. S. Kaliskiego str, 2, 00-908 Warsaw, Poland, E-mail: tmuszynski@wat.edu.pl*
****Military University of Technology, gen. S. Kaliskiego str, 2, 00-908 Warsaw, Poland, E-mail: mjaskolowski@wat.edu.pl*

Abstract

The paper presents a simulation research of dynamic stability L34 loader. Simulations were performed for specified test of the first speed gear. It examined the ability of the articulated loader to work on a slope.
KEY WORDS: *dynamic stability, articulated loader, simulation research, MSC. Adams.*

1. Introduction

The phenomenon of dynamic stability articulated loaders is an important issue, because to a large extent depend on the possibility of working the machine. The European Union a document characterized by determining the stability of the loader its nominal load is EN: 474-3: 2009 [8]. This norm longitudinal stability is determined by the maximum capacity of loader, which is 50% - 80% of tipping load. Tipping load is the load that applied to the bucket loader will lose contact between the rear wheel and the ground. However, in recent years has greatly extended the field of application of articulated wheel loaders. They are not only used for reloading work on paved horizontal surfaces, but also on the slopes. Under such conditions, the stability of the loader influence not only nominal load, but also the weight distribution and the location of the articulation turn. This leads to the need to assess the ability of loader working on slopes. As an example, the analysis was widely used in the industry loader L-34 production Huta Stalowa Wola (HSW). In order to determine the ability of the machine to work on slopes used data provided by the manufacturer in operation handbook. According to [5] limits the inclination ground, where there is a loss of stability for loader L - 34 are:

- 52% in the position of the frame upright in parallel to the tilting axis;
- 40% in the position of the frame to the inside of a twisted angle of 40°;
- 48% in the position of the frame to the outside of a twisted angle of 40°.

However, in the DTR [6] for a similar-sized excavators L - 35 M from the same manufacturer are shown limits the inclination ground:

- 57% in the position of the frame upright in parallel to the tilting axis;
- 40% in the position of the frame to the inside of a twisted angle of 40°;
- 57% in the position of the frame to the outside of a twisted angle of 40°.

The value of the maximum slope of the ground is the results of the static tests performed on tilt table. In this research, the machine is not loaded and its bucket is located at a height of 0.5 m above the ground. Based on the presented data the user cannot fully determine the ability an articulated loader to work on slopes. This is caused by the lack of information on the influence load and driving dynamics, on the permitted inclination ground. To complement the data manufacturer provides the permissible inclination ground during operation. According to [5] wheel L - 34 are the following recommendations:

- Working with bucket a lifted to maximum height:
  - Inclination of 0%. Turning angle 0 ° - 40 °. Capacities limit 68.670 kN.
  - Inclination to 5%. Turning angle of 0 °. Capacities limit 30,240 kN.
  - Inclination to 5%. Turning angle 40 °. Capacities limit 33.354 kN.
  - Slope > 5%. Working prohibited.
- Driving with standard payload without lifting bucket:
  - Inclination to 5%. Turning angle 0 ° - 40 °. Drive acceptable.
  - Inclination 6% - 10%. Turning angle of 0 °. Drive acceptable.
  - Inclination 11% - 16%. Turning angle of 0 °. Only the front downhill or entry at.
  - Slope > 16%. Drive prohibited.
- Driving without payload and without lifting bucket:
  - Inclination up to 10%. Turning angle 0 ° - 40 °. Drive acceptable.
  - Inclination of 11% - 57%. Turning angle of 0 °. Only the front entrance or entrance.
  - Slope > 57%. Drive prohibited.

However, the same manufacturer of construction equipment in the manual [6] wheel L - 35 M of similar stability makes the following recommendation:

- Lifting attachments to his full height is only allowed after stopping the machine or drive with a minimum speed or braking gently. Moving the machine is allowed on inclination up to 16%.
- Transporting the ore without lifting attachments. Permissible inclination up to 36%.
- Driving without load and without lifting attachments. Acceptable inclination up to 25%.

Volvo's manual to loader L 120, [4] published only that the work up or down slope the machine to set the load facing up the slope, do not work at inclinations greater than 30%.

The recommendations are very different from each other. The reason for this difference may not be the same methods for determining the permissible slope of the land on which it can work articulated loader. This is caused by the lack of standards and recommendations to harmonize test methods. For what is the difficulty of determining the usefulness of the machine for work on slopes. This results in an inability to clearly assess opportunities to work on the inclinations of such a charger. It is therefore to develop a method of verifying the data provided by the manufacturer.

2. Criteria for assessment stability of articulated loaders

The problem of assessing the lateral dynamic stability of construction machinery is discussed e.g. requirements in the U.S. military in specifying ability of vehicles to move over rough terrain vehicles [1, 2]. The requirements are divided into test driving stability and the stability test. Stability driving tests are shown in [3]. Tests stability is moving machine on a specified drive track (Fig. 1.) at 30% slope area. During the test required is shortly stop the machine. Crossings are made for bucket in transport position without load and nominal payload. For loaders without load transfer was performed at a speed of not less than 10 mph (~ 16 km/h) corresponding to the speed of vehicular most machines. However, drive of the nominal load is performed at not less than 3 mph (~ 5 km/h) which is equal to operating speed.
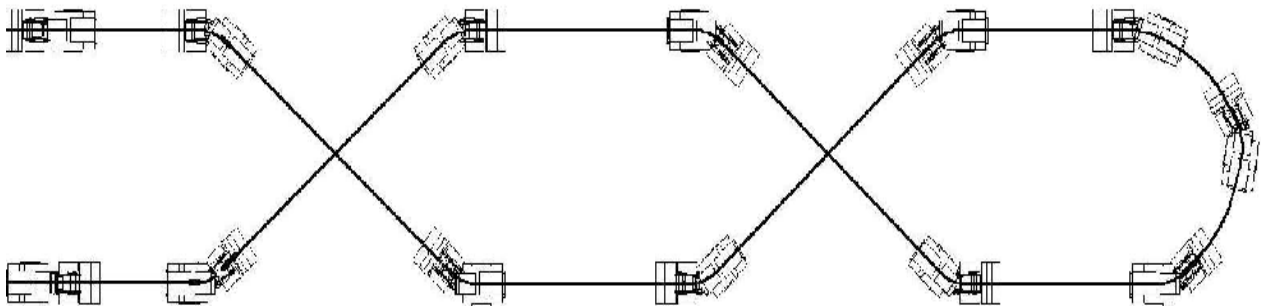
Fig. 1. Diagram of test track travel loader at 30% inclines [2]

Based on these requirements [2] in the Department of Mechanical Engineering been developed a simulation method to test the ability of the articulated loader to work on the slopes. This method consists in performing a simulation ride loader in a 30% slope along the track in the shape of a figure eight (Fig. 2). The shape of the track checks the stability of the vehicle in every possible position of the machine to the hills.
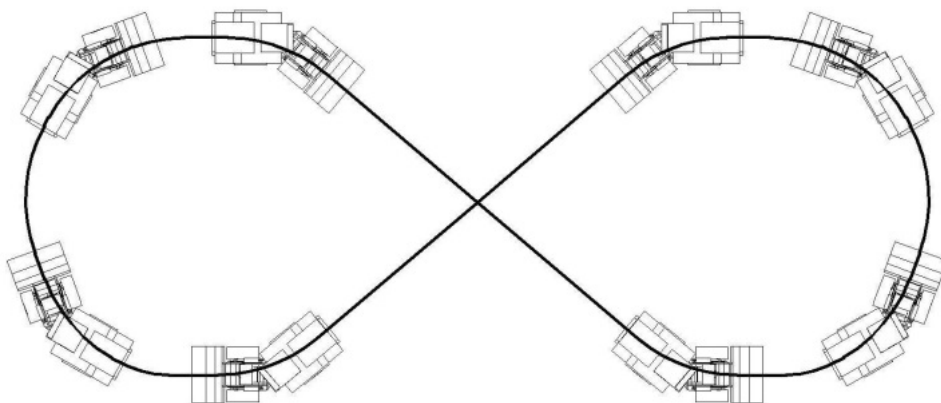
Fig. 2. Schematic track loader at 30% incline

Intensity of-turn as was applied to the test corresponds to a maximum speed at which the operator can operate the steering wheel. It is ensured through the execution the articulation angle of 40° for 1.5 seconds, after which the travels of 3 s twisted frame and then decreases the steering angle to 0 degrees in the travel time of 1.5 seconds. Drive is performed at a speed of not less than 7.4 km/h resulting from the maximum speed in first gear machine. In addition, during research examined the effect of the load on the stability of the machinery by carrying tests with half of nominal load, with one-quarter of the nominal load and without load. More than a check is subject to influence position of

bucket on the stability machine of made passing from bucket in three positions: in transport position, in a position parallel to the ground and in position raised to its maximum height above the ground.

As a criterion to assess the ability of the machine to work on slopes accepted normal response coefficient W_{nor} described pattern.

$$W_{nor} = \frac{R_p}{R_n}$$

where: R_p is the value of the minimum reaction of the single wheel on slope; R_n is the nominal value of the reaction on a single wheel on horizontal ground.

Coefficient value should be determined for each wheel machine. As the limit adopted $W_{nor} = 0$ because then following detachment wheel of the machine from the ground. In order to ensure safe operation of steering the machine hence assumed that when $W_{nor} = 0.2$ there is a loss of steering.

3. Model articulated loader in MSC. Adams

In order construct the model articulated wheeled loader with a mass 19 tons in MSC. Adams environment for testing the ability to work loader in a 30% slope been adopted, a number of assumptions and simplifications. It was assumed that the basic parameters of the numerical model such as wheelbase, dimension and weight distribution are similar to those in loader L - 34. Furthermore, in order to verify the ability to work on slopes model equipped a movable extension arm. For the analysis adopted three extreme positions:
- transport position in which the bucket is on the smallest height above the ground and closest to the line of contact with ground and front wheels,
- position parallel to the ground, where in the bucket located in the greatest distance from the line of contact with ground and front wheels,
- maximum upper position in which bucket is raised to maximum height above the ground.

Components of model were combined so as to reproduce as closely as possible the actual characteristics of the loader. To this end wheels of the bridges associated with revolute constraint allows controlling the speed of wheels, so the travel speed of the model. Thus, the revolute constraint frames of the front and the rear member model to ensure the steering angle control framework. In order to raise the extension arm model given translational constraint between the piston and the cylinder actuators, which allow controlling the speed of piston rod extension, and therefore the speed with which raises and lowers extension arm. Other components of the model connected with rigidly taking over from all the degrees of freedom given subassembly making solid body model (Fig. 3b). In order to move the specified loader model each wheel base model associated with ground contact constrain that can determine the coefficient of friction between the wheel and the ground, or to determine the adhesion of wheels to the ground. To avoid the phenomenon of loss of traction during the simulation model on a slope is assumed that the value of the coefficient of static and dynamic friction coefficient is equal to 1. Irrespective of type of material from which modeled the components of the loader MSC. Adams confers ideal rigidity, which prevents the deformation of the components including the tire. So in order to reproduce the actual deflects bridges tires combine the model with its wheels constraints elastic – damping. These constraints can give elastic properties - absorbing connection between wheel and the bridge corresponding to the actual characteristics of the tires. Based on [7] assumes that deflects front tires at 50 mm and 100 mm rear when the machine in repose and without payload. In order to achieve actual values of deflection assumed that the rigidity coefficient on the front axle is equal 23 N/mm and the rear axle 503 N/mm, while the damping coefficient is equal to 26 Ns/mm at the front and 40 Ns/mm on the rear axle (Fig. 3a).
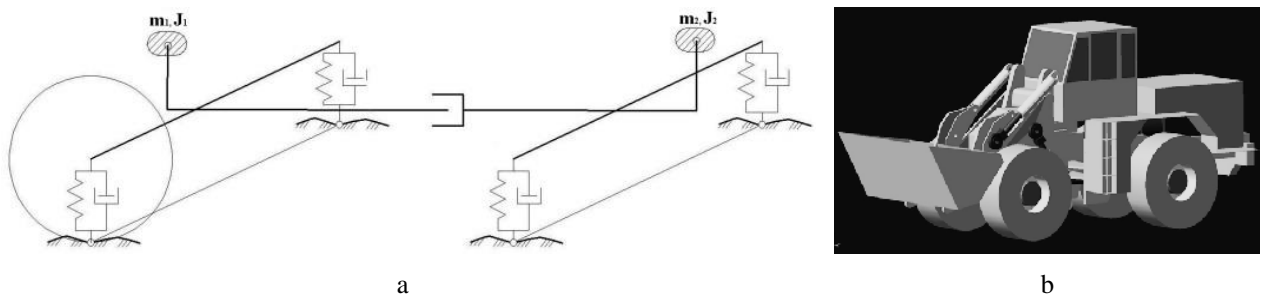
Fig. 3. Model articulated wheel loader: a – structure of the model; b – the model performed in the MSC.Adams

4. The results of research simulations

In the first phase of the research determined the nominal value of reaction to wheels loader when moving through a horizontal ground. Summary of the results presented in Table 1. In the next stage of research simulation stability articulated loader described crossing of track on 30% inclination. Sample waveforms of reaction on the wheel

loader are shown in Fig. 4 and 5. Collected the lowest reaction to value of wheel loader during passing are summarized in Table 2 However value coefficient W_{nor} are presented in Table 3.

<div align="right">Table 1</div>

<div align="center">Nominal values of the reaction to wheels loader on horizontal ground</div>

Position of bucket	Payload, kg	The value of the reaction on wheels loader, kN			
		Front axle		Rear axle	
		Left wheel	Right wheel	Left wheel	Right wheel
Transport	0	42	42	51	51
	1500	53	53	47	47
	3000	64	64	43	43
Parallel to the ground	0	44.5	44.5	48.5	48.5
	1500	55	55	45	45
	3000	70	70	37	37
Maximum upper	0	44	44	49	49
	1500	54	54	46	46
	3000	68	68	39	39
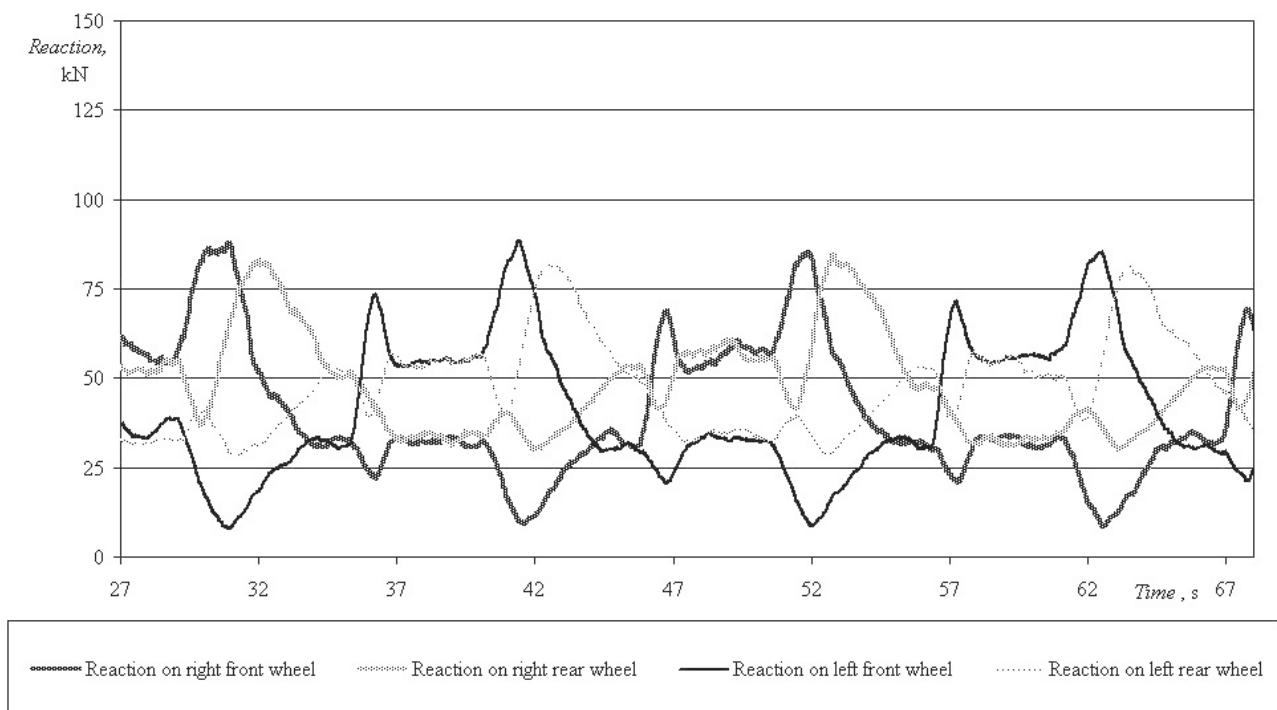
Fig. 4. The reaction on wheel of loader. Loader with bucket in transport position and without load

The conducted research simulation loader with bucket in the transport position that while driving the value of reaction to wheels front axle is reduced to, 8 kN this resulting that W_{nor} reaches a value 0.2. The minimum value of the response received on wheels loader without load. However at the rear axle response value decreased to 18 kN, and W_{nor} is equal 0.58 in the loader with half of nominal load. The minimum value of the reaction occurs when the loader executing a turn, or when there is a sharp change of direction in the other configurations, the minimum load response is higher as a result of which it was found that prevalence of W_{nor} not be reduced below the accepted requirements. During operation of the boom loader in transport position there is no risk of loss of stability.

From carried research simulation loader with bucket in position parallel to the ground follows that the reaction to wheels the front axle is reduced 0 kN ($W_{nor} = 0$) in the machine with the half nominal payload. The loader without payload minimum value of reaction is equal 6 kN ($W_{nor} = 0.13$). Value reaction at the rear axle fell to 0 kN ($W_{nor} = 0$) with a load of 3000 kg, 15 kN ($W_{nor} = 0.33$) with a load of 1500 kg and 23 kN ($W_{nor} = 0.47$) without load. Decrease of reaction to the minimum value occurs at the same time as the loaders with bucket in transport position. The minimum values of responses received on wheels loader that only Unloaded machine can maneuver on the 30% of the slope.

A study of research simulation for loader with bucket in maximum position follows that regardless of the size of the load when maneuvering response value on the wheels is reduced to 0 kN ($W_{nor} = 0$). This indicates that the machine loses stability. From this it follows that the loaders with bucket in every position cannot be working at 30% slope.
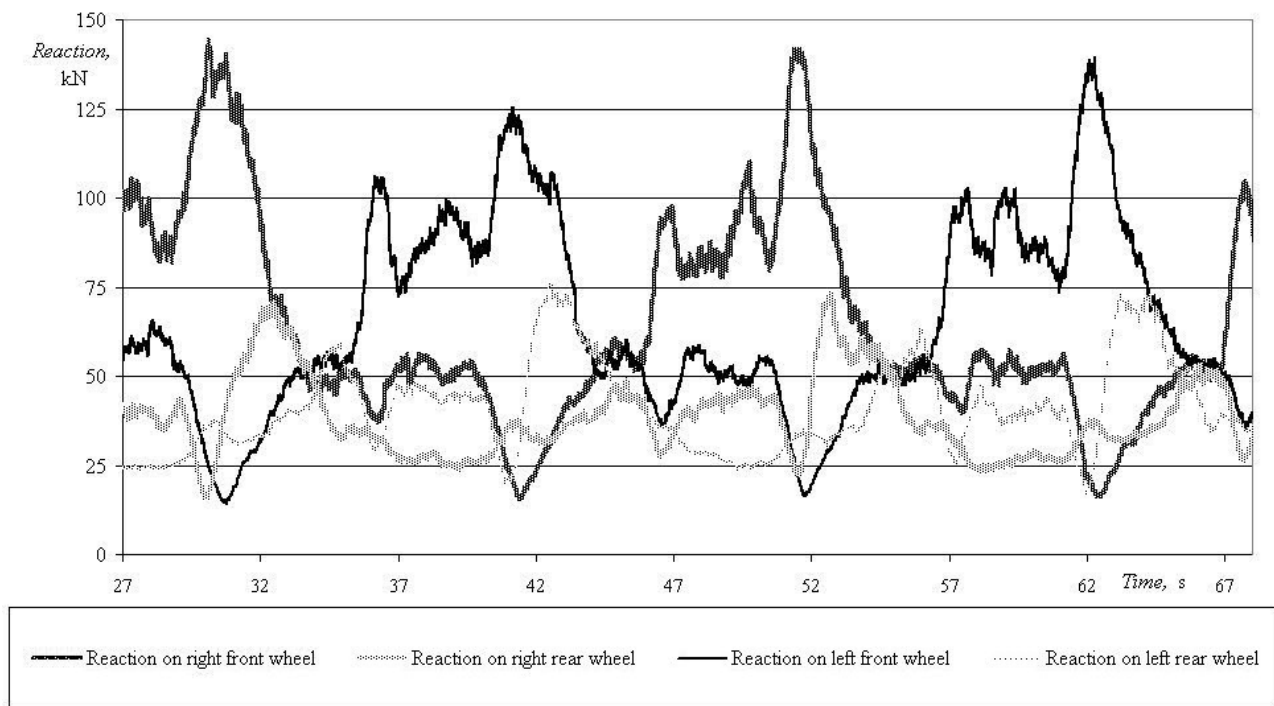
Fig. 5. The reaction on wheel loader with load 1500kg. Loader with bucket in transport position

Table 2

The minimum value of the reaction on articulated loader wheels

Position of bucket	Payload, kg	The value of the reaction on wheels loader, kN			
		Front axle		Rear axle	
		Left wheel	Right wheel	Left wheel	Right wheel
transport	0	8	8	30	30
	1500	11	11	25	25
	3000	14	14	18	18
parallel to the ground	0	6	6	23	23
	1500	0	0	15	15
	3000	0	0	0	0
maximum upper	0	0	0	0	0
	1500	0	0	0	0
	3000	0	0	0	0

Table 3

The value of the coefficient W_{nor} on articulated loader wheels

Position of bucket	Payload, kg	The value of the coefficient Wnor on wheels loader			
		Front axle		Rear axle	
		Left wheel	Right wheel	Left wheel	Right wheel
transport	0	0.2	0.2	0.58	0.58
	1500	0.21	0.21	0.53	0.53
	3000	0.22	0.22	0.42	0.42
parallel to the ground	0	0.13	0.13	0.47	0.47
	1500	0	0	0.33	0.33
	3000	0	0	0	0
maximum upper	0	0	0	0	0
	1500	0	0	0	0
	3000	0	0	0	0

5. Conclusions

Summing completed research, the stability testing methodology developed and adopted criteria for assessing the stability of fully verify the possibility to work on the slopes of the articulated loader. The simulation studies it was

found that the results differ from those published in operation handbook loader L - 34. The documentation for this given that the machine without load and bucket in transport position can be moved, twisted frame on the ground only a 10% slope. However the simulation tests performed articulated loader of the same type follows that it can move along the 30% slope. However, it has low ability to perform work on a 30% slope because only in the transport position there is no risk of loss of stability. To perform the loader works on 30% slope area should be reduced centrifugal force interacting on the machine. Reduction of the centrifugal force can be achieved by reducing the speed and increasing the loader turning radius at which the machine moves, which can result in prolonged cycle and thus lowering productivity.

Reference

1. Inch – Pound ATPD – 2301. Purchase description tractor, wheeled, all-wheel drive with attachments (High mobility engineer excavator). Army - At. Project 2420 - 003. 23 September 2002.
2. ITTC Recommended Procedures 7.5-02-05-04.1: Testing and Extrapolation Method High Speed Vehicles – Excerpt of ISO 2631, Seasickness and Fatigue. International Towing Tank Conference 1999.
3. **Konopka S., Krogul P., Łopatka M. J., Muszyński T.** Articulated engineering equipment stability simulations based on Ł34 wheel loader. Journal of Kones vol 18 No. 1. ISSN 1231-4005, str. 8, 2011
4. Ładowarka hydrauliczna. L 120. Dokumentacja techniczno – ruchowa. Podręcznik operatora. Volvo. Ref No. 482 669 6695 Polish. 20. 06. 2000.
5. Ładowarka hydrauliczna Ł - 34. Instrukcja obsługi. Kombinat przemysłowy Huta Stalowa Wola, 37-450 Stalowa Wola. AGPOL - ZW - 01 - 266/87.
6. Ładowarka hydrauliczna Ł - 35 M. Instrukcja obsługi. Kombinat przemysłowy Huta Stalowa Wola, 37-450 Stalowa Wola. HZE/10/90.
7. **Łopatka M. J**. i inni. Optymalizacja parametrów konstrukcyjnych przegubowego ciągnika kołowego ze względu na stateczność jazdy. Sprawozdanie z projektu badawczego Grant nr 0T00A01614. WAT. Warszawa 2000.
8. PN – EN: 474 – 3: 2009: Earth – moving machinery – Safety – Part 3: Requirements for loaders.

Proceedings of 8ᵗʰ International Conference ITELMS'2013

Comparison of PID and FUZZY Controller in the Cascade Tank System in Matlab/Simulink

R. Bayır*, H. M. Ertunç**, H. Demir***

*Karabuk University, Faculty of Technology, Dept. of Mechatronics Engr. 78000, Karabuk, Turkey, E mail: rbayir@karabuk.edu.tr
** Kocaeli University, Mechatronics Engineering Department, Kocaeli, Turkiye E mail : hmertunc@kocaeli.edu.tr
***Karabuk University, Technology Faculty, Dept. of Mechatronics Engr. 78000, Karabuk, Turkey, E mail: hasanfe_88@hotmail.com

Abstract

In this study present comparison of PID and FUZZY controller in the cascade tank system. In order to control cascade tank system, fuzzy and pid controller was simulated in Matlab /Simulink. The system has two tanks. The water level in the tanks and the stream provided by pump are the system parameters. The current which is applied to the motor is the only control variable in the system. In this system fuzzy controller are compared with pid controller. The signals of the system's output are observed in matlab.
KEY WORDS: *cascade tank system, fuzzy logic controller, fuzzy logic types, pid controller.*

1. Introduction

Since fuzzy logic was introduced by Lotfi Zadeh in 1965, it has had many successful applications mostly in control. This 'fuzzy' boom has generated strong interest in this area together with a boom in studying and teaching of fuzzy theory and technology. Fuzzy Logic Control Systems have many advantages such as high precision and high accuracy etc.

Fuzzy logic techniques have been adopted much more gradually in the USA and Europe. But the success of the Japanese developers is making companies like General Electric, General Motors, Hewlett-Packard, Rockwell and others take note. Starting in the 1990s, they have begun to apply it in their internal system development. For example, in the early 1990s, US companies started using fuzzy logic in the aerospace industry for applications such as rotor transmission, servo control, missile warning, automated manufacturing and navigation systems. Meanwhile, General Motors has successfully incorporated fuzzy logic control into a product as widely used as the automatic transmission downshift mechanism of the SaturnTM. However, Mitsubishi GalantTM S is offered with a standard five-speed overdrive manual gearbox and electronically controlled four-speed overdrive automatic transmission with 'fuzzy logic' shift control. Employing fuzzy logic, the electronic control unit of the transmission calibrates gear shifts and considers such inputs as a vehicle speed, throttle position and brake application, to determine whether the vehicle is going uphill or downhill and how twisty the road is before executing a shift [1].

Recently, the miscellaneous parameters in the process are controlled such as temperature, level, and etc. Some process needs to keep the liquid level in the tank such as water, chemical liquid in its. The level control is a common type of control. The level control system must be controlled by the proper controller. The objective of the controller in the level control is to maintain a level set point at a given value and be able to accept new set point values dynamically. The conventional proportional-integral-derivative (PID) is commonly utilized in controlling the level, but the parameter of those controllers must be turned by tuning method either in time response of frequency response to meet their required performances. On the other hand, the fuzzy controller is also popularly implemented in many practical industrial automation applications.

In this study, cascade tank system was controlled both PID controller and fuzzy logic controller. It was observed that fuzzy logic controller more successfully than PID controller.

2. Experimental Study

2.1 Cascade Tank System

In this simulation there are two tanks which is connected together. Water is pumped into the top from the reservoir tank like Figure1. It flows to the second tank from the bottom tank and the following flows into the reservoir tank. In the system, the only control variable of the pump motor current is applied.

The various parameters in the process of industrial are controlled such as temperature, level, and etc. Some process needs to keep the liquid level in the horizontal tank such as oil, chemical liquid in its. The level control is a type of control method for common in process system. The level control system must be controlled by the proper controller. The objective of the controller in the level control is to maintain a level set point at a given value and be able to accept new set point values dynamically.
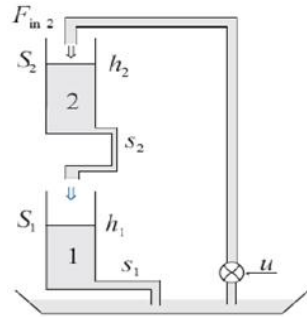
Fig. 1. Cascade tank system

The dynamic description of differential equations which are shown below:

$$\dot{h}_2(t) = \frac{F_{in,2}(t)}{S_2} - \frac{s_2 \sqrt{2 g h_2(t)}}{S_2} \tag{1}$$

$$\dot{h}_1(t) = \frac{s_2 \sqrt{2 g h_2(t)}}{S_1} - \frac{s_1 \sqrt{2 g h_1(t)}}{S_1} \tag{2}$$

$$t \dot{F}_{in,2}(t) = -F_{in,2}(t) + Q_s u(t) \tag{3}$$

where h_1 is level of the water in the lower tank; h_2 is level of the water in the upper tank; $F_{in,2}$ is flow provided by the pump.

Meaning of the parameters and set points in Eq. (1) to Eq. (3) are given in the Table 1.

Table 1

Parameters and set point value

Symbol	Parameter	Value	Unit
g	The acceleration of gravity	981	cm/s^2
S_1, S_2	Cross-sectional areas of tanks	5.30	cm^2
s_1	The water output area of lower tank	0.096	cm^2
s_2	The water output area of upper tank	0.692	cm^2
Q_s	Flow gain	33.6	cm^3/(s·A)
τ	Motor time constant	3.00	s

2.2. Simulink Block Diagram of the cascade Tank System

System using the standard Simulink blocks and it has been applied as follows,
1. Dynamic equations of the system is performed by pulling required the blocks from the library.
2. Input block of U is taken into sub-directory of sources.
3. h_1, h_2 and $F_{in,2}$ graphs are drawn.

As a result, figures of the subsystem are shown in Figure2.

Tank system was actualized as plant block in the subsystem. Cascade tank system was controlled with PID and Fuzzy Logic Controller. This simuling control system is given in Figure 3.
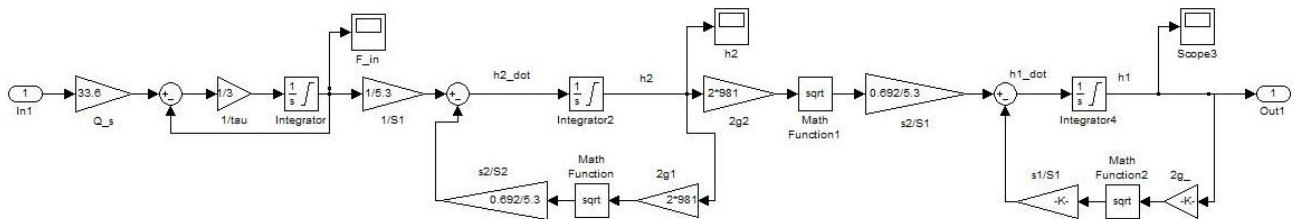
Fig. 2. Tank subsystem block
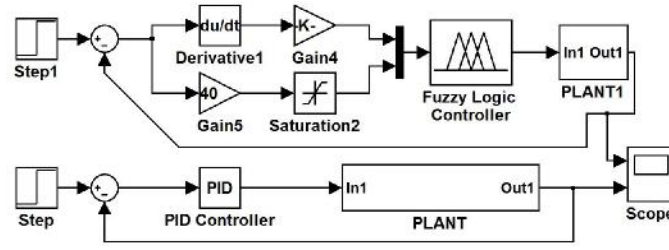
Fig. 3. PID and Fuzzy Logic Controller

2.3. PID

Proportional-integral-derivative controller (PID controller) is a generic control loop feedback mechanism (controller) widely used in industrial control systems. A PID controller calculates an "error" value as the difference between a measured process variable and a desired set point. The controller attempts to minimize the error by adjusting the process control inputs.

The PID controller calculation (algorithm) involves three separate constant parameters, and is accordingly sometimes called three-term control: the proportional, the integral and derivative values, denoted *P*, *I*, and *D*. Heuristically, these values can be interpreted in terms of time: *P* depends on the *present* error, *I* on the accumulation of *past* errors, and *D* is a prediction of *future* errors, based on current rate of change. The weighted sum of these three actions is used to adjust the process via a control element such as the position of a control valve, a damper, or the power supplied to a heating element[2].

The PID control scheme is named after its three correcting terms, whose sum constitutes the manipulated variable (MV). The proportional, integral, and derivative terms are summed to calculate the output of the PID controller. Defining $u(t)$ as the controller output, the final form of the PID algorithm is:

$$u(t) = MV(t) = K_p\, e(t) + K_i \int_0^t e(t)\, \mathrm{d}t + K_d\, \frac{\mathrm{d}}{\mathrm{d}t} e(t) \qquad (4)$$

where K_p is proportional gain, a tuning parameter; K_i is integral gain, a tuning parameter; K_d is derivative gain, a tuning parameter; $e(t) = \mathrm{SP} - \mathrm{PV}$ is error; t is time or instantaneous time (the present); τ is variable of integration (takes on values from time 0 to the present t).

PID control was actualized with PID block which located in toolbox. In the block PID proportional, integral and derivative variables entered. PID parameters were found as a result of experimental studies. These values $K_p = 10$, $K_i = 7$, $K_d = 3$.

2.4. Fuzzy Logic Control

In order to use fuzzy logic block, firstly we need to be defined fis editor membership functions and rules. Inputs and output membership functions which was solved the problem and its rules table are also shown in Figure 4, Figure 5 and Figure 6.
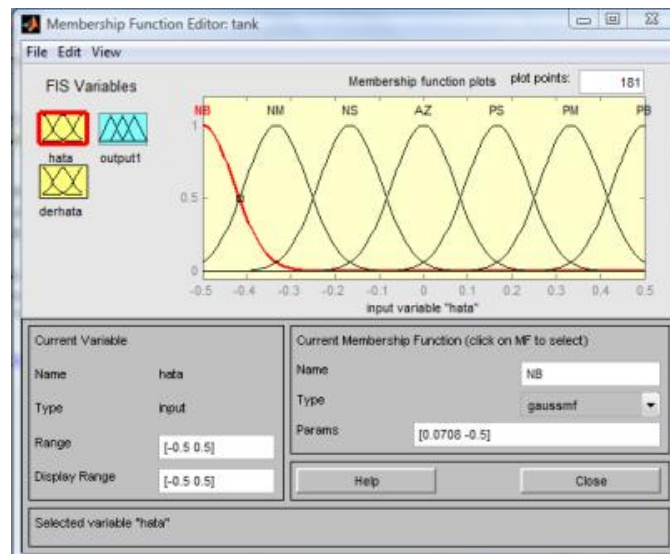
Fig. 4. The membership function of error input
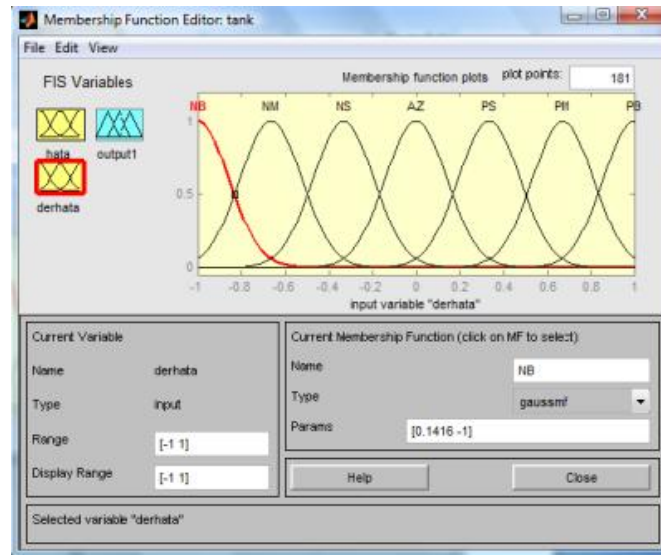
Fig. 5. The membership function of error's derivative input
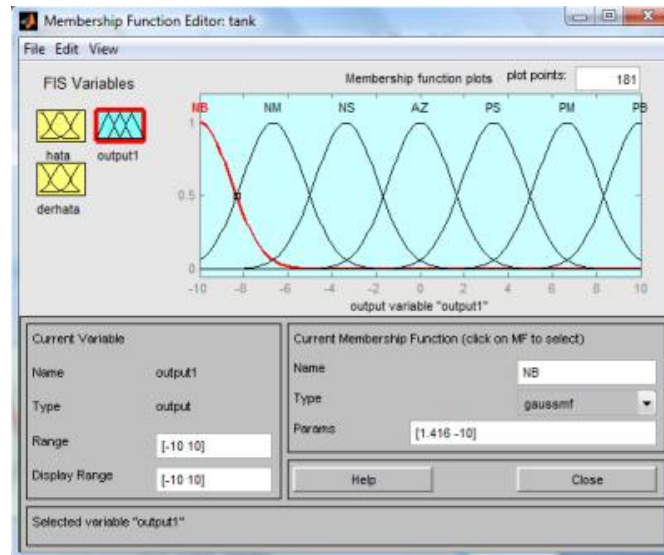
Fig. 6. The membership function of system output

Table 2

Fis editor rule table of cascade tank system

$\dfrac{e}{\dot{e}}$	NB	NM	NS	AZ	PS	PM	PB
NB	NB	NB	NB	NM	NS	NS	AZ
NM	NB	NB	NM	NS	NS	AZ	PS
NS	NB	NM	NS	NS	AZ	PS	PM
AZ	NM	NM	NS	AZ	PS	PM	PM
PS	NM	NS	AZ	PS	PS	PM	PB
PM	NS	AZ	PS	PS	PM	PB	PB
PB	AZ	PS	PS	PM	PB	PB	PB

Where: NB is negative big; NM is negative medium; NS is negative small; AZ is zero; PS is positive small; PM is positive medium; PB is positive big.

Fis editor rules table of system is shown in Table 2. There are seven membership functions of inputs that are shown in the rules table. Error input range varies between -0,5 and 0,5. Input which is derhata, range between -1 and 1. We set the output range of 10 to -10. We used as a method of Defuzzification centroid. Centroid method gives better output for the cascade tank system.

The graphs of both controllers are plotted in Figure 7.
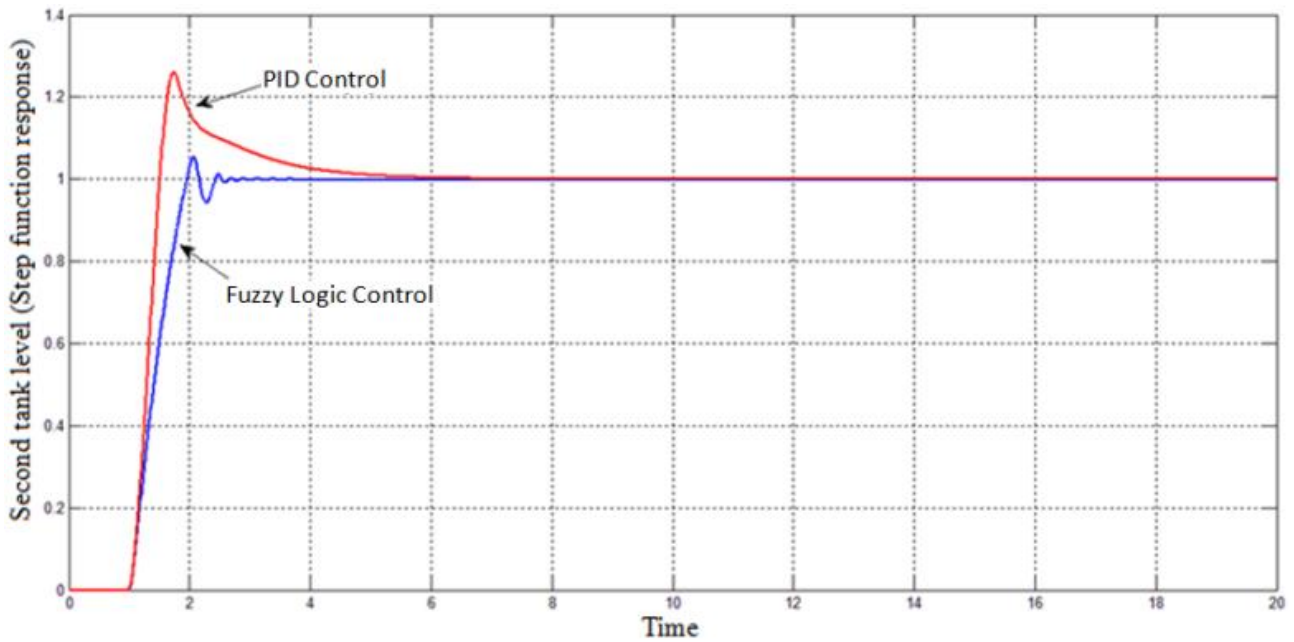
Figure 7: Comparison of PID and Fuzzy Logic Controller outputs

3. Conclusions

PID and fuzzy controller are used for built the controller in order to control the level in the cascade tank system. As a result of, the speed of responses of the level control for fuzzy logic controller is better than pid controller. Hence, it can be conclusion that:
1. The response time of fuzzy logic controller less than the pid controllers.
2. Fuzzy logic controller give the smallest state error.
3. Fuzzy logic controller make less overshoot.
4. Fuzzy logic controllers settling time is less than pid controllers. And output settled the input value as soon as possible.

References

1. **Reznik**. Fuzzy Controllers. Victoria University of Technology, Melbourne, Australia, 1997. -11p.
2. **Araki M**. PID CONTROL, Kyoto University, Japan.
3. **Kuo B., Golnaraghi F., Wiley.** Automatic Control Systems, 8th Edt., 2003.
4. **Franklin G. F., Powell J. D., Naeini A. E.** Feedback Control Systems, Prentice-Hall, 4th Edt, 2002.
5. **Nise, Wiley.** Control Systems Engineering, 4th Edt., 2004.
6. **Ogata K.** Modern Control Engineering, 3th Edt., Prentice-Hall, 1997.
7. **Dorf R. C., Bishop R. H.** Modern Control Systems, Prentice-Hall, 10th Edt., 2005.
8. **Özdaş N., Dinibütün T., Kuzucu A.** Otomatik Kontrol, İTÜ Matbaası, 1989.

Design of Control System for a Quadrotor Flight Vehicle

R. Bayır*, A. E. Coşgun**

*Karabuk University, Technology Faculty, Dept. of Mechatronics Engr. 78000, Karabuk, Turkey, E mail: rbayir@karabuk.edu.tr
**Karabuk University, Technology Faculty, Dept. of Mechatronics Engr. 78000, Karabuk, Turkey, E mail: atilcosgun@karabuk.edu.tr

Abstract

In this study, for a quadrotor's stability has been designed control system. Mechanic and software design of the machine was actualized for this purpose. To do this project four brushless motors have been used. Each motor has been controlled by an ESC(Electronic Speed Controller). The ESCs have been controlled by the microcontroller with Proportional Integral Derivative (PID) controller. To keep the quadrotor flight vehicle stable in the air a gyroscope, an accelerometer sensor and a barometer sensor have been used so that the microcontroller could detect undesired changes in the quadrotor flight vehicle's angle and adjust each motor speed accordingly to the variation. For the entire contraption's energy consumption has been used a lithium polymer battery. The performance of the system was proved in the laboratory. Thanks to PID controller, a good performance was obtained indoor areas.
KEY WORDS: *quadrocopter, quadrotor, flying robot, uav, pid controller.*

1. Introduction

The helicopter is one of the most complex flying machines due to its versatility and maneuverability to perform many types of tasks. Classical helicopters are usually equipped with a main rotor and a tail rotor. However, other types exist which use a twin rotor[1]. In order to eliminate the problem of versatility and maneuverability has been developed quadrotors which have four rotors to generate lift and propulsion. Its early designs in the 1920s and 1930s suffered from poor performance and lack of stability due to limited controls and system integrations. Today with advanced electronics, accurate sensors and control system technology these limitations are becoming more a thing of the past, technology today has allowed these systems to grow more and more appealing due to increased stability and payload capacities. To overcome these obstacles, complex integration of various sensors would have to be incorporated to allow this configuration of flight to be successful, the quadrotor [2]. The quadrotor flight vehicle is a kind of flying robot. In literature various quadrotor flying robot systems has been developed to be used in various fields. Many of them to be used for monitoring dangerous or difficult to access areas with a camera and various sensors or these types of robots could also be used for rescue operations and preventing secondary disasters [3]. In addition to, there are many studies example of its in academic and commercial field to research and development for quadrotor flying robots. In 1922, Dr. George de Bothezat had formed first quad copter vehicle. It has a similar like a X shape platform and there were four motor end of the four edges X shape platform. Thrust and yaw control had been provided with two small propeller could be adjusted its slope.

The first miniature quadrotor flying robot was designed by Area Fifty-One Technologies Company the name of Roswell Flyer in 1996. After this development, Draganflyer four-rotor aircraft was manufactured by Draganfly Company also Engager and Gyrosaucer four-rotor aircraft was manufactured by Keyence Company. Claire J. Tomlin and his team had been actualized an autonomous rotorcraft for multi-agent control project. The aim of this project that multi agent control for between the multiple four-rotor aircrafts with provided a coordination. Especially, they want to observed about collision, obstacle avoidance, path determination, and task setting [4]. Steven L. Waslander and his team had been actualized a Reinforcement Learning control for quadrotor flying robot [5]. Also, there was a study in the Salzburg University about quadrotor flying robot. They studied on about high altitude communication, real time and online system of flying robot [6]. In addition to, Handford and his team in their study they had used an 8-bit PIC-based processing unit and Micro Electro Mechanical Systems (MEMS) based sensors to detect undesired changes in the quadrotor flight vehicle's angle. They had used Proportional Integral (PI) control method for stability of quadrotor flying robot [7]. And to keep quadrotor flying robot balanced and stable Harmel and his team was tried a backstepping control method and they had designed a simulation program to actualized for this purpose [8]. Also, in the literature there is a different study which was actualized by Bouabdallah and his team. They had tried two control method at the same time Proportional Integral Derivative (PID) and Linear Quadratic(LQ) control on quadrotor flying robot. They had been actualized various simulation of it and according to their observation they had been used their data on OS4 quadrotor flying robot [9].There are a lot of study about quadrotor flying robot in Turkey too. One of them has been actualized by Mehmet Önder Efe and his team in TOBB University of Economics and Technology. The name of their project was "Rotary Wing". They have studied on about quadrotor flying robot to visual-based control, target tracking application and autonomous flight [10]. In another quadrotor study, Zehra Ceren and Erdinç Altuğ has actualized a visual-servo based control for flying robot [11].

In this paper, presents an design of control system for a quadrotor flight vehicle. A mechanical and software design of the machine have been actualized for this purpose. Quadrocopters has to have some sort of sensors to keep track of how its moving and for this project has been used an accelerometer, a gyroscope and a barometer sensor. For the quadrotor has been used a closed controlled loop to ensure its stability and manoeuvrability.

1.1. Quadrocopter

A quadrocopter is a rotorcraft machine that has four (hence quadro) rotors to generate lift and propulsion. In a typical quadrocopter design the propellers are located at the same distances from each other on a cross. Quadrocopters have different frame designs and naturally there are machines with more rotors, such as hexacopters (six rotors) or octocopters (eight rotors). Quadrocopters usually falls under the category UAV – Unmanned Aerial Vehicle. They can be used in a wide range of applications such as rescue operations, espionage, security surveillance and terrain mapping or just for fun. Quadrocopters are not commercially used in a great extent, but the ones operating are often used for photographing and filming from above. Flight principles of the vehicle is shown in Fig. 1 and the motors are numbered as No.1, No.2, No.3 and No.4. Lift is obtained from the total force by all motors. The moment around X axis is generated by the rotational speed difference between No. 2 and No. 4 motors, so as the attitude angle around X axis of the airframe changes, the thrust is converted into the component force on Y direction. Using the same principle, by using the rotational speed difference between No. 1 and No. 3 motors, it is possible to control the X direction of the airframe. Moreover, the No. 1 and No. 3 rotors are rotating clockwise while the No. 2 and No. 4 rotors are rotating in the opposite direction (counter-clockwise). The rotation around Z axis (Yaw) of the airframe is controlled by counterbalancing the moment. To keep it desired position has been tuned rotational speed of every rotor.
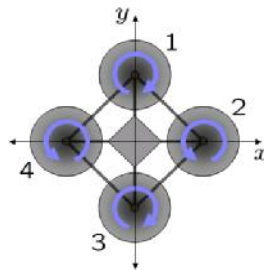
Fig. 1. Flight principles of the vehicle

2. Material and Method

In this study, quadrotor flight vehicle has been developed to keep it stable in the air. Mechanical and software design of system has been developed with considering the system constraints. The system diagram of quadrotor flight vehicle is shown in Fig. 2
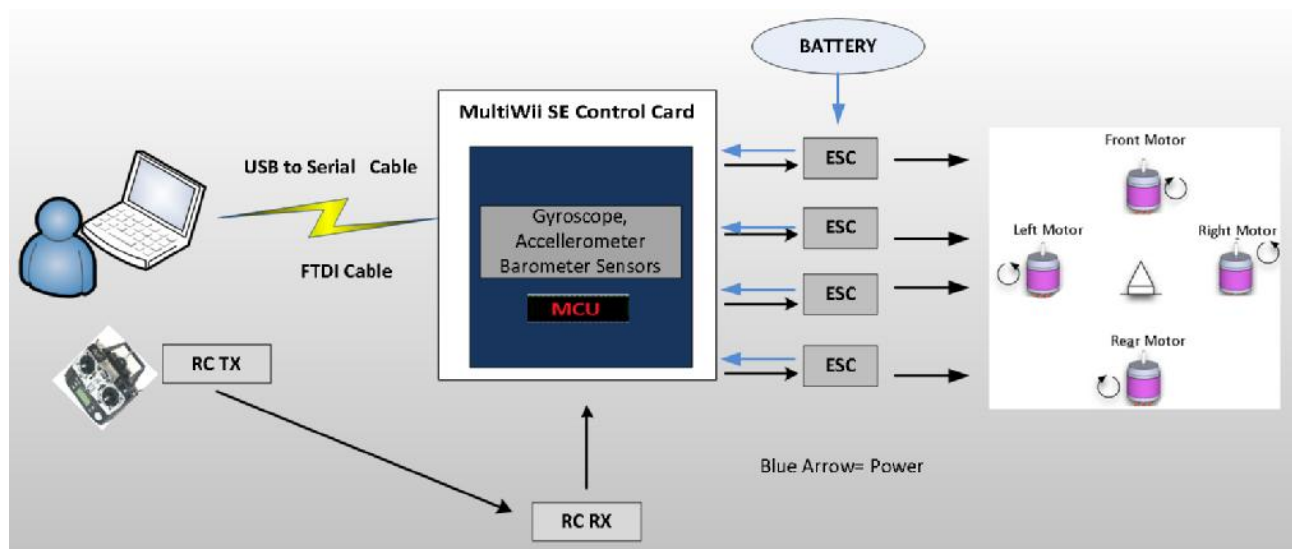
Fig. 2. The Quadrotor Blok Diagram

The specification of quadrotor is shown in Table 1. There is a six- channel radio control receiver module for quadrotor flight vehicle, the quadrotor flight vehicle has 1,700mAH 3-cell lithium polymer battery. Its hovering flight

time is about 15 min. without payload. To keep the quadrotor flight vehicle stable in the air has been used gyro sensor, accelerometer sensor and barometer sensor. Also there are four ESC to control each motor. The ESCs have been controlled by the microcontroller.

Table1

The specification of quadrotor

Parameter	Value
Maximum Diameter	570 mm
Total mass (with battery)	750 g
Payload	1100 g to 2200 g – depending on power system
Motor	GUEC GM-412S – Brushless Motor – 960 RPM / Volt
Battery	Li-Po 3S 11.1 V 1750 A
ESC	GUEC GE-183 – 18A
Gyro	ITG3200 Gyro Module – 16-bit ADC
Accelerometer	BMA180 Accelerometer Mod – 14-bit ADC
Barometer	Bosch BMP085 – Measuring range 300 to 1100 hPa
Micro controller	ATMega 328P

The quadrotor flight vehicle design consists of a carbon fiber airframe, so it has a light and strong body. The lift results from four brushless motor, and by using a special driver, the maximum speed reaches about 6720 rpm. The complete vehicle is shown in Fig. 3.

Fig. 3. The Quadrotor Flying Vehicle

The control software is implemented in Multiwii SE control card in order to stable flight of Quadrotor Flight Vehicle. It is based on Atmel's ATMega 328P microcontroller that is shown in Fig. 4. The microcontroller could detect undesired changes in the quadrotor flight vehicle's angle and adjust each motor speed accordingly to desired set referans point.
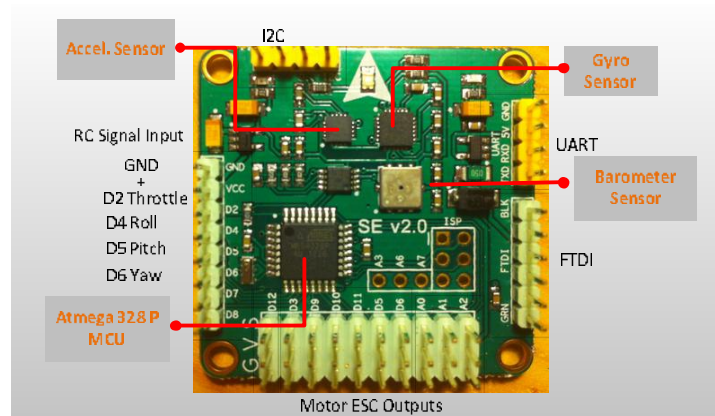
Fig. 4. Multiwii SE Control Card

2.1. Experimental Study

In order to observing of changes motor speed, airframe angels and PID values has been used a graphical user interface (GUI) that had been prepared with "Projessing" program. The GUI of quadrotor flight vehicle is shown in Fig. 5.
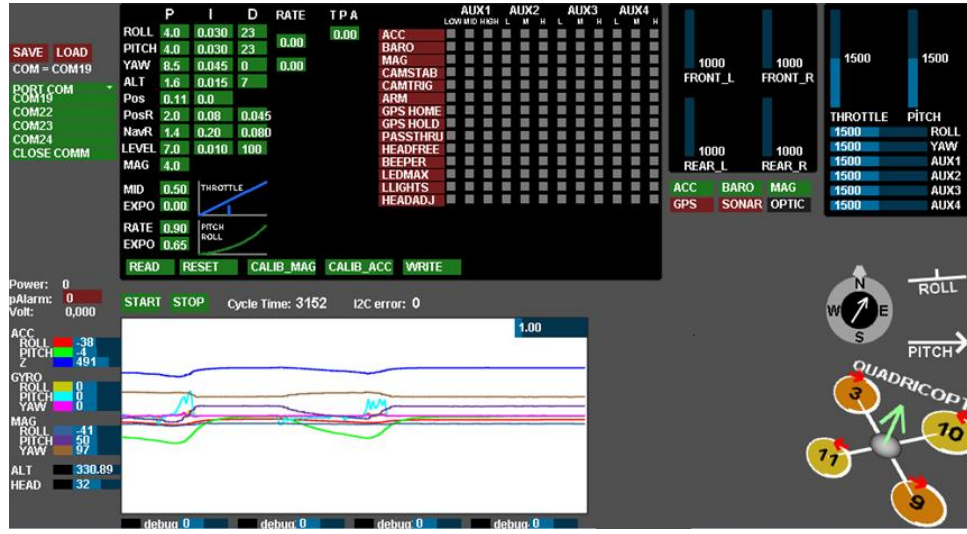
Fig. 5. The GUI of quadrotor flight vehicle

In this study, there has been also observed gyro sensor's data in the matlab/m-file to check the accuracy of it. There are gyro sensor's three data in Fig. 6. Each of them belong to result of quadrotor flight vehicle's movement in X, Y and Z axis.

a   b   c
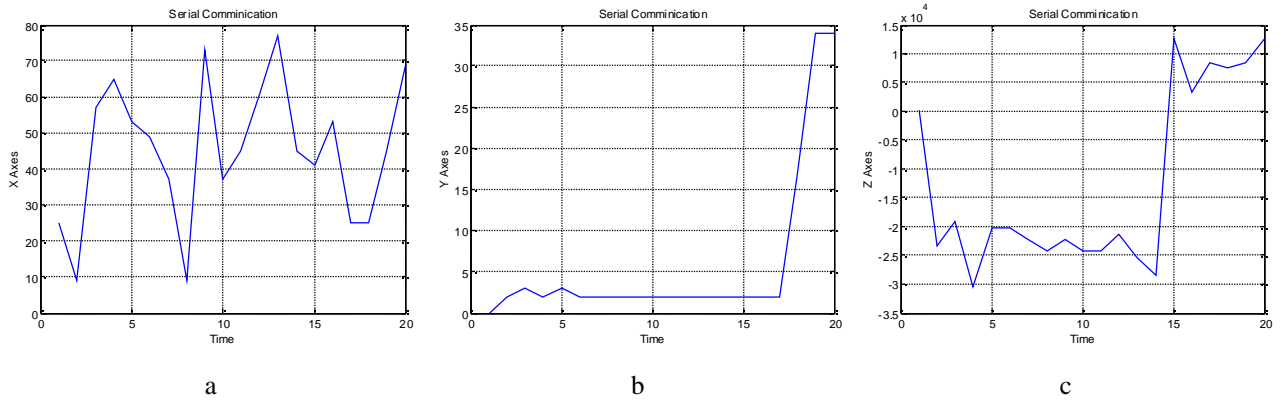
Fig. 6. The 's Data In the Matlab/M-file: a – roll test; b – pitch test; c – yaw test

In order to movement of quadrotor flight vehicle as stable , the internal PID algorithm has been applied by using gyro sensor. The PID algorithm in the controller has provided PWM to maintain a constant RPM. It has also provided optimum response and settling time. The PID controller is a closed-loop feedback system which will output a control signal u and receive feedback from the gyro sensor. The controller then calculated the difference between the desired position orientation and the current position orientation and adjusts u accordingly. The equation for a PID controller is as follows:

$$u(t) = K_p\, e(t) + K_i \int_0^t e(t)\, \mathrm{d}t + K_d\, \frac{\mathrm{d}}{\mathrm{d}t} e(t) \tag{1}$$

where: K_p is proportional gain, a tuning parameter; K_i is integral gain, a tuning parameter; K_d is derivative gain, a tuning parameter; $e(t) = ed(t) - ea(t)$ is error ($ed(t)$ is desired condition and $ea(t)$ is actual (measured) condition); t is time or instantaneous time (the present); τ is variable of integration (takes on values from time 0 to the present t).

In order to obtain appropriate PID values has been used manuel tune method. For manuel tunning K_i and K_d have been set to zero, and K_p has been changed until the system oscillates. From there, it has been set to one half that value. I has been then increased to reduce settling time without causing instability. Finally, D has been increased until the overshoot is minimized without over damping the system.

3. Conclusions

In this study control and design of a quadrotor flight vehicle system has been actualized. In order to the keep it stable in the air, the internal PID algorithm has been applied. Quadrotor has been worked well, when find appropriate PID values to the system controller. Although there are some errors of sensors' data, it has been solved with giving some delaying sampling time. PID has the potential of being a good base for the stability part of a complete quadrotor. It is flexible enough to be able to cope with inputs from more sensors and can be used in maneuvering a quadrotor.

In future, it is planned that quadrotor flight vehicle will most probably have to be stabled with additional sensors such as IR, GPS and UV. Also, by means of GPS module, automatically it would be directed the desired position. In addition to software revisions will be necessary for more stable flight. It is planned that developed system will be used by the security forces to outdoor monitoring with a camera.

Acknowledgment

References

1. **Castillo P., Dzul A., Lozano R.** Modeling and Control of Mini-Flying Machines, Berlin: Springer, 2005.
2. **Basta P. O.** Quad Copter Flight. Electrical Engineering, California State University, Northridge, May 2012.
3. **Nonami K., Kendoul F., Suzuki S., Wang W.** & **Nakazawa D.** Autonomous Flying Robots-Unmanned Aerial Vehicles and Micro Aerial Vehicles. Springer,2010.
4. **Hoffmann G., Rajnarayan D. G., Waslander S. L., Dostal D., Jang J. S.** and **Tomlin C. J.** The Standford Testbed of Autonomous Rotorcraft for Multi-Agent Control (STARMAC). 23rd Digital Avionics Systems Conference, 2004.
5. **Waslander S. L., Hoffmann G., Jang J. S.** and **Tomlin C. J.** Multi-Agent X4-Flyer Testbed Control Design: Integral Sliding Mode vs. Reinforcement Learning. IEEE/RSJ International Conference on Intelligent Robots and Systems, 2005.
6. The JAviator Project, http://javiator.cs.uni-salzburg.at/ (February 2011).
7. **Hanford S. D., Long L. N.** and **Horn J. F.** A Small Semi-Autonomous Rotary-Wing Unmanned Air Vehicle (UAV). American Institute of Aeronautics and Astronautics, Infotech@Aerospace Conference, 2005.
8. **Hamel T., Mahony R., Lozano R.** and **Ostrowski J.** Dynamic Modelling and Configuration Stbilization for an X4-Flyer. 15th IFAC Triennial World Congress, Barcelona, Spain, 2002.
9. **Bouabdallah S., Noth A.** and **Siegwart R.** PID vs LQ Control Techniques Applied to an Indoor Micro Quadrotor. Proc. of 2004 IEEE/RSJ Int. Conf. on. Intelligent Robots and Systems, Japan, 2004.
10. Dönerkanat Projesi, http://www.donerkanat.etu.edu.tr/ (February 2011).
11. **Zehra Ceren, Erdinç Altuğ.** Vision-based Servo Control of a Quadrotor Air Vehicle. IEEE International Symposium on Computational Intelligence in Robotics and Automation (CIRA2009), DCC, Daejeon, Korea, Kasım 2009.

Thermo-Stable Steels Welded Joints Microstructure and Properties of the Heat-Affected Zone Metal

Z. Bazaras*, B. Timofeev**, N. Vasileva***

*Kaunas University of Technology, Kestucio 27, 44312, Kaunas, Lithuania, E-mail: Zilvinas.Bazaras@ktu.lt
**Saint Petersburg State Polytechnic University, St. Petersburg, Russia, E-mail: timbt@rambler.ru
***Central Research Institute of Structural Materials "Prometey", 49 Shpalernaya str., St. Petersburg, Russia, E-mail: mail@crism.ru

Abstract

Heat resistant Cr-Mo and Cr-Mo-V steels welded joints heat-affected zone microstructure is presented in the paper. It is shown, that these steels have high liability to brittle fracture of the heat-affected zone metal because of age hardening at the stage of heating. Due to the optimum welding technology choice age hardening effect can be considerably reduced.
KEY WORDS: *thermo-stable steels, welded joints, heat-affected zone, microstructure, age hardening, embrittlement.*

1. Introduction

In reliable work maintenance of the energy installations, both on thermal, and nuclear stations, belongs to welded joints. During the operation various by character, place and time damages of the welded joints from thermo stable steels are observed [1, 2]. It is known, that welded joint consists of three zones: base (welded) metal, welded joint and heat-affected zone. Structure and properties of each zone are various. Thus, in the heat-affected zone there are 5 areas with different structure and properties. Most steels during the fusion welding have two areas of this zone (overheating and ageing areas) which can have the greatest properties distinction against base metal that is due to the influence of the welding thermal and deformation cycle on the material. Depending on the welding method and welding conditions these structures can be considerably different (Fig. 1). Thus, during the welding of the thermostable, chromium and molybdenum alloyed, steels hardness changes at the heat-affected zone and as a result raised liability to brittle fracture of the metal during the age hardening is observed. The purpose of this paper is such damages reasons detection and recommendation of the technological conditions of their elimination or minimization.

$\times 100$

a

$\times 500$

b
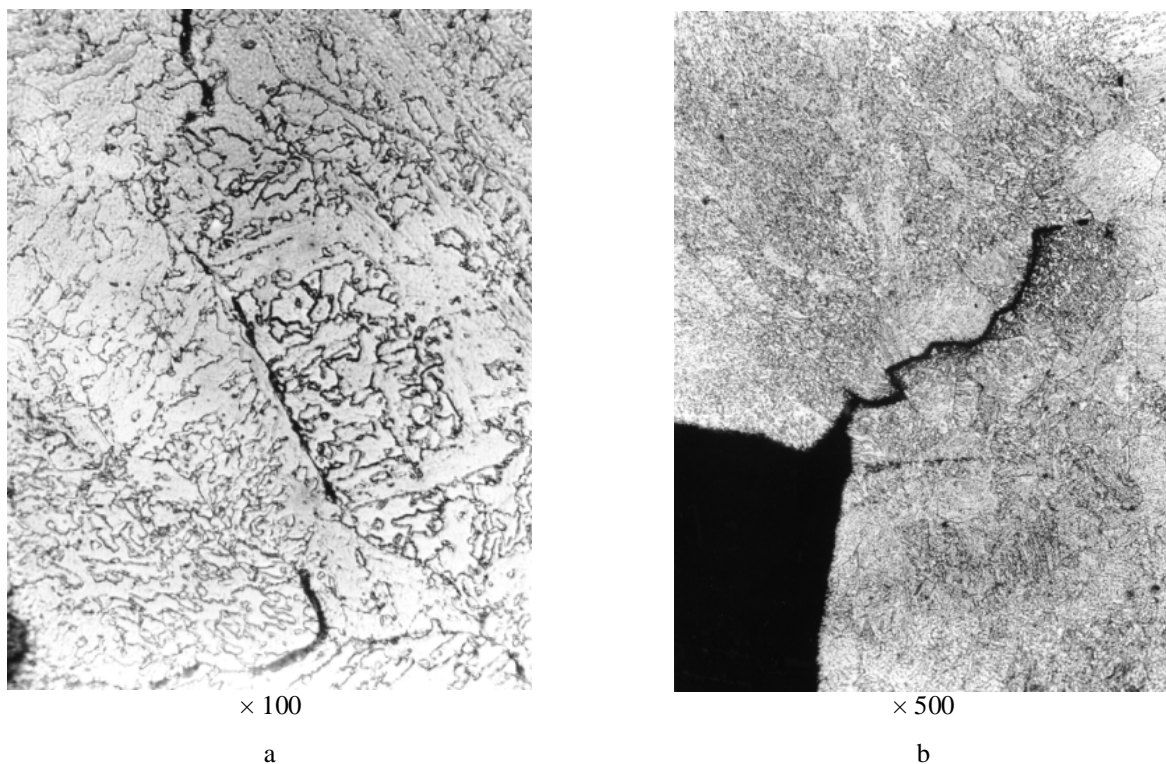
Fig. 1. Typical damages of the welded joints heat-affected zone metal: a – steel 1Cr2Mo heat-affected zone microstructure (hand electric arc welding: $V_{heat} = 200°C/hour$, $T_{temp} = 700°C$); b – steel 15Cr2MoVA heat-affected zone microstructure ($T_{heat} = 300\text{-}50°C$, $V_{heating} = 100°C/hour$, $T_{tempering} = 670°C$)

2. Research technique

For the heat-affected zone hardening effect estimation plates from steels type 15Cr2MoVA and 1Cr2Mo were undergo building-up in one pass by electrodes type N-6 with tempering at 150-200°C and 300-350°C. After tempering plates have cut across the joint on templates and Vickers hardness is measured at 10 kg loading. In each case average hardness value was accepted using 6-10 measurement. Then specimens were heating in the furnace up to the temperature of 400-750°C with constant heating speed (25, 50, 100 and 200°C/hour). At set temperature specimens took out from the furnace and measured Vickers hardness after cooling. Besides, hardness measurement were made of the welded joints heat-affected zone both steels after various tempering temperatures and different curing times that has allowed to define optimum heat treatment conditions after welding for steels type 1Cr2Mo and 15Cr2MoVA welded joints subject to the age hardening effect minimization.

3. Research results

Measurement results shows, that the effect appears already at heating. Submitted data on figure 1 shows, that heating speeds of the age hardening heat-affected zone metal influence is ambiguous. At constant heating speed hardness grows up to the certain temperature, and then it is reduced, such character is similar to hardness change in the course of time at isothermal ageing and stipulated by dispersed secondary phases precipitation at first (age hardening), and then their coagulation and matrix softening. The higher heating speed, the higher maximal hardness temperature is.

a   b
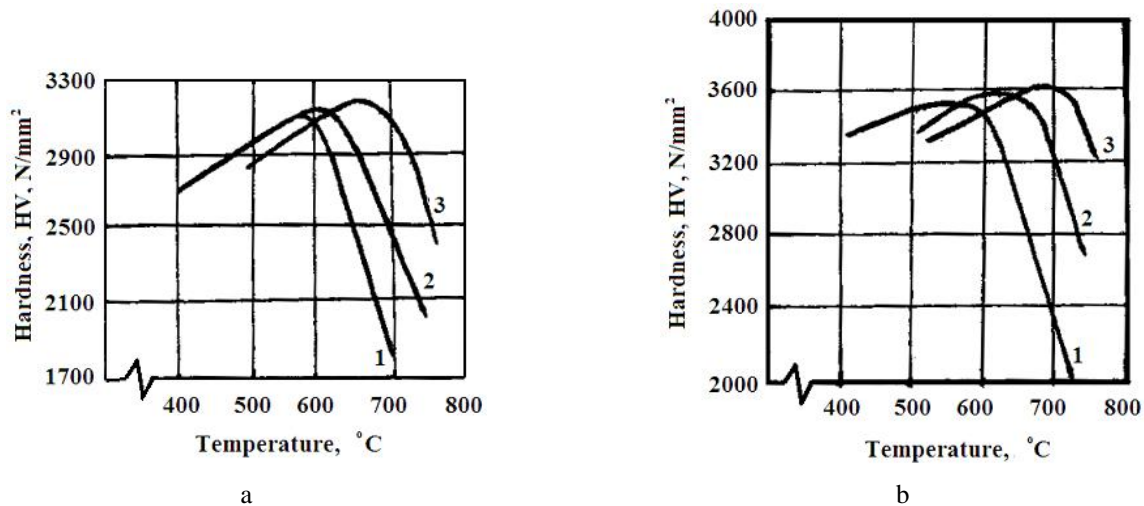
Fig. 2.   Hardness change of the welded joints heat-affected zone metal of steels type 1Cr2Mo (a) and 15Cr2MoVA (b) during heating to the set temperature with constant speed 10°C/hour (1), 100°C/hour (2) and 200°C/hour (3)

The further retention results in graceful hardness decrease (over ageing). Hardness changes analysis of the fine structure, anodic deposit chemical and phase composition has shown that solidification in researched welded joints is connected with decomposition of the supersaturated solid solution and with precipitation dispersed vanadium and molybdenum carbides. Softening during the curing time increase is caused by development of carbide coagulation. For comparison convenience of the welded joints by tendency to dispersion hardening in various factors dependence kinetic hardening curves at different temperatures have been generalized in function of Larson-Miller temperature-time parameter [1, 3]. It is shown, that an arrangement of dispersion hardening areas on a scale of temperature and time and hardening degree depend on contents and thermal stability of the strengthening carbide phases. Under identical temperature-time conditions of ageing the hardening effect of the welded joints researched steels appears differently. In values interval of the temperature-time parameter applicable to the tempering conditions after welding, the greatest propensity show the steels, alloyed by vanadium and molybdenum. In welded joints Cr-Mo thermo-stable steels with the molybdenum up to 1% after tempering dispersion hardening isn't appears practically.

Tempering temperature and duration should be accepted not only with the final welded joint properties level, but also with an opportunity of crack formation during the heat treatment. From the point of the metal level of properties final maintenance it is important to maintain only the certain size of tempering temperature-time parameter (with indifference at the expense of heating temperature or time), from the point of the crack formation prevention during tempering it is more preferable to reach the required size of parameter due to rise in tempering temperature.

It is effective to increase welded joints resistance against brittle failure during the heat treatment use multilayer welding at conditions providing prevalence of the disorientation fine-grained recrystallization structure. For the last layer structure refinement in the heat affected zone it is expedient to make annealing weld.

4. Conclusions

1. The dispersion hardening determining role in occurrence of the brittle cracks in the heat affected zone is established.
2. Dispersion hardening degree essentially depends on the welding conditions. Preheating temperature reduction and welding heat input is amplifying hardening. At the same time excessively high preheating reduces resistance of the cold brittleness. For multipass joints hardening effect is decay during the recrystallization of the heat affected zone metal dependent upon the heat of the following layers.
3. From the point of welded joints resistance against brittle failure increase welded joints heat treatment requirements are determined. For the crack formation prevention during the tempering it is necessary to increase tempering temperature.

Acknowledgements

References

1. **Shron R. Z.** Thermally stable steels welded joints strength and ductility of the power installations. Abstract of a thesis, 1976
2. **Zemzin V. N., Shron R. Z.** Welded joints properties and heat treatment. Mechanical engineering, 1978, 367 p.
3. **Shron R. Z., Nikanorova N. I.** Thermally stable steels welded joints age-hardening of the steels type 12Cr1MoV and 15Cr1MoV. Automatic welding. 1973, № 4.

Orientation in Urban or Semi-Urban Environment Using Segmentation of Homogeneous Regions

A. Česnulevičius*, A. Bartulis**, O. Fiodorova***, V. Sinkevičius****, A. Tautkus*****

*Kaunas University of Technology, S.Daukanto str. 12, 35212 Panevėžys, Lithuania, E-mail: aurimas.cesnulevicius@ktu.lt
**Kaunas University of Technology, S.Daukanto str. 12, 35212 Panevėžys, Lithuania, E-mail: alfredas.bartulis@ktu.lt
***Kaunas University of Technology, S.Daukanto str. 12, 35212 Panevėžys, Lithuania, E-mail: olga.fiodorova@ktu.lt
****Kaunas University of Technology, S.Daukanto str. 12, 35212 Panevėžys, Lithuania, E-mail: vytenis.sinkevicius@ktu.lt
*****Kaunas University of Technology, S.Daukanto str. 12, 35212 Panevėžys, Lithuania, E-mail: arunas.tautkus@ktu.lt

Abstract

The main issue in all existing unmanned transport vehicles (UTV) is their orientation in the immediate environment. UTV "*gets lost*" in urban or semi-urban environment, which contains no pre-installed guiding devices (optical or radio beacons, barcode labels, etc.). However, such an environment is full of typical large-area objects, such as sidewalks, road pavement, lawns, bushes, trees, road signs, etc. They feature pronounced properties, such as texture and colour. Such homogeneous regions can contribute in UTV orientation and navigation tasks. As computational resources in unmanned vehicles are usually limited, image processing algorithms need to be as simple as possible. Image quality depends on the brightness of light, its direction, shadows cast by other objects, and condition of the objects being analysed (dry, wet, dusty, etc.). This research analyses peculiarities of motion in urban and semi-urban environment using computer vision. The study also solves image segmentation task using colour characteristics of homogeneous regions.
KEY WORDS: *computer vision, urban and semi-urban environment, unmanned vehicle transport, homogeneous regions.*

1. Introduction

Image recognition systems can be considered as one of the main parts of motion planning systems in mobile robots and other unmanned transport vehicles. Motion planning in urban environment involves solving of multiple tasks: detection of road surface and determination of movement direction, routing, identification of stationary objects, identification and tracking of mobile objects. These issues are usually encountered in the process of enhancement of driver assistance systems or development of mobile robot control programs. Such video assistance systems can be implemented in, for example, vehicles for people with disabilities. Pedestrians with vision impairment could benefit from it too.

Compared with indoor environments, motion outdoors presents additional issues, such as brightness of the light and its direction, shadows, and condition of objects (dry, wet, dusty, etc.). Consequently, image processing algorithms being developed need to be simple, adaptive, and suitable to react to all the effects mentioned.

Movement surfaces in urban or semi-urban environments can be usually considered as homogeneous regions. Because of this, colours are very efficient parameters for segmentation of these regions.

Colour identification is one of the options for robot movement planning in urban or semi-urban environments. The following guides can be used in movement planning: road pavement (grey) with road marks (white), sidewalks (grey) with texture elements (dark grey), lawns and bushes (green), parterres (predominantly green), road signs (different primary colours). In addition, some of these guides feature standard shape.

The objective of this research is to assign objects to either one of two classes: "*road*" or "*off-road*"; this will facilitate UTV in planning its movement towards the destination. Results of the study will be used in development of the computer vision system in mobile robot designed for "Robots Intellect" competition.

2. Related works

Diversity of objects in the environment makes road object segmentation a complex task. Moreover, UTV has very limited time for decision making. Therefore, segmentation task is usually simplified down to detection of just two segments: "*road*" or "*off-road.*" Study [1] assumes that initial position of the UTV is on the "*road*"; this allows using colour characteristics of the fragment in front of the UTV to detect class "*road*" segment. Analysis is based on how the intensities of RGB components in a fragment image are distributed comparing with green colour. Further, this colour distribution is used as a pattern to recognize the class "*road*" objects. Low green colour intensity indicates that object is attributed to the class "*road.*" The method offered contributes in minimizing effects caused by object shadows.

The other option of searching for class "*road*" objects is the elimination of image segments that can be attributed to the grass class ("*off-road*" object). This task can be easily realised if the surface of grass plots is homogeneous. Analysis of colour dispersion in the HSI colour model of the image both vertically and horizontally

allows identification of the grass segment [2]. However, this method is hardly applicable for non-homogeneous greeneries (e.g., mowed lawn of the football field).

One more option to detect required segments is by using local and global dominant colour histograms (DCH) [3]. However, this method is sensitive to shadows cast by nearby objects, and its application requires several images of the same area illuminated with different intensities and directions.

Method of conditional random field (CRF) models [4] allows detecting the following object classes within an image: sky, road, marking line, trees and bushes, grass, buildings, free areas and vehicles. However, the study mentioned does not cover shadow neutralization and, according to examples provided, is more intended for highway traffic.

Methods of UTV control are usually tested during competitions [5]. This study also uses a vision-based colour segmentation algorithm suitable for urban environments. The method divides the image in front of a camera into areas of drivable and non-drivable terrain. Two areas from the front view are used for orientation. Image properties are extracted from the smaller area, while identification of the road segment uses the larger area. Reliability of the two-area analysis results decreases, when the robot starts driving along the roadside and images of grass by the road appear in the visible area. Moreover, this method usually considers shadows as non-recognized objects.

3. Experiment setup

Experimental image recognition system used for this research was based on the Open Source Computer Vision Library (OpenCV). Hardware of the experimental system consisted of the following: Logitech HD Webcam C525 EER and Olympus SP-590UZ digital camera.

Results of the research are illustrated by 6 selected images (Fig. 1). 3 pictures in the top row were captured using the webcam, while 3 images in the bottom row were shot using the digital camera.

Research involved both RGB (Red-Green-Blue) and HSV (Hue-Saturation-Value) colour models.

Fig. 1. Original pictures

4. Segmentation of homogeneous regions

The research aimed to develop a model for analysis of images from robot movement environment that would be as simple as possible and would require minimum resources.

Basic guides for UTV movement planning were pedestrian footpaths (*"road"* object) and vegetation, such as grass, bushes, and trees (*"off-road"* object). The aim was to find limit values of colour characteristics and use them for detection of both mentioned objects (image segments).

The initial stage did not use image pre-processing. Results of detected areas for class *"road"* and *"off-road"* objects are presented below. Image pixels with HSV parameters Hue = 0-255, Saturation = 0-25, and Value = 10-200 attributed to the class *"road"* object (Fig. 2).

White segments (Fig. 2) represent the class *"road"* object. Images captured by the webcam (upper 3 pictures) have no clear outlines of the class *"road"* object. Lower three pictures from the still camera feature better outlines of the class *"road"* object; however, some incorrect objects (buildings, trees, etc.) are attributed to this class too.

Fig. 3 shows segmentation results obtained by identification of regions with predominantly green colour. Here, pixels with HSV parameters Hue = 40-100, Saturation = 80-255, and Value = 50-255 assigned to the class *"off-road"* object (Fig. 3).

White segments (Fig. 3) represent the class *"off-road"* object. Process of this object identification provides more accurate results, i.e. it allows detecting image segments with certain colour properties.

Figs. 2 and 3 show segmentation results obtained by analysis of all three colour channels (HSV colour model). Fig. 4 shows results for the class *"off-road"* object analysed using thresholding of just one colour channel (Hue). Benefits of this method include possibilities to identify accurate outlines and textures of individual objects. For example, it can be used for UTV orientation and navigation along the edges of footpath tiles. However, this method is not applicable for detecting homogeneous segments in a frame.

To improve segment detection quality, images were processed additionally by colour normalization (Fig. 5-6) and histogram equalization (Fig. 7-8). Segmentation used previous ranges of HSV parameters.

Colour normalization did not significantly improve detection quality of neither class *"road"* object nor class *"off-road"* object.

Method of additional histogram equalization detects smaller objects and sharpens shadows of foreign objects. Compared with colour normalization, histogram equalization contributes to more detailed outlines and textures of individual objects for detection of the class *"road"* objects.
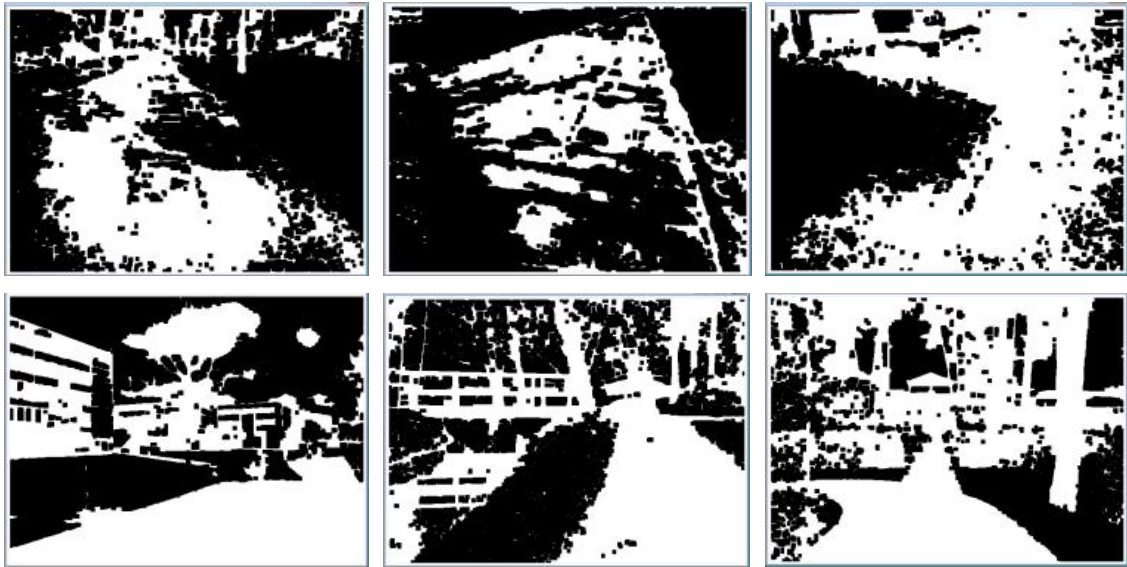
Fig. 2. Results of the class "road" objects analysis
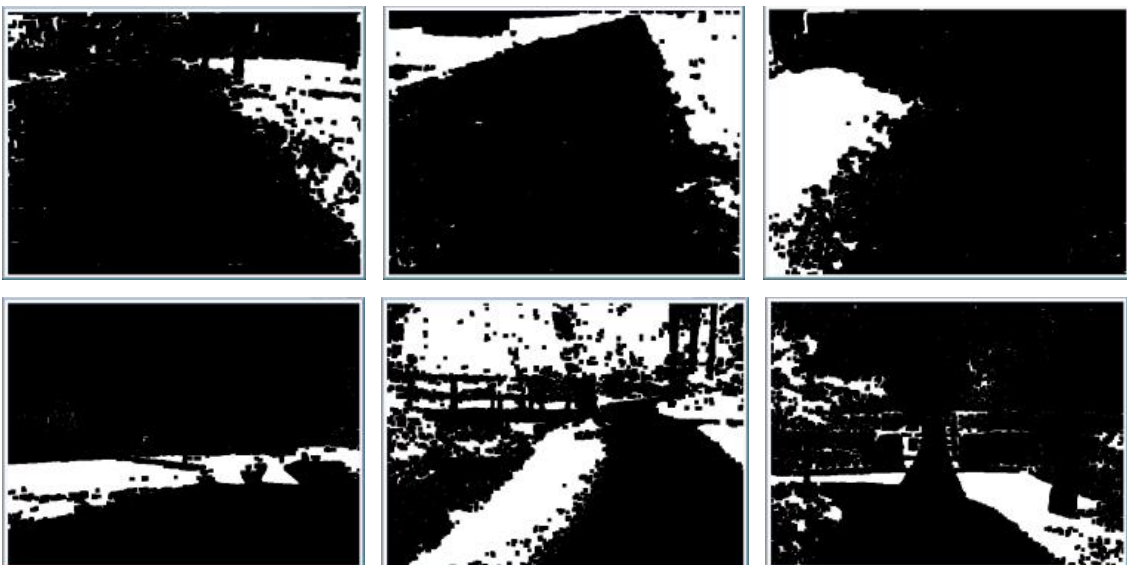
Fig. 3. Results of the class *"off-road"* object analysis
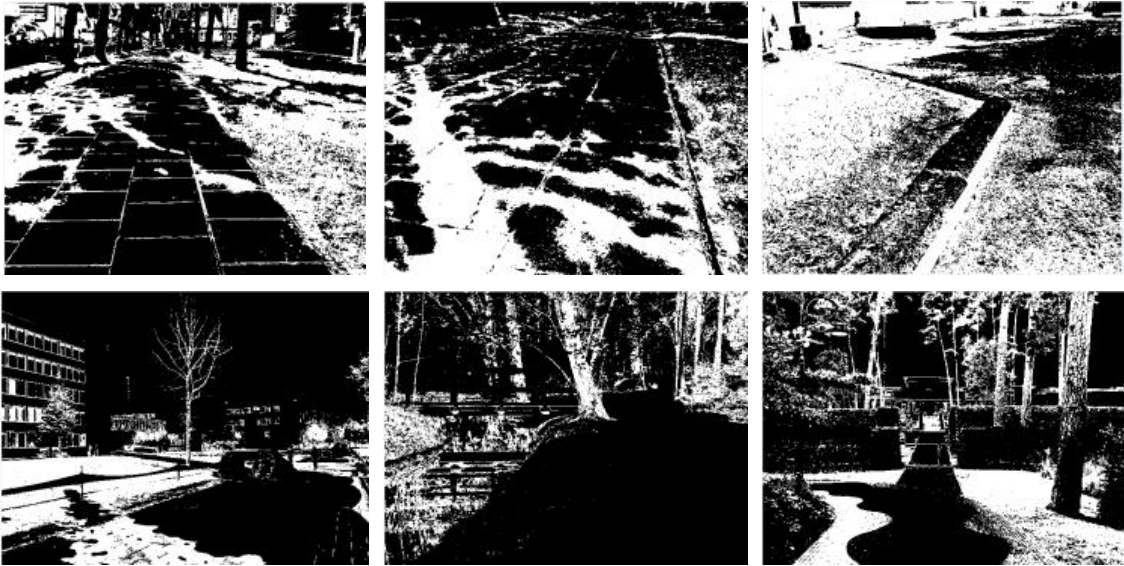
Fig. 4. Results of the class *"off-road"* object analysis after Hue channel thresholding
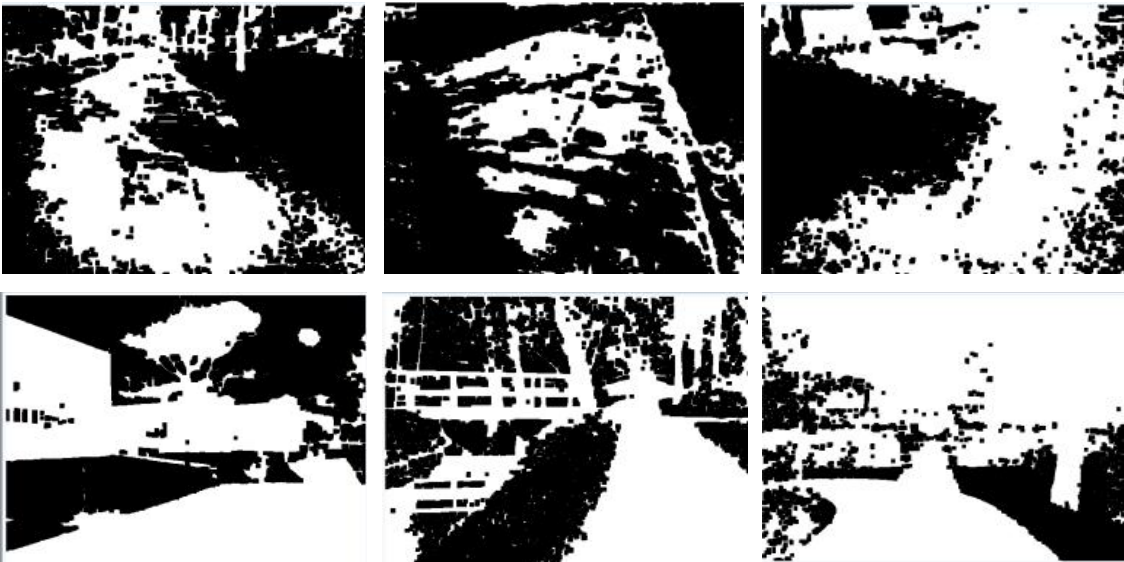
Fig. 5. Results of the class *"road"* object analysis after colours normalization
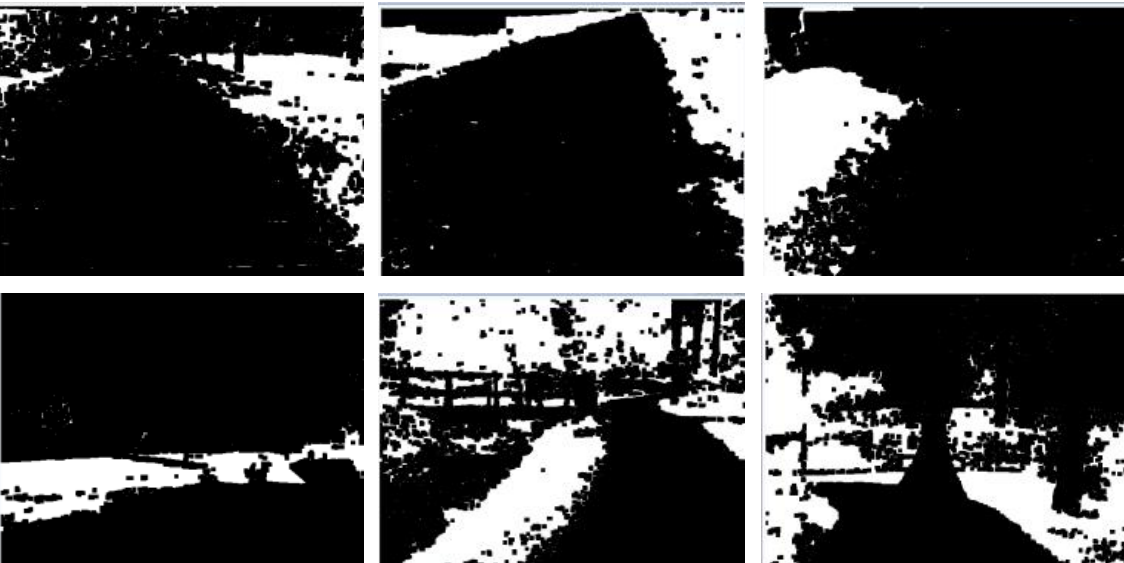
Fig. 6. Results of the class *"off-road"* object analysis after colours normalization
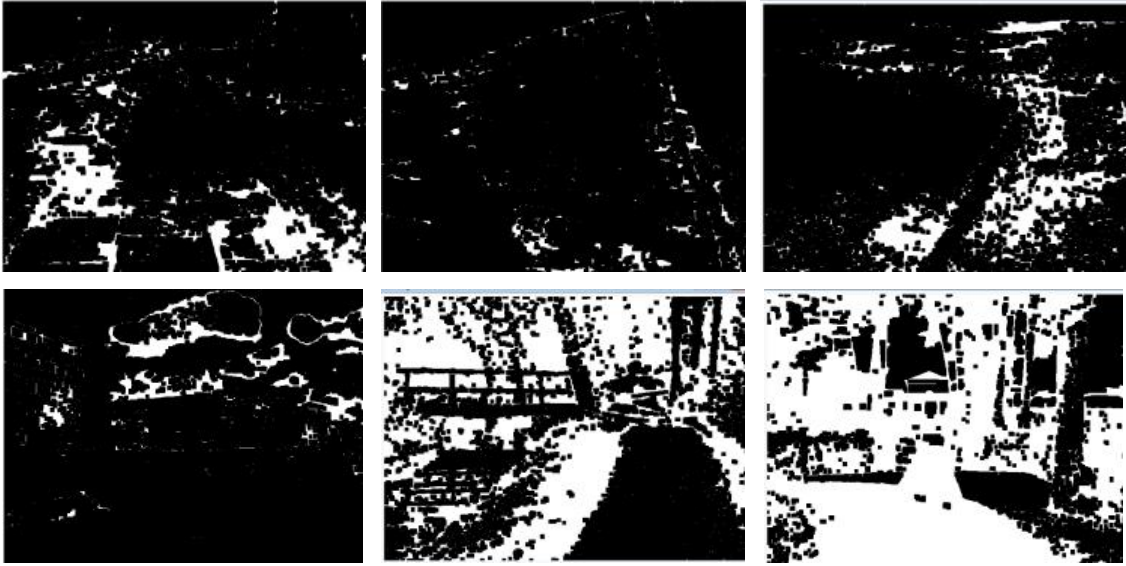
Fig. 7. Results of the class *"road"* object analysis after histogram equalization
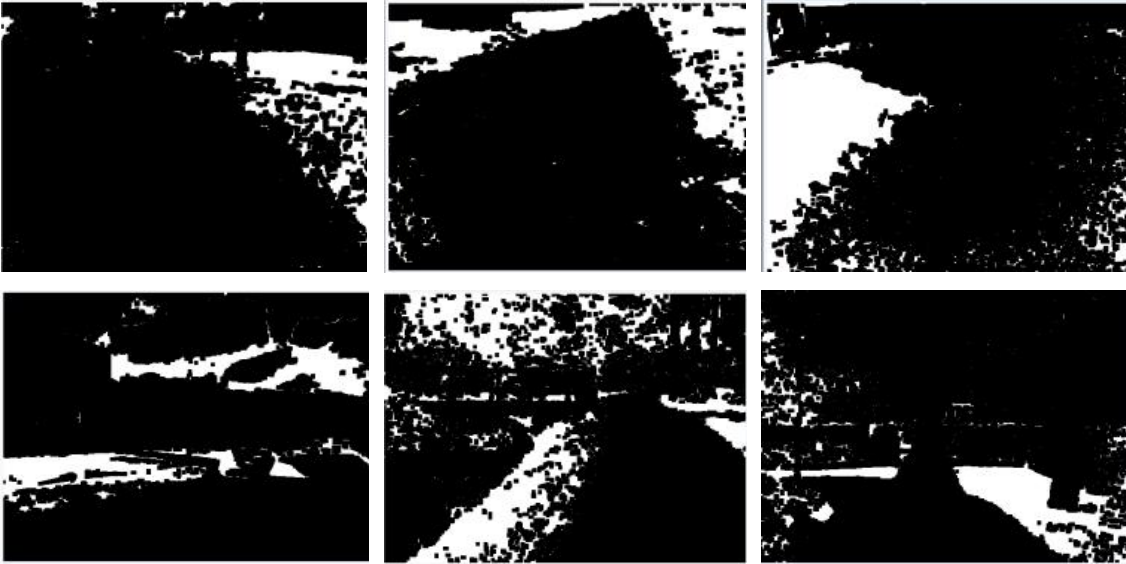
Fig. 8. Results of the class *"off-road"* object after histogram equalization

5. Adaptive segmentation

Previous experiments show that segmentation is particularly sensitive to the brightness of light and shadows from foreign objects. Further experiments involved segment detection method containing no complex calculations but data manipulations only. The purpose of the method is to make a pattern using just part of the whole captured image. This manipulation allows adaptation to the brightness of light in the environment.

It is known in advance that there is a road in front of the robot; this allows attributing objects in the immediate environment to the class *"road."* Image with dimensions *Width×Height* from the video camera is inserted into array $f(x,y,n)$ (Fig. 9a). Index *n* denotes colour as follows: $n = 1$ – Red, $n = 2$ – Green, $n = 3$ – Blue. Trapezium shaped fragment closest to the robot is taken out of the array f and inserted into array $f0$ (Fig. 9b). Base of the trapezium equals to *Width*/2, while the height equals to *Width*/5; horizontal position of the trapezium is selected in such a way that it includes only class *"road"* objects. Influence of the trapezium size and shape on segmentation has not been analysed.

The array $f0(x,y,n)$ is created from the array $f(x,y,n)$ by transferring RGB intensity values of pixels from inside of the trapezium:

$$f0(x, y, n) = \begin{cases} f(x, y, n), & x \text{ and } y \text{ are inside of the trapezium} \\ 255, & x \text{ or } y \text{ are outside of the trapezium} \end{cases} \quad (1)$$

a   b

Fig. 9. Original image *f* (a) and trapezium-shaped image cut-out *f*0 (b)

Array $f0(x, y, n)$ consists of the rage of RGB intensity values corresponding to the class *"road."* Red, green, and blue colour intensity values of a single pixel are denoted as $R0(x, y)$, $G0(x, y)$, and $B0(x, y)$. Values are calculated as follows:

$$\text{for } x = 1 \div \text{Width}, \quad y = 1 \div \text{Height},$$
$$\left.\begin{array}{l} R0(x, y) = f0(x, y, 1) \\ G0(x, y) = f0(x, y, 2) \\ B0(x, y) = f0(x, y, 3) \end{array}\right\} \tag{2}$$

Pattern of pixel colour intensities is created using two 2D 256×256 arrays GR (Green-Red) and GB (Green-Blue). Intensity values are filled in by using the following:

$$\text{for } x = 1 \div \text{Width}, \quad y = 1 \div \text{Height},$$
$$\left.\begin{array}{l} i = G0(x, y) \\ j = R0(x, y) \\ k = B0(x, y) \\ GR(i, j) = GR(i, j) + 1 \\ GB(i, k) = GB(i, k) + 1 \end{array}\right\} \tag{3}$$

Fig. 10 shows contents of arrays GR and GB. Here, each black dot denotes combinations of Green-Red or Green-Blue colour intensities, if any. Otherwise, white colour left instead.
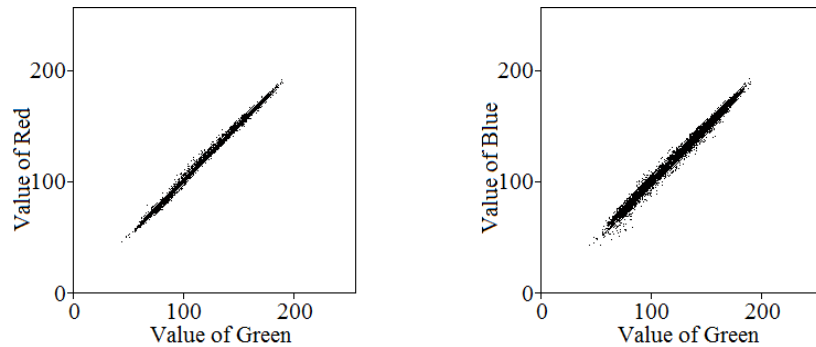
Fig. 10. Contents of pattern arrays of colour intensity combinations

In such a way, arrays GR and GB contain all possible combinations of Green-Blue and Green-Red colour intensities of pixels from inside the trapezium.

To develop a segmented image, an array G of the same size as the array f is created. The whole array $G(x, y)$ is pre-filled with zero values; black colour denotes objects that are not attributed to the class *"road"*.

Then, several simple operations are completed. Consecutive reading of RGB colour intensities of pixels from image array $f(x, y, n)$ takes place. Intensities are attributed to variables i, j and k. A check of whether values from array $GR(i, j)$ and $GB(i, k)$ elements are greater than zero is performed. If this is the case, it means that particular colour combination was detected inside the trapezium. Then maximum intensity of 255 is set to the pixel $G(x, y)$ (detected segments will be white) or the intensity from the image $f(x, y, n)$ is transferred (detected segments will be replaced by

original image). If value of $GR(i, j)$ or $GB(i, k)$ equals to zero, this means that patterns contain no such combination of colour intensity; in this case, initial zero value for pixel $G(x, y)$ remains unchanged.

$$\text{for } x = 1 \div \text{Width}, \quad y = 1 \div \text{Height},$$

$$\left.\begin{array}{l} i = f(x, y, 1) \\ j = f(x, y, 2) \\ k = f(x, y, 3) \\ G(x, y) = 255 \quad \text{if } GR(i, j) > 0 \text{ and } GB(i, k) > 0 \\ G(x, y) = 0 \qquad \text{otherwise} \end{array}\right\} \tag{4}$$

Fig. 11 shows $G(x, y)$ arrays of test images. Lower 3 images (Fig. 11) captured using high-quality digital still camera show class *"road"* object that is detected unambiguously. If a shadow happens to be inside of the trapezium pattern, shadowy areas of the road are still assigned to the class *"road"* object. If shadows on the road are outside of the trapezium outline, shadowy areas are assigned to the class *"off-road"* object. Method for considering random shadows was already presented [1]; however, it requires additional calculations.
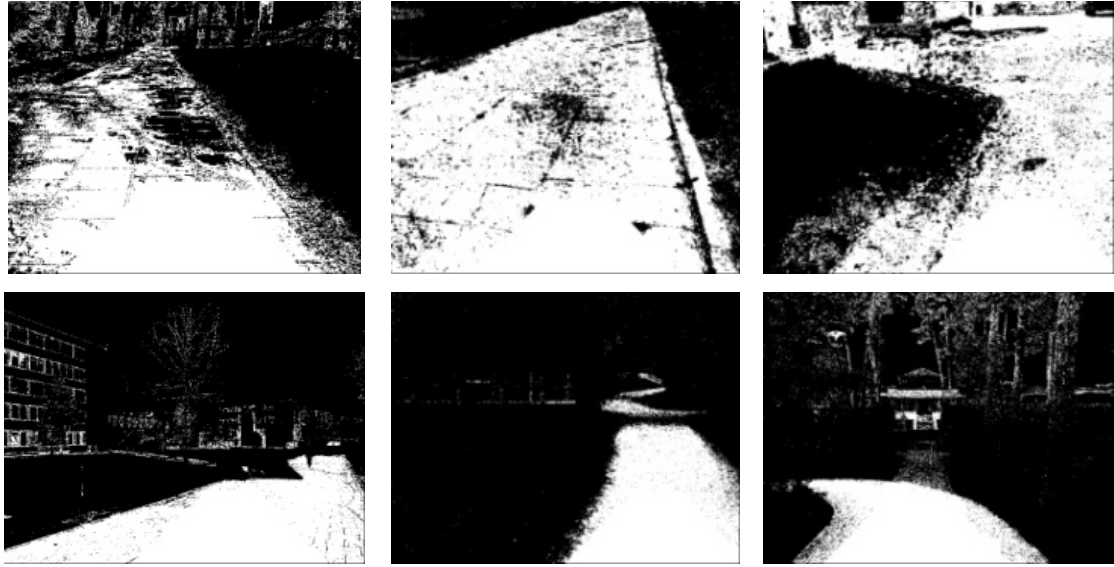
Fig. 11. Results of adaptive segmentation

Method of adaptive segmentation presented in this study is reliable in case objects detected within the trapezium outline are considered as road. Consequently, it is very important to choose correctly the size, shape, and even position of the trapezium, as these parameters highly depend on the camera height and its angle to the road.

5. Conclussions

1. To identify class *"road"* and *"off-road"* objects, segmentation by analysing HSV colour range can be used. Colour normalization does not improve significantly the quality of recognition. Histogram equalization ensures more detailed outlines and textures of individual objects.
2. Adaptive segmentation allows unambiguous detection of the class *"road"* object and prevents shadow effects in case a shadow falls inside the trapezium area.
3. Technical specification of the hardware in an experimental system impacts segmentation of homogeneous images. Recognition of images taken with a digital still camera is more accurate due to better quality of the captured image.

Acknowledgements

References

1. **ChengFa Fan, ZhuMing Li, XiuQing Ye, WeiKang Gu.** An Adaptive Method of Color Road Segmentation. Computer analysis of images and patterns: 7th international conference, proceedings / CAIP '97, Kiel, Germany,

September 10 - 12, 1997. Gerald Sommer ... (ed.). – Berlin; Heidelberg; New York; Barcelona; Budapest; Hong Kong; London; Milan; Paris; Santa Clara; Singapore; Tokyo : Springer, 1997.

2. **Kaveh Kangarloo, Ehsanollah Kabir.** Sequential Probabilistic Grass Field Segmentation of Soccer Video Images. Combinatorial Image Analysis: 10th International Workshop / IWCIA 2004, Auckland, New Zealand, December 1-3, 2004. Reinhard Klette ... (ed.).: Springer, 2004.

3. **Liyuan Li, Xinguo Yu, Weimin Huang.** Scene Context Modeling for Foreground Detection from a Scene in Remote Monitoring. Advances in Visual Computing: Third International Symposium / ISVC 2007, Lake Tahoe, NV, USA, November 26-28, 2007, Part II. George Bebis ... (ed.). – Springer-Verlag Berlin Heidelberg 2007.

4. **Christian Wojek, Bernt Schiele.** Dynamic Conditional Random Field Model for Joint Labeling of Object and Scene Classes. Computer Vision ECCV 2008: 10th European Conference on Computer Vision, Marseille, France, October 12-18, 2008. Part IV. David Forsyth ... (ed.). – Springer-Verlag Berlin Heidelberg 2008.

5. **Kai Berger, Christian Lipski, Christian ainz, Timo Stich, Marcus Magnor.** The Area Processing Unit of Caroline – Finding the Way through DARPA's Urban Challenge. Robot Vision: Second InternationalWorkshop, RobVis 2008, Auckland, New Zealand, February 18-20, 2008. Gerald Sommer ... (ed.). – Springer-Verlag Berlin Heidelberg 2008.

Proceedings of 8th International Conference ITELMS'2013

Universal Robotic Control Station for a Grouping of Unmanned Engineering Machines

A. Dąbrowska*, R. Typiak**

Military University of Technology, Kaliskiego str. 2, 00-908 Warsaw, Poland, E-mail: adabrowska@wat.edu.pl
** *Military University of Technology, Kaliskiego str. 2, 00-908 Warsaw, Poland, E-mail: rtypiak@wat.edu.pl*

Abstract

The paper presents a concept of a Universal Robotic Control Station (URCS) which use would allow a single operator to take control over multiple unmanned engineering machines and utilize them during an execution of a single complex engineering task. Presented solution allows for a one operator – one machine control with an access to data from onboard sensors of any machine at any given time and the ability to transfer control between them on the fly. The described control station is designed for military applications which require meeting specific expectations described in the article. Additionally, the control station would utilize a number of control algorithms for hardware management of transmitting control and sensory data as well as a description of possible, external algorithms for simulating autonomous behaviors for idle machines which could be executed on the control station side, thus eliminating the need to modify anything on the machine side.
KEY WORDS: *control systems, unmanned platform sensory, ergonomics, multi machine control algorithms.*

1. Introduction

Currently conducted peace keeping missions around the world require military forces to be in close proximity of civilians and civilian structures. This presents an ideal opportunity for any type of enemy force utilizing asymmetrical tactics, to bombard fortified positions from within urban populated areas. This poses a threat to soldiers conducting engineering missions both within their own bases as well as outside them. That is why, there is a visible trend of introducing unmanned machines for carrying out high threat level actions instead of sending in soldiers. However currently, there is a limited number of possible uses for these devices as they're dedicated solutions and real world engineering scenarios rarely require only one type of action to be performed. One possible solution would be to create a robust unmanned engineering machine which would be capable of completing engineering missions on its own, however, since these are a high threat level actions, the possibility of loosing such a machine is high. Another solution would be to utilize multiple, less expensive machines, which would complement each other's functionalities. This approach would decrease the possibility of loosing all units in case of any unpredicted actions. This solution does have a drawback in a sense that currently each machine comes with its own control station (Fig. 1). As such, when trying to use two or more units, one needs two or more operators. Not only that, but it's also crucial to allow them to communicate witch each other. While during missions taking place inside military installations this does not seem to be a big issue, on-site missions in remote locations, where it's crucial to keep presence at minimum to provide adequate security, high number of personnel is not the right solution.

a   b

Fig. 1.   Different control panels for unmanned engineering equipment: a – All All-purpose Remote Transport System's control panel (ARTS); b – Bobcat's Robotic Controller Kit's control panel

This drawback has been a driving factor in creating a concept of a single, flexible control station which would allow a single person to take control on a number of unmanned engineering machines and use them in rotation to complete a complex engineering task. Because each machine's functionality can be divided into a mechanical and sensory, simple switching between machines proves inadequate, as taking control over a new machine prevents from using the last machine's sensory functionality. That is why the control station should be equipped with an onboard control system which would allow for control transfer while still retaining access to sensors from each machine used.

Using multiple machines poses also a problem of remote control and interference between devices using similar wireless solutions. In standard conditions this could possibly be a major problem, but with a single control station solution, this becomes a software issue instead of a hardware one.

There are a number of issues needed to be addressed in order to create a fully functional multi machine control station. Most importantly it needs to have a clearly defined functionality as this is the base for creating any working control stand. A target consumer needs to be defined in order to asses the work environment, possible powering solutions and mobility level. Next, there needs to be a clear logic defined which would concern the controlled machines and how they influence each other and the control station. With the knowledge gained from previous steps, one can extrapolate certain requirements for communication and control hardware and programming. Such aspects as available power supply limitations and presumed mobility allows to narrow down possible hardware solutions and discard those which do not meet presented requirements. The same relation takes place with machine control algorithms. Knowledge about how the operator has to be able to interact with selected machines allows to determine the number of hardware elements which need to be in use during normal working conditions. Obviously the idea of using multiple unmanned machines for completing a single, complex engineering task puts a huge focus on enabling the operator to use multiple sensors scattered across different hardware platforms (machines). This process needs to be done both efficiently and user friendly. Burying the operator under vast amount of data and letting him sort it out is not time-efficient, a criteria which is currently being introduced more openly on the market, however, this mostly involves control schemes, not data visualization. One such solutions is using a game controlled to send steering commands to an unmanned machine (Fig. 2). This flattens the learning curve for new operators, which (as is assumed) mostly use these devices in their home entertainment systems.

Fig. 2. Complete Bobcat Robotic Controller Kit system with a gamepad controller

2. Control station's functionality requirements

Soldiers carrying out engineering tasks have access to logistical support which, most of the time, boils down to access to technical support vehicles. These vehicles then supply access to a wide range of powering solutions, from 12V through 24V DC current to 230V AC. However, there needs to be a factor of mobility taken into account. It is assumed that the described control station should have the possibility to be mounted inside most (if not any) personal carriers available. Thus, the available voltage ranges are limited to 12 and 24V DC installations. Should a single voltage value needed to be chosen, it is preferable to select the 12V DC as it is also commonly found in civilian vehicles, which than could also serve as means of transport for the control station. The problem of powering every component from a single 12V installation should not prove problematic, as a lot of currently available communication hardware is built in a way which allows powering from 9-36V DC installations. The same goes for industrial and military grade visualization units and commonly available units are effectively powered from 12V power adapters. Another argument for using the 12V power source could be that some diesel-power units are equipped with both 230V AC and 12V DC power outputs.
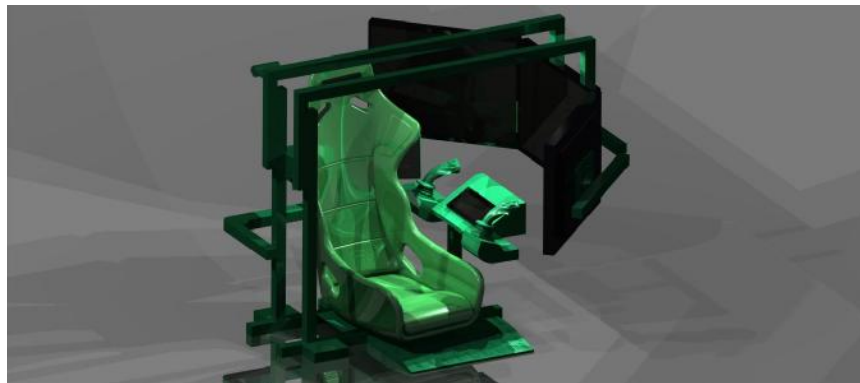
Fig. 3.   A concept design of the URCS with three sections: the operator's seat and controls, the operating panel and the visualization panel

As mentioned, a lot of effort should be put into creating the control station as mobile as possible. This would require creating a compact, but sturdy frame, preferably one that has an openwork structure to decrease mass. The idea is that the stand alone version of the control station should comprise of three detachable sections: the operator's seat and controls, the operating panel and the visualization panel. With these three parts functioning together but having the ability to be separated, it allows for using the same station within different work environments (Fig. 3). If space is not an issue, the whole set may be used. If the space is limited, the visualization part, or the operator's seat may be removed. If however the space if highly limited or in case of emergency, the operating panel should suffice to allow basic control over every machine.

3. Multiple machine control algorithms

The problem of controlling multiple machines is being tackled by many research institutes, however most of their work concerns Unmanned Aerial Vehicles (UAVs) [1, 2]. The Military University of Technology has experience in strategies of use of remote control unmanned ground vehicles [3]. The presented solution is a set of rules and logic which would be implemented in order to allow a single operator to control one of several selected unmanned machines, with other units being on standby and supporting the task currently underway. A more detailed description of the logic itself may be found in [4].

The idea is that an operator, tasked with carrying out an engineering mission is given the mission parameters and selects, from any currently available units, the ones which he decides are going to be useful. The then registers them to his control station, effectively binding them to his control until released (Fig 4). The control systems of these machines communicate with the control station, which not only tells them whose commands to obey, but also how may other machines are there in the grouping and sets an order in which the control protocol will be handled. Each machine would receive an ID by which it would communicate with the stand. After this, the process of configuration would be over and a normal work process would start.
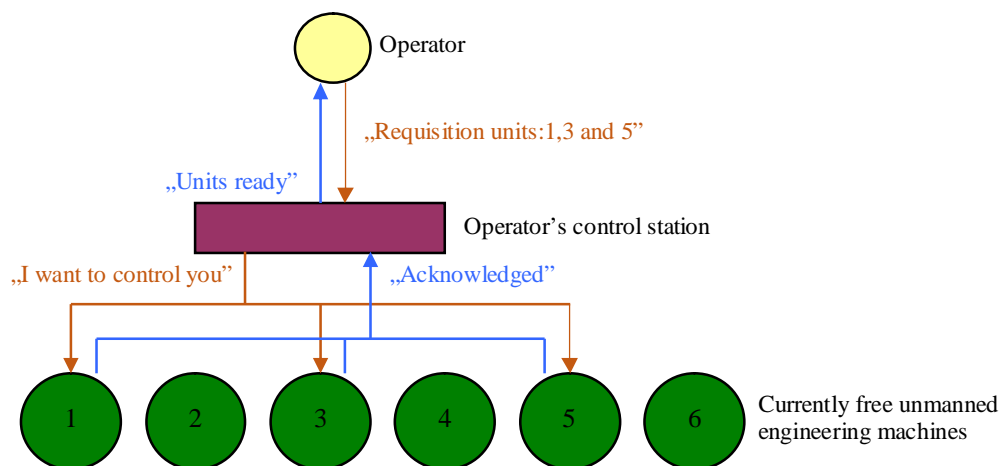
Fig. 4. A diagram describing the way for the operator to register desired unmanned engineering machines

Switching between machines would have an option to enforce a certain state upon the units currently not used. This would allow to imply certain overall behaviorism upon the grouping. For example, it could force all the machines currently not used to go into idle state, which would decrease their engine's rpm and shut down any unnecessary systems to conserve power and decrease noise. This state would also decrease fuel consumption which would benefit the effective work time of the grouping.

4. Communications and control algorithms

Because there is a need to handle a lot of data traffic between the machines and the operator's station, it has been assumed that there is going to be a set of algorithms used on the hardware side to manage both control and sensory data.

The control station should be equipped with a set of two radio transmitters, working on the same frequency band, but on different channels. The lowest channel ("control channel") would be reserved for the currently controlled machine while the other one would be used for two way communications with the rest of the units. The main link would be used to transmit both control and sensory data with as high refresh rate as possible to allow as smooth control as possible. The second link would normally be used for siphoning data from sensors to the control station, but in case of switching the currently controlled machine it would send a command to the specific unit to become active. This way, the machine would reconfigure it transmitting unit to change onto the control channel. Additionally, the currently controlled machine would receive an order to turn inactive (Fig. 5).

It is obvious that any unmanned engineering machine working in the grouping would be required to undergo a certain adaptation process to enable it to communicate with the control station. However (assuming they all use the same control signal bus, like CAN-bus, etc.) the proposed solution would only require to change the currently used transmitting unit to an "intelligent" module working on a set frequency. The on-board logic of this unit would allow it to not only manage data transfer between the machine and the operator station but would also reconfigure itself when receiving a certain command. This way, there would not be any need to change the on-board control systems of these machines. Protocol handling would also be carried out by the newly attached unit as, because of several machines using the same frequency channel, an order will need to be introduced, resulting in data transfer frequency decrease. The unit would have the ability to emulate control data if needed to keep the machine in its desired state. Since the data traffic would use the same channel the transmission unit could track information transfers to see if other machines are currently sending data. If so, the unit would keep feeding the on-board control system with data corresponding to a safe state for the machine. If the traffic would cease and control with the operator's station would be lost, the unit would have the possibility to execute a certain command (full shutdown, autonomy algorithm, etc.).

Switching control from machine #1 to machine #3
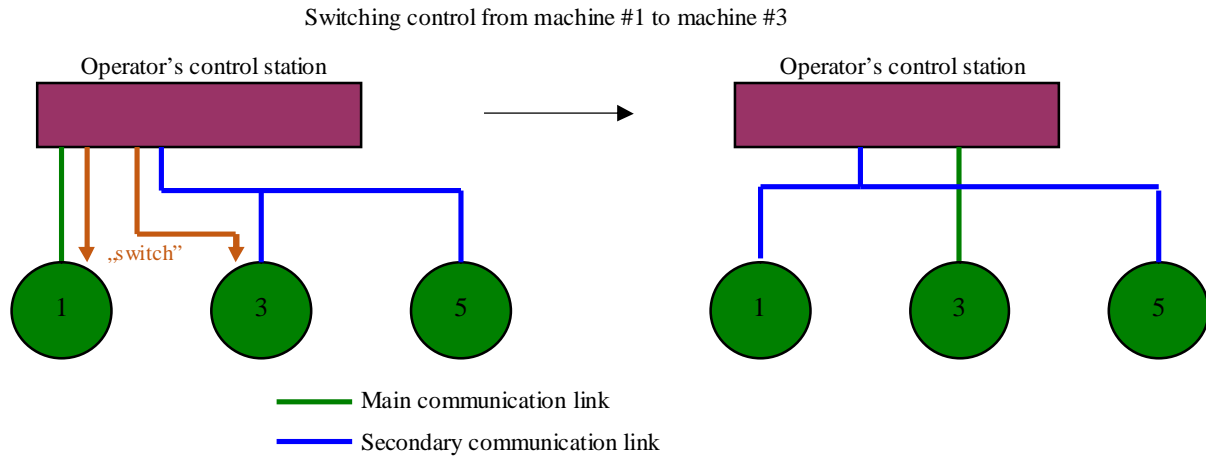
Fig. 5. Diagram describing the logic used for switching control over different unmanned engineering machines

5. Sensor data visualization and management

The described control station should be equipped with a set of visualization tools to held the operator easily obtain information he/she currently needs. Since the basic set of information used to generate control signals for the unmanned engineering machines comes from vision signals, the control station should be equipped with a set of monitors to allow natural access to these data. An analysis carried out by [5] has determined that a set of three monitors positioned in a way as to create a panoramic view is a good solution for these kinds of machines. They should be the main part of the control station's visualization panel. Other being a set of two smaller monitors positioned underneath which would serve as additional sensory visualization units (Fig. 6).
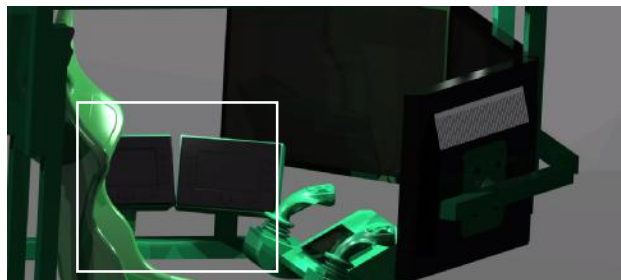
Fig. 6. URCS's additional monitors purposed with visualizing data acquired from different unmanned engineering machines

To allow easy access to data, there should be a system created to categorize data and a GUI to place that data in specific parts of the sensory monitors. That way, the operator would be able to switch between, for example thermal imaging and night vision with a push of a button. Additionally they may serve as means to display 3D maps of the environment [6, 7] This system could also interact with the control station's own system to ask for certain information to be sent. This could further decrease the traffic as data which would not be even displayed to the operator, would not be sent.

6. Control station's autonomy algorithms

The idea of a single operator's station to serve as a means to controlling multiple unmanned engineering machines could also be used as means of introducing autonomous behaviors to machines not designed for such actions. Maintaining communication with each unit allows the control station to send each its individual control data. It would of course happen at a decreased rate, so the list of available autonomous behaviors would be limited, but it could prove invaluable when carrying out tasks required from all the machines at the same time (like reaching a certain destination). A trailing mechanic described in [8] could be used on each machine, with only a single unit having the whole sensory base needed. Others could enter certain modes, which could be executed with the need of only a small amount of additional information on their part. Currently two modes are being considered: shadow mode and follow mode.

In shadow mode, each unit would receive the same data (for example "move forward at 100% speed") which would allow for a quick displacement of an entire grouping. The other one would be the follow mode, where certain data (presumably GPS) would be used to track each machine's location. After selecting a formation, the system would prioritize units and set their desired location within this formation and execute commands to make them form up on each other. These calculations would probably be done on external hardware linked with the control station's internal data bus.

7. Summary

The concept of creating a Universal Robotic Control Station which would allow for a single person to operate a number of unmanned engineering machines is a completely new approach to carrying out complex engineering tasks,. Using multiple, specialized machines may prove mode adequate in cases where space is limited and sending in a single, big machine is not a possibility. This strategy also allows for a more precise placement of different sensors which may aid the operator in his work, in comparison to every sensor being placed on a single platform. While the idea to control many machines by a single person may seem overwhelming, it needs to be stressed out that the operator is controlling a single machine at a time in a normal operation mode. In different modes, when the control is in fact sent to all the machines at once, the operator serves a role of a foreman, giving commands to a group. Carrying out relations between specific machines is to be done by the Universal Robotic Control Station's subsystems.

References

1. **Vidal. R.** Pursuit-Evasion Games with Unmanned Ground and Aerial Vehicles, Seul, 2001 IEEE.
2. **Howell A. S., Hedrick J. K.** Border patrol and surveillance missions using multiple unmanned air vehicles, Atlantis, 2004 IEEE.
3. **Typiak A., Zienowicz Z.** Utilization of remote controlled vehicle with hydrostatic driving system, Lithuania, 25th International Symposium on Automation and Robotics in Construction 2008.
4. **Typiak R.** A design of a control system for a group of unmanned engineering machines, Warsaw, IARP RISE 2012.
5. **Bartnicki A., Krogul P., Przybysz M.** Stanowisko zdalnego sterowania pojazdem bezzałogowym w zadaniach zmniejszenia zagrożenia wywołanego niekontrolowanym uwalnianiem substancji niebezpiecznych, Logistyka 2011 issue 3, ISSN 1231-5478.
6. **Typiak a., Gnatowski M.** Map Building System for Unmanned Ground Vehicle, Jastrzebia Gora, Conference on Mechatronic Systems, Mechanics and Materials 2011.
7. **Typiak A.** Use of Laser Rangefinder to detecting in surroundings of mobile robot the obstacles, Lithuania, 25th International Symposium on Automation and Robotics in Construction 2008.
8. **Dąbrowska A., Typiak A.** Nadążne sterowanie lekką platformą transportową w układzie teleoperatora, VI Międzynarodowa Konferencja Uzbrojeniowa, Waplewo, 2006.

Proceedings of 8th International Conference ITELMS'2013

Analysis of Freight Transport in Lithuania

A. Dėmenienė*, D. Striukienė**, E. Zacharovienė***, S. Kairienė****, A. Bartulis*****

*Kaunas University of Technology, Klaipedos str. 3, 35209, Panevezys, Lithuania, E-mail: alina.demeniene@ktu.lt
**Kaunas University of Technology, Daukanto str. 12, 35212, Panevezys, Lithuania, E-mail: danguole.striukiene@ktu.lt
***Kaunas University of Technology, Daukanto str. 12, 35212, Panevezys, Lithuania, E-mail: elvyra.zacharoviene@ktu.lt
****Panevėžys College, Laisvės a. 23, 35200, Panevezys, Lithuania, E-mail: saule.kairiene@ktu.lt
*****Kaunas University of Technology, Daukanto str. 12, 35212, Panevezys, Lithuania, E-mail: alfreda.bartulis@ktu.lt

Abstract

The article contains the functionality analysis of freight transport in Lithuania in 2007–2011, examining the fleets of freight transport registered in the administrative territories of Vilnius, Kaunas, Klaipėda, Šiauliai, Panevėžys, Alytus, Marijampolė, Tauragė, Utena and Telšiai, including the fleet of semi-trailer trucks, its types, the dynamics of the number of vehicles and the most popular vehicles.

KEY WORDS: *vehicle, trailers, semitrailers, administrative territories.*

1. Introduction

Substantiation of expedience of the research. The need for communications is one of those more important in our lives. The users of transportation services include all businesses of all types. In case of any interruptions in transportation, the possibilities of the people to communicate decrease and economic losses are sustained in various fields of activities.

Problem under consideration. The intended purpose of freight vehicles is to carry the goods and provide other transportation and the associated services. Successful functioning of the transport system is vital to rapid development of economics and welfare of the people. When the disturbances of the transport system become permanent (e. g., traffic jams in cities, shortage of parking places), this creates obstacles for the rational use of resources, reduces the division of labour, negatively affects the environment, economic welfare and quality of life for the people. The growth of economy results in the development of transport, too: in individual countries, there develop sectors of economy, the production of which is delivered to various countries of the world. The volumes of cargo carried by roads, shipped or flied increase. Under the conditions of economic decline following the crisis of 2008, freight rates went down; some of the international transportation companies closed down, while others had to reduce the number of trucks in their possession.

Objectives of the research:
1. To discuss the criteria for the classification of freight transport.
2. To assess the dynamics of the change in numbers of vehicles registered in Lithuania (2007–2011).
3. To assess the dynamics of the change in numbers of vehicles registered in Lithuania by administrative territories (2007–2011).

Methods of research:
- analysis of secondary statistical data;
- case analysis;
- semi-structured interview;
- analysis of documents.

When presenting the statistical data of the company and comparing the international cargo transportation in Lithuania and Russia, President of UAB Linava Algimantas Kondrusevičius mentioned that in 2013 the neighbouring Russia has about $30 \cdot 10^3$ vehicles for international transportation, whereas the members of Linava and other transport companies in Lithuania have about $24 \cdot 10^3$ vehicles [2].

When conducting the analysis of freight transport in Lithuania, it is necessary to discuss the criteria for the classification of vehicles. Based on the directives of the European Union currently in force (2007/46/EB, in 2007. September 5.), vehicles are classified to the following categories:

Category M – motor vehicles intended for the carriage of passengers and having at least four wheels or at least three wheels, if the maximum permissible mass exceeds 1 tonne.

Category N – motor vehicles intended for the carriage of goods and having at least four wheels or at least three wheels, if the maximum permissible mass exceeds 1 tonne. Seeing that our article pertains to the vehicles ascribed to this category, we are going to examine the classes the vehicles are divided into according to general mass:
- Class N1 – vehicles intended for the carriage of goods with the general mass not exceeding 3.5 tonnes (freight vehicle);
- Class N2 – vehicles intended for the carriage of goods with the general mass exceeding 3.5 tonnes, however below 12 tonnes (freight vehicle);

- Class N3 – vehicles intended for the carriage of goods with the general mass exceeding 12 tonnes [2].

Category O – trailers and semitrailers. This category is divided into the following classes:
- Class O1 – trailers with general mass not exceeding 0.75 tonnes (light trailer or trailer of a light duty car);
- Class O2 – trailers with general mass exceeding 0.75 tonnes, however below 3.5 tonnes (for a freight vehicle);
- Class O3 – trailers with general mass exceeding 3.5 tonnes, however below 10 tonnes (for a freight vehicle);
- Class O4 – trailers with general mass exceeding 10 tonnes.

2. Research

The number of freight vehicles in different regions of Lithuania shows the potential of the region for the carriage of goods. Freight vehicles registered in Lithuania carry the goods to all countries in Europe and CIS countries. High level of motorisation creates favourable conditions for the creation of jobs. It can be stated that the development of transport sector also affects the resolution of social issues in the country.

The dynamics of the change of the number of vehicles registered in Lithuania in 2007–2011 is presented in Table 1.

Table 1

Dynamics of the change of the number of vehicles registered in Lithuania in 2007–2011
(http://db1.stat.gov.lt/statbank/default.asp?w=1249, 2013)

	2007	2008	2009	2010	2011
Road vehicles, in total	1,838,385	1,938,468	1,963,055	1,954,592	1,986,050
Motorcycles	28,826	34,029	36,562	38,995	41,349
Mopeds	6,444	11,588	14,810	17,276	18,775
Light cars	1,587,903	1,671,065	1,695,286	1,691,855	1,713,277
Busses	13,997	13,824	13,360	13,261	13,086
Trolleybuses	491	488	477	467	459
Freight vehicles	126,507	128,733	126,519	113,113	113,452
Semitrailer trucks	21,076	21,375	19,806	20,808	23,327
Semitrailers	21,598	22,518	21,734	23,819	26,678
Trailers	18,162	20,379	20,036	20,400	20,905
Special vehicles	13,381	14,469	14,465	14,598	14,742

Table 2

Number of semitrailer trucks registered in the Republic of Lithuania in 2007–2011
by manufacturer (http://db1.stat.gov.lt/statbank/default.asp?w=1249, 2013)

	2007	2008	2009	2010	2011
In total, by manufacturer	21,076	21,375	19,806	20,808	23,327
DAF	2,368	2,586	2,469	2,671	3,334
Iveco	1,530	1,470	1,326	1,431	1,545
KamAZ	517	463	433	308	247
KrAZ	41	35	34	25	23
LiAZ	29	27	27	17	14
MAN	3,184	3,276	2,996	3,272	3,459
MAZ	967	897	837	647	548
Mercedes-Benz	3,077	3,046	2,673	2,973	3,313
Renault	1,379	1,414	1,364	1,607	1,846
Scania	2,694	2,756	2,578	2,693	3,081
Ural	179	172	168	128	113
Volvo	4,533	4,704	4,414	4,678	5,530
ZIL	419	377	344	252	185
Other	159	152	143	106	89
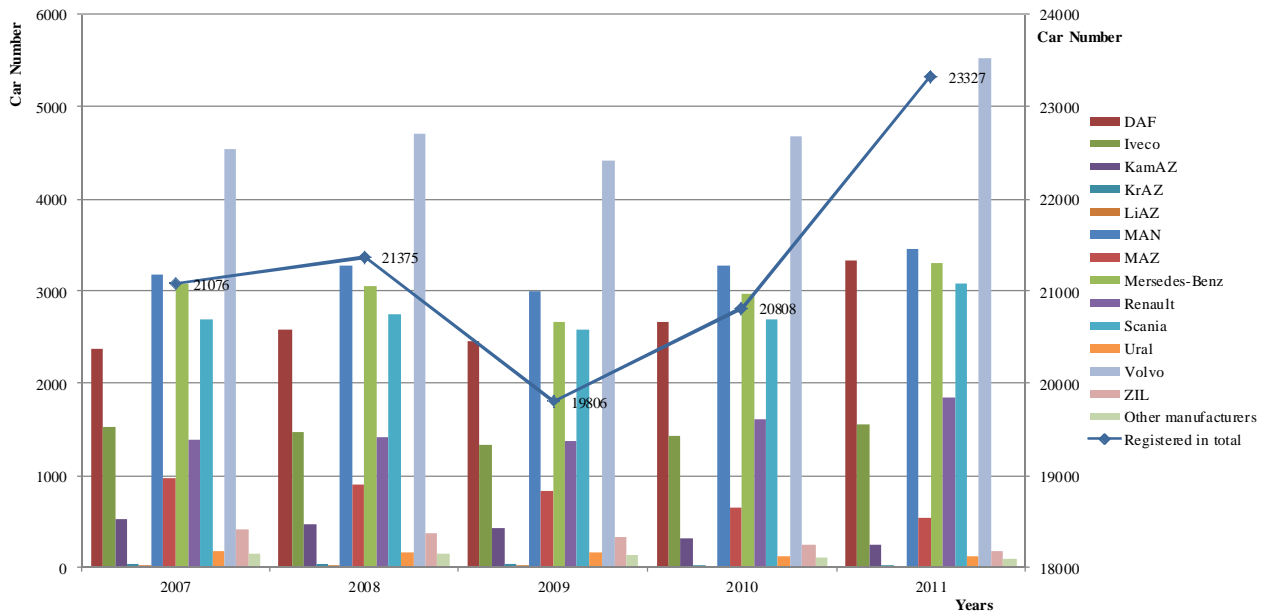
Fig. 1. Number of semitrailer trucks registered in the Republic of Lithuania in 2007–2011 by manufacturer

In Lithuania, the number of cars and other vehicles, compared to the population, is rather high. Although in the years of crisis the numbers of almost all types of vehicles went down, they started going up again from 2011. The reduction in the number of semitrailer trucks was observed until 2009, while from 2010 it went up again. Compared to 2010, the number of semitrailer trucks registered in Lithuania increased by 12.1%. According to the data of the State Road Transport Inspectorate as of 31 December 2011, there were 23,327 freight vehicles engaged in international transportation.

When analysing the changing of the number of semitrailers registered in Lithuania, certain trends are observed in the fluctuation of dynamics. Based on the data, it can be stated that the most significant reduction of the total number of semitrailer trucks registered was recorded in 2008–2009, from 21,375 to 19,806; however from the end of 2009, the total number started growing rapidly and in 2011 substantially exceeded that of the previous year.

At the end of 2011, the fleet of semitrailer trucks comprised by 3,521 vehicles more than registered at the end of 2009.

While investigating the makes of the semitrailer trucks registered in Lithuania that occupy the largest market share, it turned out that in 2007–2011, the Volvo make surely held the leading position in the truck market overcoming MAN in the second place and DAF in the third, Mersedes-Benz in the fourth and Scania in the fifth. Differences between places two and four are not significant.

Table 3 presents the distribution of freight vehicles registered in Lithuania by administrative territories.

Table 3

Number of freight vehicles registered in the Republic of Lithuania in 2007–2011 by administrative territories (http://db1.stat.gov.lt/statbank/default.asp?w=1249, 2013)

	2007	2008	2009	2010	2011
Alytus County	6,156	6,308	6,171	5,238	4,954
Kaunas County	26,003	26,387	26,591	24,656	24,935
Klaipėda County	12,824	13,075	12,817	11,216	11,290
Marijampolė County	8,250	8,332	8,076	6,674	6,597
Panevėžys County	11,774	12,087	12,334	10,198	10,175
Šiauliai County	13,392	13,406	13,302	11,212	11,439
Tauragė County	6,031	6,145	6,085	5,284	4,989
Telšiai County	6,168	6,290	6,154	5,340	5,191
Utena County	6,490	6,605	6,453	5,066	4,861
Vilnius County	29,419	30,098	28,536	27,696	28,625
Republic of Lithuania	126,507	128,733	126,519	113,113	113,452

When analysing the secondary statistical data, it can be stated that the largest number of freight vehicles is registered in five administrative territories: Vilnius (25.3 %), Kaunas (22 %), Šiauliai (10.0 %), Klaipėda (9.95 %) and Panevėžys (9 %). Seeing that these are the largest cities of Lithuania, consequently, the largest companies with rather

large vehicle fleets are established within the territories of these cities and counties. Nonetheless, it can be seen from Table 3 that the fleet of freight vehicles has been decreasing since 2008 and started going up again only in 2011; however it did not reach the level of 2008.
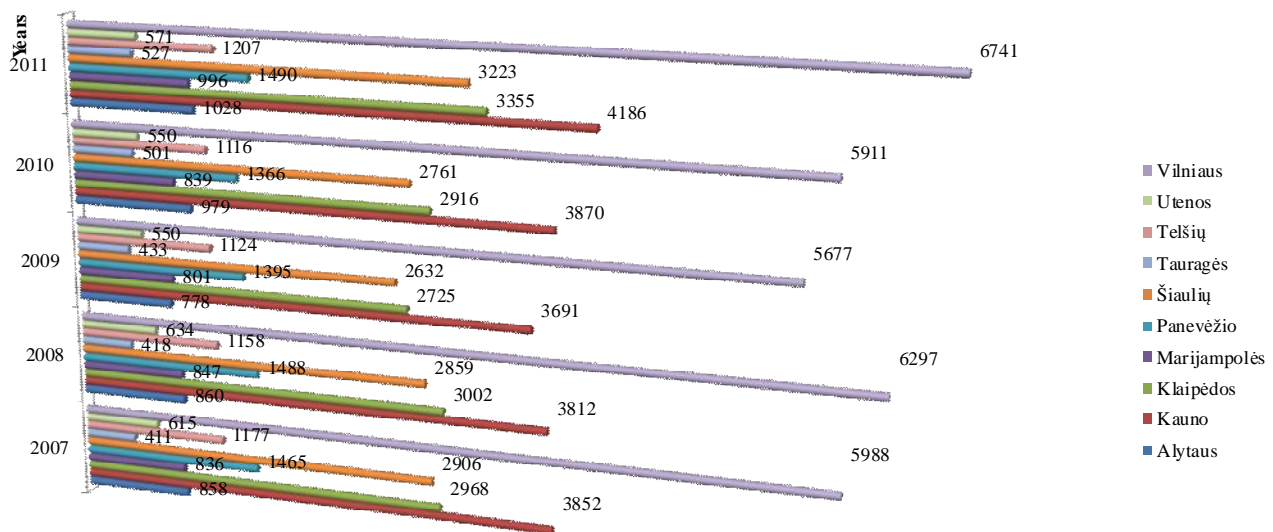
Fig. 2. Number of semitrailer trucks at the end of 2007–2011 by administrative territory

The research was aimed at analysing the fleet of semitrailer truck fleet in Lithuania and monitoring its dynamics after taking into account the criterion of administrative territories. The chart shows that the semitrailer trucks are not uniformly segmented in the territory of Lithuania. Dispersing trends can be seen according to the administrative territories of the largest cities. As many as 28.9 %, compared to the total number registered in Lithuania, are located in county of Vilnius; substantial numbers are in counties of Kaunas(17.8 %), Klaipėda (14.4 %), Šiauliai (13.8 %) and Panevėžys (6.4 %). Hence, it can be stated that the main companies engaged in transportation of goods are registered in the same territories. The examination of the secondary statistical data showed that the largest transportation companies are concentrated in the administrative territory of Vilnius.

3. Conclusions

The article discussed the criteria for classification of freight transport in line with the directives of the European Union currently in force.

The dynamics of the change in numbers of vehicles in the Republic of Lithuania in 2007–2011 was assessed.

The dynamics of the change in numbers of semitrailer trucks in the country in 2007–2011 was assessed by manufacturer.

The dynamics of the change in numbers of freight transport registered in Lithuania was assessed by individual administrative territories (2007–2011).

Acknowledgements

References

1. **Agnė Rutkauskaitė.** Kokius krovininius automobilius eksploatuoja Lietuvos transporto įmonės? < http://www.cargonews.lt/autotransportas/kokius-krovininius-automobilius-eksplotuoja-lietuvos-transporo-imones/?hash= >.
2. Statistika. Registruotų krovininių automobilių skaičius (2000-2011). < http://db1.stat.gov.lt/statbank/default.asp?w=1249 > [2013-05-10].
3. Dėl motorinių transporto priemonių ir jų priekabų kategorijų ir klasių pagal konstrukciją reikalavimų patvirtinimo. < http://www.infolex.lt/ta/78090 > [2013-05-09].
4. Homologacija. < http://web.iveco.com/lithuania/paslaugos/pages/homologacija.aspx > [2013-05-12].

Proceedings of 8th International Conference ITELMS'2013

Suggestion of a Inventory Control Model Used in the Army

J. Furch

University of Defence, Kounicova 65, 662 10, Brno, Czech Republic, E-mail: jan.furch@unob.cz

Abstract

The article deal with an inventory control model which it used the Economic Order Quantity (EOQ) model. The Economic Order Quantity model serves as the basis for determining supply order quantity. While setting the model, it is important to introduce supply classification claimed by an organization. For the army we suggest using so-called strategic (stone) reserve which means we determine a so-called ordering supply level as shown in the Q-model of a supply control system. Acquisition supply costs as well as the costs of keeping and storing the supplies are important elements when setting the model. In order to meet the requirements we have chosen a dynamic model with absolutely determined supply movement and a dynamic multi-product model with the constant level of costs used for acquiring supplies. Applying both methods already mentioned we calculate minimum total costs and select the model with lower total costs.

KEY WORDS: *economic order quantity model, supply model, ordering supply level, system of supply control.*

1. Introduction

The supply theory might be defined as the sum of mathematical methods used for modelling and optimizing processes of developed items to provide company´s smooth running. When determining a supply strategy at peace time, it is necessary to assess and balance ordering costs on the one hand, and supply preservation costs on the other. A strategy to order big amounts less frequently, for example, can lead to such increase in supply preservation costs that this will exceed ordering costs savings. The ordering costs include the costs of supply transfer settling, product manipulation costs, product storage costs, settling an invoice costs. The supply preservation costs contain supply assets, services costs (insurance, taxes), storage facilities costs, and the costs of supply deterioration risk.

2. Models for inventory control

The model of supply control can be divided into two basic groups:
1. When taking into account the way of determining an enquiry (consumption) level and lead time length, there are:
   a) stochastic models based on the probabilistic character of enquiry (consumption) and the length of lead time;
   b) deterministic models which assume the enquiry (consumption) quantity and lead time length to be precisely known;
   c) non-deterministic models where the character of enquiry (consumption) and lead time is not known.
2. When dealing with the way of renewing supplies, there are:
   d) static models where the supply is made by one-time delivery;
   e) dynamic models where an item supply is kept in stock on a long term basis and is renewed by frequent deliveries.

The supply theory models introduced above use a basic evaluation criterion based on minimizing the overall costs of purchasing, storing and keeping supplies, and in some cases even short supply costs.

The costs of acquisition supplies are expected to be the function of a delivery amount during a period under consideration. Optimization calculations include only variable costs relating to an order or a delivery. The example of such costs are enquiry (consumption) prediction costs, the costs of the raise, expedition and transfer of an order, transport costs (only if they are delivery size independent), taking delivery costs, quality check costs, the costs of processing the documentation, the clearance and settlement of the invoice, etc. The price of material or goods is included in acquisition costs only when an ordered amount matters, i.e. a quantity discount is applied.

The costs related to storing and keeping supplies cover only the costs which are the function of an average supply. They consist of a lot of different costs and generally they are the main part of logistic costs. They include the labour costs of warehouse counters, the costs of storage facility maintenance, energy costs, the hire costs of storage facilities, supply insurance, or the costs due to supply deterioration. Loss caused by tying capital in supplies represents significant part of these costs. In Table 1 there are the average annual cost rates for keeping and storing supplies expressed in the percents of a stored material value.

2.1. Dynamic determined model

When setting an ordering strategy the aim of which is to minimize the total costs of supply preservation and ordering costs, the economic order quantity model might be used. The economic order quantity model determines

optimum order quantity based on ordering costs and supply preservation costs. Order quantity is optimal when incremental ordering costs equal the incremental costs of supply preservation. Cost relations which are to be taken into account when specifying economical, i.e. optimum order quantity, are put in Fig. 1. The quantity and frequency of an order during which both costs types will be minimized is determined in such a manner that the economic order quantity is divided by a yearly product inquiry.

$$EOQ = \sqrt{\frac{2PD}{CV}} \qquad (1)$$

where: P is ordering costs per 1 order; D is yearly product inquiry or consumption; C is annual supply preservation costs; V is average costs or a supply unit value 1.
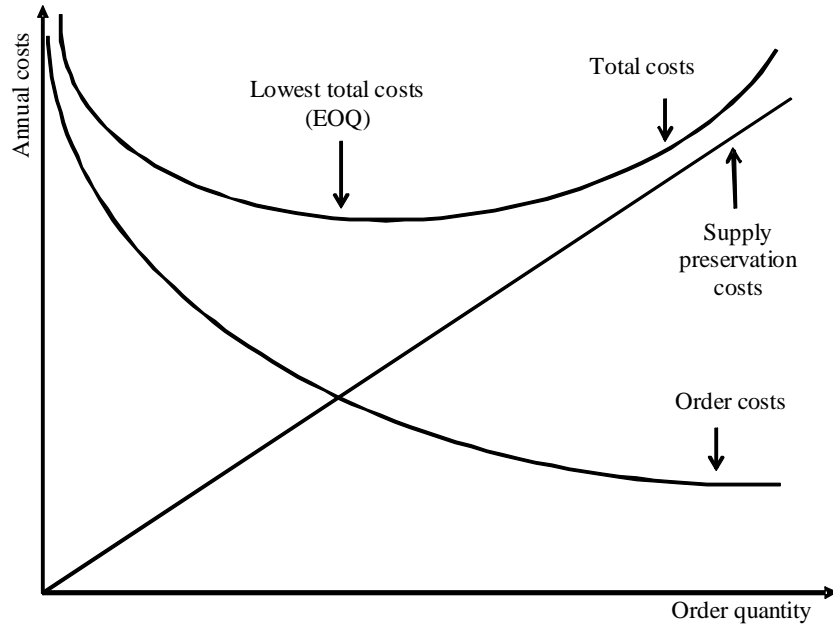
Fig. 1. Diagram of economic order quantity model 1

The simple *EOQ* model is based on the following assumptions: a continuous constant and known level of inquiry, constant and known resupply time or total resupply time, constant purchase prices independent of order quantity and order time, constant transport costs independent of order quantity and order time, satisfying all inquiry (supply depletion is not accepted).

It is not very common in practice to have constant inquiry and supply time, and also it is not easy to know when to determine them for certain, or when exactly the costs are known. Typical modifications which are to be performed in the *EOQ* model are the inclusion of shipping cost depending on traffic volume and quantity discount. The simple *EOQ* model did not take into account these both factors. If we want the *EOQ* equation to include the influence of quantity discount and shipping cost, it might be extended in the following manner:

$$Q^1 = 2\frac{rD}{C} + (1-r)Q^0 \qquad (2)$$

where: Q^1 is maximum amount whose order is economical, but markdown claim per unit will be observed; r is markdown percentage in the case that bigger amount has been ordered; D is annual inquiry expressed in units; C is the percentage of supply preservation costs; Q^0 is *EOQ* calculated from a market price.

2.2. Stochastic dynamic model

If supply consumption Q is exactly known during a certain period, between delivery frequency v and a delivery size x the following equation 1 will apply:

$$v = \frac{Q}{x} \qquad (3)$$

In practice we experience such situation very rarely. The supply consumption is mostly of a probabilistic character which means that the consumption fluctuates. The formula (3) applies only to the mean values of these

quantities. The fluctuation of the consumption and thus the real supply level around its mean value is to be balanced. Basically there are two ways of balancing the fluctuation and they are as follows:
a) Q-system of supply control – delivery frequency changes while delivery size is constant;
b) P-system of supply control – delivery size changes while the delivery interval is fixed.

Q-system of supply control. Q-system works with fixed sizes of orders and deliveries (an order size is the same as a delivery size) and balances fluctuation in consumption by changing the frequency of orders. When applying it, an ordering supply level is determined and it serves to meet the demand during the interval of supply acquisition t_p. When the real supply level reaches an ordering level, a new order is raised.

$x_1 = x_2 = x_3$
$t_{p1} = t_{p2} = t_{p3}$
$t_{o1} \neq t_{o2} \neq t_{o3}$
$t_{c1} \neq t_{c2} \neq t_{c3}$
x_o – ordering level
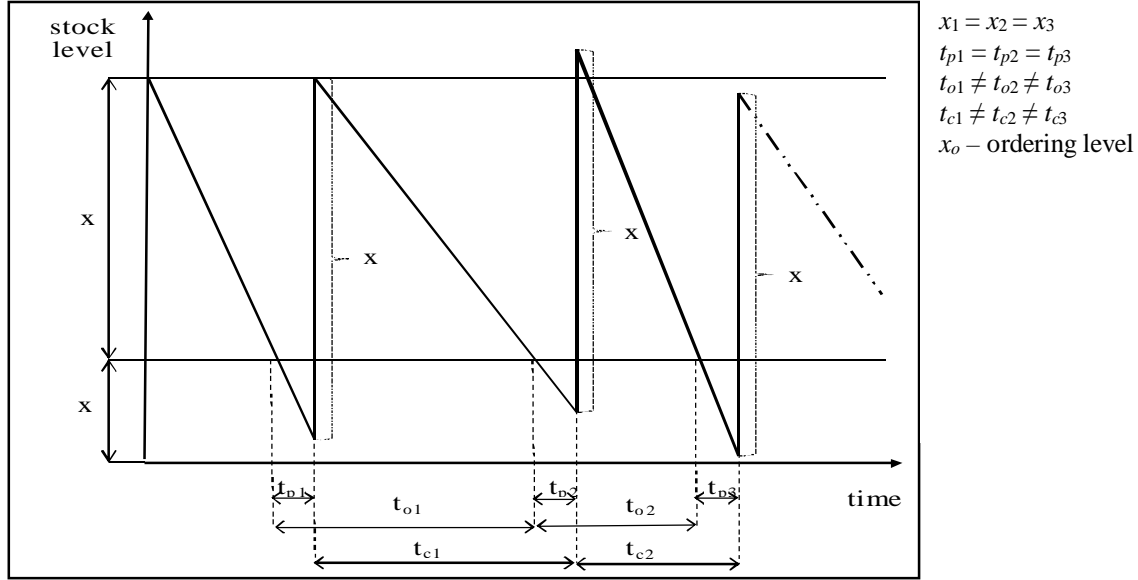
Fig. 2. Q-system of supply control

The fixed size of an order (delivery) is most frequently determined by the Harris-Wilson formula

$$x_{opt} = \sqrt{\frac{2 Q c_p}{T c_s}} \tag{4}$$

where: Q is number of purchase units for the time T; c_p is cost of purchase one unit; T is time; c_s is costs for maintenance and storage of one unit.

The safety supply for the Q-system of supply control is determined separately only for a supply acquisition interval t_p, because fluctuation in consumption automatically reflects a change in an order cycle t_o. If there is an increase in item consumption above an expected level, the real supply will fall faster at an ordering supply level and therefore a new order will be raised earlier. However, this principle of the automatic absorption of fluctuation in consumption cannot be applied during a supply acquisition interval. The company is expected to hedge itself against such fluctuations in consumption by properly set safety supplies.

P-system of supply control. The P-system is based on the principle that at the fixed reorder points of a t_k length the raised orders are generally of a different size x. It is a system in which supplies are periodically followed.

The size of an order is expressed as expected consumption per an uncertainty interval $(t_p + t_k)$ with regard to a safety supply x_p and disposition supply x_d quantity

$$x = \left(t_p + t_k\right)\overline{p} + x_p - x_d \tag{5}$$

The fluctuation of the real consumption around its mean value is balanced by the size of single orders. It is not required by the system to check constantly a supply level, only a periodical check at intervals given by a length t_k will be sufficient.

Regarding the P-system of supply control, a higher average supply is considered to be a disadvantage as compared with the Q-system of supply control, which is actually given by the higher level of a safety supply. It is rather demanding to get and have precise input data for both systems. Therefore they are not very suitable for controlling the supply of less important items. For these items it has been developed admittedly simple, but reliable system controlling supplies with two bins.
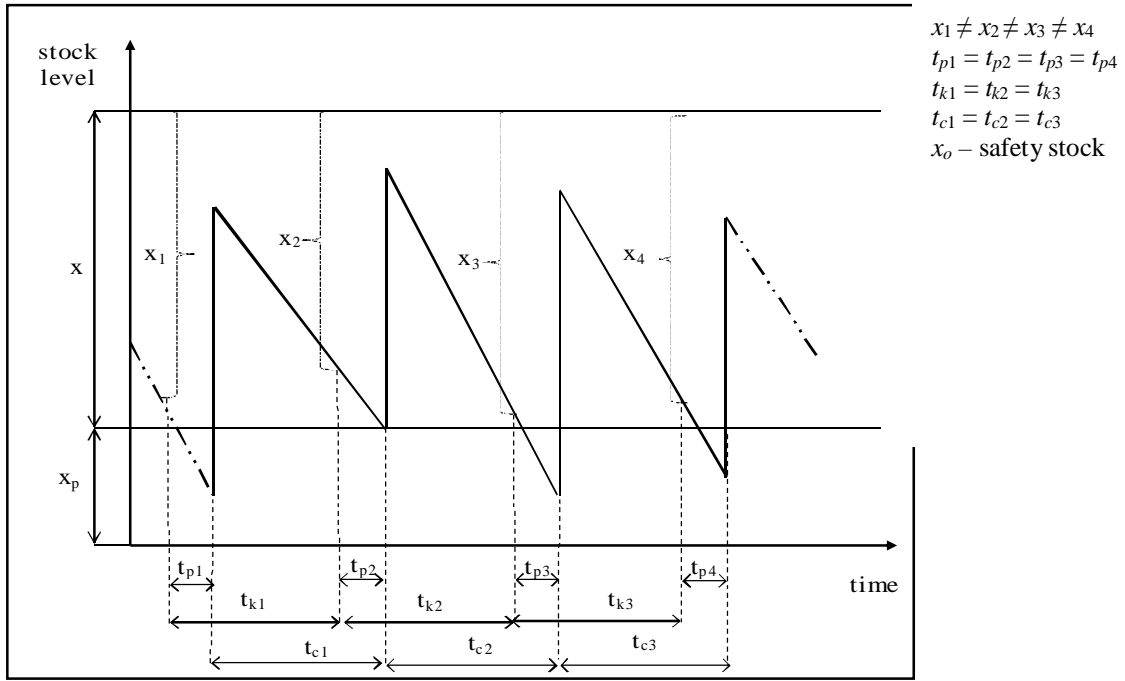
Fig. 3. P-system of supply control 2

3. Suggestion of an inventory control model used in the army

To calculate the optimization of a supply theory applied in the Army of the Czech Republic it is advisable to use a dynamic model with absolutely determined supply movement, and a dynamic multiproduct model with the constant level of supply acquisition costs. Following the established results of minimum costs used to acquire and store supplies, we select the model with lower costs.

3.1. Dynamic model with absolutely determined supply movement

It is a model which assumes that the quantity of enquiry is exactly known in advance. The aim of the optimization is to determine an optimal delivery size x_{opt} for which the total costs connected with delivery acquisition, keeping and storing supplies $N_c(x_{opt})$ during the period of a length T will be minimal.

If it is necessary to purchase Q units during the period of a length T and the supply is regularly renewed by the delivery of x units, then the number of deliveries v per a given period might be expressed by the following formula 2

$$v = \frac{Q}{x} \tag{6}$$

The costs used for acquiring all deliveries $N_p(x)$ are given by the product of a delivery amount v and one delivery costs c_p 2

$$N_p(x) = v\,c_p = \frac{Q}{x}c_p \tag{7}$$

The costs used for keeping and storing supplies $N_s(x)$ during a period t depend on the quantity of average supply x. The storing costs can be put as follows: 2

$$N_s(x) = \frac{x}{2}T\,c_s \tag{8}$$

Along with the increase in delivery size, an average carry over supply and consequently the total costs of keeping and storing supplies grow too. By summing both cost items we obtain a total cost function $N_c(x)$ which might be expressed in the following manner 2

$$N_c(x) = \frac{Q}{x}c_p + \frac{x}{2}T\,c_s \tag{9}$$

Now we set the first derivative of formula (9) equal zero and we get the Harris-Wilson equation which is put this way

$$x_{opt} = \sqrt{\frac{2\,Q\,c_p}{T\,c_s}} \tag{10}$$

When we put an optimum delivery size expression x_{opt} in a cost function $N_c(x)$, we will get the formula used for calculating minimum total costs.

$$N_c\left(x_{opt}\right) = \sqrt{2\,Q\,T\,c_p\,c_s} \tag{11}$$

Besides total minimal so-called optimum costs it is necessary to determine the time when an order is to be raised to get a new order to the store in time. Therefore it is essential to set an optimum so-called ordering supply level

$$x_o = Q\,t_p - m\,x_{opt} \tag{12}$$

where: t_p is the length of order lead time; t_c is the length of a delivery cycle; m is the amount of orders en route.

The value m will be calculated the following way

$$m = \frac{t_p}{t_c} \tag{13}$$

The calculated value m will be rounded up to whole numbers.

When following this way, the requirements listed below are to be observed:
• enquiry (consumption) should be known and constant;
• supply collection cannot swing;
• supply renewal is one-time in the form of an optimum delivery size;
• acquiring and storing costs are to be stabilized;
• purchase price is independent from order quantity;
• optimum delivery size is calculated for each supply item separately.

3.2. Dynamic multi-product model with the constant level of supply acquisition costs

This model assumes the customer will order more items to a store at once. On that account, however, an optimum delivery cycle as well as the optimum delivery size of single items will be abandoned, which can affect the costs of supply keeping and storing. This model presumes that supply acquisition costs do not depend on the number of ordered items. Furthermore, it is assumed that for the length T period the army needs to order k items of supplies with expected consumption (enquiry) Q_i of quantity units. The costs of the keeping and storing of single supply items are c_{si}. The total costs of a group order are then expressed by formula (14), provided that the items will be delivered in equal length delivery cycles. The number of deliveries v is to be also the same.

$$N_c\left(t_c\right) = \frac{T}{t_c}\,c_p + \frac{1}{2}\,t_c \sum_{i=1}^{k} Q_i\,c_{si} \tag{14}$$

If a function $N_c(t_c)$ derivative by t_c equals zero, then for an optimum delivery cycle length we will obtain the formula below

$$t_c^{opt} = \sqrt{\frac{2\,T\,c_p}{\sum_{i=1}^{k} Q_i\,c_{si}}} \tag{15}$$

Now it is necessary to determine an optimum structure (amount) of single material items delivery

$$x_i^{opt} = \frac{Q_i\,t_c^{opt}}{T} \tag{16}$$

After, we will specify the total minimal costs of supply acquisition for item group ordering in the following manner 2

$$N_c\left(t_c^{opt}\right) = \sqrt{2\,T\,c_p \sum_{i=1}^{k} Q_i\,c_{si}} \tag{17}$$

In final step it is essential to compare total costs of both versions of material ordering

$$\sum_{i=1}^{k} \sqrt{2\,Q\,T\,c_p\,c_s} \neq \sqrt{2\,T\,c_p \sum_{i=1}^{k} Q_i\,c_{si}} \tag{18}$$

4. Conclusion

The aim of inventory control is to obtain the required standard of service for an acceptable price. This might be achieved by finding a balance between storing costs and a price for providing a required service at the level claimed by the customer. Generally it might be stated that if supply quantity is high, the service price will be high too. This includes storing costs and the value of supplies placed in the warehouse. And conversely, if there is a small amount of supplies in the warehouse, storing costs and the price of supplies will be low. But drawback is the deficit in supply which might lead to secondary costs as a result of searching for a stopgap solution. The costs due to the deficit in supply are often very high especially when the production is to be stopped. Moreover, within the Army of the Czech Republic it can reduce the readiness for action of some military equipment and affect combat operations mainly in foreign missions.

Ideally, it would be good to find the way of having low service and storing costs and providing spare parts just in time. It means that the deficit in supply will not occur, but if it does, it will be only for a short time and for a low level of supplies, the percentage of which should be determined. A key aspect of supply control is dealing successfully even with supply uncertainty.

References

1. **Lambert D., Stock R. S., Ellram L**. Logistika. CP Books. Brno: 2005.
2. **Sixta J., Žižka M.** Logistika – používané metody. Computer Press. Brno: 2009.
3. **Kubát J.** Jak snižovat zásoby. *Logistika*, 2001, roč. 7, č. 11, ISSN 1211-0957, s. 16.
4. **Furch J., Kutil R.** Suggestion for a Supply Model to be Used in the Army of the Czech Republic. In: *Deterioration, Dependability, Diagnostics.* Brno: University of Defence, 2012, p. 249 – 258.

Proceedings of 8th International Conference ITELMS'2013

Research of Contact Stresses in Crossing

M. Gecas*, V. Lukosevicius**, Z. Bazaras***

*Kaunas University of Technology, Kęstučio str. 27, LT-43124, Kaunas, Lithuania, E-mail: modestas.gecas@stud.ktu.lt
**Kaunas University of Technology, Kęstučio str. 27, LT-44354, Kaunas, Lithuania, E-mail: vaidas.lukosevicius@ktu.lt
***Kaunas University of Technology, Kęstučio str. 27, LT-44354, Kaunas, Lithuania, E-mail: zilvinas.bazaras@.ktu.lt

Abstract

This article covers interaction analysis of cast crosspiece and rail carriage wheel. Also calculations and alterations of contact tension when wheel is moving through crosspiece. In order to evaluate crosspiece interaction with wheel, finite elements model using "Solidworks" was created and analysis was performed.
KEY WORDS: *shunt, crosspiece, contact tension.*

1. Introduction

This work aims to analyze the main cast crossings and wheelset interaction, and to determine how changes in the combination rolling contact stress in pieces. In order to analyze the interaction with the frog was collected wheelsets theory about the construction of the turnout, turnout marks, materials in the manufacture of elements of a turnout. the elements described in the turnout and the interaction between the axles, the potential impact location. According to Lithuania used for defect classification turnout up main crossings and bends defect list. Calculations were performed four axis wagon with a maximum permissible wagon axle load of Lithuania, which is equal to 22.5 tons. After the calculations were made up of dynamic load from the wheel mounting dependence on speed. According to this model in „Solidworks Simulation" program was carried out during the rolling wheel throught crossing simulation.Also was the contact stress in different locations to find the most dangerous place. When increasing the speed of most dangerous place was found safe speed limit. The conclusions discuss the results and compare the analytical and „Solidworks" program results compared.

2. Crosspiece types

Crosspiece – it's a piece of shunt, is used for railway transport in order to safely cross railroad intersections. Crosspieces have two mains groups:
1. Solid crosspieces;
2. Crosspieces with moving elements.
Common shunts are using sharp crosspieces. Here in section from beginning to core of crosspiece, wheel is not steered. This section is commonly called "death space". In order to be able to steer both wheels two checkrails are installed.
Angle α is an angle between core working edges and it is called crosspiece angle (Fig. 1). Tangent of this angle: core width, it's capacity and length ratio is called crosspiece sign and is marked $1/n$. Value n shows how much crosspiece length is bigger than it's width.
Crosspiece class can be determined using equation:

$$\frac{1}{n} = \frac{AB}{BO} = \text{tg}\, a$$

here: AB – perpendicular to A, mm; BO – distance between points B and O, mm.
Distance between checkrails and crosspiece core working edges cannot be lesser than 1472 mm, distance between checkrail and crosspiece flap pieces is not allowed to be higher than 1435 mm (Fig. 2).
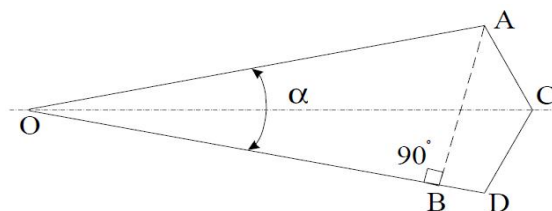
Fig. 1. Crosspiece class identification: OACD – crosspiece contour, α – crosspiece angle [1]
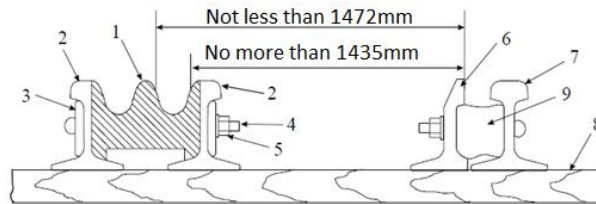
Fig. 2. Distance between checkrail and crosspiece core, between checkrail and flap working surfaces: 1 – cast core, 2 – flap, 3 – plate, 4 – bolt, 5 – nut, 6 – checkrail, 7 – rail, 8 – sleeper, 9 – insert [1]

According to construction type, solid crosspieces can be:
1. assembled from rails;
2. assembled with cast core and easy wearable flap piece;
3. surenkamos su lieta šerdimi;
4. assembled with cast core;
5. cast.

Crosspieces made from special rails are not widely used. Second type crosspieces consist of core and highly wearable flap pieces that are attached to rails. Compared to assembled crosspieces, second ones have relatively longer life time, because they are assembled from lesser parts count, however looking from construction perspective they are way more complicated. Third type crosspieces consist of cast core and flaps, which are made from ordinary rails. Cast elements are casted all in one. Main advantages are: low count of parts, high stability and durability, relatively long life time. Assembled crosspieces cast piece and all cast crosspiece is made from steel with 13% manganese. Such steel is more resistant to impact. After comparing two types of crosspieces advantages can be identified. Assembled crosspiece is better because it does not require expensive steel with manganese. In case of deterioration it is possible to replace certain parts, as flaps. Cast crosspiece has an advantage of lesser deformation probability, as whole part is casted at once.

Crosspiece with moving elements is sorted into:
1. with one moving rail,
2. with two moving rails,
3. with one moving flap,
4. with moving core.

Crosspieces with moving core is most widely used. Cores are produced from special sharp rails. This constructions enables to have continuous moving rolling surface from crosspiece to flap also dynamic forces are minimal. This enables, using such shunts that the speed used between stations can be used here. Crosspieces with moving core does not have checkrails installed, as mentioned above this is because of continuous rolling surface. Because of lower dynamic influence, crosspieces with moving core are likely to have three times longer lifetime than ordinary solid crosspieces. Disadvantage of such shunts is that synchronically movement of device must be ensured.

3. Forces acting while crosspiece in use

Static rolling parts impact is constant; all other impacts are random or statistical values. In order to determine dynamical loads such railroad characteristics should be known: rail and base elasticity modulus and rail and base relative stiffness coefficient. Four axle rail carriages which are moving at 5 m/s speed, wooded sleepers rubble ballast are given conditions. Calculations results are shown in Fig. 3. Base elasticity modulus is dependent on sleepers' type, ballast type, season of the year, railroad type. Dynamic influence is transferred trough wheels, having in mind that construction is inspected; rail road is in good condition and fulfills all characteristics.

When calculating contact tension it is enough to evaluate influence of one wheel. Calculations are made using highest dynamic load appearing probability.

Dynamical force dependence shows that even a small velocity can cause relatively high dynamical loads. Even with increasing velocity dynamic load does not increase much (Fig. 3).
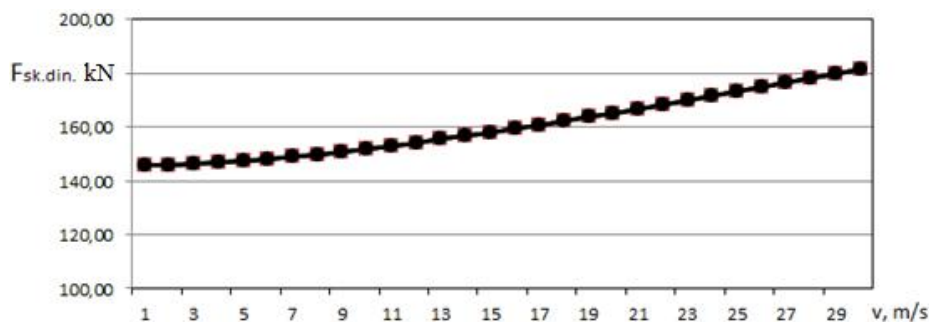
Fig. 3. Dynamic force and velocity dependance

4. Investigation results

When two bodies are interacting in small area: point or line, than contact or interfrence tensions appears. Even if those bodies acts with compression forces on each other, there is also interaction passed to other elements of this construction. In these ares triangle state of tension appears (Fig. 4). These tensions are only concentrated close to the surface area. Unfortunately for some elements these tensions can be cruicial, i.e. bearings, gears, rails. Surface area stenght of these elements is dependant on contact tensions value and when surface area is destroyed, element is no longer can be used. Because these loads are only considered in points that are very close to examined areas, there no longer can be used San - Venan principle or other tension calculation methods.
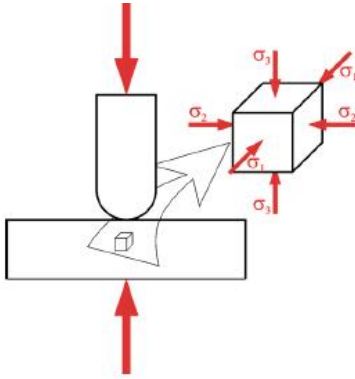
Fig. 4. Triaxial stress state [2]   Fig. 5. Wheel and crosspiece layout [3]
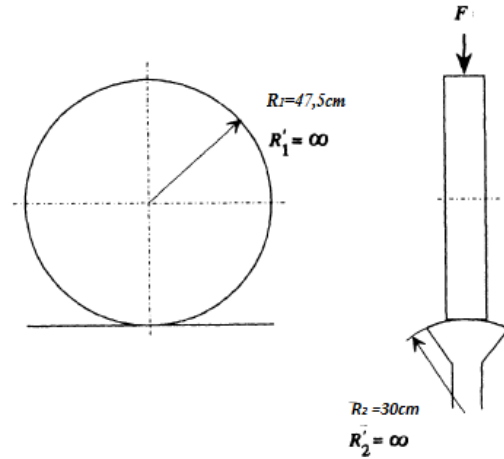
Assumptions used for contact stress calculations:
1. Contact spot can only deform elastically, Hooks law is valid.
2. Contact surface area is few times lesser than contactic elements area.
3. Pressure is acting perpendicular to a surface.

When considering wheel and crosspiece interaction, we have two steel bodies interacting with each other: when with radius of $R_1 = 0.475$ m, crosspiece which has $R_2 = 0.3$ m contact area with wheel (Fig. 5). Both steel surfaces have the same elasticity model of $E = 210$ GPa, Poisson's ratio of $v = 0.3$ and $q = 90°$ angle between interacting bodies planes. After performing calculations we can see that contact area deformation is $d = 0.132$ mm and maximal contact pressure is $p_0 = 1186$ MPa.

Analysis of contact formation and distribution was made; conclusions can be made that even if elasticity modulus excessed steel doesn't not fall apart. This is subject of triangle compression (material is compressed from all directions, meaning that no splits can appear. Using dissociation index value of $|\sigma_c| = 5\ \sigma_y$ was determined [5].

5. Calculations using "Solidworks"

In order to determine contact tension in multiple crosspiece locations, the complete model was designed in "Solidworks" (Fig. 6).
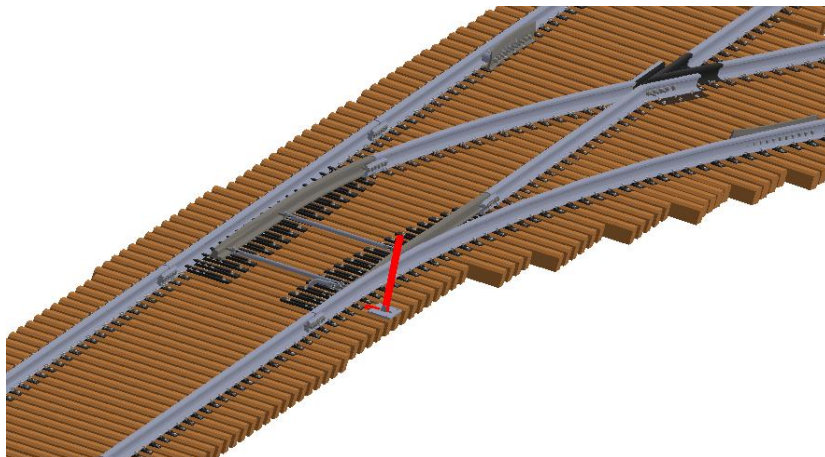
Fig 6. General view of railway turnout

Material used for wheel and coning was chosen according to ГОСТ 398-96 standard, which is used for determining steel composition, processing and mechanical properties, which are shown in Table 1. Crosspiece material was chosen according to ГОСТ 18267-82 standard, which regulates annealed rails mechanical processing and mechanical properties. Properties are shown in table 2. In order to perform analysis "Solid Works" model was created and analyzed. Crosspiece is fixed using rail flap pads. Rolling direction goes longitudinal to crosspiece blunt end. Finite element model is being used in analysis; areas of contact are refined and have improved custom mesh. Four axles railway wagon with weight of 22.5 tones was used. Wagon has velocity of 5 m/s directed to the blunt end of crosspiece. Different sets are performed while moving wheel with 50mm to crosspiece blunt end.

Table 1

Steel used for railroad wheel coning

Steel class	Plasticity limit, MPa	Relative elongation, %	Relative thinning,%	Hardness, HB
2	930-1110	Min. 10	Min. 14	Min. 269

Table 2

Characteristics of steel used for crosspiece

Plasticity limit, MPa (not less than)	1176
Relative elongation, % (not less than)	6
Contraction, % (not less than)	25
Impact viscosity (temp. 20°C), MJ/m^2	0,25

Table 3

Contact and equivalent pressure in mathematical crosspiece center

Distance from mathematical center, mm	Contact pressure,MPa	Equivalent pressure, MPa
-88	1036	553
-38	1282	788
12	1478	835
62	1963	989
82	1617	965
92	1020	671
112	2152	1011
162	1707	973
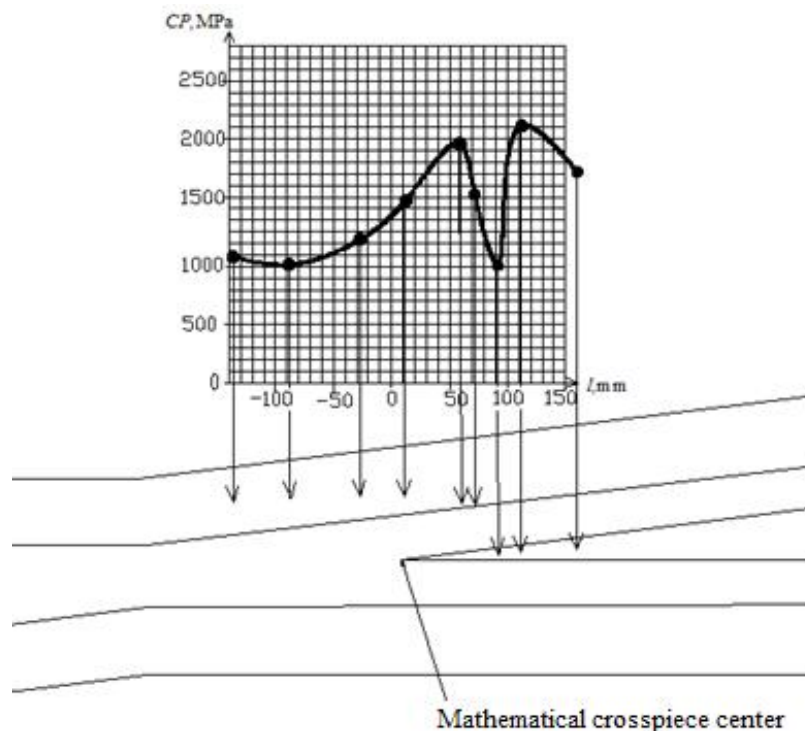
Fig. 7. Contact pressure when wheel is rolling though crosspiece

Calculations are made using 250 mm steps calculating tension in mathematical center of a crosspiece. Velocity used for calculations is 5m/s. In order to have a good result correlation, experiment is repeated twice when having high tensions. It is because wheel passes rail to the crosspiece part. Positive direction is direction of crosspiece blunt side. In highest tension experiment is repeatedly performed with increased speed. Results of calculations are shown in table 3 and Fig. 7. Pointers show points of maximal tension concentration. Coordination system is placed in crosspiece mathematical center (Fig. 7).

As we can see from the dynamic force and velocity graph, even low speed can cause relatively high dynamic loads.Increase in speed does not influence dynamic load that much.

6. Conclusions

Article covers investigation of cast 1/6 class steel crosspiece interaction with a wheel. Dynamic load were calculated: four wheel fully loaded train wagon which is going 5m/s speed and a crosspiece is operated under the force of 147.3 kN.

Calculations showed that contact tension $\sigma_y = 1176$ MPa, maximum contact pressure $p_0 = 1186$ MPa. Crosspiece steel yield strenght $\sigma_y = 1176$ MPa. Secure movement is assured.

More difficult calculations performed in the end of crosspiece, because contact area is quite small compared with with surface area of contacting pieces. Also wheel can contact with two surfaces at the same time, to determine interaction in this area, Solidworks calculations been made.

Performed calculations determined that maximal contact pressure in the distance of 112 mm is 2152 MPa. Safe value is 2940 MPa, so that means that crosspiece is safe to use. Results calculates in 1s ,taking 0.1s steps.

In order to perform investigation at higher speed, a crosspiece with moving elements, which forcs consistend surface. It is possible to lower stress in a solid crosspiece by increasing roll radius of contact surface.

Acknowledgements

References

1. Iešmų elementų konstrukcijos. Access on the internet: < http://vddb.library.lt/fedora/get/LT-eLABa-0001:E.02~2004~D_20040623_144448-49423/DS.005.0.04.ETD > [checked on 20012-05-15].
2. Vietiniai įtemptos medžiagos poveikiai. Access on the internet: < http://www.freewebs.com/auris10/XIV%20skyrius.pdf > [checked on 20012-05-15].
3. Iešmų defektų klasifikatorius. 55/k. Lietuvos geležinkeliai. 2003.
4. GOST 18267-82 standarto bėgių plienas. Access on the internet: < http://www.roadportal.ru/rail/gost18267-82/ > [checked on 20012-05-15].
5. Бандажи из углеродистой стали для подвижного состава железных дорог широкой колеи и метрополитена. Технические условия ГОСТ 398-96. Access on the internet: < http://www.metalgost.ru/gosts/GOST%20398-96.pdf > [checked on 20012-05-15].
6. **Lingaitis L. P.** Geležinkeliai. Bendras kursas. – Vilnius: Technika, 2009. – 278 p.
7. **Sakalauskas K., Laurinavičius A., Podagėlis I.** Geležinkelių inžinerija 2. Konstrukcija, priežiūra, technologija. – Vilnius: Technika, 2000. – 276 p.
8. **Podagėlis I., Povilaitienė.** Geležinkelių inžinerija. Viršutinė bėgių kelio konstrukcija. – Vilnius: Technika, 2006. – 112 p.
9. **Bazaras Ž., Dundulis R., Kalpokas J.** Geležinkelio riedmenys. – Kaunas: Technologija, 1997. – 87 p.
10. [LST EN 13232-1:2007 lt]. Standartas. Geležinkelio kelias. Iešmai ir bėgių sankryžos. Apibrėžtys.
11. [LST EN 13232-2:2007 lt]. Standartas. Geležinkelio kelias. Iešmai ir bėgių sankryžos. Geometrinės formos reikalavimai.
12. [LST EN 13232-3:2007 lt]. Standartas. Geležinkelio kelias. Iešmai ir bėgių sankryžos. Ratų ir bėgių sąveikos reikalavimai.
13. Rato ir bėgio kontakto įtempių būvio tyrimas. Access on the internet: < http://science-bsea.narod.ru/2004/mashin_2004/vorobiev_issled.htm > [checked on 20012-05-15].
14. **Pilkey, Walter D.** Formulas for stress, strain and structural matrices. Second edition. Virginia. 2005. Access on the internet: < http://fte.edu.iq/eftrathya/15.pdf > [checked on 20012-05-15].

Dissipative Structures Modeling in the Aluminium Alloy: an Energy Approach

V. Hutsaylyuk*, H. Sulym**, I. Turchyn***, Ia. Pasternak****

Military University of Technology, Gen. S. Kaliskiego Str. 2, 00-908, Warsaw, Poland, E-mail: vhutsaylyuk@wat.edu.pl
**Bialystok Technical University, Wiejska Str. 45c, 15-351 Białystok, Poland, E-mail: sulym@pb.bialystok.pl*
***Ivan Franko National University of Lviv, Universytetska Str. 1, 79000 Lviv, Ukraine, e-mail: ihorturchyn@gmail.com*
****Lutsk National Technical University, Lvivska Str. 75, 43018 Lutsk, Ukraine, e-mail: pasternak@ukrpost.ua*

Abstract

The paper presents a simplified analysis of the aluminium alloy 2024-T3 behavior under the influence of impact additional loading. Periodic distribution of the dissipative structures induced by the loading impulse is related with the standing wave produced by the latter. Simple energy approach is used to assess the frequency and wavelength of the associated standing wave and thus the distance between the bands of material dissipative structures.
KEY WORDS: *aluminum alloy 2024-T3, impact loading, dissipative structure, simplified analysis.*

1. Introduction

Structural materials, especially those used in the aircraft industry and airspace engineering, are subjected to various types of impact load during their long-term exploitation. Numerous studies have revealed a number of peculiarities in the dynamic behavior of the materials at the yield point, which had not been observed under the quasi-static loading. Recent experimental studies [1–4] have shown that the additional impact loading imposed on the prestressed samples made of elastic-plastic materials can lead to the irreversible changes in material structure, in particular to formation of the so-called *dissipative structures*. The latter are usually observed as bands placed at the approximately equal distance one from another (Fig. 1). Thus, the structure of the material essentially changes, and it possesses new mechanical properties.
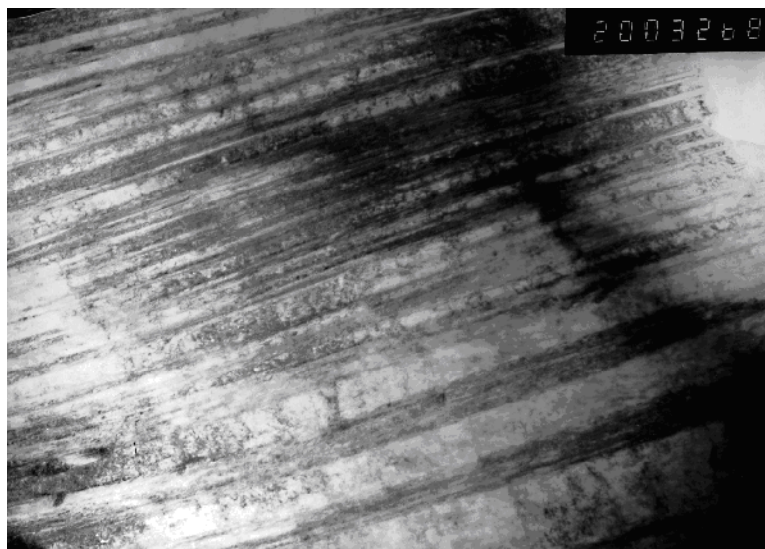
Fig. 1. Dissipative structures obtained under additional impact loading of the aluminium alloy 2024-T3 sample

Structural changes inside the material were associated with the amount of energy supplied to the sample during the impact loading [1–4]. However, these models provided only qualitative analysis of the physical processes involved in the formation of the dissipative structures. The quantitative analysis of wave propagation in the elastic-plastic aluminium sample was first held in Ref. [5]. This analysis allowed prediction of development of plastic deformations under the influence of impact load. It was observed that the increase in the loading rate essentially increases the magnitude of vibrations, and only slightly influence their frequency. Vibrations have harmonic behavior. The study of the plastic energy shows that it increases monotonically, however the total strain energy rapidly reaches its maximum and at certain time, when the plastic energy reaches its maximum, it continues to change periodically. The time, when the plastic deformation process is over, is much greater than the time, which is required by the wave to path through the plate. Thus, the patterns of plastic strains are formed by both incident and scattered waves, which can obviously induce a standing wave.

However, to this end there are no quantitative approaches, which allow simplified analysis and modeling of impact loading induced dissipative structures. The ordering of the obtained material structure indicates that certain periodic processes takes place during or just after the impact loading of the material. Most simple and obvious periodic process, which can take place after the impact, is a standing wave, which dissipates its energy at the antinodes. The latter can be related with the bands of dissipative structures.

Therefore, this paper provides simplified analysis of the standing waves, which can induce dissipative structures in the elastic-plastic materials, and relates their wavelengths with the parameters involved in the experimental processes of additional impact loading of elastic-plastic materials.

2. Energy Approach to Modeling of Dissipative Structures

Consider a prismatic sample of a length l, which cross section area is equal to S. Thus, its volume equals $V = S \, l$. Assume that during the impact loading the sample obtains some amount of energy W. Consider an associated standing wave, which energy equals W. According to [6] the mean energy density $\langle w \rangle$ of elastic wave equals

$$\langle w \rangle = \frac{1}{2} r (\Delta l w)^2 \tag{1}$$

where ρ is the density of the material; ω is an angular frequency, and Δl is the amplitude of the wave. The wave amplitude Δl can be related to the displacement of the specimen's end during the impact loading.

It is obvious that the total energy inside the specimen equals

$$W = \langle w \rangle V = \langle w \rangle Sl = \frac{1}{2} rSl (\Delta l w)^2 . \tag{2}$$

According to the energy conservation law, the energy W induced by the impact loading should be equal to the work A produced by the external force. The work A of a force equals

$$A = \int_{l}^{l+\Delta l} F dx . \tag{3}$$

Due to instantaneous character of the impact loading, one can assume that the force F is a linear function of x, i.e.

$$F = s S \approx \left(s_0 + \Delta s \frac{x-l}{\Delta l} \right) S \tag{4}$$

where s_0 is the initial stress of the sample; Δs is the change in stress during the impact loading.

Substituting Eq. (4) into Eq. (3) one can obtain

$$A = \int_{l}^{l+\Delta l} F dx = S \int_{l}^{l+\Delta l} \left(s_0 + \Delta s \frac{x-l}{\Delta l} \right) dx = S \left(s_0 + \frac{1}{2} \Delta s \right) \Delta l \tag{5}$$

Equaling Eqs. (3) and (5) the following equation can be written

$$\left(s_0 + \frac{1}{2} \Delta s \right) \frac{l}{\Delta l} = \frac{1}{2} r (lw)^2 \tag{6}$$

Noting that the deformation of a sample during the impact equals $\Delta e = \Delta l / l$, Eq. (6) writes as

$$\frac{s_0 + 0.5\Delta s}{\Delta e} = \frac{1}{2} r (lw)^2 \tag{7}$$

The left-hand-side of Eq. (7)

$$k = \frac{s_0 + 0.5\Delta s}{\Delta e} \tag{8}$$

can be determined experimentally from the obtained stress-strain curves. One can readily estimate the value of k. In the case of static or quasi-static loading with zero initial stress k is equal to the half of material Young modulus E. It is obvious that due to the inertia phenomenon the impact loading is accompanied with higher stress and lower deformations than in the case of static loading. Therefore, the constant k should be bigger (or much bigger) than the

Young modulus: $k \gg E$. The value of k is dependent on the material properties and on the deformation rate (or stress rate).

Based on Eq. (7) the angular frequency of the standing wave, which dissipate energy supplied by the impact loading is equal to

$$w = \frac{1}{l}\sqrt{\frac{2k}{r}} \tag{9}$$

The wavelength of the standing wave is equal to

$$l = \frac{2pc}{w} = 2plc\sqrt{\frac{r}{2k}} \tag{10}$$

where c is a phase velocity.

Since there are two antinodes at the wavelength λ, the distance between them, which is associated with the distance between the dissipative bands, equals

$$d = \frac{1}{2}l = plc\sqrt{\frac{r}{2k}} \tag{11}$$

The phase velocity c of the elastic wave in a solid is related to its density and Young modulus by the following dependence

$$c = \sqrt{\frac{E_0}{r}} \tag{12}$$

where $E_0 = \dfrac{E(1-n)}{(1+n)(1-2n)}$, and n is a Poisson ratio.

According to Ref. [7] the phase velocity is sensitive to the plastic behavior of the material, and when the material deformation is accompanied with plastic deformations the phase velocity is lower, than in the elastic case. Thus, one of the distinctive features of these processes is dynamic properties of materials, which primarily concern theoretical foundations of materials science and, in particular, the study of the phenomenon of formation of dissipative structures under impact supply of deformation energy. However, one can use Eq. (12) assuming that E_0 is dependent on strain and strain rate. Then Eq. (11) writes as

$$d = pl\sqrt{\frac{E_0}{2k}} \tag{13}$$

3. Analysis of the Obtained Dependence

Eq. (13) gives a useful relation between the distance d of dissipative structures, the length l of the specimen, and the characteristic parameter k, which account for the impact loading and initial stress of the sample. However, one can easily determine only the value of d, using for example a metallographic analysis. The impact modulus k given by Eq. (8) can be determined from the stress-strain curve, but the latter should be precisely plotted. This is due to the fact, that the impact loading is instantaneous, and thus due to the equipment inertia it is rather hard to determine true values of stress and strain increments. Another issue is to determine the value of E_0 for the elastic-plastic material. Further experimental studies should be held to estimate parameters involved in Eq. (13).

However, Eq. (13) allows explanation of the phenomena of dissipative structures based on the classical viewpoints of continuum mechanics. According to the analysis provided after Eq. (8) one can note that for quasi-static loading $2k \approx E_0$, and Eq. (13) results in $d \approx pl > l$. Thus, one can conclude that no dissipative structures can be observed under the quasi-static loading, since the expected distance between them is greater than the length l of the specimen. On the other hand this proves the obvious fact that no dynamic processes are observed under the quasi-static loading.

In contrast, for the impact loading $k \gg E_0$, therefore, according to Eq. (13) $d \ll l$. Thus, the phenomenon of dissipative structures and their band-like distribution can be explained by the transient elastic-plastic dissipative waves, which are induced by the impact. Besides, according to Eq. (8) the higher is the initial stress s_0 the higher is k. It is obvious that the highest values of k can be obtained when the initial stress s_0 is approximately equal to the yield stress s_y, since at this point the strain increment Δe is still small, comparing to that for higher s_0. This behavior is well agreed with the experimental studies [1–4].

4. Conclusions

This paper considers formation of dissipative structures in the elastic-plastic aluminium alloy and relates it to the standing wave initiated by the impact supply of mechanical energy. Due to the plastic irreversible deformations this wave dissipates its energy at the antinodes, thus forming the bands of dissipative structures. The simplified analysis used in this paper results in a simple equation relating the distance d of dissipative structures, the length l of the specimen, and the characteristic parameter k, which accounts for the impact loading and the initial stress of the specimen. Thus, the quantitative analysis can be held to assess the properties of elastic-plastic materials after the impact loading of prestressed samples. It is shown that the account of the equipment inertia is crucial for the assessment of parameters involved in the quantitative model of the phenomenon of nonclassical behavior of materials under the limit high-speed loads and dissipative structures formation. Besides, one of the distinctive features of these processes is dynamic properties of materials, which primarily concern theoretical foundations of materials science and, in particular, the study of the phenomenon of formation of dissipative structures under the impact supply of deformation energy.

References

1. **Chausov N. G., Voytyuk D. G., Pylypenko A. P., Kuzmenko A. M.** Setup for tests of materials with full chart failure // Problems of Strength. – 2004. – № 5. – P. 117–123.
2. **Chausov N. G., Zasymchuk E. E., Markashov L. I., Vyldeman V. E., Turchak T. V., Pylypenko A. P., Parada V. N.** Features deformation plastic materials at the dynamic non-equilibrium processes // Zavodskaya Laboratory. Diagnosis of materials. – 2009. – V.75. – No 6. – P. 52–59.
3. **Zasymchuk E. E., Markashov L. I., Turchak T. V., Chausov N. G., Pylypenko A. P., Paratsa V. N.** Features structure plastic transformation of materials in the process of shock change load // Fyzycheskaya mezomehanyka. – 2009. – V. 12. – № 2. – P. 77–82.
4. **Chausov M. G., Lucky Y. Y., Pylypenko A. P.** et al. Effect of multiple change loading on the deformation of plastic material // Mehanika i fizyka ruynuvaynya budivelnyh materialiv i konstrukciy. Zbirnyk publikaciy. – Lviv: Kameniar. – 2009. – Issue 8. – P. 289–298.
5. **Hutsaylyuk V., Sulym H., Turchyn I., Pasternak Ia., Chausov M.** Investigation of dynamic non-equilibrium processes in the aluminum alloy 2024-T3 under additional load impulse // Proceedings of 7th International Conference ITELMS'2012. – P. 79–85.
6. **Landau L. D., Lifshitz E. M.** Theory of Elasticity (3rd ed.). – Oxford, England: Butterworth Heinemann. – 1986.
7. **Liu Jin-Xia, Cui Zhi-Wen, Wang Ke-Xie.** The acoustoelastic effect on Rayleigh waves in elastic–plastic deformed layered rocks // Chinese Physics. – 2007. – Vol. 16, No 8. – P. 2180–2187.

Introduction of Investigation of Implementation Possibilities of LEAN Manufacturing System in Metal Processing Industry Using Statistical Methods

R. Jackuvienė*, R. Karpavičius**, V. Kleiza***

*Lithuanian Maritime Academy, I. Kanto str. 7, Klaipėda LT-92123, Lithuania, e-mail: r.jackuviene@lmc.lt
**AB "Fasa", Sporto str., 9 Marijampolė LT-68108 Lithuania, e-mail: rimas@fasa.lt
***Kaunas University of Technology, Daukanto 12, 35209 Panevėžys, Lithuania, e-mail: vytautas.kleiza@ktu.lt

Abstract

The article presents the LEAN investigation of the internal resources of the Lithuanian company of metal processing using the program for processing of statistical data SPSS 20. There was selected the analyzed sample; and three types of analyzes were used: descriptive, correlative and regressive. There were formed statistical-economic linear dependences, which allow forecasting the activity indexes of the company.
KEY WORDS: *LEAN, manufacturing, 5S.*

1. Introduction

The integration and "introduction" of new technologies into the market in modern global market is one of possible management modes of successful business using the up-to-date technologies to create new products, processes, and services. The basis of LEAN philosophy is to reduce the expenses as much as possible and to increase the value received by the user as much as possible [1]. The purpose of this system is to provide such value to the user as he expects. The companies, which have already applied LEAN principles in their activity notice positive changes in many areas. With the beginning of application of LEAN principles the execution time of orders gets much shorter, the work efficiency increases, the motivation of employees grows significantly, and new possibilities for their continuous development appear. Besides, the application of principles of "lean" management helped to avoid worsening of the product's quality. The implementation of LEAN principles is the essential organizational transformation that changes the employees' behavior, attitude to the clients, cooperation between the colleagues from different departments of organization, and roles of employee and manager in the company. In order to analyze the created additive value that determines the importance of main indexes in the company, we will use the methodology of statistical researches. We will use the mathematical package SPSS in order to determine the characteristics, on the basis of which we will be able to speak about necessity to apply the principles of the LEAN system in the company.

2. Investigation by statistical methods

We will select the analyzed sample in the investigation and we will us the analyses of three types: descriptive, correlative and regressive. We will use the ordinary random selection method of the sample. The ordinary random sample is the sample of n different elements from the finite population of N size, when any set of different elements n has the same probability to be selected.

In order to answer the question about the needed size of the sample and to get a representative sample, we calculate it by recording the absolute evaluation error, $d = 5\%$, at the selected significance level $a = 0.05$, standard deviation of population $s_i = 22$, standardized value of reliability level $z_{a/2} = z_{0.05/2} = 1.96$ and size of population $N = 130$. When we use [2] the formula (1), we receive the size of the sample equal to 47. Nevertheless, we are able to use the data of all the workshop's workers, thus when we satisfy the minimal requirements of sample's volume using the sample equal to 72.

$$n = \left(\frac{1}{N_i} + \frac{d^2}{s^2 \, z_{a/2}^2} \right)^{-1} \tag{1}$$

3. Stages of the empirical research

The descriptive analysis allows assessing the functions of the indexes' sample (statistics), i.e. characteristics of data location and dispersion. After we calculate the descriptive statistics for each variable, we will compare them with each other and present their interpretation. We will calculate the descriptive statistics for the number of employees (**X1**), percentage index of actually performed work hours (**X2**), number of actually performed work hours (**X3**), monthly work load (**X4**), number of planned work hours (**X5**), and percentage index of planned work hours (**X6**).

The correlative analysis can identify the relation between the aforementioned variables. Therefore we will calculate the "Pearson" correlation coefficient for each pair of variables and we will form correlative matrix and evaluate the statistical significance of correlation by calculating of probability p of the hypothesis about equality of correlation coefficient to 0, and by recording the significance level $a = 0.05$. We will consider the double correlation with $p = 0.05$ as statistically significant, and otherwise we will state that the linear connection between two variables is not statistically significant, thus the hypothesis about equality of correlation coefficient to 0 will be rejected.

In order to assess the impact of independent variables on response (dependant variable), we will use the regressive analysis. The formed model of linear regression will help us to assess the influence of the independent index on the dependent variable. When the models of linear regression of planned hours and actually worked hours are made, we will determine the influence of the employees' number on the number of hours. Probably the increase of employees' number leads to increased number of planned and actually worked hours per month.

4. Correlative analysis

We will use the correlation coefficient to evaluate the strength of connection [3]. The value of the correlation coefficient will allow making conclusion about the strength of correlation. Thus the strength measure of dependency of variables is the correlation coefficient. When we check the hypothesis about equality of correlation coefficient to zero, we will answer the question about statistical significance of dependency of variables in population. The relation determined during correlative analysis will not be interpreted as causality, only as a measure of relation.

The values of observed random dimensions X and Y are measured in the scale of intervals. The dotted evaluation of correlation coefficient is calculated using the formula (2).

$$r = \mathrm{r} = \frac{\overline{XY} - \overline{X} \cdot \overline{Y}}{\sqrt{\overline{X}^2 - (\overline{X})^2} \sqrt{\overline{Y}^2 - (\overline{Y})^2}} \qquad (2)$$

The linear relation is stronger when $|r|$ value is closer to 1. If $r = 0$, there is no linear relation.

5. Regressive analysis

The regression equation received in single-factor regressive analysis [4] links one variable Y, so called dependent variable, with another – independent variable X. When the regression equation is used, it is possible to forecast the values of dependent variable according to the independent variable using the 95% reliability.

The model of single-factor linear regression is written by formula (3).

$$Y_i = b_0 + b_1 \cdot X_{ji} + e_i \qquad (3)$$

where: $i = \overline{1, 72}$; Y is dependent variable; X is independent variable.

6. Descriptive statistics

When the economic indexes are analyzed [5], it is very important to know the statistics of their location and dispersion – they are presented in Table 1. During the analyzed period the average number of employees per month was 16. The deviations of employees' parameters from the average analyzed in different months are not big, as the standard deviation is 3.14. The asymmetry of allocation of the employees' number is also not big, as the asymmetry coefficient is equal to -0.835. The case of left asymmetry is observed because the asymmetry coefficient is below 0. This means that the allocation of the employees' number is more focused to the left from the mean of the employees' number, and usually more than 16 employees were working. As the excess coefficient of the employee's number is smaller than 0, the allocation is flat (is not sharp). The smallest number of employees was 10 employees, and the biggest recorded number per month was 20.

During the analyzed period, on average 139% of actual work hours were worked per month. In different months the dispersion of percentage index around the mean is equal to 22.2. The asymmetry of index allocation is quite big, because asymmetry coefficient is equal to -1.484. The case of left asymmetry is observed because the asymmetry coefficient is below 0. This means that the allocation of the employees' number is more focused to the left from the mean – accordingly, this determines more values of the index below 139%. As the excess coefficient of percentage index is smaller than 0, the allocation is taper. The smallest recorded value of the index was 56%, and the biggest 188%.

The number of actually worked hours is not a percentage index, but a nominal one. During the analyzed period, on average 3319 actual work hours were worked per month. In different months the dispersion of percentage index around the mean is equal to 1130. It is a very big dispersion. Big dispersion of data has negative influence on formation of forecasting models, because when such a variable is included, the model describes small amount of the data, while majority of data is allocated to the errors of the model. The asymmetry of index allocation is small, because asymmetry coefficient is equal to -0.07. The case of left asymmetry is observed, but we can regard this asymmetry as not significant because it is close to 0. As the excess coefficient of percentage index is smaller than 0, the allocation is flat, but in this case the flatness is manifested only theoretically, because the excess coefficient, similarly to asymmetry coefficient, is close to 0. The smallest number of worked hours per month was 782 h, and the biggest – 5795 h.

The monthly load of work hours on average made 2376 hours. In different months the dispersion of hours around the mean was equal to 619 hours. It is quite a big dispersion. The asymmetry of index allocation is moderate, because asymmetry coefficient is equal to -0.57 and the allocation is accumulated leftwards from the sample's mean. As the excess coefficient of monthly work load exceeds 0 (0.72), the allocation is flat. The smallest monthly work load made 434 hours, and the biggest – 3480 hours.

The number of planned work hours per month on average made 3495 hours. In different months the dispersion of hours around the mean was equal to 1381 hours. It is a very big dispersion around the mean. Big dispersion of data has negative influence on formation of forecasting models, because when such a variable is included, the model describes small amount of the data, while majority of data is allocated to the errors of the model. The asymmetry of index allocation is small, because asymmetry coefficient is equal to 0.06, thus the allocation is almost symmetrical to the mean. As the excess coefficient of monthly work load is below 0 (-0.68), the allocation is sharp. The smallest number of planned work hours per month was 742 h, and the biggest – 6560 h.

During the analyzed period, on average 104% hours were planned to be worked per month. In different months the dispersion of percentage index around the mean is equal to 18.5. The asymmetry of index allocation is small, because asymmetry coefficient is equal to -0.179. The case of left asymmetry is observed because the asymmetry coefficient is below 0. This means that the allocation of the index is more focused to the left from the mean – accordingly, this determines more values of the index below 104%. As the excess coefficient of percentage index is smaller than 0 (105), the allocation is taper. The smallest of the index was 52%, and the biggest 159%.

We present the data on actually worked hours, planned work hours and monthly work load during the analyzed period (Table 1).

Table 1

Descriptive statistics

Statistics / Descriptive	X1	X2	X3	X4	X5	X6
N Valid	72	72	72	72	72	72
N Missing	0	0	0	0	0	0
Mean	16.13	139.24	3319.44	2376.704	3495.040	104.484
Std. Deviation	3.140	22.270	1130.734	619.755	1381.480	18.564
Skewness	-0.835	-1.484	-0.072	-0.573	0.064	-0.179
Std. Error of Skewness	0.283	0.283	0.283	0.283	0.283	0.283
Kurtosis	-0.537	4.218	-0.522	0.725	-0.680	1.0590
Std. Error of Kurtosis	0.559	0.559	0.559	0.559	0.559	0.5590
Minimum	10	56	782	434.440	742	52.490
Maximum	20	188	5795	3480.00	6560	159.35

7. Conclusions

1. The results of the conducted empirical analysis show that the planned and actually worked hours do not have strong relations with the number of employees, thus we can state that it is rational to start applying LEAN manufacture in the company. The absence of strong correlation between the aforementioned signs shows uneven number of work hours, which is related to the fact that the employees have work holidays, during which their work time is not recorded.
2. The statistically significant relation between the number of planned work hours and the number of actually worked hours was received. This is based by the fact that the planning cannot be separated from observation of actual data and surveillance of manufacturing process.
3. We have determined that we cannot describe reliably the actual and planned work time subject to the number of employees using the models of linear (non-linear) regression. We have to perform determination of relations of correlation analysis.

References

1. **Šateikienė D., Pancerovas D.** Just-initime sistemos įdiegimo galimybės laivų statyboje. Klaipėdos universitetas, Jūrų technikos fakultetas. ISSN 1648-8776 Jaunųjų mokslininkų darbai. Nr. 2 (31). 2011, pp. 182 – 188.
2. **Yangb H. C., Chaob A., Yipc P. S. F.** Population size estimation using local sample coverage for open populations.Journal of Statistical Planning and Inference. Volume 113, Issue 2, 1 May 2003, Pages 699–714.
3. **Al-Mutairi D. K., Ghitany M. E., Gupta R. C.** Estimation of reliability in a series system with random sample size. Computational Statistics & Data Analysis, Volume 55, Issue 2, 1 February 2011, Pages 964-972.
4. **So Young Sohn, Su Gak Lee**. Probe test yield optimization based on canonical correlation analysis between process control monitoring variables and probe bin variables Original Research Article. Expert Systems with Applications, Volume 39, Issue 4, March 2012, Pages 4377-4382.
5. **Nilesh Thite, Babu Noushad, Gauri Kunjeer.** Contact lens prescribing pattern in India—2011 Original Research Article Contact Lens and Anterior Eye, In Press, Corrected Proof, Available online 26 January 2013.

Electric Properties of Asymmetrically Narrowed Superconducting Detectors

A. Jukna*, J. Gradauskas*, **, A. Suziedelis*, **, A. Abrutis*, V. Nargeliené**, J. Sulcas*,
V. Lisauskas**, K. Sliuziene****

**Department of Physics, Vilnius Gediminas Technical University, Sauletekio av. 11, LT-10223, Vilnius, Lithuania,
e-mail: arturas.jukna@vgtu.lt*
***Centre for Physical Sciences and Technology, Semiconductor Physics Institute, A. Gostauto 11, LT-01108 Vilnius,
Lithuania, e-mail: jonas@pfi.lt*
****Department of General and Inorganic Chemistry, Vilnius University, Naugarduko 24, LT-03225 Vilnius, Lithuania,
e-mail: adulfas.abrutis@chf.vu.lt*

Abstract

Type-II superconductor $YBa_2Cu_3O_{7-x}$ (YBCO) thin films are characterized by the critical temperature $T_c^{on} \sim 91$ K and the critical current density $J_c(78$ K$) > 3$ MA/cm^2 at temperature $T = 78$ K. Such films have found application in low-jitter ultrafast photo-switches operating in a picosecond time-scale and also as emitters of the microwave-frequency (MW) signals. Comparatively weak absorption of MW signals, possibility to control motion of Abrikosov magnetic vortices at temperatures below T_c^{on}, and well developed technologies of films fabrication and patterning are the main advantages of YBCO superconductors if compared with other superconducting materials. Our research results represent a concept of MW-detector based on asymmetrically-necked YBCO thin film devices exhibiting nonlinear current-voltage dependences in the normal material's state (i.e. degenerate semiconductor) at temperatures above T_c^{on} and also in the superconducting state (i.e. zero resistivity), at temperatures below T_c^{on}. Based on current-voltage measurement results the electric properties of devices in the normal state are explained by means of electric field induced nonuniform heating of free-carriers in the superconducting film. At temperatures below T_c^{on}, in the mixed state of the material biased with current density higher than J_c, the current-voltage dependences of the devices are predetermined by the onset of dissipative motion of Abrikosov magnetic vortices in the superconductor.

KEY WORDS: *YBCO superconductor, critical temperature, critical current, oxygen decomposed superconductor, normal state superconductor, microwave detection, asymmetrically-necked structure, asymmetric nonlinear I-V characteristic.*

1. Introduction

Superconductor thin film exhibits superconducting state (i.e. the Meissner state or in other words the state of absolute diamagnetism) at temperatures $T < T_c^{on}$ while the amplitude of bias current is below critical current I_c, and the amplitude of external magnetic field or biasing current self-produced magnetic field is below the first critical magnetic field H_{c1} of a superconductor [1]. Here T_c^{on} is the temperature of onset of the superconducting state in the film. The screening of magnetic field appears due to surface supercurrents flowing in $\lambda(T)$-thick layer of a superconductor [2]. Here $\lambda(T) = \lambda(0)[1 - (T/T_c)^4]^{-1/2}$ is the temperature dependent magnetic field penetration depth into superconductor. Generally speaking, the Meissner supercurrent in the superconductor biased at $I = I_c$ should reach maximum, equal to the depairing current of Cooper pairs: $I_{cd} = \Phi_0 S / \left[3\sqrt{2} \, p \, m_0 \, x(T) l(T)^2 \right] \sim 100$ MA/cm^2 [3]. Here $\Phi_0 = h/2e = 2.07 \times 10^{-15}$ Wb denotes magnetic flux quantum, $S = d \cdot W$ stands for the cross-section of the d-thick and W-wide film and $\xi(T) = \xi(0)(1 - T/T_c)^{-1/2}$ is the temperature dependent coherence length in a superconductor.

The most important parameter in various technical applications of superconductors is critical current density J_c, expressed as $J_c = I_c / S$, which is usually several orders of magnitude weaker than current density of superconductor's irreversible thermal damage J_{td} (i.e. $J_{td} = I_{td} / S$) [4]. It is believed that current assisted thermal damage of the film occurs due to onset of a dissipative motion of Abrikosov magnetic vortices [5] in the superconductor. Magnetic vortices and antivortices nucleate in random places at the film's edges and move perpendicularly to electric current direction. Recently it has been shown experimentally that density and character of motion of Abrikosov magnetic vortices in the superconducting films can be controlled and directed by means of insertion of artificial columnar defects in the superconducting film [5], by introducing the multilayer structures [6], or creating vortex channels for easy vortex flow [7], etc.

Superconducting devices made of thin films of $YBa_2Cu_3O_{7-x}$ type-II superconductor with $T_c^{on} \sim 92$ K and $J_c(78$ K$) \sim 3$ MA/cm^2 are demonstrated as a low-jitter ultrafast photoswitch [8] and emitter of microwave signals [9]. Weak absorption of MWs [10], controllable motion of Abrikosov magnetic vortices at $T < T_c^{on}$ [5-7], well developed technology of film fabrication [10-11] and patterning [7] are the main advantages of the $YBa_2Cu_3O_{7-x}$ superconductors if compare with other superconducting materials.

Being in the nonsuperconducting state, i.e. at temperatures $T > T_c^{on}$, type-II superconductor exhibits properties of degenerate (i.e. heavily-doped) semiconductor. Strong coupling between electrons and phonons in heavily-doped semiconductors impedes investigation of hot carrier phenomena that takes place in semiconductors. One case that hot carrier phenomenon manifest itself is so called bigradient effect arising in asymmetrically-necked semiconductor structures and being recognized through asymmetrical current-voltage characteristic [12]. Investigations of hot electron electromotive force arising in the asymmetrically-necked devices of heavily-doped n-GaAs thin films with neck shaped down to submicron dimensions revealed the dependence of voltage sensitivity of the structure on the size of the neck [13]. Moreover, the asymmetrically-necked semiconductor planar structures revealed themselves as THz radiation detectors which operation is based on electric field induced free-carrier heating effect.

Our research results represent a concept of MW detectors based on asymmetrically-necked $YBa_2Cu_3O_{7-x}$ thin film devices exhibiting nonlinear current-voltage dependences in the normal material's state (i.e. degenerate semiconductor) at temperatures above T_c and also in the superconducting state (i.e. zero resistivity), at temperatures below T_c. Based on experimental measurement results, the nonlinear current-voltage dependences of our devices switched into the normal state are explained by means of electric-field-induced nonuniform heating of free-carriers [12]. At lower temperatures, $T < T_c$, nonlinear current-voltage characteristics are explained by means of onset of dissipative motion of Abrikosov magnetic vortices in the superconducting film biased at $I > I_c$.

2. Samples and Measurement Methods

0.3-μm-thick $YBa_2Cu_3O_{7-x}$ films were fabricated using MOCVD method [11] onto $LaAlO_3$ substrates. Epitaxial films with the crystalline c-axis oriented perpendicularly to the substrate's plane exhibited metallic-like resistivity $vs.$ temperature dependence, zero-resistivity-temperature $T_{c0} = 91$ K, superconducting transition width $\Delta T_c = 0.4$ K, and critical current density J_c (78 K) ~ 1.7 MA/cm^2 at temperature $T = 78$ K.

Asymmetrically narrowed devices were made of the YBCO films by means of photolithography and chemical etching. Typical asymmetric shape of the device narrowed down to ~ $10 \div 15$ μm in the neck is shown in Fig. 1.
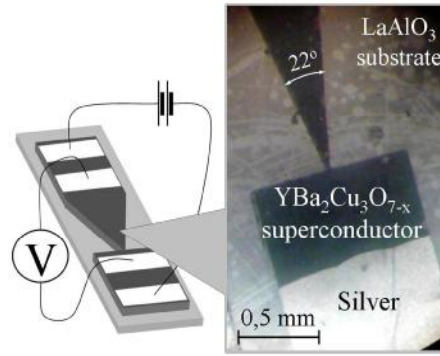
Fig. 1. Asymmetrically-necked 0.3-μm-thick $YBa_2Cu_3O_{7-x}$ device manufactured by means of photolithography and chemical etching. Silver 0.1-μm-thick contacts for 4-probe electric measurements have been deposited by thermal evaporation of silver in vacuum

The Ag contacts for electric measurements were made by thermal evaporation of ~ 0.1-μm-thick films onto the surface of superconducting devices at room-temperature. After the process of silver deposition, superconducting devices were additionally annealed at temperature $T = 375$°C for 1.5 h in oxygen ambient. The thermal treatment intensifies silver diffusion into the superconductor and causes decrease of contact resistance of metal/superconductor junctions to negligible values.

Electric resistivity and current-voltage dependences in the range of temperatures 78 K < T < 300 K have been measured by means of 4-probe dc-measurement setup and using 10-μs-pulsed electric current. We selected two groups of the samples. The asymmetrically-shaped YBCO devices attributed to the first group were characterized by a metallic-like resistivity vs temperature dependence in the range of temperatures $T > T_c^{on}$ with the onset of the superconducting state in the device at critical temperature T_c^{on} ~ $84 \div 85$ K which is characteristic temperature for YBCO thin films with oxygen depletion level of $x \leq 0.2$ [14]. For the second group of the samples we selected the YBCO devices which did not demonstrate the superconducting transition at temperatures $T \leq 78$ K. The resistivity of these devices with temperature decrease at temperatures $T > T_c^{on}$ corresponded to the oxygen depletion level of $x > 0.5$ [14]. We suppose that higher level of oxygen depletion occurred due to chemical procedures of the photolithography processes of selective etching of the superconducting film with structural defects (e.g. grain boundaries, screw dislocations, etc.) what resulted in decrease of oxygen content in the device's neck region.

To minimize the electric current induced heating of the contacts of the superconducting devices, mounted into a 50-Ω-impedance high-frequency transmission line, the current-voltage dependences at temperatures ranging from 78 K to 300 K were measured by means of 2-probe electric measurements setup. The setup uses $10 \div 100$-μs-long

square-shaped pulses of electric current from pulsed-current source at variable repetition rate of pulses ranging from 1 Hz to 10 kHz.

For MW detection measurements, the superconducting YBCO device was placed into a 10 GHz rectangular waveguide perpendicularly to its wider walls. Thus, electric pulsed-field of the MWs with adjustable electric power up to 3.3 W, pulse duration of 10 μs, and repetition rate of 100 Hz was oriented parallel to the longitudinal axis of the sample.

3. Results and Discussion

Current-voltage (I-V) characteristics measured at temperature $T = 199$ K $> T_c^{on}$ of the $YBa_2Cu_3O_{7-x}$ device with $x > 0.5$ (i.e. second group of the YBCO devices) demonstrating semiconductor-like resistivity dependence on temperature are shown in Fig. 2. The forward and reverse branches of the I-V characteristic are plotted (see vertical axis on the left) in the single quadrant (++) of the Cartesian system, thus reversing sign of current and voltage negative values. To see the asymmetry of the I-V characteristic, the parameter $\Delta I = I_1 - I_2$ for the same bias-voltage applied in the forward (1 curve in Fig. 2) and in the reverse (2 curve in Fig. 2) directions of our device is depicted as well (see vertical axis on the right). Here I_1 and I_2 are electric pulsed-current strengths at the same value of fixed voltage for forward and reverse directions, respectively.
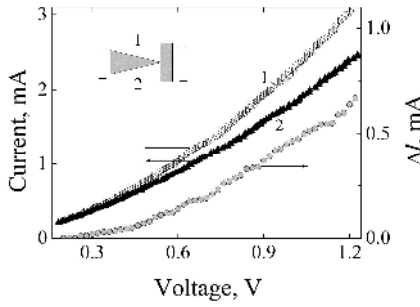
Fig. 2. The current-voltage dependence of asymmetrically-necked $YBa_2Cu_3O_{7-x}$ device biased by 10-μs-long square-shaped electric pulsed-current at temperature $T = 199$ K $> T_c^{on}$. Polarity of the applied voltage is denoted by symbols 1 (for the forward) and 2 (for the reverse) biasing directions, respectively. The parameter $\Delta I = I_1 - I_2$ determining asymmetry of the I-V characteristic for the same superconducting device at same temperature (right axis) was found to be positive in all the investigated voltage range
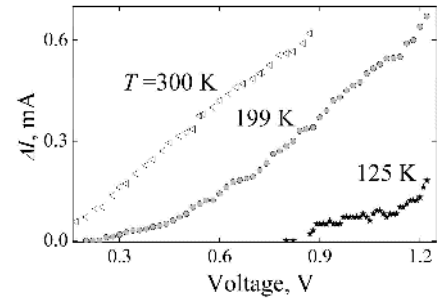
Fig. 3. The parameter determining asymmetry of current-voltage characteristic vs biasing voltage measured for the asymmetrically-necked $YBa_2Cu_3O_{7-x}$ device by means of 10-μs-long square-shaped pulsed-electric current at temperatures $T = 125$ K, 199 K, and 300 K $> T_c^{on}$. In all experimental cases the parameter $\Delta I = I_1 - I_2$ was positive. Explanation of symbols 1 and 2 see in caption of Fig. 2

The differential electric resistance of our testing device under test decreased from 714 Ω at bias voltage amplitude of $V = 0.2$ V down to 257 Ω and 330 Ω at voltage value of 1.2 V for the forward and reverse directions of biasing current, respectively. This change in differential electric resistance at higher amplitude of bias voltage can be explained by means of strong electric field assisted tunneling of charge carriers through oxygen decomposed insulating barriers (e.g. grain boundaries, screwed dislocations [15] etc.) located in the device's neck. According to our estimations, in a 10-μm-long neck of oxygen decomposed (i.e. $x > 0.5$) YBCO material a 1.2 V voltage amplitude can create up to $E \geq 100$ kV/m strength of electric field thus causing a considerable increase in electron tunneling probability of electric charge trough insulating barriers of the device.

The decrease of the electric differential resistance might be also affected by current self-induced Joule's heating of the oxygen decomposed ($x > 0.5$) device which exhibits a semiconductor-like character of resistivity change with temperature. Biasing at 3 mA with a 10-μs-long 100 Hz repetition rate of pulsed current might affect an increase in device's temperature for several degrees. The current induced heating effect was verified experimentally by measuring the I-V characteristic of the same device biased with 100-μs current pulses at the repetition rate of 100 Hz. These results of measurements confirmed that the overall change in differential electric resistance of the YBCO device at 1.2 V voltage which was mentioned above can not be associated only with the device's heating effect.

The parameter ΔI determining asymmetry of the current-voltage characteristic for the forward and reverse directions of bias current depends on electric field gradient induced nonhomogeneous distribution of hot carriers in the device's neck (the current density appears to be of the order of 50 kA/cm² at fixed voltage amplitude of 1.2 V), what results in rise of the thermoelectric phenomenon of hot carriers [12]. Our experimental results showed, that for lower values of oxygen depletion x (i.e. at higher doping levels of the p-type YBCO material), the parameter ΔI of the YBCO devices decreases (Fig. 3) with temperature decrease. A ratio $IT^{0.9\,V}(T) = (\Delta I_1 - \Delta I_2)/(T_1 - T_2) = 3.4 \times 10^{-6}$ A/K has

been calculated at fixed voltage of 0.9 V. Similar phenomenon has been already observed in asymmetrically-necked n-GaAs [13] and n-Si materials [16] and explained by means of nonhomogenous distribution of electric field, affecting drift mobility of charge carriers in these semiconductors. Thus, our results let us demonstrate that the parameter ΔI of the asymmetrically-necked YBCO devices can be controlled by means of material's temperature and its biasing conditions.

A typical current-voltage characteristic of the asymmetrically-necked $YBa_2Cu_3O_{7-x}$ device with $x \sim 0.2$ (i.e. first group of superconducting devices) of the same dimensions was measured by 10-μs-long pulsed-electric-current at fixed temperature of $T = 82$ K $< T_c^{on}$ (i.e. the device being switched into the superconducting state) and is shown in Fig. 4.
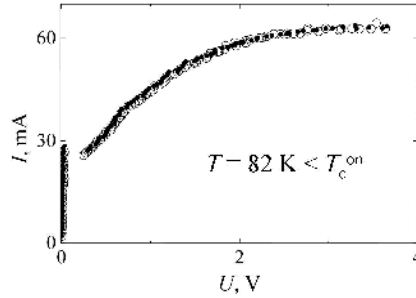
Fig. 4.   The current-voltage characteristic of asymmetrically-shaped 0.3-μm-thick $YBa_2Cu_3O_{7-x}$ device at temperature $T = 82$ K $< T_c^{on}$. Open and solid symbols correspond to opposite polarities of biasing voltage, respectively

As it is seen in Fig. 4, this device does not exhibit obvious asymmetry of the current-voltage characteristic within nonlinear part of this dependence starting with 29 mA amplitude of bias current. It has been estimated as a critical current of the superconductor resulting in critical current density $J_c(82$ K$) = 9.7 \times 10^5$ A/cm² at the narrowest part of the device, and at the same time confirming high quality of the YBCO superconducting material. The critical current is determined also as a current of onset of a dissipative motion of Abrikosov magnetic vortices in the mixed-state YBCO film biased at $I \geq I_c$.

Needs mentioning that the linear part of the current-voltage characteristic (Fig. 4) of the device staying switched in the superconducting state let us estimate electric resistance of both electric contacts as negligible for the results of our electric measurements.
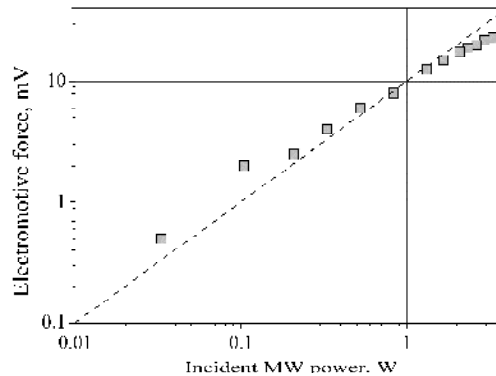
Fig. 5.   The emf voltage vs incident MW power of 0.3-μm-thick $YBa_2Cu_3O_{7-x}$ device with $x > 0.5$ measured at room temperature. The electric field component of the MWs has been oriented along the asymmetrically-shaped device's structure

In the MW detection experiments, the samples of the first group ($x \sim 0.2$) at room temperature showed extremely low value (i.e. less than tithe of mV) of electromotive force (emf) signal arising across the YBCO device,. On the other hand, the samples of the second group exhibited higher values and almost linear dependence of the emf signal on incident MW power (see Fig. 5), what is typical for emf of hot carriers in semiconductors.[13, 16].

Sublinearity of the dependence starts manifesting itself at higher power values. Heating assisted decrease of the device's electric resistivity can be proposed as a reason for this sublinearity. Moreover, analysis of temporal behaviour of the induced emf proves this assumption. Thus, the presented experimental result of MW detection is in good agreement with a presence of asymmetry of the current-voltage characteristic of our YBCO devices with $x > 0.5$ and demonstrates obvious possibility to use them as rectifier elements and microwave detectors incorporated in a superconducting YBCO electronics operating at the liquid nitrogen temperatures.

4. Conclusions

For conclusion, we have investigated asymmetrically-necked YBCO devices exhibiting nonlinear current-voltage characteristics while being in the normal (i.e. degenerate semiconductor) and in the superconducting (zero resistance) states. The electric properties of these devices at $T > T_c^{on}$ are explained by means of free carrier nonuniform heating, and at temperatures $T < T_c^{on}$ by means of onset of motion of the Abrikosov magnetic vortices in the mixed-state superconductor. We also conclude that oxygen-decomposed asymmetrically-shaped $YBa_2Cu_3O_{7-x}$ (i.e. $x \geq 0.5$) devices can be used as nonlinear elements for detection of MW radiation and as a non-superconducting rectifier in the superconducting YBCO electronic chip, which can operate at temperatures below temperature of superconducting transition T_c^{on} of the superconducting chip material.

References

1. **Laue M. V., London F., London H.** Zur Theorie der Supraleitung. Zeitschrift für Physik. 1935, v. 96(5-6), pp. 359–364.
2. **Cooper J. R., Chu C. T., Zhou L. W., Dunn B., Grüner G.** Determination of the magnetic field penetration depth in supercondicting yttrium barium copper oxide: Deviations from the Bardeen-Cooper-Schrieffer laws. Phys. Rev. B 1988, vol. 37 (1), pp. 638–641.
3. **Joss Ch., Albrecht J., Kuhn H., Leonhardt S., Kronmüller H.** Rep. Prog. Phys. 2002, vol. 65, pp. 651 – 788.
4. **Jukna A., Taneda T., Sobolewski R.** Supercond. Sci. Technol. 17, S336-S340 (2004),
5. **Lin J. -Y., Gurvitch M., Tolpygo S. K., Bourdillon A., Hou S. Y., Phillips J. M.** Phys. Rev. B 54, R12717 – R127120 (1996).
6. **Sueyoshi T., Watanabe M., Haruta M., Fujiyoshi T., Miyahara K., Ikegami T., Ebihara K., Miyagawa R.** Physica C 468, 1266 – 1269 (2008).
7. **Jukna A., Barboy I., Jung G., Abrutis A., Li X., Wang D., Sobolewski R.** J. Appl. Phys. 99, 113902-1–5) (2006).
8. **Lindgren M., Currie M., Williams C., Hsiang T. Y., Fauchet P. M., Sobolewski R., Moffat S. H., Hughes R. A., Pieston J. S., Hegman F. A.** Appl. Phys. Lett. 74(6), 853 – 855 (1999).
9. **Jukna A., Taneda T., Sobolewski R.** Supercond. Sci. Technol. 17, S336-S340 (2004).
10. **Karim R., How H., Seed R., Widom A., Vittoria C., Balestrino G., Paroli P.** Sol. St. Commun. 71, 983 – 986 (1989).
11. **Abrutis A., Kubilius V., Teišerskis A., Bigelyte V., Galindo V., Weiss F., Senateur J. P., Vengalis B., Jukna A., Butkute R.** Thin Solid Films 311, 251 – 258 (1997).
12. **Ašmontas S.** Electrogradient phenomena in Semiconductors. (Mokslas, Vilnius, 1984) pp. 140 – 152.
13. **Sužiedėlis A., Gradauskas J., Ašmontas S., Valušis G., Roskos H. G.** J. Appl. Phys. 93(5), 3034 – 303 (2003).
14. **Jones E. C., Christen D. K., Thomason J. R., Feenstra R., Zhu S., Lowndes D. H., Phillips J. M., Siegal M. P., Budai J. D.** Phys. Rev. B 47(14), 8986 – 8995 (1993).
15. **Babu N. H., Kambara M., Carwell D. A., Campbell A. M.** Supercond. Sci. Technol. 15(5), 702 – 707 (2002).
16. **Ašmontas S., Gradauskas J., Sužiedėlis A., Valušis G.** Microelectronic Engineering, 53(1-4), 553 – 556 (2000).

Identifying Electropolishing Parameters for Aluminium Surface Treatment in AAO Processes

T. Jukna*, ***, R. Kaliasas*, **, L. Jakucionis**

*Kaunas University of Technology, Faculty of Technologies, Daukanto str. 12, Panevėžys, Lithuania, E-mail: tomas.jukna@ktu.lt, remigijus.kaliasas@ktu.lt
**Panevezys College, Klaipedos str. 1, Panevezys, Lithuania, E-mail: liudas@panmc.lt
***Panevezys Mechatronics Center, S.Daukanto str. 12, Panevezys, Lithuania

Abstract

The paper presents an investigation of the electropolishing behaviour of high-purity aluminium in ethanol–perchloric acids by using anodic polarization measurement, scanning electron microscope (SEM), and atomic force microscope (AFM). The results show that the polarization potential, the $HClO_4$ concentration, and the temperature have important effects on the aluminium electropolishing behaviour.

KEY WORDS: *aluminium, electropoliching, ethanol-perchloric acid.*

1. Introduction

The self-organized, highly ordered anodized aluminium oxide (AAO) porous membrane, which has been intensively studied [1-4] over the last five decades, was recently reported to be a typical self-ordered channel material. Comparing conventional lithography, such as UV or X-ray, electron beam and scanning probe lithography, self-organization presents a cheap and efficient process for the formation of vastly different two-dimensional lateral nanometric superlattices [3, 5-7]. Anodization and electropolishing are two self-assembly techniques that can spontaneously form a two-dimensional array of quantum dots [1, 3-5, 7]. AAO has been proposed to be fabricated through anodizing highly pure aluminum sheets in various acidic solutions [3, 8, 9] without the pre-texturing treatment [4, 5]. However, several studies found that the pretreatment procedure (including annealing and polishing) and the two-step anodizing process are the essential factors affecting the quality and pore properties of AAO [3, 4, 8-10]. For polishing, several pretreatment methods, such as chemical polishing, alkaline degreasing, and electropolishing, have been used to flatten the Al sheets in order to promote the self-ordering of AAO [3, 4, 8-10]. Among these methods, a flat and smooth surface of aluminum sheets can be efficiently obtained by the employment of electropolishing. In addition, the surface roughness of aluminum sheets is believed to be changeable and controllable by varying the electropolishing conditions (e.g., solution temperature, applied potential and polishing time, etc.) [3, 9]. Accordingly, how to control the surface roughness of Al sheets by varying the electropolishing variables as well as the correlation between surface roughness and pore properties (e.g., pore size or density) are very important and interesting for AAO preparation. In this paper, the electropolishing process is investigated. In addition, the optimized parameters for electropolishing, such as electrolyte composition, temperature, applied potential, are evaluated by the electrochemical measurements.

2. Experimental

High-purity aluminium foils (purity 99.99%) of 0.3 mm thick, was used as substrate after cutting into 4x1 cm2 sized rectangular samples. After annealing under ambient N_2 at 450 C for 4h, Al substrates were degreased in ethanol, then washed in deionised water. During electropolishing the sample was used as the working electrode with an exposed area of 2 cm². The counter electrode was a stainless steel with a surface area of 1 cm².

The electropolishing solution was composed of a mixture of 70– 72% perchloric acid and 99.7% ethanol. Four mixed solution systems were used with ethanol to perchloric acid volume ratios of 6:1, 4:1, 3:1 and 2:1. The temperature was maintained at cool water and the electropolishing time was varied from 60 to 180 s.

The morphology of electropolished surface was characterized by scanning electron microscopy (SEM observations were performed on a Raith e-Line system) and atomic force microscope (Nanosurf easyScan 2).

3. Results and discussion

Fig. 1 compares the anodic polarization curves of high-purity aluminium samples in the mixed solutions with different volume ratios of ethanol to perchloric acid of 6:1, 4:1, 3:1 and 2:1. The curves no show the typical I–V characteristics for electropolishing, except 6:1 solution, but depending upon the potential applied there are three zones in electropolishing process: etching zone, polishing zone, and gassing zone [11]. In low current and in the etching zone, the thickness of insulating layer is low and weak corrosion carries out on the surface of anode. So the surface is

unsmoothed by electropolishing. By increasing voltage roughness of the specimens will be enhanced and approached it's minimum of 26 V in the mixed solution with the volume ratio of ethanol to perchloric acid as 4:1 (Fig. 2a) and 32 V in the mixed solution with the volume ratio of ethanol to perchloric acid as 6:1 (Fig. 2b).
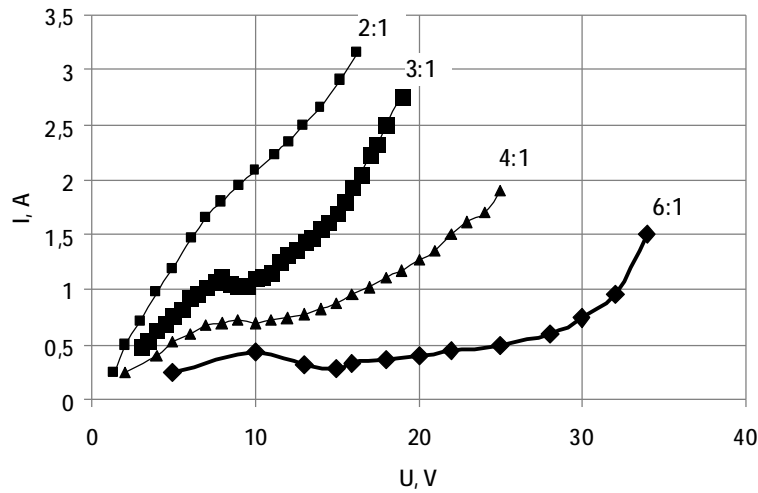
Fig.1.   Voltamperic curves of the high-purity aluminium sample obtained in mixed solutions with different volume ratios of ethanol to perchloric acid
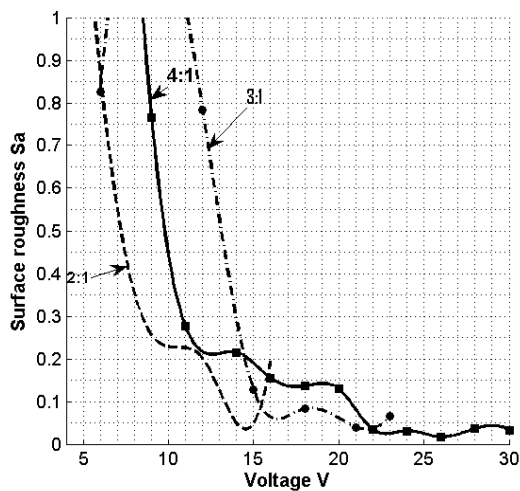
a
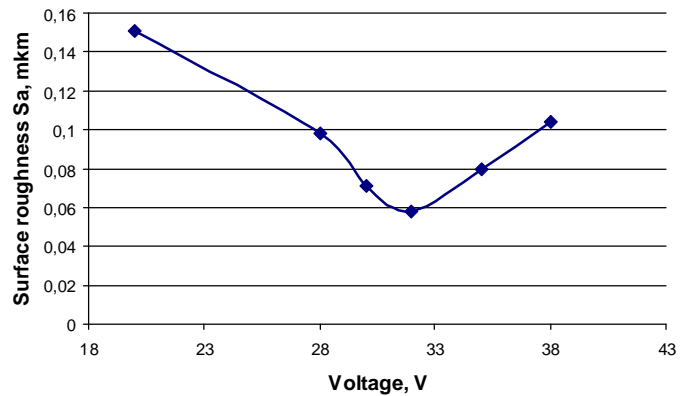
b

Fig.2.   Surface roughness S_a as a function of voltage measured in corresponding ratio ethanol to perchloric acid electrolytes at 4-6°C temperature: a – 4:1, 3:1, 2:1; b – 6:1

With respect to the effect of morphology on roughness, the typical SEM micrographs of surfaces before and after the electropolishing of Al specimens are shown in Figure 3. The Al specimen before electropolishing shows an uneven surface with considerable streaks (Fig. 3a). There are three electropolishing processes: etching zone, polishing zone, and gassing zone. In etching zone surface is concave (Fig. 3b), in polishing zone – smooth (Fig. 3c) and in gassing zone – roughness increased ago. The surface roughness was 70 nm for untreated Al and then decreased to 22 nm after electropolishing at 26 V.

Fig. 4 shows surface roughness S_a, S_q and mass loss as a function of voltage for 4:1 ethanol to perchloric acid electrolyte at temperature 4-24°C. By increasing voltage roughness S_a and S_q of specimens decrease and approached about 20 nm, simultaneously mass loss increasing.

a

b

c

d
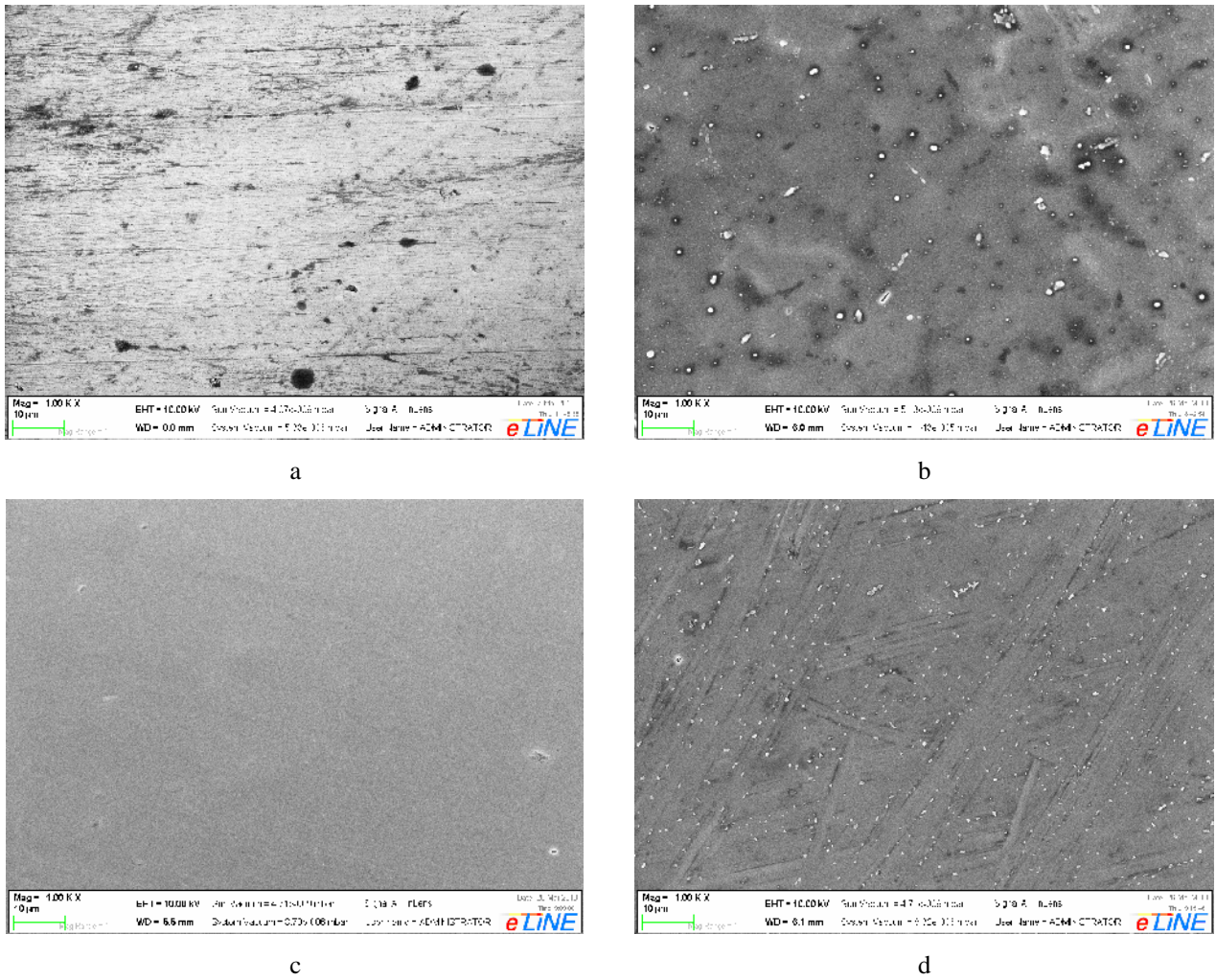
Fig. 3. SEM micrographs of the surfaces of Al specimens before (a) and after (b, c, d) the electropolishing; b – voltage 11 V in a mixture of $C_2H_5OH : HClO_4 = 4:1$ (volume ratio) for 1 min; c – voltage 26 V in a mixture of $C_2H_5OH : HClO_4 = 4:1$ (volume ratio) for 1 min; d – voltage 30 V in a mixture of $C_2H_5OH : HClO_4 = 4:1$ (volume ratio) for 1 min
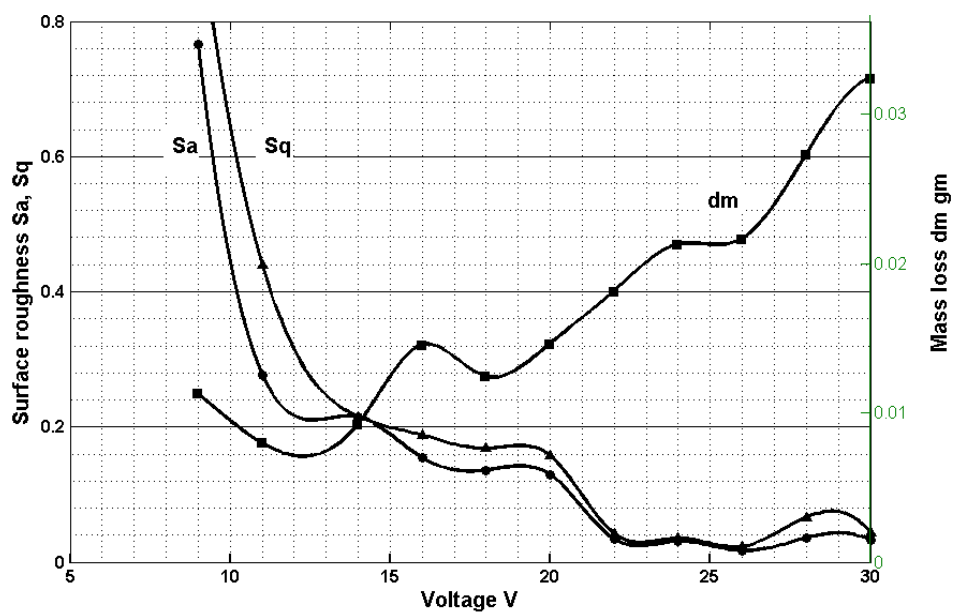
Fig. 4. Surface roughness S_a, S_q and mass loss as a function of voltage for 4:1 ethanol to perchloric acid electrolyte at temperature 4-24°C

4. Conclusions

In this work, electropolishing was used to provide smooth aluminum sheets with high purity (99.99% Al). The specimens were electropolished in an electrolyte that is a mixture of ethanol to perchloric acid. Experimental curves showed that the polarization potential, the $HClO_4$ concentration, the temperature have important effects on the aluminium electropolishing behaviour. Best surface roughness Sa was 22 nm in the mixed solution with the volume ratio of ethanol to perchloric acid as 4:1 at 26 V and 6:1 at 32 V was 31 nm.

Acknowledgements

References

1. **Jessensky O., Muller F., Gosele U.** Self-organized formation of hexagonal pore structures in anodic alumina, J. Electrochem. Soc. 145, 1998. – 3735 p.
2. **Keller F., Hunter M. S., Robinson D. L.** Structural features of oxide coatings on aluminum, J. Electrochem. Soc. 100, 1953. – 411 p.
3. **Masuda H., Hasegwa F., Ono S.** Self-ordering of cell arrangement of anodic porous alumina formed in sulfuric acid solution, J. Electrochem. Soc. 144, 1997. – L127 p.
4. **Masuda H., Yamada H., Satoh M., Asoh H., Nakao M., Tamamura T.** Highly ordered nanochannel-array architecture in anodic alumina, Appl. Phys. Lett. 71, 1997. – 2770 p.
5. **Bandyopadhyay S.** Self-assembled quantum dots: the route to novel optical, electronic, magnetic and superconducting properties, Bull. Mater. Sci. 22, 1999. – 537 p.
6. **Chik H., Xu J. M.** Nanometric superlattices: non-lithographic fabrication, materials, and prospects, Mater. Sci. Eng. R 43, 2004. – 103 p.
7. **Yuzhakov V. V., Takhistov P. V., Miller A. E., Chang H. -C.** Pattern selection during electropolishing due to double-layer effects, Chaos 9, 1999. – 62 p.
8. **Li A. -P., Müller F., Birner A., Nielsch K., Gösele U.** Hexagonal pore arrays with a 50–420 nm interpore distance formed by self-organization in anodic glumina, J. Appl. Phys. 84, 1998. – 6023 p.
9. **Ono S., Saito M., Asoh H.** Self-ordering of anodic porous alumina formed in organic acid electrolytes, Electrochim. Acta 51, 2005. – 827 p.
10. **Jessensky O., Müller F., Gösele U.** Self-organized formation of hexagonal pore arrays in anodic alumina Appl. Phys. Lett. 72, 1998. – 1173 p.
11. **Landlot D.** Fundamental aspects of electropolishing, Electrochem. Acta 32, 1987. – 1 p.

Proceedings of 8th International Conference ITELMS'2013

Investigating Resistance of Turn Six-Wheel Skid-Steer Vehicle

S. Konopka*, P. Sprawka**, T. Muszyński***, K. Spadło****

*Military University of Technology, gen. S. Kaliskiego 2 st., 00-908 Warsaw, Poland, E-mail:skonopka@wat.edu.pl
**Military University of Technology, gen. S. Kaliskiego 2 st., 00-908 Warsaw, Poland, E-mail:psprawka@wat.edu.pl
***Military University of Technology, gen. S. Kaliskiego 2 st., 00-908 Warsaw, Poland, E-mail:tmuszynski@wat.edu.pl
****Military University of Technology, gen. S. Kaliskiego 2 st., 00-908 Warsaw, Poland, E-mail:kspadlo@wat.edu.pl

Abstract

This paper presents the problem of estimating resistance of turning six wheel vehicle with skid steer and hydrostatic drive system. Due to lack of comparative analytical research results to real value, built a computer model of vehicle to simulate turning process. Simulation results were compare to real value which were obtained from the measurements on an existing vehicle in Department of Machine Building in Military University of Technology.

KEY WORDS: *skid steer turning resistance, multi-axis wheeled vehicles, hydrostatic drive system, MSC Adams.*

1. Introduction

In time of increasing mobility requirements of off-road vehicles the multi-axis handling systems are becoming more popular [1]. Using more than two axis in vehicle improves the ability to overcome terrain obstacles. This also reduce ratios of MMP and VCI [8] (while maintaining the size of the wheels), which are parameters specified the minimum load area. Further parameters of the ability to overcome terrain obstacles are also: maximum speed, pressure unit exerted on the ground and maneuverability. Maximum speed depends on engine power and transmission system, pressure unit can be modify by changing size of tires (tracks) or number of wheels. The maneuverability is forming mainly by type of steering system used in vehicle. There are three basic steering systems: Ackerman's system (Fig. 1a), articulated steer system (Fig. 1b) and skid steer system (Fig. 1c).

| a | b | c |
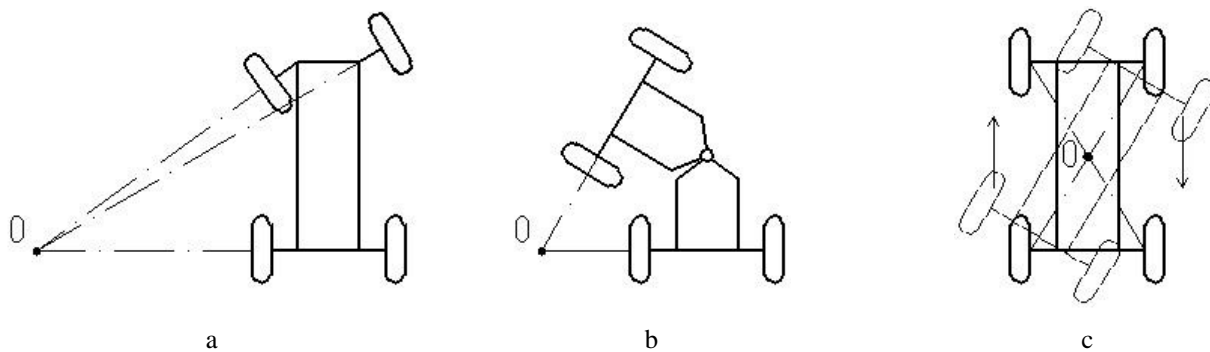
Fig. 1. Different types of steering systems [5], where: O – temporary center of vehicle rotation; a – Ackerman's system; b – articulated steer system; c – skid steer system

Each of these types are used in vehicle with different maneuverability requirements. The smallest maneuverability have vehicles with Ackerman's sterling system, the largest with skid steer system. Moreover skid steer system allows to change angle position of vehicle without move forward or backward (turning radius is zero). Due to this systems it is widely used in engineering robots.

The Department of Machine Building in Military University of Technology (KBM WAT) conducted research on high mobility Unmanned Ground Vehicle (UGV) with three axis, six wheel drive system. Due to destiny Unmanned Ground Vehicle (IED/EOD missions) the most important parameter (expect ability to overcome obstacles) is maneuverability. It improve moving in urban areas. In contrast to vehicle designed by other institutions [9, 10] the KBM's machine have skid steer turning system.

While working on it, one of the problem was valuation resistance of turn skid steer. There can be found some dependences help to determinate size of it. In literature these are theoretical dependences [1], which have not been tested on real objects.

The scince base from KBM WAT allows to compare result of analytical calculations with results obtained during verification test on real objects (Fig. 2). Futheremore, it is possible to compare both of values to results obtained in computer simulations. To this researchs were used six wheel vehicle which weighs 4200 kg with all wheel drive.

Fig. 2. Unmanned Ground Vehicle MAREK with 6x6 drive system and skid steer
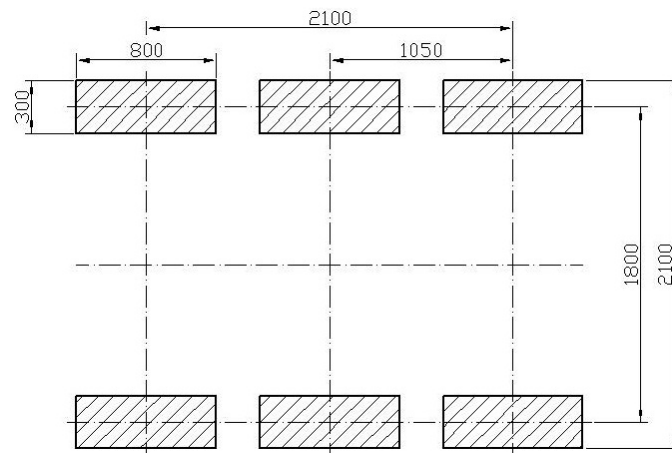
Fig. 3. Basic dimensions of the drive system Unmanned Ground Vehicle MAREK

Basic dimensions of the drive system MAREK vehicle are shown on Fig. 3. Based on the literature [1, 3, 4, 5, 7, 9] specifies that the most unfavorable moment is execution of maneuver turning in place (turning radius is zero). Execution this maneuver is possible through to use hydrostatic drive system [2]. It allows to get opposite turn of velocity vectors for left and right side of vehicle.

2. Analytical method for estimating the resistance of skid steer turning

Methods for estimating the resistance of skid steer turning multi-axis vehicles are presented in the literature [1]. There is one model similar to the tracked vehicle and two models based on the tracked model but modified to approaching it to wheeled model.

In mentioned methods were addopted a number of simplifying assumptions such as:
- none of methods take into consideration pressure distribution on individual wheels;
- was not include location the center of gravity;
- was not include influence suspensions;
- was adopted that temporary center of turning is coincidence with geometrical center of the drive system;
- were no administered information about ground adhesion coefficient in function of slip (μ = const);
- calculation can be done only for all wheel on side, without breakdown to individual wheels.

To the all calculations were taken into account parameters such a:
- B_Z = 2.1 m – external width of the vehicle;
- B_K = 0.3 m – wheel width;
- B_G = 0.3 m – track width;
- $B = B_Z − B_K$ – vehicle track spacing;
- L_G = 2.45 m – length of the track adhesion to the ground;
- C = 0.35 m – length of the wheel adhesion to the ground;
- μ = 0.85 – turning resistance coefficient.

2.1. Method I – estimating the turning resistance for tracked skid steer vehicle

For tracked drive system total torque of turning resistance can be calculated from the relations (marked according to Fig. 4) [1, 7, 10]:

$$M_{sI} = m\frac{G\,L_G}{4} \tag{1}$$

Dividing the total moment of turning resistance by radius of the driving force received driving force on one side of the vehicle.

$$P_{sI} = \frac{mG\,L_G}{4B} = \frac{mG\,L_G}{4(B_Z - B_G)} \tag{2}$$
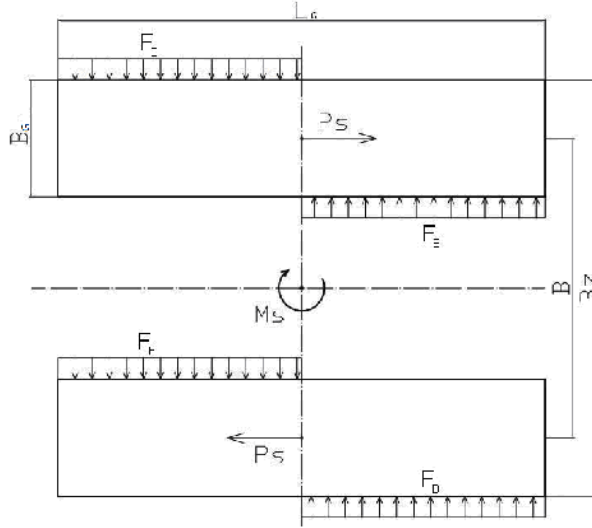
Fig. 4. Force on the tracks in skid steer, where: Ms – torque of turning resistance; Ps – resistance turning force; F_B – side force influence on track; B_Z – external width of the track; B – tracks spacing; B_G – central width of the track; L_G – length of the track contact to the ground

2.2. Method II – estimating the turning resistance for wheeled skid steed vehicle

This method involves modification of width track contact area wheeled and tracked are the same. It was assume that width of vehicle (dimension B_Z) will not change.

a   b
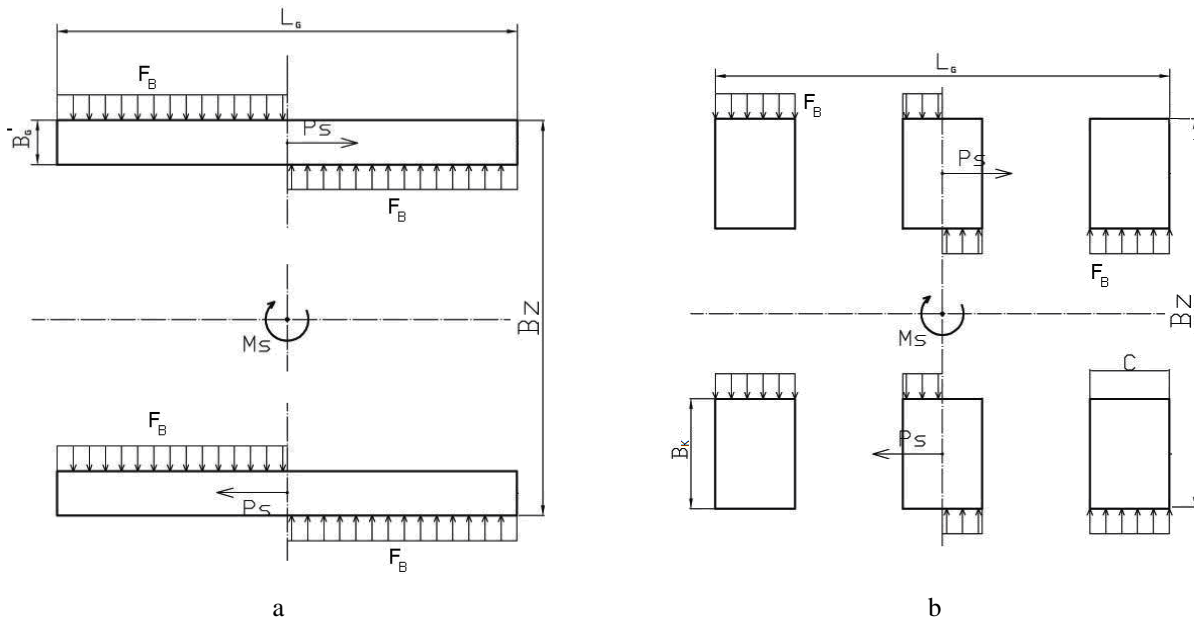
Fig. 5. Scheme showing connections between characteristic dimensions of the drive system (C is length of the wheel adhesion to the ground): a – tracked system; b – wheeled system, where

In accordance with the assumptions of equivalence contact area of the wheeled and tracked system:

$$A_G = A_K \tag{3}$$

where: $A_G = 2\,B_G'\,L_G$ is area of tracked system contact to the ground; $A_K = 6\,C\,B_K$ is area of wheeled system contact to the ground.

For this model we can use relations (1) and (2), by insert B_G' instead B_K. This will mean that for calculations of with of the wheel is set equal to the calculated with of the track (in this case $B_K = B_G'$)

$$M_{sII} = m\frac{G\,L_G}{4} \tag{4}$$

$$P_{sII} = \frac{mG\,L_G}{4\,B} = \frac{mG\,L_G}{4\left(B_Z - B_G'\right)} \tag{5}$$

2.3. Method III – replacement wheeled model

The model is based on adding and subtracting torque of turning resistance, calculated for different lengths of contact track to the ground. For six wheel drive system this method can be illustrated as in Fig. 6.

Total torque of turning resistance M_1 is determined for length L_1, torque M_2 for length L_2 and torque M_3 for length L_3.

This method of calculation cause a change of actual contact area with ground. It can cause the change of pressure unit exerted on the ground. To eliminate this problem, the factor k was entered. It is the ratio of area of tracked system contact to the ground to area of wheeled system contact to the ground.

$$k = \frac{B_K\,L_G}{B_K\left(L_1 - L_2 + L_3\right)} \tag{6}$$
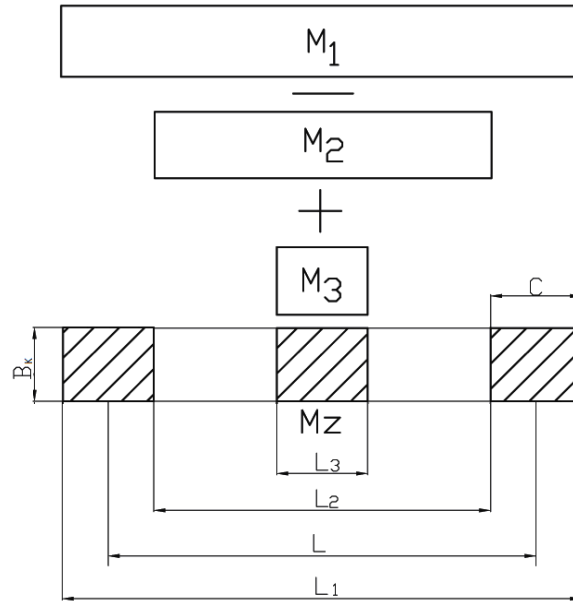
Fig. 6. Graphic interpretation of method calculations torque of turning resistance for replacement wheeled model, where: L_1 is distance between the extreme points of contact drive system to the ground for extreme axis of vehicle; L_2 is distance between inner points of contact drive system to the ground for extreme axis of vehicle; L_3 is length of contact single wheel to the ground

The final relation for three axis vehicle takes the form:

$$M_{sIII} = m\frac{G\left(L_1 - L_2 + L_3\right)}{4}k \tag{7}$$

$$P_{sIII} = \frac{mG\left(L_1 - L_2 + L_3\right)}{4\,B}k = \frac{mG\left(L_1 - L_2 + L_3\right)}{4\left(B_Z - B_K\right)}k \tag{8}$$

The table below shows the results of calculations for listed methods.

The values of the driving force for a single side of the vehicle, calculated by different analytical methods

Calculation methods	Method I – estimating the turning resistance for tracked skid steer vehicle	Method II – estimating the turning resistance for wheeled skid steed vehicle	Method III - replacement wheeled model
The values of the driving force [N]	14 343	12 974	11 156

Executed analysis shows that compare to the calculation method for the tracked driving system, method II reduced the required driving force by 10% and method III by 22%.

3. Verification analytical calculation by simulating computer model

To compare analytical results, the computer model was made [4, 6, 7, 10] (Fig. 7). Model was built in MSC Adams software. The wheels of both side were propel in opposite directions. The ground adhesion coefficient was determinate at 0.8. It responds to a moving in disintegrated ground including formation of the ground piles while wheel is in slip.
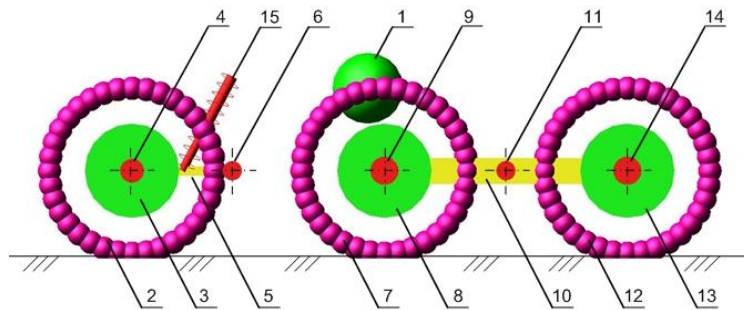
Fig. 7. Model of driving system of engineering robot, where: 1 – resultant center of gravity of the basic chassis; 2, 7, 12 – tire model of wheel (2 – front, 7 – center, 12 – rear); 3, 8, 13 – wheel rims; 4, 9, 14 – hydrostatic engine model; 5 – front arm; 6 – point of rotate front arm; 10 – rear arm (center and rear wheels); 11 – point of rotate rear arm; 15 – front suspension

In this model were adopted a few simplifying assumptions. Weight distribution of the model was created based on the masses of individual components of the drive system, suspension, hydraulic motors and other components. Weight of frame, engine and parts of body has been reduced to concentrated mass (Fig. 8).
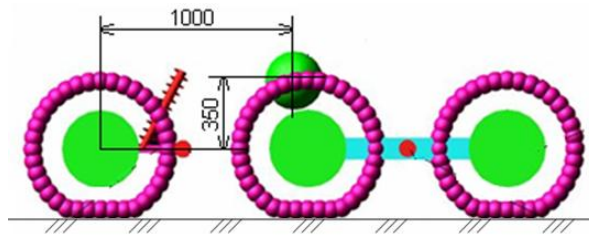
Fig. 8. Model of engineering robot with specifying the center of the gravity

Analysis of distribution elements in the vehicle allowed for estimate center of the gravity. It was taken that it is 1000 mm behind front axle and 350mm over axle. Compared computer model to analytical model the center of the gravity is shifted by 5% to the front of vehicle. It was assumed that axis spacing of the vehicle is constant and it is $L_1 = L_2 = 1050$ mm. It was addopted that wheel spacing $B = 1800$ mm. The model is equipped in susceptible wheel with free radius $r_{sw} = 400$ mm and dynamic radius $r_d = 370$ mm. Suspension is composed of single front arm with spring and shock and rear trolley mounting pendulous.

Pulsations visible on the results of the simulations (Fig. 10, 11 and 12) are effects of the cooperation wheel model with the ground. Model of wheel is shown below.

Model is made from a finite number of balls (Fig. 9a) connected to rim by spring-damping elements. Elements associated each ball with rims as shown on Fig. 9b. Pulsations are results of entering and leaving the next ball in contact with the ground. Spring and damping coefficients were chosen by comparing simulations results with results obtained from real object. Execution of a preliminary analysis (Fig. 10) showing the relations between the coefficient of adhesion

and slip at constant wheel speed. The resulting characteristic is similar to theoretical characteristic, which allows to conclude about correct of the wheel model.

ON the basis of the building model, defined pressure distribution of individual wheel. Example for right side of the wheel is shown on Fig. 11. Simulation process was performed using Newmark method of integration in steps of 0.01 s. The entire simulation took 30 s. After his time, vehicle made a 180 degree turn.
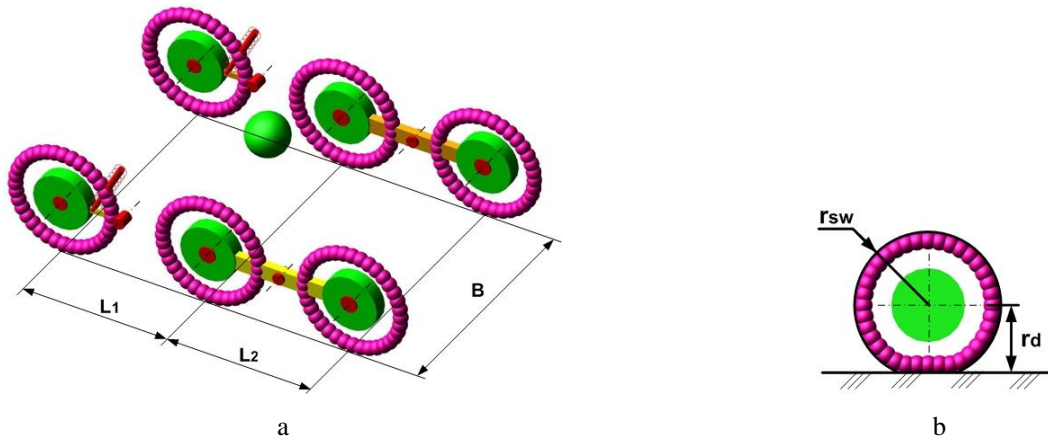
Fig. 9. Model of vehicle used to computer simulations: a – dimensions of drive system; b – model of susceptible wheel, where L_1 and L_2 are axis spacing; B is wheels spacing; r_{sw} is free radius of wheel, r_d is dynamic radius
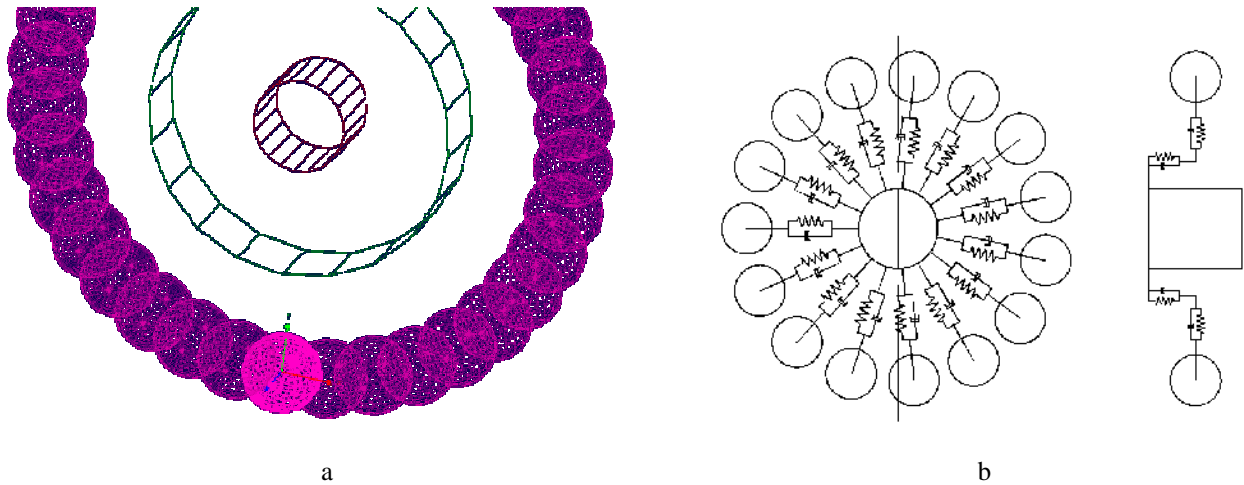
Fig. 10. Model of wheel: a – built in MSC Adams software; b – physical model of wheel
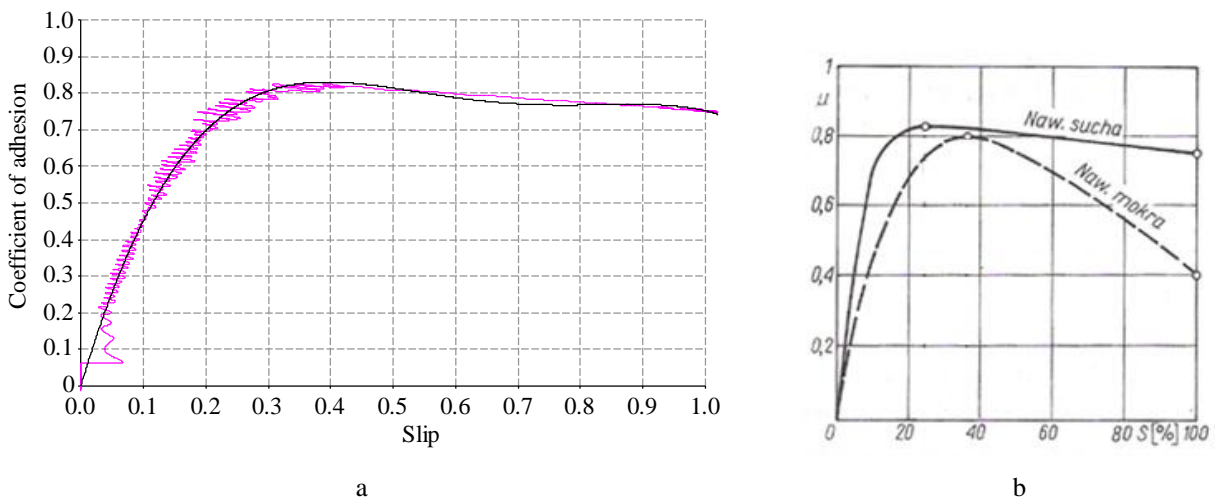
Fig. 11. The relation between the coefficient of adhesion and slip at constant wheel speed: a – simulation result; b – theoretical characteristic
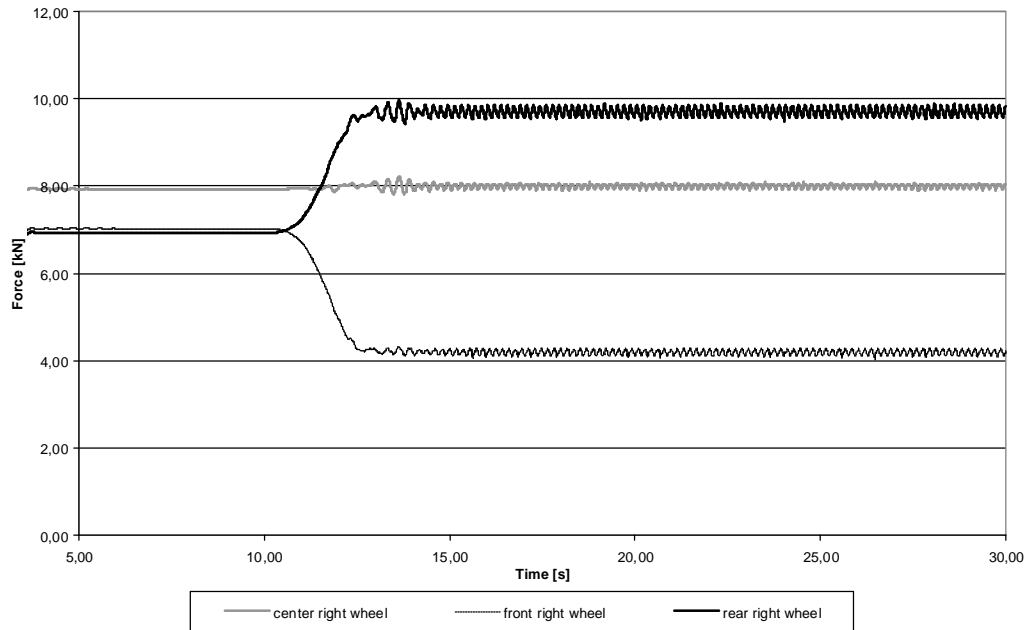
Fig. 12. Results of pressure distribution of individual wheel, 5-10 s – vehicle is stop, 10-30 s – vehicle is turning

Analyzing the pressure distribution, determinate the percentage distributions for each wheel (up to 10 s).

Above 10 s the vehicle starts to executing turning maneuver. Pressure distribution subject to change. This is coused by load and unload the individual wheels of vehicle. Results of developed driving force for individual wheels shown in Fig. 12.

Analyzing results (Fig. 12) can narrow the analysis to a few second due to stability of the loads. ON the basis of results can specify the average driving force for individual wheels. The values of driving force shows in Table 3. Total driving force developed by one side of vehicle is sum of forces for individual wheels on one side.

Table 2

Pressure distribution of individual wheel

	Front wheels	Center wheels	Rear wheels
Percentage distributions of pressure	32	36	32
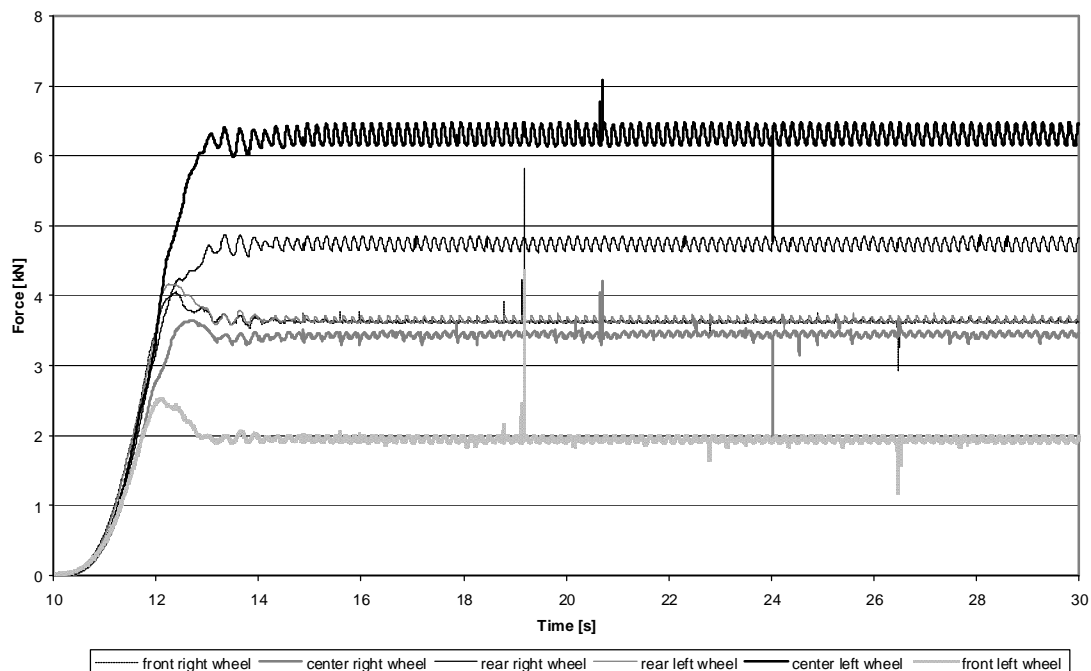
Fig. 13. The value of the driving force on the individual wheels of the vehicle

Average value of driving force developed on individual wheel

	Rear right wheel	Center Wright wheel	Front right wheel	Rear left wheel	Center left wheel	Front left wheel
Force [N]	4726	3423	3631	3642	6262	1933
Sum [N]	11780			11837		

The differences between results for each wheels are results of change pressure load for wheel.

Simulation methods in contrast to the analytical methods allows determinate required driving force for individual wheel. It also allows to change position of center of the gravity, as a result change pressure distribution. It has influence to load individual wheels.

4. Verification tests

Research on the real object was executed on UGV Marek (Fig. 2) in the Department of Machine Building in Military University of Technology. The maneuver of turn was executed on the base ground. Suspension system was working in hydraulic trolley system on center and rear axis. Front wheel was suspended independently. During the test the hydraulic oil pressure was measured at the entrance to the hydrostatic engines. This allowed to indirect calculate the driving force developed by each of wheels. An example of calculated driving force is shown in Fig. 13.

Analysis takes only results from 7 to 25 s. Rest of time was start and stop maneuver. Table 4 shows results of research and average value of driving force.
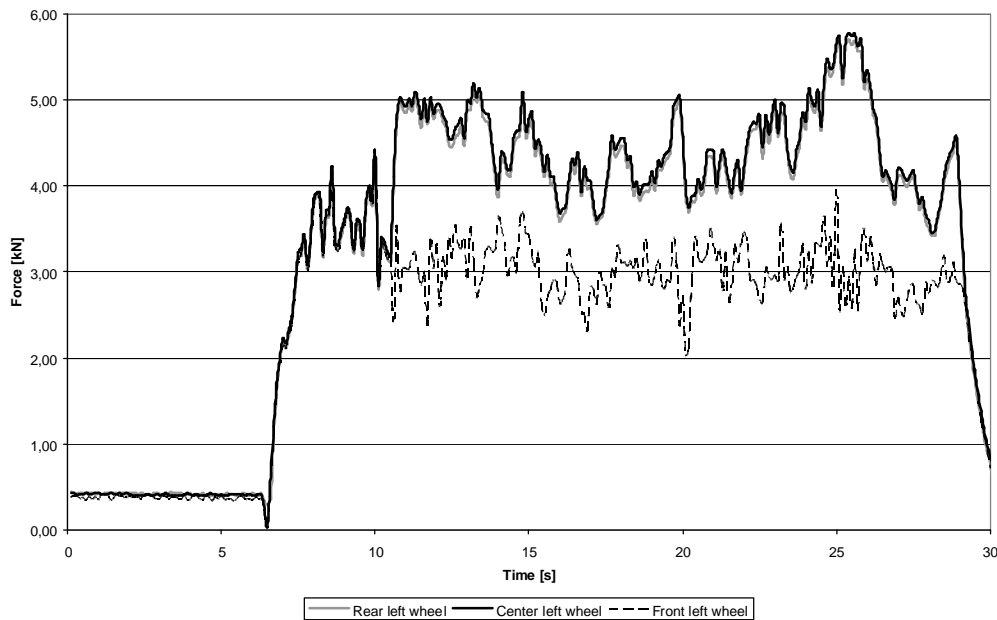
Fig. 14. Example of driving force developed by wheel on left side of vehicle

Average value of driving force developed by each wheel

	Left side			Right side		
	Rear	Center	Front	Rear	Center	Front
Driving force [N]	4280	4359	3115	3800	3832	3867
Sum [N]	11754			11499		

Reak load variations of vehicle are characterized by larger amplitude compared to analytical results. During the verification tests occurred random phenomenon which can not be simulated in computer model. For this phenomenas may be include:

• heterogeneity of ground (e. g. stones);
• small inequality of ground, which may have impact on the adjustment tire to the ground;
• formation piles of ground on sidewall of tires;
• delve tire into the ground;
• changing the tire pressure values associated with the different load.

5. Conclusion

Results of the analysis shows that analytical method allows to accurately calculated approximate value of driving force due to turning maneuver is method III – replacement wheeled model (driving force 11 156 N). Also computer simulations is close to results receive in test on real vehicle (right side 11 780 N, left side 11 837 N). This confirm well-formed model and properly chosen model coefficients. Comparable analytical and computer model value to results from real object (right side 11 754 N, left side 11 499 N) demonstrate it is possible to use analytical relation or computer model to define driving force necessary to turning maneuver. Analytical method is quickest than building a model and make a computer simulations. Computer analysis allows to determinate the size of hydrostatic units necessary to turning maneuver. Indirectly, it also allows to specifying power of engine. Analytical calculation do not allow to define driving force on individual wheel. This limits the analytical method to more advanced analysis.

References

1. **Bartnicki A., Łopatka J., Muszyński T.** Szacowanie oporów skrętu burtowego wieloosiowych platform kołowych, Logitrans 2010.
2. **Bartnicki A., Muszyński T., Sprawka P.** Hydrostatyczny układ napędowy trójosiowej platformy wysokiej mobilności o skręcie burtowym, Logistyka 2010.
3. **Li X., Yin X., Zhang Y., Yuan S.** Turning resistance coefficient model for skid-steer wheeled vehicles, Automotive Engineering 2012.
4. **Fauroux J. C.** Improving skid-steering on a 6x6 all-terrain vehicle: A preliminary experimental study, 12th IFToMM World Congress, France 2007.
5. **Morales J.** Simplified Power Consumption Modeling and Identification for Wheeled, Skid-Steer Robotic Vehicles on Hard Horizontal Ground, The 2010 IEEE/RSJ International Conference on Intelligent Robots and Systems, Taipei, Taiwan 2010.
6. **Nabaglo T., Jurkiewicz A., Apostol M., Micek P.** Construction and simulation of a 2S1 tracked vehicle model and its verification using vertical forces on the road wheels while overcoming a single obstacle, Diffusion and Defect Data Pt.B: Solid State Phenomena 2011.
7. **Prochowski L.** Mechanika ruchu, WKN, Warszawa 2008.
8. **Sprawka P.** The methods of evaluation the mobility of off-road vehicles, Solid State Phenomena Vol. 180, Trans Tech Publications, Switzerland 2011.
9. **Stania M.** Analysis of the kinematics of an eight-wheeled mobile platform, Diffusion and Defect Data Pt.B: Solid State Phenomena 2013.
10. **Tyro G.** Maszyny ciągnikowe do robót ziemnych, WNT, Warszawa 1986.
11. **Zongwei Y., Guoqiang W., Rui G., Xuefei L.** Theory and experimental research on six-track steering vehicles, Vehicle System Dynamics 2013.
12. www.hydromega.com.pl
13. www.supacat.com

Proceedings of 8th International Conference ITELMS'2013

Kinematic Discrepancy of Hydrostatic Drive of Unmanned Ground Vehicle

S. Konopka*, M. J. Łopatka**, M. Przybysz***

Military University of Technology, ul. Gen. S. Kaliskiego 2, 00- 906 Warszawa 49, Poland, Email: skonopka@wat.edu.pl
**Military University of Technology, ul. Gen. S. Kaliskiego 2, 00- 906 Warszawa 49, Poland, Email: mlopatka@wat.edu.pl*
***Military University of Technology, ul. Gen. S. Kaliskiego 2, 00- 906 Warszawa 49, Poland, Email: mprzybysz@wat.edu.pl*

Abstract

In the paper the problem of kinematic discrepancy of hydrostatic driving systems in high mobility vehicle was presented. As well as its influence on occurrence of disadvantageous effect of circulating power. Moreover, theoretical aspect of kinematic discrepancy possibility of compensation by hydrostatic driving system based on researches which used static characteristic was presented.

KEY WORDS: *high mobility, hydrostatic driver, mobile robot, kinematic discrepancy.*

1. Introduction

Tasks which have to be concluded by Unmanned Land Platforms (BPL) during rescue operations and military missions set up high requirements for their mobility and maneuver. They contain among other things BPLs' capability to move around accidental terrain (20-30 cm), grade 40% (22°), terrain of low carrying ability $CI = 150$ kPa, typical terrain obstruction as: Rubbles heaps, logs, ditched [1]. Above requirements can be fulfilled by using hydrostatic driving system (HUN) and suspension with high jump of the wheels [2].

Advantages, of hydrostatic driving systems, like stepless changing of the gear unit, securing propulsion engine from overwork, wide range of rotational speed in hydraulic engines cause that they are generally used in vehicle and machines used in heavy terrain works [3] for example in heavy work machinery.

Drive of BPL around big terrain's obstructions or with different radius of dynamic wheels, which can be caused by uneven load or different inflation pressure makes that wheels should spin around with different rotational speed (Fig. 1). The phenomena is called kinematic discrepancy and is specified by kinematic discrepancy level. Kinematic discrepancy level Δ of the system is a differences ratio of spins of the wheels ω', ω'' which are made on given part of the road (rolling without slipping) to the number of spins of the spinning wheel which has more speed [4]

$$D = \frac{w' - w''}{\max(w', w'')} \tag{1}$$

where: ω' and ω'' are angular speed of examined wheels of the vehicle.

Kinematic discrepancy of the driving system can be analyzed between wheels placed on the same axle or between driving axels. In this diploma the problem of kinematic discrepancy between axles is described.
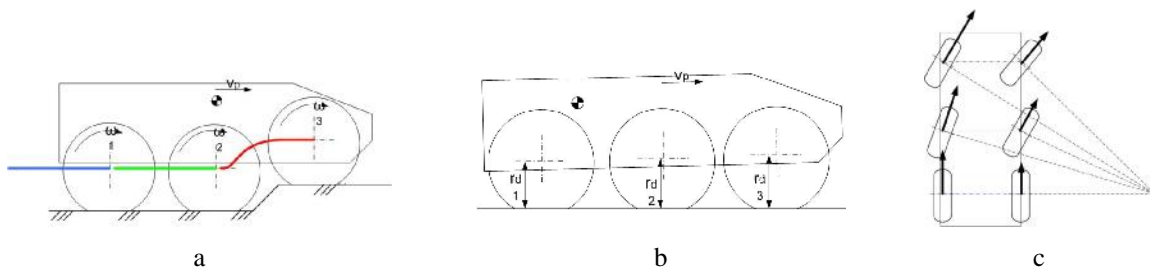
Fig. 1.   Causes of kinematic discrepancy of six-wheeler vehicle: a – moving around terrain obstructions; b – different radiuses of dynamic wheels; c – curvilinear move

BPL mobility requirements cause higher requirements for the cooperation of driving system with the surface. It is significant because when it is impossible to accommodate rational speed of the wheel to the road it leads to creating significant slipping when the wheel touches the surface (positive – when the wheel spins with lower rational speed than it can be deducted from the kinematic movement against the surface and slipping. Negative – when the wheel spins with higher rational speed than it can be deducted from kinematic movement against the surface) [5, 6]. Wheel with positive slipping is in this case is braking wheel of the vehicle, which causes that there is an additional power stream. The stream comes from the surface and is called circulating power. This phenomena causes among other things significant possibility of limitation when overcoming of terrain obstructions is considered, and what is more to lower the efficiency

of the whole driving system caused by the increase pressures in the system. In the long term effect it can cause faster usage and even damage.

Hydrostatic driving systems are characterized by high kinematic stiffness, which is connected with small compressibility of working factor, which in HUN is a kind of a medium which helps to transfer power from the pressure generator to the references. These references are hydraulic motors which are responsible for front wheel drive. This feature causes that HUN can guarantee big kinematic accuracy during movements and also at the same time it is very sensitive when kinematic discrepancy appears. This accuracy depends mostly on ouside leeks, which are caused by construction features used in the elements of the system and pressure drop in the elements [6]. These leeks help in some extent to diversify rotational speed of the wheels which is necessary to cover kinematic discrepancy and is called kinematic susceptibility. Whereas the ability to cover kinematic discrepancy by ensuring kinematic susceptibility of the system is called kinematic discrepancy compensation.

The leeks in the system should be examined in order to find out what is their influence on capability of diversifying speed of the wheels, which helps to keep the right cooperation of the wheel with surface when driving with high value of kinematic discrepancy, preventing from formatting circulating power phenomena.

In this diploma the problem of kinematic discrepancy which comes from driving around big terrain obstruction was presented, its influence on hydrostatic driving system. The action of estimating of kinematic discrepancy compensation ability in hydrostatic driving system was taken.

2. Construction solution of hydrostatic driving systems used in increased mobility vehicles

One of the method which helps to eliminate the problem of circulating power phenomena in the system is to used hydraulic differential mechanism by feeding hydraulic motors connected with each other in parallel way. The sum of all absorbing capacity of the hydraulic motors is covered by efficiency of the pump, which can be described by the relation

$$Q_p = \sum_{i=1}^{n} Q_{si} \qquad (2)$$

where: Q_p is efficiency generated by hydraulic pump; ΣQ_{si} is sum of absorbing capacity of the hydraulic motors; n is number of hydraulic motors.

However, such a solution has got one serious flaw, namely, taking into consideration the fact that pressure of motor supply and drain lines is equal because of their load, and as a result of decreasing the pressure drop in any motor, there shall occur a limitation or even an impossibility to create a driving moment on other wheels. This effect may occur in case of decreasing of the thrust of the wheels on the ground, driving on a ground characterized by a small value of the traction rate or, in extreme cases, lifting the wheels off the ground (Fig. 3).
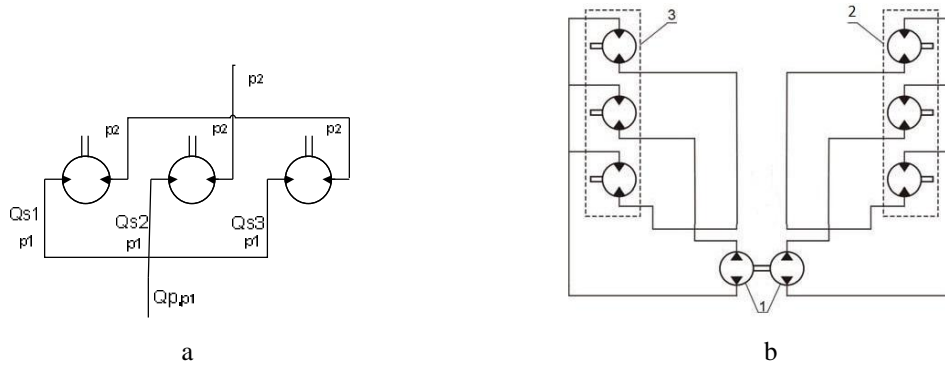
Fig. 2.   Arrangement in parallel of the supply of hydraulic motors: a – pressure drops in hydraulic system; b – diagram of connecting hydraulic motors in parallel
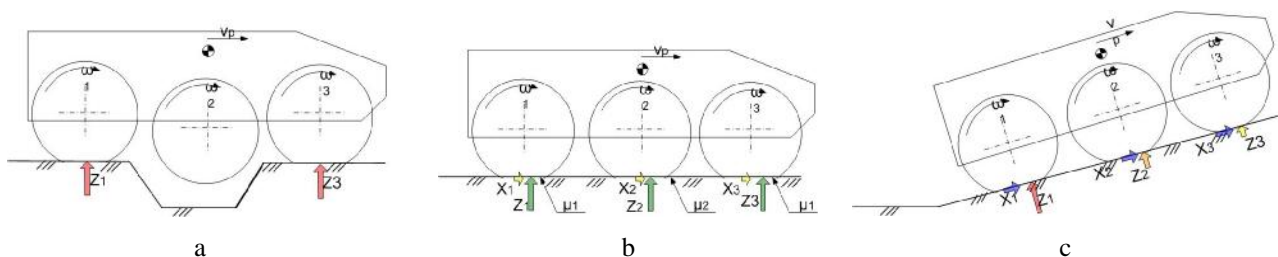
Fig. 3.   Possibility of limitation or a loss of capacity of the Hydrotronic Driving System (HDS) to generate pull force: a – overcoming a ditch; b – small value of the traction rate; c – unequal load on road wheels

The unfavourable effect described above can be eliminated by introducing a kinematic stiffness HDS of wheels that belongs to one side of the vehicle and is understood as their drive with the same speed, regardless of their load. It can be achieved by connecting motors in series or in parallel with the use of gear flow dividers responsible for dividing the working medium for motors regardless of their load (Fig. 4).

In case of a connecting motors in series, the total capacity of the supply pump is subsequently forced through the motors of a one side

$$Q_p = Q_{s1} = Q_{s2} = Q_{s3} \qquad (3)$$

where: Q_p is capacity of the pump; Q_{si} is absorbency of the hydraulic motor.

As a result, the increase of the pressure generated by the supply pomp covers the sum of pressure drops in hydraulic motors (Fig. 5a)

$$D\,p_p = \Sigma\,D\,p_{si} \qquad (4)$$

where: Δp_p is pressure generated by the positive displacement pump; $\Sigma\,\Delta p_{si}$ is sum of pressure drops in hydraulic motors.

In case of connecting motors in parallel, every of them may use the maximum pressure generated by the pump (Fig. 5b), on the other hand, total capacity id divided in a proportional way into each hydraulic motor according to the dependence (2). Using both connecting configurations in one driving system, it is possible to get a road or a ground gear.
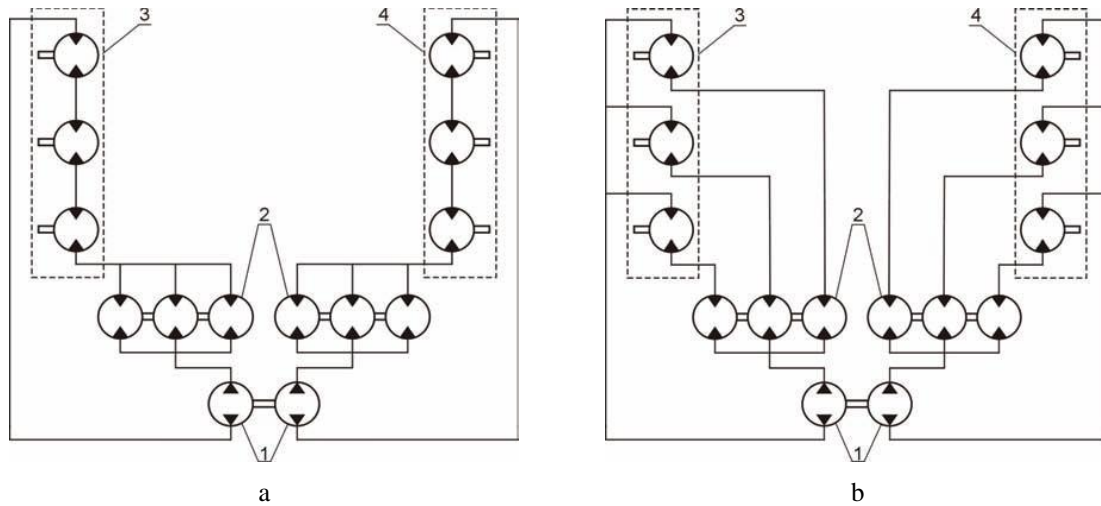
Fig. 4. Kinematically stiff driving system: a – connecting hydraulic motors in series; b – connecting motors in series with use of gear flow dividers; 1 – positive displacement pumps; 2 – gear flow dividers; 3 – hydraulic motors [8]
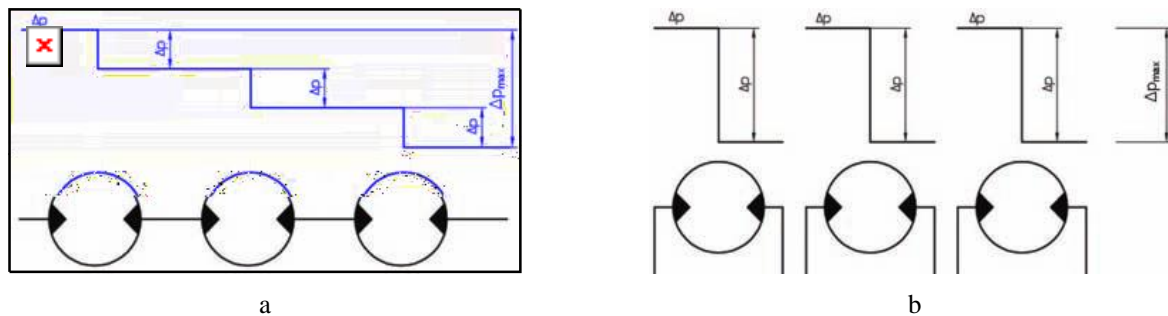
Fig. 5. Pressure drop in hydraulic motors [7]

Those types of systems are used first and foremost in all-terrain vehicles with a high mobility and where used in an engineering support robot called Marek (Fig. 6a). Suggested driving system consists of two main positive displacement pumps with a variable capacity. Each of them is responsible for the supply of the motors belonging to a separate side (1), of the working medium gear flow dividers (2) and of hydraulic motors serving for the road wheels drive (3) (Fig. 6b). The system is equipped with valves allowing to change the connection of motors in parallel or in series. The system was used to examine the capacity of compensating the kinematic discrepancy.
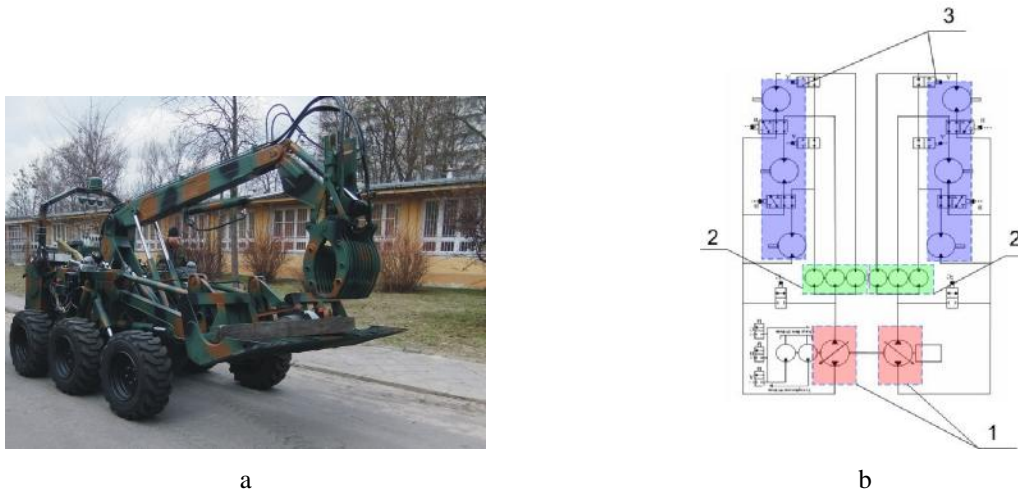
Fig. 6. Engineering support robot Marek: a – view of the vehicle; b – hydrostatic driving system: 1 – positive displacement pumps supplying the system; 2 – working medium gear flow dividers; 3 – hydraulic motors [9]

4. Compensating kinematic discrepancy in a hydraulic system

In order to examine the capacity to differentiate the rotational speed of the road wheels of the vehicle, one shall define volumetric losses in the driving system and their cumulated influence on the rotational speeds of hydraulic motor shafts. The value of those leakages may be determined on the basis of characteristics and data made available by producers of hydraulic components. In the adopted driving system of the Engineering support robot Marek (Fig. 6), the capacity of compensating the kinematic discrepancy depends on the leakages in the gear flow dividers and hydraulic motors. The leakages in the pump does not influence the capacity of compensating the kinematic discrepancy.

For the analysis of the compensation of the kinematic discrepancy one chose displacement motors with a comparable unit absorbency of about 400 cm^3 and a capacity to generate a driving moment but different in terms of their construction:

1 – gerotor engine Danfos TMT 400;
2 – piston engine Rexroth MCR5 380.

Analogically, for the analysis on chose gear flow dividers with a comparable value of nominal and working flows at the comparable nominal pressures, but different in terms of the accuracy of dividing the working medium:

1 – toothed divider by ViVoil with a 2% accuracy of the working medium flow division at the nominal working conditions;
2 – toothed divider by ViVoil with a 5% accuracy of the working medium flow division at the nominal working conditions;
3 – throttling divider Rexroth RTM, with variable characteristics of the division depending on the speed of the working medium flow (Fig. 7).
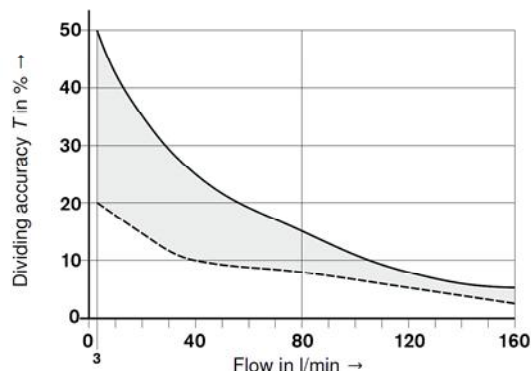
Fig. 7. Characteristics of the accuracy of dividing the throttling stream Rexroth RTM of the gear flow divider [10]

The following system working conditions were adopted for the examination:

a – driving at a low speed and with a significant resistance to motion requiring high values of driving forces which corresponds to the movement of a vehicle on a difficult terrain and with a ground gear;
b – driving with a high speed with a small resistance to motion achieved with a road gear and in a system arranged in series.

4.1. Estimating the capacity to compensate the kinematic discrepancy with the terrain mode

The analysis was performed for a vehicle moving with a speed of $v_j = 1$ m/s which, taking into consideration the dynamic radius of wheels $r_d = 0.35$ m, requires ensuring the absorbency of each of three engines with the value of $Qs = 12$ dm³/min, which results in the fact that the pump supplying the side of the vehicle should generate the capacity $Q_s = 36$ dm³/min. It was assumed that the maximum decrease of the pressure in hydraulic engines and the pressure generated by the pump, are limited by the safety valve to the value of $\Delta p_p = 30$ MPa and $\Delta p_{si} = 30$ MPa. In the assumed scope of speed, the volumetric efficiency of the gerotor engine Danfos TMT 400 is $\eta_v = 0.82$ for the assumed maximum pressure, on the other hand, for the piston engine Rexroth MCR5 380 in the same conditions $\eta_v = 0.86$ (Fig. 9).
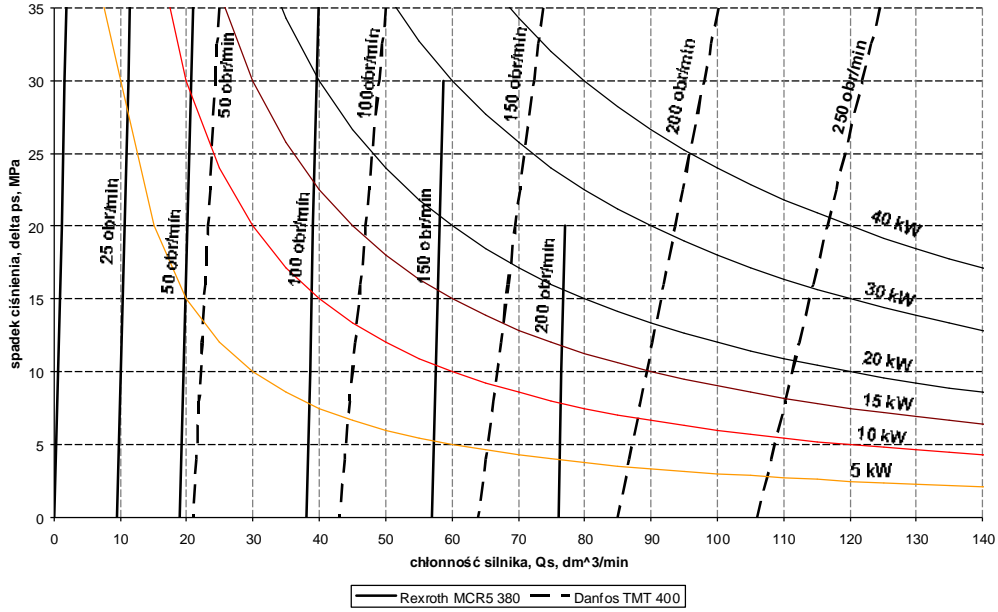
Fig. 8. Comparison of the volumetric hydraulic motors characteristics by means of a curve of the constant speed – worked out on the basis of the data provided by the producers [10, 11]

The starting point for determining the capacity to compensate the kinematic discrepancy is constituted by the balance of pressure drops generated in the gear flow divider (Fig. 9) that constitutes a kinematic coupling with the lines of the hydraulic system. As a result of the fact that the sections of the divider are connected mechanically, the sum of pressure drops in particular section must equal to zero, which is indicated by the dependence

$$\sum_{i=1}^{n} Dp_{dzi} = 0 \qquad (5)$$

where Δp_{dzi} is pressure drops in the sections of the gear flow divider.

The above results in the fact that the average of pressures in the input and output lines of the divider must be equal to each other in accordance to the dependence

$$\frac{1}{n}\sum_{i=1}^{n} p_{dziwej} = \frac{1}{n}\sum_{i=1}^{n} p_{dziwyj} \qquad (6)$$

where: p_{dziwej} is average of pressures before the gear flow divider; p_{dziwyj} is pressures after the gear flow divider.
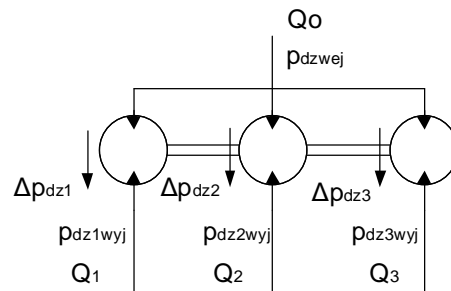
Fig. 9. Flow and pressure division in the gear flow divider

The above mentioned dependences result in the fact that the particular sections of the divider may function in the system as an engine decreasing the pressure or as a pump increasing the pressure in the line after the divider. In both cases there a leakages depending on the value of the pressure drops which results in the compensation of the kinematic discrepancy.

For the sake of the examination, it was assumed that the maximum value of the compensation of the kinematic discrepancy of the system occurs when the pressure drop in one of the engines drops to zero (the wheel rolls freely but it does not generate traction force), however, the value of the pressure drop in the other engine is maximum.

First, the case of driving straight ahead was taken into consideration (Fig. 10), where the gear flow divider is situated on the run-off line of the hydraulic motors. Assuming the pressure drops in the engine with the value of $\Delta p_{s1} = 0$ MPa, $\Delta p_{s2} = 0$ MPa, $\Delta p_{s3} = 30$ MPa, the pressures on the run-off line of the motors shall have the value of $p_1 = 30$ MPa, $p_2 = 30$ MPa, $p_3 = 0$ MPa. In connection with the pressure in the lines after the gear flow dividers and in the suction pump in accordance with the independence (6) shall have the value of $p_4 = 20$ MPa, while the increase of pressure generated by the hydraulic pump shall have the value of $\Delta p_p = 10$ MPa.

The theoretical values of the capacity to compensate the kinematic discrepancy determined according to this algorithm are indicated for a set consisting of:

1 – a toothed engine and a gear flow divider with the 5% accuracy – table 1;
2 – a piston engine and a gear flow divider with the 2% accuracy – table 2;
3 – piston engine and a throttling divider whose accuracy of division of the working medium is between 9%÷30% for the work with the efficiency $Q_p = 36$ dm^3/min – table 3.
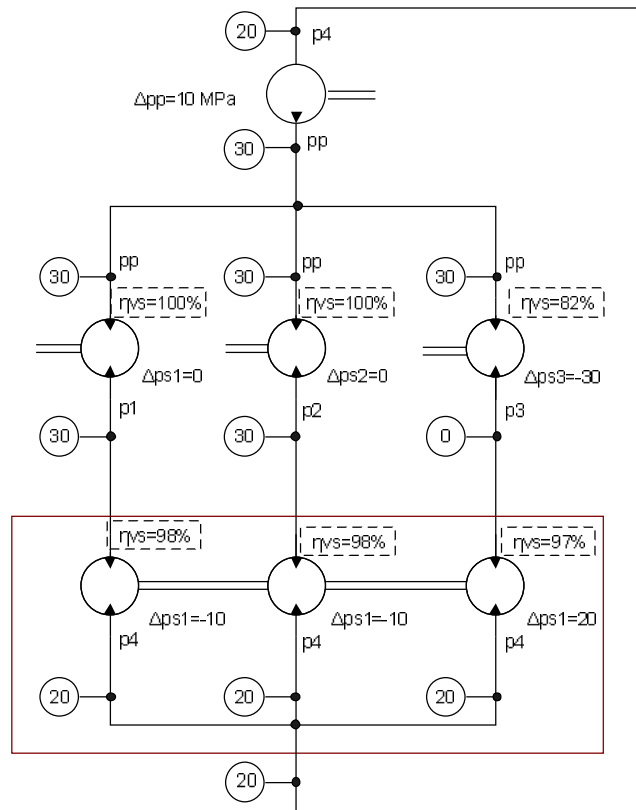
Fig. 10. Connecting in series for driving straight ahead – the numerical values of the pressures are indicated in [MPa]

Table 1

Comparison of the results of the analysis of a system constituting
of a toothed engine and a gear flow divider with the 5% accuracy

Element		Δp, MPa	η_v
hydraulic motor		30	82.0%
gear flow divider	1	-10	98.3%
	2	-10	98.3%
	3	20	96.7%
sum of leakages		Σ	77.9%
compensation of the discrepancy			22.1%

Table 2

Comparison of the results of the analysis of a system constituting
of a piston engine and a gear flow divider with the 2% accuracy

Element		Δp, MPa	η_v
hydraulic motor		30	86.0%
gear flow divider	1	-10	99.3%
	2	-10	99.3%
	3	20	98.7%
sum of leakages		Σ	84.3%
compensation of the discrepancy			15.7%

Table 3

Comparison of the results of the analysis of a system constituting of a piston
engine and a throttling divider (9-30% with the efficiency $Q_p = 36$ dm^3/min)

Element		Δp, MPa	η_v		
hydraulic motor		30	86,0%	÷	86,0%
gear flow divider	1	-10	97,0%	÷	90,0%
	2	-10	97,0%	÷	90,0%
	3	20	97,0%	÷	90,0%
sum of leakages		Σ	80,9%	÷	69,7%
compensation of the discrepancy			19,1%	÷	30,3%

Taking into consideration a case where a vehicle moves backwards in a all-terrain mode (Fig. 11) for the assumed pressure drops $\Delta p_{s1} = 0$ MPa, $\Delta p_{s2} = 0$ MPa, $\Delta p_{s3} = 30$ MPa, and assuming that the pressure in the run-off lines from engines have the value of $p_4 = 0$ MPa, then the pressure in the high pressure line for the hydraulic motors $p_1 = 0$ MPa, $p_2 = 0$ MPa, $p_3 = 30$ MPa. Thus, the pressure in the input line of the gear flow divider, in accordance with the dependence (5), shall be $p_p = 10$ MPa.
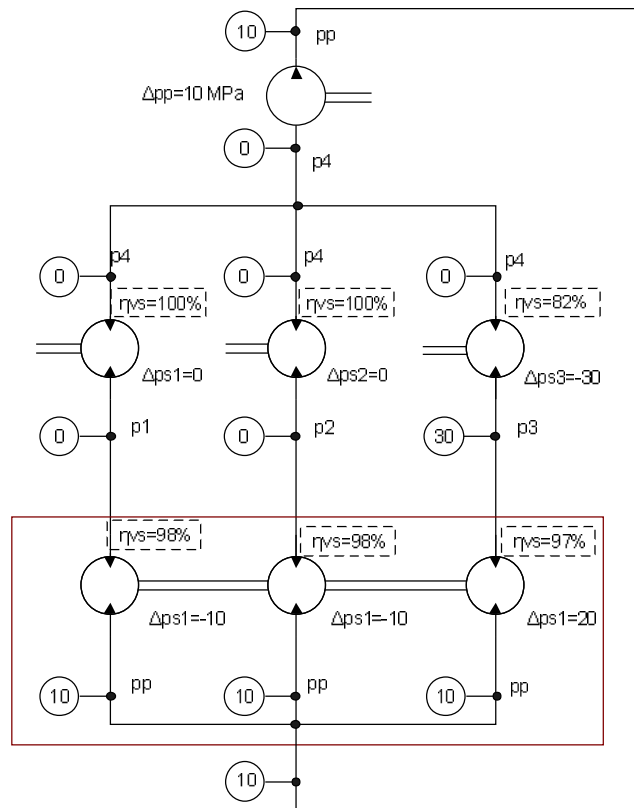
Fig. 11. Connecting the motors in parallel for driving straight ahead-numerical values of the pressures are indicated in [MPa]

The analysis suggests that by assuming analogically the same hydraulic components and values of the pressure drops in the elements, the same value of the compensation of the kinematic discrepancy is indicated.

Although, the pressure drop in the hydraulic motor is $\Delta p_s = 30$ MPa, the small values of pressure drops in other motors cause a significant decrease in the pressure generated by the pump $p_p = 10$ MPa. This is the effect of the action of two sections of the divider that took over the function of a pump (one section) and of an engine (the second section). Thus, in such case there is a necessity of protecting the line after the gear flow divider against the excessive pressure increase.

By extending the examination of the capacity to compensate the kinematic discrepancy in a system arranged in series, an analysis was performed for a bigger scope of the driving speed $v_j = 2; 3; 4; 5; 6; 7$ m/s, and for the calues of the pressure drops in the hydraulic motors $\Delta p_{si} = 30; 20; 10$ MPa. Its results are presented in the Fig. 11-13.
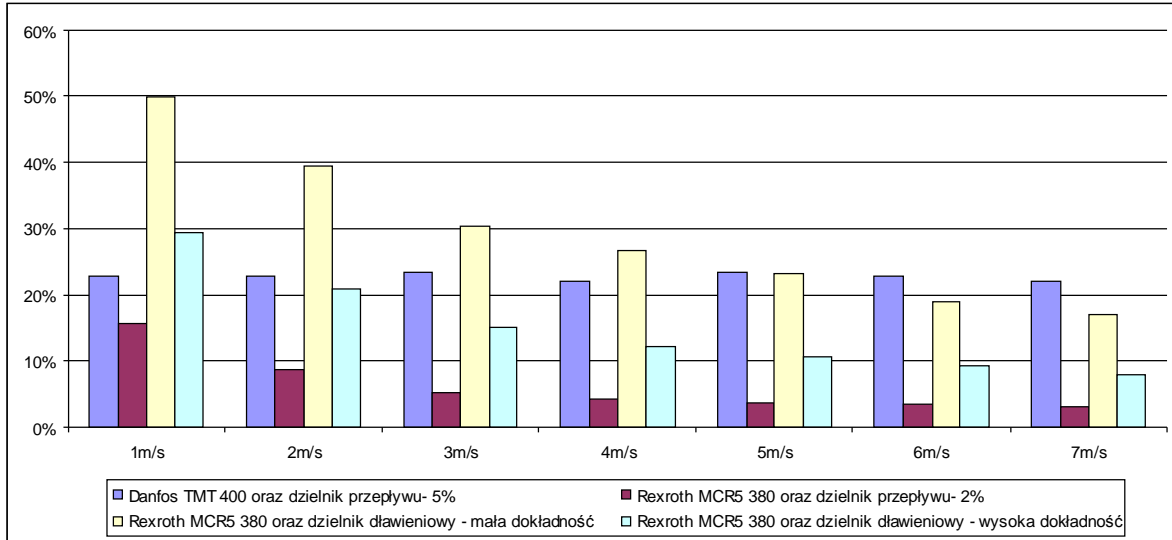
Fig. 12. Capacity to compensate the kinematic discrepancy of the system for different driving speeds in the all-terrain mode in case of a drop of pressure in the hydraulic motor $\Delta p_s = 30$ MPa
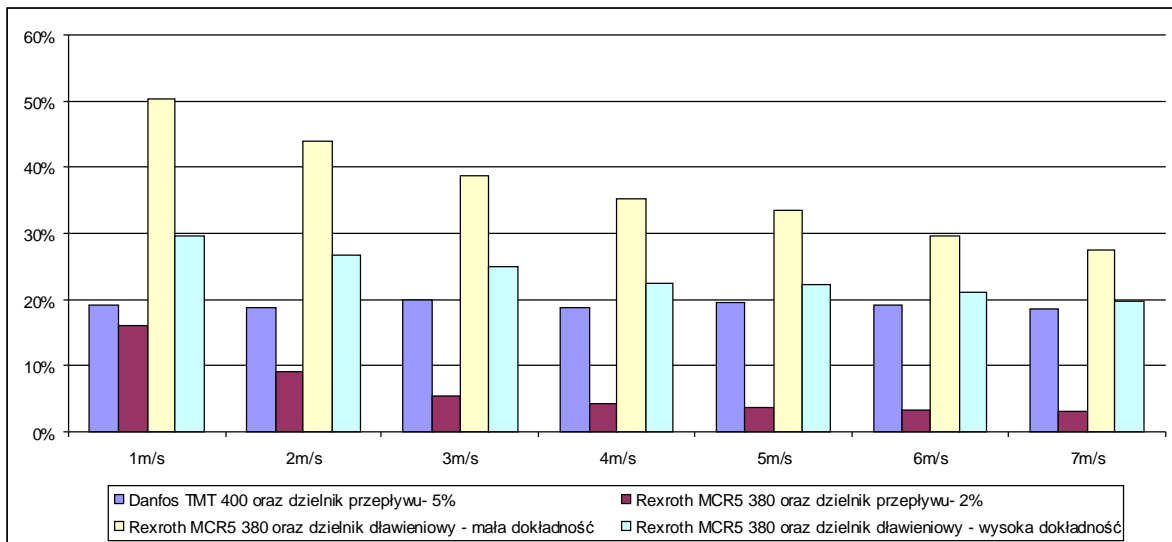
Fig. 13. Capacity to compensate the kinematic discrepancy of the system for different driving speeds in the all-terrain mode in case of a drop of pressure in the hydraulic motor $\Delta p_s = 20$ MPa
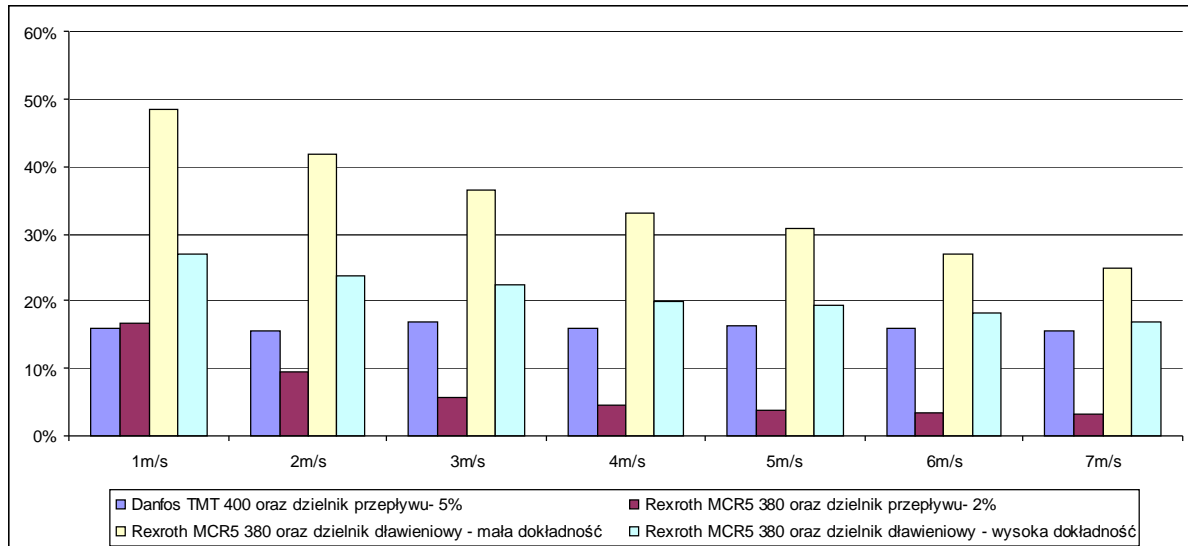
Fig. 14. Capacity to compensate the kinematic discrepancy of the system for different driving speeds in the all-terrain mode in case of a drop of pressure in the hydraulic motor $\Delta p_s = 10$ MPa

4.2. Examination of the capacity to compensate the kinematic discrepancy in the road mode

Driving in the road mode when the engines are supplied in series, assuming the speed of the vehicle $v_j = 10$ m/s. The values of pressures of the hydraulic motors were assumed analogically as for the connection in parallel. The results of the analysis are indicated in the Fig. 15.
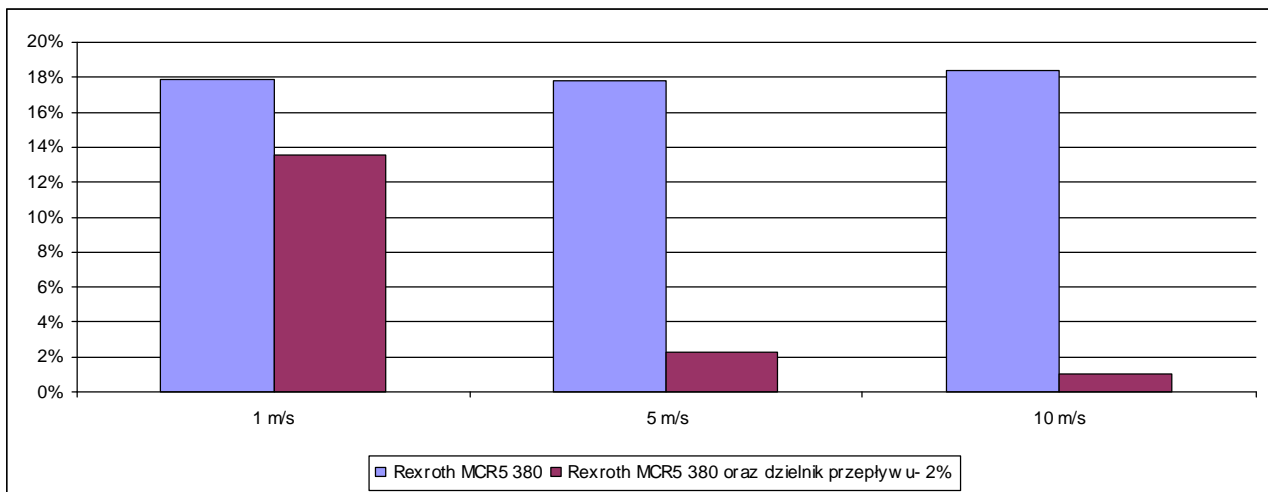
Fig. 15. Capacity to compensate the kinematic discrepancy of the system for different driving speeds in the road mode in case of a drop of pressure in the hydraulic motor $\Delta p_s = 30$ MPa

The analysis of the system arranged in series indicates that the maximum capacity of the system arranged in series to compensate the kinematic discrepancy results from the total value of leakages of one engine and is 18% for the toothed engines and 14% for the piston engines. However, it is an excessive generalization as it does not include the volumetric losses taken from each engine to the container. Taking into consideration the presence of the leakages even when driving straight ahead on a flat ground with identical values of the pressure drops, the kinematic discrepancy occurs resulting from the gradual decrease of the dose of the working medium to each next engine.

5. Conclusions

The performed analyses indicate that shaping the characteristics of the compensation of the kinematic discrepancies in a hydrostatic driving system should be performed in two ways: by choosing appropriate structure of the system and by choosing the components of the hydraulic system and analyze them prom the perspective of the whole system.

Ensuring a high efficiency of the system requires using the hydraulic motors that are characterized by the high volumetric efficiency and the efficiency of gear flow dividers ensuring a due division of the medium flow. Taking it into consideration the most, favorable characteristics were achieved by using the piston engines and the throttling gear flow divider. It allowed to achieve the maximum capacity to compensate the kinematic discrepancy for driving at small speeds between 30-50%, and at higher speeds between 8-17%.

References

1. **Sprawka P.** The methods of evaluation the mobility of off - road vehicles. Solid State Phenomena Vol. 180, Trans Tech Publications, Switzerland 2011.
2. **Budny E.** Napęd i sterowanie układów hydraulicznych w maszynach roboczych. ITE, Radom 2001.
3. **Bartnicki A., Sprawka P.** Zastosowanie hydrostatycznych układów napędowych we współczesnych maszynach i pojazdach lądowych. LOGITRANS, Szczyrk 2008.
4. **Studziński K.** Teoria I sterowanie. Samochód. WKŁ, Warszawa 1980.
5. **Comellas M., Pijuan J., Potau X., Nogue´s M., Roca J.** Active bogies, chassis levelling and transmission efficiency for avehicle operating in rough terrain. Journal of KONES Powertrain and Transport, nr 4 2007.
6. **Comellas M., Pijuan J., Potau X., Nogue´s M., Roca J.** Analysis of a hydrostatic transmission driveline for its use in off-road multiple axle vehicles. Journal of Terramechanics, nr 49. 2012.
7. **Stryczek S.** Napęd hydrostatyczny. Tom I. Wydawnictwa Naukowo - Techniczne, Warszawa 2005.
8. **Bartnicki A., Muszyński T.** Koncepcja układu napędowego dla bezzałogowej platform lądowej o skręcie burtowym, Międzynarodowa Konferencja Naukowo-Techniczna Napędy i Sterowania Hydrauliczne i Pneumatyczne, Wrocław 2010.
9. **Łopatka M. J.** Praca zbiorowa, Inżynieryjny Robot Wsparcia IOD/EOD – usuwania ładunków niebezpiecznych, Sprawozdanie z projektu rozwojowego Nr OR00001205/PBR, Warszawa 2011.
10. [10, 11, 12] Directories hydraulic components published on the official websites of manufacturers.

Simulation Research of Hydrostatic Power System Control of Engineer Robot Manipulator

S. Konopka*, M. J. Łoptaka**, P. Krogul***

*Military University of Technology, Warsaw, Poland, E-mail: skonopka@wat.edu.pl
**Military University of Technology, Warsaw, Poland, E-mail: mlopatka@wat.edu.pl
***Military University of Technology, Warsaw, Poland, E-mail: pkrogul@wat.edu.pl

Abstract

This article presents capabilities of intuition control system for engineer robot manipulator equipped with hydrostatic power drive system. For this purpose, simulation research which included nonlinearities and dynamic of electrohydraulic direct valve was conducted. Simulations was performed for two degrees of freedom, open chain manipulator. Based on simulation research, estimated trajectory of manipulator tool using selected parameters.

KEY WORDS: *manipulator, intuition control, hydraulic, kinematic, dynamic, simulation.*

1. Introduction

Development of mobility robots involves development their equipments and manipulators. One of these group are engineer robot manipulators, which name according to high functionality. In order to their effective control in teleoperation system [1-4] operator has to have a lot of experience which are result of longtime training and working with selected group of manipulators. Inexperienced operator could decrease control effectivity even 50%, an example of which are correction coefficients included rank of operator experience using by manufacturers of engineering equipment to determine efficiency of working machine [5, 6]. It becomes more complicated if it take to consideration control of hydrostatic drive system, which application to drive manipulators results of many advantages [7-9] for other kind of drive systems. In order to improve control efficiency intuition control system are being formed. Main disadvantages of this kind of systems are:

- external reference elements to correct manipulator motion;
- complex structure and stationarity control station;
- control of individual actuators manipulator.

Based on limitations of intuitive control systems proposed the concept of new control system. The idea of such a system is used to copy the horizontal and vertical movements of the operator's hands by analogous movements of the manipulator tool. In order to achievement this concept, it has to simultaneously control hydraulic control valves to properly direct the flow of the working medium with required flow to hydraulic actuators. Most commonly be accomplished using electric-operated directional control valves (DCV). Their widespread use results mainly from low prices, compared to the expensive servo valves and process control automation capabilities by applying computers and programmable logic controllers. Unfortunately, such valves are characterized by worse dynamic properties, and several times greater hysteresis of their electromechanical transducers in the case of use servo valves [8]. Although the DCVs are characterized by specified restrictions in relation to the expensive servo, it continues to be components used in automation control. It was used among others in the motion automation of equipment excavator [10-16] or hydrostatic testing of the hydrostatic drive system with load compensation [17-20]. In the literature well describes their nonlinear and dynamic properties [8, 21], but does not take into account their impact on the accuracy of tool of engineer robot manipulators. Lack of clear information about the impact of DCV on the trajectory of the manipulator tool impossible to implement the proposed control system. Taking this into account in this article such a control system simulation taking into account which include effect of nonlinearity and dynamics properties of the DCV on the trajectory of the engineer robot manipulator tools.

2. Simulation research methodology

The main objective of the simulation study was to evaluate the possibility of moving the manipulator tool across selected trajectories in its workspace. This was achieved on the basis of five horizontal trajectory and three vertical (Fig. 1), which their linear shape results from the proposed control system, and lengths due to range of manipulator workspace (Table 1).

Table 1

Lengths of considered trajectories

	Trajectory							
	1	2	3	4	5	6	7	8
Length of trajectory [m]	2.8	2.7	2.8	2.9	2.7	4.1	4.3	2.8
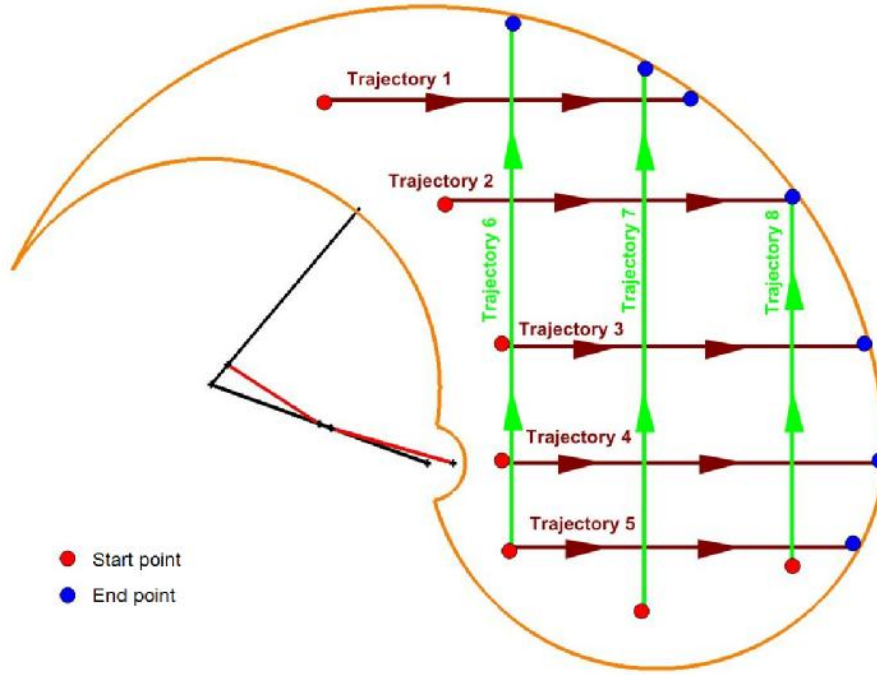
Fig.1. Scheme of considered trajectories

In order to evaluate the trajectories of the manipulator tool in relation to the established trajectories taken into account the following geometric parameters:

- $y_{max\,(+)}$ – maximum vertical direction positive deviation of manipulator tool trajectory;
- $y_{max\,(-)}$ – maximum vertical direction negative deviation of manipulator tool trajectory;
- y_k – vertical direction deviation trajectory end of manipulator tool from reference trajectory;
- x_{ks} - trajectory end position coefficient of manipulator tool

$$x_{ks} = \frac{x_k}{l} \qquad (1)$$

where: x_k is difference in horizontal distance end trajectory of manipulator tool from end of reference trajectory; l is length of reference trajectory;

- $y_{śr}$ is arithmetic mean value of trajectory of manipulator tool

$$y_{śr} = \frac{\sum_{i=1}^{n} y_i}{n} \qquad (2)$$

where: y_i is the i-th value of point deviation in vertical direction; n is quantity sampling points of trajectory;

- y_{RMS} is root mean square trajectory of manipulator tool

$$y_{RMS} = \sqrt{\frac{\sum_{i=1}^{n} y_i^2}{n}} \qquad (3)$$

- r is trajectory deviation of manipulator tool

$$r = y_{max\,(+)} - y_{max\,(-)} \qquad (4)$$

For such adopted parameters were plotted characteristics of manipulator tool deviation trajectory in vertical direction as a function of reference trajectory length. The way of describing the trajectory recognized either the vertical and horizontal deviations in relation to the reference trajectory, which would be difficult to considered them as a function of time (lack of information about trajectory end point of manipulator tool). For simulation studies model of manipulator with two degrees of freedom was developed. Hydrostatic drive system of this model includes the effect of disturbances which result from the operation of DCV, without taking into account the manipulator inertia and without

disturbances resulting from the operation of DCV and including the inertia of the manipulator. Such accepted division allowed the assessment of the influence of individual elements on trajectory of manipulator tool.

3. Structural model of the manipulator

This paper considered an open kinematic chain model of the manipulator with two degrees of freedom. Manipulator model is presented in Fig. 2 and its geometrical dimension are summarized in Table 2. As mentioned in chapter two examined two variants of the hydrostatic drive system model of manipulator. The first option includes interference resulting from a DCV, without taking into account inertia of the manipulator while second option ignores DCV interference and take into account the inertia of the manipulator (Fig. 3).
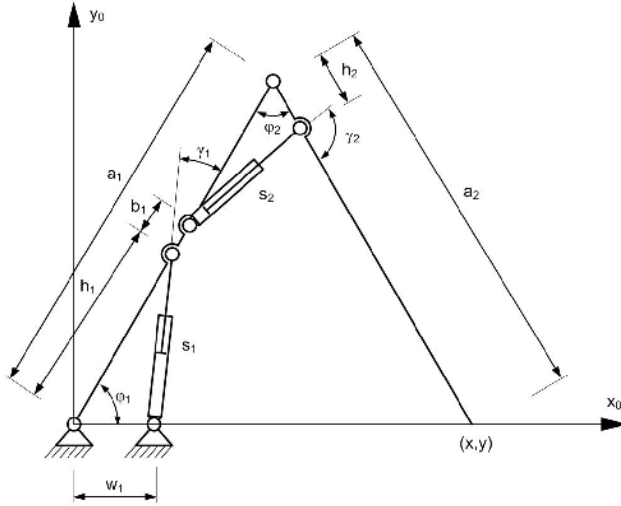
Fig.2. Kinematic model of manipulator
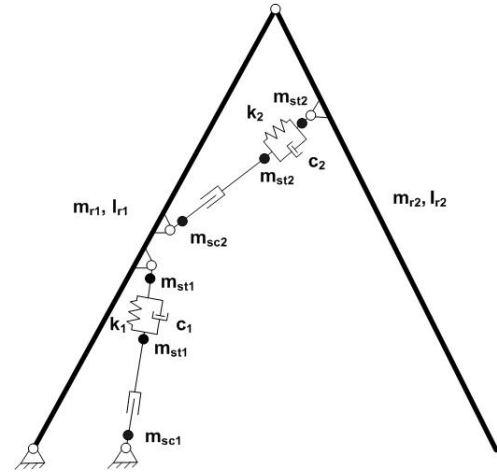
Fig.3. Structural model of manipulator

Table 2

The dimensions of manipulator model

h_1	h_2	a_1	a_2	b_1	w_1
0.8 m	0.2 m	1.8 m	1.8 m	0.1 m	0.2 m

The main assumptions used to build the model of the manipulator and its drive system are:
- individual units were considered as a homogeneous, non-deformable rod elements of known masses and mass moments of inertia;
- hydraulic actuator were considered as non-deformable elements with masses reduced to their attachment points;
- not included the occurrence of leaks in hydraulic system;
- assumed constant pressure drop at direct valve;
- assumed that pump ensures the required flow rate for each actuators;
- omitted pulsating nature of the hydraulic pump work;
- pressure in cylinder is presented as a force equal to the reduced load on the cylinder rod arising from the configuration of manipulator units.
    For the first variant:
- not included the phenomenon of compressibility working medium and elasticity of the hydraulic lines;
- take into account non-linear nature of the change of working medium flow rate as a function of displacement of spool DCV as a static characteristic;
- take into account non-linear character of proportional solenoid work in the form of hysteresis characteristic (the phenomenon of magnetism);
- included the inertia direct valve.
    For the second variant:
- not included the nonlinearities and dynamics of DCV;
- included the inertia of the manipulator, compressibility of working medium and elasticity of hydraulic lines through the damping and stiffness elements with constant parameters.
    The maximum speed of rod actuators is limited to actuators speed level of this type engineering machine, $v = 0.1$ m/s (mini excavators). Determination of parameters values of stiffness and damping elements was performed from the actual characteristics of engineer robot manipulators "Bogus" [22]. Nonlinearity resulting from a DCV was developed on the basis of the real characteristics valves of group PVG32 [23]. Includes the following nonlinearity:

- structural nonlinearity type of hysteresis, resulting from the operation of an electromechanical converter;
- structural nonlinearity as a characteristics of flow (static characteristics) that resuts from the construction of the valve.

The nonlinearity in the form of hysteresis elaborated by the relation

$$u(v_i) = v_i + \text{sign}\left(\frac{0.02 Q_N}{S_i}, \&_i\right) \tag{5}$$

where: Q_N is nominal flow rate of the working medium by the direct valve; v_i is input signal in the form of the i-th cylinder piston rod speed result of the manipulator tool motion; S_i is surface of the i-th cylinder.

Whereas the static characteristics compalied by incorporate the points from the real characteristic and interpolated them by the function of the first order (Fig. 4).
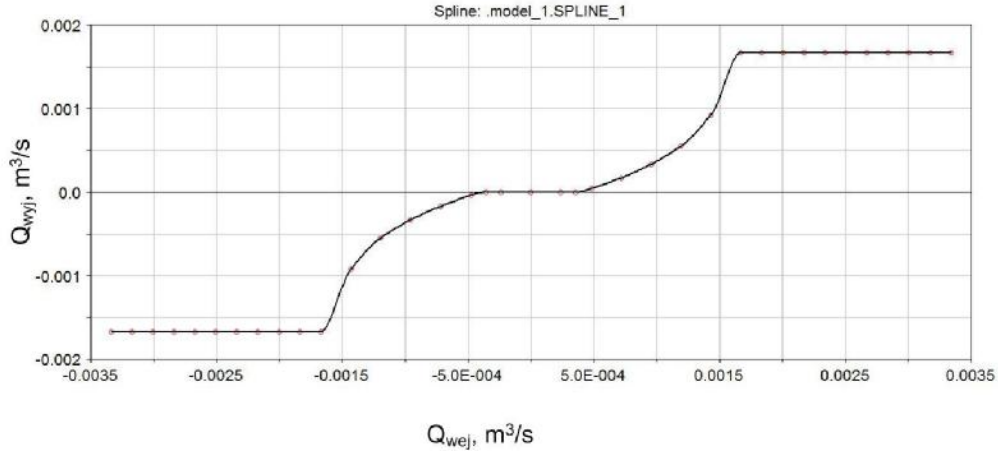
Fig.4. Static characteristic of DCV created In the MSC Adams

The inertia of the direct valve is implemented as transmittance of oscillating unit (Fig. 5) [21], where the time constant resulting from the natural frequency of system $T = 0.2$ s and dimensionless damping factor $\xi = 0.7$ was assumed. For this model was generated logarithmic amplitude-frequency characteristic in MSC Adams (Fig. 6).
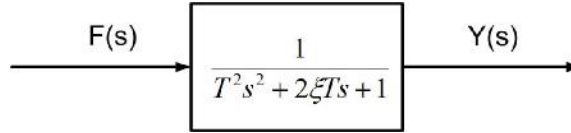
Fig.5. Block diagram describing the inertia of the hydraulic valve in the form of transmittance: T is time constant determining the speed of the system action; ξ is dimensionless damping factor determining the susceptibility of system to resonance; $F(s)$ is input signal in the transmittance form; $Y(s)$ is output signal in the transmittance form
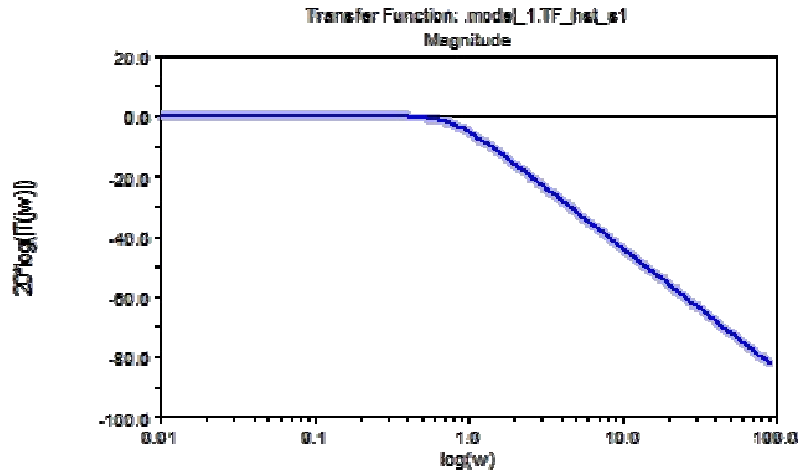
Fig.6. Logarithmic amplitude-frequency characteristic of direct valve dynamic properties created in the MSC Adams

4. Input signal

In order to control the tool of manipulator according to specific trajectory (Fig. 1) was determined the motion equations of manipulator tool resulting from submission of individual unit motion to the task of inverse kinematics [24, 25]. This task was considered for spatial dual element mechanism, which is considered manipulator. On the basis of scheme presented on Fig. 7 was determined relations on point coordinates $A(x, y)$ as a function of the angle φ_2.
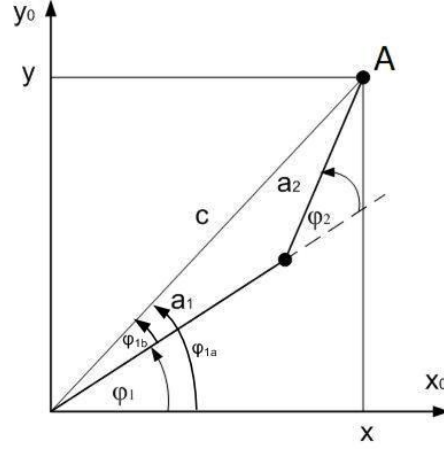
Fig.7. Scheme to determine relations on point cordinates $A(x, y)$ as a function of the angle φ_2

Using the cosine theorem

$$c^2 = a_1^2 + a_2^2 - 2a_1 a_2 \cos(p - j_2) \tag{6}$$

and taking into account

$$c^2 = x^2 + y^2 \quad \text{and} \quad \cos(p - j_2) = -\cos j_2 \tag{7}$$

and after transformation

$$\cos j_2 = \frac{x^2 + y^2 - a_1^2 - a_2^2}{2a_1 a_2} = T \tag{8}$$

On his basis, the relations on angle φ_2 is

$$j_2 = \arccos T \tag{9}$$

Whereas the angle φ_1 was determined by taking into account

$$j_1 = j_{1a} - j_{1b} \tag{10}$$

where

$$j_{1a} = \arctan \frac{y}{x} \tag{11}$$

and φ_{1b} was determined by taking into account sines theorem

$$\sin j_{1b} = \frac{a_2 \sin j_2}{\sqrt{x^2 + y^2}} \tag{12}$$

and then after appropriate transformation

$$\tan j_{1b} = \pm \frac{a_2 \sin j_2}{\sqrt{x^2 + y^2 - a_2 \sin^2 j_2}} \tag{13}$$

and substituting

$$x^2 + y^2 = a_1^2 + a_2^2 + 2\,a_1\,a_2\cos j_2 \tag{14}$$

determined φ_{1b}

$$j_{1b} = \arctan\frac{a_2\sin j_2}{a_1 + a_2\cos j_2} \tag{15}$$

Therefore the angle φ_1 is

$$j_1 = \arctan\frac{y}{x} - \arctan\frac{a_2\sin j_2}{a_1 + a_2\cos j_2} \tag{16}$$

Then, such determined relations on φ_1 and φ_2 were differentiated in terms in terms of variable x or y depending on vertical or horizontal trajectory. Symbols were adopted as presented in Fig. 2a. Based on the relations on φ_1 and φ_2 were determined velocity of cylinders

$$\dot{s}_1 = j\dot{q}_1\, h_1\cos\left(\frac{p}{2} - \dot{g}_1\right) \quad\text{and}\quad \dot{s}_2 = j\dot{q}_2\, h_2\cos\left(\frac{p}{2} - \dot{g}_2\right) \tag{17}$$

Dyscretization of relations (17) according to the following equations

$$Ds_1 = Dj_1\, h_1\cos\left(\frac{p}{2} - Dg_1\right) \quad\text{and}\quad Ds_2 = Dj_2\, h_2\cos\left(\frac{p}{2} - Dg_2\right) \tag{18}$$

were implemented to simulation program for their execution. Then specify that nominal flow from the pump is equal to the sum of flows on aqtuators Q_1 and Q_2

$$Q_N = Q_1 + Q_2 \tag{19}$$

Also were included in following relation the proportional distribution of flow for considered actuators

$$\frac{Q_1}{Q_2} = \frac{Ds_1}{Ds_2} \tag{20}$$

After appropriate transformation equations (14) and (15) were determined input signals for hydraulic cylinders as their velocities

$$v_1 = \frac{Q_N}{\left(\dfrac{Ds_2}{Ds_1} + 1\right)S_1} \quad\text{and}\quad v_2 = \frac{Q_N}{\left(\dfrac{Ds_1}{Ds_2} + 1\right)S_2} \tag{21}$$

5. The results of the simulation research

Pursuant to simulation studies were generated trajectory characteristics in vertical and horizontal coordinates of manipulator tool. The characteristics of trajectory 7 generated in MSC Adams was presented in Fig. 8 and 9. Based on these characteristics were calculated the values of geometric parameters. Theirs summary were presented in Table 3 and 4, while in Table 4 included the first variant of drive system and in Table 3 the second variant.
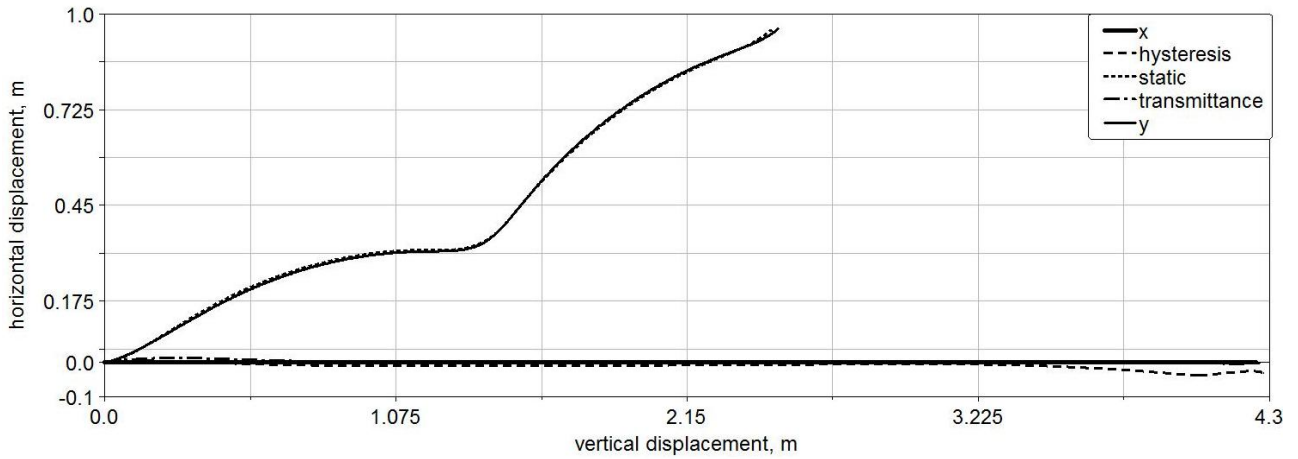
Fig.8.   The trajectory characteristics of the manipulator tool for the first variant: *x* is reference trajectory; hysteresis-manipulator tool trajectory depends on hysteresis of proportional solenoid; static – manipulator tool trajectory resulting from static characteristic of direct valve; transmittance – manipulator tool trajectory depends on dynamic properties of direct valve; *y* is manipulator tool trajectory takes into account all considered factors
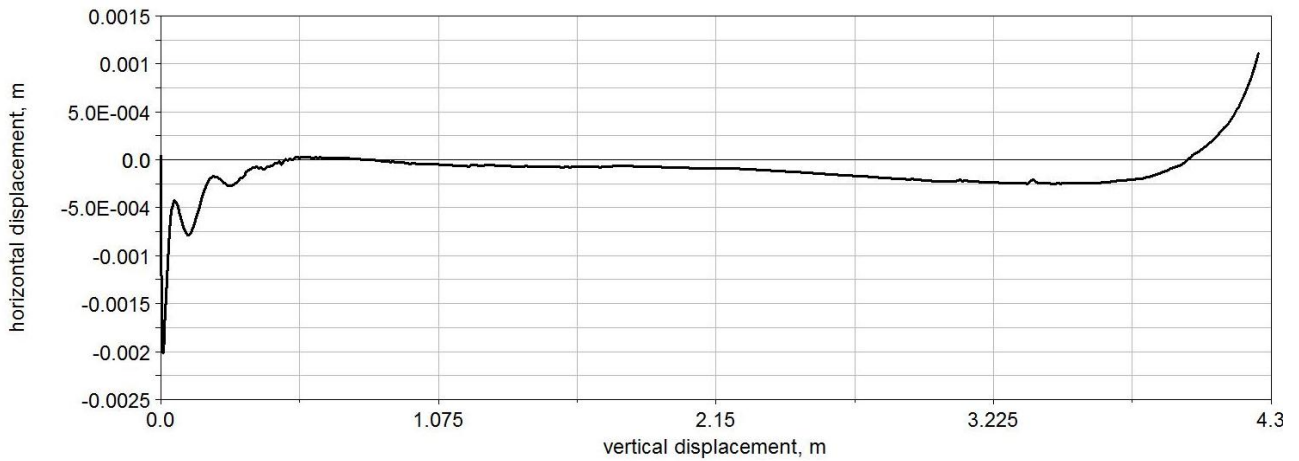
Fig.9. The trajectory characteristics of the manipulator tool for the second variant: x- reference trajectory; hysteresis-manipulator tool trajectory depends on hysteresis of proportional solenoid; static- manipulator tool trajectory resulting from static characteristic of direct valve; transmittance- manipulator tool trajectory depends on dynamic properties of direct valve; y- manipulator tool trajectory takes into account all considered factors

Table 3

Sumary of geometric parameters for the second variant of the drive system

	Trajectory							
	1	2	3	4	5	6	7	8
$y_{max\,(+)}$ [m]	0.002	0.000	0.000	0.000	0.000	0.023	0.001	0.005
$y_{max\,(-)}$ [m]	−0.016	−0.022	−0.045	−0.027	−0.034	−0.001	−0.002	−0.004
y_k [m]	−0.003	−0.022	−0.045	−0.027	−0.034	0.023	0.001	0.005
x_{ks}	0.000	0.000	0.000	0.000	0.000	0.000	0.000	0.000
y_{RMS} [m]	0.003	0.011	0.023	0.016	0.012	0.014	0.001	0.004
$y_{śr}$ [m]	−0.002	−0.008	−0.015	−0.013	−0.008	0.011	0.000	0.003
r [m]	0.018	0.022	0.045	0.027	0.034	0.025	0.003	0.009

Comparison of selected parameters for the first variant was presented in Fig. 10 and 11. On this basis it can be concluded that the main factor influence on manipulator tool trajectory is static characteristic of DCV. On the other hand Fig. 12 and 13 presented comparison of parameters *r* and y_{RMS}, which result from control system operation (the first variant) and inertia of manipulator (the second variant). On this basis it can be said that root mean square depends on manipulator inertia achieves values of around several centimeters which in the case of system operation (DCV effect) reaches up to 60 cm.

Table 4

Sumary of geometric parameters for the first variant of the drive system

		Trajectory							
		1	2	3	4	5	6	7	8
$y_{max\,(+)}$ [m]	hysteresis	0.002	0.000	0.000	0.000	0.059	0.010	0.002	0.005
	static	0.122	0.088	0.440	0.699	0.046	0.799	0.952	0.327
	transmittance	0.016	0.004	0.019	0.009	0.006	0.007	0.010	0.013
	y	0.102	0.068	0.454	0.692	0.000	0.667	0.958	0.327
$y_{max\,(-)}$ [m]	hysteresis	−0.044	−0.077	−0.250	−0.383	−0.053	−0.198	−0.040	−0.019
	static	−0.002	−0.025	−0.060	0.000	−0.208	0.000	−0.002	0.000
	transmittance	−0.007	−0.001	−0.001	0.000	−0.011	−0.005	−0.008	−0.009
	y	0.000	−0.042	−0.079	0.000	−0.206	0.000	0.000	0.000
y_k [m]	hysteresis	−0.037	−0.067	−0.250	−0.035	0.000	−0.198	−0.032	−0.010
	static	0.116	0.086	0.490	0.699	0.046	0.798	0.952	0.327
	transmittance	0.000	0.000	0.019	0.009	0.000	0.005	−0.004	0.000
	y	0.095	0.066	0.454	0.692	−0.012	0.649	0.958	0.327
x_{ks}	hysteresis	0.000	0.000	0.000	0.000	0.000	0.000	0.000	0.000
	static	0.478	0.624	0.704	0.528	0.333	0.344	0.428	0.486
	transmittance	0.000	0.000	0.000	0.000	0.000	0.000	0.000	0.000
	y	0.450	0.597	0.684	0.513	0.374	0.300	0.422	0.479
y_{RMS} [m]	hysteresis	0.031	0.055	0.122	0.147	0.026	0.117	0.020	0.011
	static	0.107	0.068	0.361	0.513	0.090	0.617	0.722	0.298
	transmittance	0.004	0.001	0.012	0.006	0.003	0.003	0.004	0.005
	y	0.090	0.052	0.322	0.527	0.087	0.506	0.604	0.252
$y_{śr}$ [m]	hysteresis	−0.025	−0.049	−0.099	−0.107	0.007	−0.094	−0.016	−0.007
	static	0.102	0.053	0.284	0.432	−0.012	0.546	0.630	0.282
	transmittance	0.001	0.000	0.009	0.005	0.001	0.002	−0.001	0.001
	y	0.087	0.032	0.237	0.448	−0.054	0.446	0.489	0.216
r [m]	hysteresis	0.047	0.077	0.250	0.383	0.113	0.208	0.042	0.024
	static	0.123	0.113	0.500	0.699	0.254	0.799	0.954	0.327
	transmittance	0.023	0.006	0.020	0.009	0.016	0.011	0.018	0.022
	y	0.103	0.110	0.533	0.692	0.206	0.667	0.958	0.327
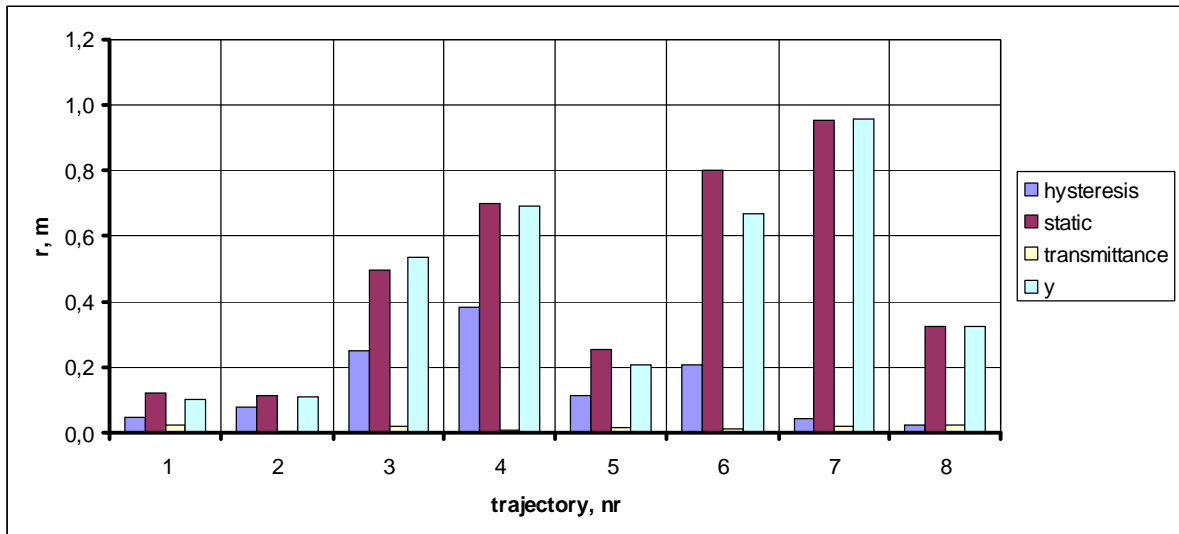
Fig. 10. Comparison of each characteristics of DCV as a function of manipulator tool trajectories for r parameter
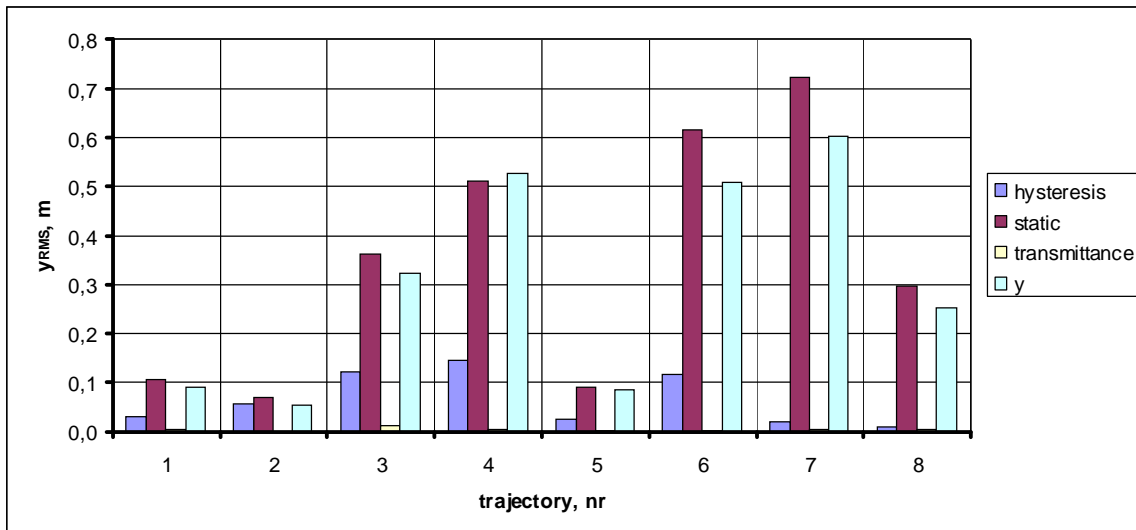
Fig. 11. Comparison of each characteristics of DCV as a function of manipulator tool trajectories for y_{RMS} parameter
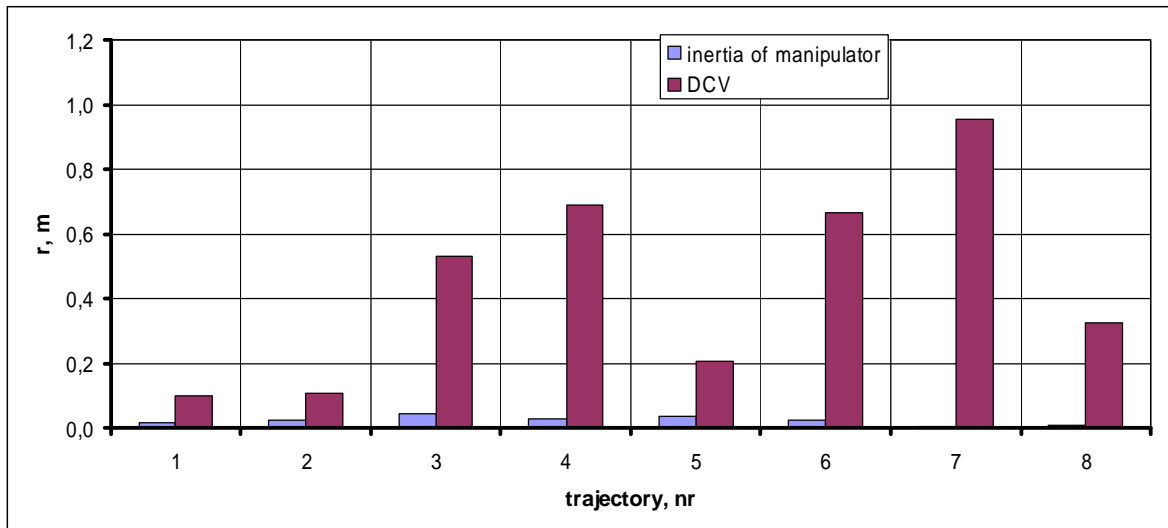
Fig. 12. Comparison of control system (DCV effect) and the inertia of manipulator as a function of manipulator tool trajectories for r parameter
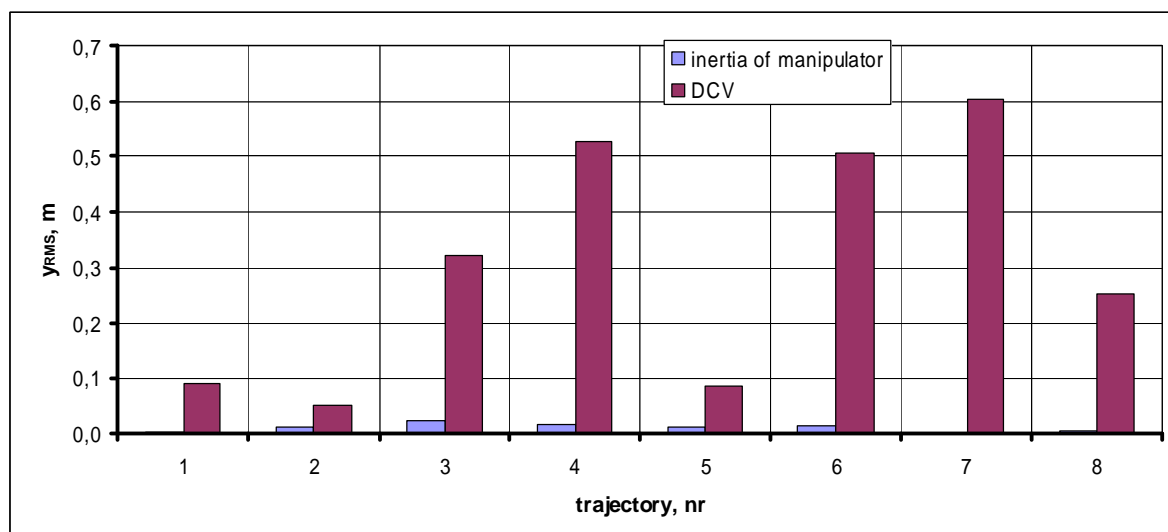
Fig. 13. Comparison of control system (DCV effect) and the inertia of manipulator as a function of manipulator tool trajectories for y_{RMS} parameter

6. Conclusions

Based on simulation studies it can be said that open loop control system for hydraulic drive system of manipulator tool is difficult to achieve. This is mainly due from the nonlinear characteristic of direct valve which depends on dead bad and saturation zone. Effect on the motion precision also depend on curvilinear part of this characteristic. The nature of the operation causes significantly reduce the trajectory of manipulator tool (limited range of operation) and an increase in vertical deviation from the reference trajectory. Influence of the manipulator inertia causes deviation of manipulator tool trajectory from reference trajectory by 2-3 cm which is a few percent of control system influence. Taking into account the limited ability to control typical DCV in open system, it is envisaged to carry out studies for control system with feedback.

References

1. **Konopka S., Typiak R.** Dobór systemu wizyjnego dla bezzałogowej szybkobieżnej maszyny inżynieryjnej. Materiały konferencyjne PRMR. 10 stron. 2011.
2. **Wen G., Xie Y. C.** Research on the tele-operation robot system with tele-presence. Proceedings of 4th International Workshop on Advanced Computational Intelligence. Pages 725-728. 2011.
3. **Ni T., Zhang H., Liu S., Yamada H.** Teleoperation system with virtual reality based on stereo vision. Proceedings of International Conference on Transportation, Mechanical, and Electrical Engineering. Pages 494-497. 2011.
4. **Jingwei H., Dingxuan Z.** A new force feedback algorithm for hydraulic teleoperation robot. Proceedings of International Conference on Computer Application and System Modeling. Volume 15. Pages 1515-1518. 2010.
5. **Poradnik Caterpillara.** Caterpillar performance handbook, edition 41. Wydawnictwo Caterpillar. USA. Illinois. Peoria 2011.
6. **Poradnik Komatsu.** Specifications & application handbook, edition 27. Wydawnictwo Komatsu. Japonia. 2006.
7. **Galal Rabie M.** Fluid power engineering. Wydawnictwo McGraw-Hill. 2009.
8. **Pizoń A.** Elektrohydrauliczne analogowe i cyfrowe układy automatyki. WNT. Warszawa 1995.
9. **Kress R. L., Jansen J. F.** Hydraulic manipulator research AT Oak Ridge National Laboratory. ANS Sixth Topical Meeting on Robotics and Remote Systems in Augusta. Georgia. April 27 – May 1 1997.
10. **Budny E., Chłosta M., Gutkowski W.** Sensitivity of the optimum bucket trajectory in controlled excavation. Automation and Robotics in Construction XVI. 1999.
11. **Budny E., Chłosta M., Gutkowski W.** Load-independent control of hydraulic excavator. Automation in Construction 12. 10 stron. 2003.
12. **Budny E., Gutkowski W.** A hydraulic open loop system for controlled excavation along prescribed path. ISARC 17. 6 stron. Taiwan. Taipei 2000.
13. **Kim D., Kim J., Lee K., Park C., Song J., Kang D.** Excavator tele-operation system using a human arm. Automation in Construction 18. 10 stron. 2009.
14. **Uusisalo J., Huhtala K., Vilenius M.** Effects of remote control on usability of hydraulic excavator. Proceedings of the ASME Dynamic Systems and Control Conference. Pages 1233-1240. 2009.
15. **Pratumsuwan P., Hutamarn S., Po-Ngaen W.** A development of tele-controller for hydraulic excavator. Proceedings of the 2012 7th IEEE Conference on Industrial Electronics and Applications. Pages 2123-2126. 2012.
16. **Yoshinada H., Okamura K., Yokota S.** Master-slave control metod for hydraulic excavator. Journal of Robotics and Mechatronics. Volume 24. Pages 977-984. 2012.
17. **Bartnicki A., Kuczmarski F.** Badanie statycznych i dynamicznych właściwości hydrostatycznych układów napędowych z kompensacją obciążenia. Przegląd Mechaniczny. Zeszyt 2/2004.
18. **Bartnicki A.** Badanie właściwości I kształtowanie sterowania hydrostatycznymi układami napędowymi z kompensacją obciążenia. Rozprawa doktorska. WAT. Warszawa 2004.
19. **Yi Y., Yu T.** The load sensing principle of proportion multi-channel valve and its application In excavator. Proceedings of the 3rd International Conference on Intelligent System Design and Engineering Applications. Pages 1469-1472. 2013.
20. **Li Y., Cui T., Jiang J., Yu C.** The principle of a novel load sensing hydraulic system and design of the electronic control system. Applied Mechanics and Materials. Pages 119-122. 2012.
21. **Konopka S., Łopatka M. J.** Podstawy konstrukcji maszyn z CAD, część 4 modelowanie ruchu maszyn. WAT. Warszawa 2005.
22. Projekt Badawczo-Rozwojowy nr. 0012/R/T00/2008/06: Bezzałogowy pojazd do wykonywania zadań w strefach zagrożenia. WAT. Warszawa 2011.
23. PVG 32 Proportional Valve Groups. Technical Information. 2011.
24. **Morecki A., Knapczyk J., Kędzior K.** Teoria mechanizmów i manipulatorów. WNT. Warszawa 2002.
25. **Crane III C. D., Duffy J.** Kinematic analysis of robot manipulators. Wydawnictwo Uniwersytetu Cambridge. Nowy Jork 2008.

Proceedings of 8ᵗʰ International Conference ITELMS'2013

Office Workers with Better Lighting Conditions Suffer Less Health Symptoms

T. Koppel*, P. Tint*

Tallinn University of Technology, Chair of Labour Environment and Safety, Ehitajate tee 5 Tallinn 19086 ESTONIA, E-mail: tarmo.koppel@ttu.ee; piia.tint@ttu.ee

Abstract

The study investigates the link between the lighting conditions in the office work environment and the health symptoms associated with poor illumination. Along with the recent studies, the important role of lighting and its effect on humans is becoming clearer. The relevance of the natural daylight is expressed by the dynamic nature of the colour temperature, the bright illuminance level and the continuous spectrum. But most modern lighting systems fail to replicate the natural daylight. This study used questionnaire data to assess the lighting conditions at office workplaces. Both natural daylight and artificial indoor lighting were assessed. 518 office workers participated in the study and were divided into six groups based on the lighting conditions at their workplaces. The groups showed clear distinctions in regard to a number of health symptoms suffered by average group member. The symptoms were seen to be more dependent on the quality of the indoor lighting, but also the natural daylight had a significant role. The workers with poor lighting conditions were seen to suffer more from fatigue, tired or painful eyes, dizziness, dry eyes, difficulties in concentrating, stress or depression headache, etc. Those people reported in average 2.8 times more symptoms than people working in adequate lighting conditions. The highest gap was detected as workers in well lit environments reported 95 per cent of them feeling productive, whereas only 37 per cent of the workers from poorly lit environments could claim the same. Although limitations do apply, as with any self-reported data, the results suggest the relevance of both indoor and natural lighting on workers psychological and physical health.
KEY WORDS: *lighting, daylight, sunlight, illuminance, health, office, questionnaire.*

1. Introduction

The focal point of this study is the natural daylight and its levels at office workplaces. The authors were motivated to conduct the study, since scientific body of research is becoming clearer on the importance of natural daylight to human being. Also, many of the modern office buildings are planned and built in a way that minimizes the occupants' exposure to the natural daylight. This is especially the case for buildings with closed inner courtyards, called atriums. Office workers with their workplaces facing the atrium are likely to receive orders of magnitude less natural light than their colleagues facing the outside of the building. Therefore the underlying question of this study was set up, whether these office workers with less natural daylight suffer more from a given psychological or physiological conditions. Also, it may be asked, if these people are as productive as others working under better lighting conditions.

The study presents a new questionnaire, specifically developed to use self-reported data to map the natural daylight conditions at the worker's workplace. Since natural daylight can not be viewed separately from the indoor lighting the latter is also addressed by the questionnaire. The composition of the questionnaire is aimed at proving or dismissing the link in between the natural daylight conditions and a given set of health symptoms that are associated with poor lighting conditions.

When one starts to compare the indoor lighting conditions to those outside, the relevance of sunlight is actually not so hard to comprehend – homo sapiens' evolution has taken place under the sun, which therefore has been an integral part of this process. The research from the field of photobiology has also attributed the light with a variety of vital roles: from regulating organism's circadian rhythms to driving the immune system. Even a new term "malillumination" has been coined to describe a health condition where insufficient natural light is seen to be the cause of symptoms similar to the chronic fatigue syndrome. Surely lighting is not the only factor influencing human health. Amongst the risk factors many can be named that endanger the well-being of the human. The office worker may be subjected to any of the following:

- unfavourable nature of work;
- nocuous social environment, such as bullying, sexual harassment or other kind of discrimination;
- micro- and nano-size particles (for example from laser printers and photocopiers);
- chemical risk factors;
- biological risk factors such as fungus, mould, bacteria, viruses etc;
- indoor climate and the air quality (temperature, humidity, ventilation efficiency etc);
- electromagnetic fields, such as those from wireless devices or nearby production facilities;
- noise and vibration (an open space office environment, nearby production or construction area);
- ergonomical risk factors (for example the body posture)

Next to the array of different risk factors, a person's individual characteristics also play a role in the development of health symptoms caused by poor lighting: age, physical fitness, receptivity to illnesses, mental strength etc. If a person is following the healthy life styles, having regular physical activities, eating healthy food, having plenty time for rest and recovery from the work, has a satisfying job – he/she is more likely to better coupe with the environmental stressors.

This study focuses solely on the lighting conditions and disregards other risk factors. Therefore the adverse effect from the poor lighting conditions needs to be remarkable and the sample size large, to detect any effects from lighting, as surely other environmental factors will contribute with a "noise". If the lighting conditions are only to produce a weak effect on humans, then this study is likely not to notice it, since the other risk factors are not controlled. Also, the personal characteristics of the respondent are also unaccounted for.

When focusing on lighting, it must be noted that it consists of many parameters, each of which may have an effect on human being. Mostly, only illuminance level is measured and considered in assessing the lighting. But there are also other light parameters that have been seen to have an effect on humans. Therefore, the lighting conditions can not be represented by a single index. A star-diagram based model, developed by Koppel, is helpful in describing the ergonomical quality of different lighting sources [1]. Next to the illuminance level, it encompasses spectrum, colour temperature, dynamic nature, flicker and the electromagnetic fields – inherent to each artificial light source (Fig. 1).
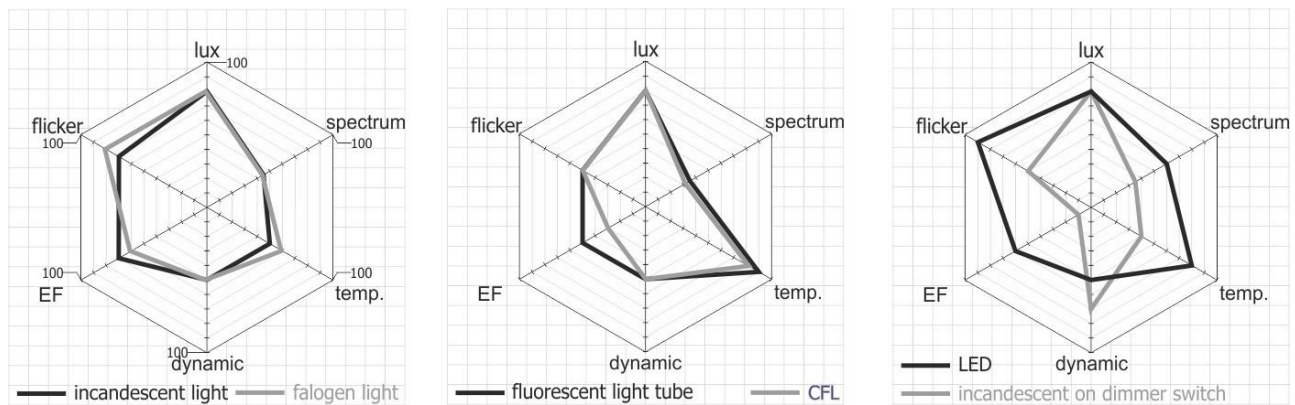
Fig.1. Representing different lighting sources on the star-diagram model [1]

Koppel's model was developed to assess single light sources without taking into account the characteristics of the room. Therefore glare and other environment dependant risk factors are unaccounted for. Also, the model includes electromagnetic fields, which are irrelevant if one only seeks to assess the properties of the natural lighting.

The star-diagram model considers natural daylight as the hallmark of ergonomic lighting and compares all the rest artificial sources to it. For example, in an open meadow, below a lonely tree several lighting conditions exist, created by the natural daylight, that the authors consider ideal for lighting requirements of the office work as pictured in Fig. 2.
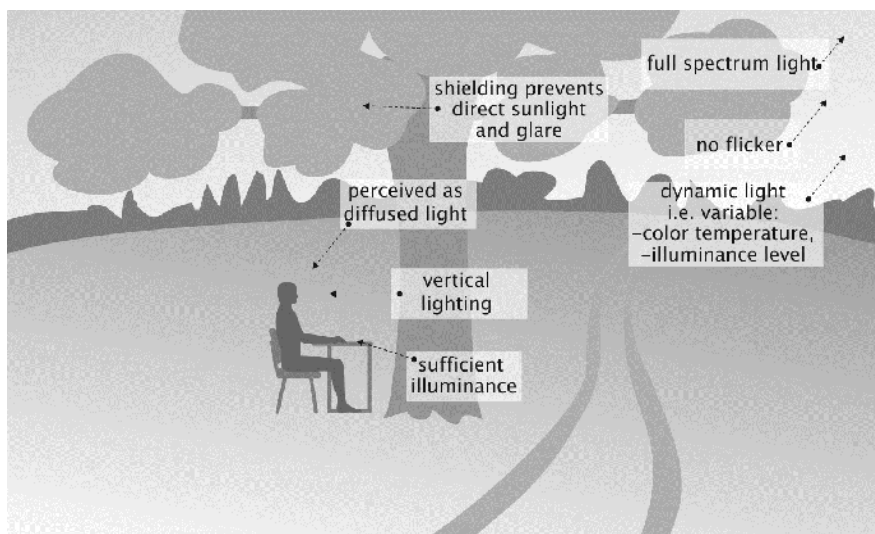
Fig. 2. The authors describe perfect lighting conditions as working below a lonely tree in an open field.

The problem with most office workplaces nowadays is that the lighting characteristics are far from those intrinsic to the natural daylight. According to the presupposition, the human being has evolved under the natural

daylight, which the organism is most accustomed to. The Sun has been the major source of lighting for hundreds of millions of years of the evolution of the man. Only fairly recently we have switched to the artificial lighting as our main light source.

The sunlight is a full spectrum light, unlike those fluorescent light tubes or CFLs (compact fluorescent light bulbs) most common in offices today (Fig. 3). The spectrum of the natural daylight is not only the spectrum of the sunlight. The atmosphere also has an absorbing and a diffusing role, as the sunlight passes through the layers of the atmosphere. This is why the sunlight appears yellowish or even reddish at the evening. Artificial light sources only try to mimic the white light but actually create only something called "pseudo white". The term describes the light that the human eye perceives as white, but is only an illusion of white since most of the wavelengths are missing. For example, the fluorescent tube creates three intense wavelengths in the blue, green and yellow region that summed together create an impression of white light.
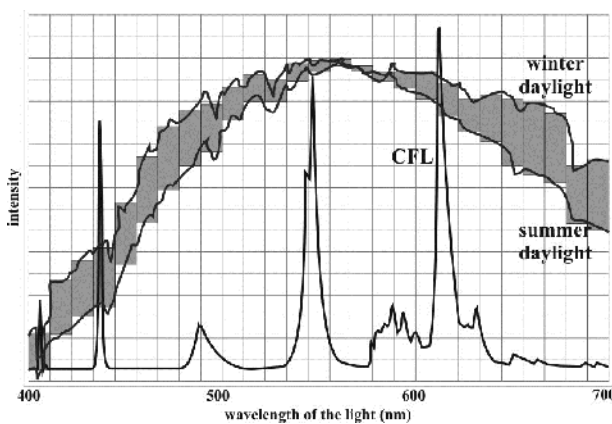
Fig. 3. The spectrum of the summer sun, the winter sun and the compact fluorescent light bulb [2]
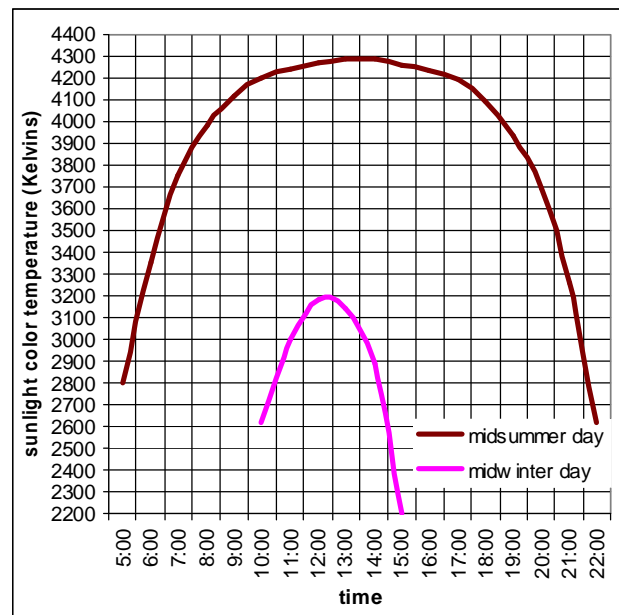
Fig.4. Sunlight color temperature during the course of the day from sunrise to sunset [2]

Also, the sunlight has no flicker which is present in most artificial lighting solutions. Older fluorescent tubes with magnetic ballasts created a significant flicker. Modern electronic ballasts are considered flicker free, but technically this is not true as still they flicker at higher frequencies (around 20-60 kHz). Such high frequencies are though considered unharmful to humans, since frequencies below 100 Hz are found to create most of the health problems. 100 Hz is still unnoticeable by human eye since most humans are even unable to detect 50 Hz flicker [3]. However, epileptic persons are considered a risk group, since flickering may induce epileptic seizures. Researchers have identified 15-18 Hz [4] and 3 Hz [5] to be most dangerous for the mentioned risk group. Migraine attacks have also been linked to flickering lights, if the person is susceptible to migraines more than other people [6]. Wilkins et al (1991) also linked flickering to eye strain [7]. Studies have also shown the appearance of light oversensitivity at the same period when the migraine attacks or in between the periods of migraine attacks [8]

When considering the illuminance level, when the daylight entering the office workplace is in a form of a direct sunlight, the excessively bright light may also create discomfort for the staff. In general, for a long period of time it has been thought that the best illuminance level would be between 500-1000 lux [9], but recent studies have shown that the limit could as fine be 2000 lux [10]. The levels of 2000 lux and above are easily exceeded by letting in the natural daylight. A human being does not only need the light for visual tasks, but also for non-visual functions where the light stimulates several biological functions i.e. adjusting the circadian rhythms. In dim environments the humans tend to become sleepy and lazy, but in well lit rooms they become alert. This is why bright light is also used for treating seasonal affective disorder (SAD) as it helps to overcome a number of conditions such as depression, lack of energy, decreased interest in work, increased appetite with weight gain, carbohydrate and sugar desire, increased need for sleep and excessive daytime sleepiness, social withdrawal, extreme afternoon slumps with decreased energy and concentration, decreased sex drive [11]. But sufficiently lit places are also found to alleviate non-seasonal depression. A meta-analysis done by Even et al (2007) concluded that bright light is an excellent candidate for treating depression in general [12]. However, treating SAD with bright light seemed to be more efficient than treating non-seasonal depression, though the research is yet inconclusive [12]. Other researchers have also found the bright light to improve social behaviour. People exposed to bright light of 1000 lux or more had less quarrelsome activity, more agreeable behaviour and overall better mood [13]. Another similar study, by Smolders et al (2012) tested illuminance levels of

200 lux and 1000 lux on human subjects [14]. Results showed that people in brightly lit environments were more alert and vital, felt less sleepy, had shorter reaction time and increased physiological arousal [14]. The study showed that even in normal conditions intense light can surely improve being alert and vital, also heightening psychological arousal. Stephenson et al. (2012) who conducted one of the recent meta-analysis concluded that mood depends partly on alertness level, whereas light influences mood by increasing alertness via circadian component, but also through a direct mechanism of activating alertness centres in the brain [15].

A shifting colour temperature is considered a vital part of the dynamic lighting conception. As the natural daylight is dynamic by its nature, the colour temperature varies from yellowish (low colour temperature, long wavelengths) to clear white (higher colour temperature, shorter wavelengths) during the day (Fig. 4). Indoor lighting has no means of varying the colour temperature, except if a special dynamic lighting system is installed. Higher colour temperatures increases humans' psychological activity, as higher wavelengths have stronger stimulus on the autonomic nervous system [16]. Philips, the manufacturer of lighting solutions, has also done research in colour temperature, with the results indicating 17000 Kelvin colour temperature to stimulate test subjects and increase their productivity [17]. Figuiero et al (2004) in their study showed that blue light (short wavelengths) eliminated fatigue and sleepiness also at night time [18].

If the office workplace is lit by the incandescent of other filament types of light bulbs, the colour temperature is low and therefore inadequate for office works. LEDs, fluorescent tubes and other gas mixture solutions provide a range of colour temperatures and from this point of view are suitable for office premises.

As demonstrated, the natural daylight consists of many parameters important to the well-being of human. The authors consider the full spectrum and the shifting colour temperature along with the bright illuminance levels to be most important factors of the natural daylight. A recent discovery of a new photoreceptor has shared more light on the mechanism these parameters have. The light is signalling the body the time of the day, regulating the biological clock, which in turn regulates circadian and circannual rhythms of many bodily processes [19]. The circadian rhythms affect the human being both physically and psychologically: sleep/wake cycles, alertness, performance patterns, core body temperature, production of hormones [20]. The discovered photoreceptor is seen to be sensitive to blue tones of the light, which are received in the eye for a period of a time, stimulating a wide range of physiological responses linked to the neuroendocrine and neurobiological systems, it can be viewed as resetting the circadian timer, suppressing nocturnal melatonin production and raising alertness [20, 21].

Many factors may influence the levels of natural daylight indoors. The shape of the building, other buildings close-by, the floor where the workplace is situated and the total number of floors in the building – all needs to be taken into account. For example in an atrium type building, having a workplace with windows facing the inner courtyard, is likely to suffer from insufficient levels of natural daylight (Fig. 5). From another end of the scale – a workplace exposed to direct sunlight will produce a glare that will likely create discomfort for the worker. Such glare could be avoided if light diffusing elements are used next to the window. Preferably such elements should be planned already in the designing phase of the building. Later improvements will be difficult to implement and are therefore usually limited to the usage of curtains.
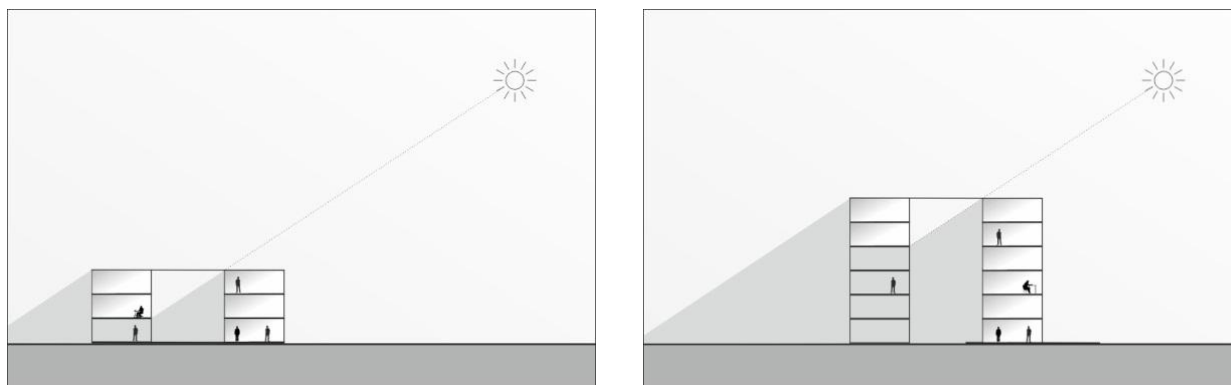
Fig.5.   The atrium type buildings have insufficient daylight at workplaces facing the inner courtyard. The higher the building the less daylight the occupants of the lower floors are to get

A large scale study, by Hwang and Kim (2011), involving 2744 occupants, conducted in the headquarters of Samsung Corporation, found that daylight indeed improves the workers' psychological health and productivity [22]. The study investigated an intervention where automatic roller shade system, controlled by the sunlight conditions, was installed. The researchers concluded that a significant correlation existed between the worker's visual comfort and satisfaction with lighting conditions and luminance distribution of the windows. Visual annoyance was seen to be in a functional relationship to the Sun elevation angle, since the workers reported less visual annoyance during the summer – as the Sun was higher, the direct sunlight did not penetrate deeply into the office space. The causes of visual annoyance were identified as glare, poor illuminance level, inadequate shade materials and logic error of the shade. After intervention the reported annoyances decreased tremendously. Another relevant conclusion was that improving

lighting conditions had no effect on the self-reported health symptoms [22].

2. Method

2.1. The questionnaire

This study is based on self-reported data. A questionnaire was developed to map both the indoor and natural daylight conditions at respondent's workplace. The researchers aimed at categorizing office workplaces based on different lighting conditions that would place the worker either into a well lit or poorly lit office environment. Therefore several factors affecting the path and propagation of light needed to be taken into account (Fig. 6).
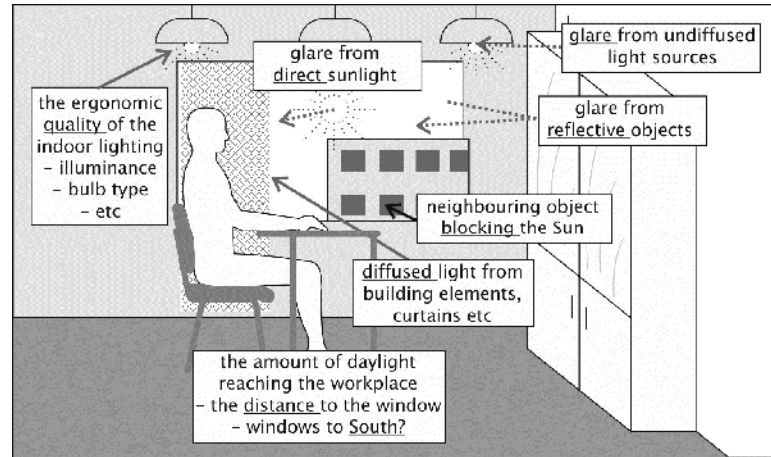
Fig.6. Factors at office workplaces affecting the lighting conditions and perceived light by the workers.

While composing the questionnaire, the authors found the most similar questionnaire from the research by Hwang and Kim (2011) which investigated lighting conditions and intervention efficiency in Samsung Corporation headquarters.

Items from Hwang's and Kim's questionnaire were used in a rephrased form [22]. However, the authors of this work do not use on-site instrumental measurements nor intervention measures, therefore the questionnaire developed, needed to have a complete set of questions to map the lighting conditions at the respondent's workplace.

The introductory part of the questionnaire explained the purpose of the survey and the potential benefit for the respondent – although the questionnaire was presented as an anonymous one, the respondent was provided with an option to leave his/her e-mail address in order to receive the results of the study. The researchers believed that the later option would stimulate the will to participate in the survey since the person is therefore able to receive feedback that will help him/her to determine the quality of lighting at his/her workplace compared to the rest of the sample.

Next to asking basic personal data, the questionnaire was divided into two main parts. The first section "Work environment and lighting" was aimed to create an overview of the lighting conditions at the individual's workplace. Also, the respondent was asked on how he/she is satisfied with the current lighting conditions. The questions were set up to reveal the main factors describing the lighting condition at one's workplace. Also, secondary factors that may affect the lighting perceived by the worker were inquired. The factors of the first section are summarized in table 1.

The second part of the questionnaire attempted to establish a link to a list of health effects. 15 symptoms or adverse health effects were presented, believed to be associated with poor lighting conditions. The respondent was asked to asses in Likert's 5-point scale the extent being affected by each of the symptoms. The respondent was to assess only his/her wellbeing at the workplace or after the work, as the effect of other environments or free-time conditions needs to be excluded. Understandably, the listed symptoms can be induced by many other environmental or medical issues, therefore no perfect correlation can not be expected. However, if the sample size is sufficient and representative, then at least a slight correlation would be expected, if indeed there is a link in between the symptoms and the lighting conditions.

The symptoms inquired were as follows: anxiety, fatigue, dizziness, headache, skin irritation or pain, eyes tired or painful, watery eyes, dry eyes, difficulty in concentrating, bad moods, restless and emotional, insomnia, frequently ill, stress or depression, cardiovascular problems. The respondent was faced with a question or a statement, which he/she then needed to assess using a given scale. Mostly Likert's 5-point scale was used, but also customized scales were needed for specific questions. The Likert's scale was presented as: 1-not at all; 2-a little bit; 3-moderately; 4-quite a bit; 5-a great deal.

Table 1

Lighting factors inquired by the questionnaire and secondary factors affecting the perceived lighting conditions

Inquired factor	Relevance to the research
Amount of natural daylight	Natural daylight is the focal point of this study. Natural daylight may enter the room being diffused (reflected or scattered by another reflective or luminescence object). Also, direct sunlight may enter the room lighting the workplace and the worker directly. This is somewhat unwanted scenario, since direct sunlight has a tendency to create glare. The preferred natural lighting is diffused lighting.
Occurrence of too bright light	The item seeks to inquire about the glare from sunlight. It is important to distinguish diffused daylight from the direct sunlight. The first creates well lit workplaces, the latter may cause discomfort.
Satisfaction with lighting conditions	There is always a chance that questions presented in the questionnaire do not map the lighting conditions entirely, leaving room for error. Inquiring about the respondent's satisfaction helps to decrease this error. However, on the other hand, satisfaction tends to be a highly subjective way to assess situations leaving much room for interpretations.
Distance to the window(s)	The farther the worker's desk is from the window the less daylight he/she receives (except for buildings with roof windows). As found by Newsham et al (2009) window access if considered to be an important factor of general satisfaction with overall lighting. The view must also be taken into account, as the worker's satisfaction does not only depend on the proximity of the window but also the satisfaction with outside view [23].
Which point of the compass do the window(s) point	When the windows face the South, then the occupants are able to benefit the most from the natural daylight. Contrariwise the case with the windows facing the North. In the northern latitudes the direction of the compass has even greater effect, on the available daylight at workplaces since in winter time there is little sunlight.
Obstacles (i.e. other buildings) blocking the sunlight from entering the room and distance to them	Even if the workplace's windows are facing the South, the Sun might be blocked by neighbouring buildings trees or other objects. Also the distance to the object blocking the Sun, must be accounted for since in some instances the buildings are placed right next to another, not only blocking the Sun, but also limiting the diffused daylight from the sky.
At which floor is the workroom positioned and the total number of floors in the building	In case of atrium or other inner courtyard type of a building the higher floors are likely to suffer less from insufficient daylight than lower floors.
Type of indoor lighting	Whether the workplace lighting consists of fluorescent light tubes or conventional filament tubes might have an effect on some individuals, as some have reported being sensitive to compact fluorescent light bulbs.
Hours per day spent at the workplace	The longer time the worker spends at the workplace, the higher the exposure to the possible poor lighting conditions. As a general rule of dosimetric studies, an individual may be resistant to adverse effects from the environmental risk factors for some time, but the more time is spent in such an unfavourable environment, the more likely the risk factors will have a toll on well-being. For example, the lecturers may spend a remarkable amount of their workday giving lectures, therefore minimizing their exposure to the lighting conditions at the workplace.

2.2. Method of delivery

The questionnaire was published on-line in two languages: Estonian and English. A free open-source questionnaire engine LimeSurvey was used to open the questionnaire at the research group's web page. The questionnaire engine collected the responses and entered them into the database without the need of researchers' supervision. The invitation to participate in the survey was distributed by means of personal e-mails. The target audience was the staff from ten universities and colleges. The email addresses were obtained from their institution's web pages. At first the researchers used the mailing lists of three faculties to distribute the invitation, but since the reply rate proved to be low, personal invitations were used for the rest and larger part of the target group.

2.3. Assessment of the data

The questionnaire consists of 34 items that can be divided into 9 groups, either predictive or response variables (Fig. 7). Some items such as the return date and the computer IP address were recorded automatically without the input from the responder. The return date data is mostly useful to analyze the distribution of returns in time in order to better select the invitation delivery date in the future studies. For example an invitation e-mail received at the Friday evening

is unlikely to draw immediate attention by the receiver. On Monday, when a majority of the office staff returns to their work, they may pay less attention to the letters received few days ago than the letters received when they work at the computer.

In the data analysis the predictive variable are compared against the predictive variables. Respondents are divided into six groups by combining different lighting scenarios. The distribution factors for natural lighting are: 1) rich natural lighting without glare, 2) rich natural lighting with glare, 3) poor natural lighting. It is important to account for the occurrence of glare since it may turn naturally well lit workplaces into stressful workplaces. The distribution factors for indoor lighting are: 1) Sufficient indoor lighting and 2) poor indoor lighting.
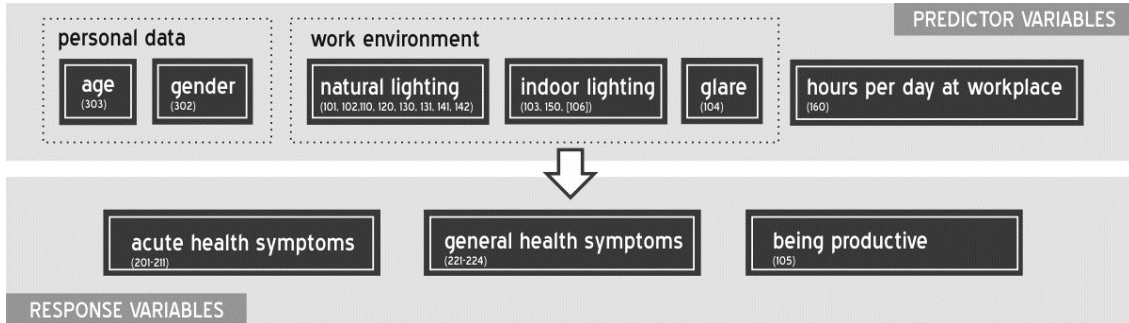
Fig.7. Questionnaire items as dived into predictor and response variables

3. Results

A total of 518 respondents participated in the survey. Based on the gender, the replies distribute to 29 per cent from males and 71 per cent from females. The respondents divide into age groups as follows:
- below 26 yrs - 5 per cent;
- 26 to 35 yrs – 25 per cent;
- 36 to 45 yrs – 24 per cent,
- 46 to 55 yrs – 24 per cent;
- 56 to 65 yrs –17 per cent;
- 66 to 75 yrs – 5 per cent;
- above 75 yrs – 0.2 per cent.

Based on the criteria set by the authors, described in the latter chapter, the sample was distributed into six groups (table 2). The groups were formed by determining the following indicators:
1. who gave high scores (5 or 4) to natural daylight conditions at their workplaces (item 102), altogether 57 per cent of the sample;
2. who reported suffering from glare (score 5 or 4 at item 104), altogether 26 per cent of the sample;
3. who reported being satisfied with current indoor lighting (average of items 103 and inverse-106 with a score more than 3.5), altogether 53 per cent of the sample. Scores are based on Likert's 5-point scales.

Table 2.

Dividing the sample into groups based on lighting conditions and the group's percentage from the total sample

The respondent's workplace...	has rich natural lighting without glare	has rich natural lighting with glare	has poor natural lighting
has adequate indoor lighting	Group 6 – 22%	Group 4 – 18%	Group 2 – 13%
has inadequate indoor lighting	Group 5 – 6%	Group 3 – 10%	Group 1 – 30%

Analyzing the results, the groups with adequate indoor lighting (2, 4, 6) clearly differentiate from the groups with inadequate indoor lighting (1, 3, 5). Groups 6 and 4 reported least number of adverse health symptoms (accordingly 1.7 and 1.4 symptoms in average for a person in the group), whereas groups 1 and 3 reported most of the symptoms (3.8 and 3.7 accordingly). Groups 2 and 5 were not far from the best, having 1.9 and 2.2 symptoms in average per person in that group. This shows that the more lighting the worker has in his/her workplace, the less symptoms he/she has to report with the emphasize on indoor lighting quality. The results from the groups 5 and 2 would suggest, that in case of one of the lighting sources is inadequate (natural or indoor lighting) the situation is not so bad as long as another source is abundant.

The most reported health symptoms by groups 1 and 3 were the same, with only the first group having somewhat increased occurrence. The most complained symptoms were 1) the fatigue and 2) tired or painful eyes, with accordingly 57 and 60 percent in group 1 and 57 and 57 per cent in group 3 reporting these items. Also people in group 1 marked those as most occurring symptoms: 31 and 21 per cent accordingly. Other symptoms in group 1 were reported

only by 7.9 per cent (median) indicating that fatigue and tired/painful eyes are common symptoms that seem to be caused by a variety of reasons, but with poor lighting conditions only intensifying them.

On another hand, groups 1 and 3 reported many other symptoms, not so common amongst group 6. The occurrences of these symptoms in group 1 was as follows: dizziness – 38, dry eyes – 36, difficulty in concentrating – 33, stress or depression – 25, headache – 21, bad moods – 19, insomnia – 19, anxiety – 18, watery eyes – 17, being restless and emotional – 17 and skin irritation or pain – 13 per cent of the group. In average people from group 1 were reporting these symptoms 2.8 times more than those in group 6, with the gap being widest within those reporting the anxiety and bad moods.

Likewise, people in group 1 and 3 were more likely to complain about not feeling productive than in the rest of the groups. The highest reported productivity was revealed amongst group 6 (95 percent of the sample) and group 4 (79 per cent). The lowest scores in groups 1 (37 percent) and group 3 (44 per cent). For an overview of the results see Fig. 8.
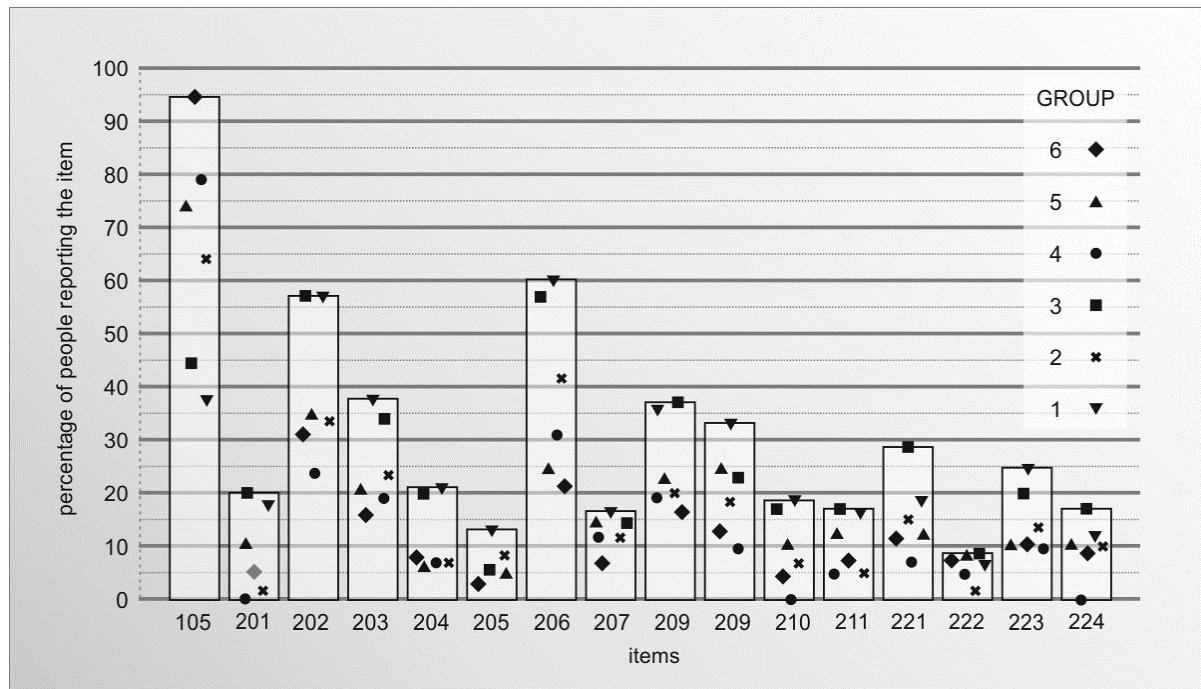
Fig. 8. Percentage of people per group reporting health symptoms or other issues (items). For item code see the appendix.

In general, women were more to report health symptoms than men. Female respondents reported 3 health symptoms in average, whereas men only 1.7. The gap is insignificant in regard to productivity, as 65 percent of the women reported being productive, whereas 71 per cent of men.

An unexpected relationship revealed itself when analysing the data based on the age group. An inverse negative correlation occurs between the age and the number of reported health symptoms. Whereas the youngest age group (those in the age of up to 25 years) reported 3.6 health symptoms in average per person and only 54 per cent from the group felt being productive, the people in the group 66-75 yrs only reported 1.3 health symptoms and 78 per cent of them felt themselves being productive.

Analysing the sample based on the time the person spends at his/her workplace revealed that people with longer working hours tend to report more acute health symptoms. Still, the relationship was not linear, but the sample can be divided into two groups: persons working at the office 1 to 5 hours per day tend report 2.2 acute health symptoms in average. After the fifth hour, the amount of symptoms increases abruptly to 2.5 and stays basically the same for lengths of 6, 7 and more hours.

As explained in the method chapter, the researchers believed that offering the respondent with an option to write down his/her email address, would help to stimulate the participation. Indeed, about 24 per cent of the respondents did discard their anonymity and registered their emails. About 21 per cent of the respondents also felt it necessary to fill out the notes section at the end of the questionnaire, describing their work conditions in more detail or expressing their concern in regard to the lighting conditions. This indicates that a large portion of the respondents indeed consider the lighting conditions relevant issue.

3.1. Limitations and future research

The conclusions are based on the results derived from the self-reported data. Whether the lighting conditions are adequate or not, they are likely not to be equally weighted by all the respondents. Respondents complained also

about other environmental issues that they believed having an effect on their health. The questionnaire need further developing, in order to better accommodate different environmental scenarios reported by the respondents. Also, inquiring about personal health characteristics, such as chronic illnesses, may help to reduce the biased in the input. The future research should also consider incorporating on-site measurements to accompany the self-reported data.

4. Conclusions and discussion

The results indicated that groups 1 and 3 reported clearly more adverse effects than others. Some indicators of group 5 would also suggest a slightly elevated risk score but average health indicators show no remarkable difference from other groups. As seen from table 2, groups 1, 3 and 5 have all been categorized under inadequate indoor lighting section. Only at group 5 the inadequate indoor lighting seems to be relieved by sufficient natural lighting conditions. Therefore, proper accessibility to natural daylight indeed eases the stress from inadequate indoor lighting. The results are even more remarkable since the test was conducted amongst the office workers residing in the northern latitudes (around 58-59 degrees North) where availability of natural daylight is limited during the winter times and SAD is common.

From the results one would expect daylight to have a role in the development of various health implications. But analyzing the indices from groups with adequate indoor lighting (2, 4, and 6) there is little difference to see. This suggests as far as indoor lighting system provides the workers with proper illumination, natural (outside) lighting has a secondary role. Although, in regard to some specific health symptoms, the exceptions do apply: in group 2 people reported up to about twice as more problems with 1) decreased ability to concentrate and 2) tired or painful eyes, than in groups 4 and 6. This indicates that more daylight has at least a psychological effect but possibly other links discussed in the first chapter may also have been confirmed. Contrary to most widely used fluorescent light bulbs with a spiky spectrum, the daylight is a continuous spectrum that will supply the human vision with full range of wavelengths of a visible light. This may explain why people under sufficient daylight conditions reported less suffering from vision related health symptoms than those mainly exposed to indoor lighting.

The relevance of lighting becomes more evident when analyzing the indicator for productivity. Again, the main contributor to the productivity seems to be adequate indoor lighting, but combined with proper daylight conditions, the score is topped. Lack of both proper indoor and outdoor (natural) lighting makes people to feel less productive. One must note that compared to the reported health symptoms, the productivity item is more subjective and therefore may not provide us with actual levels of respondents' productivity.

Group 4 (people having sufficient daylight, but with occurrence of glare) showed several anomalies not present to other groups. Although the glare is known to produce visual discomfort, this group had no one reporting problems (score 4 or 5) with 1) bad mood, 2) anxiety or 3) skin irritation or pain. Comparing these items to the group 1 (with least exposure both to the natural and indoor lighting), 19, 18 and 13 per cent of the group reported these symptoms accordingly. These anomalies may have been caused by the small sample size (N=43) but need to be investigated by future studies with larger sample size.

As the study only dealt with the lighting conditions, there are several other environmental factors that may have induced the reported health symptoms. For example a stress might be initiated by the situations in the social environment. Also there remains uncertainty in regard to the subjective nature of the reported data. One of the aims of the authors was to find out, if self-reported data can be used to assess the lighting conditions of workplaces without having instrumental measurements results. Present results have shown clear differences in between the groups exposed to different lighting conditions. Peculiarities from natural daylight and indoor lighting have been identified. The people with better lighting conditions have reported themselves to be more productive and suffer from less health symptoms.

5. The questionnaire

Next, the authors present the full questionnaire, in order for the reader to interpret the items codes as presented earlier in this article.

The questionnaire "Do you have sufficient amount of natural daylight in your workplace?"

<u>Part 1: Workplace and lighting</u>

100 Please describe the room you are working in.

		1(0) not at all	2 a little bit	3 mode-rately	4 quite a bit	5 a great deal
101	For what extent the Sun can light the room you are working at?	1	2	3	4	5
102	Do you feel that a sufficient amount of natural daylight is reaching your workplace?	1	2	3	4	5
103	Do you feel that your workplace is lit sufficiently by the indoor lighting?	1	2	3	4	5

104	Does bright light (glare) obstruct you at your work?	1	2	3	4	5
105	Do you feel productive and creative at that workroom?	1	2	3	4	5
106	Do you see it necessary to improve the lighting conditions at your workplace?	1	2	3	4	5

110	From your workplace, how far is the nearest window?	0-1m	1-2m	3-4m	4-7m	7-10m	over 10m	no windows

120	Towards which point of the compass are the windows positioned?	to North	to East	to South	to West	don't know

130	What object is blocking the Sun from shining into your workroom?	the windows face the inner courtyard	another building	the trees	other object	nothing specifically

131	If sunlight is blocked by your or another building, how far is the opposite wall from you window?	up to 20m	21-40m	over 40m	nothing specifically

The building

141	At which floor is your workroom located?	1	2	3	4	5+
142	How many full floors are there in the building?	1	2	3	4	5+

150	What is the type of the main ceiling lighting?	fluorescent or CFL	other gas mixture	incandescent (inc halogen)	LED	other/don't know

160 In average, how many hours do you spend at your workplace?
Choose one of the following answers?

up to 2h	2-3h	3-4h	4-5h	5-6h	6-7h	7-8h	8-9h	9-10h	over 10h

Part 2: Workplace and well-being

200 At your workplace (or after work) how much do you suffer from the following symptoms?

		1(0) not at all	2 a little bit	3 mode-rately	4 quite a bit	5 a great deal
201	anxiety	1	2	3	4	5
202	fatigue	1	2	3	4	5
203	dizziness	1	2	3	4	5
204	headache	1	2	3	4	5
205	skin irritation or pain	1	2	3	4	5
206	eyes tired or painful	1	2	3	4	5
207	watery eyes	1	2	3	4	5
208	dry eyes	1	2	3	4	5
209	difficulty in concentrating	1	2	3	4	5
210	bad moods	1	2	3	4	5
211	restless and emotional	1	2	3	4	5

220 In general, how much do you suffer from the following symptoms?

		1(0) not at all	2 a little bit	3 mode-rately	4 quite a bit	5 a great deal
221	insomnia	1	2	3	4	5
222	frequently ill	1	2	3	4	5
223	stress or depression	1	2	3	4	5
224	cardiovascular problems	1	2	3	4	5

Part 3. About you

301 In which department's , institution's building is your workroom? (optional)

302 Gender

Female	Male

303 Age (yrs)

If you'd like to get feedback, please leave us your e-mail. Your data is considered confidential and will not be given to anyone outside the research group.

304	E-mail (optional)	

305 Your comments here (optional)

References

1. **Koppel, T.** Assessment of the quality of lighting systems based on the star diagram model; Proceedings of the ITELMS'2012: 7th International Conference Intelligent Technologies in Logistics and Mechatronics Systems. Kaunas Technical University, by the journal "Mechanika": Kaunas Technology University, 2012.
2. **Koppel, T.** Dynamic lighting system for workplaces at northern latitudes, (2012). Scientific Journal of Riga Technical University, 5. series., Tehnogēnās vides drošība. - 3. vol, pp 39-44, 2012.
3. **Seitz, A.R., Nanez, J.E. Sr., Holloway, S.R., Watanabe, T.,** Perceptual learning of motion leads to faster flicker perception. PLoS One, 1:e28, 2006**.**
4. **Hughes, JR**, The photoparoxysmal response: the probable cause of attacks during video games, Clin EEG Neuroscience, 39(1):1-7, 2008.
5. **Harding, G., Wilkins AJ, Erba G, Barkley G.L, Fisher R.S.,** Epilepsy Foundation of America Working Group, Photic- and pattern-induced seizures: expert consensus of the Epilepsy Foundation of America working Group, Epilepsia, Sep 46(9):1423-1425, 2005.
6. **Shepherd, A.J.,** Visual contrast processing in migraine, Cephalalgia, 20(10):865-80, 2000.
7. **Wilkins, AJ, Wilkinson P., A** tint to reduce eye-strain from fluorescent lighting? Preliminary observations. Ophthalmic Physiol Opt, 11(2):172-5, 1991.
8. **Main, A., Vlachonikolis I, Dowson A**., The wavelength of light causing photophobia in migraine and tension-type headache between attacks, Headache, 40(3):194-9, 2000.
9. **Stellman, JM.**, Encyclopedia of occupational health and safety, International Labour Office, Volume 1, 1998.
10. **Aries, M.** Human Lighting Demands - Healthy Lighting in an Office Environment, Eindhoven: Technische Universiteit Eindhoven, 2005.
11. **Holick, M.F., Jenkins, M.** The UV Advantage: new medical breakthroughs reveal powerful health benefits from sun exposure and tanning", 2nd ed, ibooks, New York, 2009.
12. **Even, C., Schröder, C., Friedman, S., Friedman, S., Rouillon, F.** Efficacy of light therapy in nonseasonal depression:A systematic review, Journal of Affective Disorders 108, 11–23, 2008.
13. **Rot, M., Moskowitz, D.S., Young, S.N.** Exposure to bright light is associated with positive social interaction and good mood over short periods: A naturalistic study in mildly seasonal people, Journal of Psychiatric Research, 42, 311-319, 2008.
14. **Smolders K.C.H.J., de Kort Y.A.W., Cluitmans, P.J.M.** A higher illuminance induces alertness even during office hours: Findings on subjective measures, task performance and heart rate measures, Physiology & Behavior 107, 7–16, 2012.
15. **Stephenson, K.M., Schroder, C.M., Bertschy, G., Bourgin, P.** Complex interaction of circadian and non-circadian effects of light on mood: Shedding new light on an old story, Sleep Medicine Reviews 16, 445-454, 2012.
16. **Deguchi, T., Sato, M.,** The effect of color temperature of lighting sources on mental activity level, The Annals of physiological anthropology, 11(1), 37–43, 1992.
17. **Philips**, Activa Club, http://www.lighting.philips.com/glen/activiva, 25.04.2011.

18. **Figueiro, M., Bullough, J., Parsons, R., Rea, M.,** Preliminary evidence for spectral opponency in the suppression of melatonin by light in humans, Neuroreport, Volume 15 - Issue 2, 9 February 2004.America Working Group, Epilepsia, 46(9):1423-5, 2005.

19. **Van Bommel, W.J.M**. Non-visual biological effect of lighting and the practical meaning for lighting your work", Applied Ergonomics, 37 (2006), 461-466.

20. **Bellia, L., Bisegna, F., Spada, G.** Lighting in indoor environments: Visual and non-visual effects of light sources with different spectral power distributions, Building and Environment, 46, 2011.

21. **Daurat, A., Aguirre, A., Foret, J., Gonnet, P., Keromes, A., Benoit, O**. Bright light affects alertness and performance rhythms during a 24-h constant routine, Physiology and Behavior, 1993;53:929-36.

22. **Hwang, T. and Kim, J.T.** Effects of Indoor Lighting on Occupants' Visual Comfort and Eye Health in a Green Building, Indoor and Built Environment, 20:75, 2011.

23. **Newsham, G.R.; Brand, J.; Donnelly, C.L.; Veitch, J.A.; Aries, M.; Charles, K.E.** Linking indoor environment conditions to organizational productivity: a field study. Building Research & Information, 37, (2), pp. 129-147, 2009.

Influence of Power Steering System on Directional Stability of Articulated Wheel Loader

M. J. Łopatka

Military University of Technology, Kaliskiego Street 2, 00-908, Warsaw, Poland, E-mail: mlopatka@wat.edu.pl

Abstract

An analysis over new support vehicles for engineer corps conducted at the Military University of Technology has shown that articulated wheel tool-carriers are characterized by gigantic working possibilities and comparatively low operating costs. The low drive speeds are the main restrictive factor of their utilization for realization of military tasks. However, increasing their drive speeds is limited by the phenomenon of snaking - the lack of direction stability during straight ride. The identification of causes of the aforementioned phenomenon and a possibility of its limitation was the main aim of this research. It was conducted on articulated wheel loader weighing about 19.5 t. This vehicle was equipped with 2 types of serial arrangements of steering systems as well as with 2 research arrangements of steering systems with different gains. The conducted tests have shown that a 3-time reduction of the deviations of the vehicle drive track by suitable modernization of the steering system is possible. Moreover, spectral analyses affirmed that an increase in the snaking phenomenon according to the drive speed results from limited perceptive possibilities of the operator, who fulfils in this arrangement the role of a controller.
KEY WORDS: *articulated vehicle, directional stability, power steering systems, experimental study.*

1. Introduction

Articulated wheel tractors are used as base machines for loaders and tool carriers and possess many unique features which permit effective realization of earth carrying and hauling works constantly pushing out tracked tractors. The most significant features are:

1. the high maneuverability – the wheeled tractors with the Ackerman's arrangement of a steering system have to have about 20% shorter wheelbase to obtain similar maneuverability;
4. the better loading of equipment – during turn the equipment is always in front position (perpendicular to the direction of motion);
5. the high lifting capacity – owing to indispensable capacity of the front axis practically all wheeled loaders with weight above 8 t and lifting capacity 3 t possess an articulated construction;
6. the high working speed – the maximum speed of tracked tractors usually does not exceed 10 km/h, whereas the wheel tractors move at a speed of up to 30 km/h and even faster;
7. the high traction pulls and efficiency of work impossible to achieve with the attachments assembled on trucks – the weight of the vehicles does not exceed the road limitation (built with typical components can come to over 20 t);
8. the high cross country mobility – because of the big size of tires even with the weight of up to 20 t their ground pressures are comparable to tanks and other heavy tracked vehicles [7];
9. low running gear operation cost – it is 5-10 times lower than for high speed tracked vehicles [8];
10. the high durability and reliability with low costs of manufacturing as a result of a simplicity of construction and a serial production of components [10].

Moreover, using quick coupling permits to transform them in tool-carriers. A wide range of accessible tools and equipment allow performing many diverse tasks [9, 10].

The weakest point of articulated wheel tractors is their road mobility at high speeds, which considerably limits their wider utilization in many applications. The two phenomena responsible for this are pitching and snaking. The pitching – longitudinal swinging of the vehicles during moving over a rough surface limits the vehicle's speed to 5-10 km/h and it decreases work efficiency during carry and haul operations [3]. Increasing the efficiency of such working cycle was a challenge for construction equipment manufacturers. As a result the anti-pitching systems using transported load to dump the swing were developed and introduced – they canreduce pitching accelerations 3-times [5]. What is referred to as the snaking phenomenon is the lack of directional stability – the constant deviation of the vehicle from the chosen driving direction, which requires that the operator periodically adjust the direction of travelling [1,3,6]. The deviation from the chosen direction is caused by the minute turning angles of the vehicle frame, which are almost imperceptible to the driver and which cause the turning of the vehicle during drive. Having noticed the deviation, the operator executes the adjustment with the steering wheel, though the latter action is also encumbered with the error of the precision of the steering system as well as with that of the operator's perception. As a result, subsequent adjustments are requisite, whereas the vehicle's motion path is close to sinusoidal – hence the name of the phenomenon.

During a typical reloading cycle, which requires intense manouvering within a confined area and during which straight rides do not exceed 2-3 m, the phenomenon goes unnoticed and does not affect the efficiency of the vehicle.

In applications which require longer rides, with expected high speeds of up to 30-40 km/h, the lack of directional stability [2] is the main factor limiting the the work efficiency and the effectiveness of the vehicle utilization. The higher the speeds, the shorter the time necessary to introduce the adjustments and the bigger are the deviations from the travelling direction, which is accompanied by the widening of the necessary motion path as well as by an increased effort on the part of the operator. At higher speeds, the system's 'follow-up' feature may be lost, i.e. the operator is not capable of generating necessary adjustments and the vehicle goes off the set track.

The solution to this problem may significantly widen the scope of applications of articulated vehicles. It requires research on the limiting or eliminating the snaking phenomenon.

2. Arrangements of steering systems and requirements

Analyzing the solutions of steering systems' arrangements applied by manufacturers in articulated vehicles it is possible to divide them into two principal groups (Fig. 1):
1. hydraulic steering systems with mechanical feedback;
11. hydrostatic steering systems with hydraulic feedback.

a   b
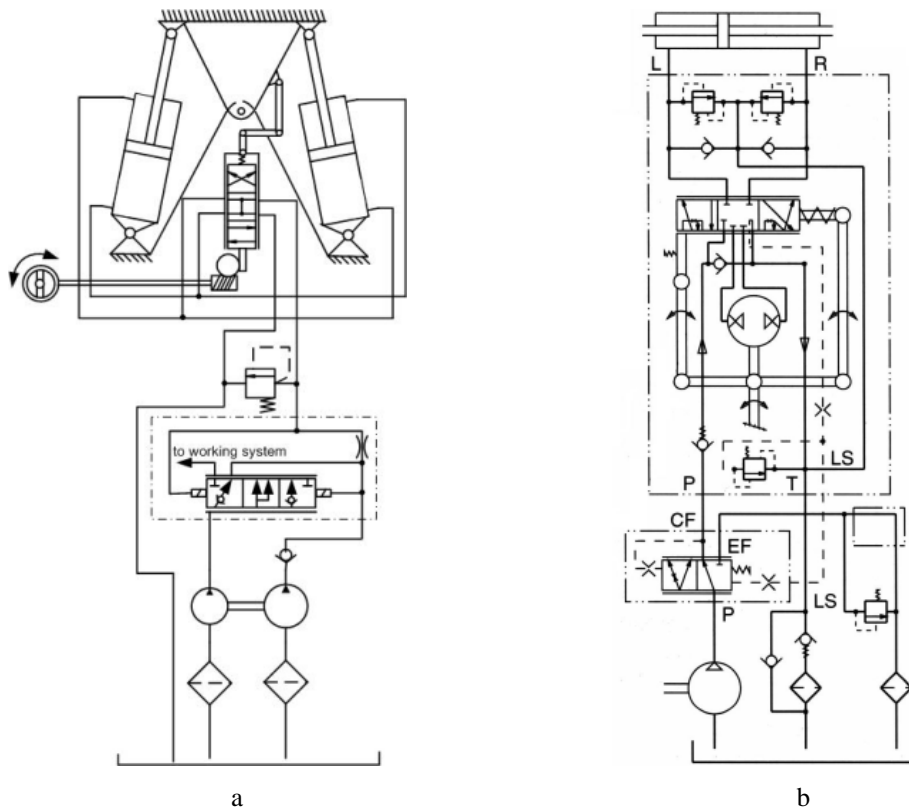
Fig.1.   Hydraulic diagrams of tested steering systems: a – hydraulic steering systems with mechanical feedback [10]; b – hydrostatic steering systems with hydraulic feedback operating in LS system with priority valve [11]

First of them is an older solution, applied in the first generation vehicles; the second solution is newer – applied at present by all manufacturers of construction machines.

Hydrostatic steering systems with hydraulic feedback replaced older solutions because they enable to obtain a higher gain. What is more, owing to Load-Sensing (LS) system and the priority valve, it was possible to eliminate the separate pump for the steering system. The increase in gain K – measured as the inverse of a number of steering wheel turns necessary for realizing the full turn – has caused the shortening of steering time and, simultaneously, the improvement of the working cycle time as well as the growth in the efficiency of the vehicle.

For the safety of the movement, arrangements of steering systems applied in articulated vehicles have to meet the requirements included in the National and ISO or SAE standards [11-13]. These requirements define, among other things, the maximum deviation Δy (dependent on the width of a vehicle) from the given track during drive at the maximum speed. Moreover, they tell that the »steering system should assure the possibility of straight drive of a vehicle at a maximum speed ... « on route » ... length at least 100 m and width 1.25 ± 0.05 of a vehicle chassis width". In road conditions these requirements can be insufficient. The investigation of the steering system arrangements has shown that the high stability of the vehicle during drive on public routes is necessary. The use of solutions which require smaller effort and lower concentration from the operator is recommended as well. For that reason, the experimental research of available steering systems was undertaken and their influence on the side drift of the vehicles was examined. Moreover, an attempt to determine basic factors responsible for the snaking phenomenon was made.

3. Experimental procedures

In order to determine the vehicle's directional stability it is necessary to determine the motion path. To estimate the operator's effort and concentration, the intensity of turning the steering wheel is required. What is more, identification of factors influencing the snaking phenomenon requires the measurement of basic parameters of the steering system. As a research object the loader SL-34 (Fig. 2) in two versions of steering system (offered by manufacturer) was used:

- Type 1 – with mechanical feedback and gain $K = 1/5.5$;
- Type 2 – with hydraulic feedback and gain $K = 1/3.2$ – operating in LS system.

a   b

Fig.2. The SL-34 loader: a – general view; b – on trial track during test

The motion path was recorded with a digital video camera. Three position markers were situated on the vehicle (Fig. 3). Two of them (A and C) were intended for marking the motion paths of the front and rear of the vehicle (both located at a distance of 2.5 m from the joint) and third (B) was fixed in the axis of the joint in order to illustrate the operator's inclination. All markers had a measuring mesh composed of white and black squares with a side length of 5 cm arranged in a "chessboard" pattern. Both the pattern and the size of the elements were chosen on the basis of earlier conducted tests – their goal was to achieve the maximum legibility and to obtain measuring accuracy dependent on the resolution of the recording system. In order to assure the necessary sharpness within the whole measuring range, the position and distance of the recording camera were carefully chosen as well. As a result, at a maximum distance between the vehicle and the camera the accuracy of the vehicle position was about $\Delta y = \pm 0.25$ cm and at the opposite end of the measuring track it was about $\Delta y = \pm 0.12$ cm.
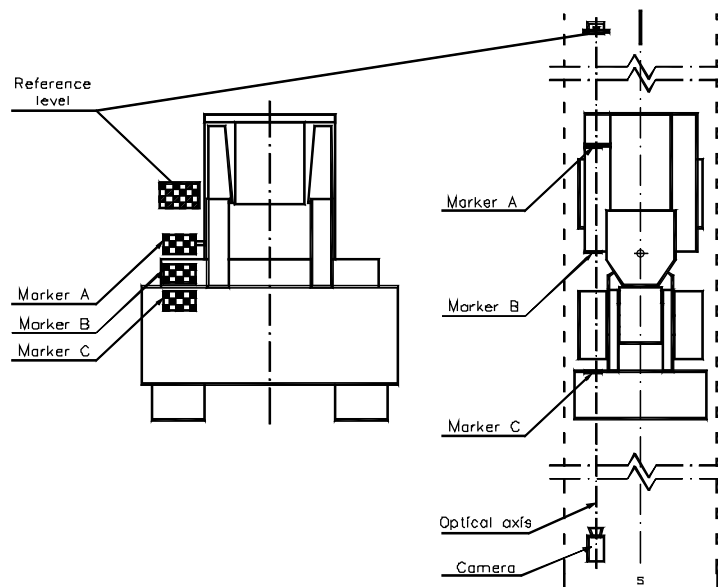
Fig. 3. Diagram of movement path measurement system

Moreover, according to the assumed guidelines, the tests also recorded:

- the change of the steering wheel turn angle $\Delta\alpha$ (with the optical sensor resolution $\pm 0.25°$);
- the change of the hydraulic cylinder length Δl (with the inductive sensors assured accuracy ± 0.25 mm);
- the pressure in the steering system (with the 4 tensometric sensors class 0.1% (0-16 MPa) – installed near the chambers of the cylinders).

All signals from the measuring sensors were acquired with a recording system which consisted of a DaqBook 100 measuring card, a computer and Snap-Master software. Records had a digital character and were sampled with 50 Hz frequency.

4. Findings and discussion

The analysis of the registered courses of movement paths obtained with a video recording method (Fig. 4) showed that the rear part of the vehicle, compared to the front part, had about 30% larger values of maximum side deviations. It mainly resulted from lower stiffness of the rear axis tires working with almost 2-times lower inflation pressure than the front ones. The character of the recorded courses is completely consistent. What is more, it should be noted that the deviation sensed by the operator (marker B) is delayed about 0.5 s in comparison with the movement of the front of the vehicle (marker C).
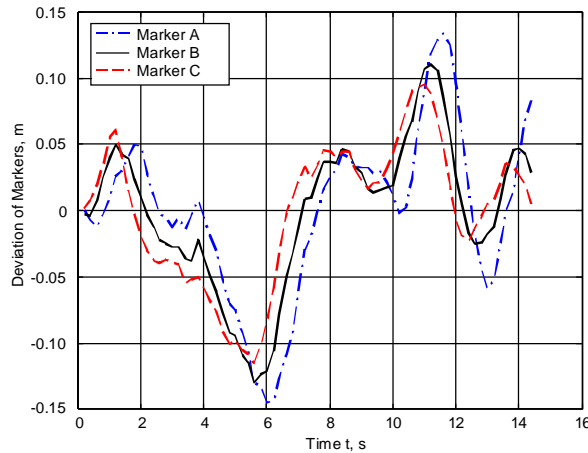
Fig. 4. Recorded movement paths of markers – steering system type 1, speed 36 km/h

The dislocation of the operator's seat from the current position in the centre to the front of the vehicle can be essential to accelerate the operator's reactions and to improve the motion stability of an articulated vehicle.

The main purpose of the experiment was to determine the influence of the applied steering system solution on the snaking phenomenon. According to the requirements [12, 13], the research should be conducted at a speed close to the maximum speed developed by the vehicle. That is why the measured road speed of the loader was kept at the level of 35-36 km/h during the tests. The recorded courses had an oscillatory character, which is shown in Fig. 5.

a

b
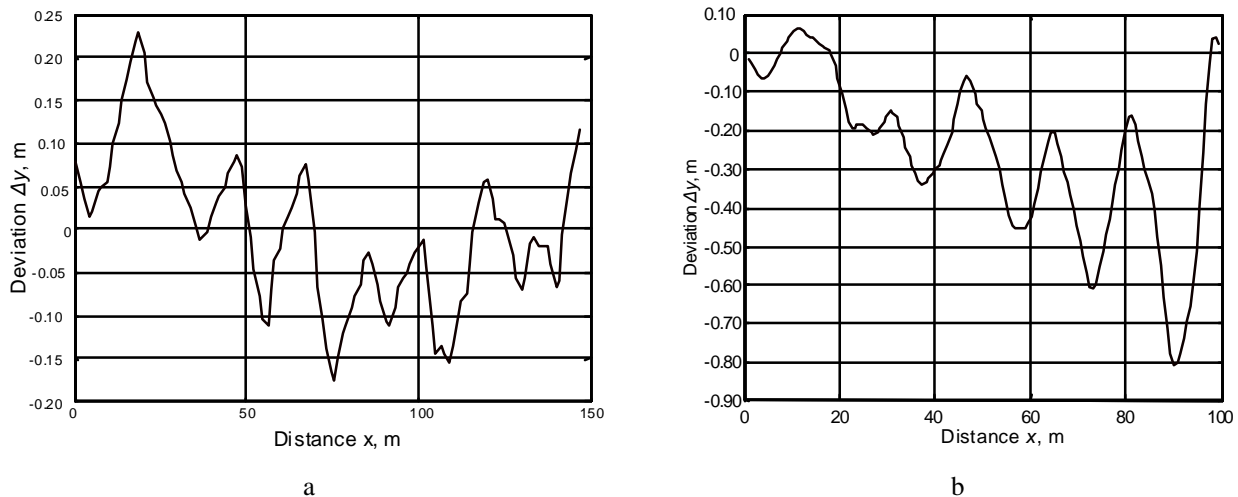
Fig. 5.   The chosen courses of lateral driver deviation at the speed of 36 km/h: a – arrangement with mechanical feedback; b – arrangement with LS system

One should pay attention to the fact that in the arrangement with the LS system the snaking phenomenon is more intensive and when the vehicle is operated by a less experienced driver the deviations can grow so significantly that the loader can lose its stability of movement (Fig. 5b). In order to find the reason of such a situation and compare the work efficiency of the studied steering system arrangements, the time delay between the signal from the sensor of hydraulic steering cylinder length Δl and the signal from the sensor of the steering wheel turn angle $\Delta\alpha$ was applied.
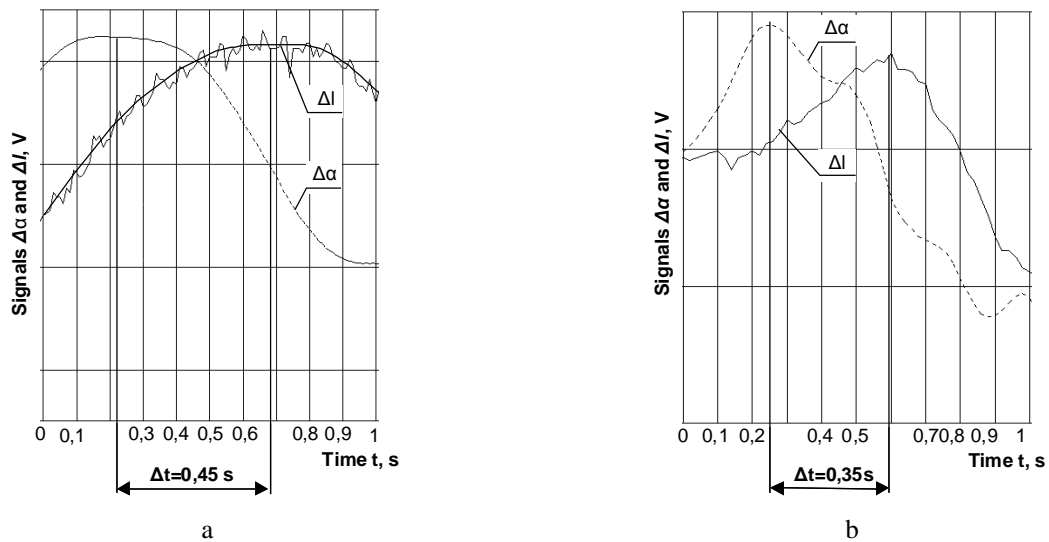
Fig. 6. Signal time delay in steering systems: a – with mechanical feedback; b – with hydraulic feedback and LS system

The obtained results (Fig. 6) showed that in the standard arrangement the time delay equals $\Delta t = 0.45$ s and it is higher than in the arrangement with the LS system, in the case of which the delay is kept at the level of $\Delta t = 0.35$ s.

One should pay attention to the fact that although in the arrangement with the LS system the signal time delay is decreased, the snaking phenomenon is more intensive. It is possible that it results from a considerably larger gain of the steering system, improving maneuverability and raising work efficiency during typical tasks, as well as from lowering the number of turns of the steering wheel necessary for the realization of a working cycle, which decreases the operator's effort.

The growth in the steering system gain as well as the growth in the signal delay is the main cause of the snaking phenomenon increasing. However, its scale depends strongly on the operator's skills and predisposition.
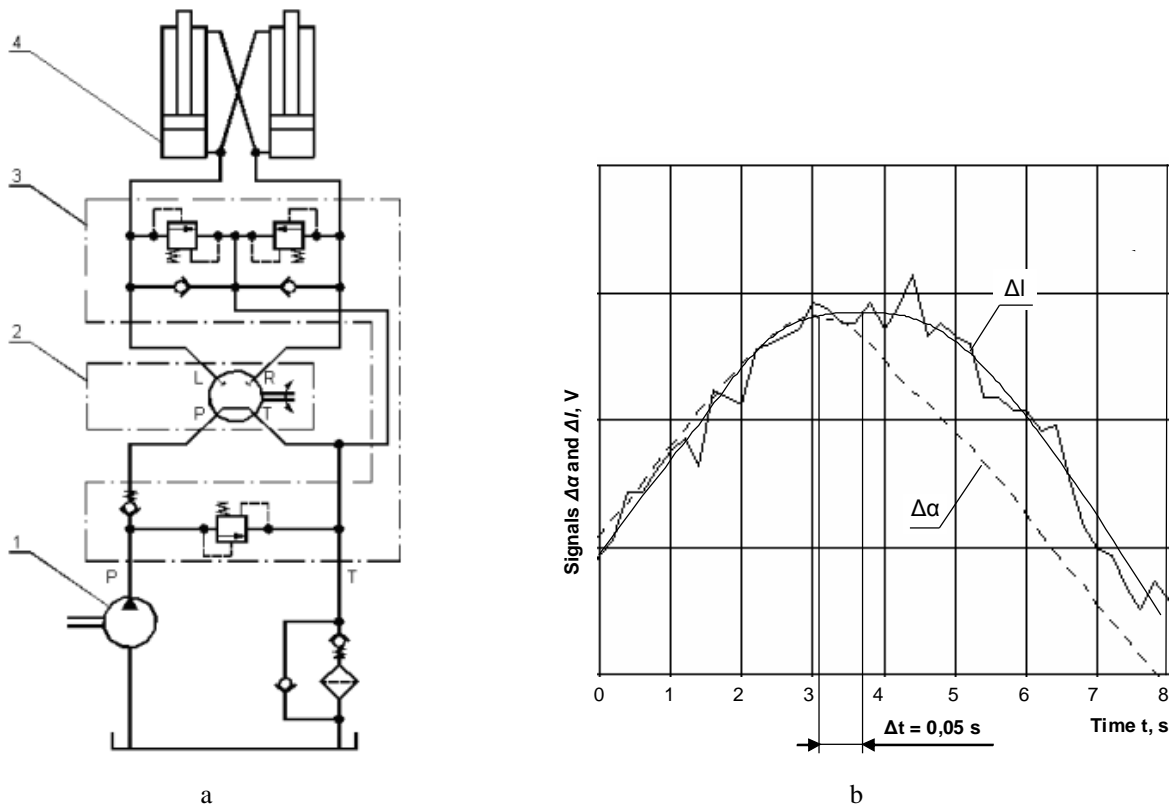
Fig. 7. Developed steering system – direct, working with hydraulic feedback and gain $K = 1/6.5$: a – diagram; b – signal time delay

In order to recognize the possibility of limiting the snaking phenomenon by decreasing the gain and signal time delays, two steering systems were designed (Fig. 7a):

- Type 3 – direct, working with hydraulic feedback and gain $K = 1/6.5$;
- Type 4 – direct, working with hydraulic feedback and gain $K = 1/16.2$.

As a result of the LS system elimination the transmission time and signal time delay in designed steering systems were shortened to $\Delta t = 0.05$ s, which is shown in Fig. 7b. Although, the signal time delay in the steering system was significantly decreased (Table 1) and the snaking phenomenon was limited to a considerably lesser extent.

Table 1

Comparison of work efficiency for selected hydraulic
steering systems of SL-34 articulated loader at speed of 36 km/h

a) Gain					b) Signal time delay in steering system			
Steering system					Steering system			
Type 1	Type 2	Type 3	Type 4		Type 1	Type 2	Type 3	Type 4
1/5.5	1/3.2	1/6.5	1/16.2		0.45 s	0.35 s	0.05 s	0.05 s
c) Average turn angle of steering wheel					d) Average change of steering cylinder length			
Steering system					Steering system			
Type 1	Type 2	Type 3	Type 4		Type 1	Type 2	Type 3	Type 4
1/5.5	1/3.2	1/6.5	1/16.2		0.45 s	0.35 s	0.05 s	0.05 s
e) Average deviation amplitude from theoretical line					f) Average period of steering wheel turns			
Steering system					Steering system			
Type 1	Type 2	Type 3	Type 4		Type 1	Type 2	Type 3	Type 4
27.4 cm	58.4 cm	18.0 cm	8.1 cm		2.60 s	2.25 s	3.25 s	4.80 s

It is caused by the fact that the smallest deviations from the theoretical track appeared in the arrangement with the smallest gain. Hence, the operator is one of the sources triggering the snaking phenomenon. Limiting the possibility of his influences by gain decrease stabilize the movement of the vehicle whereas the growth in the steering system gain leads to the loss of stability and to going off the ride track.

Assuming the value of a deviation amplitude Δy (which should not exceed 0.4 m – 25% of vehicle width) as a basic comparative parameter during research of the vehicle's movement stability, one should remember that serial arrangements of steering systems do not permit to develop safe speed above 40 km/h. Vehicles equipped with special arrangements of the steering system can be characterized by even 3-times smaller side drifts, which allows a crucial increase in the maximum achievable safe speed. However, it is advisable to use the gain limitation during drive.

5. Spectral analyses

In order to obtain a better assessment of the compared steering systems the spectral analysis for turn angle of the steering wheel $\Delta \alpha$ and deviation from the theoretical axis of movement Δy was conducted.

Fast Fourier Transform (FFT) with a zero-pole method and 6% wide Hamming window was used – specially adapted for the analysis of short period signals.
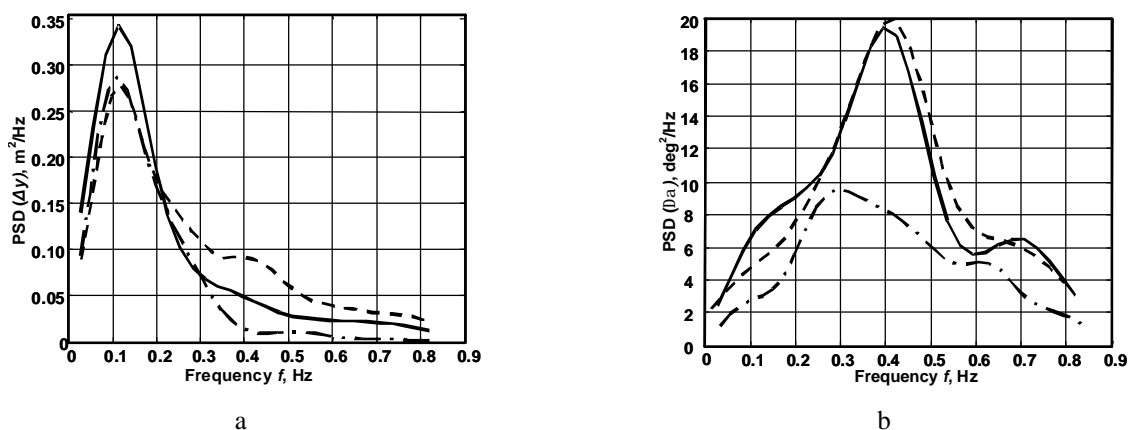
Fig. 8. The PSD of chosen courses recorded during drive of SL-34 loader at speed of 36 km/h: a – the deviation of motion path; b – the steering wheel turn angle. Where (———) denotes steering system type 1 ($K = 1/5.5$); (– – –) – steering system type 2 ($K = 1/3.2$); (– · – · –) – steering system type 3 ($K = 1/6.5$)

The acquired Power Spectrum Density (PSD) of the motion path deviation (Fig. 8a) permits to affirm that the basic frequency of yaws is situated at the level of 0.1 Hz and it is similar for all analyzed steering system solutions (it corresponds to a sinusoid wave with the length of about 100 m and the period of 10 s). Amplitudes for this frequency do

not differ significantly too. Hence, this component is not connected to the snaking phenomenon but to the operator's ability to keep straight drive direction. In arrangements with lower directional stability one can distinguish a component frequency of about 0.4 Hz (sinusoid with the period of about 2.5 s and the length of 20-25 m) but it has a considerably lower power value.

The component frequency (0.4 Hz) is clearly visible on the PSD of courses concerning the steering wheel turn angle (Fig. 8b). This is a fundamental frequency of the operator influence on the steering systems of type 1 and type 2 during moving at high speeds. Because the movement of a vehicle equipped with the steering system of type 2 was conducted at a critical speed (at the stability limit) it is probably a critical frequency of work effectiveness of the operator limited by his perception. What is more, it should be noticed that for research of the developed type 3 system the fundamental frequency of the operator's influence on the steering system is lower and is at the level of 0.3 Hz. The PSD of this frequency is definitely lower too. This testifies that in the case of vehicles equipped with serial arrangements of steering systems the high speeds of movement require more concentration and a higher effort from the operator to keep the vehicle straight on the line.

An in-depth analysis of the steering wheel turns angle PSD (Fig. 9) permits to affirm that at low speeds of the vehicle, the motion component with the aforementioned frequency of 0.1 Hz is predominant.

For higher speeds of driving which require higher concentration from the operator, the 0.4 Hz frequency appears and definitely predominates at high speeds. The character of the PSD shows that it is a resonance frequency and it is critical for the operator's perception. Moreover, it is a fundamental component of the snaking phenomenon according to figure 5 and it is generated by the operator, which is shown in Fig. 9b, 9c and 9d. The experience and skills of the driver have a considerable influence on the value of this component.
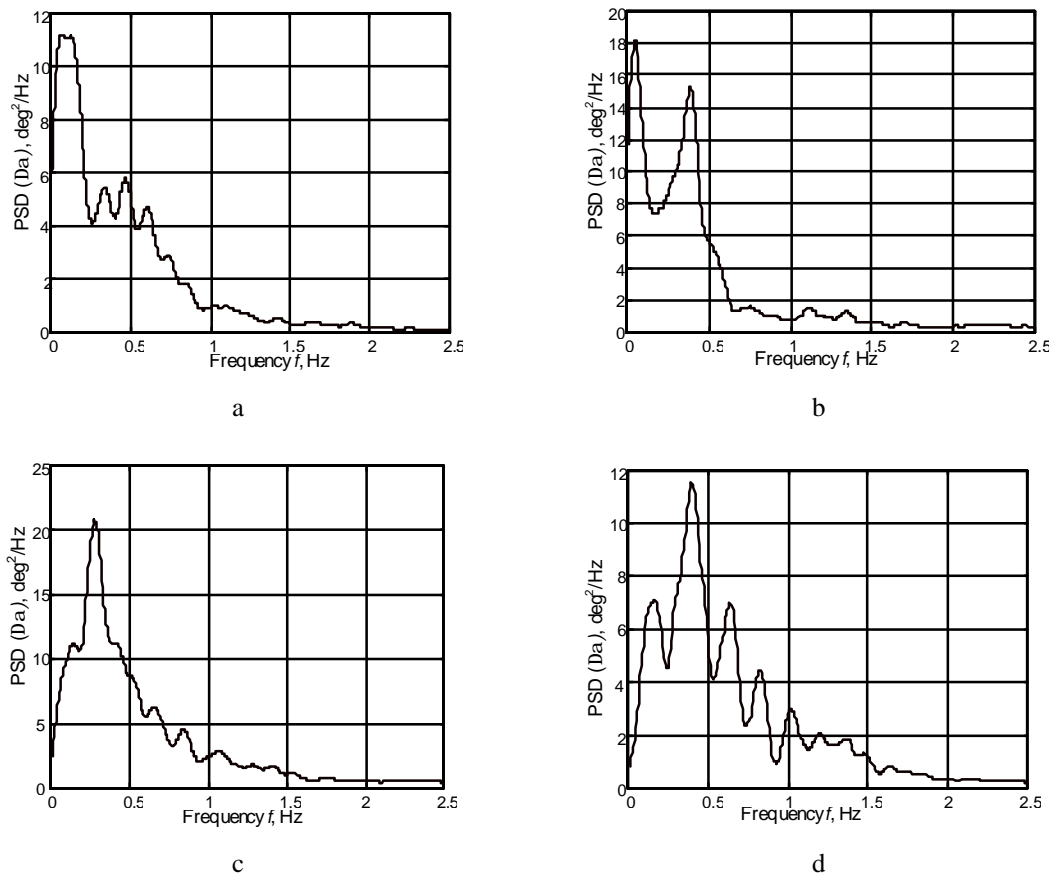
Fig. 9. PSD of steering wheel turn angle for selected drive speeds (Hamming window 3 % wide) – steering system type 3, inexperienced operator: a – $v = 6.5$ km/h; b – $v = 14$ km/h; c – $v = 20$ km/h; d – $v = 36$ km/h

The conducted analyses showed that standard arrangements of the steering system of an articulated vehicle require higher concentration and increased effort from the operator during high speed drive.

6. Conclusions

The main conclusions are:
- in articulated tractors the driver is responsible for stabilizing the steering system – however, the effects of his efforts depend a on signal time delay and gain used in an arrangement of a steering system,

- the standard arrangements of steering systems designed to achieve high operation performance in typical working cycles have a low directional stability of motion – the gain and signal time delay are too big,
- the limitation of gain and signal time delay in a steering system can reduce even 3-times the deviation and the snaking phenomenon,
- to assure high performance of operation and good stability during high speed drive it is required to use arrangements with a changing gain,
- it is necessary to apply systems with shorter time delays; this virtually eliminates the LS systems,
- it is possible to undertake works on stabilizing systems supporting the operator – however, it is necessary to better identify the causes of the snaking phenomenon.

It is possible to achieve a high speed of motion by heavy articulated tool-carriers, but it requires specially designed steering systems. Moreover, the dislocation of the operator's cabin in front of the vehicle's traveling direction is also desirable because it accelerates the reaction of the operator.

References

1. **Iida M., Fukuta M., Tomiyama H.** Measurement and analysis of side slip angle for an articulated vehicle. Engineering in Agriculture, Environment and Food, 2010, Volume 3, Issue 1.
2. **Łopatka M. J., Muszyński T., Przychodzień T.** The critical speed research of articulated wheel machinery. Mechanics and Mechanical Engineering, 2002, Volume 3, Issue 3.
3. **Rehnberg A., Drugge L.** Ride comfort simulation of a wheel loader with suspended axles. International Journal of Vehicle System Modeling and Testing, 2008, Volume 3, Issue 3.
4. **Rehnberg A., Edren J., Eriksson M., Drugge L., Trigell A. S.** Scale model investigation of the snaking and folfing stability of an articulated frame steer vehicle, International Journal of Vehicle System Modeling and Testing, 2011, Volume 6, Issue 2.
5. **Williamson C., Lee S., Ivantysynova M.** Active vibration damping for an off-road vehicle with displacement controlled actuators, International Journal of Fluid Power, 2009.
6. **Zhu Q., Liu G., Song D.** The study of dynamic characteristic of full hydraulic power steering system based on AMESim, 3-rd International Conference on Manufactuting Science and Engineering, Xiamen 2012.
7. **Łopatka M. J.** Mobility of Combat Engineer Equipment, Report, Military University of Technology, 1998 Warsaw.
8. **Łopatka M. J.** Combat Engineer Squad Support Vehicle on the MTLB chassis, Report, Military University of Technology, 2000 Warsaw.
9. **Łopatka M. J.** Light Combat Engineer Equipment for Airborne and Rapid Reaction Forces. Report, Military University of Technology, 2001 Warsaw.
10. **Łopatka M. J.** Wheeled Dozer as a Counter Obstacle and Road Maintenance Vehicle, Report, Military University of Technology, 1996 Warsaw.
11. Ognibene SPA – Form 494933, Power steering system.
12. SAE J1511/ISO 5010 Steering for off-road, rubber-tired machines, Society of Automotive Engineers 1994.
13. SAE J1790 Self-Propelled Sweepers and Scrubbers Steering Requirements Single-Circuit Hydraulic Servo-Assisted Systems, Society of Automotive Engineers 1998.
14. PN-85/M-47042 Układy kierownicze jazdy maszyn na podwoziach kołowych. Wymagania i metody badań (in Polish), Polish Organization for Standardization 1985.

Proceedings of 8th International Conference ITELMS'2013

Sustainability of Government Debt in the Baltic States

R. Mazgelis*, S. Bekesiene**

Gen. J. Žemaitis Military Academy of Lithuania, Šilo 5A, LT-10322 Vilnius, Lithuania, E-mail: rimgaudas.mazgelis@mil.lt
**Gen. J. Žemaitis Military Academy of Lithuania, Šilo 5A, LT-10322 Vilnius, Lithuania, E-mail: svajone.bekesiene@mil.lt*

Abstract

In this paper we are evaluating a government debt forecasts in Lithuanian and Latvian cases. The Maastricht criteria about government debt were used to check if these two countries are strong enough economically to adopt euro. For these investigations was used Eurostat data. Government debt was calculated by Blanchard model. Polynomial regression and seasonal adjustment was offered to estimate GDP growth, budget balance and consequently to calculate the forecast of the government debt. Additional, was shown, that Blanchard model can be applied to calculate forecast of minimal investment as percent of income in *t*-th years. The algorithm scheme for investment is presented.

KEY WORDS: *Blanchard model, polynomial regression, algorithm schema.*

1. Introduction

The fast build-up of government debt in an environment of financial instability and low growth has enlarged the need for an assessment of government debt sustainability [3]. The risks to debt sustainability need to be closely monitored in euro area countries. To assess the size of these risks, conventional debt sustainability analysis has become a core element of enhanced country surveillance. Such an analysis is, however, subject to several limitations. It depends crucially on the choice of underlying assumptions and analytical tool and its findings are subject to considerable uncertainty. Therefore is a more comprehensive approach to debt sustainability assessments, comprising a more systematic in-depth assessment of country-specific risks. This would need to include a systematic monitoring of a broad set of fiscal liabilities and private sector imbalances, replacing the current ad hoc approach to accounting for such risks. Moreover, more emphasis should be placed on accounting for fiscal and economic behavior in response to shocks. In addition, the crisis has shown that apart from addressing medium-term risks to debt sustainability, there is also a need to account for short-term refinancing risks, which tends to further strengthen the case for safety margins in public finances in normal times. To limit risks to debt sustainability in the euro area, government debt-to-GDP ratios should be brought to levels safely below 60%. In this respect, the commitment to establish within the new Treaty on Stability, Coordination and Governance in the Economic and Monetary Union a new fiscal compact comprising a "debt brake" is a welcome step towards achieving more rigorous budgetary discipline in the euro area.

However, conventional debt sustainability analysis is subject to several limitations, which means that the results need to be interpreted carefully. In fact, the outcome of debt sustainability analyses depends crucially on the choice of underlying assumptions and analytical tool and is subject to considerable uncertainty. Furthermore, particular care is needed, as debt sustainability assessments can also have a direct impact on sustainability itself: increases in government bond yields that are based on unfavorable sustainability assessments by financial markets could create a vicious circle of increasing government debt refinancing costs and furthering debt sustainability risks.

As recent developments in the euro area have shown, this negative spiral accelerates further if unfavorable debt sustainability assessments, for example by credit rating agencies, have a negative impact on banks' balance sheets. Nowadays the sustainability of the government debt is one of the important problems. It's very important for the financial markets, for the government and for the investors who purchase the debt. In a research of government debt budget balance plays an important role. Budget can be with a surplus, deficit or balanced. Budget balance – difference between revenues and spending [2]. A positive balance is called budget surplus, a negative balance – budget deficit. Euro zone countries and non euro zone countries which want to adopt euro have some restrictions about the size of government debt. Maastricht Pact and Stability and Growth Pact have determined restrictions about government finances. If a country of European Union wants to adopt euro, it has to satisfy Maastricht criteria's:

1. Inflation level of a country must not be more than 1,5% higher than the average of inflation indices in three countries of EU having the lowest level of inflation.
2. Annual budget deficit must not exceed 3% of a GDP in the end of the year.
3. The ratio of government debt to GDP must not exceed 60%.
4. Applicant country should have joined the exchange rate mechanism under the European Monetary System for two consecutive years, and should not have devalued its currency during the last two years.
5. Long term interest rates should be no more than 2% higher than the average of similar yields in three EU member states with the lowest inflation.

Countries that are not in the Euro zone every year give the information about their economy by the Maastricht (convergence) programs.

This paper deals with government debt forecasts in Lithuanian and Latvian cases to check if these two countries are strong enough economically (by the Maastricht criteria about government debt) to adopt euro [6]. Eurostat data was used [4, 5]. Blanchard model was used to calculate government debt. Polynomial regression and seasonal adjustment was offered to forecast GDP growth and budget balance and so to calculate the forecast of the government debt.

2. Mathematical model

Blanchard model was used in these investigations because of possibility to apply integral calculus for annual and quarterly data. The ground information about this model is introduced below.

$$B(t) - B(t - \Delta) = m(t)G(t)\Delta$$

where: $B(t)$ – nominal government debt at the moment t; $\mu(t)$ – budget balance as a percent of GDP; $G(t)$ – nominal GDP from moment $t - 1$ to t; Δ – time change.

If we divide the equation by the $G(t)$, we have:

$$\frac{B(t)}{G(t)} - \frac{B(t - \Delta)}{G(t)} = m(t)\Delta$$

For a small Δ we can write this equation:

$$\frac{B(t)}{G(t)} - \frac{B(t - \Delta)}{G(t - \Delta)}(1 - \Delta\frac{G'(t - \Delta)}{G(t - \Delta)}) = m(t)\Delta$$

where $G'(t - \Delta)$ is the derivative of G at the moment $t - \Delta$.

If we mark government debt as percent of GDP – $b(t)$, GDP growth – $g(t)$, after some calculations we have a differential problem:

$$b'(t) = m(t) - b(t)g(t), \quad t > 0, \quad g(0) = g_0, b(0) = b_0$$

where: b_0 – initial government debt; g_0 – initial GDP growth.

This problem has a solution:

$$b(t) = e^{-\int_0^t g(s)ds}[b_0 + \int_0^t m(x)e^{\int_0^x g(s)ds}dx]$$

This solution is used to calculate government debt. It was tested with annual and quarterly data of Eurostat and compared with government debt from statistical data and European Commission forecasts [6-8]. European Commission considers government debt sustainable if the present value of future income is greater than or equal to the current debt, it means:

$$b_0 \leq \sum_{t=1}^{\infty}(pb)_t r_t$$

where: $r_t = \frac{1 + g_t}{1 + i_t}r_{t-1}$; $r_0 = 1$; b_0 – initial debt as percent of GDP; g_t – GDP growth; i_t – interest rate on the government debt; $(pb)_t$ – primary budget balance as percent of GDP; t – time (years).

3. Results and Discussions

The same model and methods were used for calculations of both countries government debt. Government debt as a percent of GDP was calculated using Blanchard model with the integral expression form of the debt presented by Kregždė [1, 3]. The solution from above was used like as recursive expression:

$$b(t) = e^{-\int_{t-1}^t g(s)ds}[b(t - 1) + \int_{t-1}^t m(x)e^{\int_0^x g(s)ds}dx]$$

Integrals were calculated using trapezoid formula, where $g(0)$ – GDP growth in 2000-th years, $\mu(0)$ – budget balance in 2000-th years and so $b(0)$ – debt as percent of GDP in 2000-th years.

In case we have GDP growth and budget balance statistical data, we can use regression and calculate forecast of them and so using the forecasted data and integral model government debt forecast can be calculated [7]. Linear regression for annual data was not confident, because too low determination coefficient was gotten. Exponential and logarithmic regressions did not give enough determination coefficients.
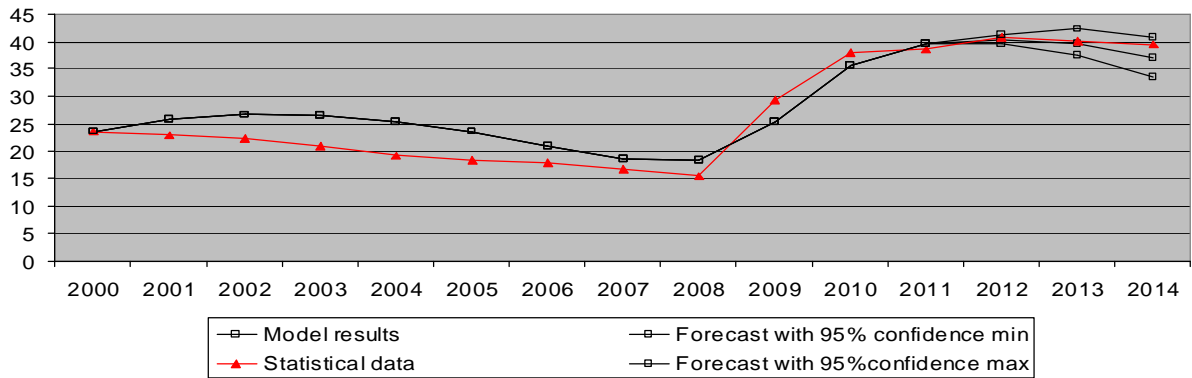
Fig.1. Government debt with forecast for Lithuanian data (annual)
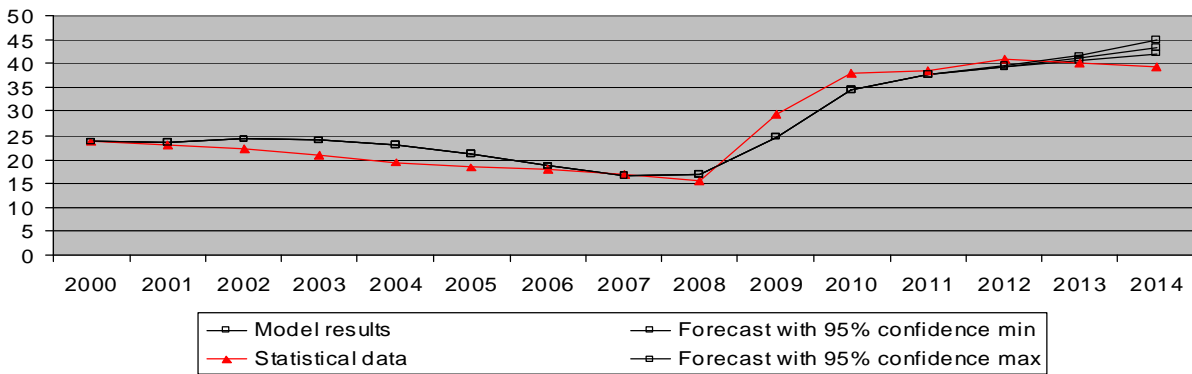
Fig.2. Government debt with forecast for Lithuanian data (quarterly)

Polynomial regression was offered to get confident results. Forecasted budget deficit for both countries – Lithuania and Latvia – was gotten over 3%, so it does not satisfy Maastricht criteria [6-8]. Having in mind that both countries' governments want to adopt euro, they should decrease their budget deficit to 3% or less, so budget balance equal to 3% was taken into calculations. Confidence intervals were calculated for forecasts using 95% confidence level. Forecasts were compared with European Commission's forecasts. European Commission's forecasts in the graphs continue statistical data curves.

Table 1

Government debt with forecast for Lithuanian data (annual)

Annual data	2000	2001	2002	2003	2004	2005	2006	2007	2008	2009	2010	2011	2012	2013	2014
Model results	23.6	25.7	26.8	26.4	25.4	23.6	21	18.6	18.2	25.3	35.7	39.6	40.4	39.8	37
Statistical data/EC forecast	23.6	23	22.2	21	19.3	18.3	17.9	16.8	15.5	29.4	38	38.5	40.7	40.1	39.4

Table 2

Government debt with forecast for Lithuanian data (quarterly)

Quarterly data	2000	2001	2002	2003	2004	2005	2006	2007	2008	2009	2010	2011	2012	2013	2014
Model results	23.6	23.4	24.3	23.9	23	21.1	18.7	16.5	16.8	24.7	34.5	37.7	39.4	41	43.3
Statistical data/EC forecast	23.6	23	22.2	21	19.3	18.3	17.9	16.8	15.5	29.4	38	38.5	40.7	40.1	39.4

More modifications are needed for quarterly data. Polynomial regression was not enough in this case. Quarterly data is seasonal. Seasonal adjustment with moving average was offered for quarterly data. Forecasts using quarterly data were calculated with 95% confidence level and compared with European Commission's annual forecasts [8]. For

Lithuania country all results are shown in the tables 1 and 2, also in the graphs Fig. 1 and 2. Government debt with forecast for Latvian data are introduced in Tables 3 and 4. All data visualization is shown in the graphs Fig. 3 and 4.
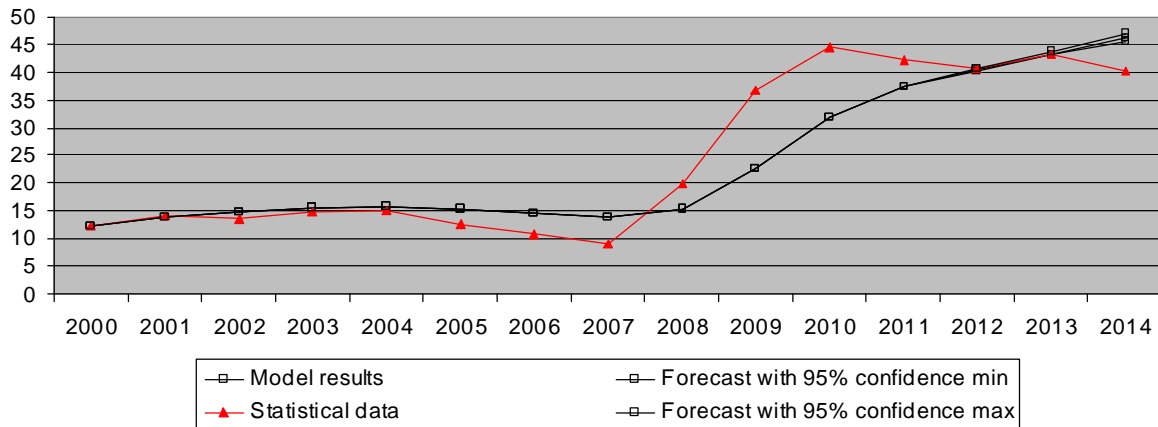
Fig.3. Government debt with forecast for Latvian data (annual)
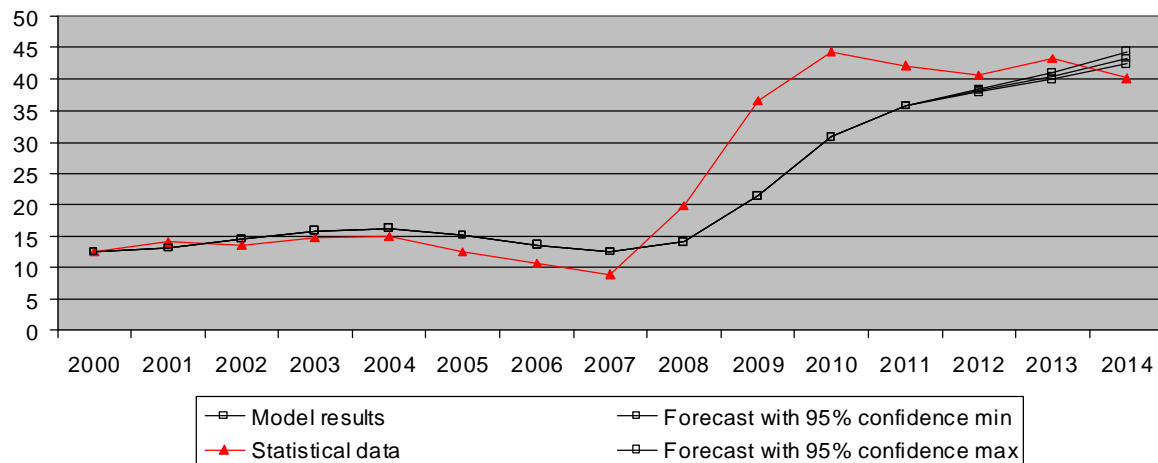
Fig.4. Government debt with forecast for Latvian data (quarterly)

Table 3

Government debt with forecast for Latvian data (annual)

Annual data	2000	2001	2002	2003	2004	2005	2006	2007	2008	2009	2010	2011	2012	2013	2014
Model results	12.4	13.7	14.8	15.7	15.9	15.3	14.5	13.7	15.3	22.5	31.9	37.5	40.5	43.3	46.2
Statistical data/EC forecast	12.4	14.1	13.6	14.7	15	12.5	10.7	9	19.8	36.7	44.5	42.2	40.7	43.2	40.1

Table 4

Government debt with forecast for Latvian data (quarterly)

Quarterly data	2000	2001	2002	2003	2004	2005	2006	2007	2008	2009	2010	2011	2012	2013	2014
Model results	12.4	13.1	14.5	15.9	16.3	15.2	13.6	12.4	14	21.5	30.7	35.8	38.2	40.5	43.4
Statistical data/EC forecast	12.4	14.1	13.6	14.7	15	12.5	10.7	9	19.8	36.7	44.5	42.2	40.7	43.2	40.1

We see that curves for both countries are not identical. If a country use privatization funds to pay for the debt, then model shows higher debt than it's given in statistical data. If the government of the country borrows funds at the end of the year to keep the budget needs for the next year satisfied, then the model shows lower debt, because then in statistical data the government debt at the end of the year is given. Also some deviation can occur because of accounting problems.

Latvian forecasts show that their government debt should not exceed 60% of GDP and so should satisfy Maastricht criteria. Additional indices of Latvia also satisfy all the other Maastricht criteria's, which means Latvia should be strong enough economically to adopt euro in 2014.

Although Lithuanian forecast of government debt satisfy Maastricht criteria, inflation level exceeds the limit and is not satisfying Maastricht criteria.

4. Model application for personal accounts

Investing isn't just for the prosperous. Almost anyone can devote at least a little money to investments, keep close tabs on it, and wind up with more money than they started with. If you have a few thousand or even a couple hundred you don't need right away, here are some suggestions on how to make the most of it. Obviously, this depends on your age and financial goals, but here are some specific recommendations you can use today.

Let's say we want to invest some money with annual (quarterly, monthly, weekly...) contributions. If we know annual income, how many we can spend for contributions and interest rates of the banks, Blanchard model with offered methods for forecasting can be applied to calculate forecast of minimal investment as percent of income in t-th years. The same differential problem is used:

$$b'(t) = m(t) - b(t)g(t) , \quad t > 0, \, g(0) = g_0, \quad b(0) = b_0$$

In this case b would be investments as percent of income, g – income growth, μ – contributions as percent of income. The algorithm scheme, which is introduced below in the Fig. 5, shows the investment steps of the process. As you can see in the Fig. 5, this algorithm is realized multiplex intellectual task solving schema for two levels developing. The first level is constructed for the self containment as process logic and analysis of consumer objectives. There are determining possibilities and prerequisites for individual investment progress. The second level of algorithm is constructed for Blanchard model with offered methods for forecasting.
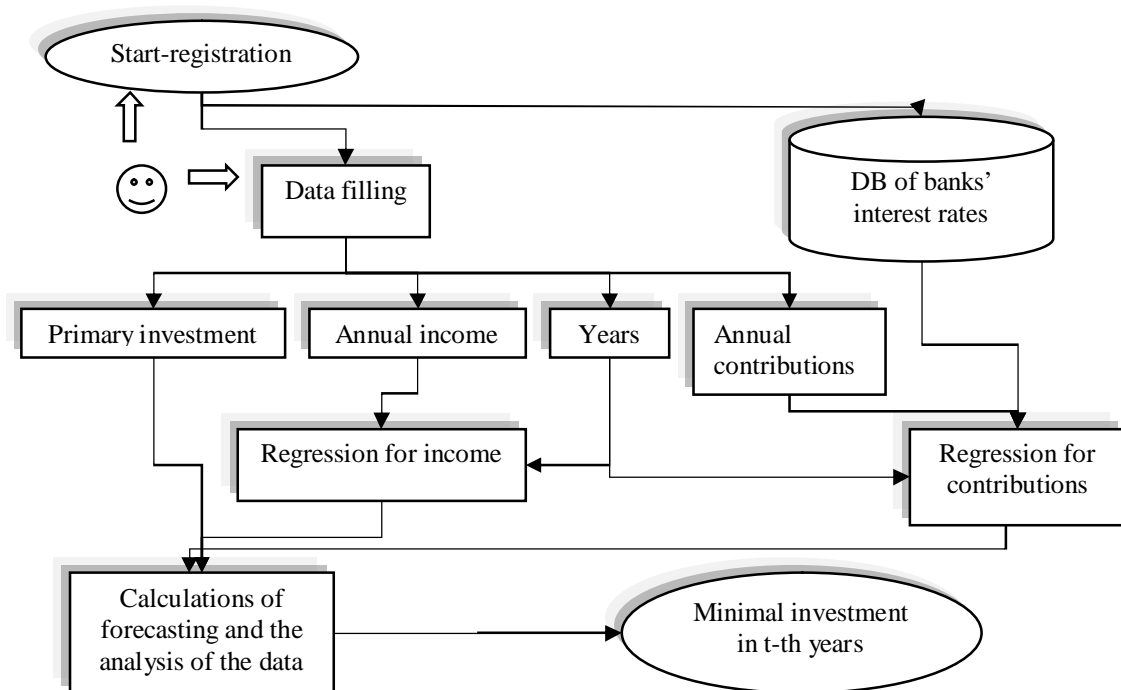
Fig.5. Government debt with forecast for Lithuanian data (quarterly)

As you can see, this algorithm is constructed in typically way [10-12]. Firstly, user must start from registration and filling the data. Also the customer can chose the primary investment size, which is then calculated as percent of income, annual (quarterly, monthly, weekly, …) income size and contributions, which are then calculated as percent of income, and also duration (in years) of investment must be filled in.

The program calculates regression for contributions using the banks' interest rates from the database, the investment duration and the contributions. Regression for income using the duration and the income is also calculated. Having the regression for income and for contributions, forecasts of them are calculated. These forecasts and primary investment size are applied for the model and the forecast of investment using the Blanchard model is calculated [2, 3]. The program as a result gives the minimal size of investment in the t-th years of investing.

5. Conclusions

Model gives confident results for government debt. One of the most important advantages of the model is that it can be calculated for any interval and any type of data – annual, quarterly, monthly or even daily if we would just have such data.

In case of privatization model shows greater level of debt than it's given in statistical data and in case of lump sum borrowings it shows lower level of government debt.

The model gives more confident results when more data is given.

Having GDP growth and budget balance data, regression can be applied to calculate forecasts of them and so forecast of government debt then can be calculated using the model. Regression is not enough for quarterly data, seasonal adjustment must be applied.

Latvia should satisfy Maastricht criteria and government debt should not exceed 60% of GDP. All another criteria are satisfied so Latvia will be strong enough economically and should adopt euro in January of 2014. Lithuania should also satisfy the criteria about the government debt, however the criteria about the inflation is not satisfied yet.

Introduction of the euro would contribute to economic stability, which is necessary for further growth: it would drastically reduce the credit interest rates for Lithuanian businesses and residents, eliminate additional currency exchange costs, simplify payments, reinforce the security of investments and decrease the economic risks for the State, thus making Lithuania much more attractive for investors.

Blanchard model can be applied not only for the government debt calculations. Blanchard model with offered methods for forecasting can be applied to calculate forecast of minimal investment as percent of income in *t*-th years.

References

1. **Kregždė A.** Sustainability of Government Debt. Lithuanian Case, 2012.
2. Lietuvos Respublikos Finansų Ministerija (2012). Valstybės skola 2011.
3. **Blanchard O.**, **Chouraqui J.C., Hagemann R.P., Sartor N.** The sustainability of fiscal policy: New answers to an old question, OECD Economic Studies No15. 1990.
4. Lietuvos Respublikos Finansų Ministerija. Biudžetas. Valstybės skolos valdymas. < http://www.finmin.lt/c/ portal/layout?p_l_id=PUB.1.52 >.
5. Europen Commission. Eurostat. Statistics Databases. < http://epp.eurostat.ec.europa.eu/portal/page/portal/ eurostat/home/ >.
6. European Commission. Eurostat. Valdžios sektoriaus finansų statistika.
7. http://epp.eurostat.ec.europa.eu/statistics_explained/index.php/Government_finance_statistics/lt
8. European Central Bank. Eurosystem. Mastricht (convergence) criteria.
9. < http://www.ecb.int/ecb/orga/escb/html/convergence-criteria.en.html >.
10. European Central Bank. Eurosystem. The size and composition of Government debt in the Euro area. Occasional paper series. No 132. October 2011. < http://www.ecb.europa.eu/pub/pdf/scpops/ecbocp132.pdf >.
11. European Commission. Main features of countries forecast. May 2013.
12. < http://ec.europa.eu/economy_finance/eu/forecasts/2013_spring_forecast_en.htm >.
13. **Smaliukienė R., Bekešienė S.** Decision Support System in Career Counseling for Retired Military Officers, ISBN 9789955258360, 2010, Kaunas: Technologija,. p. 86-90.
14. **Bekešienė S., Smaliukienė R.** Intelligent Technologies in Development of Leadership Competence, ISBN 9789955258360, 2009, Kaunas: Technologija,. p. 66-71.
15. **Bekešienė S., Kleiza V., Malovikas A.** Military Specialist Preparation Features in Nowadays Environment, ISBN 9789955258360, 2009, Kaunas: Technologija,. p. 158-163.

Alternating Current Scanning Electrochemical Microscopy for Investigation of Conducting Surfaces

I. Morkvenaite-Vilkonciene*, P. Genys**, A. Ramanavicius*, **

*Department of Physical Chemistry, Faculty of Chemistry, Vilnius University, Naugarduko str. 24, 03225 Vilnius, Lithuania
**Laboratory of Bio-Nanotechnology, Department of Materials Science and Electrical Engineering, Institute of Semiconductor Physics, State Research Institute Centre for Physical Sciences and Technology, Savanorių ave. 231 LT-02300, Vilnius, Lithuania

Abstract

Alternating Current Scanning Electrochemical microscopy (AC-SECM) allows to investigate surfaces by mean of Electrochemical Impedance spectroscopy (EIS) in the volume of solution and to create the map of electrochemical activity. For the investigation of some biological materials, immobilized on surface, the insulating substrate is usually applied, because of too strong signal from conducting surface. However, the immobilization the biological materials on gold surface is very simple, some cells can be immobilized on the gold surface without additional surface modification. For investigation of influence of such substrates to measurements, the study of conductive, non-conductive and surface in between is performed. Two surfaces were investigated – gold and quartz, when UME is positioned in different zones of surface: conductive, non-conductive and in the transition point of these two areas. Impedance was recorded in five frequencies from 10 kHz to 100 kHz, the highest electrochemical activity contrast in the highest frequency was found, which is very useful for corrosion studies, but it is determined as noise signal in the investigation of biological specimens.
KEY WORDS: *scanning electrochemical microscopy, ultramicroelectrode, constant-height mode, alternating current, electrochemical impedance spectroscopy, conductive surface, insulating surface.*

1. Introduction

Scanning Electrochemical Microscopy (SECM) is a tool for electrochemical characterization of various surfaces, e.g. conductive and non-conductive areas in comparison with Atomic Force Microscopy (AFM) [1] or corrosion studies [2]. AC-SECM combined with AFM tip modified for electrochemical measurements shows good image resolution (electrochemical activity contrast), then the scan is performed in higher frequencies [3]. Alternating current scanning electrochemical microscopy allows imaging of the surface conductivity and electrochemical activity by mean of Electrochemical Impedance Spectroscopy (EIS). AC-SECM is a sensitive tool for measuring of solid and liquid properties and complex interfacial processes such as charge transfer, adsorption/desorption phenomena or electrodeposition/dissolution [4] without any mediator. The current that flows between counter and working electrodes is a response to a small sinusoidal excitation signal with small magnitude of voltage in the desired range of frequency. The measured data are analyzed using alternating current (AC) theory. The current magnitude, the phase shift and impedance are monitored as a function of the position of the working electrode. The impedance on the conducting surface is lower than that over an insulating material, because the electrical field lines can pass though the conductor in order to shortcut the way to the counter electrode [3].

2. Experiments

Scanning Electrochemical Microscope from Sensolytics (Bochum, Germany) was used for imaging the conductivity of gold and quartz substrate in constant-height mode. Equipment consists of a typical electrochemical cell
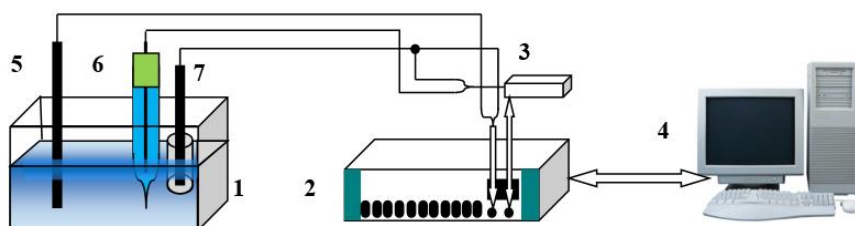
Fig. 1. The electrochemical cell and equipment connection schematic. 1 – cell, 2 – potenciostat/galvanostat, 3 – differential amplifier, 4 – computer, 5 – counter electrode, 6 – reference electrode, 7 – scanning ultramicroelectrode

(Fig. 1), connected to a potentiostat, which controls sinusoidal oscillation signal of voltage between working and reference (RE) electrodes and performs current measurement between working and counter electrodes.
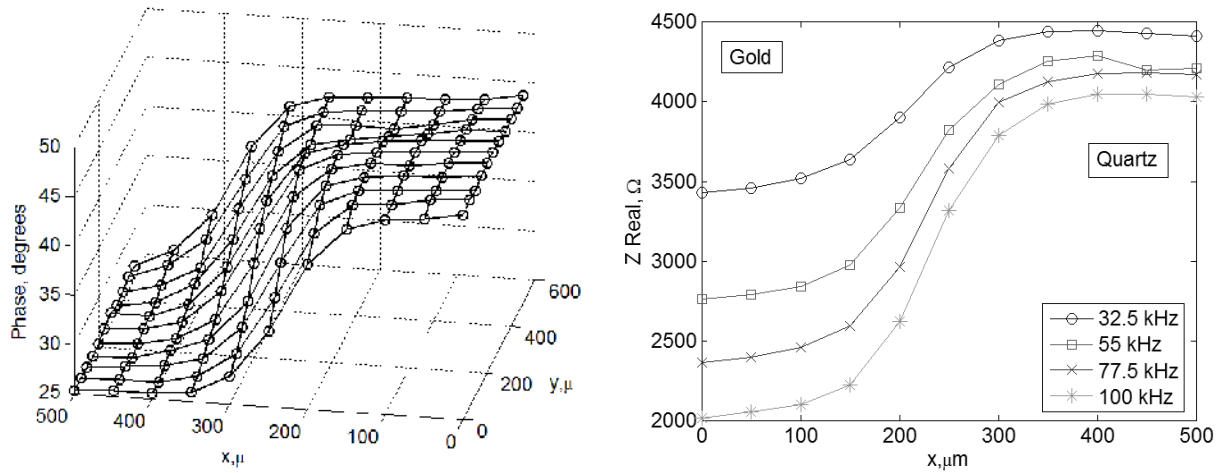
Fig. 2. Phase shift measurement of the quartz-gold substrate, was achieved in the same time as impedance measurement (left). The "o" markers show the points for impedance measurement in x-y plane. Right side: Real part of complex impedance measurement in different frequencies. The image resolution is improved at higher frequency

The WE is moved by the positioner in the 40 µm distance from gold substrate in the constant height with scanning speed of 50 µm/s in the distilled water medium. Working electrode is an ultramicroelectrode (UME) with a radius of 10 µm, fabricated from platinum wire, sealed in the borosilicate glass. The reference electrode used in this experiment is Ag/AgCl 3M KCl, the counter electrode was platinum wire. The amplitude signal was applied 10 mV RMS, measurements were performed in five frequencies from 10 kHz to 100 kHz. The 500×500 µm surface area was scanned, including quartz and gold substrates in one picture. The measured data includes impedance and phase in every chosen points of surface, as it is shown in Fig. 2, where the measured phase map is plotted. In the x-axis from 0 µm to 500 µm measurement were performed from gold to quartz. It means, that the gold surface is at the distance from 0 µm to 250 µm, and quartz surface in the picture covers the remaining part (250 µm to 500 µm). Since the lines with points in x-axis are similar, just the first line of the axis, when $y = 0$ µm, is showed in Fig. 2 right part. The x-coordinates correspond to figure 2 left part. Real part of the impedance, drawn as a function of coordinate, reveals the resolution of the scanned profile. The 100 kHz frequency provides better resolution, where the contrast between insulating and conductive areas is the highest. For the determination of electrochemical processes, occurred on different areas of conductivity, the Real and Imaginary part of impedance is compared as a function of applied frequency (Fig. 3). The Real part of impedance is the highest on quartz surface, and Imaginary part has the stronger influence on gold surface.
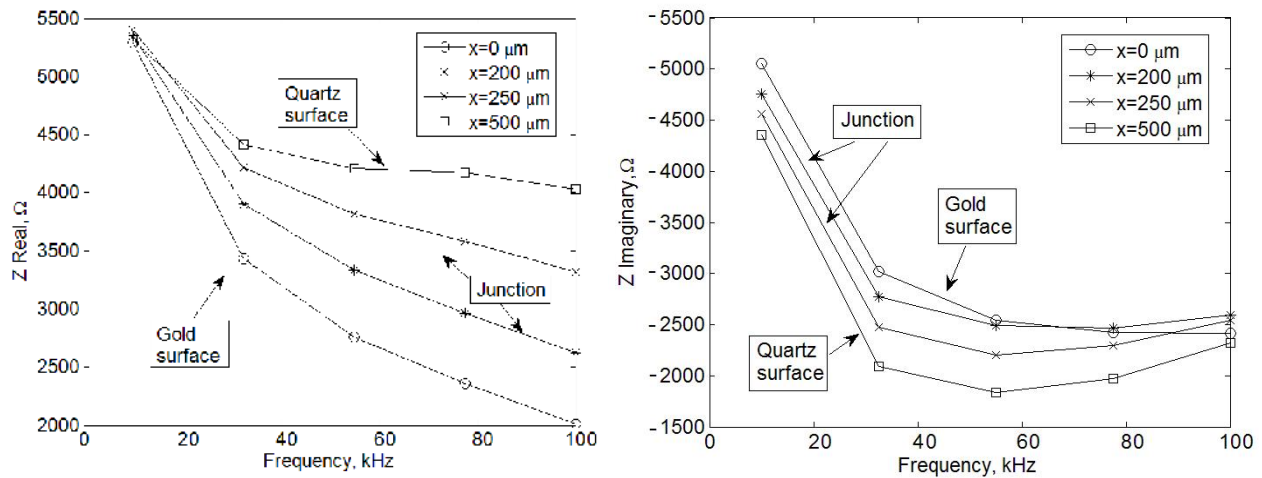
Fig. 3. Real and Imaginary parts of impedance dependence on applied frequency in different zones of surface, starting from gold substrate ($x = 0$ µm) to quartz ($x = 500$ µm). The junction between quartz and gold is showed in coordinate from 200 µm to 250 µm

Since the Real part shows dissipation of energy and resistance for moving charges between the double-layer on the electrodes, we can see from the figure 3 that this resistance is lower in higher frequencies, and the resistance difference between insulating and conductive substrates becomes very high when frequency increases. The biggest influence of Imaginary part on the gold surface shows that the double layer is formed on gold surface, but this phenomenon is not strongly expressed by different conductivities of substrate, and in highest frequency the results are very similar.

3. Conclusions and future developments

The AC-SECM technique shows good results for imaging of surfaces of different conductivity. Real part of impedance, which can be associated with charge transfer resistance and energy dissipation, shows that on gold surface in high frequencies this resistance is two times lower. For investigation of surfaces of different conductivity, such as corrosion studies, this phenomenon is very useful, because of high electrochemical contrast in the picture. However, the impedance measurements show that very strong signal is achieved in high frequencies, and this signal can influence measurements of some immobilized biological species on gold surface. This effect can be eliminated by using lower frequencies. New approach seems very promising for evaluation of surfaces of biosensors [5-7], biologically active nanomaterials [6, 7] and biolelectronic devices [8].

Acknowledgement

References

1. **Eckhard K., Shin H., Mizaikoff B., Schuhmann W., Kranz C.** Alternating current (AC) impedance imaging with combined atomic force scanning electrochemical microscopy (AFM-SECM). Electrochemistry Communications 2007,9:1311-1315.
2. **Eckhard K., Etienne M., Schulte A., Schuhmann W.** Constant-distance mode AC-SECM for the visualisation of corrosion pits. Electrochemistry Communications 2007,9:1793-1797.
3. **Eckhard K., Kranz C., Shin H., Mizaikoff B., Schuhmann W.** Frequency dependence of the electrochemical activity contrast in AC-scanning electrochemical microscopy and atomic force microscopy-AC-scanning electrochemical microscopy imaging. Analytical Chemistry 2007,79:5435-5438.
4. **Ballesteros Katemann B., Schulte A., Calvo E. J., Koudelka-Hep M., Schuhmann W.** Localised electro-chemical impedance spectroscopy with high lateral resolution by means of alternating current scanning electrochemical microscopy. Electrochemistry Communications 2002,4:134-138.
5. **Lapenaite I, Ramanaviciene A., Ramanavicius A.** Current trends in enzymatic determination of glycerol. Critical Reviews in Analytical Chemistry 2006,36:13-25.
6. **Kausaite-Minkstimiene A., Mazeiko V., Ramanaviciene A., Ramanavicius A.** Enzymatically synthesized polyaniline layer for extension of linear detection region of amperometric glucose biosensor. Biosensors & Bioelectronics 2010,26:790-797.
7. **Ramanavicius A., Kausaite A., Ramanaviciene A.** Self-encapsulation of oxidases as a basic approach to tune the upper detection limit of amperometric biosensors. Analyst 2008,133:1083-1089.
8. **Ramanavicius A., Kausaite A., Ramanaviciene A.** Potentiometric study of quinohemoprotein alcohol dehydrogenase immobilized on the carbon rod electrode. Sensors and Actuators B-Chemical 2006,113:435-444.

Characterization of Biosensor Surface by Scanning Electrochemical Microscopy

I. Morkvenaite-Vilkonciene*, I. Astrauskaite*, A. Ramanavicius*, **

*Department of Physical Chemistry, Faculty of Chemistry, Vilnius University, Naugarduko str. 24, 03225 Vilnius, Lithuania
**Laboratory of Bio-Nanotechnology, Department of Materials Science and Electrical Engineering, Institute of Semiconductor Physics, State Research Institute Centre for Physical Sciences and Technology, Savanorių ave. 231 LT-02300, Vilnius, Lithuania

Abstract

Application of Scanning Electrochemical Microscopy (SECM) is spreading very fast. The SECM based techniques are very attractive for the evaluation of biological materials and investigation of other important parameters in bioelectrochemistry, such as enzyme kinetics, heterogeneous electron transfer kinetics, and diffusion. The main part of SECM is Ultramicroelectrode (UME), which can characterize electrochemically conducting surfaces by measuring current flowing through electrode at selected point of specimen. The well-known enzyme glucose oxidase (GOx), immobilized on insulating substrate and immersed in glucose containing solution, is applied for the development of biosensor models and surfaces of such GOx-based biosensors could be evaluated by SECM. The most important factor in biosensor design is enzyme activity, which depends on temperature, duration of experiments, pH and many other factors. In recent research the substrate generation/tip collection (GC) mode was used for SECM measurements of GOx-based surface. The scan in the horizontal direction provides concentration profile of hydrogen peroxide. The enzyme immobilization was controlled by Atomic Force Microscopy. The highest enzyme activity was registered in the center of enzyme drop.
KEY WORDS: *scanning electrochemical microscopy, ultramicroelectrode, glucose oxidase, biosensor, glucose sensor, atomic force microscopy.*

1. Introduction

Development of biosensors recently is an important issue in bioanalytical chemistry. Due to wide spreader diabetes mellitus the most advanced area in this field is related to design of glucose biosensors [1-5]. These sensors usually are based on the application of glucose oxidase (GOx) [1-5]. Moreover enzyme glucose oxidase is used for remove of traces of oxygen and/or glucose from different foods, as a source of hydrogen peroxide in food preservation and in gluconic acid production, also for various clinical applications. Therefore the evaluation of GOx activity in sensor's active layer is very important issue. For this purpose Atomic Force Microscopy [1], photoluminescence [2] and electrochemical [3-5] are applied usually. Scanning Electrochemical Microscopy (SECM) is a new tool suitable for localized electrochemical characterization of various surfaces, like glass, metal, polymer, biological materials [6]. The technique is used to study heterogeneous and homogeneous reactions, for high-resolution imaging of the chemical reactivity, electrical conductivity, enzymatic activity [7] and topography of various interfaces, and for microfabrication [8, 9]. The SECM can be used as miniaturized biosensor [10] for glucose, lactate, and oxygen detection in single cells [11]. Moreover scanning electrochemical microscopy (SECM) can be used for imaging an localized spatial characterization of enzymatic activity [12] and for investigation of biocatalytic reactions inside the enzymatic layer [13]. SECM current–distance curves enables the determination of kinetic information about GOx after fitting to numerical models [14]. Kinetics analysis indicates that GOx maintains a large enzymatic activity [15]. However, number of researches provide different results, because of different immobilization conditions of GOx. Resolution studies of scanning electrochemical microscopy (SECM) shows quantitative correlation of the loss in resolution and the increase in distance between tip and sample [16]. To determine the right distance for appropriate measurement resolution, the current-distance curve has to be obtained by the approaching of the tip to biosensor surface.

2. Experiments

Sample preparation. Glucose oxidase (EC 1.1.3.4, type VII, from *Aspergillus Niger*, 215.266 units mg−1 protein) was purchased from Fluka. d-(+)-Glucose was obtained from Carl Roth GmbH&Co (Karlsruhe, Germany). Before investigations glucose solutions were allowed to mutarotate overnight. All solutions were prepared using deionised water purified with water purification system Millipore S.A. (Molsheim, France). The solution buffer was prepared by mixing sodium acetate trihydrate, potassium chloride, monopotassium phosphate, Sodium phosphate dibasic which were obtained from Reanal (Budapest, Hungary) and Lachema (Neratovice, Czech Republic). 25% glutaraldehyde solution was purchased from Fluka Chemie GmbH (Buchs, Switzerland).

Plastic cell was evaporated by glutaraldehyde 25% for 10 min, Gox 1 mg/ml 0.5 µL was sprayed on the surface to get little drops and dried in the room temperature. Then again Gox drop was evaporated 10 min by glutaraldehyde 25% and washed with buffer.
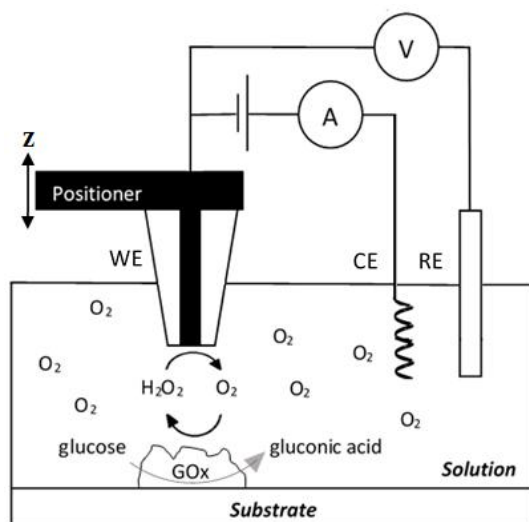
Fig. 1. Scheme of the experiments

Measurements. Sensolytics SECM (Bochum, Germany) was used for experiments. Equipment consists of typical electrochemical cell (Fig. 1) with working (WE), reference (RE) and counter (CE) electrodes, the working electrode can be moved by positioner in the vicinity of investigative substrate in the big conductivity solution. For our measurements, the buffer solution with pH 6.6 was used to keep long activity of enzyme. Working electrode is ultramicroelectrode (UME) with a radius of 10 µm, fabricated from platinum wire, sealed in the borosilicate glass. Counter electrode was platinum wire. The UME was used for scanning of surface in the 40 µm distance. The distance was determined by registration of approach curves, then it is moved by positioners in z direction [17]. The potentiostat gives some desired potential between WE and CE, and resulting current flowing in the WE-CE loop is measured. The reference electrode used in this experiment is Ag/AgCl 3M KCl, the potential 0.6 V is keeping constant vs. RE. Current flow is caused by hydrogen peroxide reduction reaction, occurred at the UME tip.

Contact mode atomic force microscopy was used for the imaging of modified surface. The BioScope II, Veeco Instruments Ltd. (Santa Barbara, USA) was used for AFM experiments.

3. Results

Enzyme glucose oxidase is the catalyzer, which catalyzes the reaction between oxygen and glucose. The reaction products are gluconolactone and hydrogen peroxide. Further the gluconolactone reacts with water, and gluconic acid is formed. The chemical reactions occurs at the enzyme surface:

$$Glu + O_2 \xrightarrow{GOx} Gluconolactone + H_2O_2 \qquad Gluconolactone + H_2O \rightarrow gluconic\,acid$$

The resulting current on UME depends on the quantity of hydrogen peroxide near the surface. The image formed from current values from scanned zone can be of better resolution if more products is generated from
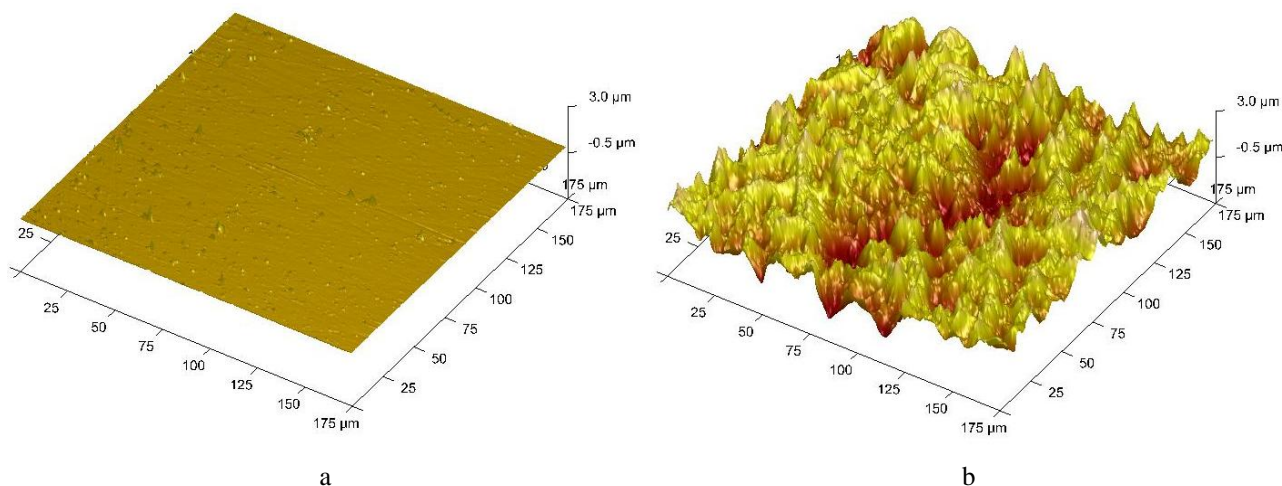
Fig. 2. Atomic force microscopy measurement for enzyme glucose oxidase immobilization control: a – without enzyme; b – with enzyme
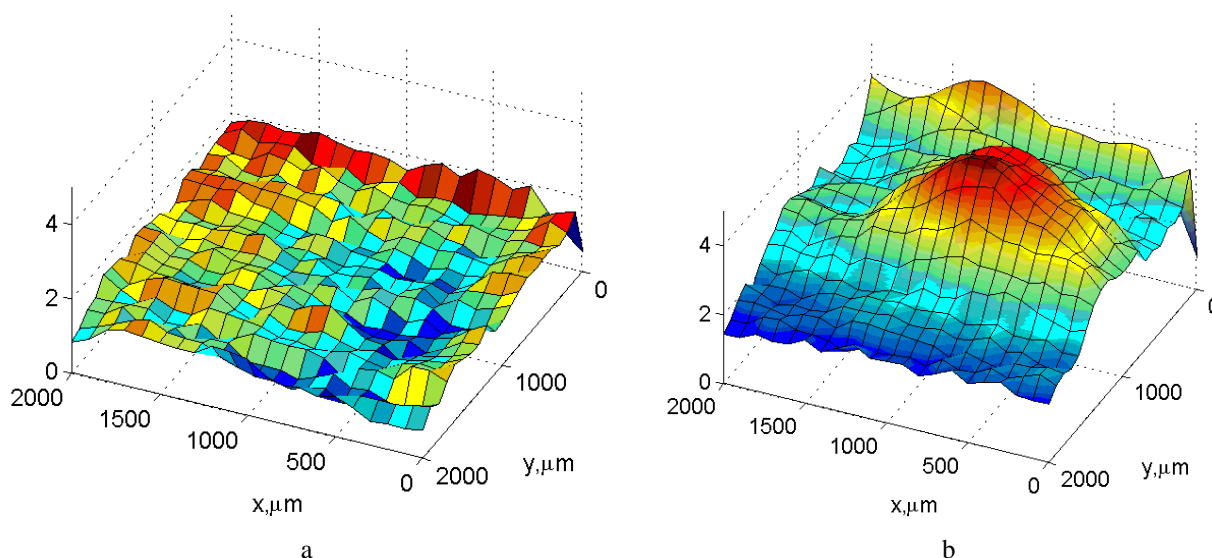
Fig. 3. Scanning Electrochemical Microscopy measurement of enzyme Glucose oxidase: a – in buffer; b – with glucose 30 mM in buffer. Z-axis shows the measured current and have no relations with topography of surface

electrochemical reaction described above. This can be achieved by adding more reacting chemicals, such as glucose. Another way for the improvement of resolution is based on application of some mediators suitable for charge transport from surface to electrode.

For GOx immobilization control Atomic Force Microscopy was used (Fig. 2). These measurements were performed in all steps of immobilization, as described in section 2. Comparing the measurement results with the plastic surface measurement shows the good quality of immobilization.

GOx activity is measured in buffer or in 30 mM of glucose (Fig. 3). The picture shows that no activity is measured if no reagents for chemical reaction is in the solution.

4. Conclusions

For biosensor surface characterization SECM and AFM measurements were applied. The enzyme glucose oxidase is biosensor's active part, therefore enzyme's activity describes biosensors quality. AFM measurements shows that immobilization of enzyme was efficient by comparing unmodified and GOx-modified surfaces. The investigation of GOx-modified surface shows best image of biosensors surface activity resolution in the presence of 30 mM of glucose in buffer.

Acknowledgement

References

1. **Ramanaviciene A., Kausaite-Minkstimiene A., Oztekin Y., Carac G., Voronovic J., German N.**, et al. Visualization of red-ox proteins on the gold surface using enzymatic polypyrrole formation. Microchimica Acta 2011,175:79-86.
2. **Ramanavicius A., Ryskevic N., Kausaite-Minkstimiene A., Bubniene U., Baleviciute I., Oztekin Y.**, et al. Fluorescence study of glucose oxidase self-encapsulated within polypyrrole. Sensors and Actuators B-Chemical 2012,171:753-759.
3. **German N., Ramanavicius A., Voronovic J., Ramanaviciene A.** Glucose biosensor based on glucose oxidase and gold nanoparticles of different sizes covered by polypyrrole layer. Colloids and Surfaces a-Physicochemical and Engineering Aspects 2012,413:224-230.
4. **German N., Ramanavicius A., Voronovic J., Oztekin Y., Ramanaviciene A.** The effect of colloidal solutions of gold nanoparticles on the performance of a glucose oxidase modified carbon electrode. Microchimica Acta 2011,172:185-191.
5. **Ramanavicius A., Kausaite A., Ramanaviciene A.** Self-encapsulation of oxidases as a basic approach to tune the upper detection limit of amperometric biosensors. Analyst 2008,133:1083-1089.
6. **Amemiya S., Guo J. D., Xiong H., Gross D. A.** Biological applications of scanning electrochemical microscopy: chemical imaging of single living cells and beyond. Analytical and Bioanalytical Chemistry 2006,386:458-471.

7. **Wilhelm T., Wittstock G., Szargan R.** Scanning electrochemical microscopy of enzymes immobilized on structured glass-gold substrates. Fresenius Journal of Analytical Chemistry 1999,365:163-167.
8. **Bard A. J., Mirkin M. V.** Scanning Electrochemical Microscopy: Marcel Dekker; 2001.
9. **Evans S. A. G., Brakha K., Billon M., Mailley P., Denuault G.** Scanning electrochemical microscopy (SECM): localized glucose oxidase immobilization via the direct electrochemical microspotting of polypyrrole-biotin films. Electrochemistry Communications 2005,7:135-140.
10. **Bracamonte M. V., Bollo S., Labbe P., Rivas G. A., Ferreyra N. F.** Quaternized chitosan as support for the assembly of gold nanoparticles and glucose oxidase: Physicochemical characterization of the platform and evaluation of its biocatalytic activity. Electrochimica Acta 2011,56:1316-1322.
11. **Ciobanu M., Taylor D. E., Wilburn J. P., Cliffel D. E.** Glucose and lactate biosensors for scanning electrochemical microscopy imaging of single live cells. Analytical Chemistry 2008,80:2717-2727.
12. **Kasai S., Hirano Y., Motochi N., Shiku H., Nishizawa M., Matsue T.** Simultaneous detection of uric acid and glucose on a dual-enzyme chip using scanning electrochemical microscopy/scanning chemiluminescence microscopy. Analytica Chimica Acta 2002,458:263-270.
13. **Csoka B., Kovacs B., Nagy G.** Investigation of concentration profiles inside operating biocatalytic sensors with scanning electrochemical microscopy (SECM). Biosensors & Bioelectronics 2003,18:141-149.
14. **Burchardt M., Wittstock G.** Kinetic studies of glucose oxidase in polyelectrolyte multilayer films by means of scanning electrochemical microscopy (SECM). Bioelectrochemistry 2008,72:66-76.
15. **Zigah D., Pellissier M., Fabre B., Barriere F., Hapiot P.** Covalent immobilization and SECM analysis in feedback mode of glucose oxidase on a modified oxidized silicon surface. Journal of Electroanalytical Chemistry 2009,628:144-147.
16. **Borgwarth K., Ricken C., Ebling D. G., Heinze J.** Surface analysis by scanning electrochemical microscopy: Resolution studies and applications to polymer samples. Fresenius Journal of Analytical Chemistry 1996,356:288-294.
17. **Morkvenaite-Vilkonciene I., Ramanavicius A.** Imaging Glucose Oxidase by Scanning Electrochemical Microscopy. In: 2nd International Conference on Nanotechnologies and Biomedical Engineering. Chisinau, Moldova: Technical University of Moldova; 2013. pp. 597-600.

Proceedings of 8th International Conference ITELMS'2013

Testing the Immune Algorithms for Electrical Transport Using Mathematical Methods

A. Mor-Yaroslavtsev*, A. Levchenkov**

Riga Technical University, Kronvalda bulv. 1, LV-1010, Riga, Latvia, E-mail: andrejs@rtu.lv
**Riga Technical University, Kronvalda bulv. 1, LV-1010, Riga, Latvia, E-mail: anatolijs.levcenkovs@rtu.lv*

Abstract

Objective of this paper is to test the immune algorithms for an intelligent rolling stock safety system which could provide a possibility for railway transport to avoid dangerous situations. The authors examine the algorithms used in artificial immune systems and ways how they can be used together and provide data for each one other via communication protocols, then create a simulation for further analysis with mathematical methods.
The authors review data analysis methods used to detect, predict and control undesirable rolling stock travel conditions.
KEY WORDS: *immune algorithms, classification, railway transport.*

1. Introduction

The research aims to develop a way for the electric railway transport to avoid dangerous situations.

Objective of this paper is to test the immune algorithms for an intelligent rolling stock safety system which could provide a way for railway transport to avoid dangerous situations.

Artificial immune systems (AIS) were mentioned in some papers in mid 1980s but became a subject in its own right in 1994 in papers on negative selection by For-rest et al. [1] and Kephart et al. [2]. Currently the systems are actively explored for possible use cases. Dasgupta et al. [3] investigated a real-valued negative selection algorithm for aircraft fault detection. Watkins et al. [4] presented a simplified version of a clonal selection algorithm called AIRS (Artificial Immune Recognition System) and Negi [11] implemented an AIS for urban traffic control which responds to undesirable situations.

The authors examine the algorithms used for data analysis in artificial immune systems and ways how they can be used together and provide data for each one other, then create a simulation for further analysis with mathematical methods.

2. The system analysis and design

During journey the rolling stock driver may experience many undesirable situations and have to make decisions on how solve them. The situations may include such examples as:
- the last car from the flow is still on the level crossing 25 seconds before the train arrival, while the safety regulations require the crossing to be cleared at least 35 seconds before train arrival;
- a daredevil is running across the tracks somewhere in the urban zone;
- there is a red signal on the railway traffic light;
- there is a wide but harmless rod lying between the tracks, etc.

Each of these situations requires different actions or no action at all. The driver may have to apply brakes, speed up, continue the steady movement and in any case communicate the information to the control center and other drivers.

The desired result conforms to at least two require-ments:
- there are no casualties;
- the train is on schedule.

A common situation is illustrated on Fig. 1, where L is a locomotive and I is an invading object on tracks.

The authors offer the intelligent rolling stock safety system functional design which is presented on Fig. 2.
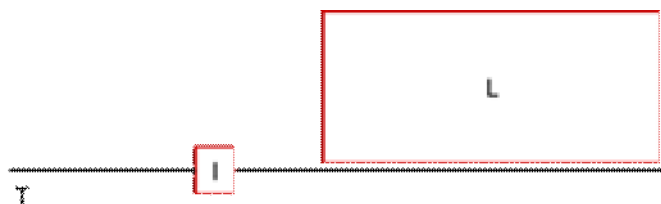
Fig. 1. A common unwanted situation on the railway tracks
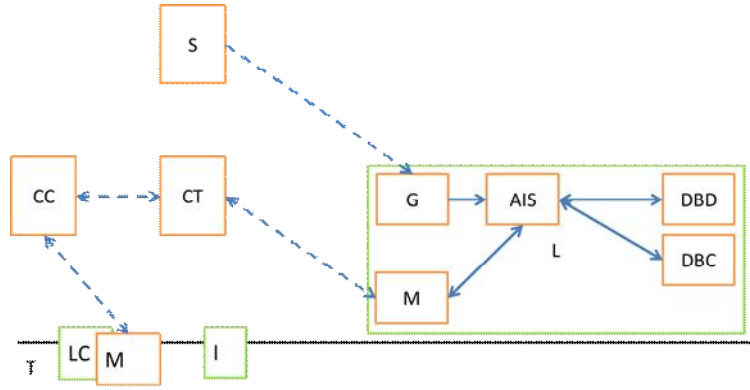
Fig. 2. The intelligent rolling stock safety system functional design

The invading object I is picked up by sensors S and the data is transmitted to the nearest cell tower CT, which relays it to the control center CC and nearest locomotives wireless modems M. Through the same modem the locomotive L receives data about closest neighbors' rolling stock position and status, railway segment profile and maximum allowed speed.

L also hosts: a positioning receiver G which receives data from a positioning satellite ST; data analysis module AIS which communicates to the immune detector database DBD and control cell database DBC. Depending on the results of control cell maturation the module makes a decision and executes it by sending a control signal or displaying an alert to the driver.

The information is also communicated to the device on a level crossing LC through a similar modem M.

The principles behind AIS, DBD and DBC are discussed further in the article.

3. Mathematical formulation

Let $U \in R$ be problem space:

$P \in U$ – set of known "good" situations;

$S(t) \in U$ – current situation which changes with time t;

$D = \{D_1, D_2, \ldots, D_n\} \notin P$ – set of detectors;

$C = \{C_{D1(1)}, C_{D1(2)}, \ldots, C_{D1(p)}, C_{D2(1)}, \ldots, C_{Dn(p)}\}$ – set of control cells affiliated to detectors;

$E = \{E_1, E_2, \ldots, E_m\}$ — set of encountered situations;

$W = \{W_{E1D1}, W_{E1D2}, \ldots, W_{E1Dn}, W_{E2D1}, \ldots, W_{EmDn}\}$ – set of detector weights in different situations;

Distance between two points on a sphere:

$$d = 2R \arcsin\left(\sqrt{\sin^2\left(\frac{lat_A - lat_B}{2}\right) + \cos(lat_A) \times \cos(lat_B) \times \sin^2\left(\frac{lon_A - lon_B}{2}\right)}\right)$$

Conditions intriduced by using embedded device:

$T = \{t_1, t_2, \ldots, t_n\}$ – the embedded device must work in real time;

$V = \{v_1, v_2, \ldots, v_n\}$; $v_i = x_i \times y_i \times z_i$; V^* – min V – size of the device;

$T_{test1} < T_{test2}$ – time to test prototypes;

$E = \{e_1, e_2, \ldots, e_n\}$; E^* – min E – energy consumption;

$IZ = \{iz_1, iz_2, \ldots, iz_n\}$; IZ^* – min IZ – install and use costs;

$P = \{p_1, p_2, \ldots, p_n\}$; P^* – min P; $AT = \{at_1, at_2, \ldots, at_n\}$; AT^* – min AT – speed and memory.

Additional limitation outside of mathematical scope is input and output UI.

The requirements for the chosen algorithm A_n:

$T_{An} \to$ min – completion time for the algorithm

$Pr_{An} \to$ max – precision of the algorithm's result

$E_{An} \to$ min – energy consumption while running the algorithm

$(x_B \times y_B \times z_B) \to$ min – embedded device dimensions

$ST_B \to$ max – reliability of the device and algorithm

$IP_B \to$ min – install and use costs

Hypothesis: the immune algorithm will complete faster and give more precise answers.

4. The general algorithm

The possibilities for learning implementation are the following: either make the system fully automatic and let it discover all the data by itself; or set two-stage learning with the initial training and continuous self-improvement.

Therefore the intelligent rolling stock safety system general algorithm is such:
1. Fill in the initial values *D* for DBD by running the negative selection training routine.
2. Run in real time the detection routine using the negative selection algorithm.
3. Determine the possible situation identifiers (detectors which matched above a given threshold).
4. Assign weights to the detectors based on their «distance» to the situation.
5. Retrieve a population of control cells *C* from DBC which are related to the activated detectors.
6. Run the control cell maturation routine using the clonal selection algorithm.
7. Execute the found optimal solution.
8. Communicate the information to the control centre CC.
9. Continue from step 2.

The most feasible way to implement such a safety system would be, like in case of hybrid IDS [5], through the two phases of anomaly detection and determination of their type to draw a conclusion. In this case the incoming data from the sensors is the set of antigens. The data includes but is not limited to speed, acceleration, voltage, rotation and operational temperature.

The algorithm uses AIS negative selection and clonal selection algorithms as the basis. The problem in AIS is represented as an antigen and solution candidates as antibodies which are randomly generated from the library of available solutions or genes. The evaluation of affinity or degree of binding between the antigen and the anti-body is similar to complementarity level in biological *IS* and it defines the fate of each individual antibody as well as termination of the whole algorithm.

Negative selection algorithms need training samples only from one class (self, normal), thus, they are especially suited for the tasks such as novelty, anomaly or change detection including those in engines and other devices. The key advantage of anomaly detection systems is their ability to detect novel attack patterns for which no signature exists, while their most notable disadvantage is a larger false positive rate. This algorithm produces a set of detectors capable to recognize non-self patterns. The action following the recognition varies according to the problem under consideration. In the case of transport safety control system it could be an alarm or issue of an immediate stop signal depending on the detected situation.

The detectors and the caught dangerous conditions are stored in immune memory for further processing and to provide further information about the consequences of the attack and possible future actions instead of simply reporting the incidents.

In clonal selection algorithm, individual antibodies are replaced, cloned and hypermutated until satisfactory level of affinity is reached. Partial replacement of the solutions' population with fresh randomly generated candidates maintains diversity which allows solving a wider set of problems. The probability of cloning or hypermutating a candidate depends on its affinity. While usually cloning is proportional and hypermutation is inversely proportional to each candidate's affinity, there's also a version of this algorithm called AIRS [4], which is a bit closer to a genetic algorithm and where hypermutation happens on an independently random rate.

5. The experiment

The computer experiment plan was such:
- build a computer model for each of the solution methods;
- input data about the device;
- simulate various road situations;
- run the models for many iterations;
- statistically analyze the output and draw conclusions about the devices and algorithms with such methods as t-tests and z-tests.

The test run of the real-valued negative selection algorithm on the computer in 2-dimensional problem space shows the detectors showed good coverage of the nonself space and stable detection of nonself antigens. The population should have stayed the same but after 3 generations the detector population decreased but still detected the pathogens. The chosen actions did not differ much probably because of implementation which needs further research and improvement.

The field experiment involved controllers on the locomotive and in the railway traffic light control box interacting with a server and each other. The data set for the experiment was taken from the two controllers in the field attached to a locomotive and a traffic light control box. The data exchange scheme is presented on Fig. 4.

The communication between the controllers was facilitated by GPRS modules and a server running on a PC; the data was exchanged using a set of custom text messages on top of an open protocol which facilitates observation and control of the whole process with a wide range of tools for PCs and mobile phones. Through the chain of software tools – communications and data collection server, an instance of PHP script (could be anything capable of network and database communication) – the data was piped from the controllers to the database tables.

Upon receiving the data about its own and the traffic light location the locomotive embedded device calculates the distance between them according to the formula of distance between points on a sphere.
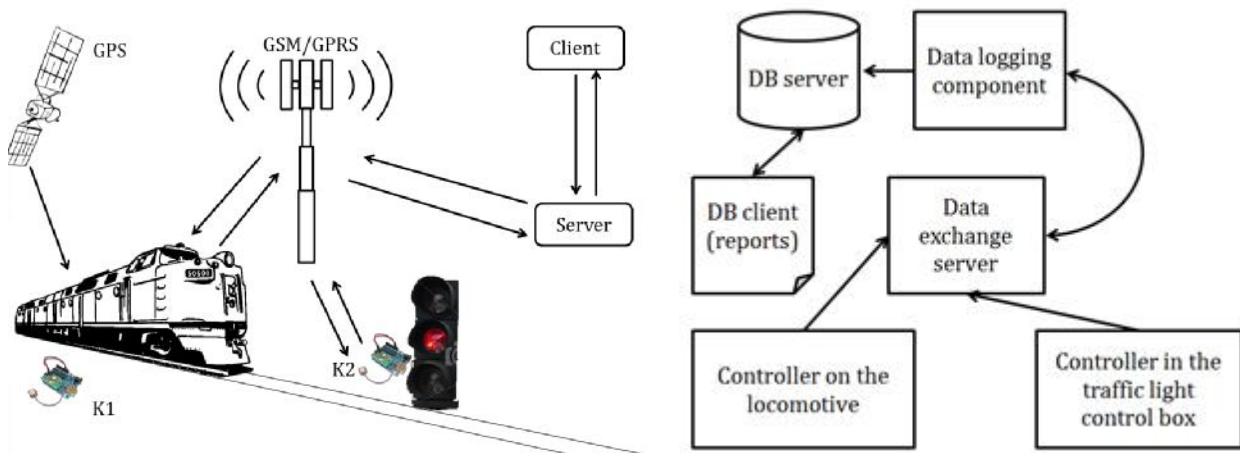
Fig. 3. The experiment overall and data exchange plan

When the braking distance matches or exceeds the calculated distance and the traffic light is set to red, the device immediately activates the train brakes.

Some signal instability was detected in the GPS feed and some data overflow in the exchange process.

6. Conclusions

- Learning process for the intelligent rolling stock safety control system should consist of two phases:
  - o Initial training and detection – immune negative selection algorithm,
  - o Classification and improvement – clonal selection algorithm;
- The embedded program needs a position and distance prediction routine to handle lost or late data due to unstable radio signal;
- An alternative protocol should be established to avoid flooding the serial link with all the devices variables' values;
- The authors need to assess the possibility to run the data analysis on the embedded devices themselves using these algorithms in real time.

References

1. **Forrest S., Perelson A. S., Allen L., Cherukuri R.** Self-nonself discrimination in a computer. In proceedings of the 1994 IEEE Symposium on Research in Security and Privacy. Los Alamitos, CA.
2. **Kephart J. O.** A biologically inspired immune system for computers. In proceedings of Artificial Life IV: The Fourth International Workshop on the Synthesis and Simulation of Living Systems, 1994. MIT Press.
3. **Dasgupta D., K. Krishna Kumar, Wong D., Berry M.** Negative Selection Algorithm for Aircraft Fault Detection. In proceedings of ICARIS 2004.
4. **Watkins, Timmis J., Boggess L.** Artificial Immune Recognition System (AIRS): An Immune-Inspired Supervised Learning Algorithm. 2003. Kluver Academic Publishers.
5. **Powers S. T., He J.** A hybrid artificial immune system and Self Organising Map for network intrusion detection. Elsevier IS 179, 2009.
6. **Bereta M., Burczynski T.** Immune K-means and negative selection algorithms for data analysis. Elsevier IS 179, 2009.
7. **Musilek P., Lau A., Reformat M., Wyard-Scott L.** Immune Programming. Elsevier IS 179, 2009.
8. **Gorobetz M., Alps I., Levchenkov A.** Mathematical Formulation of Public Electric Transport Scheduling Task for Artificial Immune Systems. Proceedings of ITELMS '2009, Kaunas.
9. **Masutti T. A. S., de Castro L. N.** A self-organizing neural network using ideas from the immune system to solve the traveling salesman problem. Elsevier IS 179, 2009.
10. **Tavakkoli-Moghaddam R., Rahimi-Vahed A., Mirzaei A. H.** A hybrid multi-objective immune algorithm for a flow shop scheduling problem with bi-objectives: Weighted mean completion time and weighted mean tardiness. Elsevier IS 179, 2009.
11. **Klūga A.** Satelītu radionavigācijas sistēmas. RTU, 2010.
12. **Negi P.** Artificial Immune System Based Urban Traffic Control. Texas A&M University, 2006.

Mechanical Properties of Laser-Welded Joints in the Difficult-to-Weld Steels

B. Nasilowska, T. Slezak, L. Sniezek, J. Torzewski

Military University of Technology, gen. S. Kaliskiego 2 str., 00-908 Warsaw, Poland, e-mail: tslezak@wat.edu.pl

Abstract

Laser welding for joining elements made of structural difficult-to-weld steels is very promising. This technology is characterized by high welding speed, less heat input with simultaneous deeper welding penetrations – in comparison with conventional methods, relatively narrow welds and reduced heat-affected zone (HAZ), which minimizes the residual stresses and distortions. This paper presents the results of the mechanical properties study of welded joints two different types of steel being used in the responsible structures: high-strength fine-grained steel S1100QL and austenitic steel 1.4541 (X6CrNiTi18-10).
KEY WORDS: *welded joints, laser welding, austenitic steel, high strength steel, residual stresses.*

1. Introduction

The basic criteria determining the applicability of the materials for steel structures is their weldability. It is defined as the possibility to make joints by welding of the required physical properties, capable for transmitting loads prescribed for the type of construction, the implementation of which that material is planned to be used (def. J. Pilarczyk). Factors limiting the weldability of steel are mainly lamellar and crystallization cracks, hydrogen embrittlement, toughness and hardness of the heat-affected zone (HAZ). The basic parameter describing the weldability is carbon equivalent CE (or CET) [1]. Many types of steel that are difficult or impossible to weld using conventional arc welding may be joined with a laser beam, without having to modify the welding process [2]. Unquestionable advantages of laser beam welding are: small amount of the heat input, narrow HAZ and small distortions of welded structure. In economic terms the advantages include high welding speed and one-pass full penetration. The great disadvantages of this process are: high cooling rate, metal evaporation, the precise fit-up requirements for the joint geometry and accurate guidance the beam along the weld due to the high depth-to-width ratio of fusion zone (FZ). Selected methods of effective prevention the faults by proper welding parameters are presented in [3-4].

Austenitic stainless steel resistant to corrosion (e.g. 1.4541) and high strength steel (e.g. S1100QL) are more often used in steel structures because of their characteristics. Austenitic stainless steel (1.4541) is widely used in the chemical industry e.g. for the construction of heat exchangers, pipelines and tanks for hazardous media, parts of pumps working in acid environment or in the food industry for components exposed to aggressive preservatives. The structural steel S1100QL is used for welded structures exploited in heavy loads having the existing exploitation parameters. These steels are used e.g. for the jibs of cranes and car lifts, pressure vessels and mobile bridges [5-6]. Strengthening mechanism is based on advanced thermo-mechanical treatment resulting in fine-grained structure stabilized by carbide precipitates. Welding as a zonal heat treatment causes local damage of the structure and loss of the initial properties.

The major aim is to provide connections with the best strength properties by reducing the grain growth in the heat-affected zone and taking control of phase transitions. These conditions are particularly important in the process of welding structural steel plates with large thickness when multiple welding passes are required. Difficulties in welding of the described steels are mainly caused by the necessity of use low linear welding energy and to control the cooling time $t_{8/5}$ between consecutive welds. Application of laser beam in joining high-strength steels allows avoiding these difficulties by manufacturing weld in one pass.

There is required the development of modern welding methods minimizing heat input and providing suitable strength and impact resistance. Moreover, joints obtained in this way are characterized by inconsiderable welding distortions [7]. These deformations are particularly important making the construction of prefabricated elements, which are finally adjusted on site. Excessive distortions can be reversed by mechanical or thermal methods, for example by flame heating. If this operation is carried out not shipshape then it can lead to grain growth and the degradation of mechanical properties. Thus, there is great interest in the use of laser beam processing to minimize the heat input while ensuring full penetration in the weld. The use of the high energy density welding technique can reduce the total heat input required for fulfillment the construction joints by reducing the total energy in a single weld performance and also in the case of multilayer welds.

2. Research procedures

In the research were used two grades of steels in the form of plate: high-strength structural steel S1100QL of a thickness 6 mm and austenitic steel 1.4541 of a thickness 5 mm. The chemical composition and strength properties of the steels are shown in Table 1.

The microstructure of examined steels is shown in Fig. 1 and 2. Steel S1100QL is characterized by fine-grained martensitic-bainitic structure with a grain size of 4-10 μm, made by the controlled thermo-mechanical

treatment. The presence of vanadium alloying element affects the permanent carbides locking grain growth. As a result of hot rolling there have occurred band texture (Fig. 1a), with a number of ferrite precipitates within small amount of cementite released during the bainitic and martensitic transformations.

The structure of 1.4541 steel consists of austenite grains with an average size of 20 μm with many re-crystallization twins (Fig. 2b), which were formed during the fabrication of the pipeline components using hot forming implemented by rolling. During metallographic examination between austenitic matrix was revealed grains the band δ ferrite separations, formed during the metallurgical process (Fig. 2). There was shown also titanium nitride precipitates forming local galvanic micro-cells conducive to develop pitting corrosion.

Laser beam welding was carried out at the Centre for Laser Technologies of Metals in Kielce with the CO_2 continuous operation TRUMPH laser (Fig. 3). Laser is equipped with a numerically controlled table and its maximum power is 6.0 kW. The nominal spot diameter was 0.43 mm. Joints were made with the following welding parameters:

- for steel 1.4541:
  - constant beam power P = 4.5 kW, weld travel speed v = 1.1-3.0 m/min;
  - constant weld travel speed v = 1.5 m/min; beam power P = 2.5-6.0 kW;
- for steel S1100QL:
  - constant beam power P = 5.0 kW, weld travel speed v = 0.8-1.5 m/min.

The details of processing parameters used in the study are presented in Table 2. The nominal heat input Q from the laser beam can be obtained from the following equation:

$$Q = \frac{P \cdot 60}{v} \ [\text{kJ/mm}] \tag{1}$$

where P is the laser power [kW], and v is the weld travel speed [mm/min].

Table 1

Mechanical properties and chemical composition (W_t %) of the examined steels

	Mechanical properties			Chemical composition							
	$R_{0.2}$ [MPa]	R_m [MPa]	A [%]	Si	Mn	Cr	Mo	Ni	V	Ti	N
S1100QL	1197	1363	11.8	0.40	1.06	0.70	0.69	2.02	0.07	–	–
1.4541	250	550	35	0.36	1.44	18.44	–	10.07	–	0.51	0.05
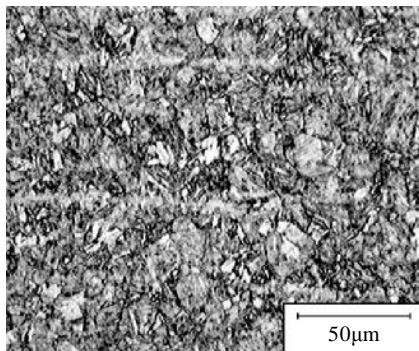
a
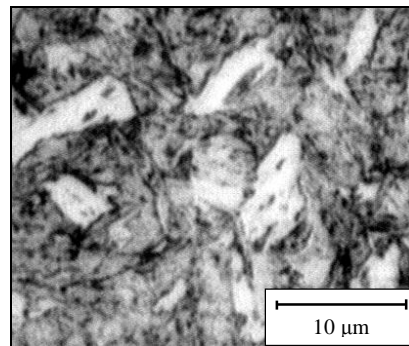
b

Fig. 1. Microstructure of as-received S1100QL steel
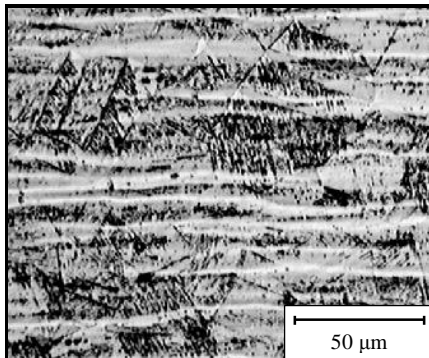
a
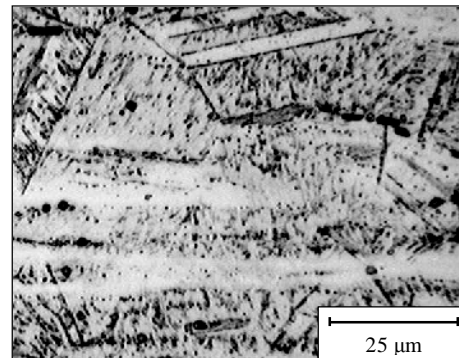
b

Fig. 2. Microstructure of as-received X6CrNiTi18-10 steel
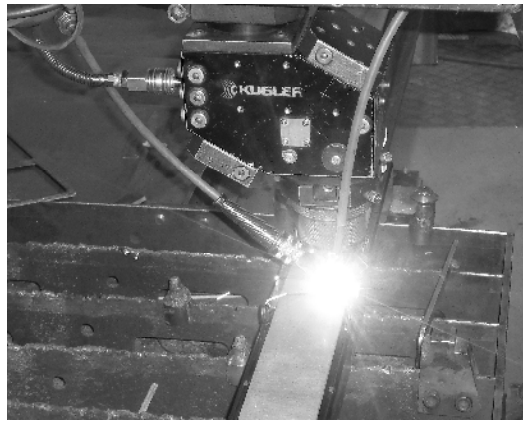
Fig. 3. Processing using TRUMPH laser CO_2

      Butt joints were made without any filler material and shielded using helium at a flow rate of 10 L/min. Laser beam spot was positioned on the surface of the specimen.

      After welding, received joints were prepared for metallographic examination. The sections were cut out from each weldment transverse to the welding direction. These sections were used for preparation the metallurgical specimens. They were ground, polished with aluminum oxide and then etched. Austenitic steel was etched electro-chemically. The weld bead morphology and macrostructure of the welded joints were examined using a metallographic microscope equipped with an image analysis program. For some selected specimens, the microindentation hardness profiles across the welds were measured using a 100G test load with a Vickers microhardness machine [8]. Measurement of microhardness was carried out within ~1 mm from the specimens surface at the face of weld side. The interval of the measuring points was 0.2 mm (in case of large changes 0.1 mm).

Table 2

Processing parameters used

Welding number	Welding speed [m/min]	Laser power [kW]	Heat input [kJ/mm]	Welding umber	Welding speed [m/min]	Laser power [kW]	Heat input [kJ/mm]
Austenitic steel 1.4541				cont.			
# 1	1.5	**2.5**	0.10	# 13	1.8	**4.5**	0.15
# 2	1.5	**3.0**	0.12	# 14	2.0	**4.5**	0.14
# 3	1.5	**3.5**	0.14	# 15	2.2	**4.5**	0.12
# 4	1.5	**4.0**	0.16	# 16	2.4	**4.5**	0.11
# 5	1.5	**5.0**	0.20	# 17	2.8	**4.5**	0.10
# 6	1.5	**5.5**	0.22	# 18	3.0	**4.5**	0.09
# 7	1.5	**6.0**	0.24	**S1100QL steel**			
# 8	1.1	**4.5**	0.25				
# 9	1.2	**4.5**	0.23	# 21	0.8	**5.0**	0.38
# 10	1.4	**4.5**	0.19	# 22	1.0	**5.0**	0.30
# 11	1.5	**4.5**	0.18	# 23	1.2	**5.0**	0.25
# 12	1.6	**4.5**	0.17	# 24	1.5	**5.0**	0.20

      One of the key factors affecting the safety assessment of welded structures is the knowledge of the actual state of stress. Then, it is important to determine the residual stresses caused by the carried out welding process during the analysis of actual material effort [9-10]. Residual stresses are generated by the non-uniform heating of elements and the shrinkage of metal entailed by the thermal cycle. The internal forces are caused by local heating up of relatively narrow area in which the metal expands and shrinks during cooling. The changes of stresses value are caused by movement of temperature field, the position of the welded junction and phase changes in the HAZ.
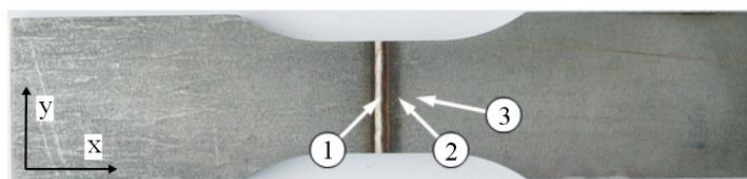
Fig. 4. Schematic of residual stresses measurement in laser weldment

Measurement of the stresses in welded joints were carried out at the Light Metals Division of the Institute of Non-Ferrous Metals in Skawina with X-ray diffraction method using STRAINFLEX PSF-2M apparatus. It was performed at three points: weld (1), heat affected zone (2) and paternal material (3) and in two directions respecting the weld axis: perpendicular X and longitudinal Y, as shown schematically in Fig. 4.

3. Results of research

Laser welding of steel 1.4541 has resulted in full penetration of the specimens for all beam parameters (Fig. 5). Differences which are closely related to the amount of heat input occurred in the fusion zone. In some cases, the porosity appeared as single bubbles (Fig. 5b, e). It can be noted that with the increase of the laser beam travel speed, also the height-to-width ratio of the weld face increases, what in terms of strength is unfavorable phenomenon. This shape influences the growth of the weld shape factor and reduces the fatigue strength [11]. At lower travel speeds (case # 8) weld has a lower symmetry, which may adversely affect the state of residual stresses and welding distortion. This shape of the weld is due to the worse stability of weld eye at lower speeds.
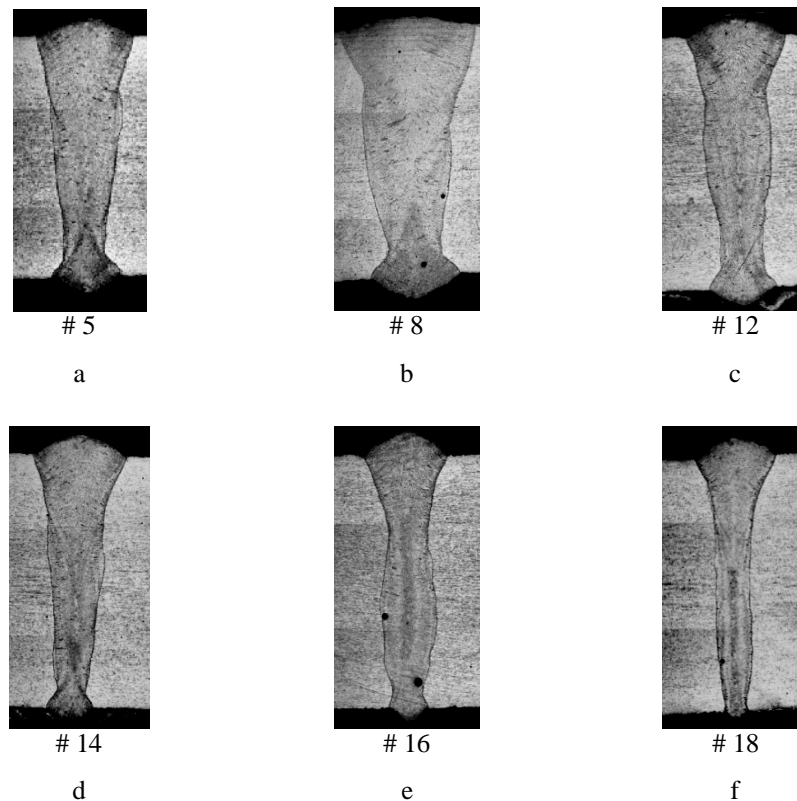
Fig. 5. Laser-made welds of 1.4541 steel – parameters of welding in Table 2

There were also obtained excellent results during performing laser-made butt joints on S1100QL steel elements with the assumed welding conditions (Fig. 6). Welds are characterized by symmetry and a small height of the face and the root of weld. In some conditions the outline coincides with the surface of the work piece (Fig. 6a). At the highest speed of welding, as in the case of austenitic steel, face is characterized by the worst shape (Fig. 6c). On the image of the specimen # 24 is shown the local lack of melting the fusion face near the root (1). This is due to the difficulty of positioning the laser beam accurately on the axis of welding and a large value of the depth-to-width ratio of fusion zone (for # 24 width is ~ 1 mm in some areas). There is important a slight width of the zone of weld with HAZ, which is from 2.3 mm at the narrowest point (for # 24) to 4.5 mm (for # 21).

The results of microhardness HV0.1 measurement of the austenitic steel welds are shown in Fig. 7. The horizontal axis shows the distance from the weld axis. There are no significant changes in the welded joints and HAZ, especially at higher welding speeds (Fig. 7a and c). There is noticeable an inconsiderable increase of the hardness in the weld area in relation to the paternal material. Whereas, there can be highlighted the area of lower hardness in heat-affected zone (up to 170 HV) of the specimen made at greater heat input (Fig. 7b).

The results of Vickers hardness test for S1100QL steel are shown in Figure 8. The microhardness distribution is similar in all cases and changes significantly. Weld and partly heat affected zone have microhardness 360-380 HV. In the normalized area it increases up to about 420 HV and then rapidly decreases to 285 HV in the re-crystallization zone. Next, the hardness is gradually increasing to 335 HV (the hardness of the paternal material). Measuring points of the HV0,1 maximum values are marked on the Fig. 6 with black "X" symbols.

Residual stress measurement results are presented in Fig. 9. In both cases, the values measured in the *X* direction (defined in Fig. 4) are indicated by the solid lines, whereas in the Y direction – the dashed lines.
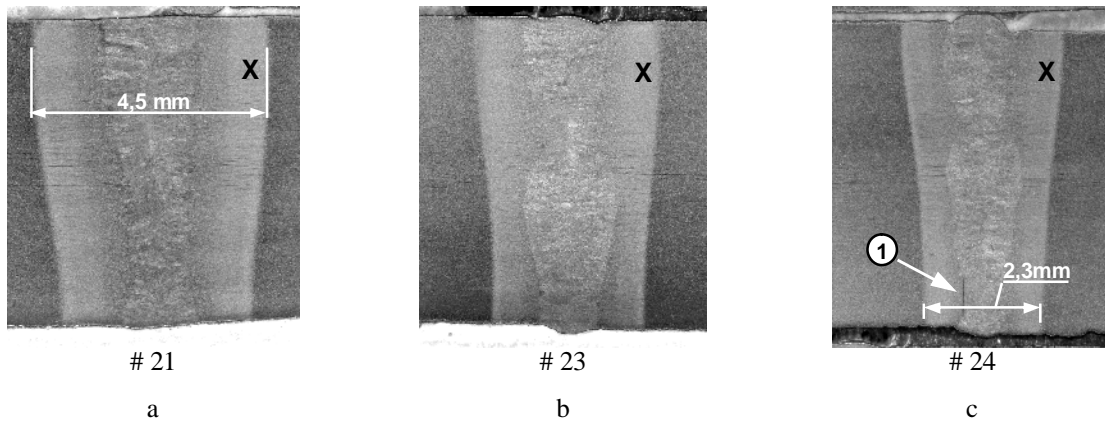
Fig. 6. Laser-made welds of S1100QL steel (description in test) – parameters of welding in Table 2
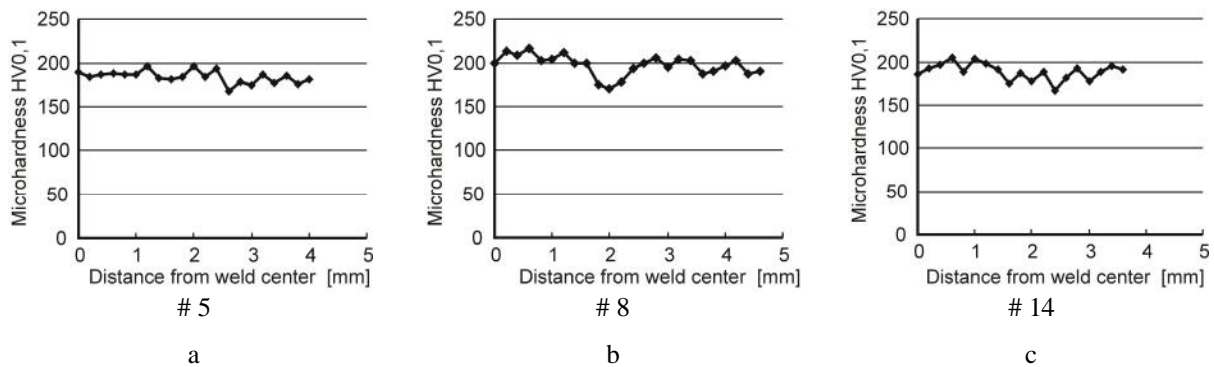
Fig. 7. Microhardness distribution in welds of 1.4541 steel
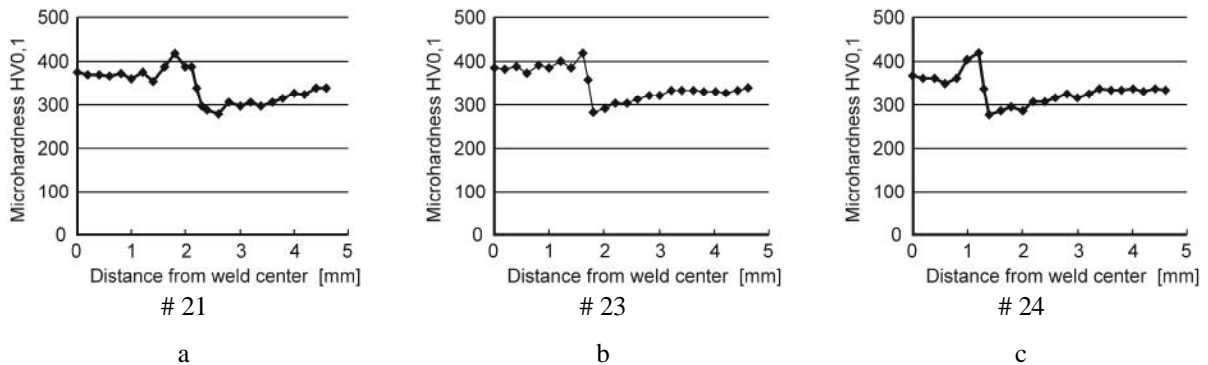
Fig. 8. Microhardness distribution in welds of S1100QL steel
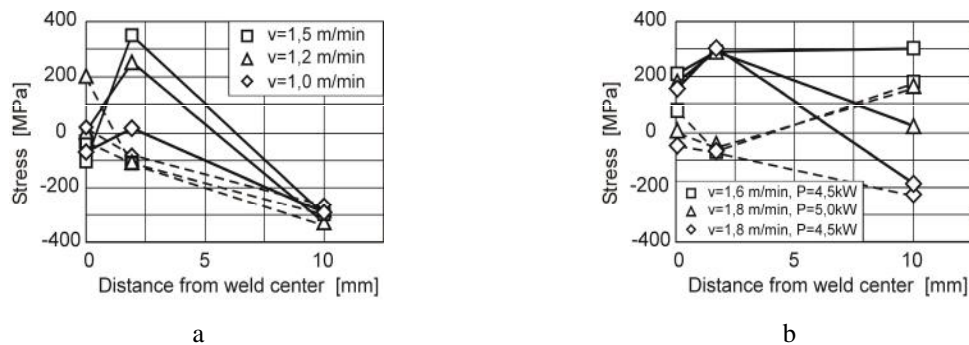
Fig. 9. Residual stresses in laser-welded joints: a – S1100QL; b – 1.4541 steel (description in text)

Comparing the two above plots it is clear that austenitic stainless steel is more sensitive to the effects of welding process. This is reflected in the range of adverse tensile stress area.

The increase of laser beam travelling speed at constant laser power causes the rise of the residual stress value measured in the direction perpendicular to the weld axis. In second direction it is approximately constant (Fig. 9a). This is directly related to the amount of heat input and cooling rate. At higher welding speed crystallization of the melting metal progresses very quickly and it also entiles high tensile stresses in the HAZ (about 350 MPa). Greater amount of heat input at lower speed allows stress relaxation in the HAZ and tensile stresses reduction.

Welding conditions of austenitic stainless steel (Fig. 9b) indicated by a square and a triangle have the same value of the heat input rate of 0.17 kJ/mm. In the vicinity of the weld, stresses measured in the same direction are approximately equal. High value of the stress in the X direction is due to the shrinkage of the weld in the same direction. It can be seen that simultanous incerse of the travel speed and welding power leads to reduction of the tensile stresses range. Furthermore, a small increase of welding speed (diamond symbols) reduces the level of stresses in paternal material to compressive, measured at a distance of 10 mm from the weld axis.

4. Conclusions

The application of laser beam in joining the difficult-to-weld materials allows obtaining the required quality of weldment, both for the fine-grained structural steel S1100QL and austenitic 1.4541. Obtained joints are characterized by a small range of heat-affected zone and the preferred shape of the face and root of weld, which significantly affects their strength properties. The strengthening mechanism of the steel, which results directly from their chemical composition and processing, influences on changes in microhardness and residual stress state. Reducing the amount of heat input in steel 1.4541 by increasing the laser beam travel speed reflects in favorable changes in distribution of the residual stresses. In the case of S1100QL steel, an increase of the heat amount influences on the stress distribution positively but it extends the width of the weld cross-section with higher values of microhardness.

References

1. EN-1011-2:2009. Welding – Recommendations for welding of metallic materials – Part 2: Arc welding of ferritic steels.
2. EN-1011-6:2006, Welding – Recommendations for welding of metallic materials – Part 6: Laser beam welding.
3. **Klimpel A., Lisiecki A.** Laser welding of butt joints of austenitic stainless steel AISI 321. Journal of Achievements in Materials and Manufacturing Engineering, Vol. 25, Issue 1, November 2007, pp. 63-66.
4. **Yan S.** et al. CW/PW dual-beam YAG laser welding of steel/aluminum alloy. Optics and Lasers in Engineering, Vol. 48, Issues 7-8, July-August 2010, pp. 732-736.
5. **Günther H. P.** Use and Application of High-Performance Steels for Steel Structures (Structural Engineering Documents 8), IABSE, 2005.
6. **Glodeža S.** et al. Fatigue and fracture behaviour of high strength steel S1100Q. Engineering Failure Analysis, Vol. 16, Issue 7, October 2009, pp. 2348–2356.
7. **Cao X.** et al. Hybrid fiber laser – Arc welding of thick section high strength low alloy steel. Materials and Design 32 (2011), pp. 3399-3413.
8. EN ISO 9015-2:2011. Destructive tests on welds in metallic materials – Hardness testing – Microhardness testing of welded joints.
9. **Śnieżek L.** et al. Analiza trwałości zmęczeniowej rurociągu przemysłowego (in Polish), Wojskowa Akademia Techniczna, Warszawa 2010.
10. **Nasiłowska B., Śnieżek L.** et al. Trwałość zmęczeniowa laserowych połączeń spawanych stali austenitycznej stosowanej na rurociągi przemysłowe (in Polish), XXIII Symposium on Fatigue Failure and Fracture Mechanics, May 2010, Bydgoszcz - Pieczyska, Poland, pp. 93-94.
11. **Mazanek K., Śnieżek L., Ślęzak T.** Fatigue research of welded joints of high strength S960QL steel (in Polish), Biuletyn WAT, Vol. LXII, Warszawa 2013, pp. 253-269.

Vehicle Moving Evaluation with Simulating Technologies Support

V. Neumann

University of Defence, Kounicova 65, 66210, Brno, Czech Republic, E-mail: vlastimil.neumann@unob.cz

Abstract

The paper presents evaluation of defined vehicle to overcome basic obstacles – step and straight ditches. Basic tool for analysis was used mathematic simulation – especially usage of software ADAMS MSC software. In this software was created mathematic model and this model was tested in different defined states. Analysis and simulation are basic inputs for next development of the vehicle. The vehicle does not have any problem to overcome given step obstacle, but possibility of overcoming defined straight-walled ditches is limited at this vehicle configuration.
KEY WORDS: *simulation, moving, obstacle, model.*

1. Introduction

The aim of this paper is to evaluate moving capabilities of a new design vehicle through basic obstacles with simulating technologies support. This new vehicle is constructed as carrier of special extensions. Maximum speed of the carrier is set to 30 km/h. Maximum dimensions of the vehicle were determined for achieving of maximum mobility (tactical and operational) – width 1700 mm, length 2000 mm, clearance 300 mm. The carrier consists of 3 wheel axles – all-wheel drive, independent suspension of all wheels.

Basic parameters are shown in the Fig.1.

Basic obstacles were selected (according to AVTP-1):
- Step (Fig. 2.) – $h = 300$ mm;
- Staight-walled ditches (Fig. 3.) – $a = 800$mm, h is not defined.
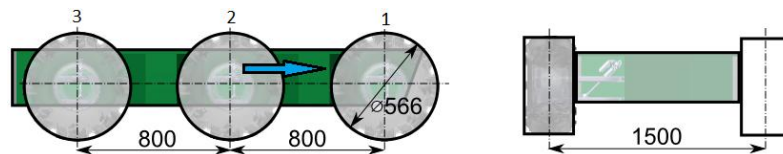
Fig. 1. Basic parameters of the carrier
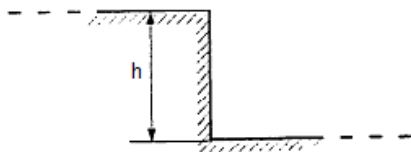
Fig. 2. 1st obstacle – step   Fig. 3. 2nd obstacle - staight-walled ditches
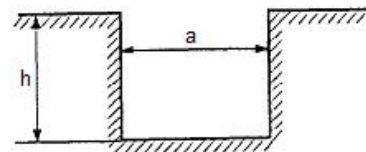
2. Vehicle model

Software ADAMS (Automatic Dynamic Analysis Mechanical Systems) of MSC software was used for mathematic model creating. This software enables testing of virtual prototypes and optimization of their power and safety, without creating of numerous physical prototypes. This tool uses simulation for analysis of complex behaviour of mechanical systems. Created model is shown in the Fig. 4.

Creating mathematic model consists of:
- 37 moving parts;
- 32 revolute joints;
- 6 translation joints.

Basic parts of the model are:
- chassis;
- axles with suspension;
- wheels;
- terrain.
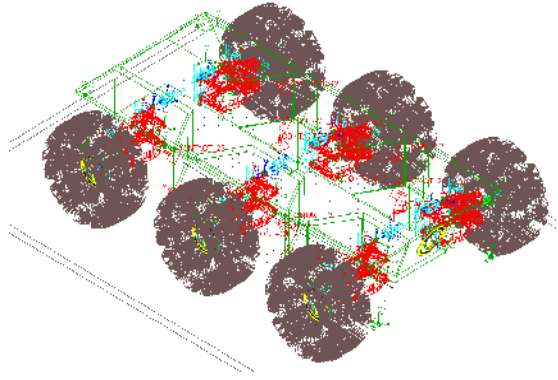
Fig. 4. Created mathematic model

The model has 12 degrees of freedom and enables to simulate vehicle ride on define terrain defined speed. During simulation are recorded basic physical quantities (location, speed, acceleration, load…) of all parts of the model. This model enables to create other modification or states – load changes, change of center of mass, ride without wheel(s)…

3. Simulations

In total eight simulations were proceeded and they are described in the next paragraphs.

3.1. Step crossing

Theoretical high of the step is defined for all-wheel drive vehicles by:

$$h = \left(1 \div \frac{4}{3}\right) r = 283 \div 377 \, \text{mm} \tag{1}$$

where h is high of the step; r is wheel radius.

Desired step high (300 mm) is smaller than maximal theoretical rate (377 mm) – vehicle should overcome the obstacle. This statement was proved by simulation (Fig. 5.).

Fig.5. Vehicle overcoming the step obstacle

3.2. Staight-walled ditches (perpendicular)

Vehicle capability (for vehicles with two and tree axles) of overcoming of straight-walled ditches is limited by sticking wheels in the trench. Maximal trench width (perpendicular entering) is defined by:

$$a = \frac{3}{2} r = 425 \, \text{mm} \tag{2}$$

where a is width of the trench; r is wheel radius.

Desired width (800 mm) is bigger than theoretical rate (425 mm) – vehicle is not capable to overcome the obstacle. This statement was proved by simulation (Fig. 6.).

Vehicles with three axles can overcome this obstacle by appropriate technique of driving. It is necessary to speed up in front of trench – inertial force works against vehicle overturning. In this case vehicle is theoretically able to overcome obstacle define by:

$$a = \frac{3}{2} r + L = 1225 \, \text{mm} \tag{3}$$

where a is width of the trench; r is wheel radius; L is wheelbase.

This manner depends on driver skills and character of a terrain. Possibility of overcoming obstacle by this manner was proved by simulation (Fig. 7.).

Because usage of this manner can be limited, other possibilities were analysed and simulated.
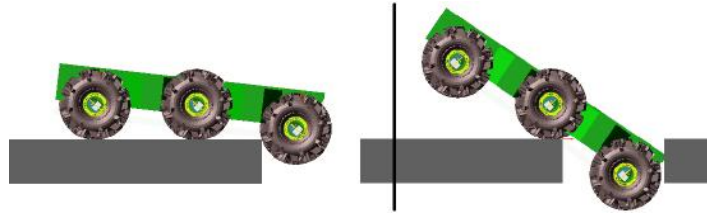
Fig.6. Perpendicular overcomming the trench (small constatnt speed)

Fig. 7. Overcoming the obstacle by appropriate technique of driving

3.3. Staight-walled ditches – active suspension system

The mathematic model was added by active suspension system – spring length was changed during the movement (Fig. 9.). Vehicle speed was low.

Usage of this system decreased vehicle overturning. The model with active suspension system overcame the trench (Fig. 8.). Next option is to change position of center of mass or combination of both systems.
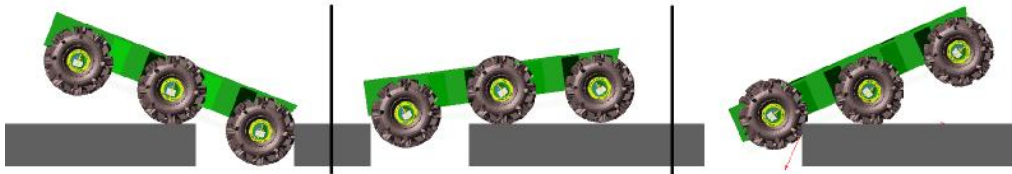
Fig.8. Simulation with active suspension system
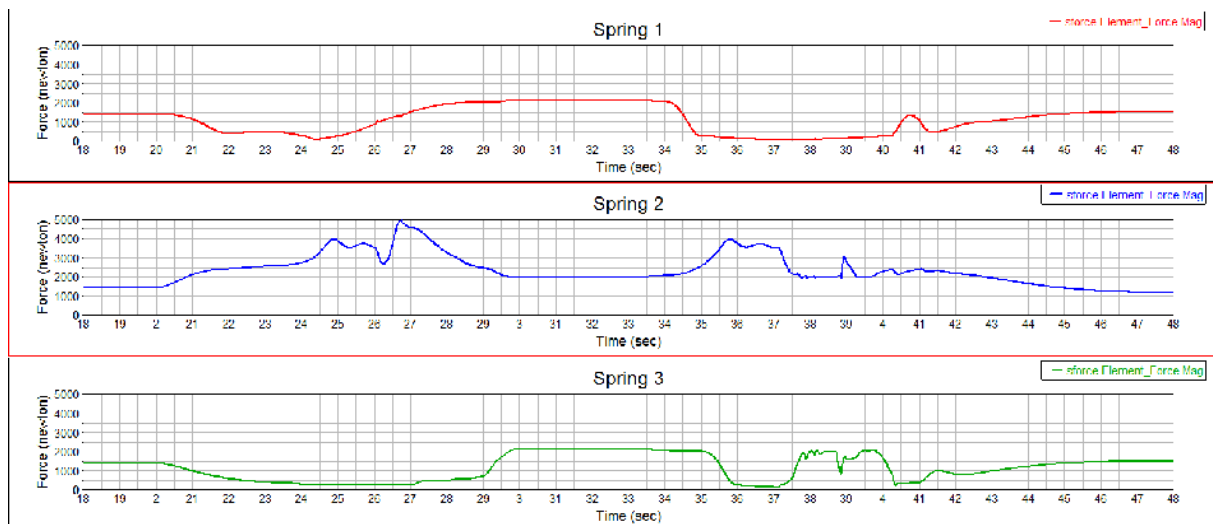
Fig.9. Force of the springs during the silumation (with active suspension)

3.4. Staight-walled ditches – moving with higher speed

This simulation was divided in to two phases. The 1st phase – vehicle speed was the maximum – 30 km/h. The 2nd phase – find the minimum possible speed for overcoming the obstacle. Outcomes from simulation with speed 30 km/h are shown in the next figures.
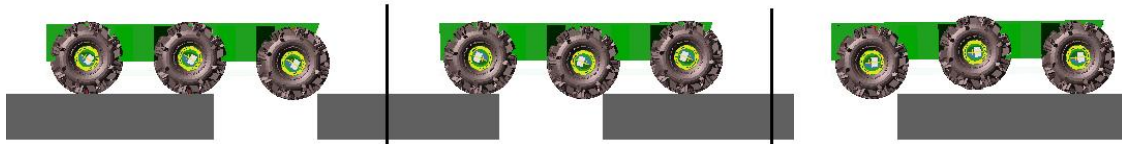
Fig.10. Staight-walled ditches – speed 30 km/h
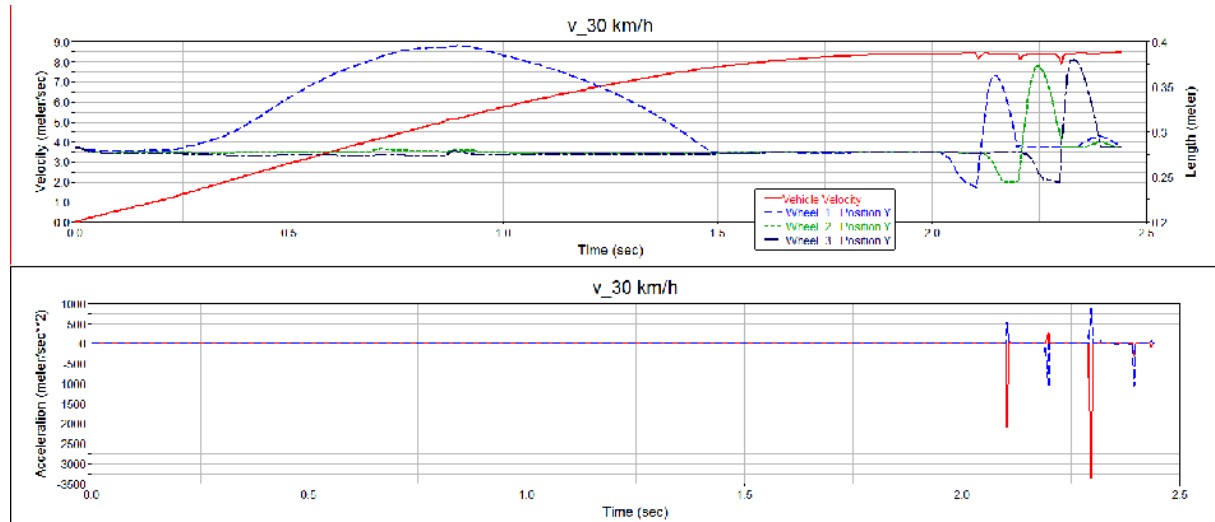
Fig. 11. Staight-walled ditches – speed 30 km/h. Upper graph: red line – vehicle speed, blue line – Y position of 1st wheels; green line – Y position of 2nd wheels; black line – Y position of 3rd wheels. Llower graph: red line – chassis accleration in X axis; blue line – chassis accleration in Y axis

By the next simulations was set the minimal speed for overcoming the trench – 8 km/h. Outcomes from simulation with speed 8 km/h are shown in the next figures.
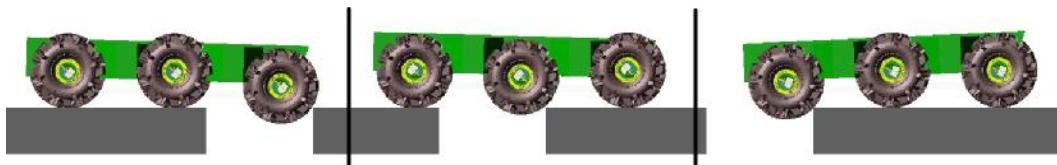
Fig. 12. Staight-walled ditches – speed 8 km/h
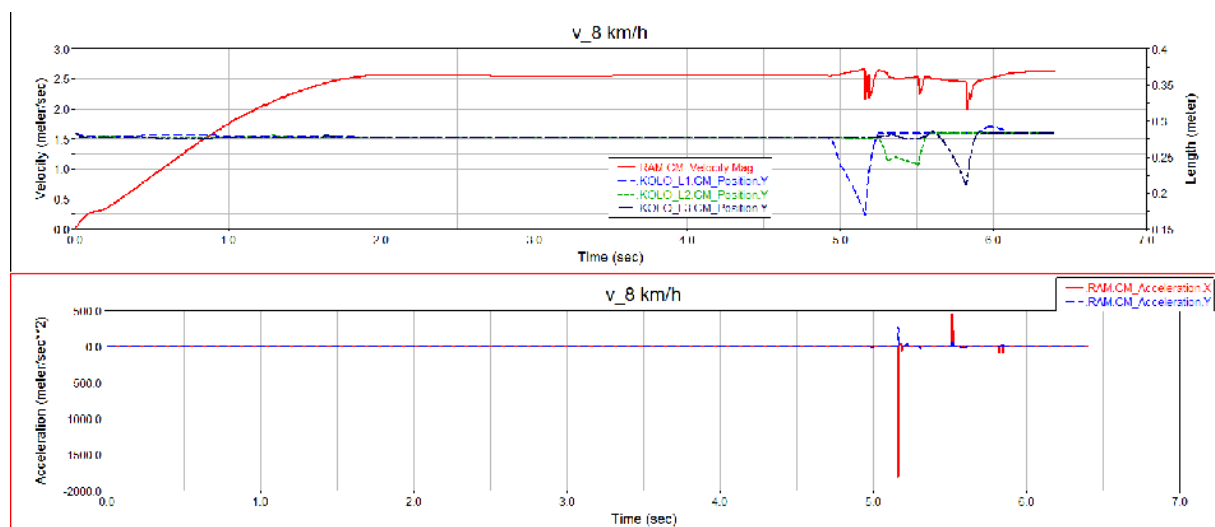
Fig. 13. Staight-walled ditches – speed 8 km/h. Upper graph: red line – vehicle speed; blue line – Y position of 1st wheels; green line – Y position of 2nd wheels; black line – Y position of 3rd wheels. Llower graph: red line – chassis accleration in X axis; blue line – chassis accleration in Y axis

3.5. Staight-walled ditches - diagonally

Next set of simulations was focused on possibility to overcome the trench diagonally (constant low speed). Minimal angle from transverse axle of vehicle was found 10° and maximal angle from transverse axle of vehicle was found 60°. Outcomes from simulations are shown in the next figures.
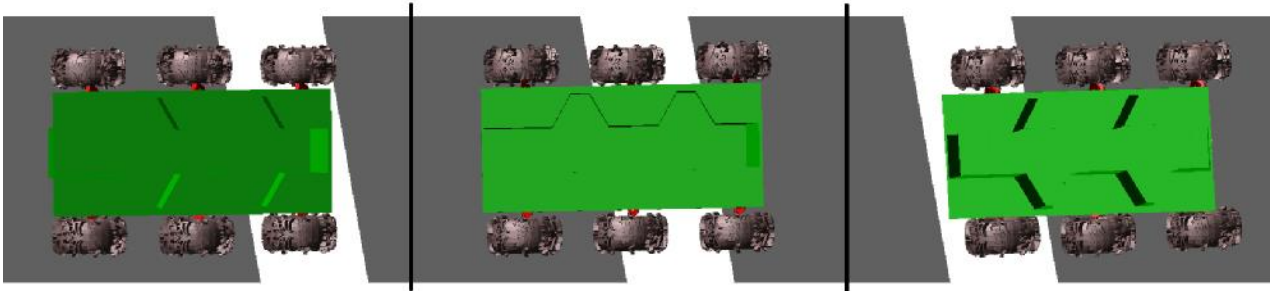
Fig.14. Staight-walled ditches – 10°
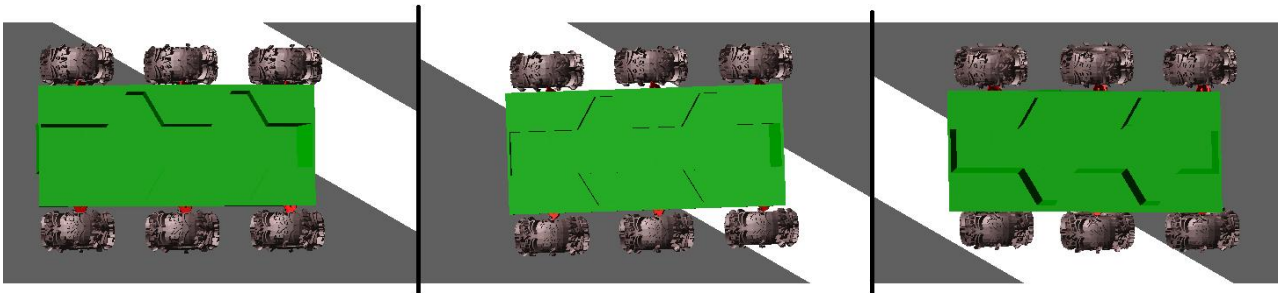
Fig. 15. Staight-walled ditches – 60°
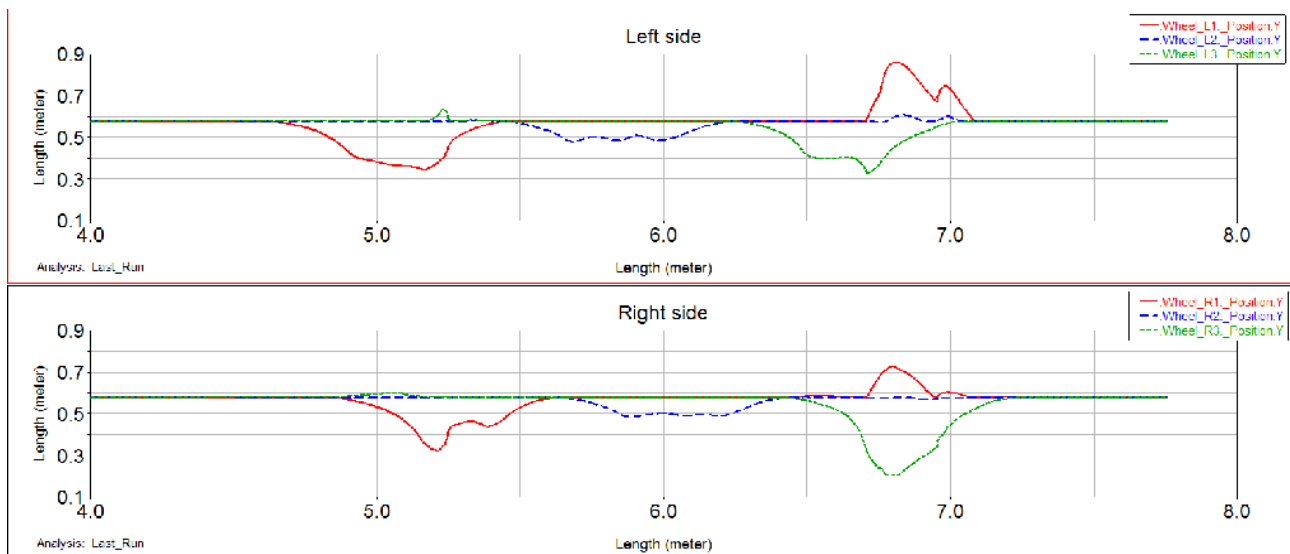
Fig. 16. Staight-walled ditches – 8°. Upper graph: red line – Y position of 1st left wheel; blue line – Y position of 2nd left wheel; green line – Y position of 3rd left wheel. Lower graph: red line – Y position of 1st right wheel; blue line – Y position of 2nd right wheel; green line – Y position of 3rd right wheel
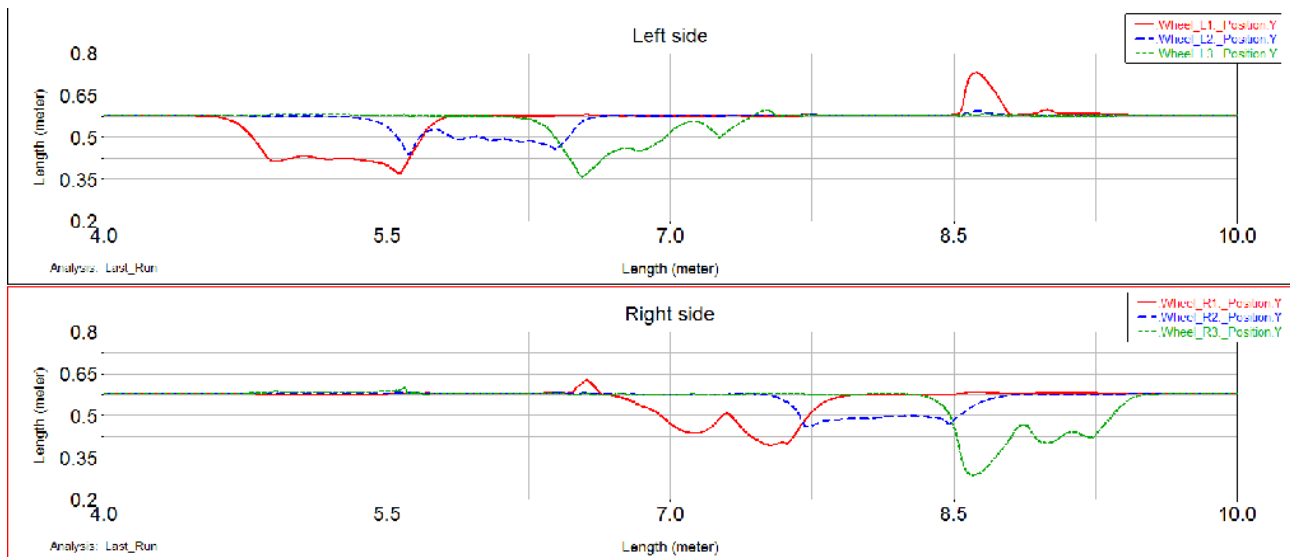
Fig. 17. Staight-walled ditches – 8°. Upper graph: red line – Y position of 1st left wheel; blue line – Y position of 2nd left wheel; green line – Y position of 3rd left wheel. Lower graph: red line – Y position of 1st right wheel; blue line – Y position of 2nd right wheel; green line – Y position of 3rd right wheel

4. Conclusion

From accomplished analysis and simulations were made next statements:

- vehicle does not have any problem to overcome given step obstacle;
- possibility of overcoming the trench can increase some active system – active suspension system or active change of position of center of mass;
- without active system vehicle is able to overcome staight-walled ditches with minimal speed 8 km/h – this manner brings increasing of load of wheels, axles, suspension and chassis (dynamic load, impact);
- vehicle is able to overcome trench diagonally at rate of angles (from transverse axle of vehicle) 10-60°.

Created analysis and simulation are basic inputs for next development of the carrier. If it is necessary to achieve overcoming the staight-wallted ditches in any case, the vehicle construction has to be changed – use some active system, change wheel radius, wheelbase. Possibility of overcoming defined obstacles is limited at this vehicle configuration.

References

1. Allied vehicle testing publications. AVTP-1. 1994. 839p.
2. **Vala M., Braun P.** Vojenská kolová vozidla II: Teorie pohybu vozidel. Brno: VA. 1999. U 1221/2. 391p.

The Stress State in Two−Layer Pipes Subjected to Internal Pressure

N. Partaukas*, J. Bareišis**

*Kaunas University of Technology, Daukanto str. 12, 35212, Panevėžys, Lithuania, E-mail: n.partaukas@gmail.com
**Kaunas University of Technology, Daukanto str. 12, 35212, Panevėžys, Lithuania, E-mail: jonas.bareisis@ktu.lt

Abstract

The stress state in two−layer pipes subjected to internal pressure is analyzed. The stresses obtained by FEM are compared to the stresses determined by analytical techniques proposed by different authors. It was found that assumptions on which analytical models are based can be inadequate. Therefore, the stresses calculated by those techniques can differ significantly from the stresses obtained by FEM. In order to accurately predict the stress state and the strength of layered pipes more sophisticated technique must be developed.
KEY WORDS: *layered pipes, stress state, finite element analysis.*

1. Introduction

Multi−layered structural element (MSE) is a physical body with a finite number of layers, made of two or more different materials. MSEs like composite materials can often replace traditional homogeneous materials. Layered structures are used because of their high strength, resistance to corrosion, lightweight construction and increased material savings [1-3].

MSEs are used in many different areas, such as water supply, heating systems, oil and gas pipelines and reservoirs. Recently layered structures are widely used in buildings and construction industry. For example, beams and columns reinforced with steel or composite jackets [4-6].

Layered structures have many advantages in comparison to conventional ones. Usually they are stronger and more resistant to abrupt failures. For example, a pipe made of poly−ethylene reinforced with a 0.2 mm thick layer of aluminium foil, increases its strength by about 65% [9].

To use a higher strength potential in MS's effectively, accurate methods for stress estimation are necessary. Several analytical techniques for the stresses in layered pipes are proposed [7, 10]. In Ref. [10] formulas for radial and hoop stresses in two−layer thick pipes subjected to internal pressure are presented.

When pipes are thin, radial stresses can be ignored like higher−order terms in comparison to hoop stresses. The latter can be considered as a constant across the wall of each layer. The technique for stresses in such pipes is presented in [7].

In each case, the authors assume that layer displacements are only restricted in radial direction. So displacements in axial direction are unrestricted. Therefore, pressure can neither induce normal stresses in axial direction, nor shear stresses between the layers.

Such an assumption greatly simplifies the mathematical model, but in real structures layers are bonded together and cannot slip freely along each other. So layer displacements in axial direction are restricted. This can induce significant normal stresses in axial direction and shear stresses between the layers.

Some research already demonstrated that such assumptions are not always reliable [11-15]. Therefore, the stress state can be more complicated than predicted by those techniques. The main objective of this research is to compare the results obtained by FEM and analytical techniques [7, 10].

The subject of the present research is two−layer pipe, subjected to internal pressure. Materials of the layers are isotropic, homogeneous and linearly elastic. The MSEs considered are made of layers with the thickness much smaller than their length.

The results presented are compared to those which were obtained by the method of FEM and according to the techniques proposed by other authors. The detected differences among results are analyzed, as well as the validity and limitations of the corresponding techniques are ascertained.

In present study we assume that the structure subjected to lads is in static equilibrium. Layers are bonded together without slip. The FEM simulation was performed with Ansys 13.0.

2. Methods and results

The geometry, loads and stresses in a layered pipe are presented in Fig. 1a. We assume that external loads in the axial direction of the pipe are absent. Usually in piping systems some flexible elements for axial displacement compensation are used. In such case, axial loads are insignificant, therefore can be ignored. So this assumption more or less corresponds to the real strain state of the pipe.

In order to determine the limits within a particular calculation technique to be used, it is necessary to know the differences between the results obtained by various techniques. The differences determined indicate those situations in which their assumptions become inadequate. Thus, the results of the appropriate technique can become inaccurate.

Consider a two-layer pipe subjected to internal pressure $p_{0,1} = 6.67$ MPa (see Fig. 1). Pipe dimensions: $d/h = 0.300$, $D/h = 0.500$, $\psi_1 = 0.750$, $\psi_2 = 0.250$, $t_1/h = 7.92 \cdot 10^{-2}$, $t_2/h = 2.08 \cdot 10^{-2}$. Where ψ_1 and ψ_2 are volumetric ratios of internal and external layers respectively.
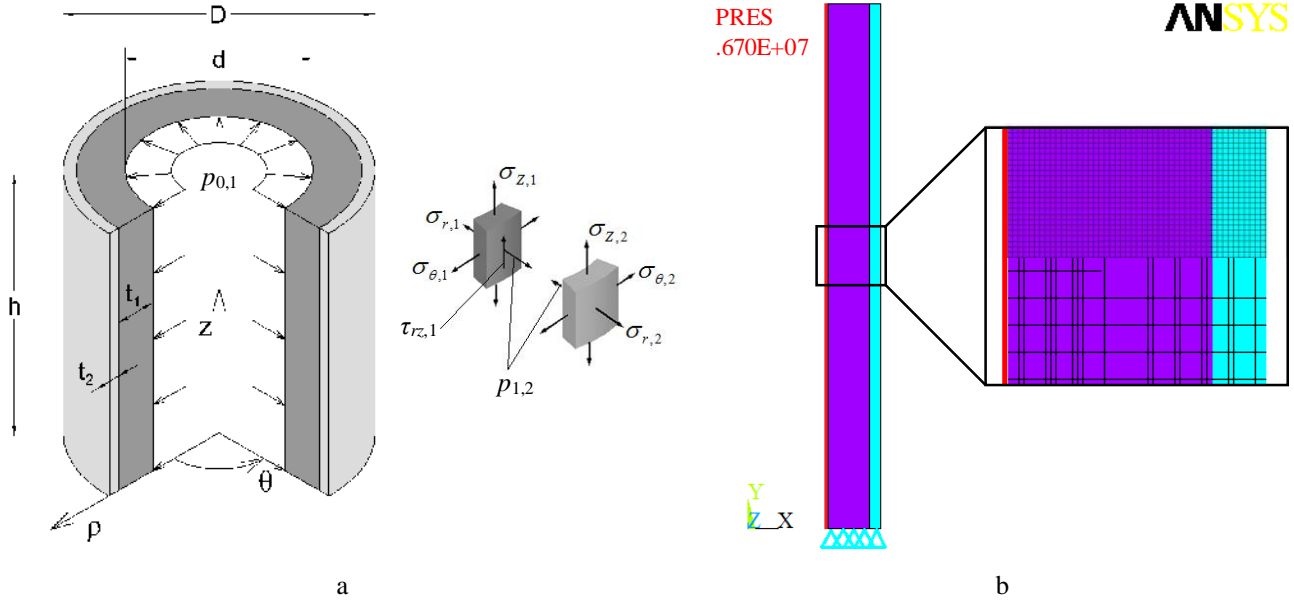
Fig. 1. Geometry and stress state in two–layer pipe subjected to internal pressure (a) and corresponding FEM model (b)

Mechanical properties of the materials: $E_1 = 0.700$ GPa, $E_2 = 70.0$ GPa, $v_1 = 0.340$, $v_2 = 0.420$. Those values roughly correspond to mechanical properties of Poly–ethylene and aluminium.

Let's assume that $h = 1$ m, then according to [10] contact pressure between the layers:

$$p_{1,2} = \frac{2 \cdot p_{0,1}(R_i^2 - 1)^{-1}}{\left(\frac{R_i^2 + 1}{R_i^2 - 1} - n_1\right) + \frac{E_1}{E_2}\left(\frac{R_o^2 + 1}{R_o^2 - 1} - n_2\right)} = \frac{2 \cdot 6.67 \times 10^6 (1.5\bar{2}8^2 - 1)^{-1}}{\left(\frac{1.5\bar{2}8^2 + 1}{1.5\bar{2}8^2 - 1} - 0.340\right) + \frac{0.700 \times 10^9}{70.0 \times 10^9}\left(\frac{1.0\bar{9}1^2 + 1}{1.0\bar{9}1^2 - 1} - 0.420\right)} = 4.4\bar{0}4 \times 10^6 \text{ Pa} \quad (1)$$

where: $R_i = 1 + 2\dfrac{t_1}{d} = 1 + 2\dfrac{7.92 \times 10^{-2}}{0.300} = 1.5\bar{2}8$, $R_o = \dfrac{D}{d + 2 \cdot t_1} = \dfrac{0.500}{0.300 + 2 \cdot 7.92 \times 10^{-2}} = 1.0\bar{9}1$.

The radial and hoop stresses in each layer are found according to Lame (*G. Lamé*) equations. For internal the layer:

$$s_{\frac{r,1}{q,1}}(r) = \frac{r_1^2 p_{0,1} - r_2^2 p_{1,2} \pm (p_{1,2} - p_{0,1})r_1^2 r_2^2 r^{-2}}{r_2^2 - r_1^2} = \frac{(0.15\bar{0})^2 \cdot 6.67 \times 10^6 - (0.22\bar{9}2)^2 \cdot 4.4\bar{0}4 \times 10^6}{(0.22\bar{9}2)^2 - (0.15\bar{0})^2} \pm$$

$$\pm \frac{(4.4\bar{0}4 - 6.67) \times 10^6 \cdot (0.15\bar{0})^2 \cdot (0.22\bar{9}2)^2 r^{-2}}{(0.22\bar{9}2)^2 - (0.15\bar{0})^2} = \left(-2.7\bar{0}4 \, \mathbf{m} \, \frac{0.089\bar{1}8}{r^2}\right) \times 10^6 \text{ Pa} \quad (2)$$

where: $r_1 = \dfrac{d}{2} = \dfrac{0.300}{2} = 0.15\bar{0}$, $r_2 = \dfrac{d + 2 \cdot t_1}{2} = \dfrac{0.300 + 2 \cdot 7.92 \times 10^{-2}}{2} = 0.22\bar{9}2$, $r_3 = \dfrac{D}{2} = \dfrac{0.500}{2} = 0.25\bar{0}$.

Similarly for the external one:

$$s_{\frac{r,2}{q,2}}(r) = \frac{r_2^2 p_{1,2}}{r_3^2 - r_2^2}\left(1 \, \mathbf{m} \, \frac{r_3^2}{r^2}\right) = \frac{(0.22\bar{9}2)^2 \cdot 4.4\bar{0}4 \times 10^6}{(0.25\bar{0})^2 - (0.22\bar{9}2)^2}\left(1 \, \mathbf{m} \, \frac{(0.25\bar{0})^2}{r^2}\right) = \left(2\bar{3}.2 \, \mathbf{m} \, \frac{1.\bar{4}5}{r^2}\right) \times 10^6 \text{ Pa} \quad (3)$$

According to [10], it is assumed that normal stresses in axial direction and shear stresses between the layers are equal to zero. Radial and hoop stresses vary across the wall. Then stress intensity depends on the radius:

$$s_{e,1}(r) = \sqrt{7.3\bar{1}2 + \frac{0.023\bar{8}6}{r^4}}\,\text{MPa}\,; \quad s_{e,2}(r) = \sqrt{5\bar{3}8 + \frac{6.\bar{3}1}{r^4}}\,\text{MPa} \tag{4}$$

According to [7], only the hoop stresses exist, which are constant across the wall of each layer:

$$s_{e,1} = s_{q,1} = \frac{p_{0,1} r_1 E_1}{E_1 t_1 + E_2 t_2} = \frac{6.67 \times 10^6 \cdot 0.15\bar{0} \cdot 0.700 \times 10^9}{0.700 \times 10^9 \cdot 7.92 \times 10^{-2} + 70.0 \times 10^9 \cdot 2.08 \times 10^{-2}} = 0.46\bar{3}5 \times 10^6\,\text{Pa} \tag{5}$$

$$s_{e,2} = s_{q,2} = \frac{p_{0,1} r_1 E_2}{E_1 t_1 + E_2 t_2} = \frac{6.67 \times 10^6 \cdot 0.15\bar{0} \cdot 70.0 \times 10^9}{0.700 \times 10^9 \cdot 7.92 \times 10^{-2} + 70.0 \times 10^9 \cdot 2.08 \times 10^{-2}} = 46.\bar{3}5 \times 10^6\,\text{Pa} \tag{6}$$

The results calculated by [7], [10] and FEM are presented in Fig. 2-4 and Table 1. The stresses in cross–section of the wall are depicted in Fig. 2 (FEM results are taken at the cross-section where $z = h - 5\,t_1$). The numerical values of stresses in each layer are presented in Table 2. Stress variation in axial direction at the contact between the layers is presented in Fig. 3 and 4.
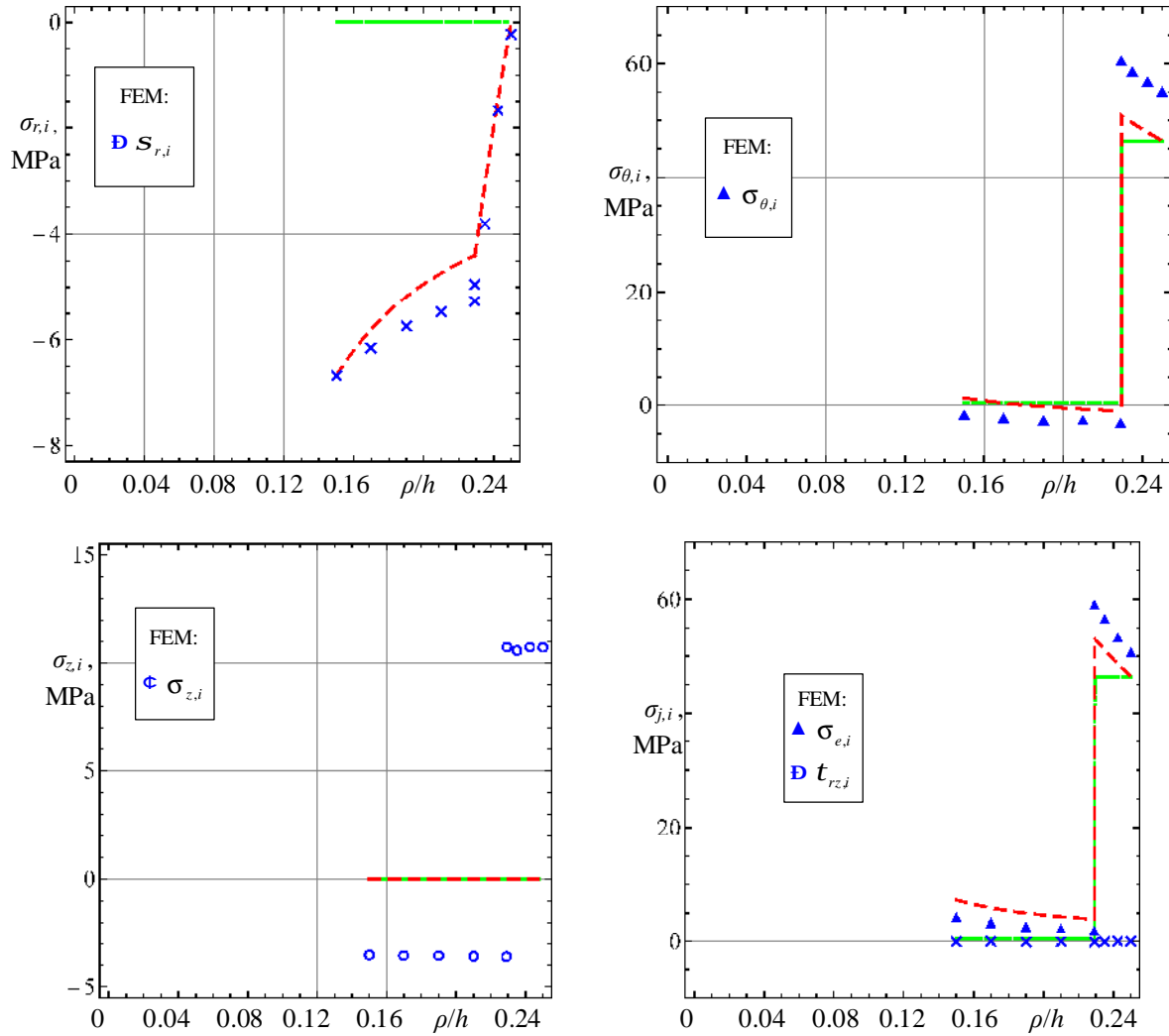
Fig. 2. Stress variation in a cross section, according to: [7] (——), [10] (— —) and FEM (• , ▲, ›)

Table 1

Comparison of results obtained by [7], [10] and FEM

i	$\sigma_{r,i}$, MPa			$\sigma_{\theta,i}$, MPa			$\sigma_{z,i}$, MPa			$\sigma_{e,i}$, MPa		
	FEM	[7]	[10]	FEM	[7]	[10]	FEM	[7]	[10]	FEM	[7]	[10]
1	-6.67	0	-6.67	-1.67	0.464	1.26	-3.53	0	0	4.37	0.464	7.38
2	-5.12	0	-4.40	60.5	46.4	50.8	10.7	0	0	59.2	46.4	53.1

Note: stress values are taken at the internal surface of each layer.

Stress variation along the *oz* axis at the contact between the layers is presented in Fig. 3 and Fig. 4. It should be noted that radial stresses in Fig. 4 are presented with a different scale on the left axis.
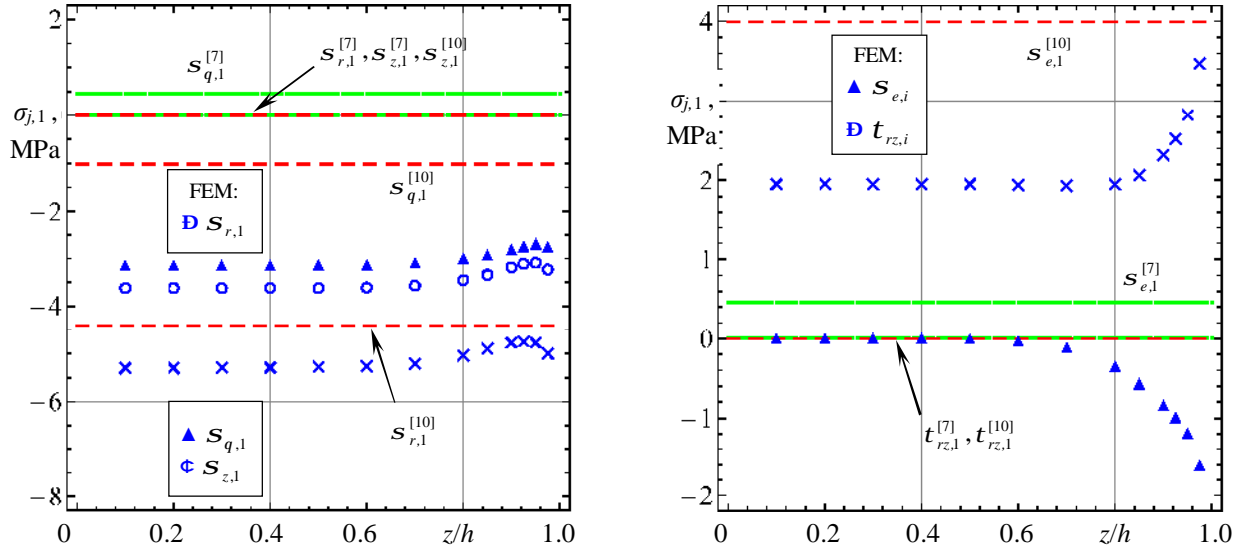
Fig. 3. Stress variation along the axis *oz* in PE layer, according to: [7] (——), [10] (— —) and FEM (• , Ñ , ›)
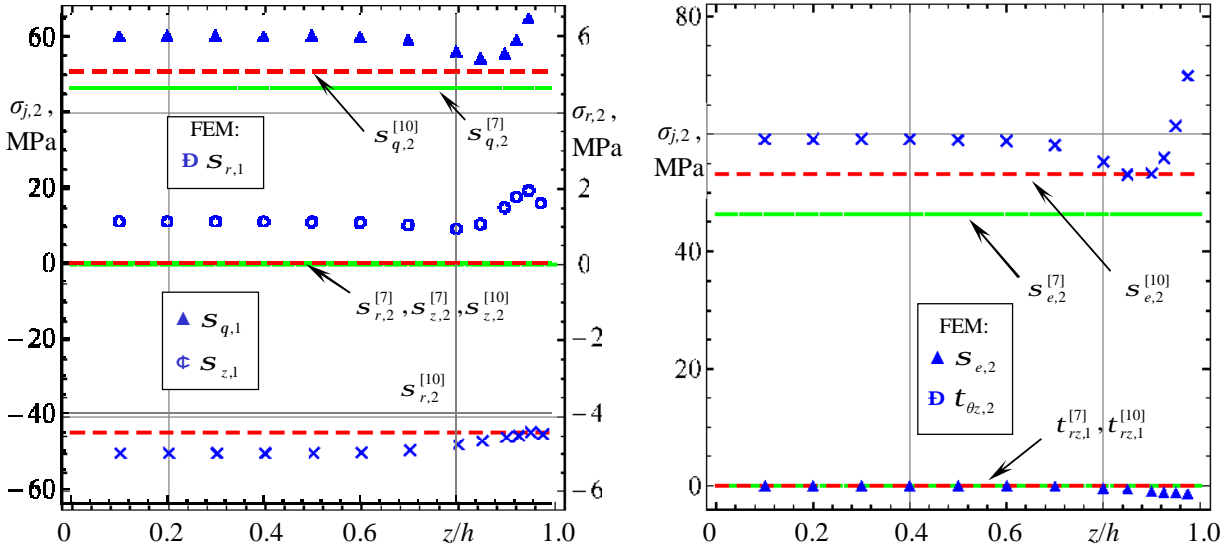
Fig. 4. Stress variation along the axis *oz* in Al layer, according to: [7] (——), [10] (— —) and FEM (• , Ñ , ›)

3. Discussion and conclusions

From the results presented it is obvious that stresses obtained by FEM and in analytical terms differ significantly (Fig. 2-4). For example, a stress value in the internal layer according to [7] and [10] differs respectively by 89% and 69% in comparison to FEM. For the external one those differences are respectively 22% and 10%. Even if the differences in aluminum layer are much smaller, still they are too large to ignore.

The differences in stress intensities can be explained by comparing the constituents of the stress state. According to the techniques [7], [10] axial stresses ($\sigma_{z,i}$) are absent. An FEM result indicates that they exist in both layers. In the internal layer they are approximately equal to the stress intensity. In the external one they approximately correspond to 20% of the stress intensity. Consequently, the assumption about the non–existence of axial stresses or even their relative insignificance is fallible.

Axial deformations of the layers cause stresses in the axial direction. The layers during deformations remain bonded together; this restrains the possible displacements in the axial direction. As a result, stresses in the axial direction appear. A similar effect in MSEs subjected to different loading conditions has been reported previously [11–15].

By analyzing radial stresses we see that the contact pressure between the layers according to FEM is about 14% higher than the one calculated by [10]. Therefore, the hoop stresses according to [10] are lower than the ones obtained by FEM.

Even higher differences were observed comparing the results according to [7]. That can be attributed to the fact that the layers are not thin (Fig. 1). Therefore, radial stresses cannot be considered as higher order terms in comparison to the hoop stresses. Nonetheless, techniques [7] and [10] give more or less similar values of stress intensities in the external layer. Consequently, we can expect that for the thin wall pipe both techniques will produce similar results.

FEM results confirm the assumption that the shear stresses at the layer contact are higher order terms in comparison to other stresses. Actually, this is only true at some distance from the free edge of the pipe (Fig. 3, 4). In the other case shear stresses cannot be ignored.

Stress variation along the axis (Fig. 3, 4) suggests that two different zones can be distinguished there. In the regular zone the material is only to subjected normal stresses. Here the stresses can be considered as constant along the axis. Contrary to this, at the zone of irregular stress distribution they vary widely. In addition, significant shear stresses arise.

By referring to the results presented we conclude that:

1. In a layered pipe subjected to internal pressure stresses in the axial direction arise. Those stresses cannot always be considered as insignificant, when compared to the other stress state components.
2. Shear stresses between the layers can be treated as higher order terms only at the sections far from the end of the pipe. Closer to the free edge, stresses vary widely in the axial direction.
3. By using the techniques which ignore the influence of axial deformations, essentially different stress/strain state and their values can be obtained in comparison to those obtained by FEM. The differences between the stress intensities can be smaller, but even then they can differ significantly.
4. In order to accurately predict the stress state and the strength of layered pipes, a more sophisticated technique must be developed. This technique should consider the stress/strain state which emerges in layered pipes subjected to internal pressure more accurately.

Acknowledgements

References

1. **Lifshitz J.M., Dayan H.** Filament-wound pressure vessel with thick metal liner. Composite Structures, 1995, 32(1-4), pp. 313-323.
2. **Nezbedova E., Knesl Z., Vlach B.** Analysis of fracture behaviour of multilayer pipes. Plastics, Rubber and Composites, 2007, 36(5), pp. 207-212.
3. **Chen P.-Y. et al.** Structure and mechanical properties of selected biological materials. Journal of the Mechanical Behavior of Biomedical Materials, 2008, 1(3), pp. 208-226.
4. **Kuranovas A., Kvedaras A.K.** Behaviour of hollow concrete-filled steel tubular composite elements. Journal of Civil Engineering and Management, 2007, 13(2), pp. 131-141.
5. **Tamuzs V. et al.** Behavior of concrete cylinders confined by a carbon composite: Prediction of strength. Mechanics of comosite materialks, 2007, 43(5), pp. 657-665.
6. **Kvedaras A.K., Kudzys A. Valiunas B.** Reliability verification for composite structures of annular creoss section. Mechanics of Com posite Materials, 2009, 45(4), pp. 407-414.
7. **Wang X., Li M.D., Yu Z.Y.** Self-strengthening research of fiber reinforced pressure vessel with metallic liners. Journal of reinforced Plastics and Composites, 2001, 20(16), pp. 1390-1413.
8. **Ivanov S.G. et al.** Modeling the mechanical behavior of metal-reinforced thermoplastic pipes under internal pressure. Mechanics of Composite Materials, 2005, 41(1), pp. 57-70.
9. **Bowman J.** Long-term behaviour of an aluminium-reinforced polyethylene pressure pipe. Journal of Materials Science, 1993, 28(4), pp. 1120-1128.
10. **Farshad M.** Determination of the long-term hydrostatic strength. Polymer Testing, 2005, 24, pp. 1041-1048.
11. **Partaukas N., Bareišis J.** The stress state in two-layer hollow cylindrical bars. Mechanika, 2009, 15(1), pp. 5-1.
12. **Liu B., Feng X., Zhang S.-M.** Young's modulus of composites beyond the Voigt estimation due to the Poisson effect. Composites Science and Technology, 2009, 69, pp. 2198-2204.
13. **Lu Y., You Z.** Formulization of asphalt concrete stiffness for specific microstructures based on discrete element method. In Paving Materials and Pavement Analysis: GeoShanghai 2010 International Conference, 2010, June 3-5, Shanghai, China. pp. 135-149.
14. **Partaukas N., Bareišis J.** Poisson's ratios influence on strength and stiffness of cylindrical bars. Mechanika, 2011, 17(2), pp. 132-138.
15. **Partaukas N., Bareišis J.** Numerical Analysis of Free Edge Effect in Out-Of-Plane Loaded Sandwiches. In Mechanika 2012: 17th International Conference, 2012, April 12-13 2012, Kaunas, Lithuania. pp. 218-223.

Adaptive System of Smooth and Accurate Braking of Railway Transport

A. Potapovs*, M. Gorobetz**, A. Levchenkov***

*Institute of Industrial Electronics and Electrical Engineering, Riga Technical University, 1, Kalku Street, LV-1658, Riga, Latvia, Andrejs.Potapovs@rtu.lv
**Institute of Industrial Electronics and Electrical Engineering, Riga Technical University, 1, Kalku Street, LV-1658, Riga, Latvia, mihails.gorobecs@rtu.lv
***Institute of Industrial Electronics and Electrical Engineering, Riga Technical University, 1, Kalku Street, LV-1658, Riga, Latvia, anatolijs.levcenkovs@rtu.lv

Abstract

This article considers the structure and operation principles of a new adaptive system of starting and accurate braking of railway transport. This system is based on the application of embedded intelligent device, the existed braking equipment of the railway transport, auxiliary mechanical parts as well as adaptive searching algorithms playing a significant role in the effectiveness of the proposed system. The article contains definitions of the functions of the main blocks of the systems under consideration and their mathematical descriptions. Additionally the algorithm of system operation is described. The prototype of the proposed device was tested, the obtained results, advantages and further development opportunities were considered.
KEY WORDS: *adaptive systems; intelligent control, railway transport.*

1. Introduction

In the industry of railway transport during the last years great steps are taken for the increasing of movement speed of this transport. The intensity of the transport is also constantly increasing. These facts also results in the necessity to solve different problems appearing with the increasing speed of transport. One of these problems is safety level that should be maintained at the same or even higher level than before. For this purpose a new adaptive system for the railway transport starting and accurate braking was developed directed to the automatic stopping if railway transport applying the operational braking mode.

Applying for the system functions of the previously developed equipment [2], it can fully operate with an improved level of railway transport safety. The positive aspects of the system can also include the fact that comparing with those previously developed it allows control the speed of a vehicle at any sector of a route and decrease it up to a particular value determined by the norms of railway safety. The process of the development of the proposed systems requires its mathematical model and prototype, deep analysis of it and testing for detection of the system's drawbacks and further improvements. The testing of the prototypes often discovers some problems that is not possible to find by means of theoretical analysis only.

Therefore the article also considers the description of the equipment components that are applied in one common braking control system with the use of global positioning system as well as wireless connection system providing the basic operational functions: timely determination of the of the location of the objects and data transfer among the basic units of the system. The application of the programming logic controllers gives an opportunity to solve complex tasks of the railway transport control.

2. Purpose and Tasks

The basic purpose of the authors is to realize an analysis of the selected algorithm of the adaptive system operation of railway transport starting and accurate braking and testing of this system and its basic elements under the laboratory and real work conditions.

Main objectives of the work:
- To describe the main elements of the adaptive system of the railway transport starting and accurate braking.
- To define functions realized by the basic elements of the system.
- To develop mathematical model and operation algorithms of the basic elements of the system.
- To test the system's elements in the laboratory and working conditions.
- To test the prototype of the device under real operation conditions and analyse the obtained results.

3. Basic elements and functions of the new adaptive system of railway transport soft and accurate braking

As it was mentioned above the task of the adaptive system of starting and accurate braking of railway transport is to improve safety without any cardinal changes in the existing control system of the trains decreasing in parallel the impact of human factor on the process of railway transport routing.

Therefore, one of the most important questions is to integrate the basic elements of the adaptive system of railway transport starting and accurate braking in order not to decrease the functionality and safety level of the existing control system.

The basic functions of the proposed system are realized by means of 3 types of devices - equipment of locomotive (LI) [3], equipment of the way sector (CPI and equipment of the control centre (VCI).

The descriptions of the physical components of LI and CPI are available in the stated information sources. The principal block diagram of the basic elements of the proposed system is given in Fig. 1.
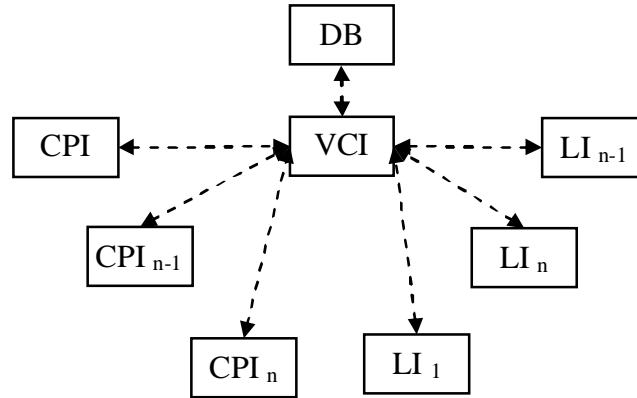
Fig. 1. Block diagram of the information flow of main elements of the adaptive system of starting and accurate braking of railway transport

The system should provide the application of more control devices (VCI) (for example, one VCI device for a particular area, for a particular station of number of way sectors) with the purpose to divide its load and take get a possibility substitute the functions of each device for the case of failures.

It is also necessary to provide the connection of each VCI device to the general data base of information saving (DB) with the purpose to synchronize its operation and for the constant initialization and further use of the actual data.

The locomotive equipment that basic elements of which are marked with yellow (fig. 2) is installed at the locomotive or other railway train equipped with pneumatic braking system. Its electric pneumatic valve (EPV) and auxiliary electric manometer (M) are integrated into the railway transport braking system (BrM). The relay of device emergency control (R) is connected to the unit of railway emergency braking control (ABM) to stop the train if it is necessary. The device also contains the modulus of global positioning (GPS) and Global System for Mobile Communication (GSM) the purpose of which is to provide the main programming logic controller (PLC) with the necessary information about the location of railway transport, speed, railway infrastructure equipment operation conditions and other necessary information from the data base of the control centre or other trains.

The equipment of the way sector is installed in the main enclosure of railway station control relays(Fig. 3) with the purpose to read the conditions of the device (railway crossing (DP)) and indications (for traffic lights (L)). The way sector is also equipped with GSM module for the sending of the information from the control relays to the central control. The device is connected to the correspondent contact groups of the control relay of the crossing (PKR) and control relays of the traffic lights (LKR).

The principal scheme of the new adaptive railway transport braking system integration:

LOK – locomotive or any other unit of ;railway transport;

VAG – wagons of the rolling stock (e.g., cargo wagons);

K – compressor for the compressed air generation;

AV – emergency valve for the decreasing of air compressing;

GR – main reservoir for the compressed air storage;

MK – controller of a locomotive driver manually regulating the braking system of railway transport;

GSR – relay of the air compressing (is actuated whet the pressure BrM is decreased for 3 kgf/cm2)

GSP – commutator of electric train;

ABM – control unit of emergency braking;

BrM – air main of braking system;

KR – reservoir for storage of compressed air at each wagon;

G – air divider, servicing for the dividing of the air flow according to the control regime of each braking system;

BC – braking cylinder driving the the power of air pressure to the braking shoe;

ATM – accepted marking for environment;

VVS – control system of the train.

The locomotive device (LI) contains the following main elements:

- D – display of the information output;
- R – control relay of the emergency braking regime;
- EPV – electric pneumatic valve for the for the regulation of air pressure for braking;

- M – manometer for the measuring of the air pressure in barking system;
- PLC – main programming logic controller;
- GPS – modulus of the global positioning system;
- GSM – Global System for Mobile Communication.
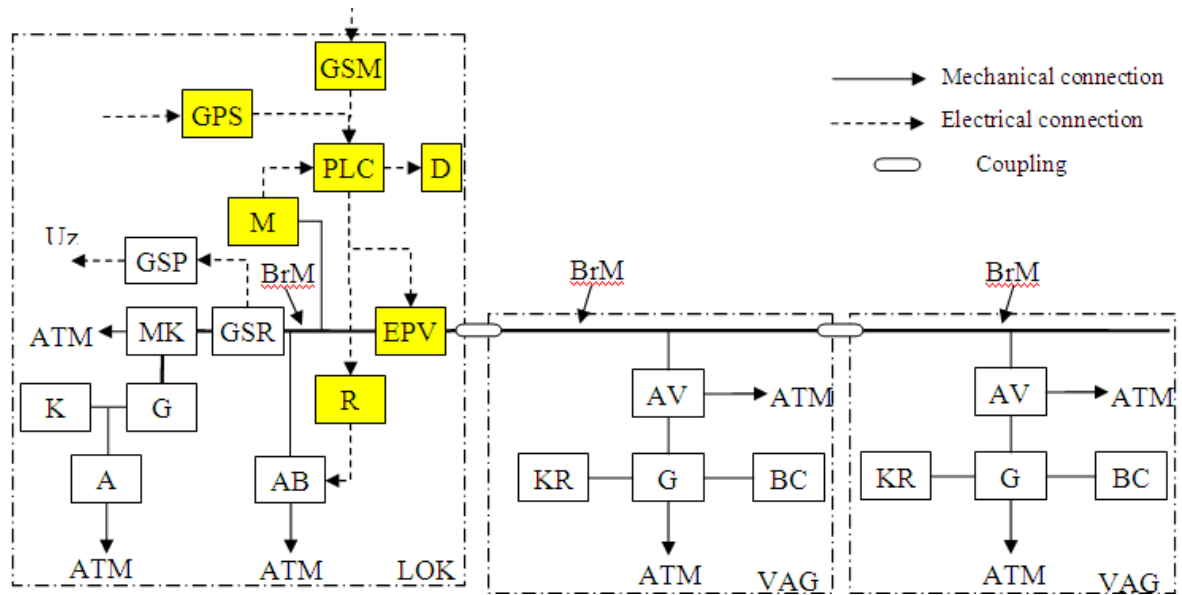
Fig. 2. Principal scheme of the integration of the new adaptive system of railway transport starting and accurate braking
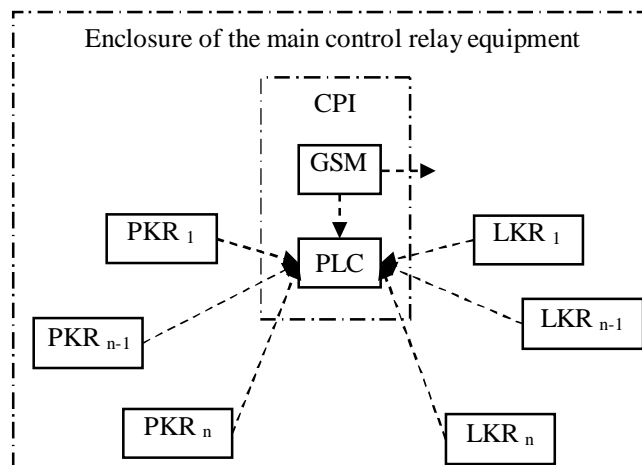
Fig. 3. Block diagram of the sector device

4. Mathematical models and operation algorithms of the main units of the new system

To date three main types of system equipment are assigned. Therefore further the algorithm of the operation of this device will be considered separately.

Briefly the algorithm of the control centre operation can be described in the following way:

a) VCI gets the information (location, route and identification number) from each particular railway vehicle equipped with LI;

b) VCI defines the railway vehicles moving along one route and are close to each other and sends them the identification numbers with the purpose to give them an opportunity to exchange with data for avoiding a potential collision;

c) Using data from data base DB and obtained information from railway transport VCI defines the zone of this vehicle movement and the movement restrictions within this zone;

d) VCI sends the obtained information from DB to LI for further processing;

e) In the case if there is a station in the zone LI obtains the identification number of this station for communication with the CPI of the station and information about the readiness of the route, for the information of the traffic lights situated on this route and any possible restrictions.

The following functions are in the basis of operation algorithm of the distance sector:

- Main PLC of CPI onto its input contacts obtains the signals about the conditions of the crossing, prepared routes and traffic lights;
- CPI sends the obtained information to VCI input into data base and control in the real time;
- On demand CPI sends the obtained information from a railway vehicle LI;
- CPI realizes possible diagnostics of the emergency regimes and in necessity VCI as well as LI send the emergency signal.

The special attention will be turned to the description of the locomotive operation algorithm.

First of all let us describe the basic functions completed by the devices:

- Processing of the information obtained from VCI;
- According to the obtained identification number a communication takes place with CPI of the station or LI of railway transport;
- Determination of the necessity to realize the working braking because of possible collision or some restrictions on the route;
- Approximate determining of emergency braking distance of railway transport using the available data;
- Realization of the working braking process;
- Realization of the emergency braking process.

The algorithm of the emergency braking operation of railway transport applying LI is described according to [3]. For the realization of soft working braking process an adaptive searching algorithm is applied , as well as special learning algorithm. The purpose f the learning algorithm is to define the effectiveness of the train braking system in the cases when the working braking is applied. The analogue of this value in the calculations of railway transport braking is marked as and called as a braking factor. This factor means the development of total power of braking of the rolling stock over the whole weight of the rolling stock.

But the application of this value is complicated due to the necessity in its calculation (formula 1) of input information that practically impossible to obtain

$$n_p = \frac{m_1\, n_1\, k_1 + m_2\, n_2\, k_2}{Q + P} \tag{1}$$

where, m_1 – number of wagons; n_1 – number of wagons axes; k_1 – specific power of pressing of cargo wagons braking shoe; m_2 – number of locomotives; n_2 – number of locomotive axes; k_2 – specific power of pressing of locomotives braking shoe; Q – total mass of wagons, t; P – mass of locomotive, t.

Therefore it is necessary to introduce a factor of efficiency of a new braking system (BSef), that according to the available parameters processing describes the condition of the whole rolling stock or of one unit of the braking system (the effectiveness of braking under different conditions).

The learning algorithm determines BSef (2) at the moments when the braking is realized by driver manually.

Manometer M installed on LI fixes the decreasing of air pressure in the braking main BrM.

If a working braking step is fixed then the changing of speed and acceleration of of the realised braking are also fixed.

There parameters are enough to calculate the approximate value of BSef factor.

$$BS_{ef} = f(\Delta P; \Delta V; a_{br}) \tag{2}$$

where, ΔP – changing of the air pressure in the braking main realizing one braking step; ΔV – changing of the railway transport speed realizing one braking step; a_{br} – average braking acceleration of railway transport realizing one braking step.

For higher effectiveness of the system operation the calculation of this factor is required at each step of working braking as well as at each speed of movement, description of the way profile and at fixing the outside conditions; in opposite cases the factor is accepted as low as possible within this or that zone. With possible changes of the rolling stock (e.g. changing number of wagon, etc.) the calculation of factor BSef is repeated.

The application of this factor is foreseen during the working of the adaptive searching algorithm, completing the theoretical curves of the railway transport movement during the automatic adaptive and soft braking. The introduction of BS_{ef} factor allows to improve the effectiveness and safety of braking process. The curves can be similar to those in Fig. 4.

Fig. 4. demonstrates the theoretical curves of the speed and braking acceleration (red colour line) of a cargo train model and the same curves resulted in the system's operation time realising the soft and accurate braking before the stop point (blue colour line). In accordance with higher BSef (the defined higher railway transport braking system effectiveness) the higher realised theoretical braking acceleration is preset and opposite.

This value can be accordingly accurately defined while testing the prototype of the system device.
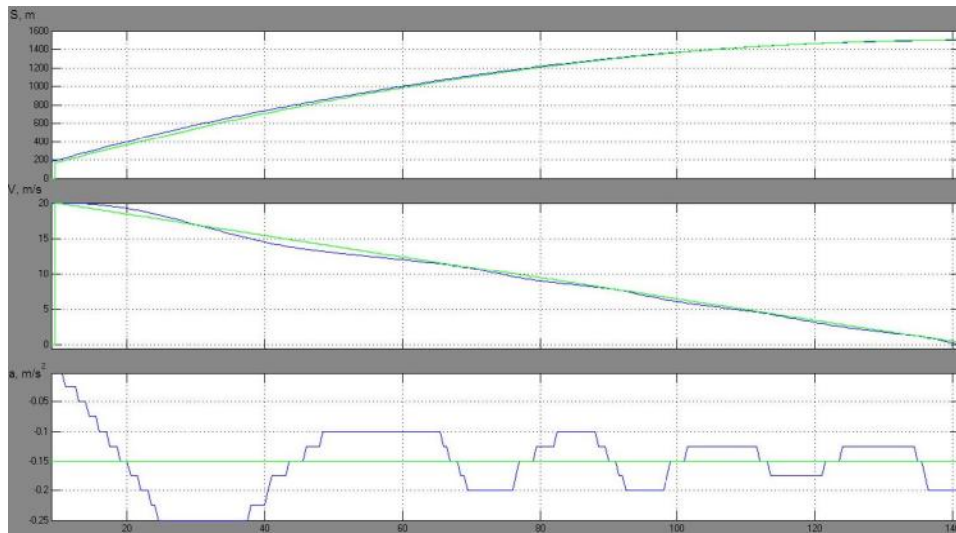
Fig. 4. Dependence of the model movement parameters on time

In compliance with the made before analysis of the searching algorithm [4] the basis of the adaptive searching algorithm operation is the application of adaptive searching together with the integrated testing and working steps modifying them.

The modification of the selected algorithm results in the introduction of a differential unit (Fig. 5, yellow marked) following the controlled parameters changing with time and making the whole system operation significantly more effective (decreasing pulsations of the regulated parameters according to the theoretical values and increasing the accuracy of the railway rolling stock stop point).
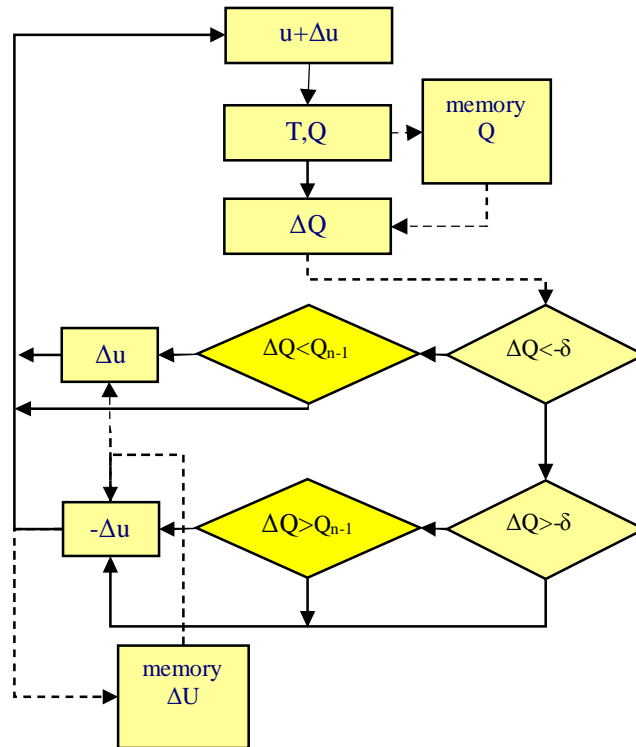
Fig. 5. The algorithm of the adaptive searching with integrated testing and working steps with a differential units

5. Analysis of the results and evaluation of the operation effectiveness of the prototype device

At the moment the following results are achieved:
- The prototypes of the system's devices are able to stop the railway rolling stock with a necessary accuracy (using working braking with accuracy +/- 2m; using emergency braking with accuracy +/-10 m from a particular safety point).

- To date PLC control program on the basis of adaptive searching algorithm allows generation of control signals according to which the driver realizes the steps of the braking or cancels it (as a perspective the electric pneumatic valve is regulated).
- A mathematical model of railway transport braking system and its control is developed describing the functional interdependency of the changes of distance, speed, braking acceleration and air pressure of braking main.
- During the control computer model validation the railway transport adaptive braking systems are fixed; and the stop locations of the model are compared with those being pre-set, that allows to conclude that the operation of total parametric adaptive algorithm is precise and corresponds to the real railway transport braking system.

6. Conclusions

The proposed algorithm of the train adaptive and accurate braking works effectively enough that allows continue the further investigations in this direction.

The testing and its results proved that the proposed system completes its tasks and main functions according to the necessary plan.

For the improvement of the effectiveness of the algorithm operation it is necessary to complete an analysis of application of another adaptive algorithm that is the task of further authors' publications.

References

1. **Rui Calçada.** Track-Bridge Interaction On High-Speed Railways. CRC Press, 2008. – 215 p.
2. **Andrejs Potapovs, Mikhail Gorobetz, Anatoly Levchenkov**. Use of Adaptive Control Algorithms for Smooth Braking of Train Using PLC. To jut out "*52th Annual Scientific Conference",* Latvia, Riga, 2011.
3. **Gorobecs M., Greivulis J., Ļevčenkovs A., Balckars P., Ribickis L.** Vilciena avārijas bremzēšanas iekārta. Patenta Nr. LV13978, Patenti un preču zīmes 2009, №5.
4. **Charles L. Philips, Royce D.** Harbor Feedback control systems. New Jersey, 1998. – 615 p.
5. **Gong Tao.** Adaptive control design and alalysis. Wiley-interscience, 2003. – 637 p.

Development of Neural-Network Based Control Algorithm for Train Adaptive and Smooth Braking System

A. Potapovs*, M. Gorobetz**, A. Levchenkov***

*Institute of Industrial Electronics and Electrical Engineering, Riga Technical University, 1, Kalku Street, LV-1658, Riga, Latvia, Andrejs.Potapovs@rtu.lv
**Institute of Industrial Electronics and Electrical Engineering, Riga Technical University, 1, Kalku Street, LV-1658, Riga, Latvia, mihails.gorobecs@rtu.lv
***Institute of Industrial Electronics and Electrical Engineering, Riga Technical University, 1, Kalku Street, LV-1658, Riga, Latvia, anatolijs.levcenkovs@rtu.lv*

Abstract

This paper provides a new insight into the smooth and precise adaptive railway transport braking system design. The first phase of the development is described and includes a development of a necessary mathematical and computer model. Components of new adaptive braking system and their interactions are defined. Mathematical model contains equations that describe the movement of the train and the pneumatics braking system of the train, as well as offering new features of the developed system, which will adaptively adjust the service brake modes and will perform real-time system diagnostics without any human interaction. The computer model and simulation results are described in this position paper.
KEYWORDS: *adaptive control systems, intelligent control, railway transport embedded devices, modelling.*

1. Introduction

Nowadays the industry of railway transport is developing new solutions for increasing a capacity and speed of the railway. These actions are followed by various problems that connected with railway transport movement safety, which has to be at least at the same or higher level than before [1].

Authors are solving the safety problem and propose to develop new smooth and precise adaptive braking system of the rolling stock. This new system is aimed to reduce various deficiencies of existing railway safety systems. The purpose of the system is an automatic braking of the rolling stock using service braking and previously developed safety functions [2], which allow to stop the train before another railway vehicle, before a level-crossing where a road vehicle is stuck or before the signal with restrictive aspect. Usage of emergency braking has negative effect and not recommended if regular service braking might be performed. Therefore, the new proposed system is based on authors' previously developed railway safety systems and may increase safety level of the train and the railway system as a whole.

After real field test experiments [3] authors concluded that efficiency of the previously developed railway safety system is not sufficient, because the system does not adapt to various working environment conditions and may work imprecise if the rolling stock contains various wagons.

Therefore, the research and development of new smooth and precise adaptive train braking system, which is now patented [4], is going on. This process contains some development stages and the first one is described in this paper.

2. Purpose and Tasks

The main problem of classical approach for smooth target braking calculation is a necessity to receive data about various parameters of the train and railway infrastructure such as length of train, mass of train, braking coefficients, condition of braking system, slopes and curves of the track etc.

The purpose of this paper is to analyse a possibility to apply the adaptive control algorithms in the management of a train braking system, with the purpose to accomplish a smooth and precise (according to a stop point) braking, and also build a prototype of a smaller embedded device which would perform automatic train stopping before the red light.

Adaptive algorithms provides new approach, when the braking control system is self-adjusting to current conditions of the braking and performs the process adaptively without additional sensors and data.

The evolution stages of the proposed system are connected with the development of the mathematical model and the computer model of train movement and work of the pneumatics braking system un development of mathematical and computer model of smooth and precise braking control are described in literature [5].

Main objectives of this paper:
1. Development of the adaptive control algorithm using neural networks, for the new braking control system, based on the developed mathematical un computer models;
2. Simulation of self-organization of the adaptive braking control system using developed algorithms.

3. Proposed Structure of Braking System of Rolling Stock

Objects of braking system of rolling stock are: steel rails - S, locomotive - L; wagon - V; steel wheels - R; brake pads - K; brake cylinder - BC, stopping transmission levers - PS; air splitter - G; stock air tank - KR; main reservoir - GR; air pipe with fittings - GV; compressor – LK; brake control devices - BV; release valve - AV, automatic mode - AR.
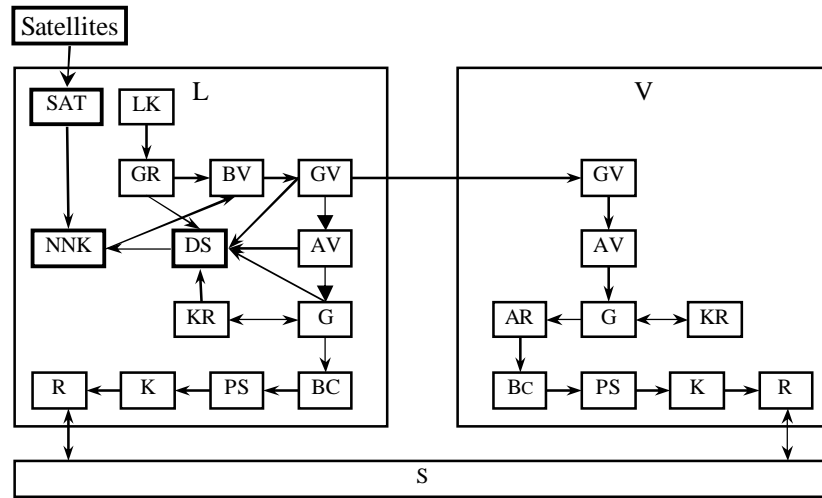
Fig. 1. Structure of proposed braking system with diagnotics devices

Fig.1. presents structure of existing braking system improved with new devices for diagnostics of braking system:
- NNK – Neural-network based adaptive braking controller;
- DS – Sensors, that measures current state of the braking system and train motion;
- SAT – receiver of satellite navigation signals.

4. Main working principle of the smooth and precise adaptive braking system of the rolling stock

The working principle of the proposed system is based on the software for programmable logic controller (PLC) with implemented adaptive control algorithm using neural network training. The goal is to perform a precise train braking and stop at the target point using service mode, but not emergency braking. The braking process consists of two braking steps. The first step is performed from time moment t_2 till t_3, the second one – from t_5 till t_7 shown in Fig. 2.
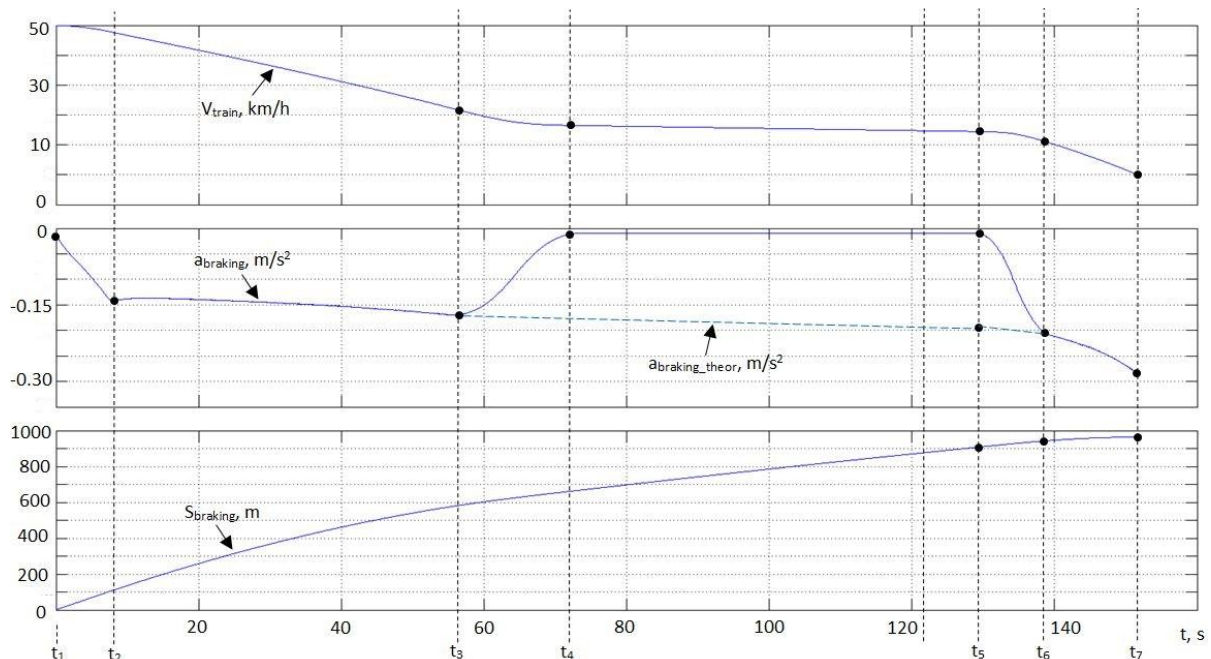
Fig. 2. Graphics of train motion parameters by performing two step braking in time

During self-learning the control program gets data, which provides direct and indirect characteristics of current status and condition of the braking system and its efficiency. This data should be in accordance to external conditions, state of the braking system and selected mode. More detailed description of the system and its elements may be found in a paper [5].

5. Usage of Neural Networks for proposed smooth and precise adaptive braking system of the rolling stock

The hypothesis is provided, that neural networks may be used for self-training of the control system during the braking process. The self-learning is performed as during the regulation of braking system work by driver and during the automatical train braking while performing the first braking step.

It is worth to mention that interest of using artificial neural network has been grown in last few years. The application of them is a research subject in fields much far from control systems such as philosophy, psychology, physiology

Artificial Neural networks may change their behavior in dependence on the external environment. There are different configurations of neural networks exist, but the organization of neurons in layers copies the structure of the human brain. Therefore, multi-layer structure is selected for the solution of the task. It has more advantages than signle-layer networks and have efficient algorithms for training.

As the braking process is continuous the previous input and output values make sense and the feedback is needed, because it ensures the neural network with the memory, similar to the short-time memory of the human being.

After some experiments, authors have chosen the Elman network [6], as a one type of recurrent networks, where feedback is implemented not from the output of the network, but from the hidden layer neurons. It allows taking in account prehistory of the observed processes and storing the information for the correct and precise control strategy. These networks may be used in the control systems of the moving objects, because the main particularity is the storing of the sequences.

On the base of the Elman network the RAAM (Recurrent auto-associative memory) network is built. RAAM - is a double Elman network with the structure 2N-N-2N, which is usually used for compressing and encoding of the information. The input of this network is a bit signal containing 2N bits. Usually, the network has size 20-10-20, where the first 10 bits are named "left" and the last 10 bits are "right".

In the beginning the left matrix gets zero bit vector (0000000000), but the right matrix gets the code of the symbol or the sentence (for example, 0010000000="A"). Then the same is fed to the output matrix elements. Using the back-propagation method the network is trained. After that 10 bits from the hidden layer are input to the left matrix, but the right matrix gets the next symbol.

In case of the smooth and precise control braking, inputs of the neural network are (figure 3):

- Train speed (V, km/h);
- Train moving distance (S, m);
- Train braking acceleration (a_{br}, m/s^2);
- Braking main line air pressure (P_{br_m}, MPa);
- Driver cotrol valve position (P, n);
- Slope of the track profile (i, ‰);
- External temperature (t, ºC).

Outputs of neural network are control signals according to five braking modes.
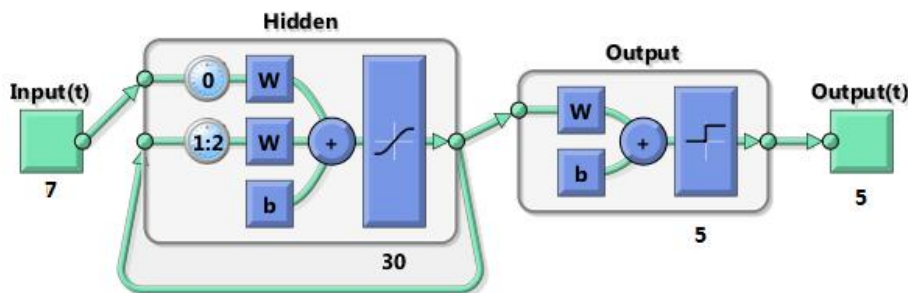
Fig. 3. Elman network structure with recurrent layer is selected as adaptation mechanism for automatic train braking system

6. Simulation results after training

After the training of the selected neural network, following simulation results are obtained. In figure 4 the upper line shows the value of the neural network output, but lower line is a real signal, which is generated by the computer model.
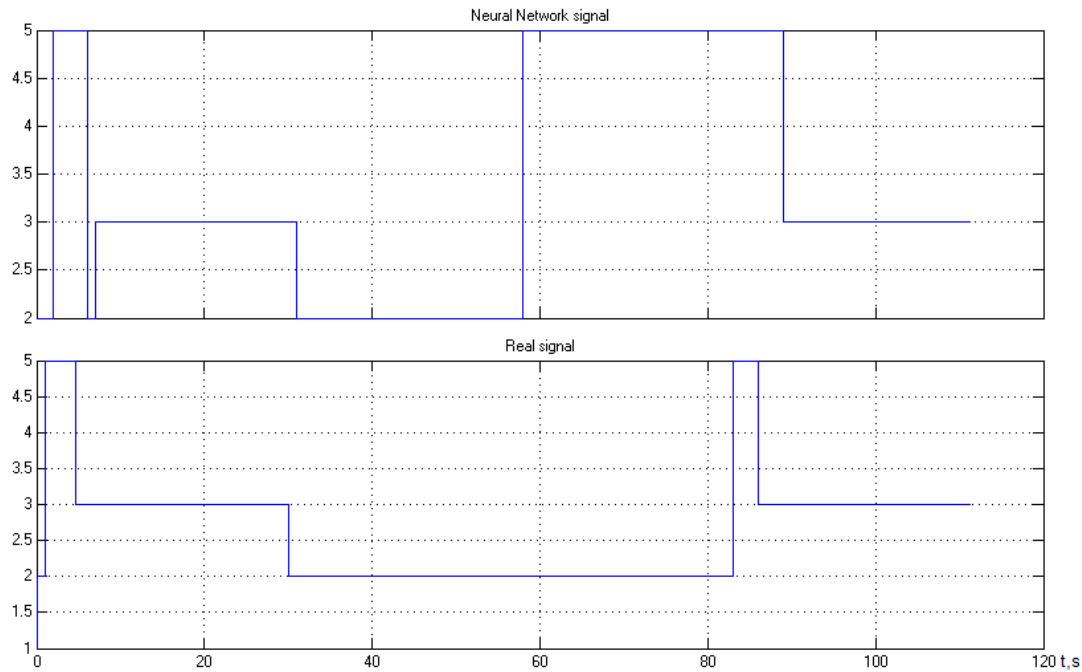
Fig. 4. Modeling results

7. Analysis of the results and evaluation

The operation effectiveness of the prototype device at the moment the following results are achieved may be evaluated as following:

- The neural network is trainable for control of the train motion and of the smooth and precise braking process, using parameters of the computer model;
- The integration of neural network into the model of the smooth and precise braking system computer model has been performed successfully;
- The tendency of neural network to learn and repeat the control signal is obvious, bur at this stage the results of training has a performance error.

8. Conclusions

The proposed neural network is workable in general, but needs further improvement. The tuning and adjustment of the training data set, data frequency and number of neurons is needed to get better results. Also efficiency of the neural network may be increased using additional elements for precision of the neural network input signal in accordance to exploitation conditions of the braking system of the rolling stock.

For the improvement of the effectiveness of the algorithm operation it is necessary to complete an analysis of application of another adaptive algorithm that is the task of further authors' publications.

References

1. **Wang J. F., Wang H. H.** & **Lin Z.** (2012). Research on a new type of train control system used at 350km/h // WIT Transactions on the Built Environment, 127, 51-60.
2. **Gorobecs M., Greivulis J., Ļevčenkovs A., Balckars P., Ribickis L.** Train Emergency Braking Device // Patent Nr. LV13978, 2009.
3. **Potapovs A., Gorobetz M., Levchenkov A.** 2012. Opportunities of adaptive control algorithms application in railway control systems. // ITELMS, 2012. y., 141 - 146 p.
4. **Potapovs A., Levchenkov A., Gorobetz M., Holodov S., Birjulin I.** Train smooth and precise automatic braking device. // Patent appliction Nr. P-13-43, 2013.
5. **Potapovs A., Gorobetz M., Levchenkov A.** Mathematical Model of Smooth and Precise Braking Adaptive Control System. // 54th Annual Scientific Conference of Riga Technical University, 2013.
6. **Elman J. L.** Finding structure in time. // Cognitive Science. – 1990. – P. 179-211.

Benefits of Eco-Driving Case Study

L. Pelenytė-Vyšniauskienė*, T. Šilinskas**, A. Bartulis***

Kaunas University of Technology, Panevėžys Institute, Klaipėdos g. 1, LT-35209 Panevėžys, Lithuania, E-mail: linapelenyte@gmail.com
**Kaunas University of Technology, Panevėžys Institute, Klaipėdos g. 1, LT-35209 Panevėžys, Lithuania, E-mail: pretendent@gmail.com*
***Kaunas University of Technology, Panevėžys Institute, Klaipėdos g. 1, LT-35209 Panevėžys, Lithuania, E-mail: alfredas.bartulis@ktu.lt*

Abstract

Eco-driving is introduced as a new standard of driving which allows to use the most up-to-date technologies of transport vehicles in the best way possible as well as to increase the traffic safety. Eco-driving as one of the components of consistent mobility significantly contributes to the protection of climate and the reduction of pollution.

Style of eco-driving is not only recognized as a new modern style of driving in the largest European countries but also becomes more and more popular, particularly among younger drivers.

Training of eco-driving is one of the goals which governments of many European countries recognize as a measure for the reduction of environmental pollution.

KEY WORDS: *eco-driving, ecology, fuel, motor car.*

1. Introduction

Operation of a transport vehicle based on the eco-driving principles not only protects the environment but also reduces the fuel consumption along with the costs spent for running and spare parts of a motor car, namely tyres, brakes, engine and other elements of a motor car are in service for a longer time. Moreover, eco-driving is considered a safe driving and therefore any consequences caused by car accidents may also be lesser.

In 2010, program ECOWILL (Ecodriving – Widespread Implementation for Learner Drives and Licensed Drivers) was started to implement in the Western Europe. Trainings of eco-driving have been foreseen in 13 European countries, also including Lithuania [1].

At the end of 2011, under project ECOWILL, the first driving instructors participated in the training on teaching methodology of eco-driving in Lithuania. At the end of January 2013, modifications of Appendix II to EC Directive 2006/126/EB had to come into effect, establishing that eco-driving should be definitely included into the driving examination in order to obtain a driving licence of B category.

It is supposed that irrespective of a make of the motor car driven, its age and technical parameters, it is possible to reduce the fuel consumption by 5-10% without any additional investments and only by a single driver's efforts. In the course of trainings under project ECOWILL in Lithuania, an average economy of fuel achieved came to 13-15%.

Aim of this article is to achieve a better understanding of what economic benefit could be achieved with the adaptation of the general eco-driving principles as well as to verify the fuel consumption in usual driving and eco-driving. In addition to that, to verify the time input and fuel expenses.

2. Eco-driving study

Two different motor cars were selected for the study, namely Hyundai i30, year 2009, engine capacity 1.6 l, fuel – diesel, fuel consumption in a city indicated by the manufacturer is 5.7 l/100 km and Volkswagen Golf, year 1988, engine capacity 1.6 l, fuel – gas, fuel consumption not indicated by the manufacturer.

The first driving by both motor cars was the control driving carried out in a usual mode, meanwhile the eco-driving principles were applied during other drivings. In total, four drivings were made within the same route. It was the route of Šiauliai State Enterprise „Regitra" which is followed when passing the practical driving examination for B category. The route comprises 15 km within the city territory. The route is characterized by many crossroads, traffic-lights, pedestrian crossings and also heavy traffic. The study commenced at 9.26 a.m. and was finished at 11.32 a.m.

Before to conduct the test, the driver of the motor car participated in the eco-driving training for 7 hours where it was accentuated to change gears earlier, to foresee driving in the car traffic, to maintain the permanent speed while the engine is running at low rotation speed.

The following eco-driving elements were adopted in this experiment:
1. While driving, to try keeping the constant speed as long as possible, to drive with a higher gear on as well as to keep the engine running at low rotation speed. In the course of this experiment it was attempted not to exceed 1500 rpm.

3. To avoid traffic jams in order to use brakes and to reincrease the speed less often.
4. In order to reduce the speed (driving down the hill, approaching the traffic-lights), not to switch the gear off but only to remove the feet from the accelerator pedal as early as possible.
5. To verify the pressure in tyres before every driving.
6. To use air conditioning and other electrical devices in the motor car only when it is necessary.

Results of the study obtained are illiustrated in Tables 1 and 2 and Fig. 1-4.

Table 1

Comparison of the study results related to Hyundai i30 and Volkswagen Golf

Motor car data	Usual driving		Eco-driving	
	Fuel consumption, l	Time, min	Fuel consumption, l	Time, min
Hyundai i30 (year 2009, 1.6 l diesel)	1.26	21	1.05	23
Volkswagen Golf (year 1988, 1.6 l gas)	1.72	20	1.00	22

It is shown it Table 1 that when eco-driving was applied, the fuel consumption for Hyundai i30 decreased by 8.3%. If during the control driving the fuel consumption within the route came to 1.26 l, when eco-driving was applied 1.05 l of fuel was consumed. When driving Volkswagen Golf, 42% of fuel was saved. During the control driving with this motor car, 1.72 l of fuel was consumed, meanwhile only 1 l of gas in eco-driving.

The time difference between usual driving and eco-driving in the route selected is barely 2 min. This time difference is equal to both motor cars.

Fig. 1 shows the fuel consumption with Hyundai i30, when usual and eco-driving was applied.

Fig. 2 shows the fuel consumption with VW Golf, when usual and eco-driving was applied.

Fig. 3 shows the time input with Hyundai i30, when applying usual and eco-driving style.

Fig. 4 shows the time input with VW Golf, when applying usual and eco-driving style.

Price for 1 liter of diesel fuel is 4.54 LTL, VAT included. Price for 1 liter of gas is 2.47 LTL, VAT included.

Price for 1 km in usual driving (when driving in lower gears, 2000-3000 rpm) and not observing the eco-driving rules specified in this chapter) with the motor car using diesel fuel is as follows:

$$1.26 \text{ l} / 15 \text{ km} \cdot 4.54 \text{ LTL/l} = 0.38 \text{ LTL/km}$$
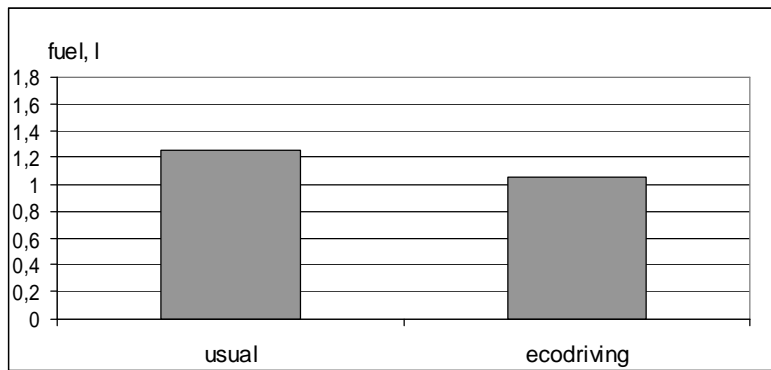
Fig. 1. Fuel consumption with Hyundai i30
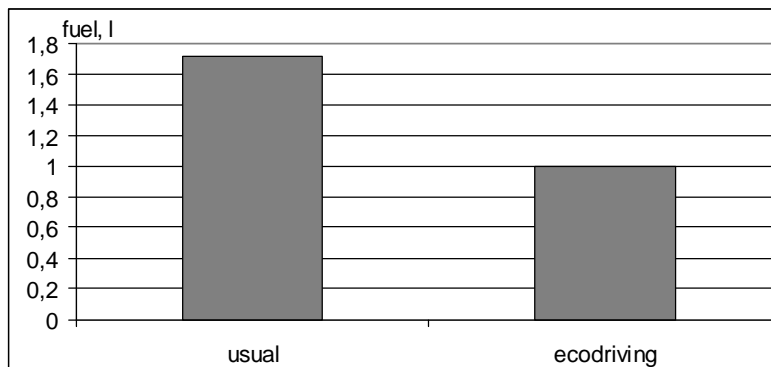
Fig. 2. Fuel consumption with Volkswagen Golf
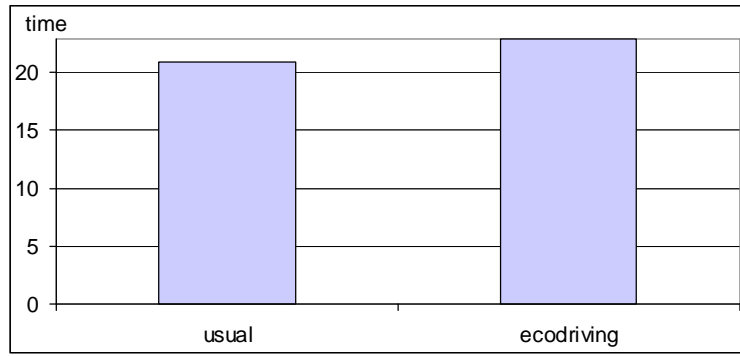
Fig. 3. Time input with Hyundai i30
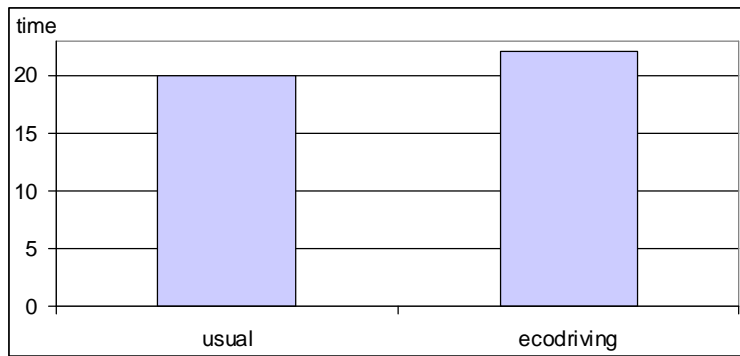
Fig. 4. Time input with Volkswagen Golf

Price for 1 km in eco-driving with the motor car using diesel fuel:

$$1.05 \text{ l} / 15 \text{ km} \cdot 4.54 \text{ LTL/l} = 0.32 \text{ LTL/km}$$

The difference between usual and eco-driving is therefore obvious, namely it is 6 cents for every kilometer driven in the city.

If an average driver drives approximately 1000 km per month in the city, having applied the eco-driving skills, he would save around 60 LTL or about 10 litres of fuel (Table 2). If this method of driving is selected, it would be possible to save approximately 120 litres of fuel or around 720 LTL per year.

Meanwhile, the price for 1 km in usual driving with the motor car driven by gas:

$$1.72 \text{ l} / 15 \text{ km} \cdot 2.47 \text{ LTL/l} = 0.27 \text{ LTL/km}$$

Price for 1 km in eco-driving with the motor car driven by natural gas:

$$1.0 \text{ l} / 15 \text{ km} \cdot 2.47 \text{ LTL/l} = 0.17 \text{ LTL/km}$$

Therefore, the difference between usual and eco-driving of the motor car using gas is even higher than that established in the case of the motor car using diesel fuel, namely it is as much as 10 cents for every kilometer driven in the city (Table 3).

If a driver, having adapted his eco-driving knowledge, drives around 1000 km per month in the city, he would be able to save 100 LTL and as much as 1200 LTL or 486 litres of natural gas per year.

Table 2

Hyundai i30

Input type	Distance driven, km							
	Usual driving				Eco-driving			
	1	15	100	1000	1	15	100	1000
Fuel, l	0.08	1.2	8	80	0.07	1.05	7	70
Price, LTL	0.38	5.70	38.00	380.00	0.32	4.80	32.00	320.00

Table 3

Volkswagen Golf

Input type	Distance driven, km							
	Usual driving				Eco-driving			
	1	15	100	1000	1	15	100	1000
Fuel, l	0.11	1.72	11.5	109	0.07	1	6.7	69
Price, LTL	0.27	4.05	27.00	270.00	0.17	2.55	17.00	170.00

As you can see from the results specified in Tables above, fuel consumption by both motor cars for 100 km during control, usual driving and while applying the eco-driving principles exceeds the fuel rates foreseen by the manufacturer. This could be explained in several ways. One of the explanations could be that the motor cars used for the study are not new, namely one of them is 4 and another 25 years old. Another explanation would be related to the route singularities. As it was mentioned in the beginning of the article, this route has many crossroads, traffic-lights, pedestrian crossings and also heavy traffic. Moreover, the study was conducted during working hours when the traffic is even more intense.

If to compare results of this study with the studies conducted by different authors [2, 3], it would be possible to conclude that the fuel consumption also corresponds to the study results obtained by others.

3. Conclusions

As it was proven by this experiment, the fuel consumption in eco-driving with Hyundai i30 decreased by 8.2%. When driving Volkswagen Golf, as much as 42% of the fuel consumption was saved.

The time difference between usual driving and eco-driving in the route selected is barely 2 min. This time difference is equal to both motor cars.

With the assessment of the minor time difference it is possible to state that eco-driving helps to save money. In this case, every kilometer driven by means of eco-driving in the city with Hyundai i30 helps the driver to save 0.06 LTL. Meanwhile, when using VW Golf driven by natural gas, we are able to save 0.10 LTL out of every kilometer driven in the city.

Acknowledgements

References

1. http://www.ecodrive.org/en/what_is_ecodriving/
2. **Beusena B., Broekxa S., Denysa T., Beckxa C., Degraeuwea B., Gijsbersa M., Scheepersa K., Govaertsa L., Torfsa R., Panisa L.** Using on-board logging devices to study the longer-term impact of an eco-driving course Transportation Research Part D: Transport and Environment, Volume 14, Issue 7, October 2009, Pages 514–520.
3. **Saboohia Y., Farzanehb H.** Model for developing an eco-driving strategy of a passenger vehicle based on the least fuel consumption. Applied Energy. Volume 86, Issue 10, October 2009, Pages 1925–1932.

Advances of Ultrasonic Sensing in Microchannels

E. Sapeliauskas*, D. Viržonis**

*Department of Electrical Engineering, Kaunas University of Technology Panevezys Institute, Daukanto 12, LT-35212 Panevėžys, Lithuania, E-mail: evaldas.sapeliauskas@stud.ktu.lt
**Department of Electrical Engineering, Kaunas University of Technology Panevezys Institute, Daukanto 12, LT-35212 Panevėžys, Lithuania, E-mail: darius.virzonis@ktu.lt

Abstract

The summary of the scientific research of capacitive micromachined ultrasonic transducers (CMUT) for the resonance measurements is given in the review. Implementations of CMUTs as the resonance gas-phase chemical sensors, microfluidic manipulators, biochemical affinity sensors and sensors of the fluid properties are reviewed. The special attention to works on CMUT application for fluid manipulation in microchannels, fluid properties setting, and specific protein interaction detection is given there.
KEY WORDS: *CMUT, sensors.*

1. Introduction

Today's requirements for safety, environmental protection, and health diagnostics calls for the operative, informative and reliable detection of various species in gas and liquid medium. This increase the demand of chemical sensors and their availability. Resonant mass sensors (gravimetric sensors) with a functional active surface coating can be used there. One of the gravimetric sensors embodiments are several kinds of microelectro-mechanical (MEMS) resonators with a very wide range of applications. Capacitive micromachined ultrasonic transducers (CMUT) are one of the modern MEMS type resonators. This alternative to piezoelectric transducers was invented by Stanford University researchers. CMUT advantages are: wide dynamic range, broad working bandwidth, and good energy efficiency. These transducers can be produced using sacrificial layer or wafer bonding technology [1-3]. Both technologies are suitable for high-density ultrasonic transducers or gravimetric sensor matrix formation. A wide range of applicability of them to measure various analytes is determined by the large selection of functional layer materials, which can be coated over the CMUT surface. CMUT like other micro-systems (MEMS) technology-based resonant sensors, has significant miniaturization capabilities, and can be superior by their throughput than classical chemical analysis systems. The review of CMUT use for resonance measurements was made in this article.

CMUT in its construction is equivalent to capacitors with one moving plate. Vacuum and dielectric silicon compounds are between two electrodes. Hermetically sealed membranes with three important advantages compared with competing sensor platform (microcantilevers) are the basic elements constituting CMUT arrays. This kind of the basic elements makes CMUT advantageous compared with competing sensor platform (for instance, microcantilevers). First, a thin vibrating plate contacts with the environment only from one side, and the bottom side of the membrane is above the vacuum gap. This reduces the energy loss, and the resonance quality factor is received larger than the cantilever sensors.
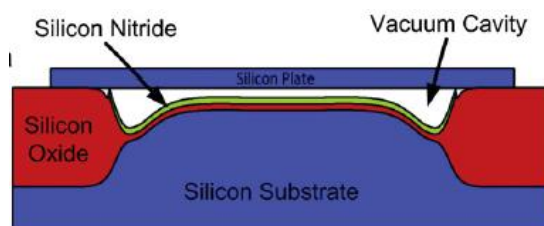
Fig. 1. CMUT cross-sectional diagram [10]

The second, it is very convenient to connect CMUT cells electrically to the parallel connected arrays by 100 - 1000 items. Such multiresonator has two main advantages: the broad electric indepence interval where the device can be impedance-matched to connect with microelectronic chips and has a greater reliability compared to a single resonator system. In addition, if necessary, a number of separate resonators can be connected into a general array. Third, CMUT manufacturing methods are fully developed (can be fully compatible with CMOS technology) [3, 4]. The multiresonator structures should have the undamped resonance with the comparatively high (100-400) quality factor. 10^{-15} g/cell CMUT sensor sensitivity to mass change is already demonstrated [5], as well as outstanding informatively when recording specific protein interaction [6].

2. Using of CMUT as a sensor in the gaseous medium

In order to effectively identify the airborne substances, CMUT resonance membrane can be covered with absorbing layer that would be specific to the desired analyte. Good sensitivity and selectivity for the analyzed substance are necessary qualities for absorbent layer [7]. Park et. al. [10] selected dimethylmethylphosphonate (DMMP) as the simulation of sarin, which is a nerve paralyzing gas during development of CMUT sensor. Poliaminohydrochloride (PAAM), polyethylene glycol (PEG), and polyvinyl alcohol (PVA) are the most affordable materials for sensitive DMMP layer formation. Polyisobutylene (PIB) was selected for the tests [8]. Its features are the most optimal for DMMP detection; 0.2 nl of PIB melted in solvent were placed on CMUT surface using an inkjet printing device [9]. Thin layer of polymer absorbent coating remains on CMUT surface already after a few seconds after evaporation of the solvent. As determined by atomic force microscope, this way covered polymer thickness made about 50 nm. The influence of such film thickness on the resonant frequency and measurement quality is very low and makes about 0.64% of resonance deviation that was before membrane coating.

Instead of slow and costly CMUT input impedance measurement authors suggested to use the low-noise oscillator circuit for the resonant frequency monitoring. Such approach allows performing real-time measurements using digital frequency meter connected to the oscillator circuit output [10]. 26 hour experiment was performed where gas injection into the specimen chamber was replicated 200 times to check for the measurement repeatability. CMUT sensor responded to all DMMP attacks without significantly changing the output signal. Sensitivity change uncertainty made 4.7% of the measured value over 26 hours and this only confirmed a slight degradation of resonator and polymer. Systematic errors also contributed to this slight change in the long-term experiment. For example, the gas flow controller used in the experiment had 1% accuracy error to the flow, and it affected the uncertainty during valves opening/closing. Authors note that CMUT can be still developed as a chemical resonant sensor. Membrane density and thickness can be further reduced for a greater sensitivity achievement. In addition, mass estimation resolution can be improved by increasing the resonator quality coefficient Q:

$$Q = 2p\frac{E}{W}$$

where E is the energy, accumulated in the resonator; W is the amount of energy, dissipated per cycle.

Detection limit is determined by frequentative system noise with a power inversely proportional to the power of resonator's Q. In addition, chemical sensitivity can be improved by selecting more sensitive and more selective functional materials [10].

3. Fluid mixing in microchannel

Ultrasound, on the contrary to the large fluid mixing or cleaning equipment, is a relatively rarely used in microchannel devices. Fluid and gas flow in sub-millimeter sized microchannels is no longer turbulent, and laminar flow prevents reagents from mixing there. Traditionally, ultrasound is widely applied for macro fluid flow measurements in pipes. Its use in micro fluid measurements is quite limited due to the ultrasonic transducer size incompatibility with microchannels. Now it has become possible because of transducers fabrication technologies development. Biomedical industry was one of the first to benefit from this progress. Mobile micro analysis systems and lab-on-chip are the main customers for the microfluidic technology. The microchannel and ultrasonic transducer integration leaving behind the traditional micro-systems in their functionality is described in [11]. The ultrasonic transducer made from thin layer zinc oxide (ZnO) film has been used. The microfluidic device was retrofitted by 10 μm wide zone ultrasonic ZnO interdigital transducers.

Authors of [11] emphasize the importance of precision monitoring and measurement of fluid temperature in micro channel. For instance, it is necessary to maintain the exact temperature while studying proteins and DNA; it requires the instruments with accurate temperature. DNA amplification by cyclically changing the temperature is possible only with good temperature determination capabilities. Authors proposed the acoustic fluid temperature measurement method. The measurement is based on sound propagation in the liquid velocity change, during the temperature change. The observed velocity change was fitted to the fluid calibration curve.
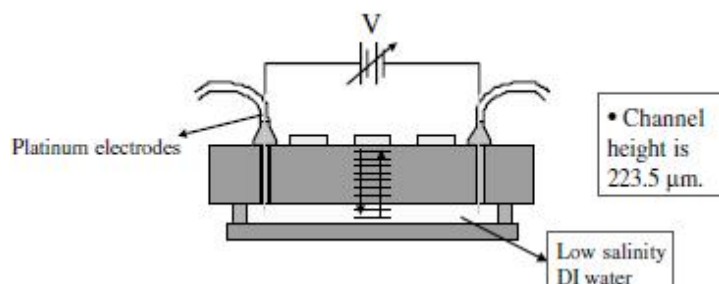
Fig. 2. The device scheme, used for the temperature measuring experiment [11]

Second experiment of [11] was about mixing the fluid. The fluid flow in microchannel is characterized by laminar flow method. Fluid mixing in microchannel is a very complicated task, because it can flow without mixing in all length of microchannel. This occurs due to the low Reynolds number in the microchannel and not formation of the fluid turbulent flow. Fluid mixing in microchannel occurs because of diffusion. The radio frequency AC voltage source wasused to generate the ultrasonic waves in the channel through the transducer. The transducer created acoustic field pressure change inside the microchannel caused fluid mixing. Fluid mixing zone above the transducer is shown in Fig. 3.
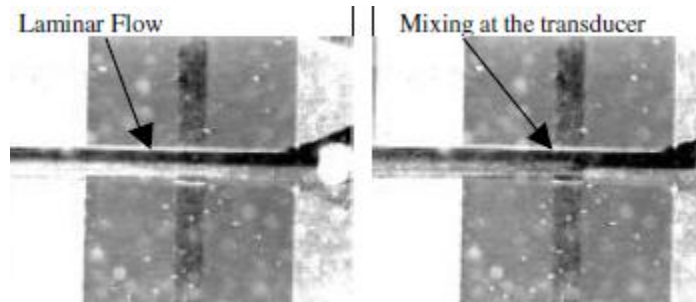
Fig. 3. Laminar fluid flow in microchannel and the conducted mixing affected by transducer energy [11]

This mixing method has many advantages compared to conventional mixing techniques. Mixing is instantaneous and is going on in a very small area. The other advantage of ultrasonic mixer is that the device is very small compared to the static mixer; and the direct contact with the fluid, as in electrophoretic method, is unnecessary. This mixing method is relatively simple and can be implemented for mixing at different channel locations.

Volume pressure waves, created by CMUT device, are accompanied by the side transitional processes of various characters (mechanical waves of various types) that are particularly undesirable in medical visualization equipment. One type of the laterally formed waves is mechanical oscillations, propagating on fluid and solid body interface; they are called interface waves. This type of waves can be used for fluid mass, density, and viscosity measurements [12]. To create a standing surface wave in all fluid and the sensor sensitive elements array contact area is the main task of this type of CMUT sensor.
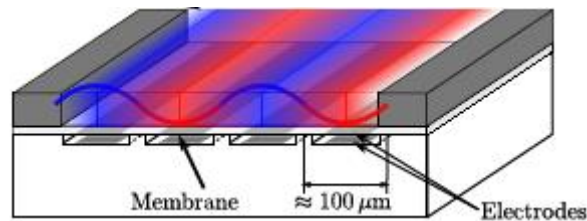
Fig. 4. CMUT model, creating volume pressure waves [12]

Reflectors on array edges limit the surface wave energy dispersion outside the sensor and ensure a high level quality mechanical vibration coefficient Q. Interface wave propagation direction is controlled by excitation of adjacent interdigital CMUT elements in different phase and in such way creating constructive wave interference on the desired side. Resonance formation conditions are met when the interfering wave length is coordinated with the distance between different operating phases of the interdigital CMUT element "fingers". Typically, the distance of the wave propagation direction satisfies the condition $d = \lambda / 2$. There are two main interface wave attenuation factors: fluid viscosity and membrane material damping. According to authors, if compared with the shear-mode piezoelectric transducers operating in thickness mode, CMUT membrane arrays design allows more freedom for viscosity and density measurement as interface wave characteristics can be commanded by changing the mass of the membrane, material density and stiffness. In addition, the resonant CMUT device frequency can be controlled by bias [12], [13].

CMUT physical parameters were calculated by the Finite Element Method (FEM). Resonant frequency depends on the device geometry and the wave phase velocity. CMUT modeling using FEM consists of three steps. In the first step the membrane was analyzed for a critical voltage U_{krit}, when membrane collapses into the bottom electrode. The second step is the static harmonic analysis of the whole sensor array. U_{bias} makes approximately 95% of U_{krit} applied to the membrane cell. Static deformation from the fluid and bias voltage was calculated by using linear matrixes. After the measurements and FEM calculation results, it was found that the unloaded in air membrane resonance happens at 8 MHz. The sensor was tested in air, water, baysilone M50, and rape seed oil It was found that resonance in water is less attenuated than in rape seed oil. The discrepancies in large viscosity values range was found after the comparison of equivalent circuit model, FEM, and measured data. Measurement and FEM data coincided at low viscosity. However, measurement result value does not change over 50 mPa range. One assumption that the membrane was not completely cleaned from oil using standard methods of treatment can be done and for this reason a very thin layer of low viscosity oil could remain on the CMUT membrane and influence the result.
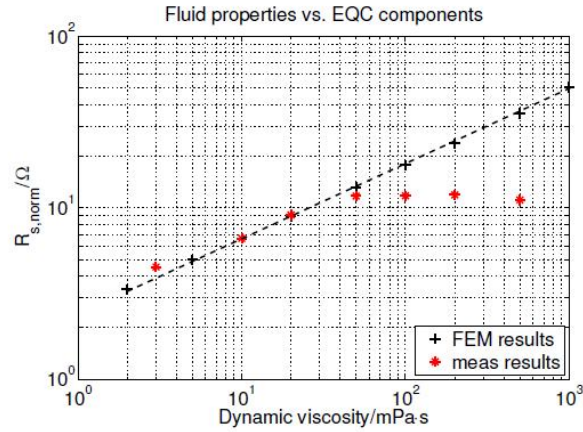
Fig. 5. Material viscosity relationship with normalized real part of the electromechanical impedance: measurement and FEM results [12]

4. CMUT use for immunosensors

Authors of [6] used CMUT elements equally modified by the same bovine leukemia virus (BLV) antigen gp51, which is one of the two major proteins of bovine leukemia virus. Antibodies against this antigen remain for a long time in infected bovine blood serum. 1.5 µl of protein aqueous solution (1 mg / ml) was placed on the transducer elements for covalent Gp51 immobilization. The solution was applied on active surface element, and dried. The drying time was 10 min in air and nitrogen atmosphere. Modified CMUT elements were kept for 20 minutes over 5% of glutaraldehyde solution. Immobilized proteins later were washed from the surface by distilled water. The transducer was dried after washing and the initial resonant frequency and impedance were measured. The washing procedure was repeated until no longer resonant frequency and impedance values displacement occurred. The modified transducer element surface was exposed for 20 min by three times diluted uninfected cattle blood serum in order to avoid possible non-specific proteins in blood interaction and the results distortion. The monitoring data obtained by authors are presented in Fig. 6 (curve 3). The transducer was washed with distilled water after this test phase. The transducer was dried after each wash in order to avoid electric breakdown because of open contacts. The experiment was repeated 3 times using diluted BLV infected bovine serum, 10 times diluted BLV infected cattle blood serum and 3 times diluted uninfected cattle blood serum sample. Infected cattle blood serum containing anti-gp51 interacts with gp51 proteins adsorbing them to the surface of the transducer.
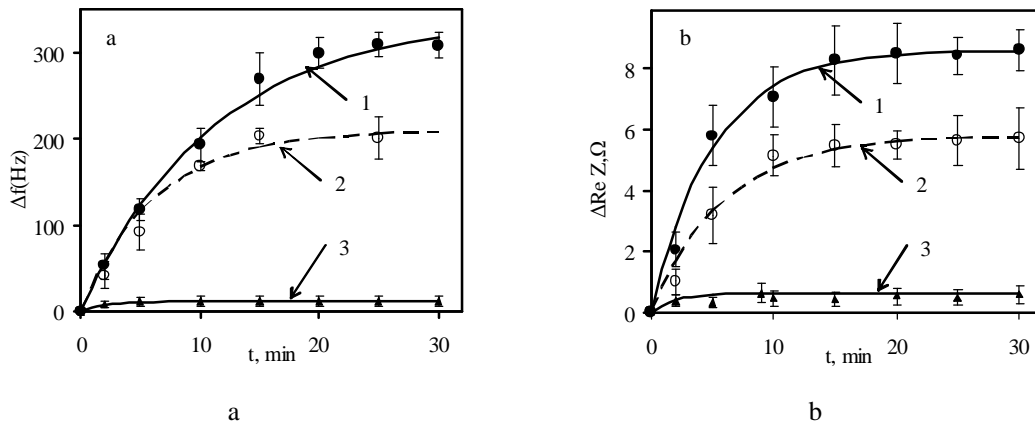
Fig. 6. CMUT resonant frequency dependence on time (a) and the real part of electromechanical impedance change depending on the blood serum containing anti-gp51 antibodies (b): 1 – three times diluted BLV-infected cattle blood serum sample; 2 – 10 times diluted BLV infected cattle blood serum sample; 3 – three times diluted uninfected BLV cattle blood serum sample [6]

The obtained non-specific interaction results depend on the CMUT modification procedures: non-specific sorption is about 15%, if CMUT membranes before measurements were 10 min. affected by three time's diluted BLV-free bovine serum. This suggests that non-specific interaction can be significantly reduced by incubating the similar protein concentrations into solution, but long before the experimental influence reduces CMUT sensor sensitivity. As authors suggest, this effect must be assessed in the development of this type of biosensors. Substantial

CMUT element parameter change was observed only in the case where the modified CMUT element was exposed by BLV infected blood serum. This parameter was 10 to 25 times lower when CMUT element is exposed by healthy cattle blood serum. Authors explain this by antigen - antibody (Ag-Ab) complex formation on the modified CMUT element in BLV infected cattle blood serum [6].

5. Conclusions

CMUT is an excellent technical platform for resonant gravimetric sensors, as CMUT basic elements (membrane cells) have a very low moving mass. Some authors demonstrate 10^{-15} g/Hz sensitivity during the analyte (DMMP) detection in gaseous environment. Using of CMUT as a resonant sensor in fluid environment is problematic because most fluids greatly dampen membrane movement, so the resonance quality is low. Mechanical resonant structures allow improving the quality of resonance (e.g. creating a standing wave composing in the liquid and solid interface) are created in order to compensate the loss of resonance quality. This setup allows measuring fluid viscosity and density. Applying CMUT for biochemical detection (identifying immunosorbent protein interaction) it was found that specific protein interactions and the total protein mass increase on the sensor surface influenced two sensor parameters, such as: electromechanical impedance and the resonant frequency. They are partly dependent on each other and potentially can be used for setting the different properties of the adsorbed analytes.

Acknowledgements

Literature

1. **Haller M. I., Khuri-Yakub B. T.** A surface micromachined electrostatic ultrasonic airtransducer // IEEE UltrasonicsSymposium, 1994.
2. **Mikalajūnas M., Viržonis D., Grigaliunas V., Tamulevičius S., Kaliasas R.** An Impact of the Residual Stress on the Sacrificial Release of Microelectromechanical Membranes. ISSN 1392–1320 Materials Science (Medžiagotyra). Vol. 13, No. 1. 2007.
3. **Virzonis D., Grigaliunas V., Repecka V., Mikolajunas M.** Capacitive micromachined ultrasonic transducer and its fabrication method. Europatent patent application EP 2 145 696 A1.
4. **Ergun A. S., Huang Y., Zhuang X., Oralkan O., Yarahoglu G., Khuri-Yakub B. T.** Capacitive micromachined ultrasonic transducers: fabrication technology. IEEE Transactions on Ultrasonics, Ferroelectrics and Frequency Control 52 (2005) 2242–2258.
5. **Lee H. J., Park K. K., Cristman P., Oralkan O., Kupnik M.** and **Khuri-Yakub B. T.** 2008 IEEE Ultrasonics Symposium, 2008, p.1951.
6. **Ramanaviciene A., Virzonis D., Vanagas G., Ramanavicius A.** Capacitive micromachined ultrasound transducer (cMUT) for immunosensor design // Analyst. Cambridge: The Royal Society of Chemistry. ISSN 0003-2654. 2010, Vol. 135, iss. 7, p. 1531-1534.
7. **Graber N., Lüdi H., Widmer H. M.** The use of chemical sensors in industry, Sensors and Actuators B: Chemical 1 (1990) 239–243.
8. **Patel S. V., Mlsna T. E., Fruhberger B., Klaassen E., Cemalovic S., Baselt D. R.** Chemicapacitive microsensors for volatile organic compound detection, Sensorsand Actuators B: Chemical 96 (2003) 541–553.
9. **Bietsch A., Zhang J., Hegner M., Lang H. P., Gerber C.** Rapid functionalization of cantilever array sensors by inkjet printing, Nanotechnology 15 (2004) 873–880.
10. **Kwan Kyu Park, Hyunjoo Lee, Mario Kupnik, Ömer Oralkan, Jean-Pierre Ramseyer, Hans Peter Lang, Martin Hegner, Christoph Gerber, Khuri-Yakub Butrus T.** Capacitive micromachined ultrasonic transducer (CMUT) as a chemical sensor for DMMP detection. Sensors and Actuators B: Chemical. 2011, Elsevier.
11. **Jagannathan H., Yaralioglu G. G., Ergun A. S., Degertekin F. L.** and **Khuri-Yakub B. T.** Micro-Fluidic Channels with Integrated Ultrasonic Transducers. Proceedings of 2001 IEEE Ultrasonics Symposium, pp. 859-862 (2001).
12. **Thr˙anhardt M., Eccardt P. -C., Mooshofer H.** and **Hauptmann P.** A resonant CMUT-based Fluid Sensor: Modeling and Simulation. Sensors and Actuators A: Physical, vol. Article in Press, 2009.
13. **Eccardtand P. -C., Daft C.** Micromachined Ultrasound Transducers for Medical Imaging: Fabrication and System Implications. VDI Kongress Sensoren und Mess-systeme, Freiburg, February 2006.

Characteristics and Performance of the Silicon Solar Cells Improved by Complex Porous Silicon Structure

E. Shatkovskis, R. Mitkevčius, V. Zagadskij, J. Stupakova

Department of Physics, Vilnius Gediminas Technical University, Sauletekio al. 11, LT-10223, Vilnius, Lithuania

Abstract

Porous silicon technology was adapted to modify and improve characteristics of mono-crystalline silicon solar cell. Solar cells under study were 450 μm thick, with a thin n-type emitter (0.5 – 0.7) μm. The porous silicon structure was manufactured inside the cell by electrochemical technology, using HF: ethanol = 1:2 electrolytes, under illumination of 50 W halogen lamp. The etching current was computer-controlled in the limits of (6-14) mA/cm^2; etching time was set in the interval of (10-20) s, to compose the porous texture inside the emitter volume. Investigation of the current-voltage characteristics in the solar cell samples was carried out under illumination of 5000 K Xenon lamp. The studies reveal that porous silicon structures positively affect the parameters of dark and lighted solar cells. It has been shown, that the formation of porous silicon structure causes (11-15)% increase in fill factor of current-voltage characteristics and approximate 31% increase in maximum power output. The study on spectral dependence of fill factor increase was performed. It revealed, that the increase of fill factor is observed in wide spectral range – (450 – 850) nm, where ~60% of the solar energy is located under air mass AM1.5. The physical mechanisms that cause the improvement in performance of the modified solar cells are discussed.
KEY WORDS: *solar cells, silicon, porous silicon.*

1. Introduction

Photoelectric conversion of solar radiation into electricity is one of the most promising techniques in creating ecologically clean energy, so, great interest is seen recently in the research field of solar cells and improvement of their efficiency. Building-integrated photovoltaics (BIPV) can become mainstream with an estimated 6.6 GW installed in 2021 as the European Commission's Net-Zero Energy Buildings (NZEBs) standards lead to likely widespread adoption across the continent, according to a report from Lux Research. The most of global solar cell production is based on mono-crystalline or multi-crystalline silicon simultaneously with creation of new types of solar cells. Laboratory-derived silicon solar cell efficiency is at 24.5%. However, the efficiency in industrial solar cells does not exceed 20% [1, 2]. Theoretical limit of crystalline silicon solar cell efficiency is considered to be at 31 percent [3]. The goal of silicon solar cell research and development is to reach this theoretical limit in order to make solar cells competitive with existing energy sources. One of the obvious and the most popular method to improve solar cell performance is based on the reduction of reflection from the cell surface. For this purpose lower refractive index material layers are produced on the solar cells surface. Layers can be quarter wavelength thick, but then it has the selective properties in respect of solar spectrum, which are not desired. One of the most significant improvements in silicon solar cell efficiency was invented by Martin Green and co-authors, who proposed to create textured cell surfaces instead of mirror flat [1, 2]. Right now, texturing of silicon solar cell surfaces is applied all the time. Attempts were made to apply porous silicon structures for enhancement in the silicon solar cell efficiency after re-discovering porous silicon [4]. Fabricating porous silicon anti-reflective coatings were mostly frequent [5-7]. It has been shown that manufacture of approximately quarter-wavelength layer of porous silicon on solar cell surface results in some increase in solar cell conversion efficiency in comparison to the initial one. Similar attempts to enhance the efficiency of silicon solar cells were made later [8-10]. Essential reflection losses reduction in silicon solar cells have been achieved using so-called black silicon.The essens of black silicon technology lies in nano-scale texturing of silicon surface using local nano-scale metal-catalysed wet chemical etching. It was shown that black silicon nanoscale texturing of silicon surface results in an almost complete suppresion of reflectivity in the broad spectral region, and in an considerable (by 36-42%) increase of the short circuit current [11]. It was shown additionally that wet black silicon nano-scale texturing can be applied to all forms of silicon solar cells (single-, poly-, or multi-crystalline) as well as to thin silicon films. Black silicon nano-scale texturing process is almost independent of the surface orientation, doping, and affects only the topmost 200-300 nm thick near-surface layer [12]. Somewhat close results were obtained using electrochemical etching also [13]. Recently, porous silicon structure was applied to enhance the efficiency of the epitaxial silicon solar cell. Chirped Bragg reflector was produced at first in the conventional p-type silicon substrate [14, 15]. The reflector is made of porous silicon layers using electrochemical technology. Then epitaxial n-type emitter was grown on the porous silicon structure. Chirped broadband porous silicon reflector effectively returns non-absorbed photons to the p-n junction increasing the solar cell efficiency. Of course, the Bragg reflector manufacture is relatively complex. This may result in more expensive production of such solar cells. In this work, we applied a simpler porous silicon technology to improve parameters of a regular, fully completed solar cells. In contrast to known method of formation of the functionally important porous silicon structure (texture) on the surface of solar cell plate, we create it buried in the emitter volume, to some extent analogously to production of the

chirped Bragg reflector in silicon wafer [14, 15]. Alongside, the solar cell surface is left almost unchanged in this case [16, 17]. In our study we used completed mono-crystalline silicon solar cells produced in a manner consistent with the industrial manufacturing process [18]. Fill factor and spectral peculiarities of current-voltage characteristics were studied on solar cells modified by hidden emitter texture. We show that fill factor of the crystalline solar cell current-voltage characteristics and solar cell performance can be improved by porous silicon structure, which is hidden in the solar cell emitter volume. The shown improvement in silicon solar cell performance is useful in improving efficiency of diverse solar cells by usage of buried emitter structures.

2. Experiment

Standard p-type, (100) orientation, 450 μm thick mono-crystal silicon wafers have been used in solar cell production. The n-type emitter was made by conventional phosphorus diffusion procedure [18]. It was $(0.5 \div 0.7)$ μm thick. Continuous lower and grid upper contacts were made of copper by vacuum sputtering. Finally, surface of cells was protected by tens of nanometers thick silicon nitride layer. For the experiment, solar cell panels were cut into (5×10) mm^2 samples. The copper wire has been attached to upper and lower contacts with silver paste. After that, all metal contacts were protected by chemically resistant and electrically-tight sealing-wax. Porous silicon layer manufacture was carried out in a teflon electrochemical cell. Anode was the protected entire lower solar cell contact, while the cathode made of platinum was in contact with electrolyte. Before the manufacture of hidden porous silicon structure, samples were placed in a fluoride acid for few minutes in order to remove the protective layer of silicon nitride. Electrochemical porous silicon technology is sensitive to many technological parameters, such as density of electrolyte, concentration of charge carriers (mainly holes), temperature and others [4]. Some special efforts are required to stabilize this technology. Moreover, we carry out electro chemical etching process under illumination. Production of porous silicon structure has been carried out in the HF: ethanol = 1:2 volume ratio electrolytes. Samples were illuminated by 50 W halogen lamp light during etching. Etching current was controlled by a computer in the limits of (6-14) mA/cm^2, etching duration was limited to (10-30) s. Electric charge passing through the unit of the area was controlled in the range of (260-420) mC/cm^2, so, the manufactured porous silicon structure consists of two porous silicon layers: low porosity top layer (about 20 – 40 %) and main higher porosity lower layer with P ~ (50 – 70) %, most of which was hidden in the emitter volume. It results in relatively unaffected solar cell surface with main texture located in a volume, unlike the works done so far. Simplified scheme of modified solar cell sample is shown in Fig. 1.
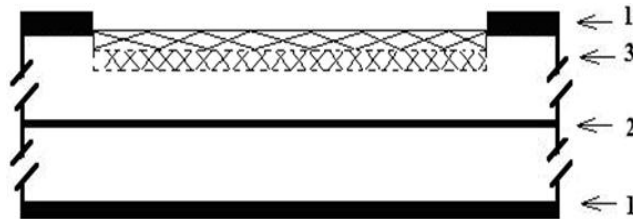
Fig. 1.   Scheme of modified solar cell: 1, 1'– entire and grid metallic contacts; 2 – p-n junction; 3 – hidden porous silicon structure (buried texture).

Original, as well as the modified solar cells were tested by measuring the electric characteristics of samples. The measurements were performed using computerized equipment package consisting of multimeters Tektronix CFG 253, Ketley 2000, Metex MXD 4660 and oscilloscope Tektronix TDS 3032B. Investigation of solar conversion efficiency in spectrally integrated regime was performed using a 35 W Xenon lamp with the spectrum close to 5000 K black body radiation spectrum. Halogen 50 W lamp and grating monochromator were used for illumination of solar cell samples during the measurement of spectrally resolved peculiarities of the current-voltage characteristics.

3. Results and Discussion

Fill factor F of the current-voltage characteristics is one of the most important parameters studied to estimate the solar cell quality. Fill factor being defined exactly as a ratio of the area under the real current-voltage characteristic curve and the area of the product of short-circuit current I_{sc} and open circuit voltage U_{oc} (electromotive force of solar cell). The simplified fill factor form, defined as the maximum solar cell output power P_{max} divided by product of short-circuit current and the open circuit voltage, is used as well. Solar cell efficiency η and fill factor F are associated by close-to-linear dependence. So, the change in fill factor value reflects simultaneously a change in solar cell conversion efficiency. The current-voltage characteristics of a solar cell can be measured using an external voltage source as well as by measuring the current, created by illuminated solar cell, and voltage on different impedance loads. We used the past method, because it allows direct determination of the optimal loading of the solar cell during an experiment. Current-voltage characteristics of two solar cell specimens are shown in Fig. 2 under illumination of xenon lamp before and after manufacture of porous silicon structure. The samples differ in illumination area and in the current density used
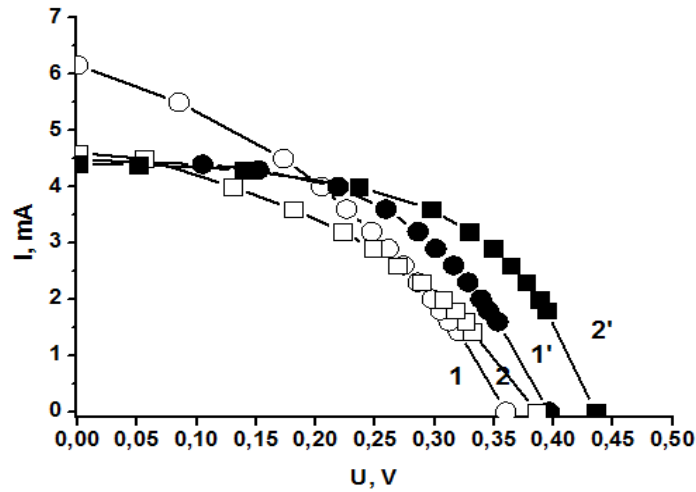
Fig. 2. Current-voltage characteristics of solar cell samples under illumination: 1 and 2 – before the manufacture of porous silicon structure; 1' and 2' – after the manufacture of porous silicon structure

at the second etching stage during manufacture of buried texture. The results presented in the figure show, that the porous silicon structure may increase the short circuit current I_{sc} and the open circuit voltage U_{oc}, as well as decrease it. It is difficult to determine the change in fill factor visually. The consistent calculation showed, however, that fill factors of current-voltage characteristics have increased in both samples investigated. Fill factor of one sample has increased by 11%, while the other sample shows an increase of 15%. The shown fill factor increase means the enhancement in the solar cell energy conversion efficiency as well. We have analyzed the experimental data of electric power dependence on voltage, to find the maximum power created by solar cell at the balanced loading. We found out that the maximum power increases by about 31 percent, thus, we found that the electric power generation in solar cell increases more than the fill factor of current-voltage characteristics in modified solar cells by manufacture of a buried texture inside the emitter volume. To figure out more specifically what causes the fill factor increase, we perform spectrally resolved measurements of current-voltage characteristics under illumination of halogen lamp light passed through the grating monochromator. Different light quanta convert to electricity with different efficiency because of the spectral dependence of light absorption coefficient $\alpha(\lambda)$ and different effectiveness in charge carrier passage through the p-n junction. Both factors influence the peculiarities of current-voltage characteristics and its fill factors at different wavelengths of incident light. The current-voltage characteristics for one of modified solar cells, illuminated by spectrally-resolved light are presented in Fig. 3. Note that the generated current is significantly lower compared to a specimen illuminated by integral radiation presented in Fig. 2. Analogously to the case of integrated lighting we found the fill factors F_1 and F_2 of each current-voltage curve for two modified samples 1 and 2 as well as fill factors F_o of each curve for the unmodified sample. It has been revealed, that the greatest increase in fill factor is in spectral range of 450 nm to 750 nm. The most of sun's spectral energy in this region (~60%) is under air mass AM1.5. We calculate the relative increase in fill factor $(F_{1,(2)} - F_o) / F_o = \Delta F_{1,(2)} / F_o$ for different wavelengths of incident light from the experimental data. The results presented in Fig. 4 reflect the specific peculiarities of a buried porous silicon texture influence on the efficiency of silicon solar cells. Generally the influence of buried porous silicon texture on fill factor is evident in wide spectral region. The greatest increase in relative fill factor was found in vicinity of wavelengths $\lambda \cong 550$ nm, whereas the relative increase in F is dropping at longer wavelengths. The absorption of light in porous silicon differs from crystalline one when quantum confinement effect occurs [4]. However, the confinement effect is not obligated for transmittance reduction in silicon plates containing porous silicon and for enhancement in its photosensitivity. Increase in photoconductivity of silicon wafer can be caused by "trapping" of light in porous layer [8]. Such effect was observed in a narrow spectral region at wavelengths close to 1100 nm for silicon wafers with textured back surface. In contrast to results observed in the paper cited we observe the enhancement in solar cell performance starting in very short wavelength region of visual spectrum and, allowed by our measurement technique, it continues up to sufficiently long wavelengths. Moreover, the greatest increase in the solar cell current-voltage characteristic's fill factor was observed in the blue-yellow region. We consider few effects which may be responsible for improvement in the characteristics of a solar cell. The main one is thought to be light scattering on the textured area which is effective for all wavelengths despite the well-known classic proportion to the wavelength squared. The close-to fractal composition of buried porous silicon texture causes weak light scattering dependence on the wavelength of incident light for all spectra, except the region near $\lambda = 550$ nm [4]. The scattering of incident light on buried texture results in change to the light propagation direction and consequently increases the optical path resulting in a more complete absorption of the excitation quantum. The scattering indicatrix depends on porosity of buried texture and on wavelength of incident light. This dependence is important by allowing control of the technological parameters to find the optimal effect for this option. This effect is somewhat similar to "light trapping" [7]. Underlying difference in our approach is
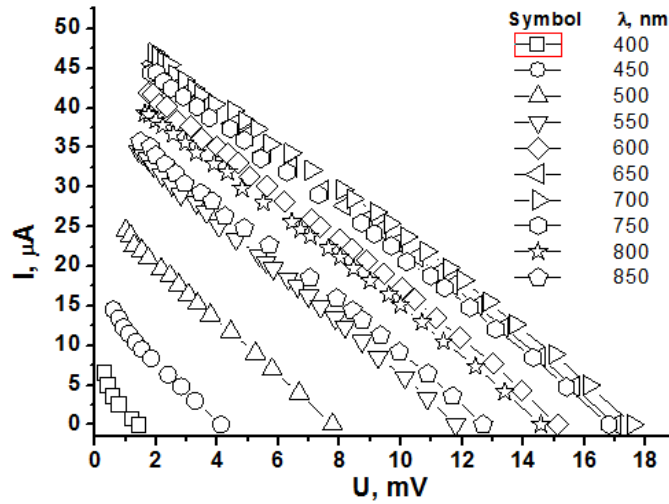
Fig. 3. Current-voltage characteristics of modified solar cells under illumination in different spectral regions
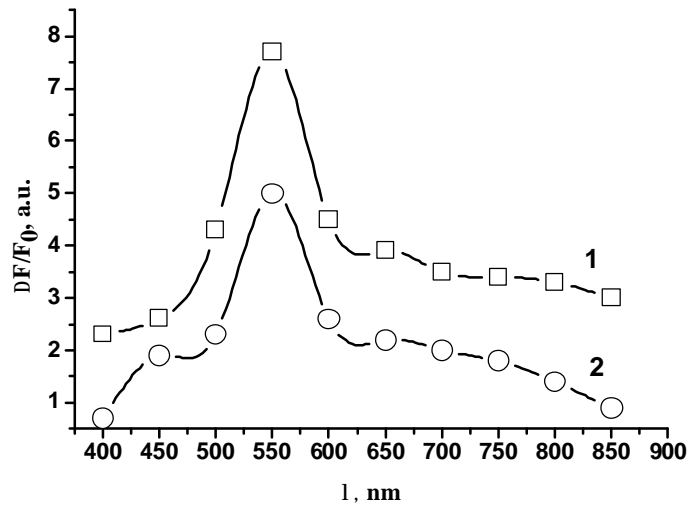
Fig. 4. Relative enhancement in current-voltage characteristics fill factor $\Delta F_{1,(2)} / F_o$ in different spectral ranges for two samples that differ by technological parameters.

the positioning of the texture in the emitter volume. Situating it closer to the p-n junction results in better collection of the excited charge carriers, enhancing the collection coefficient. In general, the greatest increase in the fill factor of current-voltage characteristics was found in vicinity of wavelengths $\lambda \cong 550$ nm. It might be the case, because of cumulative result of several different effects. First of them may be caused by influence of porosity on the effective optical path length d* in the porous area defined by the condition $\alpha(\lambda)\, d^* = 1$. Ignoring repeated reflection, optical path length in porous area is $\alpha(\lambda)\, d^* = \alpha(\lambda)\, d\, /\, (1 - P)$; where P is porosity and d is thickness of the absorbing element layer in silicon. In this case the path length of non-absorbed light may increase by 2-3 times. This increase is particularly important in blue-yellow spectral region where the light absorption coefficient α for silicon is greater than 10^5 cm^{-1}, so penetration depth $d = 1/\alpha \cong 100$ nm is much thinner than the thickness of solar cell emitter. Another effects increasing selective fill factor enhancement at $\lambda \cong 550$ nm may be highlighted as follows: i) possible reduction of the surface recombination rate in porous material [4, 20]; ii) porous structure has better anti-reflective properties [5]; iii) possible re-emission of blue incident light reaching maximum spectral sensitivity of a silicon cell [16 19]. To sum up, all these effects result in a better collection of excited charge carriers, consequently resulting in enhancement of the fill factor and improvement in the solar cell performance.

Conclusion

In conclusion, it has been shown for the first time that the buried porous silicon structure placed in the emitter volume of a mono-crystalline silicon solar cell increases fill factor of the current-voltage characteristics, improving its performance. The increase in fill factor is found in a wide spectral range – (450÷850) nm, where up to ~60% of the energy emitted by sun is located under air mass AM1.5. The most relative increase in fill factor has been observed at wavelengths of $\lambda = 550$ nm. In general, the following effects result in fill factor increase: i) scattering of incident light

across buried texture causing a change in propagation direction and increase in optical path length, thus improving absorbance of light quanta; ii) cumulative influence in a reduction of light absorption coefficient in porous silicon, a reduced surface recombination rate in porous area, possible anti-reflective properties of porous silicon layer and, finally, possible input of re-emission of blue-yellow incident radiation close to the maximum spectral sensitivity of silicon solar cell.

References

1. **Zhao J., Wang A., Green M. A., Ferrazza F.** Appl. Phys. Lett. 73, 14 (1998).
2. **Miles R. W., Zoppi G., Forbes I.** Materials Today, 10(11), 20 (2007).
3. **Schockley W., Queisser H. J.** J. Appl. Phys. 32, 510 (1961).
4. **Lehmann V.** Electrochemistry of silicon. Willey-VCH Weinheim, (2002).
5. **Prasad A., Balakrishnan S., Jain S. K., Jain G. C.** J. Electrochem. Soc., 129, 596 (1982).
6. **Menna P., Di Francia G., La Ferrara V.** Sol. Energy Mater and Solar Cells, 37, 13 (1995).
7. **Grigoras K., Krotkus A., Jasutis V., Sulienė D., Pačebutas V., Nijs J., Szlufcik J.** Lithuanian. J. Phys. 35(3), 247 (1995).
8. **Pačebutas V., Grigoras K., Krotkus A.** Physica Scripta., 69, 255 (1997).
9. **Lipinski M., Panek P., Bastide S., Levy-Clement C.** Porous Semicond. Science and Technology, 3d Intern. Conference, Ext. Abstr. 97, Techical University of Valencia, Spain (2002).
10. **Ramizy A., Hassan Z., Omar K., Al-Dauri Y., Mahdi M. A.** Appl. Surface Sci., 257, 6112, (2011).
11. **Koynov S., Brandt M. S., Stutzmann M.** Phys. Status Solidi. (RRL), 1, R53 (2006).
12. **Koynov S., Brandt M. S., Stutzmann M.** Appl. Phys. Letters., 88, 203107 (2006).
13. **Ma L. L., Zhou Y. C., Jang N., Lu X., Ge J., Ding X. M.** and **Hou X. Y.** Appl. Phys. Lett.,88, 171907 (2006).
14. **Kuzma-Filipek I., Duerinckx F., van Kerschaver E., van Nieuwenhuysen K., Beaucarne G., Poortmans J.** J. Appl. Phys., 104, 073529 (2008).
15. **Pavesi L.** Rivista del Nuovo Cimento, 20(10), 1 (1997).
16. **Samuoliene N., Sirmulis E., Stupakova J., Gradauskas J., Zagadskij V.** and **Shatkovskis E.** Acta Phys. Polonica, A119 (2), 137 (2011).
17. Nr 5819, Saulės elementas su paslėptos tekstūros emiteriu. E. Shatkovskis, V. Zagadskij, R. Mitkevicius, Lietuvos Respublikos Valstybinio patentų biuro oficialus biuletenis 2012/03, 2012-03-26 / Official Bull. State Patent Bureau of the Republic Lithuania, Patentai/Patents-5817-5821, 3, psl 15, 2012 Vilnius.
18. **Szlufcik J., Sivoththaman S., Nijs J. F., Mertens R. P., van Overstraeten R.** Proc. IEEE, 85(5), 711 (1997).
19. **Yerochov V. Yu., Melnik I. I.** Renew. Sustain. Energy Reviews, 3, 291 (1999).
20. **Kopitkovas G., Mikulskas I., Grigoras K., Šimkienė I., Tamošiūnas R.** Appl. Physics, A73, 495 (2001).

The Mechanical Properties of Composites AA2519-Ti6Al4V Obtained by Detonation Method

L. Sniezek*, I. Szachogłuchowicz*, K. Gocman*

Military University of Technology, gen. S. Kaliskiego 2 str., 00-908 Warsaw, Poland, e-mail: lsniezek@wat.edu.pl

Abstract

One method of manufacturing a metallic composite layer is explosive combining. The aim of creating metallic composites (plated coating) is to obtain a combination of desired properties of different metals. This paper presents the results of selected mechanical properties of AA2519-Ti6Al4V composites (prepared by detonation method), which were examined during monotonic tensile test and bending, micro and nanohardness measurements and with the use Charpy impact test.

KEY WORDS: *explosive welding, layered composites, mechanical properties of the composites.*

1. Introduction

Explosive welding is a process of a great technological importance to the possibility of modern metal composites production. It is an important complement to traditional plating production methods, such as welding or rolling mill. Bimetals obtained this way, and multi-layered composites consisting of more than two materials have unique structural properties. They are characterized by: high strength, corrosion resistance and in case of the association of appropriate materials – also a large ballistic resistance. Materials connectable by conventional methods can be explosion bonded. It is also possible with metals and their alloys, for which traditional technology has no alternative. Combined materials can vary significantly in their properties, for example steel-aluminum, steel-titanium, or aluminum-titanium. In addition to the production of new materials, the main reason to support the use of this technology are the economic effects in the form of large savings due to lower consumption of expensive metals and their alloys of specific characteristics. However, it should be noted, that for some base material the technology to obtain this type of connection, very difficult and complex, has been controlled only by the individual manufacturers, which results in extremely high prices of these products.

At present, this technology is most often used for joining sheets of different metals, non-weldable by conventional methods. The products produced by this method are used mainly in the manufacturing industry to improve the wear resistance and corrosion. Another very important use of explosive welding is to combine materials non-weldable by conventional methods. Studies on metals explosive welding combining are not heavily represented.

In paper [1] the structure and mechanical properties of composite materials of different types of steel after explosive welding, then subjected to heat treatment were analysed. The presented study helped to determine the scope of the subsequent heat treatment of the composites obtained from alloy steel which provide high mechanical properties with an acceptable degree of structural heterogeneity. Moreover, it has been disclosed that the diffusion zone obtained in the course of making composites with different types of steel has clearly visible structure and chemical inhomogeneity phase depending on the heat treatment method. The authors have determined the optimum explosion welding parameters for composites of various types of steel (blast velocity – $v_w = 3750$ m/s impact velocity $v_c = 400$ m/s) to ensure high tensile strength combination of materials ($\sigma_{det} = 400$-420 MPa) . Extensive discussion concerning the determination of the lower explosive limit of connection parameters ensuring the proper execution of the connectors is shown in the article [2]. The authors describe comprehensively the existing concepts and models of the merger and they also referred to the evolution of views on the possibility of obtaining the correct connector with fixed parameters: the impact velocity and angle of impact. In addition, a new parameter was introduced- pressure deformation impulse, understood as the pressure at the interface, depending on the collision circumstances and the time of pressure impulse action.

The work [3] was devoted to modeling the acceleration of the upper plate involved in explosive welding. Three numerical models describing the impact of the pressure caused by the outbreak of the upper plate connection were presented. The results indicated that the computer analysis allows prediction of kinematic parameters of explosive welding process. The study of structural and mechanical properties of metallic composites produced by explosive welding and annealing subjects were the subject of paper [4]. This paper presents the results of research on composite Al-Al3Ti-Ti composed of even 21 layers of aluminum and titanium. In such a complex combination a connection with the characteristic wave and without it was noticed on metallographic specimen. Connection structure of the material obtained was examined by TEM and SEM microscopy and by X-ray diffractometer. Impact strength of composites was determined on specimens notched "v" using Charpy impact test. Samples annealed showed lower impact strength and yet they were not fully broken in contrast to the sample without heat treatment. In [5] a study studied for a combined detonation sheets of stainless steel and titanium has been conducted. The plates were connected by oblique location of explosive striking plate. Welds were examined using optical and scanning electron microscope (SEM). Studies were

also performed on tensile, shear and bending as well as hardness and corrosion resistance were checked. Observations at the optical microscope and scanning showed the presence of flat or corrugated transition layer between the metal, depending on the force applied to connect the explosion metals. It was also found that the grains in the vicinity of the transition zone have been extended parallely to the direction of the explosion. Although the test specimens were bent by 180° they did no delaminate and did not break. As a result of these observations, it was found that explosively welded components made of titanium and stainless steel can be safely used in industry, even in the form of a bent.

Paper [6] presents the results of theoretical and experimental research on explosively bonded metal alloy of titanium and stainless steel. The aim of the study was to determine the effect of explosion on the thickness and structure of the transition layer between the metals. Optical microscopy showed that the transition from smooth to wavy transition zone occurs with increased explosive force, as described in the article [5]. Observations made by SEM also showed the presence of molten especially in the transition zone on the side against the waves and the zones growth with the increasing strength of the explosive.

Issues concerning the martensitic transformation and changes of the physical properties of the composite metal "steel-titanium" resulting from the explosive welding were described in the article [7]. This paper focuses on the analysis of a very narrow transition layer between titanium and stainless steel. It was observed that the combination of elements is present only in the layer of a width of about 6-2 µm into the titanium and 4 µm into the steel. Annealing implemented by the authors had a positive impact on the distribution of micro-connectors. It was found that the main effect on the properties of the explosive welding bimetallic composite is the plastic deformation, which increases the hardness of the alloy and the partial reduction of martensitic transformations.

The processes occurring during explosive welding are well described in the world literature [8]. Althought the phenomenon occurring during the production of multilayer composites containing in their structure the intermetallic phases of the Al-Ti are well described in the literature [9-13], the information on the formation of such a connection using explosive welding methods are quite scarce. Composite materials containing titanium aluminides, produced during the manufacture of Al-Ti joints are widely used as a construction material in the field of aeronautical engineering.

2. Research procedures

Adopted practical aim of the work included examination of selected mechanical properties of the layered composite material system of alloys: Ti6Al4V/AA1050/AA2519 and Ti6Al4V/AA2519, with the resulting diffusion layer type Al3Ti. It was assumed that such material will be characterized by unique properties, combining the beneficial properties of titanium and aluminum alloys (high strength, high ductility and low specific gravity) and Ti-Al based intermetallic alloys phases of Ti-Al (high hardness and rigidity). The tests were made by a layer composite explosive materials in the form of the underlying aluminum alloy AA2519 (AlCuMgMn + ZrSc) and titanium alloy Ti6Al4V. The chemical composition and strength properties of the base materials are provided in Tables 1 and 2.

Table 1

Mechanical properties and chemical composition of the Ti6Al4V alloy

Mechanical properties			Chemical composition [*wt* %]							
$R_{p0,2}$ [MPa]	R_m [MPa]	A [%]	O	V	Al	Fe	H	C	N	Ti
950	1020	14	< 0.20	3.5	5.5	< 0.30	< 0.0015	< 0.08	< 0.05	residue

Table 2

Mechanical properties and chemical composition of the AA2519 alloy

Mechanical properties			Chemical composition [*wt* %]							
$R_{p0,2}$ [MPa]	R_m [MPa]	A [%]	Si	Fe	Cu	Mg	Zn	Ti	V	Zr	Sc
312	335	6.5	0.06	0.08	5.77	0.18	0.01	0.04	0.12	0.2	0.36

Sheets of base materials with a thickness of 4 mm were pooled by the explosive in the Department of Technology Energetic "EXPLOMET". Cooperation with the plant allowed to undertake research aimed at obtaining and determining the performance of engineering plastics in the form of Al-Ti composite layer with specific properties, Which does not have a solid material. During manufacturing of the connection (joints) an additional intermediate layer of AA1050 alloy with the thickness of 0.6-0.8 mm was used.

3. Results of research

3.1. The strength properties

The study of mechanical properties under axial tension were carried out on the flat samples, in accordance with DIN EN ISO10002-5: 2004. Strength properties determined from the monotonic tension are presented in the Fig. 1. Static three-point bending test was conducted in accordance with DIN EN ISO 6892-1. The study was conducted for the

three variants of the load, unloading the sample from the side of: alloy AA2519 (A) and Ti6Al4V alloy (B). The results in the form of stress σ_b waveform changes depending on the deflection f is shown in Fig. 2.

$R_{p0,2}$ [MPa]	R_m [MPa]	E [GPa]	A [%]
468	619	154	11.6

	$R_{p0,2}$ [MPa]	R_b [MPa]
A	400	985
B	395	952
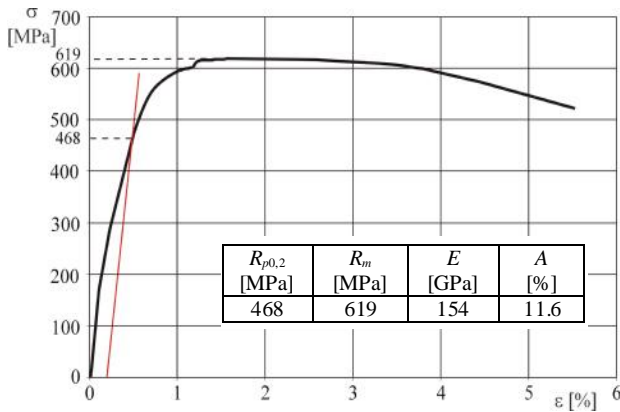
Fig. 1. Monotonic tensile test of flat AA2519-Ti6Al4V laminated composite
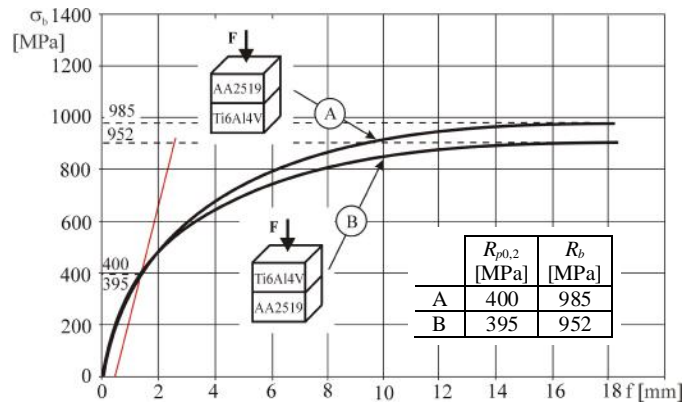
Fig. 2. Monotonic bending flat samples AA2519-Ti6Al4V laminated composite

During the bending test, no significant differences in the value of the yield strength $R_{p0,2}$ and flexural strength R_b of specimen loaded on the AA2519 alloy and Ti6Al4V alloy side were registered. Certain limitations of the range of shaping technology of tested composites showed bending test, which is used for determining the ability of the plastic deformation of samples due to bending forces. A positive test result of bending to an angle of 180° with mandrel with the thickness of 18 mm was obtained only for samples loaded from the aluminum alloy side. (Fig. 3a). Loading the sample on the side of the titanium alloy lead to cracking and loss of cohesion of the connection (Fig. 3b).
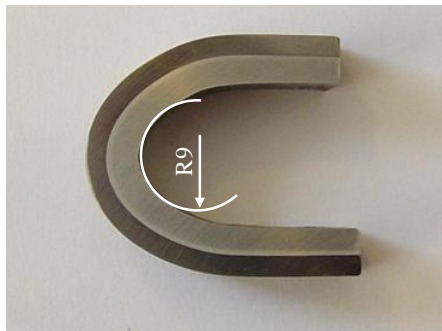
a
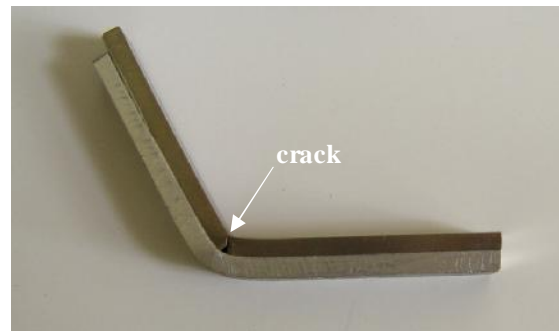
b

Fig. 3. Probes after technological bending test; sample pay the on the side of melt AA2519 (a) and the sample pay the on the side of alloy Ti6Al4V (b)

3.2. Microhardness

Selection of appropriate parameters allowed for the direct explosive connection of AA2519-Ti6Al4V alloys as well as the connections with intermediate layer of AA1050 alloy (Fig. 4a). In the latter case, the connection between AA1050-AA2519 alloys possess characteristic corrugated interface, while Ti6Al4V-AA1050 interface is flat. Distribution of microhardness across Ti6Al4V-AA1050-AA2519 connection, taking into account microhardness of materials in initial state, is presented in the Fig. 4b.

Although the time of the diffusion is short, the diffusive nature of the process of formation of Al-Ti joints and thermo-mechanical processes caused that in a narrow area of transition zone there is a segregation of elements which resulted in local changes of mechanical properties. Such measurements can be carried out in a classical instrumental method (with indentation) and by sclerometric method. Sclerometric hardness measurement is realized by scratching the surface with constant load and measuring the width of the scratches. Based on the calibration curve (width scratch versus load) made of the reference material of known hardness, the hardness of test material is calculated. The study used a set of UNMT (Universal Nano & Micro Tester) which allows very shallow scratches and measuring the hardness of areas with a width of a few nanometers. Transition zone AA2519-Ti6Al4V connection with produced scratches is shown in the photograph (Fig. 5).

If the morphology of the surface (Fig. 6a) was appropriate to produce scratches, the parameters of test (scratch length of 10 μm, and the load – 3.5 mN) were determined. The area of the measurement was carefully selected in order to avoid irregularities of surface along the track of the tip which could affect the results. After the test the surface of the sample was scanned again and the width of the scratches (1-6) were measured (Fig. 6b).

Results of hardness measurements at the measuring points illustrated in Fig. 6b is shown in a bar graph (Fig. 7).

a

b
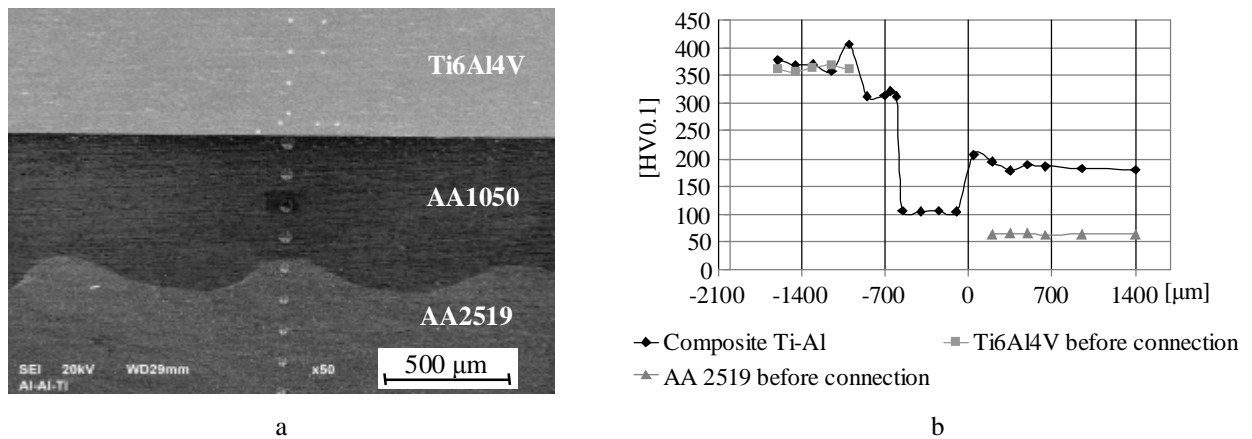
Fig. 4. Area of Al-Ti explosive connection in a form of wave AA2519-AA1050 interface and flat Ti6Al4V-AA1050 interface (a) and a graph of changes in the microhardness of the connection zone (b)
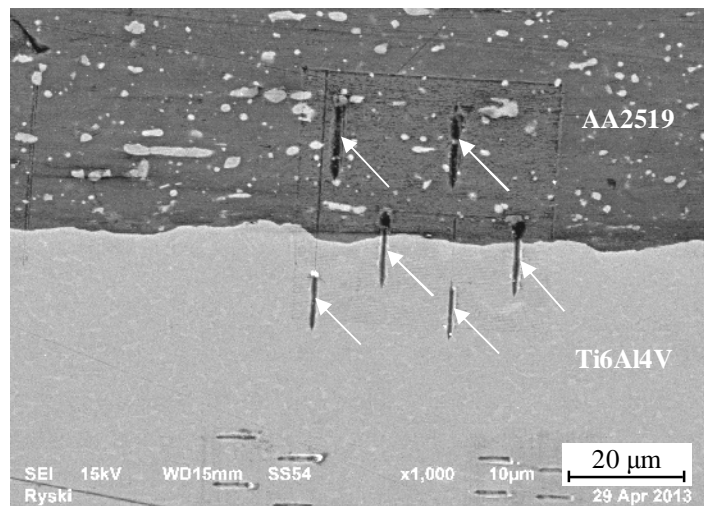
Fig. 5. Area connection AA2519-Ti6Al4V made by explosive traits that identify the hardness

a

b
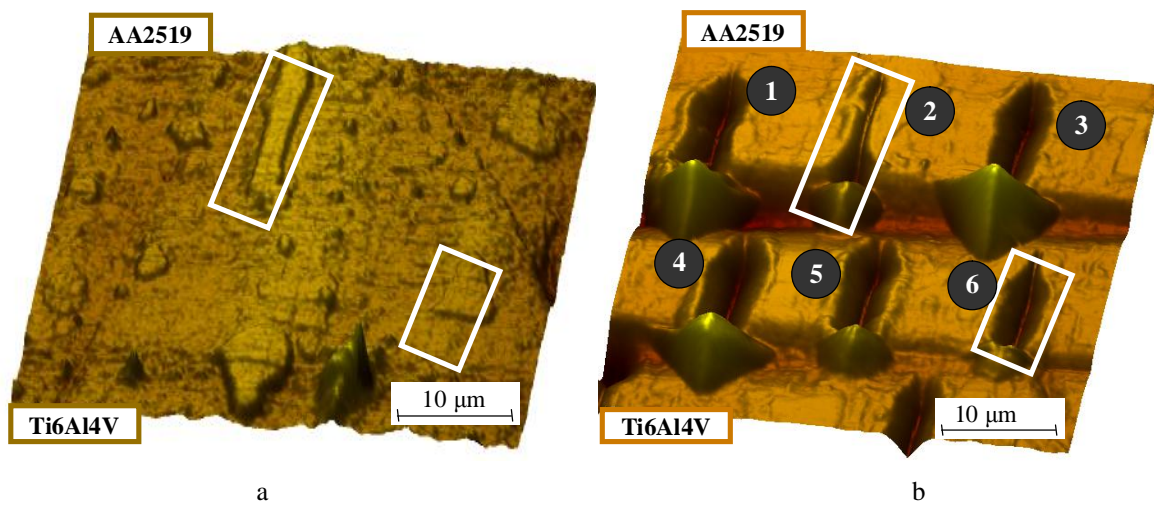
Fig. 6. The morphology of the surface of AA2519-Ti6Al4V transition zone (a) and selected scratches obtained by sclerometric hardness measurements (b)
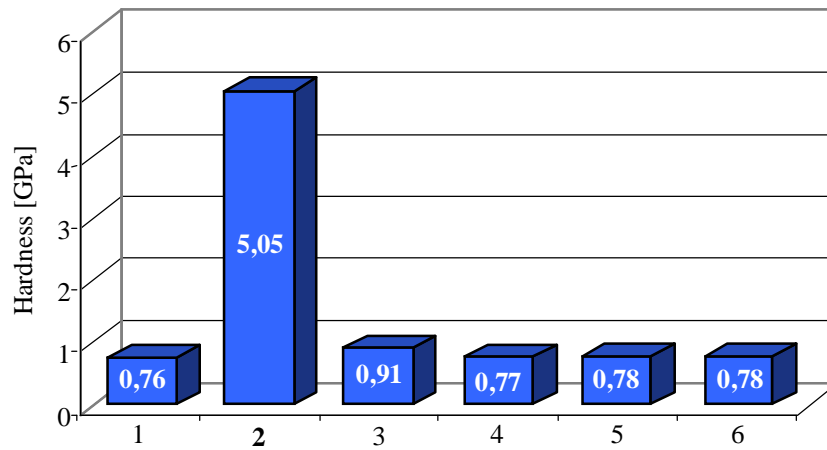
Fig. 7. Results of sclerometric hardness measurements in AA2519-Ti6Al4V transition zone (see text)

A significant increase of hardness in point (2) is probably the result of measurement within the Al3Ti particle (with a hardness of 300-340 HV) deployed in a soft matrix of aluminum alloy (67 HV). This hypothesis will be verified in further research using electron microscopy.

3.3. Toughness

Toughness measurements were performed according to standard EN 10045-1 for samples with indented V-notch. Three groups of specimens were examined: with V-notch on the side of AA2519 alloy layer (Al variant), V-notch on the side of Ti6Al4V alloy (Ti variant) and in the frontal plane of connection (Al-Ti variant) – Fig. 8.

During the test of samples of "Al variant" and "Al-Ti variant" delamination in the interface of AA2519 were registered. That delamination occurred in places where there was no characteristic wave.

Impact test results are presented in a bar graph in Fig. 9. The highest fracture toughness value was obtained for the sample made in the "Al variant" while a minimum – for "Al-Ti variant".
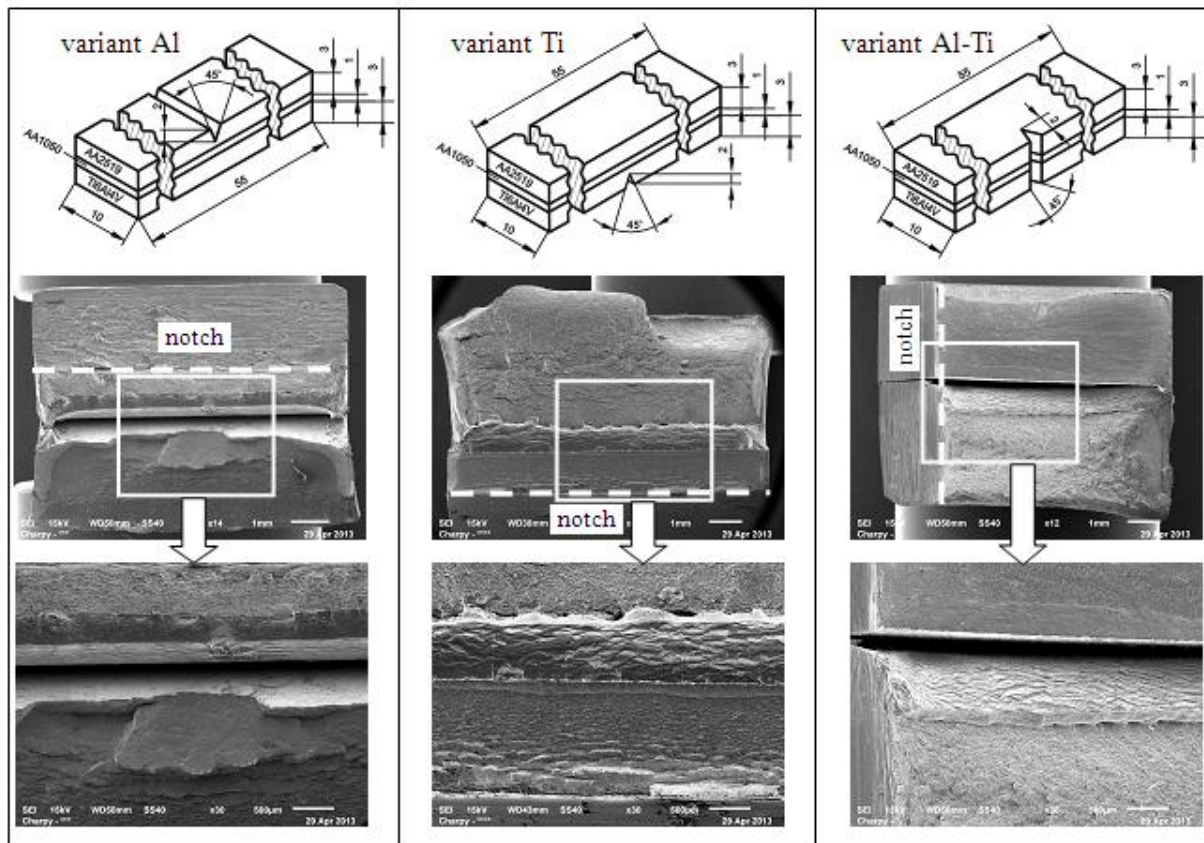
Fig. 8. Fracture of samples as a result of impact resistance tests with V-notch on the side of AA2519 alloy layer (Al variant), V-notch on the side of Ti6Al4V alloy (Ti variant) and in the frontal plane of connection (Al-Ti variant)
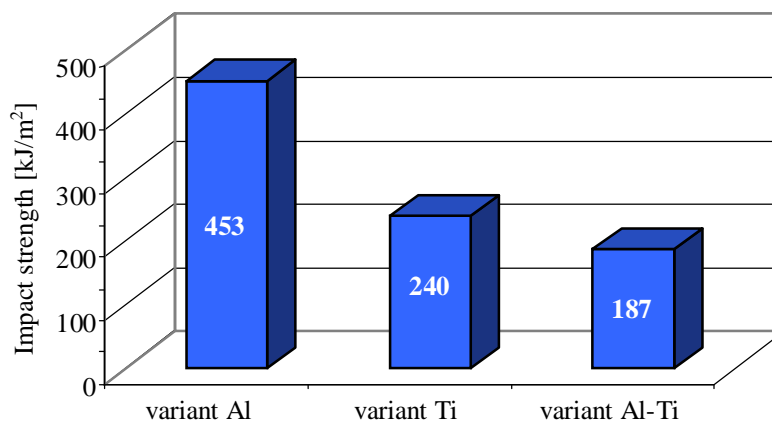
Fig. 9. The results of measurement of AA2519-AA1050-Ti6Al4V connection toughness (See text)

4. Conclusions

Combining explosive is a process of great technological importance for the possibility of the production of modern composites. The results of experiment of connection AA2519 and Ti6Al4V alloys are optimistic. The joints have satifactory resistance and susceptibility to plastic deformation during the bending under the assumption that the inner layer of the composite is made of aluminum alloy. The results set the direction for further research to determine the effect of annealing parameters in high vacuum or in a protective gas atmosphere on the microstructure, phase transitions and stability of the structure and the fatigue properties of composites of the Al-Ti, obtained in the process of combining explosive.

Acknowledgment

References

1. **Trykov P., Stepanishchev I. B., Trudov A. F., Arisova V. N.** Structure and properties of explosion-welded composites from steels of different kinds, Metal Science and Heat Treatment, Vol. 46, Nos. 3–4, 2004.
2. **Lysak V. I., Kuzmin S. V.** Lower boundary in metal explosive welding. Evolution of ideas, Journal of Materials Processing Technology, 212 (2012), pp. 150–15.
3. **Benak M., Taraba B., Turna M.** Contribution to modelling the effect of explosive on accelerated material in explosion welding, Annals of DAAAM for 2009, Volume 20, No. 1.
4. **Bataev I. A., Bataev A. A., Mali V. I., Pavliukova D. V.** Structural and mechanical properties of metallic–intermetallic laminate composites produced by explosive welding and annealing. Materials and Design, 35 (2012), pp. 225–234.
5. **Nizamettin Kahraman, Behcet Gulenc, Fehim Findik.** Joining of titanium/stainless steel by explosive welding and effect on interface, Journal of Materials Processing Technology, 169 (2005), pp. 127–133.
6. **Akbari Mousavi S. A. A., Farhadi Sartangi P.** Experimental investigation of explosive welding of cp-titanium / AISI 304 stainless steel, Materials and Design, 30 (2009), pp. 459–468.
7. **Belyaeva S., Rubanik V., Resninaa N., Rubanik V. Jr, Rubanik O., Borisova V.** Martensitic transformation and physical properties of 'steel–TiNi' bimetal composite produced by explosion welding, Phase Transitions, Vol. 83, No. 4, April 2010, pp. 276–283.
8. **Findik F.** Recent developments in explosive welding, Materials and Design 32 (2011) 1081–1093.
9. **Wierzchoń T., Ossowski M.** The structure and selected properties of composites: titanium alloy Ti6Al2Cr2Mo – intermetallic phases of the Ti-Al composites (in polish) Composites, 6 (2006) pp. 50-53.
10. **Peng L. M., Wang J. H., Li H., Zhao J. H., He L. H.** Synthesis and microstructural characterization of Ti–Al3Ti metal–intermetallic laminate (MIL) composites, Scripta Materialia, 52 (2005), pp. 243–248.
11. **Xu L., Cui Y. Y., Hao Y. L., Yang R.** Growth of intermetallic layer in multi-laminated Ti/Al diffusion couples, Materials Science and Engineering, A 435–436 (2006), pp. 638–647.
12. **Rohatgi A., Harach D. J., Vecchio K. S., Harvey K. P.** Resistance-curve and fracture behavior of Ti–Al3Ti metallic–intermetallic laminate (MIL) composites, Acta Materialia, 51 (2003), pp. 2933–2957.
13. **Vecchio K. S.** Synthetic multifunctional metallic–intermetallic laminate composites JOM, 57 (2005), pp. 25–31.

Proceedings of 8th International Conference ITELMS'2013

Optimization of the Sports Car Space Frame

V. Spangelevičius*, V. Lukoševičius**, V. Dzerkelis***

*Kaunas University of Technology, Kęstučio str. 27, LT-43124, Kaunas, Lithuania, E-mail: vilius.spangelevičius@stud.ktu..lt
**Kaunas University of Technology, Kęstučio str. 27, LT-44354, Kaunas, Lithuania, E-mail: vaidas.lukosevicius@ktu.lt
***Kaunas University of Technology, Kęstučio str. 27, LT-44354, Kaunas, Lithuania, E-mail: vytautas.dzerkelis@stud.ktu.lt

Abstract

This article covers the optimization of sports car vehicle space frame and the principals and requirements for topological optimization. Space frame is designed according the rules of international contest "Formula Student". In order to determine if construction has optimal design, several static and topological calculation sets are made.
KEY WORDS: *sports vehicle, space frame, topology optimization.*

1. Introduction

Vehicles frame – it's a robust construction which is used to connect suspension and all the components in one unit and withstand loads arising when vehicle moves. The main objective is to consolidate all the wheels with frame, and make frame resistant to bending and torsion. There also should be made a precise placement of the components like engine and transmission. Also space frame has to withstand all the external loads while vehicle is in use.

Frames used for sports cars differ from the ones used on regular vehicles. Main difference is when designing frame of sports vehicle, constructor tries to optimize its mass as much as possible. The advantage is clear – lower mass leads to a higher acceleration. There is also a trend to make frames from lither and stronger materials. However there is usually no possibility to replace materials for such standard components as engine, steering or exhaust system. That's why space frame elements of suspension and power supply system are usually objects for optimization.

Space frame used for this article is made from seamless cold rolled precise E355+N normalized low carbon steel pipes. In accordance to "Formula Student " rules all the pipes inner and outer diameters correspond all the requirements, however this makes optimization quite trough task. Static calculations are performed using three different load sets, which mostly reflect loads occurring while vehicle is use.

Main goal of this paper is to investigate if designed space has optimal design, also to perform static calculations, topological optimization and compare initial model with optimized one. Using finite element method and load sets strength calculations are made [4].

2. Strength and stiffness requirements for sports car space frame

According "Formula student" contest rules space frame has to fulfill set of specific requirements which will be analyzed in this paragraph. This helps to understand the way that was used when designing this specific space frame. Only main requirements are covered in this theoretical part. Minimal requirements for materials: main components of space frame must be made from round on square profile low carbon steel not exceeding 0.1% carbon [2].

Material specifications used when performing strength calculations for buckling and bending cases are not allowed less than specified in Table 1.

Requirements for welded single one piece parts are provided in Table 2.

Table 1

Minimal characteristics of materials

Parameter	Value
Elastic modulus E	200 GPa
Yield strength s_y	305 MPa
Maximal strength s_u	365 MPa

Table 2

Materials mechanical characteristics requirements

Parameter	Value
Yield strength s_y	180 MPa
Maximal strength s_u	300 MPa

3. Requirements for frame geometry

In any critical situation the hands or head of the driver cannot cross lines when car is in subject to roll over. Frame should have special enforcements allowing to protect foots and head. When sitting in working position driver's helmet should have at least 50.8 mm clearance from tangent line drawn from main hoop to small hoop (Fig. 1). The same applies to the tangent line in the back view. Helmet is also not allows to cross line drawn parallel to main hoop [3].
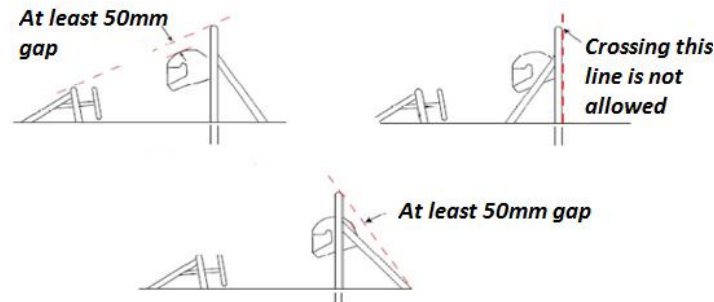
Fig. 1. Drivers head position to main hoop

Maximal pipes bending radius, which is measured from center line of the pipe, should be three times bigger than the outer diameter of the pipe. Bends must be smooth and are not allowed to have any cracks. Head and foots protecting pipes are connected together using special reinforcement plates. Aluminum and titan alloys cannot be used for main hoop, because of their mechanical properties. Main hoop should be connected to the frame in both sides, starting in one lowest side and ending in another. Angle between main hoop and vertical position should not exceed 10 degrees. Looking from front direction main hoop width at the bottom part cannot be lesser than 380mm [3].

Leg protection part has to be constructed so that the reinforcements are positioned from left to right. If leg protection parts exceeds ten degrees angle from vertical position, there should be made additional reinforcements insuring security.

The leg protection part should cover the entire frame from lower to top point. This part is also not allowed to be lower than steering wheel rack. If there are any additional or oblique reinforcements leg protecting part then can be combined from several pipes. Distance between steering wheel and leg protecting hoop cannot exceed 250mm. Oblique reinforcements are recommended.

Without requirements mentioned above, there are some specific ones for the rear part of the frame. In case of roll over, construction is not allowed to be deformed, as this might cause danger for the driver. Triangle shapes should be considered to be used as much as possible, as they tend to spread impact energy to whole construction not the single pipe or part of it. Triangle shapes also lowers risk of frame damage. Points where pipes consolidate should be considered to be points where suspension brackets are fastened. This way allows distribution of forces coming from suspension to the frame. It also protects construction from deformation of single pipes and allows reduction of mass and material usage [3].

4. Static calculations of sports car space frame

In order to validate designed construction, three static analyses are performed using finite element modeling package Ansys 13.0. Optimal frame design should withstand forces acting from suspension mountings and also forces arising from driver and component mass. Any construction deformations while vehicle is moving causes steering deteriorations, which might be crucial when vehicle is making fast turns or face bumping from the ground surface. Another crucial factor is ability to protect the driver if construction is being damaged or in case of accident. There are three specific and most common load scenarios occurring while vehicle is in use (Fig 2).
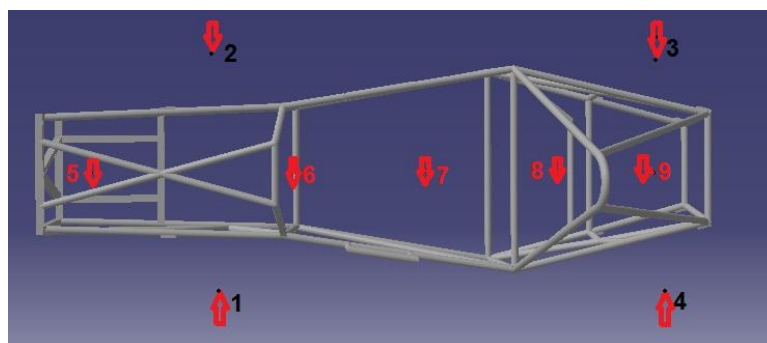
Fig. 2. Boundary conditions and restrains fixture points

Every scenario has its boundary conditions and specific load sets, which are used when calculating stress and axial deformations.

- No.1. Bending which is caused from mass of components- Points 1-4 fixed, points 5-9 with attached remote loads caused from components weight;
- No.2. Front torsion – points 3-4 fixed, in points 1-2 acting opposite forces with value of 1500N, points 5-9 with attached remote loads caused from components weight;
- No.3. Rear part torsion ,front is fixed in points 1-2, in points 3-4 acting opposite forces with value of 1500N, points 5-9 with attached remote loads caused from components weight.
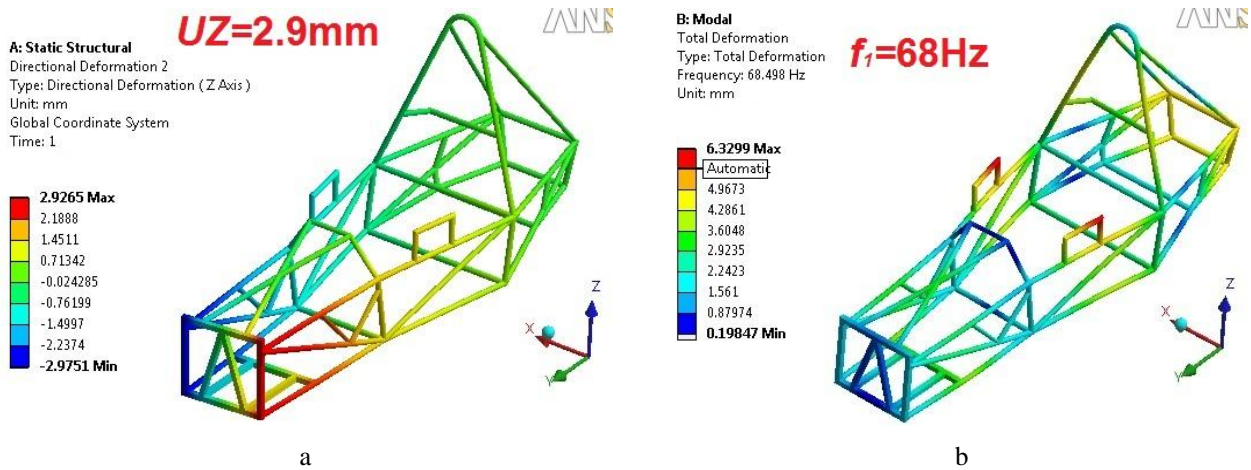
Fig. 3. Displacement and natural frequencies calculations results: a) – 1st load scenario, when front is being rotated; b – scenario, when natural frequencies are calculated

Static analysis shows (Fig. 3) that displacement in front part of the frame is 3mm and 1mm in the rear part of the frame. Assumption is made that it is appropriate to perform topological optimization in order to reduce displacement in front part. Mass reduction is also one of the goals. Modifying pipes arrangement and adding additional elements, or decreasing inner diameter of pipes could help increase stiffness and natural frequencies.

5. Topology optimization

Main principle of topology optimizations is that by having initial part shape and knowing boundary conditions-forces, fixtures, outside influence, one can choose the optimal way of material and shape distribution. Optimization method is based on the way that initial model is solved using loads cases and algorithms. Program than decides and shows points with largest element concentration, meaning that material should be in those points. Using this data graphical approximation of points where higher stiffness is needed can be made. Also preliminary shape can be defined and designed.

In order to perform topological optimization it is necessary to prepare suitable model – template. This template has same shape as initial designed frame, but is made from solid plates, which imitates places where pipe profiles are located. It also creates space for optimization. Thickness of these plates is a little bit bigger than an outer diameter of pipes used for frame. Points where suspension is attached are simulated by adding rectangle pads, pads are also added at points where components mass is acting (Fig. 4).
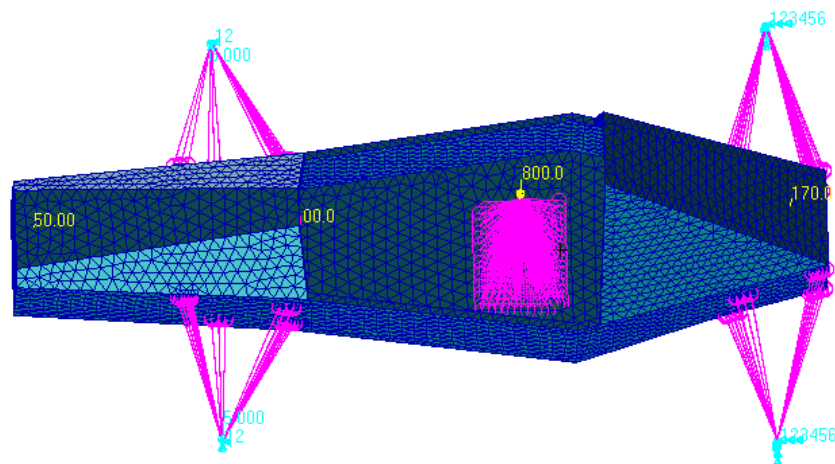
Fig. 4. Template model for topological optimization

Topological optimization algorithm uses all the load sets acting on space frame. It takes every load set right after another; this makes calculation more accurate and helps to reflect results which are close to the real case. Load steps, load values and restrains position is the same as used in static calculations. In order to ensure that the system calculates most optimal result, high mass reduction of 70% was used. Maximum iterations number used for experiment was 50. Not all scenarios required such high number of iterations, but this number ensured that optimization algorithm is fulfilled. Results are shown (Fig. 5) below. There was restrain modification made and just a sliding movement is limited, reflecting load cases in a dynamic way.
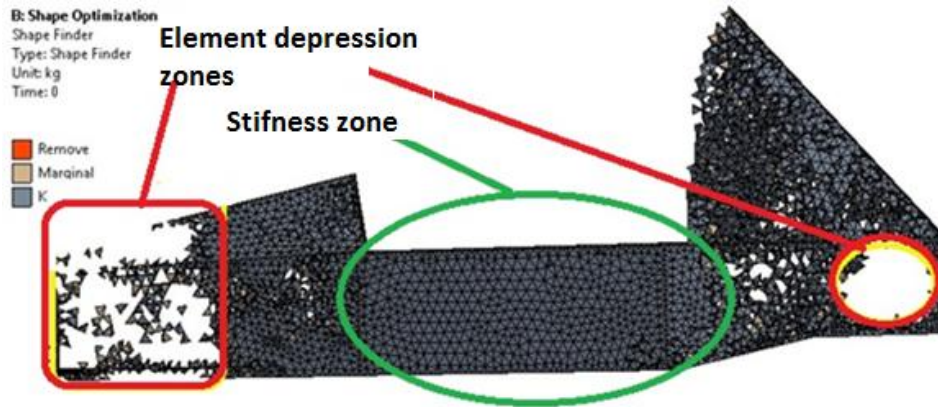
Fig. 5. Side view after optimization, 50 iterations used; mass reduction percent – 70%

Looking from the side, in front section of the frame a big depression of elements can be seen, this is because the part of construction after restrains is not subjected to any high loads, front of the car only has pedal and steering system and partially influenced by mass of the driver. Restraining just a sliding movement has a big influence as points subjected to high loads has high element concentration and this means that in these points construction should improve. In rear part between front and rear restrains, elements concentrates mostly on the sides of construction, meaning that this part should have highest stiffness. Main hoop is not taken in redesigning considerations as any change will make it not to comply with existing rules.
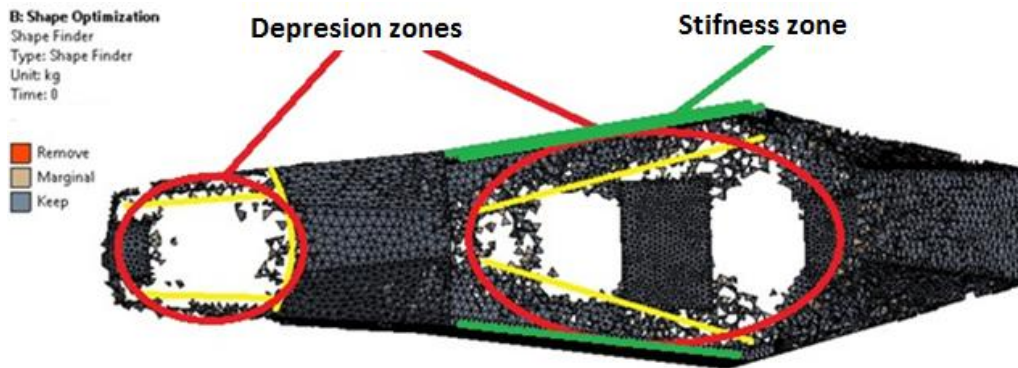
Fig. 6. Top view after optimization, 50 iterations used; mass reduction percent – 70%

Looking from the top elements (Fig. 6) tend to concentrate in areas where construction is being subjected to high loads, meaning that this area need to be stiff. High elements depressions can be noticed in places where components masses are placed. As front section is only subjected to loads coming from component masses, elements are kept just in those zones, removing all other ones.

After performing topological optimization on designed template there was several assumptions made. Middle section has to be improved, either increasing diameters of pipes or adding some reinforcements. A front and rear section after connection points does not require such high stiffness, as these areas are only subjected to loads from components mass. Suggestion is to increase the thickness of middle section pipes from minimal 1.5 mm to 2 mm. Pipes in the front and rear should have a reduction in wall thickness to lowest allowed in the rules – 1.25 mm, as wall thickness for initial model was 1.5 mm. Some restrains might be used in front section, where leg protection hoop starts.

- Green color marks round front and rear section profiles, whose wall thickness was reduced from 1.5 mm to 1.25 mm (Fig. 7).
- Red color marks middle section pipes, whose wall thickness was increased from 1.5 mm to 2.0 mm.
- Orange color marks front square pipes which have been left unchanged.
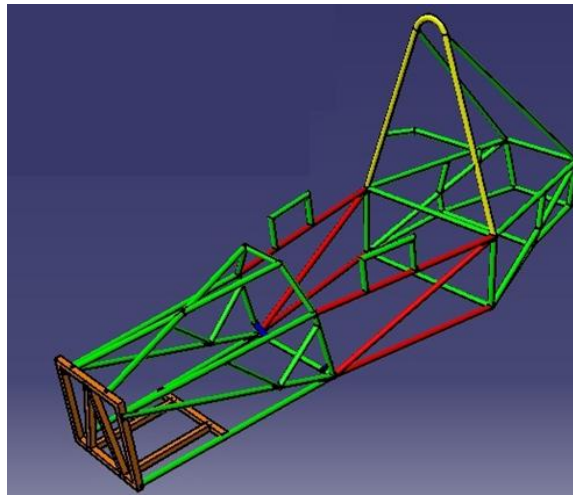
Fig. 7. Improved frame model

Static calculations on improved model were performed using same load steps and load values that were used for initial model. Displacement of front and rear part also natural frequencies was calculated. Results shows that improved construction tends to deform in quite similar as initial one, however values of displacement and natural frequencies have changed.

After comparison of the results it is clearly seen (Table 5) that all the parameters including displacement values and natural frequencies have been improved. Stiffness when turning front part has been improved 1.8 times, turning rear part 2.17 times, and this is noticeable improvement. Weight of construction decreased by 0.5 kg and this gives some improvement in sprung mass reduction. Natural frequencies were improved by 11%, which has influence on its dynamic stability.

Table 5

Static analysis comparison of initial and modified space frame

Parameter	Initial design	Modified design
Displacement rotating front section	$U_Z = 2.9$ mm	$U_Z = 1.6$ mm
Displacement rotating rear section	$U_Z = 1.3$ mm	$U_Z = 0.6$ mm
Natural frequencies	$f_1 = 68$ Hz	$f_2 = 77$ Hz

6. Conclusions

Topological optimization was performed using ANSYS finite element modeler. After analyzing optimization results it is clear that changes performed on construction gave a positive result. Static and dynamic stability of construction when turning front section improved 1.8 times, when turning rear section 2.17 times and natural frequencies increased by 1.13 times. Optimization was successful; construction became stiffer and a bit lighter.

Acknowledgements

References

1. **Willliam F. Milliken** and **Douglas L. Milliken.** Race car vehicle dynamics. Society of Automotive Engineers Inc. 1995. p. 73-285.
2. **Bendsoe M. P., Sigmund O.** Topology Optimization Theory, Methods and Applications. Berlin. 2003. p. 53-68.
3. "Formula Student" contexts rules book. Acess on the internet: < http://www.formulastudent.com/docs/fs2012-docs/fs2012-rules-final.pdf?sfvrsn=0 > [checked on 2013-05-05].
4. Standards of SAE steels, 2012. Acess on the internet: < http://www.westyorkssteel.com/AISI_steel.html > [checked on 2013-05-10].
5. Basics of topological optimization. Acess on the internet: < http://www-personal.umich.edu/~kikuchi/ GMcontents/topology.pdf > [checked on 2013-05-10].

Proceedings of 8ᵗʰ International Conference ITELMS'2013

Tools and Processes for Affordable Machines

P. Stodola*, J. Stodola**

*University of Defence Brno, Faculty of Economics and Management, K 110, Kounicova str. 65, 662 10, Brno. Czech Republic, E-mail: petr.stodola@unob.cz
**University of Defence Brno, Faculty of Military Technology, K 202, Kounicova str. 65, 662 10, Brno. Czech Republic, E-mail: jiri.stodola@unob.cz

Abstract

In this article, integration refers to a concurrent approach to making products which closely binds the independent phases of the classic serial product lifecycle and re-engineers the design, analysis, manufacturing, and support processes towards ensuring the efficiency of the overall product development process. Integration enables designers to manage processes and share data effectively, and enables tools to interoperate. By most accounts, an order-of magnitude reduction in overall cycle-time and cost can be achieved when integration of business, design and production processes is standard engineering practice.

KEY WORDS: m*odeling, simulation, design, engineering, integration, up-to-date methods.*

1. Introduction

Beginning in the 1980s, advancements in computer software and hardware began to make it possible to support the product development, manufacturing, operation and maintenance processes. In companies in the machinery industries, traditional drawing boards were replaced by Computer Aided Design (CAD) which assists the engineer in the creation, modification, analysis, and optimization of design. On the manufacturing side, CAM systems were development to help with the planning, control, and management of production operations. CAD/CAM systems are an integral part of the engineering process. Over the last thirty years, evolutionary refinements in computers and Computer-aided technologies (Cax) have significantly improved the capabilities within the many areas of product development. Mechanical design, for example, has benefited from Finite Element Analysis (FEA), process simulation, product visualization, Manufacturing Resource Planning (MRP). The application of these advanced technologies has improved the efficiency and accuracy of the many disciplines within the product development process. Paradoxically, despite investing heavily in Cax tools, training and services, many companies have discovered that their operating cost have increased and their expectations of immediate gains in productivity and efficiency remain largely unfulfilled. Decades of decomposing the product development process into specialized disciplines have led to a system mode of engineering design in which communication between the separate disciplinary groups is limited. The result is multidisciplinary "isolation" in their development of complex systems. Additionally, as the number and capabilities of the Cax tools has increased, the isolation of the functional groups within the engineering process has occurred as well. Accordingly one of the greatest engineering challenges is the effective integration of product development and manufacturing disciplines, processes and tools. In this subchapter, integration refers to a concurrent approach to making products which closely bins the independent phases of the classic serial product lifecycle and re-engineers the design, analysis, manufacturing, and support processes and share data effectively, and enables tools to interoperate. Advanced computer environments are essential to realizing the benefits of integration. Cax and Information Technology (IT) infrastructures are necessary to provide the foundational architecture that ensures that all information needed for product realization is available at every step of the process, from creation of the initial product concept to its translation to delivered product, in the form that directly supports each function. These infrastructures also enable information to flow seamlessly throughout the development, production, and support lifecycle, ensuring that the right information is available to all who need it. And they provide interoperability of tools and management of information throughout the process. This implies optimization, not only of individual processes, but also of the total product/process/resource environment [1].

2. Processes, Tools and Affordability

When a company or organization embarks on the development of a new product/system or modification to an existing product it typically follows a well defined process. There is no one right process for a given organization or product; the appropriate process must belong to the system of companies capabilities and resources, market forces or customers requirements, and possibly competitor capabilities and resources. Several well known processes for product development are: DEsign for Six Sigma (DESS), Integrated Product Development (IPD), Lean Engineering and Manufacturing, Concurrent Engineering (CE), Integrated Product Teams (IPT), and the System Engineering Approach (SEA). For example, in [2] there is a list of principles of Integrated Product Development such as:
1.   Understand needs and manage requirements;

2. Manage and plan product development;
3. Use product development teams;
4. Integrate process design;
5. Develop robust design;
6. Integrate CAD, CAM, and CAE tools;
7. Simulate product performance and manufacturing processes electronically;
8. Create and efficient development approach;
9. Improve the design process continuously etc.

In the complex study [3] by NATOs identified the emerging technologies commonly known as Concurrent Engineering, Integrated Design and Virtual Manufacturing as important for NATO member countries. The study emphasized the necessity of integration of tools and processes as a consequent evolution of the basic idea of concurrent engineering. Effectively combining people, processes and technologies was deemed an important prerequisite to achieving product affordability and advancement in the state-of-the-practice. In the development of complex mechanical systems, affordability is an important driver for the technologies and processes within the complete lifecycle of a mechanical system (machines etc.). Affordability enhances international collaboration and in turn, globalization. In addition, the classical drivers system development such as rapidly growing computer power and, in parallel, the increasing power of simulation, optimization and visualization tools contribute towards improving the affordability of mechanical system. Only with this integrated process can characteristics such as dependability, reliability, maintainability and productivity together with affordability of a product be optimized.

3. Value of Integration of Tools and Processes

The term Integrated Design referred to in this volume comprises the following key elements:

- Design information integration that makes data available, as soon as they are generated, by means of multimedia display technologies to all who need to know in engineering design organization, while maintaining a clear distinction between the proposed and approved states of design.
- Acceleration of the design decision by extensive use of mathematical modelling and simulation combined with Multidisciplinary Design Optimization (MDO) at the detailed system levels, to assist human creativity.

I the engineering design process as practiced today, the design freedom, measured by the number of variables and choices designer can still change, reduces rapidly from 100 % at the beginning of the design process to near 0% at the end of validation phase [3]. On the other hand the amount of knowledge about the object of design increases sigmoid ally from near 0% to almost 100%. Paradoxically then, as more knowledge is gained, the less freedom is available to act on that knowledge. This paradox has its consequence in cost. The cost of the final product rises rapidly reflecting design decisions made early in the design process [3]. Being based on incomplete knowledge these cannot be the best decisions, but they cannot be adjusted as new information becomes available because of the above paradox. Obviously, faster generation of knowledge, fed into decision making and longer preservation of design freedom would result into a better design. The associated accumulation of the committed cost would then not only be restrained, but also the final cost would be reduced because of designers exploiting more complete and better information available as the process unfolds in time. The message that weaves throughout this subchapter is that the above improvements may now be implemented to make the design process radically more efficient and cost-effective, and points to the technologies for design integration and the methods of the Multidisciplinary Design Optimization (MDO) as the twin, synergistic enablers already available. The expected benefit in development of new vehicles may be conservatively estimated as at least 50% design cycle time reduction. Alternatively, assuming a fixed design time limit it will translate into a higher capability or into the vehicles reduces lifecycle cost owing to the larger variety of design options that may be explored within given time and resource budget allocated to design process. Thus, more than one way of exploiting the new paradigm will be available to be chosen from to suit the situation at hand. There are several successful and well-publicized examples of the application of integration of tools and processes in the development of complex machinery systems. Design Build Teams (DBT) and a "Working Together" management strategy, personal form all disciplines – design, manufacturing, operation, procurement, customer support, and others – worked concurrently in the development of the vehicle parts and systems. Central of this new design/build process was Cax system based on Computer Aided Three-dimensional Interactive Application (CATIA) and Finite Element Analysis System. Using CATIA, engineers modelled the parts as 3D solids and used Electronic Pre-assembly Integration on CATIA software to develop a complete 3D virtual mock-up of the complete machines. With this system, designers could check pre-assembly interfaces for complete machines, as well as develop integrated Bills-of-Material (BoM) and detailed manufacturing process layouts to support final assembly. In the project, is also modelling the full behaviour of the machine throughout its lifecycle, including operations and maintenance. In addition to using CATIA, designers are combining Multidisciplinary Analysis (MDA) and Product Lifecycle Management (PLM) tools to manage and streamline the design process (see Fig. 1) [3], [4]. The Integrated Multidisciplinary Analysis workflow used to optimize the machine configuration is illustrates in Fig. 4 [3, 4]. The multitude of connections show why, in a successful machine, the mutual influences of the design element must be accounted for. The Loads Analysis Process that appears as one of many elements in Fig. 2 [3] appears in Fig. 3 [3] to highlight that this process itself comprises many coupled elements. This demonstrates the coupled system approach extending downwards through the top-down machine hierarchy toward greater detail definition.

Fig. 1. Multidisciplinary Analysis with Products Lifecycle Management

Fig. 2. Integrated Multidisciplinary Analysis

Fig. 3. Loads Analysis Process

Product Lifecycle Management (PLM) is a strategic business approach that applies a consist set of business solution that support the collaborative creation, management, dissemination, and use of product definition information:
a) supporting the extended enterprise (customers, design and supply partners, etc.);
b) spanning from concept to end of life of a machine;
c) integration people, processes, systems, and information.

For example, in the vehicle project, enlist a full suite of PLM tools to define its PLM architecture (see Fig. 4) [3].
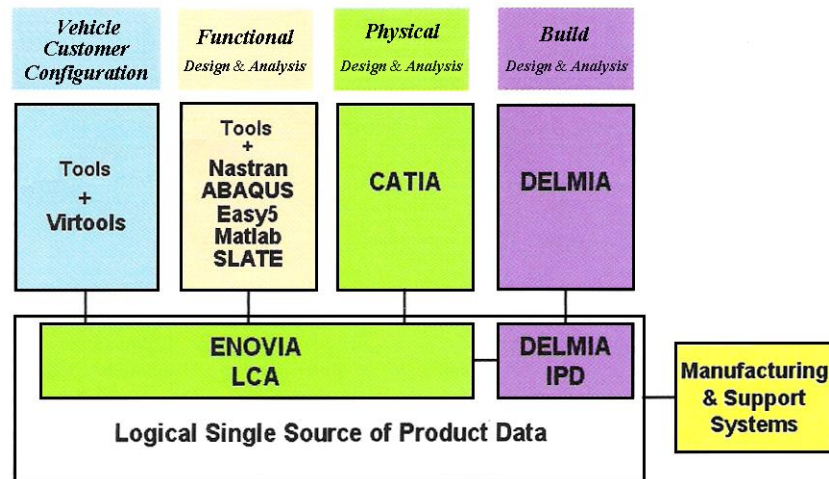
Fig. 4. Product Lifecycle Management Architecture

Functional design and analysis, including MDA, is carried out using vehicle tools and a variety of third party tools such as ENOVIA, ABAQUS, CATIA, DELMIA, and MATLAB, among others. The final act, the product testing and verification, also heavily depends on the integration of information (see Fig. 5) [3].
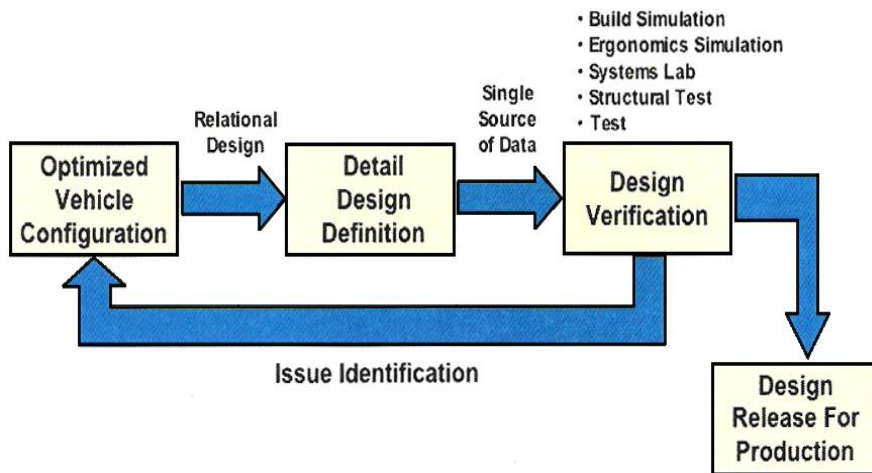
Fig. 5. Linkage of Multidisciplinary Analysis with Product Lifecycle Management

The feedback loop "Issue identification" is one that makes possible to improve the product and solve problems as new information becomes available downstream of the whole development process. The key point is that such a feedback loop could not operate without integration. In the past, the feedback loop like this was severely limited by the time it took to move the data, information, and knowledge up and down the line [4]. The value of the multidisciplinary analysis and product lifecycle management linkage in the integrated design for special vehicle is illustrated in Fig. 6 [4]. Each of the three boxes points to the benefits from multidisciplinary integration in design and manufacture stated from perspective of the entire product development process. The overarching benefit is that integration makes it possible to bring new products to market much faster.

4. Machine Design Attributes

Modern high performance vehicles are designed to optimally meet the customer's specifications. These specifications in turn are the translation of a wide spectrum of requirements like performance, mission profile, safety, manufacturing constraints, environmental constraints, human factors, etc., into engineering tasks to be optimally solved by the designer. Within this wide spectrum there are many spectrum of requirements which may lead to conflicting design tasks. The challenge for the designer is to find an affordable best compromise. This means in practice to apply powerful simulation models and optimization procedures in combination with high performance computing early design process [5]. The very complex design specification is one of the commonalities for all kind of high performance computing design. Looking deeper into the vehicle design from a system point of view more commonality can be discovered.
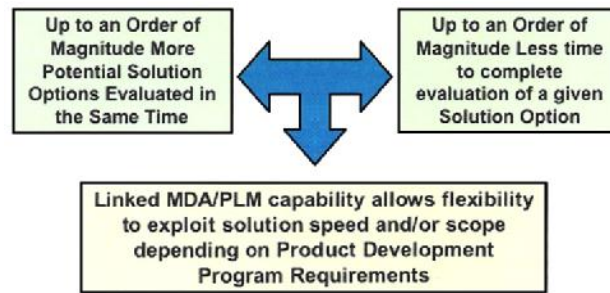
Fig. 6. Value of Multidisciplinary Analysis Lifecycle Management linkage

All categories of vehicles are composed of major subsystems which are in principle:
- mechanical and structural systems,
- propulsion systems, and
- guidance-control, communication and navigation systems etc.

These subsystems are, in turn, coupled in a manifold varying from linear to non-linear, and weakly to strongly coupled. The main differences for all categories of mechines however are to a large extent characterized by the environment in which they operate. The impact of the interdependency between the environment and the machine guide the design of the whole machine, its shape and structure, propulsion, control system etc. Despite the afore mentioned differences, the design methodology is very similar for all categories of machines and follows more or less design paradigm which states:
- have the different functions and the corresponding subsystems only weakly and linearly coupled;
- treat and optimize each function and subsystems more or less independently of the others;
- treat and optimize the whole machine is this fashion and integrate all functions and subsystems.

According to this paradigm all vehicles are designed in system procedure and disciplinary tools can be applied easily and independently. With the growing complexity of machines, however, design paradigm has been diminished. Hand in hand rapidly increasing computing power, number of software tools and the enormous economic pressure to reduce design cost [6], a paradigm shift in design methodologies has system place and the postulation for parallel design processes increased. The consequence is that tools and design process of a machine must be combined to an integrated process which can handle the various design methodologies and the coupling of disciplines, tools and computational power as well. Accordingly, the organization and approach to design must be unified into a process in which the design integration technologies combine with a body of methods provided by mathematical modelling, simulation, and multidisciplinary design optimization to support human creativity.

5. Multidisciplionary Design Optimization

The design process for machines is complex and multidisciplinary. Consequently, in order to arrive at an optimized design solution, an interdisciplinary approach must be followed. Multidisciplinary Design Optimization (MDO) may be regarded broadly as a methodology (body of methods, techniques, and other tools) for support of a design process on objects affected by a variety of interacting physical phenomena. As such, MDO needs integration of tools and computing hardware and software as its infrastructure is also needs analysis solution and optimization algorithms from contributing disciplines and specialties. It is important to always emphasize that MDO assists a designer but does not substitute for the designer; design is a creative process driven by human ingenuity. In addition to highlighting the integration of tools and processes, multidisciplinary design optimization is often considered as a technology that current state-of-the-practice is moving toward. Computation-based design is a rapidly evolving field. Mature technologies for the simulation and analysis of complex physical system are non available in most engineering disciplines. For example, in machine applications, the dynamics and structures disciplines each propose their own state-of-the-art methods for respectively simulating the behaviour of the stress and strain of structures. High fidelity computer codes now solve 3D Navier-Stokes equations for a full machine in Computational Fluid Dynamics (CFD) and Complete Finite Element model (CFE) in Computational Structural Mechanics (CSM). In parallel to the development of this state-of-the-art, high fidelity models for simulation physical systems, design methods have been developed to help engineers in making the best possible design within defined constraints [7]. In spite of the fast evolution of isolated disciplines, only timid efforts have been targeted to the design optimization as a whole. However, as the high fidelity models in isolated disciplines mature, there are incentives in using these in a more global design environment. The result has given rise to the development of MDO as a distinct discipline whose goal is to develop methodologies and tools to tackle the formidable challenges of integrating high fidelity physical models into a design environment that allows the synergism of mutually disciplines to be full exploited.

6. Conclusion

As mentioned previously, it is important to recognize that to reduce the time and cost to develop new machines and modify existing machinery systems, at least two issues needed to be addressed: the integration of tools and processes, and issues surrounding the qualification of the system [3]. Despite the progress that has been made in the integration of tools and processes, these integrated systems fall far short of being able to design a producible product without relying on the age old process passing limited information back and forth between the various engineering groups in an ad hoc manner. For example, multidisciplinary optimization is still so limited in the technologies that are integrated into MDO environment that the resulting "optimized" design is not optimal because it has neglected so many other disciplines. The growth of integration of tools depends on the whims of the researchers and tool developers to bring selected technologies together [4]. To proceed in the more orderly fashion, goals must be set that describe the disciplines that are to be integrated, and the benefits of integrating each discipline. Before moving further into this discussion, it may be beneficial to pause and explain what we mean by qualification. Qualification consists of ensuring that the machine can meet its mission performance requirements and to do it safely. The mission performance requirements are issues of concern to the customer. The safety issues are of concern to the regulatory agencies. When addressing only the safety issues, the term certification is used. It is apparent that higher fidelity analyses could be incorporated into a set of integrated tools and processes, but risk qualification may not be quite so easy. Traditional risk "qualification" methods are highly subjective making it difficult to assess the risk of a design in an automated system. However, there is a movement afoot called "Uncertainty Qualification" that holds the promise of providing an objective assessment of risk based on the uncertainty of the system. Yet, this alone is not sufficient to overcome the scepticism of certifying officials. The scepticism of certifying officials is not consistent. What one official may approve, another may not. This depends largely on the experience of the certifying official with the technology in question and the evidence shown that demonstrates the suitability of that technology. This raises the question of whether or not this issue can be overcome. In order to reduce the variance in what technologies are and which are not permitted, it seems reasonable to collect as much information as possible on that technology, regardless of source, and have it available for the certifying officials [5]. One way of retrieving this information would be to associate it with the design through hyperlinks. If the information is associated in an appropriate manner, it could also be useful to the engineers in developing the design. Incorporating information in an integrated tools and process environment presents new challenges that require moving beyond the classical MDO environments and embracing distributed systems. Integrated tools and processes is thus truly the backbone for qualification by analysis. Integration of all other issues associated with the qualification of a new system into a "single" distributed, integrated design system is essential to achieve significant reductions in system development time and cost.

References

1. Technologies for Enterprise Integration, Integrated Manufacturing Technology Road mapping. IMTI, Inc. Knoxville 2005. http://www.IMTI21.org.
1. **Crow K.** The Principles of Integrated Product Development. http://www.npd-solutions.com/principles.html DRM Associates, 2002.
2. **Sehra A., Read A. J., Hoenlinger H., Luber W., Stodola J., Follen G., Hoenlinger M.** at all. Integration of Tools and Processes for Affordable Weapons. Final Report of the NATO RTO Research Task Group AVT 093, Paris 2006, -324 p.
3. **Stodola J., Stodola P.** Architecture of Tools and Processes for Affordable Vehicles. *Transactions on Transport Science*. Ministry of Transport, Prague. Vol. 1, Nr. 1. 2008 ISSN 1802-971X, pp. 29–36.
4. **Stodola J.** Advances in Special Technique. Monograph. 1. edition. UoD Brno, 2010. ISBN 978–80–7231–716–5, -202 p.
5. **Novotny P., Pistek V., Stodola J.** Virtual Engine – a Tool for Military Truck Reliability Increase. AiMT Volume 1 Issue 1. 2007. Brno. ISSN 1802–2308.
6. **Stodola J., Stodola P.** *Mechanical System Wear and Degradation Process Modelling*. Transactions of FAMENA. Volume 3, No. X. Zagreb. 2010. ISSN 1333–1124.

Technology of Pile-Columns with Reinforced Concrete Ring Installation

S. Sušinskas*, A. Stasiškis*, R. Baltušnikienė*

*Kaunas University of Technology, Daukanto str. 12, 35212, Panevezys, Lithuania, E-mail: stk@ktu.lt

Abstract

The paper deals with industrial building foundation and presents an investigation of pile-column with reinforced concrete ring installation technology. The dependencies of relative foundations costs, reinforced concrete ring driving time and energy consumptions are given. These data enables proper selection of pile foundation type.
KEY WORDS: *pile, column, reinforced concrete ring.*

1. Introduction

Building industry is one of most important industry in each country economy. There is a need to build faster and use new materials and technologies. Pile foundation is one of strongest foundations but has quite big cost compare with strip foundations. Pile foundations are used not only for high buildings, but they are used more and more in one or a few floor industry buildings.

It is known that piles foundation is used in cases with difficult geologic site investigation data, when strong soil lies deep and upper soil layers are weak. The pile – column foundation technology has a good perspective in industry building constructions. A geotechnical site investigation of Lithuania and technical – economic calculations shows that single pile – column foundations is the best economically based foundation solution in 45% from whole Lithuania industry buildings [1].

The struggle worldwide competition in construction industry, forces to minimize building design, construction and maintenance cost. The cost becomes a vital factor for successful business. The foundation costs comprise 2.5-6% of whole costs, and takes 6-10% of building time. The cost of different foundation depending on pile length, depth and foundation area is shown in Fig 1.
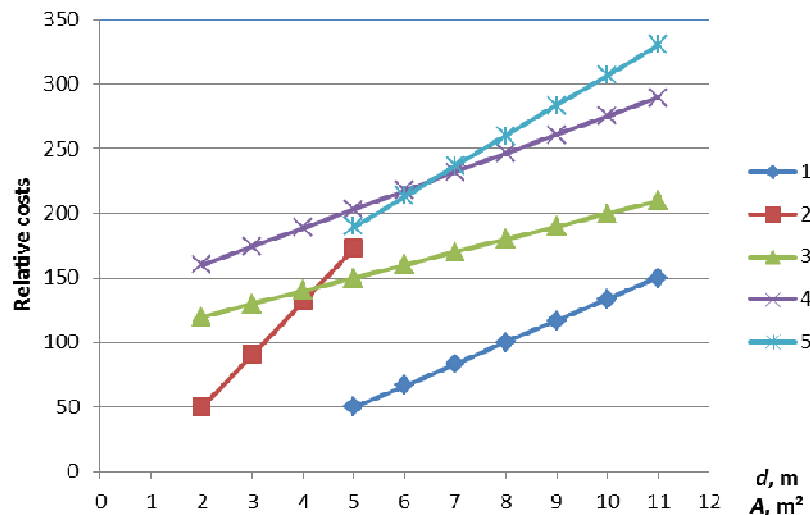
Fig. 1. Relative foundation costs: 1 – single pile 400×400 mm; 2 – drilled concrete ∅1000 mm; 3 – monolythic concrete depth 2 m; 4 – monolythic concrete depth 2.5 m; 5 – four piles 300x300 mm with monolythic head; d – pile length or foundation depth, m; A – foundation area, m²

Using pile foundation in the constructions enables to minimize ground work up to 80%, when all ground work costs is 30% from whole foundation cost. A lot of soil is removed and later putted back and condensed while making excavations for foundations. Also the consumption of material is less, for example concrete usage is 40% less. Using pile – column with reinforced ring foundation enables to minimize foundation costs 14 – 20%.

The complex and labor consuming task is to design pile – column connection. In this paper we will not discuss it, because this task was analyzed and solved in previous author work [2].

The pile – column construction could be realized in 3 different ways (Fig. 2): 1) with reinforced concrete ring; 2) with removable steel ring; 3) with steel ring. The selection of appropriate and economy based construction is analyzed in [3, 4].
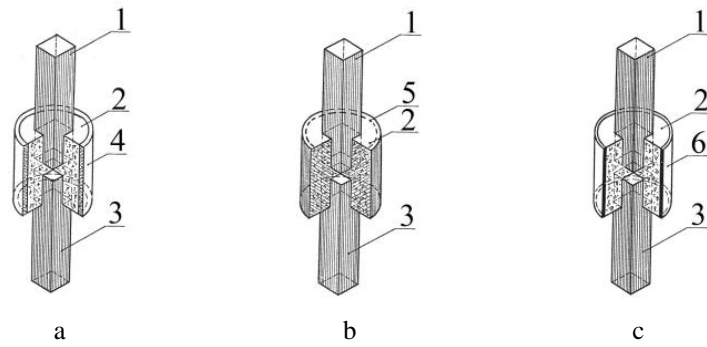
Fig. 2.   Pile – column construction: a- with reinforced concrete ring; b – with removable steel ring; c – with steel ring.
1 – column; 2 – concrete; 3 – pile; 4 – reinforced concrete ring; 5 – reinforcement structure; 6 – steel ring

2. The construction technology

The technology of pile – column with reinforced concrete ring is used for building constructions from assembled reinforced concrete elements as building foundation and holding construction. The technology is basically used for one or many floor industry buildings. Technology consists of 4 stages:
1.   Driving reinforced concrete ring using punch;
7.   Driving the pile;
8.   Forming column outlet;
9.   Column installation.
The column mounting could be realized in two alternative ways, which are described in Fig. 3

Fig. 3. Pile – column installation alternatives

The punch is consists of steel tube (wall thickness 12 mm) core filled with birch wood, 40 mm stiffeners, bottom plate and bottom ring, upper plate (diameter as reinforced concrete ring outside) Fig. 4. The conductor is used, to ensure proper position of ring Fig 5.
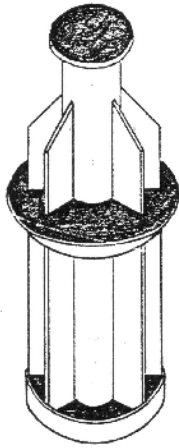
Fig. 4. The punch
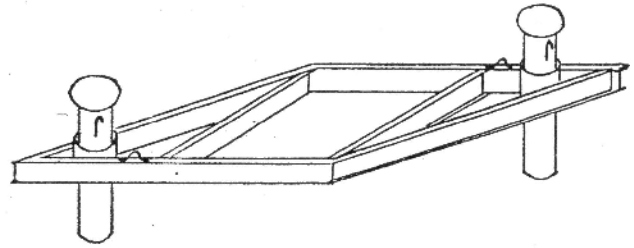
Fig. 5. Reinforced ring conductor

3. Economic feasibility

In order to better understand pile – column installation process, the soil parameters q_c (cone resistance) and f_{zl} (average side friction) were chosen as having main impact to the duration of reinforced concrete ring driving. The dependences among time and above mentioned parameters was defined:

$$y = 383.89 + 9.313q_c^2 + 0.076f_{zl}^2 \tag{1}$$

where: y is punching time, s; q_c is cone resistance, MPa; f_{zl} is average side friction, kPa.

The energy needed to drive reinforced concrete ring is calculated:

$$y = 1474.78 + 9.636q_c^2 \tag{2}$$

4. Conclusions

The proposed pile column installation with reinforced concrete ring technology could be used when cone resistance is in sand soil less than 10 MPa, clay soil – less than 4 MPa. Single pile – column foundation construction main advantage is the absence of valuable ground work cost (soil transportation and consolidation costs) compared with usual 4 piles – column foundation. The work cost is approx. 2.5 times less, and summary cost 1.5 – 2 times less. Consumption of concrete is 2 times, of metal – 1.5 times less.

Acknowledgements

References

1. Внедрение технологии возведения сваи - колонн для снижения трудовых и материальных затрат / экономия ресурсов при выполнении технологических процессов в строительстве: тез. докл. респ. конф. - Вильнюс , 1985, с. 38-39.
2. **Sivilevičius H., Daniūnas A., Zavadskas E. K., Turskis Z., Sušinskas S.** Experimental study on technological indicators of pile-columns at a construction site. // Journal of Civil Engineering and Management / Vilnius Gediminas Technical University, Lithuanian Academy of Sciences. London, Vilnius: Taylor & Francis, Technika. ISSN 1392-3730. 2012, Vol. 18, no. 4, pp. 512-518.
3. **Sušinskas S., Zavadskas E. K., Turskis Z.** Multiple criteria assessment of pile-columns alternatives. // The Baltic Journal of Road and Bridge Engineering. Vilnius: Technika. ISSN 1822-427X. 2011, Vol. 6, iss. 3, pp. 145-152.
4. **Zavadskas E. K., Sušinskas S., Daniūnas A., Turskis Z., Sivilevičius H.** Multiple criteria selection of pile-column construction technology // Journal of Civil Engineering and Management / Vilnius Gediminas Technical University, Lithuanian Academy of Sciences. London, Vilnius: Taylor & Francis, Technika. ISSN 1392-3730. 2012, Vol. 18, no. 6, pp. 834-842.

The Comparison of Pile-Columns with Reinforced Concrete Ring and Steel Ring Installation

S. Sušinskas*, A. Stasiškis*, R. Baltušnikienė*

Kaunas University of Technology, Daukanto str. 12, 35212, Panevezys, Lithuania, E-mail: stk@ktu.lt

Abstract

There exist a lot of foundation systems and installation technologies. The paper deals with industrial building foundation selection and presents the comparison of different pile-column foundation installation technologies.
KEY WORDS: *pile, column, reinforced concrete ring, steel ring.*

1. Introduction

Pile foundations are used more and more in building constructions despite building height. By setting up pile foundations instead of traditional foundations that use spread footing, the poor soil conditions have almost no impact on the foundation. Piles are used when persists large structural loads, settlement intolerant structures, low strength soils at or near ground surface. Piles could be made from timber, concrete and steel (H or pipe piles). Pile foundation implementation enables to minimize ground work and material consumption, there is no need to do any deep excavation or draining of the area, nor is there the need to install any sort of bracing or other temporary foundation. Pile foundation is most progressive foundation type [1].

2. The construction technology

The paper deals with 5 different pile with ring installation alternatives [2-4]. All of them use precast concrete piles. The technology of pile – column is used for building constructions from assembled reinforced concrete elements as building foundation and holding construction. The technology is basically used for one or many floor industry buildings. Technology consists of 4 stages: driving ring (reinforced concrete or steel) using punch; driving the pile; forming column outlet; column installation. Pile installation alternatives and short description are shown in Table 1.

Table 1

Pile with ring installation alternatives

Alternative	Short description
a1	Driving the reinforced concrete ring using a punch Fig. 1a, driving the pole Fig. 1b, construction, positioning and adjustment of the mounting jig for the column Fig. 1c, placing in situ concrete, and column mounting Fig. 1e. Hammer 1.8 t.
a2	Driving the reinforced concrete ring by applying a punch Fig. 1a, driving the pile Fig. 1b, placing in situ concrete mixture basement with a nest for the column mounting Fig. 1c, and column mounting Fig. 1e. Hammer 2.5 t.
a3	Driving the steel ring by applying a punch Fig. 1a, driving the pile Fig. 1b, placing in situ concrete mixture basement with a nest for the column mounting Fig. 1c, and column mounting Fig. 1e. Hammer 1.25 t.
a4	Driving the steel ring by applying a punch Fig. 1a, driving the pile Fig. 1b, placing in situ concrete basement with a nest for the column mounting Fig. 1c, removing the steel ring, and column mounting Fig. 1e. Hammer 1.8 t.
a5	Drilling the leader bore with 0.8 m in diameter and 1.0 m in height, driving the reinforced concrete ring Fig. 1a, driving the pile Fig. 1b, positioning and adjusting the mounting jig for the column, placing in situ concrete mixture Fig. 1d, and column mounting Fig. 1f. Hammer 1.8 t.

Driving the reinforced
concrete ring

a

Driving the pole

b

Positioning and adjusting
the mounting jig

c

Placing *in situ* concrete base-
ment with a nest for the column

d

Column mounting

e

Column mounting

f
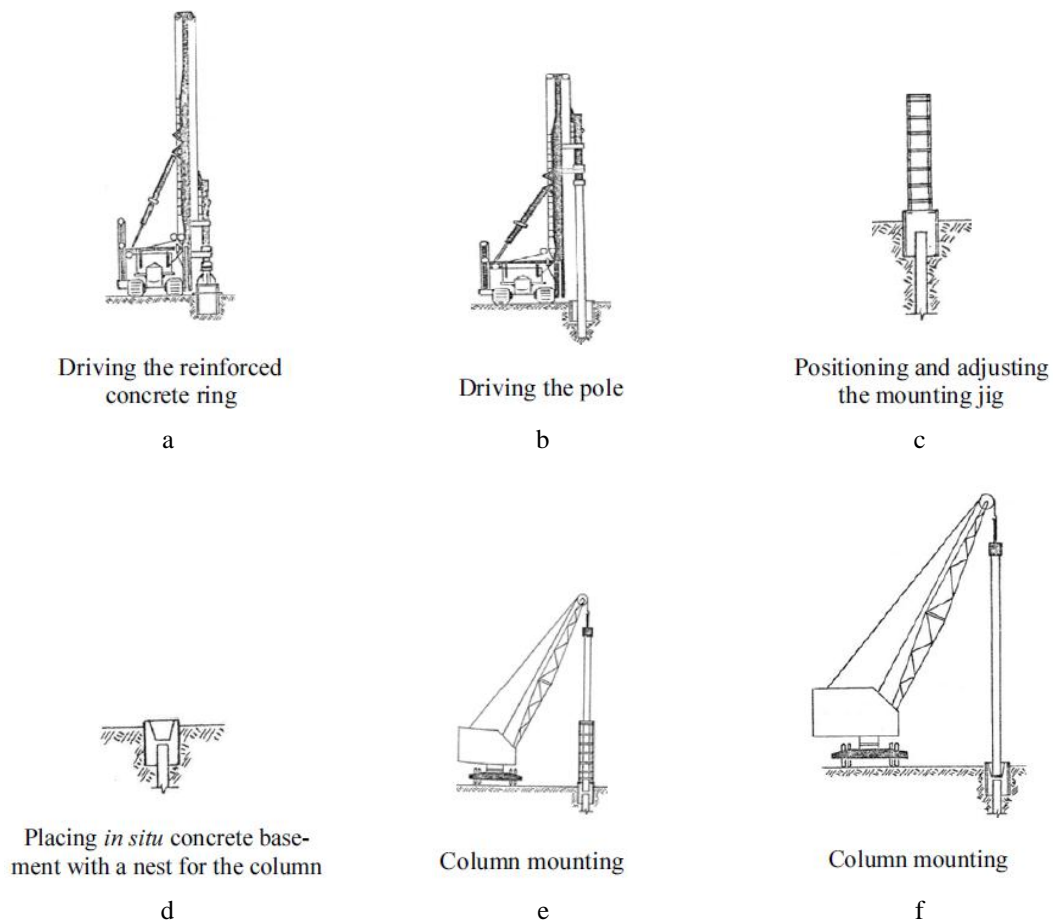
Fig. 1. Pile – column installation steps

3. Evaluation of alternatives

As pile – column alternatives slightly varies, calculations are done with different soil strength and hammer parameters. Ring driving time of different alternatives is shown in Fig. 2. The energy consumption is shown in Fig. 3.
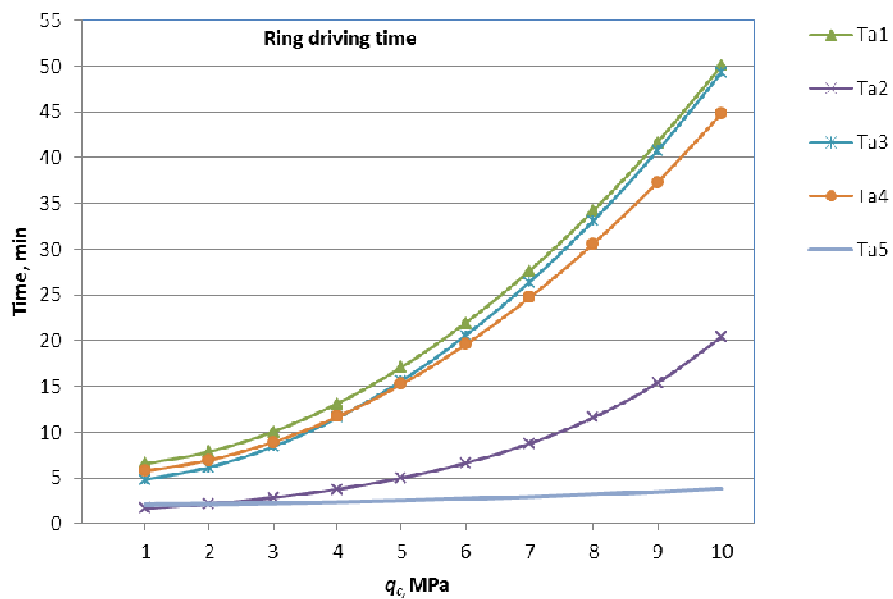
Fig. 2. Ring driving time, min
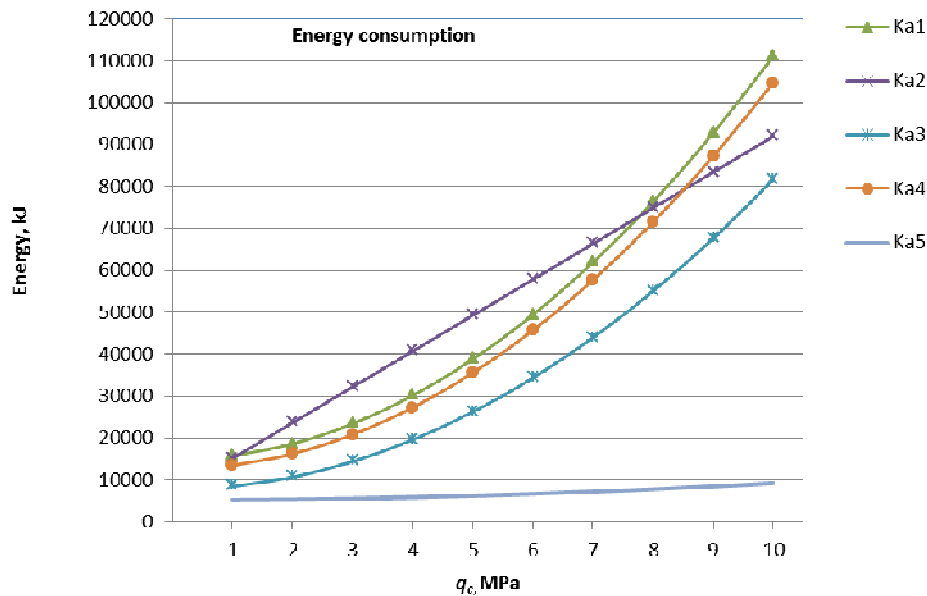
Fig. 3. Ring driving energy consumption

As pictures show, ring driving time is when cone resistance q_c and average side friction f_{zl} are bigger. Also driving time is less, when hammer mass is bigger. Steel ring driving requires less time than reinforced concrete ring at the same soil parameters. It is explained by different punch and ring area. The energy consumption for alternatives with the reinforced concrete ring is bigger than for alternatives with steel ring except alternative a5, when primary drilling is used. The a5 alternative has 8 – 10 times less energy consumption in comparison to others.

4. Conclusions

The showed that ring driving is possible and gives economic habit in clay soil up to 4 MPa strength and in sand – up to 10 MPa strength (strength is defined by static cone penetration tests). If soil strength is higher, the drilling leader bore must be used.

As investigation showed, according to needed workforce, costs, concrete quantity, steel quantity and machine time, the best alternative is a5, next a4, a1, a2 and a3.

Acknowledgements

References

1. Внедрение технологии возведения сваи - колонн для снижения трудовых и материальных затрат / экономия ресурсов при выполнении технологических процессов в строительстве: тез. докл. респ. конф. - Вильнюс , 1985, с. 38-39.
2. **Sivilevičius H., Daniūnas A., Zavadskas E. K., Turskis Z., Sušinskas S.** Experimental study on technological indicators of pile-columns at a construction site. // Journal of Civil Engineering and Management / Vilnius Gediminas Technical University, Lithuanian Academy of Sciences. London, Vilnius: Taylor & Francis, Technika. ISSN 1392-3730. 2012, Vol. 18, no. 4, p. 512-518.
3. **Sušinskas S. Zavadskas E. K., Turskis Z.** Multiple criteria assessment of pile-columns alternatives. // The Baltic Journal of Road and Bridge Engineering. Vilnius : Technika. ISSN 1822-427X. 2011, Vol. 6, iss. 3, p. 145-152.
4. **Zavadskas E. K., Sušinskas S., Daniūnas A., Turskis Z., Sivilevičius H.** Multiple criteria selection of pile-column construction technology // Journal of Civil Engineering and Management / Vilnius Gediminas Technical University, Lithuanian Academy of Sciences. London, Vilnius: Taylor & Francis, Technika. ISSN 1392-3730. 2012, Vol. 18, no. 6, p. 834-842.

AC Induction Motor Speed Stabilization Technique Based on Amplitude Control

M. Šapurov*, V. Bleizgys**, A. Baškys***, R. Zubavičius****

*Vilnius Gediminas Technical University, Naugarduko str. 41, LT– 03227, Vilnius, Lithuania, E-mail: martynas@stagelite.lt
**Vilnius Gediminas Technical University, Naugarduko str. 41, LT– 03227, Vilnius, Lithuania, E-mail: vytasbl@gmail.com
***Vilnius Gediminas Technical University, Naugarduko str. 41, LT– 03227, Vilnius, Lithuania, E-mail: algirdas.baskys@vgtu.lt
****Vilnius Gediminas Technical University, Naugarduko str. 41, LT– 03227, Vilnius, Lithuania, E-mail: zubavicius.raimondas@gmail.com

Abstract

The frequency converter supplied AC induction motor speed stabilization technique using motor slip control based on the variation of motor supply voltage amplitude has been proposed. The amplitude of voltage is varied in real time in such a way that for any motor load the motor slip would be constant. The proposed technique ensures lower motor phase steady state current and motor slip as compared to the case when conventional scalar control is used. The developed technique has been investigated experimentally. The obtained results were compared to results gained using conventional scalar control technique.
KEY WORDS: *AC motor, efficiency, slip, frequency converter, control system.*

1. Introduction

The speed of AC induction motor supplied by the frequency converter is controlled by the variation of AC voltage and phase frequency. Additionally, the appropriate amplitude of AC voltage has to be provided at given phase frequency for proper operation of motor. Since the speed of AC induction motor depends not only on phase frequency but on motor slip as well, the minor speed change at given phase frequency can be realized by the variation of AC voltage amplitude [4, 8, 9].

Different techniques are used to vary the amplitude of AC voltage generated by the frequency converter. All these techniques can be singled out in to the two groups: scalar and vector control [1–9]. The scalar control is based on the steady–state model of motor [4]. The linear law of ratio voltage amplitude to phase frequency (U_A / f_p = const) should be applied in order to keep the magnetizing flux of the motor unchanged according this model. The scalar control is applied if dependence of speed to load is known in advance, or if rotation speed is not monitored [1–3, 8, 9].

If the motor load changes randomly and constant rotation speed has to be ensured vector control of motor is used. The vector control is based on the dynamic model of the motor. The instant values of speed and flux of motor should be provided to the frequency converter for full implementation of vector control. However, it is complicated to obtain these parameters. Therefore, sensorless vector control method can be used for rotation speed stabilization [3, 9]. Differential equations of motor dynamic model must be solved and motor current transient have to be measured in real time for the realization of sensorless vector control. Only high performance DSP can implement such complex algorithms.

This paper presents the motor speed stabilization technique based on the AC voltage amplitude control using scalar control with motor speed feedback. Proposed technique performs speed stabilization by stabilizing rotor slip.

2. Amplitude control-based speed stabilization technique

Proposed technique performs rotor speed stabilization using motor slip control varying the AC voltage amplitude.
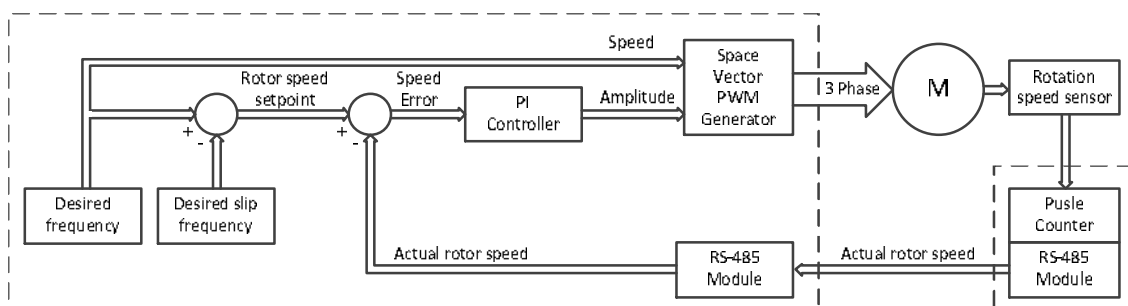
Fig. 1. The block diagram of amplitude control-based AC induction motor speed stabilization system

The block diagram of amplitude control-based AC induction motor speed stabilization system is presented in Fig. 1. Desired slip value is gained by adjusting amplitude. Amplitude control is implemented using Proportional-Integral (PI) controller. For operation of PI controller the signal from rotor speed sensor have to be provided. The control error value is obtained by rotor speed setpoint and actual rotor speed subtraction. The rotor speed setpoint is calculated by desired frequency and desired slip frequency subtraction. Where slip frequency dependence on desired frequency is $f_{slip} = S f_d$, (S – slip, f_d – desired frequency). The sensor of motor actual speed transmits the data to the PI controller via RS-485 interface.

3. Amplitude control-based motor speed stabilization technique implementation

Frequency converter implements proposed technique employing dsPIC30F6010A DSP microcontroller. The motor torque and rotation speed measurement circuits are realized using PIC18F4550 microcontroller. Frequency converter is equipped with two serial interfaces: one is dedicated to measurement of motor speed for feedback control, the other one provides PC with operating data. The motor speed data is being sent to the PI controller ten times per second, because of this, PI controller refresh rate is also limited by 10Hz. However, motor speed transients are slow, therefore, this limitation is irrelevant.

The frequency converter, which implements the proposed amplitude control-based motor speed stabilization technique, was investigated using AC induction motor test bench [1, 2]. The block diagram of test bench is presented in Fig. 2. It consists of 4 kW AC induction motor (speed 2890rpm at f_p = 50 Hz), frequency converter, motor torque and rotation speed measurement circuits. The 5.5 kW DC generator acts as adjustable motor load. The load torque is varied by changing of generator electrical load and rotor current.
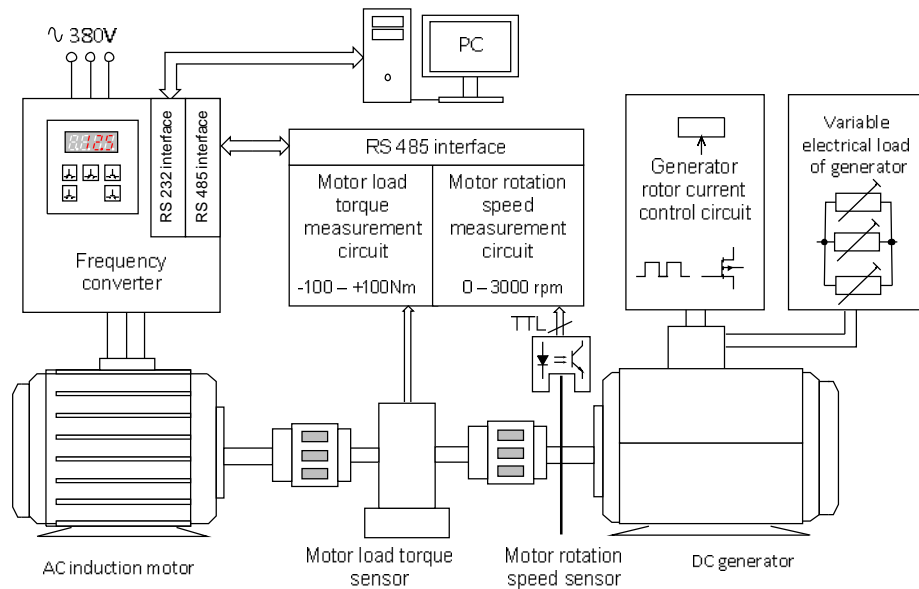
Fig. 2. The AC induction motor test bench

4. Amplitude control-based motor speed stabilization technique versus conventional scalar control

AC induction motor speed stabilization technique based on amplitude control was compared to conventional scalar control technique experimentally. The nominal value of slip at full motor speed and nominal load, specified by the manufacturer, is used as the desired slip value in the proposed control technique (Fig. 1). The motor load disturbance pulse (load torque bounce 2 to 12 Nm and back) response was investigated. The obtained transients for the desired frequency f_d = 25 Hz are presented in Figs. 3-7. It is seen that the amplitude control-based motor speed stabilization technique allows us to lower the motor steady state current and slip (compare the transients given in Figs. 4a and 5a with these presented in Figs. 4b and 5b). This fact shows that employment of proposed technique improves the frequency converter supplied AC induction motor efficiency and lowers the motor temperature as compared to the case when conventional scalar control is used. However, the transients of motor speed, current and slip obtained using amplitude control-based motor speed stabilization technique are characterized by higher overshoots. This fact indicates that proposed technique is effective if the load disturbances act with the low frequency.

The response of frequency converter output voltage amplitude modulation index m (m is the ratio of voltage amplitude with the 540 V amplitude) to AC induction motor load pulse disturbance, when motor speed is stabilized by amplitude control-based motor speed stabilization technique, is presented in Fig. 6a. It is seen that the modulation index have to be changed from 0.3 up to 0.7, i.e. the amplitude should be changed from 160 V up to 380 V, to keep the constant value of speed, when motor load changes from 2 Nm to 12 Nm and phase frequency is 25 Hz and is constant.
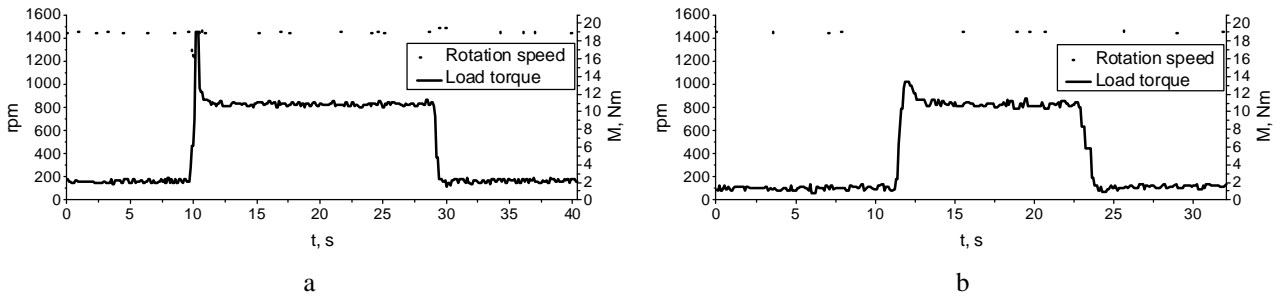
Fig. 3. The AC induction motor speed response to pulse disturbance of load, when amplitude control-based motor speed stabilization technique (a) and conventional scalar control (b) are used
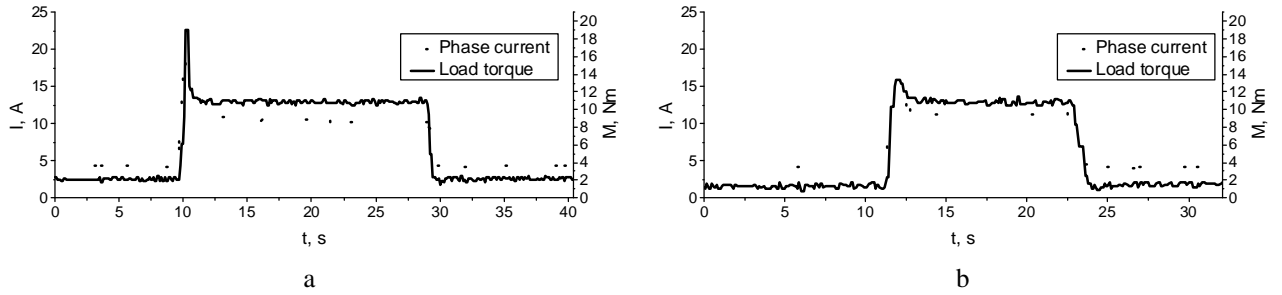
Fig. 4. The AC induction motor current response to pulse disturbance of load, when amplitude control-based motor speed stabilization technique (a) and conventional scalar control (b) are used
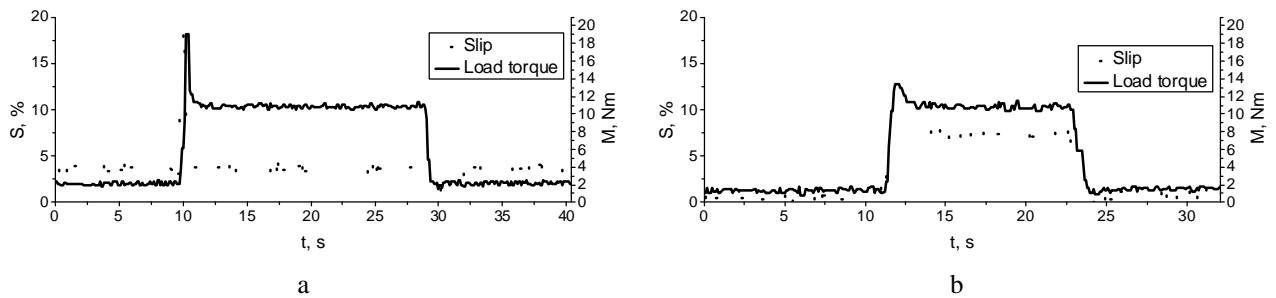
Fig. 5. The AC induction motor slip response to pulse disturbance of load, when amplitude control-based motor speed stabilization technique (a) and conventional scalar control (b) are used
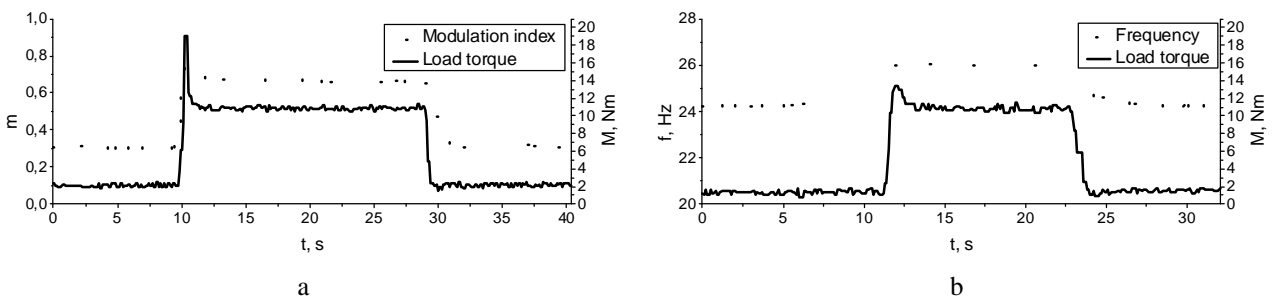
Fig. 6. The response of frequency converter output voltage modulation index (a) (motor speed is stabilized by amplitude control-based motor speed stabilization technique, phase frequency is 25 Hz) and phase frequency (b) (motor speed is stabilized using conventional scalar control based on variation of phase frequency) to AC induction motor load pulse disturbance

The response of frequency converter output voltage frequency to AC induction motor load pulse disturbance, when motor speed is stabilized using conventional scalar control based on variation of phase frequency, is given in Fig. 6b. The increment of phase frequency by 2 Hz is required to stabilize the speed in such a case.

The AC induction motor phase steady state current and phase current overshoot values at different phase frequency are presented in Fig. 7. The results where obtained for the cases when proposed amplitude control-based motor speed stabilization technique and conventional scalar control are used. It is seen that the steady state current

values using proposed technique, as compared to the conventional scalar control, are lower for the all analyzed phase frequencies.

a

b
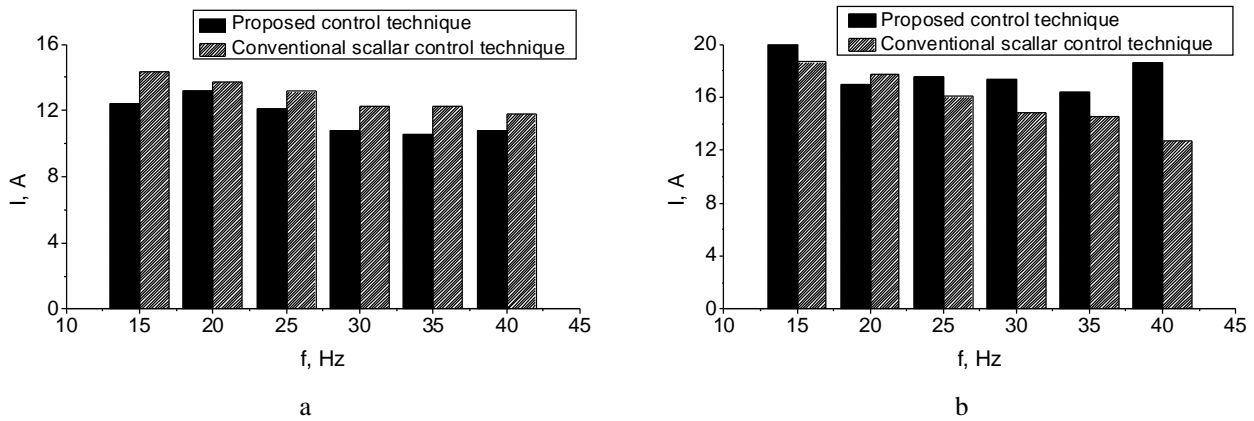
Fig. 7. The AC induction motor phase steady state current (a) and phase current overshoot (b) values at different phase frequency for the cases when amplitude control-based motor speed stabilization technique and conventional scalar control are used

5. Conclusions

The proposed AC induction motor supply voltage amplitude control-based motor speed stabilization technique allows us to vary the amplitude in such a way that rotor slip is kept constant. The employment of proposed technique enables to lower the motor steady state current and slip as compared to the case when conventional scalar control is used. However, the transients of motor speed, current and slip obtained using amplitude control-based motor speed stabilization technique are characterized by high overshoots. Therefore, the proposed technique is effective if the load disturbances act with the low frequency.

References

1. **Bleizgys V., Baskys A., Lipinskis T.** 2011. Induction Motor Voltage Amplitude Control Technique Based on the Motor Efficiency Observation. Electronics and Electrical Engineering, Kaunas: Technologija, No. 3(109), p. 89-92. ISSN 1392-1215, ISSN 2029-5731.
2. **Baskys A., Bleizgys V., Gobis V.** 2009. The impact of output voltage modulation strategies on power losses in inverter. Electronics and Electrical Engineering. Kaunas: Technologija, No. 6 (94), p. 47–50. ISSN 1392-1215.
3. **Valentine R.** Motor Control Electronics Handbook. –McGraw-Hill, 1998. – 754p.
4. **Neacsu D.** 2001. Space Vector Modulation. In Proc. 27th Annual IEEE Industrial Elec-tronics Society Conference, IECON'01, Denver, USA, December 2001, p. 1583–1592.
5. **Monmasson E.** 2010. Power Electronic Converters: PWM Strategies and Current Con-trol (ISTE). Wiley-ISTE. p. 608 ISBN-10: 1848211953. ISBN-13: 978-1848211957.
6. **Eltom A. H., Demirbas A.** 2009. Motor System Energy Efficiency in the Nylon Indus-try: a Comparison of PWM and Square Wave Inverters. International Electric Machines and Drives Conference. IEEE IEMDC 2009. Miami, Florida, USA: May 3–6, 2009. p. 604–609. ISBN 978-1-4244-4252-2.
7. **Vafakhah B., Masiala M., Salmon J., Knight A. M.** 2009. Space-Vector PWM for In-verters with Split-Wound Coupled Inductors. International Electric Machines and Drives Conference. IEEE IEMDC 2009. Miami, Florida, USA: May 3–6, 2009. p. 860–867. ISBN 978-1-4244-4252-2.
8. **Salt D., Drury D., Holliday D.** 2009. The Nonlinear Voltage Distortion Effect of an Extended IGBT Turn-off Time in Sinusoidal PWM VSI Applications. International Electric Machines and Drives Conference. IEEE IEMDC 2009. Miami, Florida, USA: May 3–6, 2009. p. 1812–1817. ISBN 978-1-4244-4252-2.
9. **Sira-Ramirez H. J., Silva-Ortigoza R.** 2010. Control Design Techniques in Power Elec-tronics Devices (Power Systems). Springer. 441 p. ISBN-10: 1849966052. ISBN-13: 978-1849966054.

Proceedings of 8th International Conference ITELMS'2013

Vehicle Stability under Crosswinds

A. Tautkus*, D. Micevičienė**

*Kaunas University of Technology Panevėžys institute, Daukanto str. 12, LT-3521, Panevėžys, Lithuania, E-mail: arunas.tautkus@ktu.lt
**Kaunas University of Technology Panevėžys institute, Daukanto str. 12, LT-3521, Panevėžys, Lithuania, E-mail: diana.miceviciene@ktu.lt

Abstract

The present thesis investigates the dependence of the automobile Audi B4 critical driving speed under crosswinds; depending on the vertical center of gravity height, track width and road surface roughness.

In this paper, the automobile side and lift force coefficients $C_{S,L}$ where calculated by the application of the finite element analysis using a flat model (central transverse – section model) in assumption that its area (contour area of the automobile's profile projection to the plane parallel with the direction of movement) corresponds to the area of the profiled contour of the Audi 80.

The critical speed of vehicle was calculated using the Baker stability calculation methodology.

The main parameters which influence the stability of the car under crosswind speed, depending on the vertical center of gravity height, track width and pavement surface roughness.

KEY WORDS: *automobile, crosswind, stability.*

1. Introduction

Cars, trucks, motorcycles become particularly unstable exposure to sudden crosswind's gusts, driving them on bridges and overpasses. Increasing dimensions, the maximum allowable speed results in decreasing vehicle stability. Under sudden crosswind gusts, vehicle's stability is determined by the aerodynamic performance of the car, its dynamic characteristics (weight, tire and suspension characteristics) as well as the driver's reaction. Actually of these factors together ensures the overall stability of the vehicle as most authors state [1-6].

The aim of the paper – to establish the maximum (safe) speed of vehicle Audi B4 under sudden crosswind gusts, considering the vertical center of gravity height, track width and pavement surface roughness. This paper presents the research methods. The crosswind's drag coefficient $C_{S,L}$ is established by finite element method using the software package ANSYS. The computing of the maximum driving speed is performed using the methodology of Baker stability calculation employing the software package MATLAB. This paper presents the simulation results.

2. Research methods

The main causes of vehicle accidents under the affection of crosswind gusts are divided into three cases [1]:

- rollover accidents;
- sideslip accidents;
- rotating accidents.

The schemes of the cases are presented in Fig.1.

The aerodynamic forces and moments depend on a number of geometrical parameters and air flow.
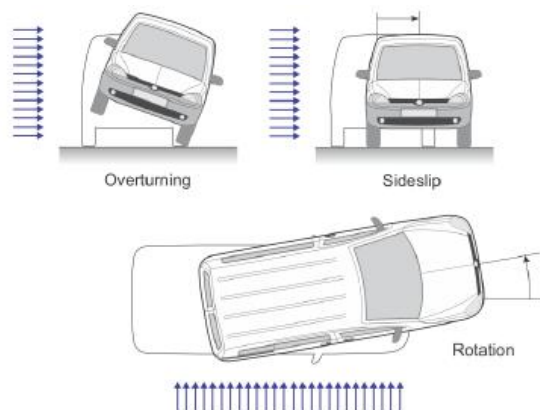
Fig. 1. Examples of possible vehicle accidents under the crosswind influence [1]

The aerodynamic characteristics are described by aerodynamics coefficients:

- Drag Coefficient C_D;
- Side force Coefficient C_S;
- Lift Coefficient C_L [2].

Drag coefficients depend on the shape of the body and of its position in the flow.

Aerodynamic effectiveness of the vehicle is determined by the drag coefficient [2, 3]:

$$C_{D,S,L} = \frac{F_{S,L}}{r\,A} \tag{1}$$

$$F_{D,S,L} = C_{S,L}\,A\,\frac{r\,v^2}{2} \tag{2}$$

where: $F_{S,L}$ – drag force of total flow, N; v – vehicle speed, m/s; ρ – density of environment in which the vehicle moves (air density), kg/m³; A – area of vehicle's front projection, m².

The scheme of computational forces and moments are presented in Fig. 2.
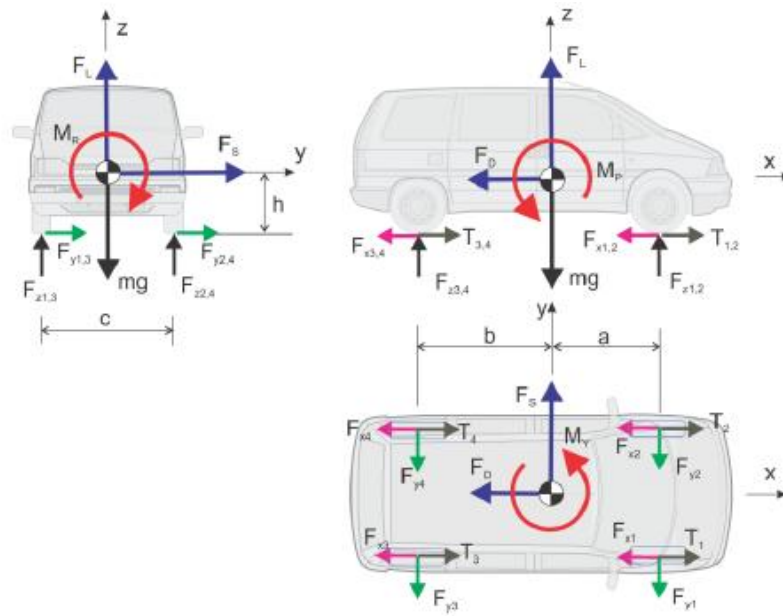
Fig.2 . The scheme of computational forces and moments

After calculation of aerodynamic drag coefficients, as well as knowing the car's wheel traction coefficients, there is a passibility to identify are important parameters of the movement of the vehicle, depending on the crosswinds:

- Critical croswind's speed, overturning the car about its horizontal axis – $V_{overturn}$;
- Critical croswind's speed, overturning the car about its vertical axis and challenging sideslip – $V_{sideslip}$.

Critical overturning speed is calculated according to the formula (3):

$$V_{overturn} = \sqrt{\frac{2\,m\,g}{r\,A} \cdot \frac{c}{2\,h\left(C_S + C_R\right) + c\,C_L}} \tag{3}$$

where: m – general vehicle weight, c – vehicle track width, h – the distance from the ground surface to the vehicle's center of gravity.

Critical croswind's speed challenging vehicle's sideslip is calculated according to the formula (4):

$$V_{sideslip} = \sqrt{\frac{2\,m\,g}{r\,A} \cdot \frac{m_1\,a + m_2\,b}{(a+b)C_S + (m_2\,a + m_1\,b)C_L + (m_1 - m_2)h(C_D + C_P)}} \tag{4}$$

where: m_1 and m_2 – front and rear wheel traction coefficients; a and b – distances from the vehicle's front and rear axle to the center of gravity.

Aerodynamic drag coefficients were found using the finite element method.

3. Model of finite element for determination of aerodynamic drag coefficients

Investigating the dependence of the drag coefficients on the vehicle geometry and velocity, the data was obtained with finite element software package ANSYS. The coefficients were calculated for a flat model considering that the investigative vehicle model's area corresponds to actual vehicle's area around the central cut.

Finite element model geometry shown in Fig. 3.

Finite element model input results demonstrates Fig. 4.
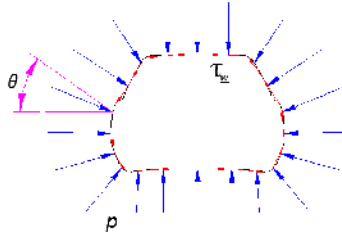
Fig. 3 Finite element model geometry
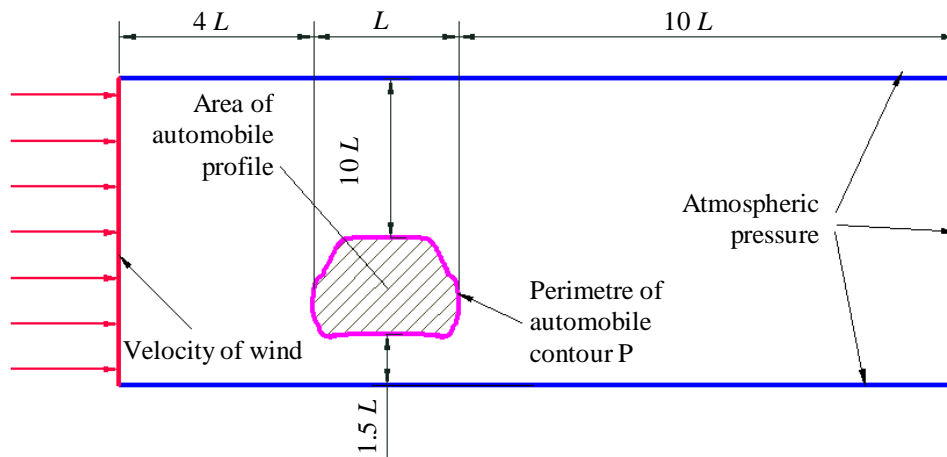
Fig.4 Finite element model input results

The program calculates the airflow's pressure only to the vehicle's contour p and shear tension on the contour. Knowing these values the drag coefficient is calculated according to formula 5 [3, 4]:

$$C_{S,L} = \int p \cos q \, dA + \int t_w \sin q \, dA \tag{5}$$

where: θ – the angle between the vehicle contour's (at any point) normal and the vector of the movement.

Determination of the coefficients values $C_{S, L}$, the following assumptions were made:

- the road way does not move in respect of the vehicle;
- the vehicle's surface roughness and surface discontinuity is not considered;
- the influence of temperature is ignored.

The accuracy of $C_{S, L}$ coefficients' values depends on on the size of the finite element. While cutting grid calculation results become more accurate. There was carried an analysis allowing to determine the optimal grid of finite elements for solving the air flow's task. It was considered that C_S value is proper, if differs not more than 15% from estimated C_S with the densest grid. It is also acceptable to use the same grid and its density level for estimation of C_L coefficient values as for C_S ones.

After the simulation, it was found that the best option for calculation of aerodynamic coefficients is a medium density grid. It is presented in Fig. 5.
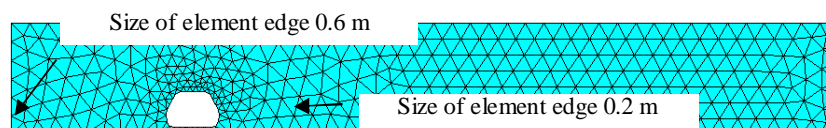
Fig. 5. The grid for calculation model of aerodynamic coefficients

4. Reaserch results

For the research was chosen a car model Audi B4. The research results are enumerated below:
1. Determined values of the drag coefficients $C_{S, L}$ at varying wind speeds ranging from 5 to 40 m/s;
2. Estimated air inlet angle at different vehicle weights and at changing wind speeds of 5 to 40 m/s;
3. The critical velocity of driving which provokes vehicle's slipping or overturning was calculated. Its was manipulated with the following parameters:
    o Vehicle's weight – from 1270 to 1750 kg;
    o The vertical position of the center of gravity – from 0.34 to 0.84 m (in the case of overturning);
    o Track width – from 1.2 to 1.7 m (in the case of overturning).

Changing the speed of crosswinds from 5 to 40 m/s the values of drag coeficients $C_{S, L}$ are determined. Results of the simulation are presented in Fig. 6.

a   b
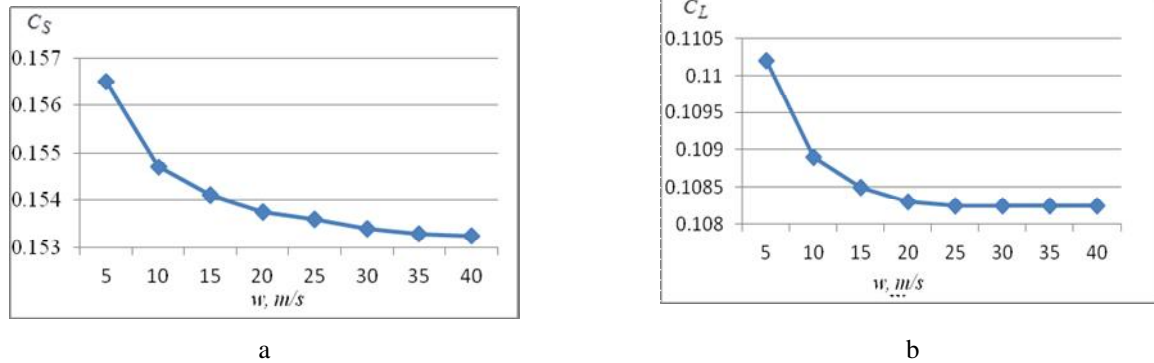
Fig. 6 Dependence of coeficient's C_S (a) and C_L (b), values on speed of crosswinds

In response to growing crosswinds' speed the values of coeficients $C_{S, L}$ vary very slightly.

Under investigation of dependence of critical driving velocity on the vehicle's weight, the former parameter varied from 1270 kg to 1750 kg (fully loaded). It was considered that the vertical center of gravity was constant. As Fig. 7 demonstrates, increasing vehicle weight increases the critical velocity as well.

a   b
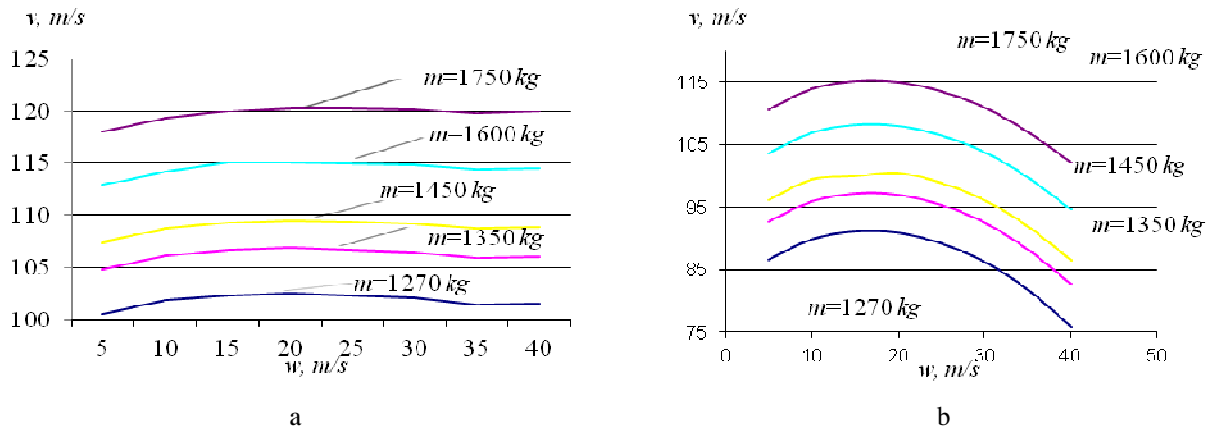
Fig. 7. Dependence of critical velocity v, on crosswinds in the case of slipping (a), in the case of owerturning (b)

By increasing the speed of the crosswinds from 5 m/s to 25 m/s the critical velocity of the car – at which its starts sliding – increases to 25 m/s. Exceeding the limit of these 25 m/s, the critical velocity speed of the car starts slightly decreasing. When the speed of the crosswinds reaches 35 m/s, the critical velocity speed begins slighty growing (Fig. 7a). It was established that increasing the crosswind's speed up to 20 m/s, the critical vehicle's velocity at which the car owerturns, slighty grows, then starts decreasing and finally does not demonstrate any growth tendency. The tendency is quite different in comparison with the case of slipping. The investigation showed that under the influence of crosswinds the critical velocity speed – at which the vehicle overturns – is lower in comparison with the velocity of slipping, so the car tends to overturn rather then slip at coefficient of friction $\mu = 0.463$.

Further investigation was conducted evaluating the car's center of gravity height on critical speed. The research results are presented in the Fig. 8.
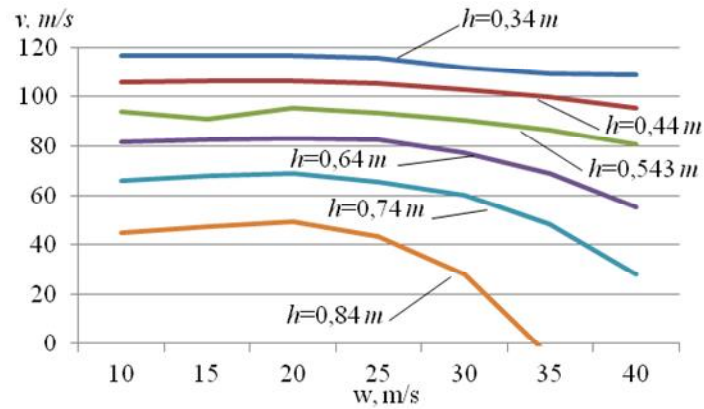
Fig. 8. Dependence of critical vehicle's velocity on the variating position of the center of gravity

Fig. 8 demonstrates that the greatest influence on the stability of the car is when the center of gravity height is greater than 0,543 m. After reaching crosswind's speed 25 m/s the critical vehicle velocity speed (provoking the overturn of the car) turns into a sharp decline. Descending the vertical center's of gravity height h increases the vehicle's stability.

The third parameter that was evaluated during the simulation was the track width of the car (car width). Simulation results are presented in Fig. 9.
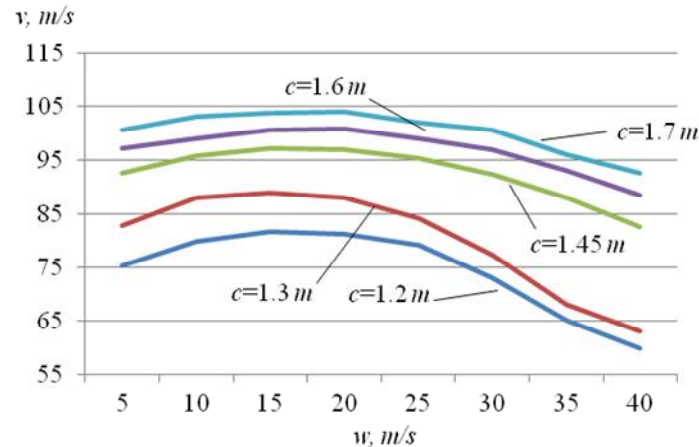
Fig. 9. Dependence of the critical car's velocity on the crosswinds speed v in response of changing car width

Changing the width of car's track from 1.2 m to 1.7 m, the critical vehicle's velocity speed growths up to 25 m/s. If the width of car's track fluctuates between 1.2-1.3 m the critical vehicle's velocity speed turns into a sharp decline. The Fig. 9 shows that the crosswind increases risk for the cars with the track width range 1.2-1.3 m.

5. Conslusions

Drag coefficient C_L changes in the range 0.1102-0.108 when crosswinds' speed varies from 5 to 40 m/s. The coefficient's values decrease with increasing wind speed.

By increasing the speed of the crosswinds from 5 m/s to 25 m/s the critical velocity of the car – at which its starts sliding – increases to 25 m/s. Exeeding the limit of these 25 m/s, the critical velocity speed of the car starts slightly decreasing. When the speed of the crosswinds reaches 35 m/s, the critical velocity speed begins slighty growing.

It was established that increasing the crosswind's speed up to 20 m/s, the critical vehicle's velocity at which the car owerturns, slighty grows, then starts decreasing and finally does not demonstrate any growth tendency. The tendency is quite different in comparison with the case of slipping.

Increasing the weight of the car from 1270 to 1750 the critical velocity speed influencing the slip varies ≈ 14 m/s and influencing overturn ≈ 25 m/s.

Descending the car's vertical center of gravity height (standard of Audi B4 – 0.543 m) influences the critical vehicle's velocity speed – it increases on average about 25 m/s. If increasing the height critical vehicle's velocity speed fluctuates in the range 94-44 m/s (at crosswind's speed 10 m/s). The position of vertical center of gravity doesn't affect the slip the speed.

With increase in vehicle track width from 1.3 to 1.7, the critical vehicle's velocity, influencing the slip, increases from 80 to 104 m/s (at crosswind's speed 10 m/s). If the standard car's track width of 1.45 m, the critical velocity speed reaches ≈ 97 m.

If the standard car's track width is less (1.45 m) the critical velocity sharply declines if the crosswind's speed exceeds of 25 m/s. The track width does not influence or affect vehicle's velocity at which the car slips.

After modeling and research, it was established that a vehicle would be much more stable at turns in roads under influence of crosswind's gusts, if the chassis would be made up of active elements within an independent suspension type. These suspension components are installed in most modern cars.

References

1. **Baker C. J.** A Simplified Analysis of Various Types of Wind-induced Road Vehicle Accidents. Journal of Wind Engineering and Industrial Aerodynamics, 1986. 22: p. 69-85.
2. **Gillespie T. D.** Fundamentals of Vehicle Dynamics. 1992: SAE Inc.
3. **Евграфов А. Н.** Аэродинамика автомобиля. – Москва, 2010. – 355p.
4. **Гухо В. Г.** Аэродинамика автомобиля. – Москва: Машиностроение, 1987. – 422 p.
5. **Ghosh S., Hunt J. C. R.** Spray jets in a cross-flow. Journal of Fluid Mechanics, vol. 365, June 1998, p. 109-136.
6. **Hubner M., Stork T., Becker U. U., Schnieder E.** Lateral stabilization of vehicle-trailer combinations against crosswind disturbances by means of sliding control. 16th Mediterranean Conference on Control and Automation Congress Centre, Ajaccio, France, June 25-27, 2008: p. 431- 438.

Proceedings of 8ᵗʰ International Conference ITELMS'2013

The Computer Workers' Working Conditions Influencing the Health in Modern Buildings

P. Tint, D. Karai, K. Oha, T. Koppel, V. R. Tuulik, V. Tuulik, K. Meigas

Tallinn University of Technology, Ehitajate str. 5, 19086, Tallinn, Estonia, E-mail: piia.tint@ttu.ee

Abstract

The paper is aimed at improving the workplace ergonomics. The psychosocial character of computer workers' health risks in modern buildings is investigated. The influence of indoor climate conditions on development of health damages at workplace are also taken into consideration. The computer workers (accountants, secretaries, etc.) often work in static posture. 295 workers from different enterprises and firms were questioned about the health risks in the work environment and health disturbances connected with their work. For the investigation Kiva questionnaire and Workability Index were used. The results show that the computer workers assess their health status considerably high. They are optimistic in solving the problem that the monotonous work with computers will continue and believe that their health status in the future will stay in the same level using the steadily enhancing rehabilitation means. The most injured regions of the body were the right wrist and the neck. The rehabilitation means have to be developed and the possibility for rehabilitation must be made available to the greatest possible number of workers. The novelty of the study is that the work conditions (indoor climate, lighting) are closely connected with the development of musculoskeletal disorders (MSDs) in glazed buildings. Low temperatures ($< 20°C$ in office) in winter and high temperatures and draught in summer; deficiency of day-lighting etc. are supplementary factors for developing the MSDs.

KEY WORDS: *indoor climate, modern buildings, health disturbance, musculoskeletal disorders.*

1. Introduction

The modern glazed buildings (including atrium-type) are very common for office-rooms in cold and hot climates [1]. The new type of construction is used for high-school buildings and in commercial centres. The biggest successes of atrium-type buildings are their appearance and heat savings in the rooms closed to the atrium. Some problems with work conditions also occur: ventilation of the rooms [2, 3], the deficiency of natural lighting (in the rooms closed to the atrium) [4, 5]; in towns the houses are built too close to each other and the modern wall materials can disturb the office-workers in the building of the opposite side. The spotted wall material (Fig. 2) of the opposite side house (Fig. 1) reflects in sunny days the sunlight directly to the computer screen of the office-workers in atrium A.

Fig. 1. Two new-style university buildings: atrium-type building A (left) and the library (right)

Fig. 2. The spotted material of the library building disturbs the students and office-workers of atrium-house A in the opposite side

There are other types of glazed buildings (high, 10 story houses) that give good natural lighting in winter where there is usually deficiency of it; but it might be too cold on the 8ᵗʰ or higher floor in -30°C of outdoor temperatures. That kind of buildings are too hot in summer and the temperature of the indoor air might raise over 30°C. The surveillance of the ventilations systems is expensive. The non-regulated ventilation (draught, the cold air blowing onto the employee in winter from the ventilation system); sick building syndrome [6, 7] in the rooms where the windows cannot be opened etc. can cause health problems of physiological and psychological character to the office-workers [8].

The work with computers causes musculo-skeletal disorders (MSDs) to the people if they work continuously and without pauses. The hands, neck, shoulders and back fatigue occurs caused by the static posture for accountants,

secretaries etc. [9]. There are connections between the work conditions and health disturbances [10]. MSDs of the computer professionals are associated in addition to the individual and psychosocial factors also with the organizational factors like the length of the rest breaks, rotation, printing and sitting duration of the worker and with the factors related to the workplace (the possibility to regulate the work chair and work table; the placement of the screen, keyboard and mouse) [11, 12]. In the recently published workplace meta-analysis, the basic biomechanical risk factors for musculoskeletal pain occur are repetitive movements, awkward positions and lifting of loads. The first two of them always are present in the work with computers. Consequently, it is important to deal with the computer workstation ergonomics, with the aim to prevent computer-related health problems. Different intervention studies have been conducted for the musculoskeletal pain reduction and prevention; and a variety of intervention methods have been used. Of these, the most common are physical exercising, stress management training, ergonomics-related training, workplace reorganization, new tools (such as obtain of a chair, safety device, keyboard, forearm) and keeping rest intervals. One as well as a combination of different methods are used. Articles overviews show that the intervention has not caused the negative or harmful influence on the ergonomics and health of the workers [13]. The effectiveness of the intervention is assessed in the review articles as unclear because the different studies give or does not give the same effect of the intervention. Coming from that, Kennedy [14] had made recommendations for carrying out the intervention studies. It is always recommended to choose also the control-group; to carry out the intervention with sufficiently large number of respondents. If the number of investigated persons is small, then it is better to test the intervention group and control group; not to use the variety of intervention methods on a number of different small-group of persons, to choose the duration the intervention method from 4 to 12 months; to choose the intervention with combined of different methods, as it is likely to effect. In spite of the increase of the MSDs as occupational and work-related diseases in Estonia, there are not sufficient adequately performed investigations on the health of office workers. To prevention of the musculoskeletal pain it is important to raise the staff awareness and direct their attention to the problems associated with computer work.

The measured work environment conditions were: the air temperature, humidity, air velocity in the workplace [5]; the workplace lighting, as well as the carbon dioxide concentration in the work room [6]. The studied rooms were taken from different houses of the university having no windows, rooms with un-openable windows, openable windows, but closed to the atrium [1]. The atrium A has a transparent of light roof and the slope between the roof and the wall. This type of design gives to the workers better working conditions [2, 3]. The paper in the field of indoor environment focuses on two issues: the cleanness of the air in the office space with modern design and the absence or shortage of natural light [7].

The present work also contains a survey of office workers, the extent of which they are satisfied with working conditions in the glazed buildings. Furthermore, the employees' perceptions were also examined, such as the lack of natural light disturbs them or not.

Novelty of the study consists in the individual approach to the workers and their opinions. One worker may not feel the shortage of the natural light, but she feels air temperature discomfort. Different people have different health disturbances (except of flu that may catch a great number of people simultaneously). The indoor climate quality in buildings is related to the workers wellbeing including job satisfaction, motivation and productivity. The European Standard EN 15251:2007 sets the new demands for previously socialist-countries for indoor climate (IC) quality: for air temperature, humidity, velocity (ventilation), carbon dioxide concentration, noise and lighting in office and research-rooms. The investigation and modelling of the air quality in the office rooms has become a very important issue in many countries of different climate (in cold and warm area). The prevention of rising the concentration of carbon dioxide (CO_2) over the norms (800 ppm over the out-door CO_2 concentration) and ventilation of the rooms have new approaches to improve the situation.

Objectives of the study were: to investigate the working conditions through the measurements in the work environment and the health risk analysis by the specialists and using the questionnaires for office-workers.

2. Methodology/Material/Approach

In the study the indoor air quality assessment in 7 different glazed buildings office-rooms was carried out (Table 1). The measurements of working conditions (microclimate, lighting, concentration of carbon dioxide) were carried out. Measurements in the work environment are based on ISO, EN DIN, EVS standards: EVS-EN-ISO 7726:2003 "Thermal environments – Instruments and methods for measuring physical quantities"; EVS-EN 15251:2007 "Indoor environmental input parameters for design and assessment of energy performance of buildings addressing indoor air quality, thermal environment, lighting and acoustics", EVS 894:2008+A1:2010 "Daylight in dwellings and offices". The measuring equipment used for microclimate: TESTO 435. TESTO 435 enables also the measurements of CO_2. Measurements of lighting the workplaces were performed using the light-metre TES 1332 (ranges from 1-1500 lx). Dust was measured with HazDust EPAM-5000.

The work conditions of the Estonian workers (n=350) using the computer in their everyday work were investigated. The workers' opinion on the existing work conditions was assessed (295 answers). Nordic questionnaire, Kiva questionnaire and Work Ability Index (WAI) [15, 16] were the basis for compile the questionnaire. The questionnaire consisted of 67 questions (an example in Table 2) which all were directed to determination mostly psychological and physiological hazards in the work environment. The preventive (rehabilitation) measures were also recommended.

The Kiva questionnaire consists of the following questions:
1. Have you enjoyed coming to work in the last weeks?
2. How meaningful do you regard your job?
3. How well do you feel in control of your job?
4. How well do you get on with your fellow-workers?
5. How well does your immediate superior perform as superior?
6. How certain you are that you will keep job with this employer?
7. How much can you influence factors concerning your job?

3. Results

The results are given in three parts: the natural lighting conditions in atrium-type buildings; the results of measurements of indoor air indicators in the investigated offices and the investigation of the opinion of workers on physiological and psychological risk factors in the work environment.

3.1. The natural lighting in the atrium-type buildings' offices

Recent biomedical studies have shown that besides visual function, light plays also an important role in human wellbeing. Due to the recent discovery of a novel photoreceptor in the eye the necessity for dynamic lighting has become clearer. Light is signalling the time of the day by the means of the newly discovered photoreceptor cells and a separate nerve system to our biological clock, which in turn regulates the circadian (daily) and circannual (seasonal) rhythms of a large variety of bodily processes [17]. In the building B the natural lighting conditions worsened a lot in 2012 when 3 additional floors were built after. The area on atrium is only 4×4 metres.
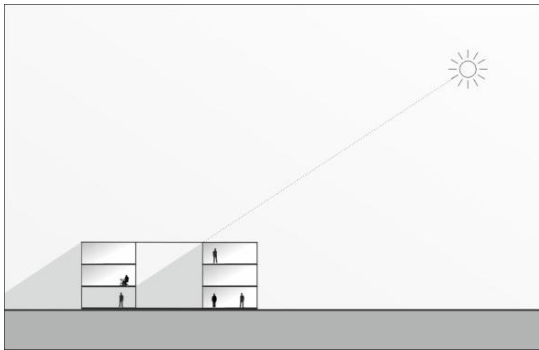
Fig. 3.   Three-story building B (built in 2010) with the atrium with closed roof

Fig. 4. The atrium of the 3-story building B
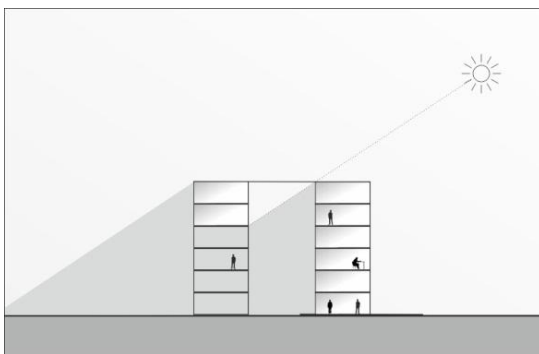
Fig. 5.   The building B is 6-story (3 additional floors were built after in 2012)

Fig. 6. The atrium of the 6-storey building

3.2. The results of the measurements in the investigated offices

The health complaints at work are often caused by badly designed workplace, but these shortages are closely connected with indoor climate conditions (bad microclimate, excessive noise, insufficient lighting). Sometimes the psychosocial factors also take place as not good relations between the employers and employees, stress coming from home or street with the workers to the workplace etc.). Therefore these three components were investigated thoroughly. The results of indoor climate investigations are given in Table 1.

Table 1

Results of measurements indoors in glazed buildings

Room type	Indoor air temperature, °C, $U = 0.6$ °C		Indoor air humidity, %, $U = 2.0$%		Natural lighting, lx (Sept.-March), $U = 10.4$%	Concentration of carbon dioxide, measured	Concentration of dust in the air
	Cold season	Warm season	Cold season	Warm season		CO_2, ppm $U = 10$%	mg/m³ $U=10$%
Building A, rooms closed to the atrium	20-22	24-28	15-25	35-75	5-250	500-750	0.0020
Building A, rooms closed to outdoors	18-22	22-28	20-30	40-75	350-600	350-1200	0.0015
Building B, rooms closed to the atrium	18-20	20-24	10-21	35-65	25-350	541-897	0.0015
Building B, rooms closed to outdoors	17-20	22-28	15-30	40-70	350-600	478-1152	0.0011
1.Glazed office- rooms (on 8th floor)- built in 2008	22-24	25-29	34-41.5	35-65	344-914	620-715	0.0015
2.Glazed office-rooms (ground floor), built in 1980s	20-22	28-30	22-23	35-65	495-890	537-998	0.0030
3.Glazed office-rooms in a small town, built in 1960s	18-20	25-26	34-40	35-65	390-765	447-750	0.0012

U – the uncertainty of measurements; the dust concentration in the smoking room (building B) was 0.099 mg/m³.

The main results of the investigation: the indoor air is too dry in winter season (relative humidity 10-20%); the air temperature in the workrooms depends on the rooms' location in the building and the relaxation time of the temperature is too high (the rooms are not heated or cooled with enough speed according to the sudden changes of the outdoor air temperature); if the room area is smaller than 10 m² per worker, then the concentration of CO_2 is over the limits (> 800 ppm); noise is a problem when the ventilation is working in a very high capacity. The concentration of dust is low and the moisture in the rooms (causing bad smell) is observed only in the first floor closed to the atrium. The artificial lighting was mainly sufficient in the investigated firms.

3.3. The investigation of the opinion of workers

The workers were questioned on satisfaction with the indoor air temperature, humidity of the air, the ventilation and the deficiency of natural lighting in the rooms closed to the atrium. If the windows were to the direction of the opposite side (to outdoors), then there were no complaints about lighting. Sometimes the workers complained about the fluorescent lamps that these were too strong and there was a pain in the eyes at the end of the work-day.

The questionnaire (based on Nordic, WAI, Kiva questionnaires) was presented to the computer-workers by internet to conclude the relationship between the workers and the employer, the development of diseases (particularly the MSDs) etc. A total of 295 (291 correct answers) people from different institutions (computer-workers from the university, hospitals and enterprises) answered the questionnaire. Among them there were 94 men and 197 women. The respondents were divided into two groups: **A,** age < 40 (40 not included) - 137 persons and **B,** age >39 (40 included) – 152 persons. The average age of the group **A** was 30.97 years and the group **B** - 54.5 years. People who answered, had been working in the same occupation accordingly 4.81 years (group **A**) and 17.38 years (group **B**). On the average the respondents were university educated and married. Over 90% of the respondents were engaged in mental work in both groups (**A** and **B**). The example of the questions and answers (from the Nordic questionnaire) is given in Table 2. The most annoys the mentally working people the lack of the opportunity to influence on their own job content and the reduction of the work motivation or desire to work therefore. To the question "Does your immediate superior encourage you to speak up, when you have different opinion?" The answer was: sometimes.

Work Ability Index questionnaire revealed the workers current performance with the best level of life. Both groups evaluated it with 8 in the scale of 1-10. In the group **A** some musculoskeletal orders occurred in 86 (62.7% of all) people, among them 22 (16%) cases were by the physician-diagnosed; cardiovascular diseases were mentioned by 22 people (17%), 10 (8%) of them were the physician-diagnosed; visual disturbances occurred in 20 persons (16%) (15 physician-diagnosed). The problem of overweight in this group occurred in 25 (20%) persons, 22 were diagnosed by a doctor. The diabetes occurred in two people. In the group **B** 114 people (74.0% of all) had the musculoskeletal disturbances (to 67 or 43.5% of the persons the disease was diagnosed by the physician); about cardiovascular diseases complained 9 persons (6%), 10 of these diseases were diagnosed by the physician); visual disturbances occurred in 13 persons (23%); 7 cases of which were diagnosed by the doctor. Overweight in this group occurred in 14 (25%) people –

all these cases had been diagnosed by the doctor and diabetes didn´t occur. The question "At what age are you planning to retire?" was presented to the both groups. The answer was 67.0 years for the group **A** and 67.1 years for the group **B**.

Kiva questionnaire (scale 1-10) revealed that the group **A** enjoyed coming to work by 6.5 points, by 8.0 points the workers considered their work important; the possibility to influence on their own work content was evaluated by 6.7, the relationships with co-workers with 8.4 points and with the boss it was assessed with 7.5 points. To the confidentiality that the worker will continue with the same employer was given 7.5 points (of 10). Group **B** enjoyed coming to work by 7.3 points, the importance of the work was assessed by 8.5 points. 8.5 were given to the relationships with co-workers and with the boss 7.1 points. An average of 6.8 points was confident that they will continue with the same employer in the future, and 6.8 points were given to the possibility to have impact of their work process.

Table 2

Do the following issues harm/hinder how you cope at work or how you manage to do your work?

The question	(Value: 0) do not exist/do not harm	(Value: 1) harms a little	(Value: 2) harms a lot	(Value: 3) cannot say	
a) things related to health or functional ability (group **A**)					100%
a) things related to health or functional ability **B**					100%
b) things related to education or know-how **A**					100%
b) things related to education or know-how **B**					100%
c) issues relates to the work environment or the physical load of the job A					100%
c) issues relates to the work environment or the physical load of the job B					100%
d) issues related to the work community or the mental burden of the job **A**					100%
d) issues related to the work community or the mental burden of the job **B**					100%
e) reduction of work motivation or desire to work **A**					100%
e) reduction of work motivation or desire to work **B**					100%
f) difficulties outside work (in the family, the economic situation etc.) **A**					100%
f) difficulties outside work (in the family, the economic situation etc.) **B**					100%
Total	45%	38%	15%	2%	
Total	57%	32%	6%	6%	

4. Rehabilitation

The work is repetitive for info-technology workers, the movements, made by the right and left hand, are different. The probability of developing the carpal-syndrome disease is higher for info-technology workers who use the mouse. As the number of musculo-skeletal disorders has risen caused by the work with computers so the rehabilitation methods are very important. The authors of the present study suggest the following: the complex treatments of these syndromes include active and passive methods of physiotherapy. The active part is organized by the physiotherapist. Systematic application of physical education, exercise therapy improves the functional capacity of the organism to physical stress. The role of the physical therapist in the occupational health team is to ensure that an optimum work environment exists for the prevention of injury and for the rehabilitation of work-related impairment, activity limitation,

and participation restrictions. There are also physical therapies which influence the tissues metabolic activity and have positive influence on the repairing process. These are massage, physical agents therapies and water immersion therapy. The most important is the workplace ergonomic design (Fig. 7) to prevent the health damages.

| a | b | c |
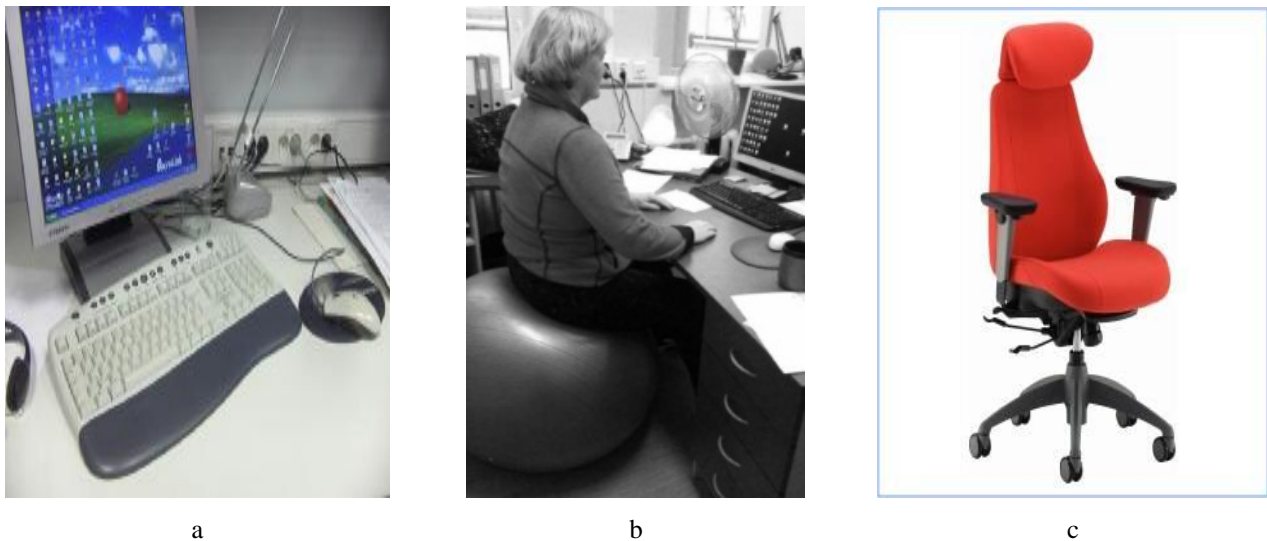
Fig. 7.   Ergonomic solutions of the workplace: a – ergonomic key-board; b – ball as a chair; c – ergonomic chair

5. Discussion

The ergonomics of workplaces has to be considered in the design of workplaces. If the house in already built it is possible to improve the work conditions, but it takes time and money. The standard EVS-EN 15251 has to be presented during the design of workplaces. The glazed buildings are very modern, but also include problems (like insufficient lighting or ventilation, too many workers in one room, the windows cannot be opened etc.). The info-technology workers often work with under-lighted working conditions although there is a possibility to raise the lighting to the normal limits (400 – 500 lx). The work in the office is monotonous. The risk scores for right and left hand are different. The questioning of the workers showed that the workers working with computers are focused on their own workplace and work-tools. The interior architect has to follow the ergonomic principles of workplaces from the beginning of the building use. The expectation of having to remain in a sitting position when working with computers should be diminished. The rehabilitation is necessary for both type of the workers (engaged in info-technology or original office-work: accountants, secretaries etc.). Despite the stress sometimes felt by the workers, time pressure, work interruption and intense periods in the work, the respondents were satisfied with their jobs. This was demonstrated both by Kiva and WAI questionnaires. The respondents had sufficient latitude to work, relationships with colleagues were good and the workplace atmosphere was good also; despite of some shortcomings in the organizational factors the employees were satisfied with the management. Work stress was felt by the 2/3 of the respondents "only a little" or "to some extent". In small doses, stress is good – such as when it helps to conquer the fear or gives extra endurance and motivation to get something done.

Based on the investigation by the age groups (**A** under 40 years and **B** over), it might be concluded that the number of visual disturbances in the group **A** has increased as the people begin to use the computers in the younger age. The analogous disturbing phenomenon was observed in the assessment of the health status of the workers: the **A** group of the respondents (workers under 40 years) assessed their health status worse. The health status assessed "good": accordingly by 55% of people in the **B** group and 43% in the **A** group.

The work in the offices is monotonous and the workload might be high. The risk scores for right and left hand are different. The interior architect has to follow the ergonomic principles of workplaces from the beginning of the building use. The expectation of having to remain in a sitting position when working with computers should be diminished. The rehabilitation is necessary for young and ageing workers.

The authors of the present study suggest the following: the complex treatments of these syndromes include active and passive methods of physiotherapy. The active part is organized by the physiotherapist. Systematic application of physical education, exercise therapy improves the functional capacity of the organism to physical stress. The role of the physical therapist in the occupational health team is to ensure that an optimum work environment exists for the prevention of injury and for the rehabilitation of work-related impairment, activity limitation, and participation restrictions. There are also physical therapies which influence the tissues metabolic activity and have positive influence on the repairing process. These are massage, physical agents therapies and water immersion therapy.

6. Implementations

The results could be used in the improvement of workers' working conditions particularly in the cold or hot season or areas; for regulation the ventilation in the rooms; for improvement the ergonomics of workplaces, improvement of lighting.

Acknowledgements

References

1. **Traumann A., Tint P.** The quality of indoor climate in offices in atrium-type buildings // Proceedings of the 6th International Conference "Intelligent Technologies in Logistics and Mechatronics Systems", ITELMS'2011, 2011, p.33-38.
2. **Mergi C. A., Al-Dawoud A-S.** Integration of ventilation in the design of commercial buildings- application to atrium buildings in hot/humid climate. *Architecture and Environment,* 2007, 6, p.14-27.
3. **Seppanen O. A., Fisk W. J., Mendell M. J.** Association of ventilation rates and CO_2 concentrations with health and other responses in commercial and institutional buildings. *Indoor Air*, 1999, 9, p.226-252.
4. **DeKay M.** Day lighting and urban form: an urban fabric of light. *Journal of Architectural and Planning Research*, 2010, **27**(1), p.33-56.
5. **Sharples S., Lash D.** Daylight in atrium buildings: A Critical Review. *Architectural Science Review*, 2007, 50(4), p.301-312.
6. **Fang L., Wyon D. P., Clausen G., Fanger P. O.** Impact of indoor air temperature and humidity in an office on perceived air quality, SBS symptoms and performance. *Indoor Air,* 2004, 14(Suppl 7), p.74-81.
7. **Jones A. P.** Indoor air quality and health. *Atmospheric Environment*, 1999, 33, p.4535-4564.
8. **Brauer C., Mikkelson S.** The influence of individual and contextual psychological work factors on the perception of the indoor environment at work: a multilevel analysis. *Int Arch Occup Environ Health*, 2010, 83, p.639-651.
9. **Da Costa R. B., Viera E. R.** Risk factors for work-related musculoskeletal disorders: a systematic review of recent longitudinal studies. *American Journal of Industrial Medicine* 2010, 53, p.285–323.
10. **Janwantanakul P., Praneet P., Jiamjarasrangsri V., Sinsongsook T.** Prevalence of self-reported musculoskeletal symptoms among office workers. *Occupational Medicine,* 2008, 58, p.436–438.
11. **Woods V.** Musculoskeletal disorders and visual strain in intensive data processing workers. *Occupational Medicine,* 2005, 55, p.121–127.
12. **Van den Heuvel S. G., De Looze M. P., Hildebrandt V. H., The K. H.** Effects of software programs stimulating regular breaks and exercises on work-related neck and upper-limb disorders. *Scand J Work Environ Health*, 2003, 29(2), p.106–116.
13. **Brewer S., Van Eerd D., Amick B. C., Irvin E., Daum K. M., Gerr F., Moore J. S., Cullen K., Rempel D.** Workplace interventions to prevent musculoskeletal and visual symptoms and disorders among computer users: A systematic review. *J Occup Rehabil*, 2006, 16, p.325–358.
14. **Kennedy C. A., Amick B. C., Dennerlein J. T., Brewer S., Catli S., Williams R., Serra C., Gerr F., Irvin E., Mahood Q., Franzblau A., Van Eerd D., Evanoff B., Rempel D.** Systematic Review of the Role of Occupational Health and Safety Interventions in the Prevention of Upper Extremity Musculoskeletal Symptoms, Signs, Disorders, Injuries, Claims and Lost Time. *J Occup Rehabil*, 2010, 20, p.127–162.
15. **Näsman O.** Metal Age and Kiva-questionnaire. Assist in navigation towards well-being at work. Mediona OyAb. The Archipelago Academy for Well-being at Work. Available at < http://www.mediona.fi/pdf/KANSI%20 Metal%20Age%20ja%20Kiva-kysely% >.
16. **Tuomivaara S., Ketola R., Huuhtanen P., Toivonen R.** Perceived competence in computer use as a moderator of musculoskeletal strain in VDU work: An ergonomics intervention case. *Ergonomics,* 2008, 51(2), p.125-139.
17. **Van Bomml W. J. M.** Non-visual biological effect of lighting and the practical meaning for lighting your work, *Applied Ergonomics,* 2006, 37, 461-466.

Ladar – Aided Navigation System for Unmanned Ground Vehicles

A. Typiak

Military University of Technology, Kaliskiego str. 2, 00-908 Warsaw, Poland, E-mail: atypiak@wat.edu.pl

Abstract

A typical unmanned and remotely operated vehicle is usually equipped with cameras which give insufficient information about the nearest environment and an operator has difficulties in driving such a vehicle in unknown environment. In this paper, a problem of the vehicle nearest area map building based on additional devices is considered. The vehicle is equipped with SICK LMS lasers, inclinometer and radars. Combining information from the devices allows to build a map which helps an operator to drive the vehicle more efficiently.
KEY WORDS: *laser telemeter, navigation system, 3D map building, unmanned ground vehicle, surroundings recognition.*

1. Introduction

There are a number of navigation trends that improve the ability to navigate in all sorts of environments. While GPS has been the driving factor behind most of these trends, it has its limitations, which become more evident over time as we are starting to be more and more dependent on this type of navigation.

The problem of integrated navigation is to combine the outputs of different types of sensors (Fig. 1). Navigation sensors, like any system have strengths and weaknesses. For examples, GPS has exceptional accuracy, but it is subject to outages due to the loss of satellite signals. Internal sensors rely only on gravity and platform dynamics, which cannot be jammed, but they exhibit errors that grow over time and eventually become unacceptable. There is no one set of sensors can be used for operations in all environments. This is implies that ultimate solution will be a modular system in which a suite of sensors can be selected for a give situation and a high level integration scheme will adaptively integrate those sensors in an optimal fashion. Navigation Kalman filter design requires a careful error analysis and model development for each sensor to be integrated.
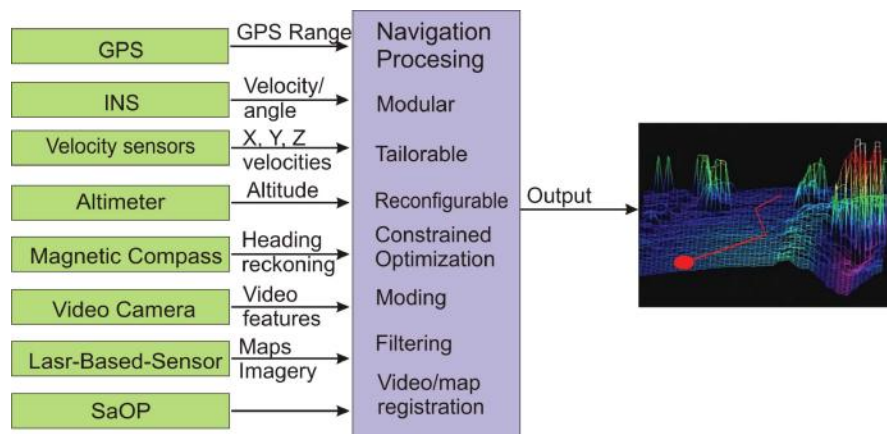
Fig. 1. Modular, adaptive, multisensory integrated system to providing robust navigation

While GPS is very good in determining the position of an object in an open space and at high altitudes, the closer to the ground level and the more complex the environment, the data accuracy starts to decrease. And even though recent advancements in high-precision GPS is allowing to acquire more and more accurate data, determining the precise position i.e. in an urban environment is still impossible.

Summarizing the navigation requirements in a manner similar to [2, 3], it would be desirable to develop a navigation system that supports:
- an indefinite mission duration;
- real-time 3D location performance;
- localization in urban environments and inside residential and most commercial buildings;
- operation in an unknown (unmapped) or sparsely known (partially mapped) environment;
- localization from the power-off condition and requires no separate starting location initialization of the user equipment;
- individual isolated user terminals, etc.

For the reasons described above, alternative navigation techniques have been and are currently being developed to help fill this navigation gap. At least three broad categories of alternative navigation techniques exist:
1. Image/Ladar/Doppler/DR aiding of inertial;
2. Beacon-based navigation (including pseudolites);
3. Navigation using signals of opportunity.

Fig. 2 shows a block diagram of the Ladar-based navigation method. The desired features ("lines" or "planar surfaces") are extracted from the Ladar scans and used to estimate the navigation solution that is comprised of changes in Ladar position and orientation.
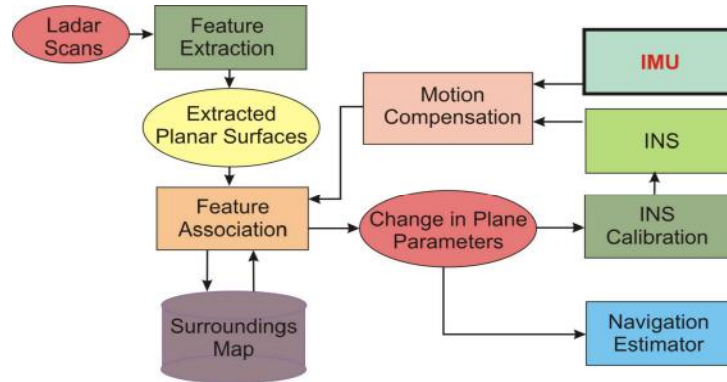
Fig. 2. Scheme of calculating vehicle route that uses images of a scanning LADAR

In order to use a planar surface for the estimation of position and orientation changes, this planar surface must be observed in both scans and it must be known with certainty that the plane in one scan corresponds to the plane in the next scan. Hence, the feature association (or matching) procedure establishes a correspondence between planes extracted at the current scan time epoch and the planes extracted at previous scan epochs. The navigation routine stores planes extracted from previous scans into the plane list, which is initialized with the planar surfaces of the first scan, If a new planar surface is observed during one of the following scans, the plane list is updated to include this new plane. The feature matching procedure uses position and orientation outputs of the INS to predict the planar surface location and orientation at the current scan time based on planar surface parameters observed at previous scan time epochs. If the predicted planar surface parameters and the parameters of one of the extracted planar surfaces match closely, a successful association is declared. Following successful feature association changes in the associated planar surface parameters are used to estimate the navigation and attitude solution. Furthermore, these changes in planar surface parameters are also applied to periodically re-calibrate the INS to reduce drift terms in inertia navigation outputs in order to improve the quality of the INS-based plane prediction used by the feature matching procedure.

The position and orientation data from the INS is also used to compensate for the motion of the vehicle (Ladar) during the scans in those cases where such motion could introduce significant distortions to Ladar scan images. The above method results in the calculation of a relative navigation solution. Estimating local frame position and orientation in one of commonly used navigation frames (e.g. East-North-Up and Earth -Centered-Earth-Fixed frames) allows for the transformation of the relative navigation solution into an absolute navigation solution. Navigation herein is performed in completely unknown environments.

2. Feature – based laser scan matching

Recently [4] proposed a promising algorithm (HAYAI) to solve self-localization problem of high speed robots. Although this method is a fast and feature based method for scan matching, it suffers from the lack of satisfying robustness property of feature extraction and it is well-suited for high range sensors. In this paper the idea of this approach is borrowed for the scan matching and similar arguments are given regarding the computation cost and precision of feature based scan matching. However, by introducing appropriate algorithm for extracting features, and modeling existence features' uncertainty, the robustness of the method is improved significantly, even for low range sensors. The main idea behind the proposed algorithm in this paper is to address the issue of feature matching extracted from two consecutive scans, such that they can be integrated based on their covariance, in order to form accurate displacement estimation [1]. Analyzing different sources of errors which affect displacement estimation process, appropriate uncertainty models is developed for each feature extracted from the scan. Incorporating these models in displacement estimation, results in more accurate estimations.

The following subsections describe the implemented data filtering techniques, extraction and matching of the used features as well as the mathematical background and practical matters of calculating the optimal transformation between two scans.

Scanning is noisy and small errors may occur, namely Gaussian noise and so-called salt and pepper noise. The latter one arises for example at edges where the laser beam of the scanner hits two surfaces, resulting in a mean and

erroneous data value. Furthermore reflections, e.g., at glass surfaces, lead to suspicious data. We propose two fast filtering methods to modify the data in order to enhance the quality of each scan, typically containing scanner's data points. The data reduction, used for reducing Gaussian noise, works as follows. The scanner emits the laser beams in a spherical way, such that the data points close to the source are more dense. Multiple data points located close together are joined into one point. The number of these so-called *reduced points* is one order of magnitude smaller than the original one. A median filter removes the outliers by replacing a data point with the median value of the *n* surrounding points (here: *n* = 7, covering an angle of [1]. The neighbor points are determined according to their number within the scan, since the laser scanner provides the data sorted in a counter-clockwise direction. The median value is calculated with regard to the Euclidean distance of the data points to the point of origin. In order to remove salt and pepper noise but leave the remaining data untouched, the filtering algorithm replaces a data point with the corresponding median value if and only if the Euclidean distance between both is larger than a fixed threshold (see Fig. 3).

a

b
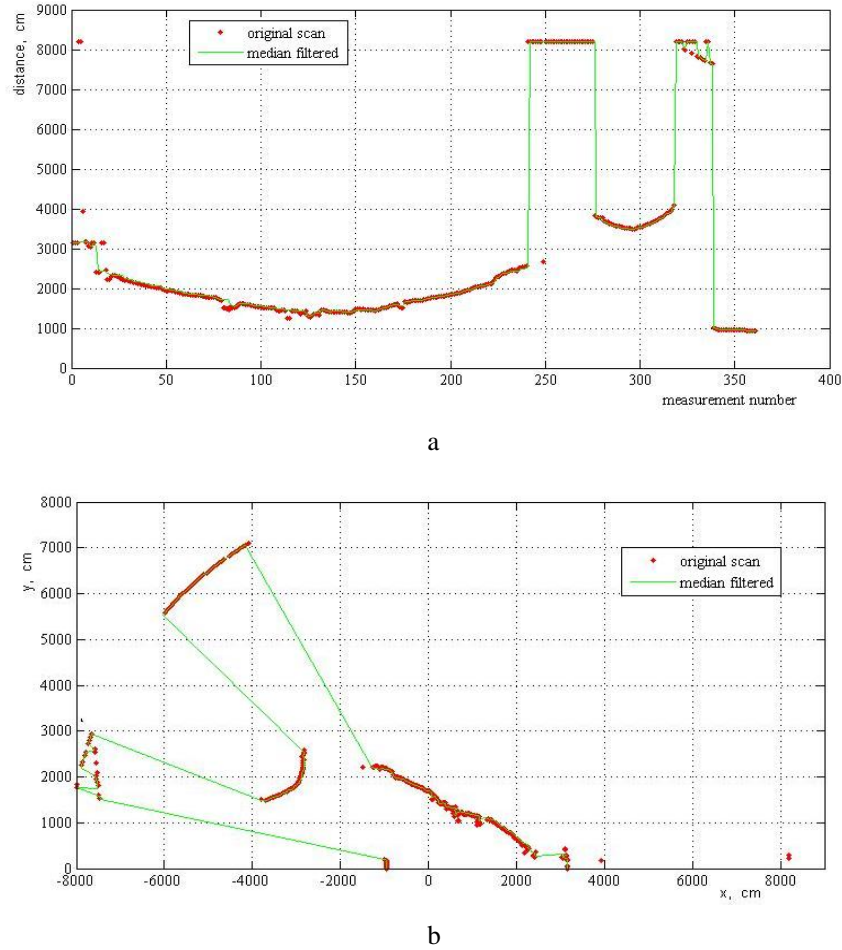
Fig. 3. Median filter: a – polar coordinates; b – Cartesian coordinates

To estimate the planar surface parameter using 2D Ladar scanners can be used by intentionally rotating the Ladar scanner. Now the multiple observed lines can be transformed to a common frame using IMU/INS data associated to form lines belonging to the same planar surface. Multiple of these lines can be used to estimate the planar surface parameters. More details of this method can be found in [2, 4].

3. Extracting features from laser range finder data and it's parsing

One of the crucial factors of correctly controlling an unmanned ground vehicle is creating an algorithm which would allow for a fast and precise localization of the vehicle within its surrounding. Measuring absolute translocation based on INS sensory data may be used only on short distances and flat, hard surfaces, since the measurement errors increase with time. One of the methods for supporting the localization system is using 2-D laser finders or ultrasonic sensors, however laser sensors allow to 'see' a wider area near the vehicle and have a higher accuracy of measurement [1, 3].

Some techniques of data analysis are applied to the scan *S*, provided by the scanner, in order to extract features from the scan. Desired features are divided into two types: features corresponding to the jump-edges and those corresponding to the corners detected in the scan. Formal notation for the scan *S* is given by:

$$S = (p_i)_{i=1\ldots n} \tag{1}$$

$$p_i = [d_i, q_i]^{\mathrm{T}} \tag{2}$$

where d, q are polar coordinated of the j-point.

In order to detect jump-edges in scan, scan points are divided into some clusters consisting of consecutive scan points in their natural order. As a result, every cluster features a dedicated start point (p_i) and an end point (p_j), in which, i and j are indices of points in whole scan S, and also $i < j$. Therefore, k'th cluster is defined

$$c_k = \{ p_m \ p_m \in S, \quad i \le m \le j \tag{3}$$

Clustering procedure is as following:

1. $p_i \in c_i$ and for all points in scan like the distance:

2. $d_i = \| p_{i+1} - p_i \|$ is calculated, then

$$p_{i+1} \in c_k \quad \text{if} \quad (p_i \in c_k, \ d_i \le d_m) \tag{4}$$

$$p_{i+1} \in c_{k+1} \quad \text{if} \quad (p_i \in c_k, \ d_i > d_m) \tag{5}$$

where: d_m is the maximum distance between two consecutive points within a cluster.

The start and end point of each cluster are good candidates for being a feature. On the other hand all features have to be invariant with respect to robot's displacement. Thus, only invariant points are reliable for being selected as a feature and thus must be chosen. There are two cases in which one can see variation in end-cluster features.

1. Clusters correlated to objects partially occluded by the other object. The start or the end point of a cluster, which is established by occlusion, is a growing (variant) point with respect to robot's displacement, and is not a good feature as illustrated in Fig. 4.
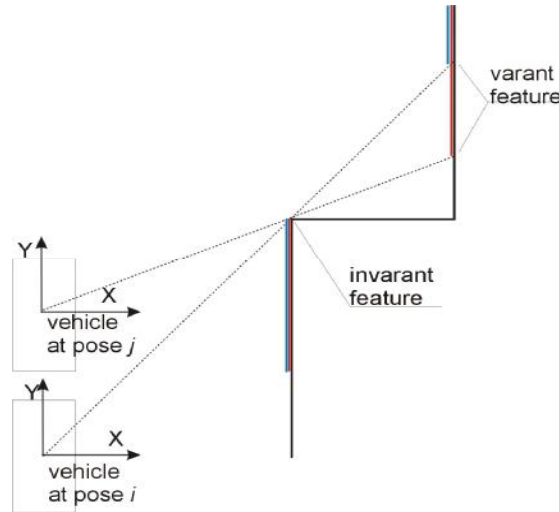
Fig. 4. Extracting variant and invariant features

Therefore, the feature selection can be found by the following routine, given p_i the start or end point of cluster k_k,

$$\text{if } |q_i - q_{i-1}| < q_r \text{ and } r_i > r_{i-1} \text{ and } p_i \text{ is start of } k_k \Rightarrow p_i \text{ is not feature}$$

$$\text{if } |q_i + 1 - q_1| < q_r \text{ and } r_i > r_{i+1} \text{ and } p_i \text{ is end of } k_k \Rightarrow p_i \text{ is not feature}$$

otherwise p_i is a feature.

2. Second class of features corresponds to the corners within the clusters. In [1] filters with small lengths are introduced to operate on the sequence of distance values (r_i) of points in the scan. Because of their small length, this method suffers from the lack of global sight on the scan data and some global information is missed. For example it may choose some features on flat walls due to scan noise. Therefore, in this paper it is proposed that for detecting corner features, at first a line fitting algorithm is applied as a global filter. In the literature several approaches are developed to solve the problem of extracting line segments from a sequence of points, with different speed and accuracy. Reference [1] has compared the state-of-art methods for line extracting, and reported that for real-time applications, split-and-merge algorithm is the best choice by its fair correctness and superior speed. Thus,

split-and-merge algorithm is used in here for line fitting within each cluster. Due to the primary clustering, merging stage is often not required, and if required it is very fast. The parameter specifying a line reads as:

$$l_k = \left[a_k, n_k, \bar{k} \right] \tag{6}$$

where: α_k is the angle between line and x axis; n_k is the number of associated scan points in line; $\bar{k}$ is the length of l_k.

If intersection of two successive lines, l_q and l_{q+1}, satisfies two following conditions, p_s, which is the end point of l_q, is introduced as a candidate corner feature.

<u>Condition 1.</u> $\left| a_{q+1} < a_q \right|$ exceeds the minimum threshold Da_{th}.

<u>Condition 2.</u> For both l_q and l_{q+1}, either $len_q > len_{q+1}$ or $n > n_k$. The len_{th} is the minimum acceptable length and n_{th} is the minimum acceptable number of points of lines intersected at this corner. The p_s may be not the exact corner point. Thus, using local information around p_s, the following algorithm tries to find the nearest point to exact corner feature.

First, two points $p_i \in l_q$ and $p_j \in l_{q+1}$ are selected which have distance r to p_s (Fig. 5). The r is proportional to len_q and len_{q+1}. The p_i and p_j are connected by a straight line and for all scan points, p_m, lying between p_i and p_j, $i < m < j$, distance to this line is calculated. The scan point, produces the maximum distance, is named p_{s1}. If $p_{s1} = p_s$, procedure is terminated and p_s is selected as a corner feature. If $p_{s1} \neq p_s$, then $p_{s1} = p_s$ r is decreased and the above procedure is recursively called until $p_{s1} = p_s$.

Finally, each corner feature is specified by, $[p_s, \alpha_{pre}, \alpha_{next}]$ in which p_s is the feature point in scan and "s" is its index in the whole scan. A_{pre} and α_{next} are angles of two consecutive lines established this corner. Moreover, each start (end)-cluster feature is specified by point p_s of scan and α_{pre} (α_{next}) which is the angle of line connecting to that.

After extracting features from two consecutive scans, matching algorithm, based on a dissimilarity function, has to be calculated. Owing to the fact that features' topology cannot change fundamentally from one scan to the other, below dissimilarity function between p_i and p_i', two features from two consecutive scans, is introduced as:

$$d(p_i, p_j') = \left\| p_i - p_j' \right\|_2 + B \tag{8}$$

If $\left| a_{next_i} - a_{next_j}' \right|$ or $\left| a_{pre_i} - a_{pre_j}' \right|$ − (which one exists) exceeds a maximum threshold, the p_i and p_j are not matched, and B becomes infinity, otherwise $B = 0$.
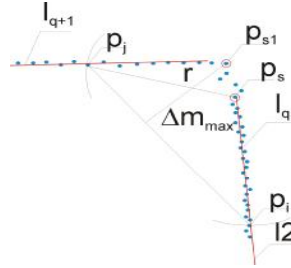
Fig. 5. Calculate a corner on the base data from LRF (specification in the text)

After dissimilarity matrix is constructed, at each step the minimum value element of this matrix is chosen, its corresponding row and column are omitted and correlated features are matched, until all rows and columns of dissimilarity matrix are omitted or the minimum value of elements exceeds a maximum matching distance.

4. Experiments

As it was mentioned before our system only supports driverless vehicles equipped with a set of cameras. An operator drives the vehicle mainly based on the camera pictures. Therefore we don't focus on any particular model of a vehicle. Our system is mounted on a metal frame (except radars) and the frame is mounted on a vehicle. We have tested several different kinds of vehicles and results are as described in the previous section. Among others we tested the system on a vehicles presented on Fig. 6. Results were comparable due to reasons beyond our control the vehicle enclosure significantly limited the point cloud.

The software system consists of two programs made in a client-server architecture. The server is a program installed on the on-board computer. Its task is to read data cyclically from all described above devices by RS-232 and Ethernet connections as well as preparing and sending data to the client in fixed format frame. The frames are sent with the frequency of 20 ms. After receiving data, the client module shifts map for the distance the vehicle moved, creates new list of obstacles and assigns them to the map. The size of each frame is about 11kb and sending a frame each 20ms requires 6 MBit/s connect.

Fig. 6. Two elements vehicle with our frame mounted on it

Aggregated data received from devices described above are represented as a point cloud. This point cloud is used to build a map. We assume that size of the map is 40m. (the laser scanners maximal range is 20m), the vehicle is always in the center of the map and data out of the map are forgotten. We consider obstacles 3m below and 12m above the vehicle. Fig. 7 presents the relations between the vehicle and the map.

System described in this article is designed to work on a remotely controlled vehicle which is driven mainly from camera signals. The main task of our system is to improve an operator to drive the vehicle more safety and more precisely.
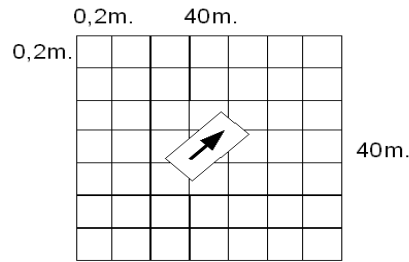
Fig. 7. Relations between the vehicle and the map

Keeping this in mind, we must present our map fulfilling the following requirements:
- System must work in real time - the vehicle goes with maximal speed about 10km/h and data must be presented on time.
- The map must improve detecting actual orientation of vehicle - It is hard to control orientation based only on cameras.
        The map must be able to monitor and alert if the path in front of the vehicle is impassable.
        Keeping a model of the map as voxels allows presenting the map to the operator in different ways. We are still exploring the best way of presenting the map and for the time being we have three different views. These are: a typical 2.5D map, profile before the vehicle and a polar-coordinated map. Fig. 8 shows the idea behind the method.
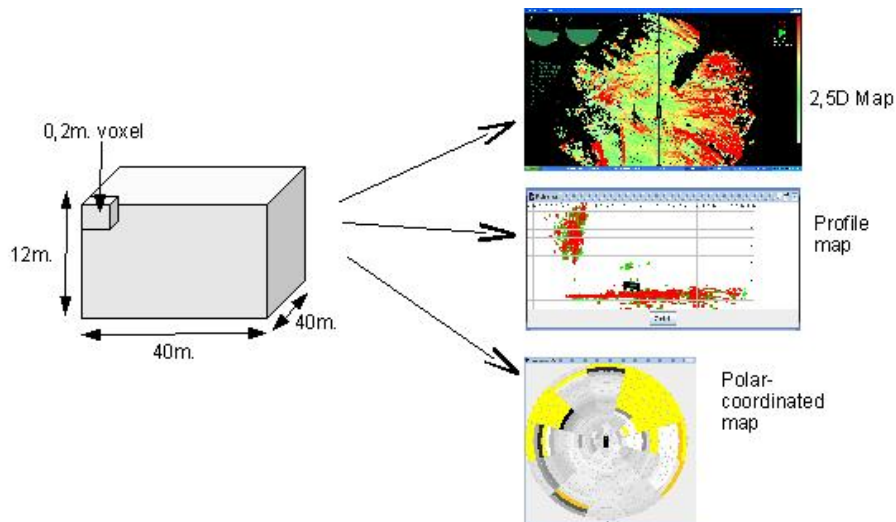
Fig. 8. 3D map model and its different views

The typical 2.5D map is the mostly used view. It shows the whole area around the vehicle. The terrain form and height is presented in different colors. Here light green color represents the deepest place (-2 m. or less), while the red – the highest (more than +1 m.). We assume, that point (0, 0, 0) is in the central laser scanner (central front point). Fig. 9a presents the place where experiments have been done (a) and 2.5D maps (b, c, d). The Fig. 9b shows the map built in the place where the photo was taken. Notice the building wall and two trees before it. During the experiment the gate was open, that's why the wall between trees is not detected. On the both sides of the vehicle the impassable obstacles were detected. We use two inclinometers, a universal one (designed by Military University of Technology) CP-1 and another designed for airplanes (MIDG). Two green circles show the indications of both inclinometers. The former seems to be too sensitive while the latter is rather too slow.

a

b

c

d
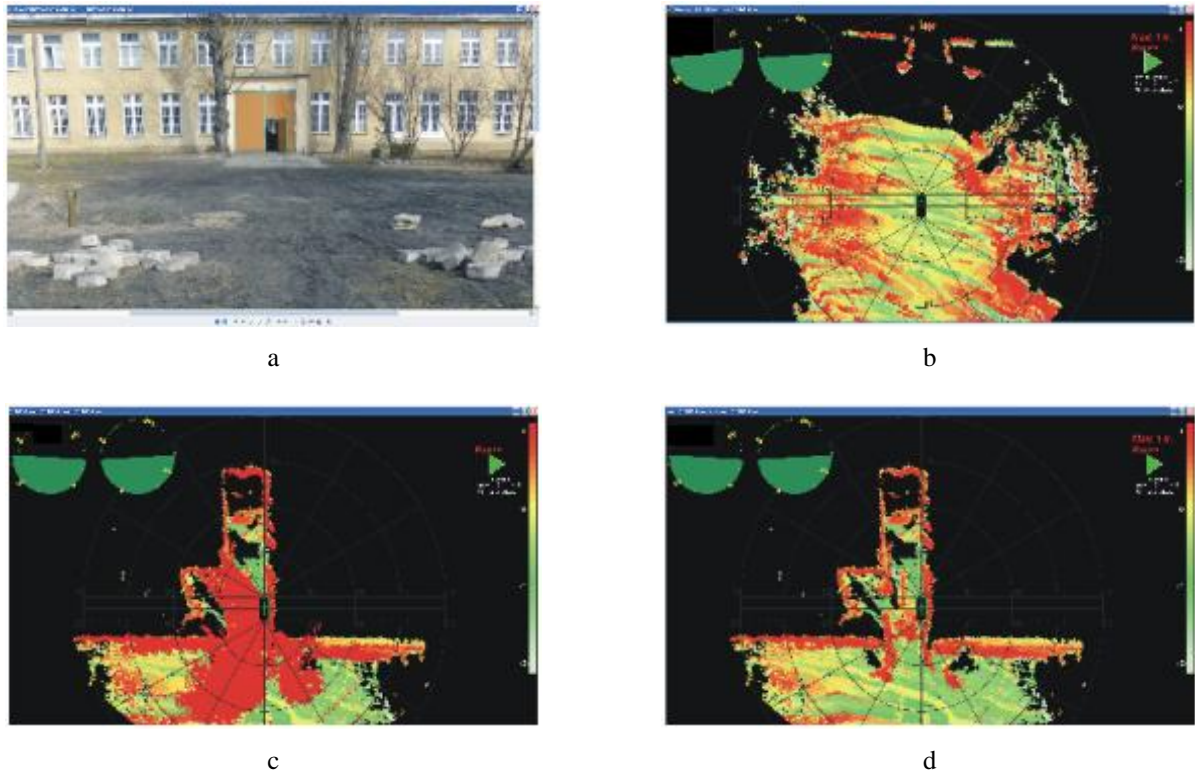
Fig. 9. A place where experiments have been done and a typical 2.5D maps (described in text)

One of the useful advantages of our map model and its 2.5D view is possibility to look under the highest obstacles. Fig. 9c, d show entrance the vehicle into the garage. Fig. 9c shows that all obstacles and the area is hardly readable, because the ceiling as well as the trees before the building covers obstacles below. Due to keeping the 3D map model it is possible not to display obstacles above certain height. Fig. 9d shows the same area where obstacles over 1m above vehicle are rejected. Now the area around the vehicle is readable.

The second type of the map is a profile one. In this view only the area in front of and behind the vehicle are presented. The aim of this view is to warn the operator of impassable area in front of the vehicle. Fig. 10 shows the necessity of this kind of map (left) and a view of it (right). The vehicle is located below a tree in front of the garage. The garage is open and obstacles in it are detected (the right part on the picture). Red and green colors represent obstacles on respectively left and right sides of the vehicle.
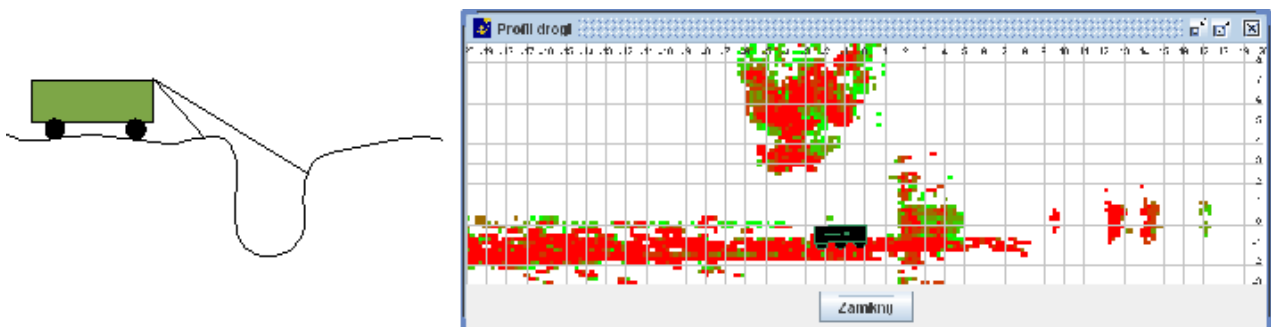
Fig. 10. The idea behind the profile map (left) and the view (right), notice a tree over the vehicle and a wall in front of it

5. Summary

Results of research carried out so far on detecting the location of objects using a laser telemeter show, that this method may be used to create an effective system for detecting and localizing objects in a 3D environment surrounding the vehicle or machine. Recent researches on depicting a 3D environment are now a basis for research on detecting the position of moving objects. Processing the data acquired from a laser telemeter, GPS and a digital map will allow building of a geodetically oriented 3D map of the surrounding.

Resolving problems with navigation and steering of those types of vehicles will allow expansion of it's applications from a military point of view in the upcoming few years, to a wide range of applications in times of crisis with direct human life threat.

In this paper an unmanned vehicle operator assist system is presented. The operator drives the vehicle based mainly on views from cameras which are installed on the vehicle. Our system supports the operator and builds an aggregated local map of the environment based on data from 5 laser scanners and shows the operator the environment in real time. There is a 3D model of a map which is presented in 3 different ways. All computation are done in real time on typical industrial and standard PC.

6. Conclusions

The future holds a lot of promise for the continued development and deployment of unmanned vehicles of all types. Applications and missions suitable to unmanned vehicles will continue to be identified and robotic technologies will further evolve to fill those needs allowing more complex missions to be performed using unmanned systems.

Results of research carried out so far on detecting the location of objects using a laser telemeter show, that this method may be used to create an effective system for detecting and localizing objects in a 3D environment surrounding the vehicle or machine. Recent research on depicting a 3D environment are now a basis for research on detecting the position of moving objects. Processing the data acquired from a laser telemeter, GPS and a digital map will allow building of a geodetically oriented 3D map of the surrounding.

Resolving problems with navigation and steering of those types of vehicles will allow expansion of its applications from a military point of view in the upcoming few years, to a wide range of applications in times of crisis with direct human life threat.

References

1. **Aghamohammad A. A., Taghirad H. D., Tamjidi A. H., Mihankhah E.** Feature Based Laser Scan Matching For Accurate and High Speed Mobile Robot Localization, 3rd European Conference on Mobile Robots, Freiburg, Germany 2007.
2. **Stahn R., Heiserich G., Stopp A.** Laser Scanner-Based Navigation for Commercial Vehicles, IEEE Intelligent Vehicles Symposium, Istambul, 2007.
3. **Będkowski J.** Intelligent Mobile Assistant for Spatial Design Support, Journal of Automation in Construction 2012.
4. **Bedkowski J., Maslowski A., De Cubber G.** Real time 3D localization and mapping for USAR robotic application, Industrial Robot: An International Journal, Vol. 39 Iss: 5, 2012.

Determination of Stress Strain State in Two-Layer Pipe Subjected to Hydrostatic Pressure at Plane Strain Condition under Elastic Loading

D. Vaičiulis

Kaunas University of Technology, Daukanto 12, 35212 Panevėžys, Lithuania, E-mail: dainius.vaiciulis@ktu.lt

Abstract

The analytical method for stress strain state determination in two-layer pipe at plane strain condition under elastic loading is presented. Solution was obtained by assuming that: two-layer pipe materials are isotropic and linearly elastic; layers of pipe are fitted without the tightness. Dependences of maximum stress intensity on ratio of separate layers elasticity modulus, ratio of separate layers thickness and Poison's ratio are also presented.
KEY WORDS: *two-layer pipe, hydrostatic pressure, plane strain condition, stress strain state, elastic loading.*

1. Introduction

Two or more layer pipes are widely used in industry and household since multilayer pipes combines the advantages of each layer for the functional and structural requirements. Typical multilayer pipes consist of a mild internal layer (for example, some kind of polymer) and a hard external layer, i.e. a reinforcing (protecting) layer. Investigation of multilayer pipes usually carried out experimentally or by using FEA [1-4].

Long pipes typically are analyzing at plane strain condition (for example, buried pipe segments which are in enough distance from fault movement zones) [2, 5]. Analytical method for determination of stress state in two-layer pipe subjected to internal and external pressure at plane strain condition and elastic loading is presented in work [5]. But in this work does not gived analytical expressions of integration constants. Therefore solution presented in work [5] is inconvenient for practical application.

The analytical method for stress strain state determination in two-layer pipe under elastic loading at plane strain condition is presented in this paper.

2. Determination of stress strain state

The two-layer pipe may be divided in two pipes (layers). In this paper the internal layer parameters (excluding radiuses) are indicated by subscript "1" and external layer parameters – by subscript "2" (see Fig. 1). Due to acting internal or (and) external hydrostatic pressure (hereinafter the "hydrostatic pressure" will be called simply the "pressure") the contact pressure $p_{1,2}$ on the contact surface of 1st and 2nd layers appears.

The stress strain state at plane strain condition (axial strain $e_z = 0$) is determined by using these assumptions:

- layers are fitted without the tightness (nominal external radius of internal layer is equal to nominal internal radius of external layer), therefore the contact pressure $p_{1,2} = 0$ when $p_{in} = p_{ex} = 0$;
- both two-layer pipe materials are isotropic and linearly elastic, i.e. $s_{i\,max\,1} \leq s_{e1}$ and $s_{i\,max\,2} \leq s_{e2}$; where $s_{i\,max}$ is maximum stress intensity; s_{e1} and s_{e2} are limits of elasticity of 1st and 2nd layers materials respectively;
- an internal or (and) external pressure are the only loads on two-layer pipe;
- a two-layer pipe does not loose stability.
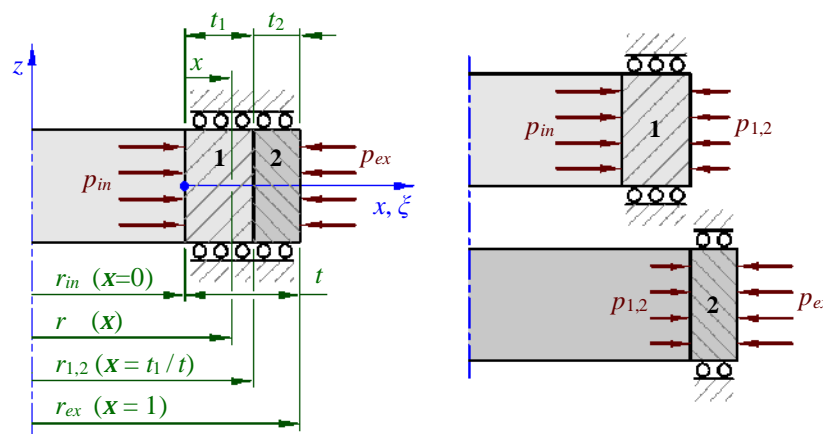
Fig. 1. Scheme of two-layer pipe subjected to internal pressure at plane strain condition

Solution was done by use the relative geometrical parameters: $s_1 = t_1 / r_{in}$, $s_2 = t_2 / r_{in}$, $s = t / r_{in} = s_1 + s_2$, $\xi = x / t$ ($0 \leq \xi \leq 1$), $\rho = r / r_{in} = (r_{in} + x) / r_{in} = 1 + \xi s$, $\rho_{in} = 1$, $\rho_{1,2} = 1 + s_1$, $\rho_{ex} = 1 + s$ (Fig. 1). The range of ξ at 1st pipe is [0; s_1 / s] (or [0; t_1 / t]) and at 2nd pipe – [s_1 / s; 1].

Radial and hoop stresses may be determined by Lame's equations [6]:

$$\left. \begin{matrix} s_{r1} \\ s_{q1} \end{matrix} \right\} = \frac{p_S}{(1+s_1)^2 - 1} \left[C_{in} \left(1 \mp \frac{(1+s_1)^2}{(1+xs)^2} \right) - C_{1,2}(1+s_1)^2 \left(1 \mp \frac{1}{(1+xs)^2} \right) \right] \qquad (1)$$

$$\left. \begin{matrix} s_{r2} \\ s_{q2} \end{matrix} \right\} = \frac{p_S}{(1+s)^2 - (1+s_1)^2} \left[C_{1,2}(1+s_1)^2 \left(1 \mp \frac{(1+s)^2}{(1+xs)^2} \right) - C_{ex}(1+s)^2 \left(1 \mp \frac{(1+s_1)^2}{(1+xs)^2} \right) \right] \qquad (2)$$

where: $p_\Sigma = p_{in} + p_{ex}$ (the p_{in} and p_{ex} shown in Fig. 1 have positive values); $C_{in} = p_{in} / p_\Sigma$; $C_{1,2} = p_{1,2} / p_\Sigma$ and $C_{ex} = p_{ex} / p_\Sigma$. In Eqs. (1)-(2) the upper sign must be used for radial stress s_r calculation and lower – for hoop stress s_θ calculation.

Radial displacement u by estimating that $e_\theta = u / r$, $e_\theta = [s_\theta - v(s_r + s_z)] / E$ and $s_z = v(s_r + s_\theta)$:

$$u = \frac{r(1+v)}{E} \left[(1-v)s_q - v s_r \right] \qquad (3)$$

where v is Poisson's ratio; E is modulus of elasticity.

When pressure is applied the radial displacement of 1st layer external radius must be equal to radial displacement of 2nd layer internal radius, i.e. $u_{1\,|\,r=r_{1,2}} = u_{2\,|\,r=r_{1,2}}$. From this condition and Eqs. (1) – (3) can be expressed parameter $C_{1,2}$:

$$C_{1,2} = 2 \frac{C_{in}(1-v_1) + C_{ex} C_{sEv}(1-v_2)(1+s)^2}{1 + (1+s_1)^2(1-2v_1) + C_{sEv}\left[(1+s)^2 + (1+s_1)^2(1-2v_2) \right]} \qquad (4)$$

where $C_{sEv} = \frac{(1+s_1)^2 - 1}{(1+s)^2 - (1+s_1)^2} \cdot \frac{E_1}{E_2} \cdot \frac{1+v_2}{1+v_1}$.

Stress intensity at plane strain condition by estimating that $s_z = v(s_r + s_\theta)$

$$s_i = \sqrt{(s_q - s_r)^2 - v(1-v)(s_q + s_r)^2 + s_r s_q} \qquad (5)$$

Strains e_r and e_θ can be calculated by generalized Hooke's law. Strain intensity at plane strain condition

$$e_i = \frac{1}{1+v} \sqrt{e_r^2 + e_q^2 - e_r e_q} \qquad (6)$$

The most heavily loaded zones in 1st and 2nd layers always are their internal surfaces (see Fig. 2). Therefore the sum of internal and external pressures when maximum stress intensity in 1st layer is equal to limit of elasticity s_{e1} may be determined from Eqs. (1) and (5) ($x = 0$):

$$p_{S\,max\,1} = s_{e1} \frac{s_1(2+s_1)}{\sqrt{3(1+s_1)^4(C_{in} - C_{1,2})^2 + \left[1 - 4v_1(1-v_1) \right]\left[C_{in} - C_{1,2}(1+s_1)^2 \right]^2}} \qquad (7)$$

Analogically the sum of internal and external pressure when maximum stress intensity in 2nd layer is equal to limit of elasticity s_{e2} may be determined from Eqs. (2) and (5) ($x = s_1 / s$):

$$p_{S\,max\,2} = s_{e2} \frac{s(2+s) - s_1(2+s_1)}{\sqrt{3(1+s)^4(C_{1,2} - C_{ex})^2 + \left[1 - 4v_2(1-v_2) \right]\left[C_{1,2}(1+s_1)^2 - C_{ex}(1+s)^2 \right]^2}} \qquad (8)$$

In this paper presented method for determination of stress strain state is valid when sum of internal and external pressure does not exceed maximum value $p_{\Sigma\,max}$, i.e. $p_\Sigma \leq p_{max}$:

$$p_{S\,max} = \min(p_{S\,max\,1}, p_{S\,max\,2}) \qquad (9)$$

Both two-layer pipe layers will have the equal strength when $p_{\Sigma\,max\,1} = p_{\Sigma\,max\,2}$. This condition can be satisfied by an appropriate selection of materials and wall thicknesses of 1st and 2nd layers.

It is common to use the Standard Dimension Ratio (SDR) as method of rating pressure piping. The SDR is ratio of the pipe external diameter and the thickness of the pipe wall: $SDR = 2\,r_{ex}/t$. Therefore ratios s and s_1, presented in this subchapter, can by expressed as:

$$s = \frac{2}{SDR - 2} \quad \text{and} \quad s_1 = \frac{2t_1/t_2}{(SDR - 2)(1 + t_1/t_2)}$$

3. Validation of the proposed method

There are compared two-layer pipes of two structures:

- M-H (mild – hard) – modulus of elasticity of internal layer material E_1 is less than this one of external layer ($E_1 < E_2$);
- H-M – modulus of elasticity of internal layer material is major than this one of external layer ($E_1 > E_2$).

Here and further stresses are presented as the ratio with the sum of internal and external pressures: $s_r' = s_r/p_\Sigma$, $s_q' = s_q/p_\Sigma$, $s_z' = s_z/p_\Sigma$ and $s_i' = s_i/p_\Sigma$.

Comparison of stress strain components obtained analytically and determined by FEA is presented in Figs. 2 and 3. The largest disagreement for stresses does not exceed 0.3% and for strains – 0.1%.
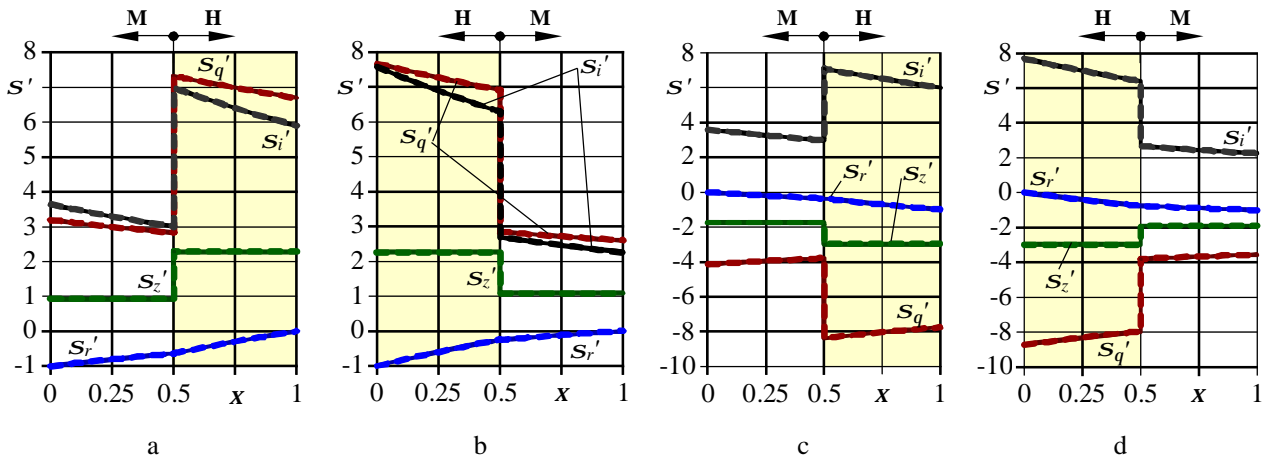
Fig. 2. Distribution of stresses s_i, s_q, s_r and s_z in the thickness of two-layer pipe wall determined analytically (——) and by FEA ($- - -$) when $s_1 = s_2 = 0.1$ (SDR12), $E_M/E_H = 0.4$, $v_M = 0.42$, $v_H = 0.34$ (where subscript M indicates mild material and subscript H – hard): a – structure M-H and $p_\Sigma = p_{in}$; b – structure H-M and $p_\Sigma = p_{in}$; c – structure M-H and $p_\Sigma = p_{ex}$; d – structure H-M and $p_\Sigma = p_{ex}$
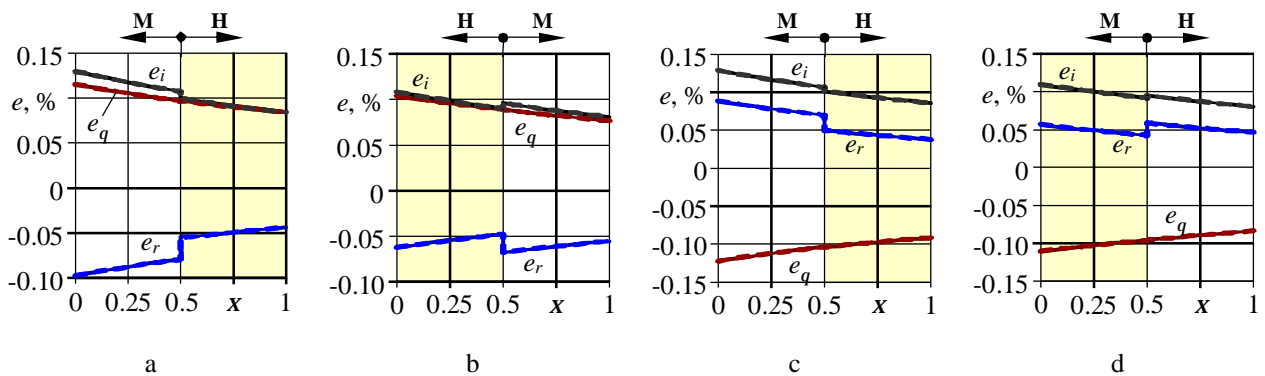
Fig. 3. Distribution of strains e_i, e_q and e_r in the thickness of two-layer pipe wall determined analytically (——) and by FEA ($- - -$) when $s_1 = s_2 = 0.1$ (SDR12), $E_M/E_H = 0.4$, $v_M = 0.42$, $v_H = 0.34$ (where subscript M indicates mild material and subscript H – hard): a – structure M-H and $p_\Sigma = p_{in}$; b – structure H-M and $p_\Sigma = p_{in}$; c – structure M-H and $p_\Sigma = p_{ex}$; d – structure H-M and $p_\Sigma = p_{ex}$

4. Analytical analysis

How maximum stress intensities depend on ratios E_1/E_2 and s_1/s_2 in separate layers is shown in Fig. 4. With increasing E_1/E_2 the $s_{i\,max\,1}$ increases but $s_{i\,max\,2}$ decreases. The maximum stress intensity $s_{i\,max\,1}$ in H-M structure ($E_1/E_2 > 1$) increases with decreasing 1st layer thickness and in M-H structure ($E_1/E_2 < 1$) increases negligible with

increasing 1st layer thickness. The maximum stress intensity $s_{i\,max\,2}$ when $E_1/E_2 > (\approx 0.7)$ negligible increases with increasing 2nd layer thickness and when $E_1/E_2 < (\approx 0.7)$ increases with decreasing 2nd layer thickness. Under external pressure maximum stress intensity in 1st layer $s_{i\,max\,1}$ is larger than under internal pressure when $E_1/E_2 > 1$ and in the 2nd layer when $E_1/E_2 < (\approx 0.7)$. Thus, the maximum stress intensity always appears in material with a major elastic modulus.

Dependency of $s_{i\,max}$ on E_1/E_2 and Poisson's ratio are shown in Figs. 5 and 6. Under internal pressure the Poisson's ratio significant influence on value of stress intensity $s_{i\,max\,1}$ has only for M-H structure at low value of E_1/E_2 ratio, i.e. $E_1/E_2 < 0.1$ (Fig. 5a). Under external pressure the Poisson's ratio affects value of stress intensity $s_{i\,max\,2}$ only
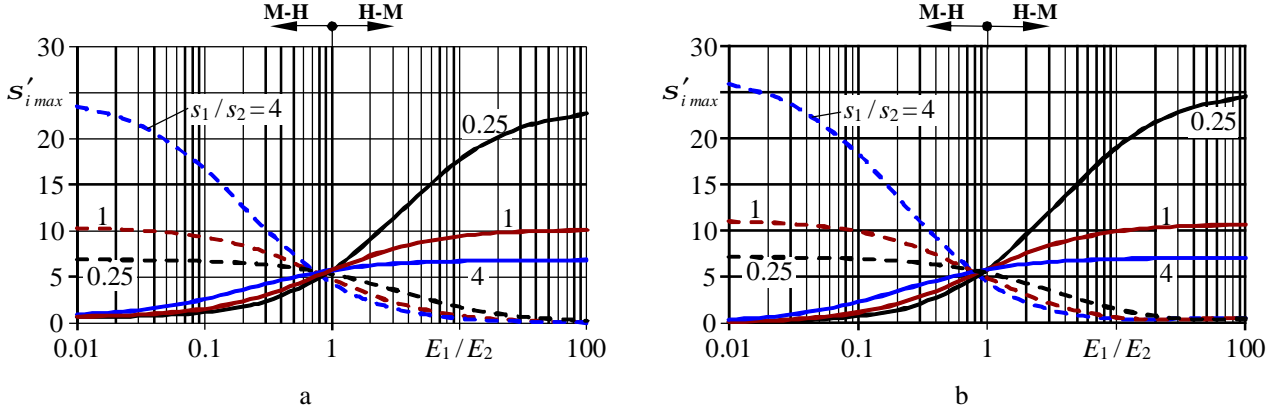
Fig. 4. Dependence of maximum stress intensities $s_{i\,max\,1}$ (——) and $s_{i\,max\,2}$ (– – –) on ratios E_1/E_2 and s_1/s_2 when $s = 0.2$ (SDR12), $v_1 = v_2 = 0.3$: a – under internal pressure ($p_\Sigma = p_{in}$); b – under external pressure ($p_\Sigma = p_{ex}$). Numbers near the curves indicate the value of the ratio s_1/s_2
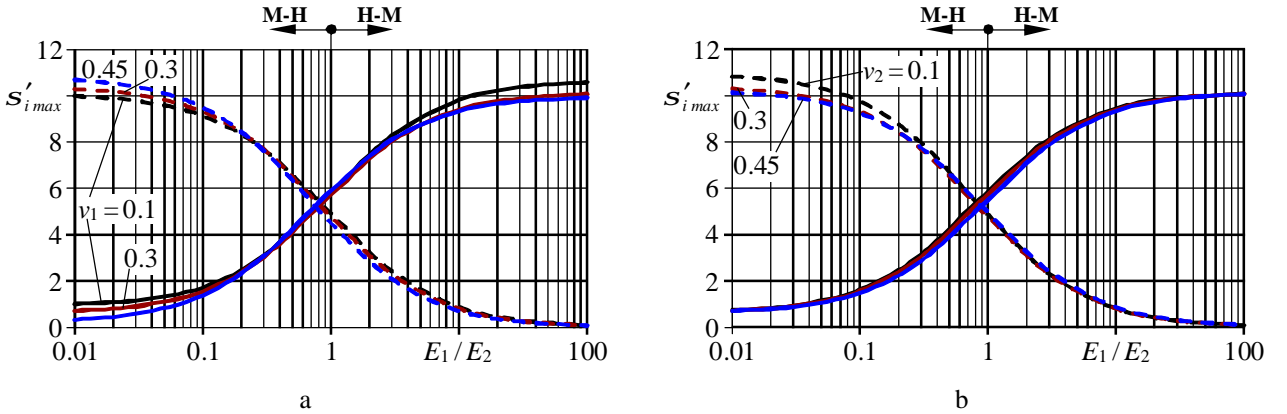
Fig. 5. Dependence of maximum stress intensities $s_{i\,max\,1}$ (——) and $s_{i\,max\,2}$ (– – –) on E_1/E_2 and Poisson's ratio under internal pressure ($p_\Sigma = p_{in}$) when $s = 0.2$ (SDR12), $s_1/s_2 = 1$: a – dependency on v_1 when $v_2 = 0.3$; b – dependency on v_2 when $v_1 = 0.3$. Numbers near the curves indicate the value of the Poisson's ratio v_1 or v_2
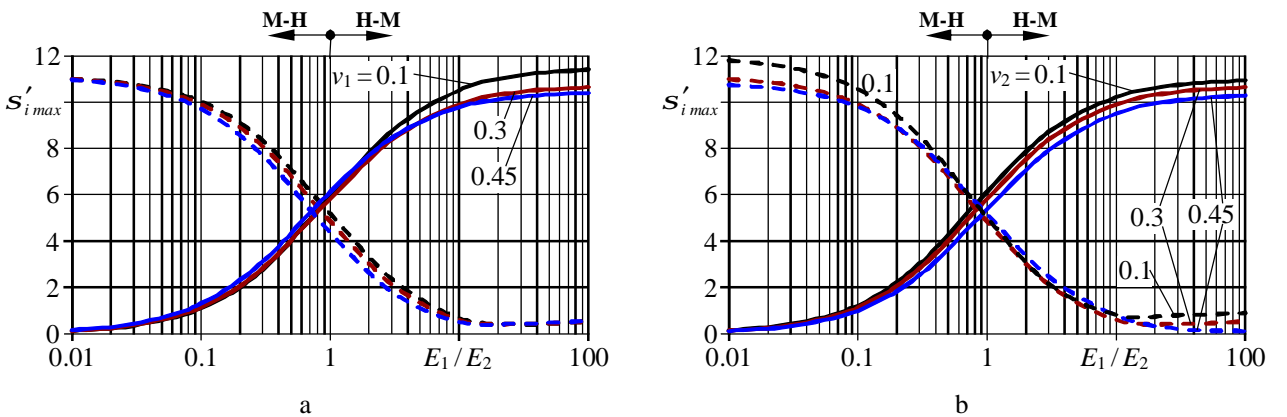
Fig. 6. Dependence of maximum stress intensities $s_{i\,max\,1}$ (——) and $s_{i\,max\,2}$ (– – –) on E_1/E_2 and Poisson's ratio under external pressure ($p_\Sigma = p_{ex}$) when $s = 0.2$ (SDR12), $s_1/s_2 = 1$: a – dependency on v_1 when $v_2 = 0.3$; b – dependency on v_2 when $v_1 = 0.3$. Numbers near the curves indicate the value of the Poisson's ratio v_1 or v_2
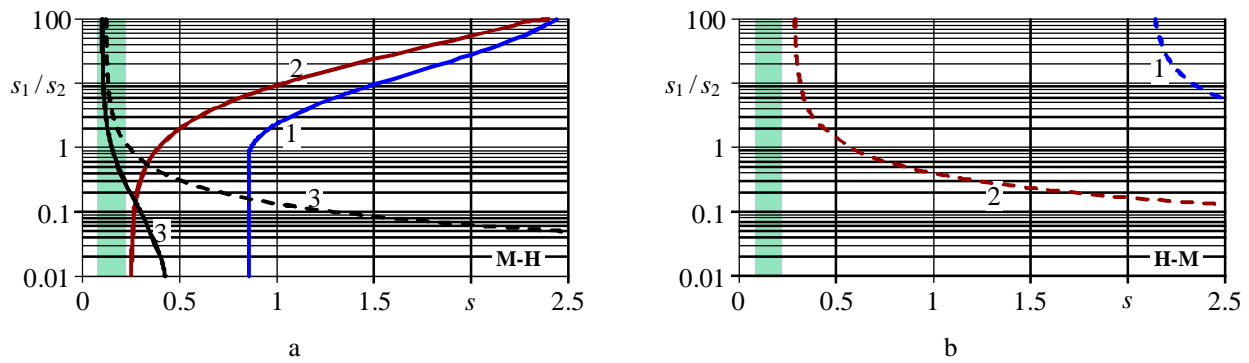
Fig. 7. Dependence of s_1/s_2 on s when both two-layer pipe layers have the same strength ($p_{\Sigma\,max\,1} = p_{\Sigma\,max\,2}$): a – M-H structure, 1 – PE-AL, 2 – PE-ST, 3 – AL-ST; b – H-M structure, 1 – AL-PE, 2 – ST-PE, 3 – ST-AL; (———) – $p_\Sigma = p_{in}$; (– – –) – $p_\Sigma = p_{ex}$; PE – polyethylene of raised temperature resistance ($E_{PE} = 0.65$ GPa; $\nu_{PE} = 0.42$; $s_{e\,PE} = 20$ MPa); AL – aluminum alloy ($E_{AL} = 69$ GPa; $\nu_{AL} = 0.34$; $s_{e\,AL} = 145$ MPa); ST – steel ($E_{ST} = 200$ GPa; $\nu_{ST} = 0.28$; $s_{e\,ST} = 340$ MPa). The vertical wide bar show range of real values of s

for the H-M structure at high value of E_1/E_2 ratio, i.e. $E_1/E_2 > 10$ (Fig. 6b). For other cases stress intensity changes negligible with changing Poisson's ratio (increase of the Poisson's ratio in 4.5 times leads to change of stress intensity in only 1.07-1.2 times).

Actually can be more than one pair of materials which have very similar E_1/E_2 and significantly different s_{e1}/s_{e2}. Therefore it is investigated how ratio s_1/s_2 depends on s when both pipe layers are made from specific materials and have the equal strength, i.e. is satisfied condition $p_{\Sigma\,max\,1} = p_{\Sigma\,max\,2}$ (see Fig. 7). Three pairs of materials were analyzed in this paper (PE – polyethylene of raised temperature resistance, AL – aluminum alloy and ST – steel). The higher accuracy of s required to maintain the condition $p_{\Sigma\,max\,1} = p_{\Sigma\,max\,2}$ then tangent of graphs, shown in Fig. 7, is closer to vertical. From analyzed materials only AL-ST structure of two-layer pipe can have equal strength when s is in the range of values which is using in practice.

5. Conclusions

The method for determination of stress strain state in two-layer pipe under plane strain condition is presented in this paper. By FEA it is proved that accuracy of this method is good. The analysis of stress state shown:
1. The most heavily loaded zones of two-layer pipe under internal or external pressure are in the internal surfaces of 1st or 2nd layer.
2. Stress intensity negligible depends on Poisson's ratio then $0.1 \le E_1/E_2 \le 10.0$.

Acknowledgements

References

1. **Bai Y., Xu F., Cheng P., Badaruddin M. F., Ashri M.** Burst Capacity of Reinforced Thermoplastic Pipe (RTP) Under Internal Pressure. ASME 30th International Conference on Ocean, Offshore and Arctic Engineering. Rotterdam, the Netherlands, June 19–24, 2011. Volume 4: Pipeline and Riser Technology, pp. 281-288.
2. **Gondle R., Siriwardane H.** Finite element modelling of long term performance of buried pipes. The 12th international conference "International Association for Computer Method and Advances in Geomechanics". Goa, India, 1-6 October, 2008, pp. 3993-4000.
3. **Liu M., Wang Y.-Y., Yu Z.** Response of Pipelines under Fault Crossing. Proceedings of the Eighteenth International Offshore and Polar Engineering Conference Vancouver, BC, Canada, July 6-11, 2008, pp. 162-165. Web source: < https://www2.lirmm.fr/lirmm/interne/BIBLI/CDROM/ROB/2008/ISOPE_2008/data/papers/I08TPC-682Liu.pdf >.
4. **di Prisco C., Galli A.** Soil-pipe interaction under monotonic and cyclic loads: experimental and numerical modelling. Proceedings of the First Euro Mediterranean Symposium in Advances on Geomaterials and Structures. Hammamet, Tunisia, 3-5 May 2006, pp. 755-761.
5. **Eraslan A. N., Akiş T.** Deformation Analysis of Elastic-Plastic Two Layer Tubes Subject to Pressure: an Analytical Approach. Turkish J. Eng. Env. Sci., 2004, pp. 261-268. Web source: < http://journals.tubitak.gov.tr/engineering/issues/muh-04-28-4/muh-28-4-5-0403-3.pdf >.
6. **Feodosjev V.** Strength of materials. – Vilnius: Mokslas, 1977. – 524 p. (in Lithuanian).

Proceedings of 8th International Conference ITELMS'2013

Analysis and Testing of Liquid Loaded CMUT Oscillator

G. Vanagas, D. Barauskas, D. Viržonis

Kaunas University of Technology Panevėžys Institute, dept. of Electric Engineering.Daukanto12, 35212, Panevėžys, Lithuania, E-mail: gailius.vanagas@ktu.lt

Abstract

In this work we were aiming to overcome the limitations of the resonant sensing with capacitive micromachined ultrasound transducers (CMUT) in liquid loaded conditions. We developed the CMUT-resonated oscillator circuit with the loopback amplifier, which is capable to maintain stable oscillations, when CMUT is loaded by the liquid. We demonstrated the real-time record of the liquid loading by dropping a 10 µL drop of two different liquids on the surface of CMUT and recording the oscillator output frequency in the real time. Since immersion to the different liquids gave different peak shifts of the oscillator output frequency (205 kHz for oil, 166 kHz for isopropanol), we claim this setup to be sensitive to the liquid properties. The relationship of the oscillator output frequency to the CMUT resonance frequency was found to be non-linear and stability of the oscillator operation was achieved at the price of decreased sensitivity.

KEY WORDS: *MEMS, resonant sensing, CMUT, oscillator.*

1. Introduction

Microfabricated resonant chemical and biochemical sensors [1-6] are advantageous over other resonance sensing techniques, such as quartz crystal microbalance (QCM), because of great potential to reduce the sensor dimensions and integrate the sensitive element(s) with other sensor components, such as readout electronics and/or microfluidic devices [1, 5]. Capacitive micromachined ultrasound transducers (CMUT) were demonstrated as resonant chemical sensors of the gaseous species [2], sensors of the fluid mass density and viscosity [4] and as sensors of specific interaction of proteins [6]. The liquid environment, which is the case in microfluidic applications, introduces significant energy losses of the motion of CMUT membrane cells [5, 7].Therefore their sensitivity for added mass loading in liquids is much lower than in gaseous medium due the lower resonance quality factor. Moreover, CMUT overdamping can be the cause of stopping the oscillator circuit used for resonance frequency measurement. In this work we aimed to develop the oscillator, which would be exhibiting stable operation in significant energy loss conditions.

2. Sensoric informativity of membrane damping and resonance frequency shift

CMUT sensor is built of an array of electrostatically actuated cells, which have the structure shown in Fig. 1 as a cross-section.
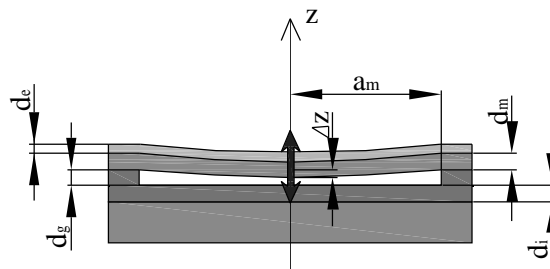
Fig. 1. Cross-sectional sketch of the single CMUT membrane cell with critical dimensions shown

Kinetic and potential energies of the membrane cell can be expressed by following equations:

$$W_k = \frac{1}{2} m \left(\frac{dz}{dt} \right)^2 \tag{1}$$

$$W_p = \frac{1}{2} k_s z^2 \tag{2}$$

where: z is the independent coordinate of the membrane displacement (Fig. 1); m stands for the moving mass of the membrane, which is determined by the membrane material, dimensions and shape; k_s is equivalent spring constant of the membrane. For circular, perimeter-fixed membrane with the radius a_m, the spring constant can be calculated as follows [8]:

$$k_s = \frac{64 p\, D}{a_m^2} \tag{3}$$

where $D = \dfrac{E\, d_m^3}{12\left(1 - n^2\right)}$.

CMUT membrane motion is damped by the surrounding medium and internal losses. The damping of the mechanical resonator can be described by the Rayleigh function:

$$H_s = \frac{1}{2} b_v \left(\frac{dz}{dt}\right)^2 \tag{4}$$

Here b_v is the damping coefficient. We can find the energy loss caused by the damping:

$$dW_s = -F_s\, v_m\, dt = -b_v\, v_m^2\, dt = -b_v \left(\frac{dz}{dt}\right)^2 dt = -2 H_s\, dt \tag{5}$$

which means that damping energy change rate $\dfrac{dW_s}{dt} = -2 H_s$. The F_s in (5) stands for the damping force and v_m is the speed of the membrane displacement. Kinetic and potencial energies and Rayleigh function H_s can be interrelated by the Lagrange equation:

$$\frac{d}{dt}\left(\frac{\partial W_k}{\partial \dot{z}}\right) - \frac{\partial W_k}{\partial z} + \frac{\partial H_s}{\partial \dot{z}} + \frac{\partial W_p}{\partial z} = F_\Sigma(z, t) \tag{6}$$

where: $F_\Sigma(z, t) = F_E(z, t) + F_l(z, t)$ is the net force acting over the membrane with the electrostatic component $F_E(z, t) = -\dfrac{\partial W_E}{\partial z} = \dfrac{U^2\, e_0\, A_e}{2\left(d_g - \Delta z\right)^2}$ (U is the voltage accross the CMUT electrodes, A_e is the effective area of the electrodes, ε_0 is the vacuum dielectric constant); $F_l(z, t)$ is the net sum of the rest of the forces acting over the membrane. Assuming $\dfrac{\partial W_k}{\partial z} = 0$, we can derive from (6) the differential equation describing the dynamics of the CMUT membrane as a mass-spring-damper system:

$$m \frac{d^2 z}{dt^2} + b_v \frac{dz}{dt} + k_s\, z = F(z, t) \tag{7}$$

If membrane is loaded by additional mass, $m = m_m + m_a$, where m_m is the moving mass of the membrane, and m_a is the additional mass. If membrane is immersed in a liquid, membrane loading by the equivalent mass with approximate value of $m_a = 0.25\, r\, p\, a_m^3$ can be assumed [9], where ρ_v is the mass density of the liquid. In sensoric applications, m_a can be attributed to the mass of adsorbed species. The most common parameter of the CMUT sensor is the resonance frequency, which depends on the additional mass. The self-resonance of the membrane loaded by the additional mass at zero-loss conditions is described as follows:

$$w = \sqrt{\frac{k s}{m_m + m_a}} \tag{8}$$

However, this equation does not take in to account the influence of the electrostatic force, which acts over the membrane during operation. If we estimate only the static case, electrostatic force acting over the membrane can be found by the following equation:

$$F_a(\Delta z) = \frac{U^2\, e_0\, A_e}{2\left(d_g - \Delta z\right)^2} - k_s\, \Delta z = \frac{U\, n}{2} - k_s\, \Delta z \tag{9}$$

Here n is electric to mechanical energy conversion coefficient:

$$n = \frac{e_0 \, U \, A_e}{\left(d_g - \Delta z\right)^2} \tag{10}$$

Now we can estimate the well known "spring softening" effect, which causes the effective membrane spring constant to be less than equation (3) says:

$$k_{seff} = \frac{\partial F_a(\Delta z)}{\partial \Delta z} = k_s - \frac{U^2 \, e_0 \, A_e}{\left(d_g - \Delta z\right)^3} = k_s - k_e \tag{11}$$

This will in turn decrease the resonance frequency, according to (8).

Next informative parameter of sensoric CMUT is damping coefficient (b_v, second term in (7) equation), which can be used for estimation of the energy dissipation due the viscoelastic interaction of the membrane with the added species. The net membrane damping b_v can be decomposed to the internal loss component b_{vs} and external dissipative component b_{va}:

$$b_v = b_{vs} + b_{va} \tag{12}$$

Energy dissipation to the external medium is a function of many parameters of said medium, like mass density, speed of sound and viscoelastic parameters [11]:

$$b_{va} = \frac{A_m^2}{A_v} \sqrt{r \left[\frac{1}{x_s} + j w \left(2 h_2 + h_1\right)\right]} \tag{13}$$

where: A_m is the moving (active) area of the membrane; A_v is the entire membrane area; ρ is the mass density of the medium; ξ_s is adiabatic compressibility; c_s is sound velocity in the fluid; η_1 and η_2 are first and second coefficients of viscosity respectively. If species with pronounced viscoelastic properties will be adsorbed on the membrane's surface, internal loss coefficient b_{vs} will change similarily as described by the equation (13) with only difference that A_m is to be accounted for the actual area coated with adsorbed species. Therefore, identification and measurement of external dissipative coefficient b_{va} will lead to the estimation of the mass density and viscoelastic properties of the medium in which transducer is operating. Finding the coefficient of internal losses will give the estimation of the mass density and viscoelastic properties of the species adsorbed on the membrane. In many cases, when CMUT is operated in fluids, $b_{vs} \ll b_{va}$, therefore identification and measurement of b_{vs} is challenging. In practical measurements, frequency spectra of electromechanical impedance of CMUT can be obtained by network analyzer or echo impulse can be converted to the frequency domain by the Fourier transform [7]. The quality factor of the resonance or central frequency peak $Q = \frac{f_0}{\Delta f}$ can be used as the loss measure (Δf is the width of the resonance peak at -3 dB), because it can also be related to the damping coefficient b_v [10]:

$$Q = 2 p \, f_0 \frac{m_m}{b_v} \tag{14}$$

Here m_m is the moving mass of a membrane, which can be modified by the added mass of adsorbed species and/or equivalent mass loading of the medium. If CMUT is not loaded, i.e. is operating in vacuum or in other low-density medium, it will exhibit high Q values. If it is damped by the liquid, the central frequency peak will have the quality usually equal or less than 1 [7]. To clarify if low Q CMUT operation can still be tracked by the oscillator circuit we performed the experimental research with the custom-designed oscillator.

3. Experimental methods and devices

Agilent 4395A spectrum/impedance analyser with integrated 40 V voltage supply was used to record the frequency response of CMUT. The circuit diagram of the experimental oscillator is shown in Fig. 2. Oscillator design is based on modified Butler type circuit (operated by VT2) with the loopback amplifier (VT1). This kind of the oscillator circuit has great potential to work with low Q resonator, since it has greater self-generation sensitivity than cirquits used by Lee et. al. [2].
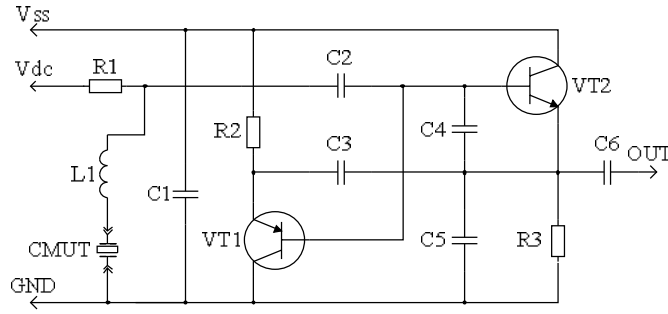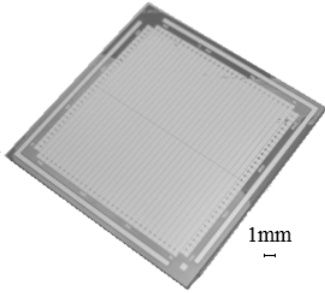
Fig. 2. Oscillator circuit with the loopback amplifier

By adjusting the R2 value one can balance the circuit to operate both transistors in linear regime. Also, C3 can be used to adjust the sensitivity of the loopback gain. We were unable to achieve both stable oscillations and linear operation of the transistors during our experiments, because we had to increase the loopback gain by increasing the value of C3 10 times above the value, which still maintains the linear operation point. Additionally we introduced the adjustable coil (L1 = 6.84 in our case), which was used to fine-match the oscillator's operating frequency with CMUT central frequency.

Digital dual-input oscilloscope Fluke 199C was used to record the oscillator output. The frequency value was calculated by using built-in fast Fourier transform operator. In our experiments we used the single 0.5×8 mm element form the linear CMUT array, which main parameters are presented in the Table 1.

Table 1

Dimensions of cmut cell

Parameter	Notation	Value
Membrane form		Square
Membrane side lengh	$2 \cdot a_m$	38 µm
Dimensions of the element		500×8000 µm
Number of membranes in transducer element		1600
Thickness of membrane	d_m	1.0 µm
Vacuum gap	d_g	0.15 µm
Dielectric layer	d_i	0.35 µm
Electrode side lengh	a_e	$a_e = a_m$
Electrode thickness	d_e	0.3 µm
Electrode material	Au	$E = 75$ GPa, $\rho = 19300$ kg/m^3, $v = 0.42$
Membrane material	Si	$E = 148$ GPa, $\rho = 2329$ kg/m^3, $v = 0.18$
Material of dielectric layer	SiO$_2$	$e_i' = 3.7$
Collapsevoltage		67V
CMUT overall image		

4. Harmonic analysis by finite element method

To estimate the harmonic behavior of liquid damped CMUT and to determine the potential sensitivity of sensoric CMUT operation we developed the finite element model, which is schematically shown in Fig. 3. Finite element analysis package ANSYS (Canonsburg, PA) was used. Membrane was divided by 2D PLANE42 elements and the vacuum gap – by TRANS126 elements. Voltage was applied to the bottom of the membrane, which was perimeter fixed. Constant pressure and bias voltage were applied as the initial conditions. Surrounding medium was simulated as the half-sphere divided by 2D FLUID29 elements. The same elements with non-reflective ("infinite") medium boundry properties were applied at the edge of the half-sphere. Structural and acoustic medium was interfaced with the fluid – structure interface. Structural damping was adjusted to meet the experimental Q value of 100.
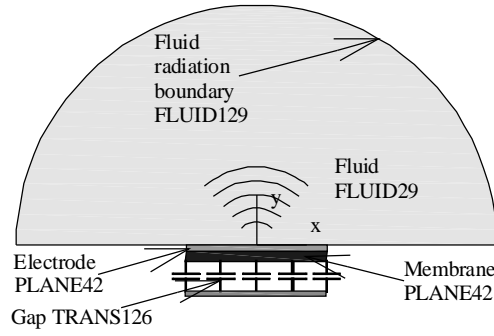
Fig. 3. Structure of finite element model

Electromechanical impedance of a CMUT cell was calculated after the harmonic analysis was done. Equivalent displacement of the membrane available from the finite element modeling

$$\Delta z_{eff} = \frac{1}{a_m} \int_0^{a_m} \Delta z(a_m)\, da_m \tag{14}$$

was converted to the electrical part of the impedance according to the equation

$$Z_m = j\frac{1}{wC} = \frac{\mathrm{Im}\,\Delta z_{eff}}{w\,e_0\,A_m} + j\frac{d_g - \mathrm{Re}\,\Delta z_{eff}}{w\,e_0\,A_m} \tag{15}$$

5. Simulation results

Design data of CMUT cell presented in Table 1 was used for simulation. Simulated fundamental resonance mode as a function of the cell dimensions and the sensitivity of the fundamental mode of corresponding membrane size to the added mass are shown in Fig. 4. Analytical results obtained by the equations (7) to (11) are presented for comparison. It was assumed that bias voltage of 0.8 U_{coll} was applied. It was also assumed that added mass (10^{-21} kg/μm^2) do not build any extra film on the membrane's surface (i.e. do not change the elasticity modulus) nor introduce any additional losses. Some difference between FEM and analytical results come from non-linearities, which are not estimated in analytical calculations. It can be seen that larger membranes exhibit more sensitivity to the added mass, however their fundamental frequency is lower and the absolute frequency shift value is smaller. We also found from this simulation the linear relationship between the membrane loading and fundamental resonance frequency of the CMUT cell. Fundamental frequency shift due to the added mass is practically insensitive to the bias voltage.
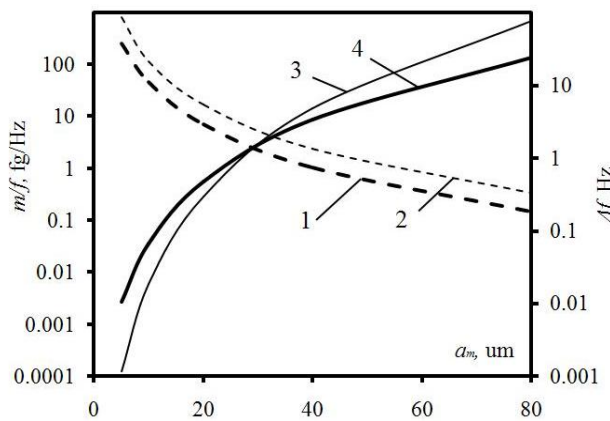
Fig. 4. Simulated relationships of the fundamental resonance mode to the membrane dimensions and corresponding sensitivity of said mode to the added mass of 10^{-21} kg/μm^2: 1 – frequency shift (FEM); 2 – frequency shift (analytical); 3 – sensitivity (analytical); 4 – sensitivity (FEM)

6. Experimental results

Output of the oscillator circuit with different bias voltages applied to CMUT is shown in Fig. 5a. This experiment was carried to find out how the oscillator circuit follows the changes of the resonator frequency. The

resonator (CMUT) was operated in the air in this case. Partially non-linear operation of the circuit is obvious; however it was not possible to balance it for fully linear operation over the whole extent of the experimental conditions. Particularly it was not possible to prevent it from stopping to oscillate when CMUT was immersed in the liquid. Meanwhile, non-linearly tuned circuit exhibited stable operation in immersion. It can be observed that the period of the oscillations increase when the CMUT bias voltage (V_{dc}, according to Fig. 2) is increased. This is normal manifestation of the "spring softening" effect (see Eq. (11)).

Relationship of the CMUT air resonance frequency to bias voltage was also measured by the network analyzer and measured values were compared to the corresponding output frequency of the oscillator (Fig. 5 b). It can be noted that oscillator output frequency is nearly linear in respect of the bias voltage while CMUT resonance frequency is highly non-linear function of the bias voltage. However the linearization is achieved at the price of decreased sensitivity of the frequency output to the resonator (CMUT in this case) resonance frequency change.
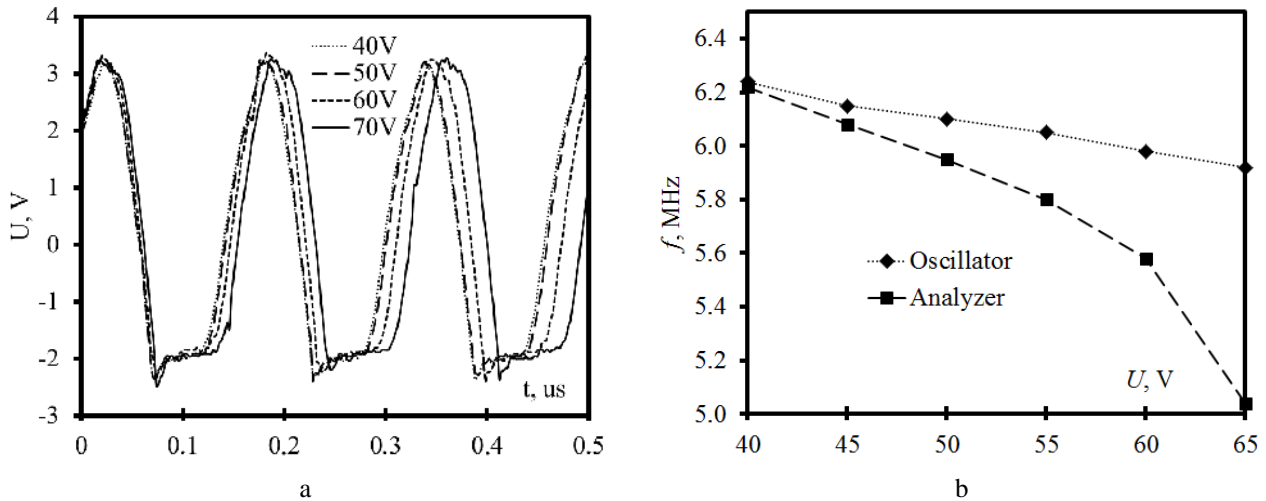
Fig. 5. Frequency relationship to the bias voltage: a – oscillator output in the case of CMUT resonating in air with DC bias range from 40 to 70 V; b – frequency to voltage relationships measured as oscillator output and as CMUT air resonance frequency measured by the network analyzer

We also tested the operation of the oscillator when CMUT is operated in damped conditions, i.e. is immersed in the liquid. Thin gray line in the Fig. 6 shows the real-time plot of the recorded oscillator output data when 10 µL drop of the transformer oil (Neste TRAFO 10X, 895 kg/m³ mass density) was dropped on the CMUT surface by the manual pipette. CMUT was operated with 50 V bias. The oscillator output frequency value suddenly dropped by 200 – 210 kHz (205 kHz average over 5 experiments) after applying the oil (extra mass and damping) with following slow recovery, which corresponds to the gravity-driven spreading of the oil spot to the neighbour structures of the CMUT element and decrease of the oil mass remaining on the sensitive surface. The same experiment was repeated with the 10 µL of the
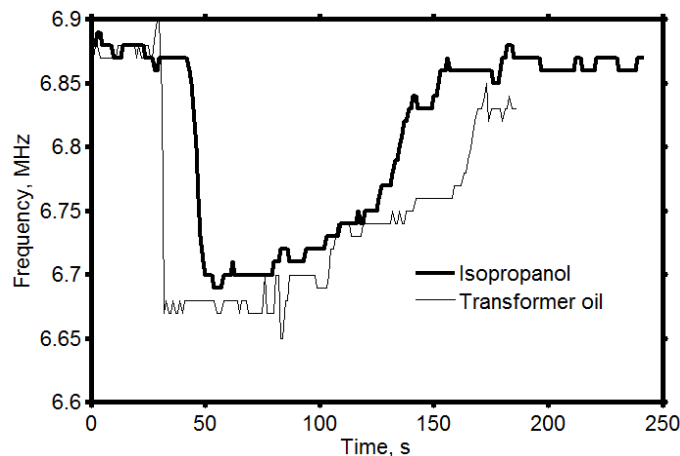
Fig. 6. Real-time plot of the oscillator output frequency during the drop loading experiment

isopropanol (786 kg/ m³ mass density). Thick black line in Fig. 5 shows sensor loading dynamics: after initial drop by 166 kHz (average over 5 experiments) the frequency recovers back to the initial value, since in this case not only spreading of the liquid spot, but also comparatively rapid evaporation decreases the mass of the liquid over the sensor

surface. Here we also emphasize that frequency change due the oil loading is greater than in the case of isopropanol loading, which can be explained by different mass densities of both liquids (isopropanol is lighther than oil).

7. Conclusions

We have demonstrated the operation of oscillator circuit with the loopback amplifier, which uses CMUT as electromechanical resonator. It was also shown that this setup is useful for mass sensing application even if the resonator is damped by the liquid. However, this is possible only when the oscillator circuit is not tuned to work in the linear regime. The oscillator exhibits the linear response to the CMUT bias voltage change, which also means that there is no linear relationship between the resonance frequency of CMUT structure and the output of the oscillator.

We demonstrated the dynamics of the mass loading by two different liquids: transformer oil and isopropanol. Different frequency shifts (205 and 166 kHz, correspondingly) were measured in both cases. This allows claiming this resonator-oscillator setup to be suitable to work as a sensor of the liquid properties, because larger frequency shift can be associated with the loading by the liquid with greater mass density.

Credits

References

1. **Johnston M. L., Kymissis I., Shepard K. L.** FBAR-CMOS Oscillator Array for Mass-Sensing Applications. IEEE Sensors Journal, vol. 10, No. 6, pp 1042 – 1047, June 2010.
2. **Lee H. J., Park K. K., Krupnik M., Oralkan O., Khuri-Yakub B. T.** Chemical Vapor Detection Using a Capacitive Micromachined Ultrasonic Transducer", Anal. Chem., vol. 83 (24), pp. 9314-9320, 2011.
3. **Ismail A. K., Burdess J. S., Harris A. J., McNeil C. J., Hedley J., Chang S. C.** and **Suarez G.** The principle of a MEMS circular diaphragm mass sensor. J. Micromech. Microeng. 16 (2006) 1487–1493.
4. **Thranhardt M., Eccardt P. -C., Mooshofer H., Hauptmann P., Degertekin L.** A resonant CMUT sensor for fluid applications. Sensors, 2009 IEEE , vol., no., pp.878,883, 25-28 Oct. 2009.
5. **Virzonis D., Vanagas G., Kodzius R.** Integration of Capacitive Micromachined Ultrasound Transducers to Microfluidic Devices. In: Microfluidics: Control, Manipulation and Behavioral Applications. Ed. by Stefano Panzarella and Walter Maroni, pp 127 - 150. Nova Publishers, New York 2013.
6. **Ramanavičiene A., Viržonis D., Vanagas G., Ramanavičius A.** Capacitive micromachined ultrasound transducer (CMUT) for immunosensor design, Analyst, vol.135, pp. 1531–1534, 2010.
7. **Vanagas G., Mikolajūnas M., Grigaliūnas V., Viržonis D.** Finite-element analysis of microelectromechanical membranes vibration // Materials science = Medžiagotyra. 2009, Vol. 15, no. 4, p. 296-301.
8. **Bao M.** Analysis and Design Principles of MEMS Devices. Elsevier B.V., 312p., 2005.
9. **Senlik M. N., Atalar A., Koymen H., Olcum S.** Radiation Impedance and Equivalent Circuit for Immersed CMUT Array Element. IEEE Ultrason. Symp., pp. 1951–1954, 2006.
10. **Lohfink A., Eccardt P. C.** Linear and Nonlinear Equivalent Circuit Modeling of CMUTs, Ultrasonics, Ferroelectrics and Frequency Control, IEEE Transactions, vol. 52, no. 12, 2005.
11. **Antlinger H., Clara S., Beigelbeck R., Cerimovic S., Keplinger F., Jakoby B.** Sensing the characteristic acoustic impedance of a fluid utilizing acoustic pressure waves. Sensors and Actuators, A 186, pp. 94 – 99, 2012.

Anti-lock Braking System (ABS) Performance Study

K. Videikis*, L. Pelenytė-Vyšniauskienė**

Kaunas University of Technology, Panevėžys Institute, Klaipėdos g. 1, LT-35209 Panevėžys, Lithuania, E-mail: kestutis.videikis@gmail.com
**Kaunas University of Technology, Panevėžys Institute, Klaipėdos g. 1, LT-35209 Panevėžys, Lithuania, E-mail: linapelenyte@gmail.com*

Abstract

The article deals with passenger car automatic braking system (ABS) performance – stopping distances at different speeds, road surface, and turning off ABS. In the scientific literature, and different sources of information, opinions supporting the effectiveness of ABS – some passenger car experts say that the ABS shortens the braking distance, others argue the contrary, that lengthens.

In-kind test method tested passenger cars ABS operation efficiency. The sample of urban driving speeds (20 km/h, 35 km/h, 40 km/h). Presented cars with ABS and without ABS braking results and conclusions.

KEY WORDS: *Anti-lock braking system, Automatic Braking System (ABS), automatic ANTI- braking system, braking distance, ABS efficiency.*

1. Introduction

Anti-Block braking system (ABS) was created in 1978, but in practice started to use cars for approximately 10 years. This system helps to optimize stop the car on any road surface. Depending on the type of road surface and tire wear on each wheel grip on road surfaces is different.

The basic idea of ABS is to prevent the wheels to stop completely during sudden braking. If that happens, the control over vehicle is lost and it can skid in an undesirable direction. ABS does not allow the wheels to be stiffened and thus enables the driver to operate the vehicle normally, although the brake pedal is pressed to the end [3].

ABS function is as follows - during braking to prevent the blocking of the wheels, the brake force distribution between the wheels according to their adhesion to the supporting surface area. In result – optimum braking performance. ABS systems advantages:

- improves braking performance;
- improves vehicle stability and steer ability during braking;
- gentle stop without jerking;
- increases opportunities to design higher-speed vehicles;
- longer pavement life [1].

ABS are now standard in most cars model equipment. Auto ABS system prevents the brakes completely lock up during heavy braking, the car remains more manageable, and the driver has a better chance to avoid the obstacle. ABS brake system also reduces the braking distance and improves driving safety [2].

The analysis of literature of notable scientists, specialists, researchers and so on shows disagreement: ABS reduces braking distances or increases? Study object is to research car braking distance with ABS and without ABS.

Fig.1. With ABS the car easier to control

2. ABS performance examination

When analyzing of similar studies and experiments, it is important to note that a technologies evolving from simple ABS operation, to learning ABS, which analyzes the results of the breaking analyzes and accordingly to the data improves ABS performance efficiency. However, it was not observed that it would be investigated at least one same vehicle in one case with ABS, otherwise – technologically disconnecting ABS unit.

The study carried out in a sudden-emergency braking experiment collecting stopping distance and acceleration-deceleration of the accelerometer data. Choose speeds, which are often driven in the city (20 km/h, 35 km/h and 40 km/h). The study was conducted in 1ha aerodromes area. Before running the car accelerometer is activated. Well into continuing to speed, driving up the starting flag and the brake pedal is pressed as quickly and strongly. Measure the stopping distance. Preserves the accelerometer data. Detachable ABS facility and the test repeated. The research was done at different road surfaces: asphalt dry, asphalt wet, snow-covered asphalt.

The experimental study has been used:
- acceleration, deceleration gauge "AccDrive109;
- braking distance measuring equipment.

Table 1

Test car

VW GOLF V	
ABS	on/off
Year	2005
Engine capacity (in liters)	1.4
Fuel	Gasoline
Power (kW)	55
Unloaded weight (kg)	1264
Tires identical	M+S
Tire tread depth (mm)	3
Body	Hatchback
Drive wheels	Front
Brakes	Disc

3. The results of the study

The study provided 18-braking test results: the stopping distance under typical conditions with ABS and without ABS, rating ABS or without ABS broke effectively, accelerometer data, accelerometer table for each braking test. Accelerometer tables show the x-axis time in seconds (s) and y-axis acceleration change (m/s^2).

3.1. Road surface – dry asphalt

The first test is carried out when the car is running dry roads, 20 km/h. The test results are seen in Fig. 2 and 3. We see that:
- in the case without ABS stopping distance – 1.45 m; seceleration: max. – 12.42 m/s^2, average – 7 m/s^2;
- with ABS stopping distance – 1.35 m, deceleration: max. – 15.56 m/s^2, average – 8 m/s^2.

We can see that with ABS braking is more effective. The deceleration of the brake test confirms that the data is correct. Test data from asphalt surface coating also present in Fig. 20.
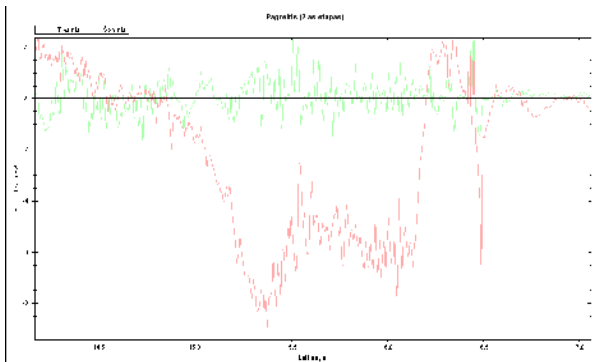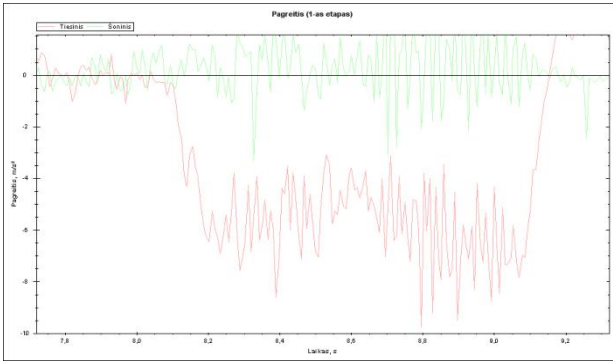

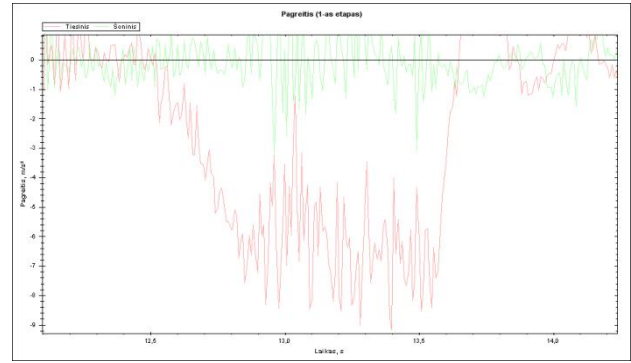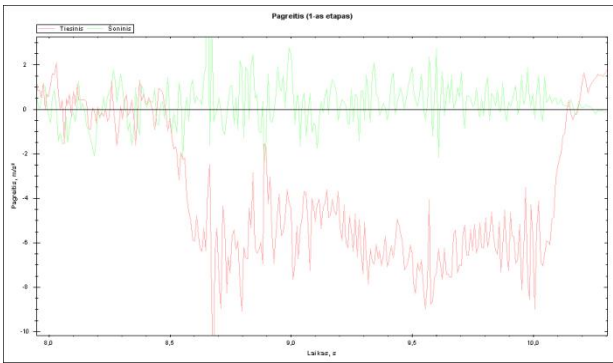Fig.2. Car without ABS speed before braking – 20 km/h   Fig.3. Car with ABS speed before braking – 20 km/h
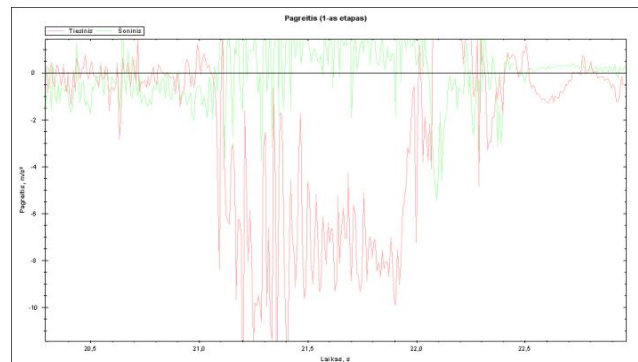
The second test is carried out when the car is running dry roads, 35 km/h. The test results are seen in Fig. 4 and 5:

- without ABS stopping distance – 5,2 m, deceleration: max. – 9.3 m/s², average – 7 m/s²;
- with ABS stopping distance – 4,7m, deceleration: max. – 11.2 m/s², average – 7 m/s².

We can see that with ABS braking is more effective. The deceleration of the brake test confirms that the data is correct. Test data from asphalt surface coating also present in Fig. 20.
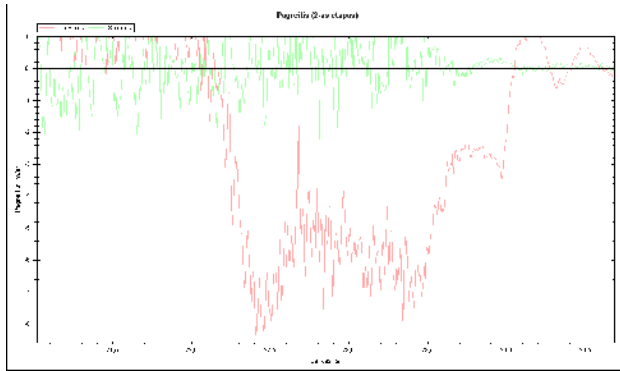
Fig.4. Car without ABS speed before braking – 35 km/h
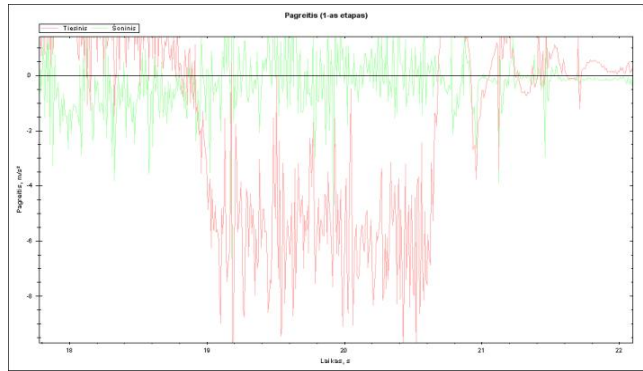
Fig.5. Car without ABS speed before braking – 35 km/h

The third test is carried out when the car is running dry roads, 40 km/h. The test results are seen in Fig. 6 and 7:
- without ABS stopping distance – 10 m, deceleration: max. – 9.32 m/s², average – 6 m/s²;
- with ABS stopping distance – 8,7m, deceleration: max. – 14.79 m/s², average – 7 m/s².

We can see that with ABS braking is more effective. The deceleration of the brake test confirms that the data is correct. Test data from asphalt surface coating also present in Fig. 20.
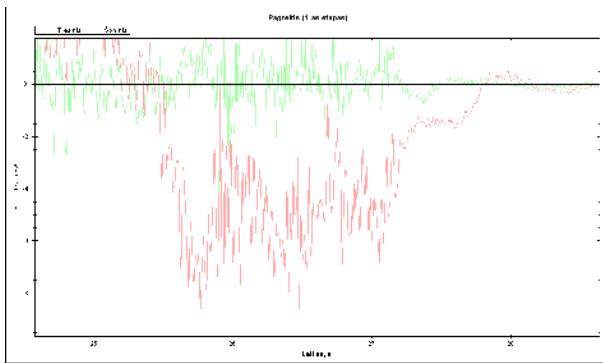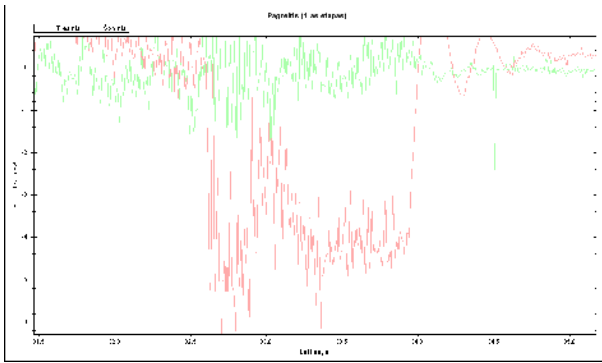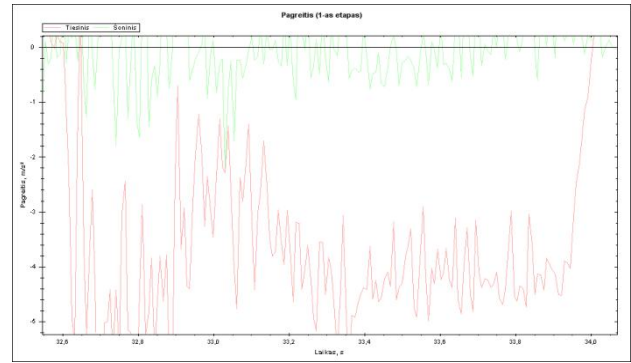

Fig.6. Car without ABS speed before braking – 40 km/h
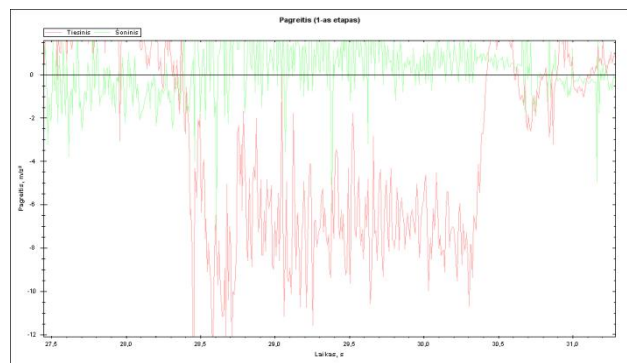
Fig.7. Car without ABS speed before braking – 40 km/h

3.2. Road surface - wet asphalt

The fourth test is carried out when the car is running wet asphalt roads, 20 km/h. The test results are seen in Fig. 8 and 9:
- without ABS stopping distance – 2.6 m, deceleration: max. – 9.77 m/s², average – 6 m/s²;
- with ABS stopping distance – 2.8m, deceleration: max. – 9.21 m/s², average – 6 m/s².

We can see that with ABS braking is worse. The deceleration of the brake test confirms that the data is correct. Test data from asphalt surface coating also present in Fig. 21.

The fifth test is carried out when the car is running wet asphalt roads, 35 km/h. The test results are seen in Fig. 10 and 11:
- without ABS stopping distance – 5.3 m, deceleration: max. – 12.05 m/s², average – 6 m/s².
- with ABS stopping distance – 4.9 m, deceleration: max. – 12.47 m/s², average – 7 m/s².

We can see that with ABS braking is more effective. The deceleration of the brake test confirms that the data is correct. Test data from asphalt surface coating also present in Fig. 21.

The sixth test is carried out when the car is running wet asphalt roads, 40km / h. The test results are seen in Fig. 12 and 13:
- without ABS stopping distance – 15.4 m, deceleration: max. – 8.92 m/s², average – 6 m/s²;
- with ABS stopping distance – 13 m, deceleration: max. – 12.55 m/s², average – 7 m/s².

We can see that with ABS braking is more effective. The deceleration of the brake test confirms that the data is correct. Test data from asphalt surface coating also present in Fig. 21.

Fig.8. Car without ABS speed before braking – 20 km/h

Fig.9. Car without ABS speed before braking – 20 km/h

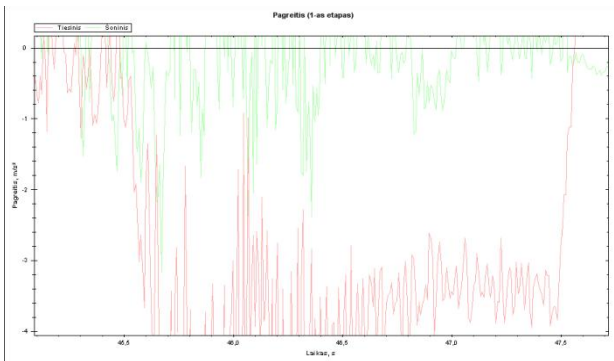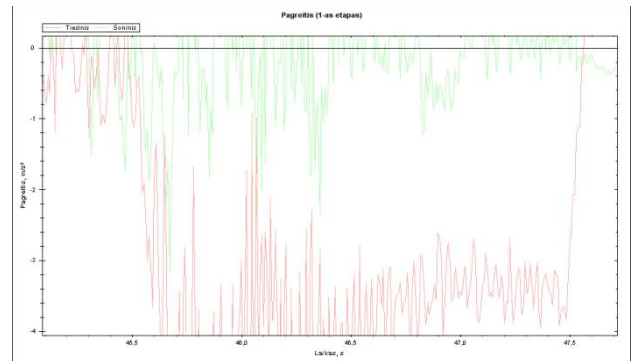Fig.10. Car without ABS speed before braking – 35 km/h
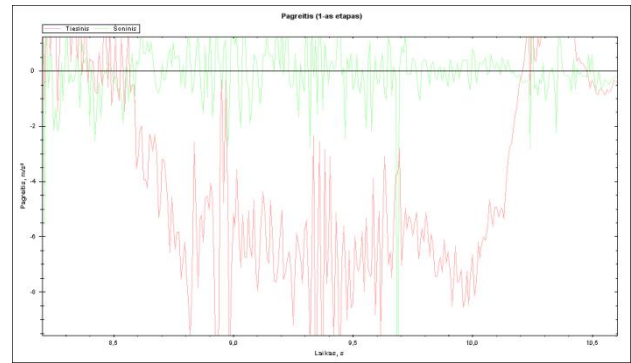
Fig.11. Car without ABS speed before braking – 35 km/h
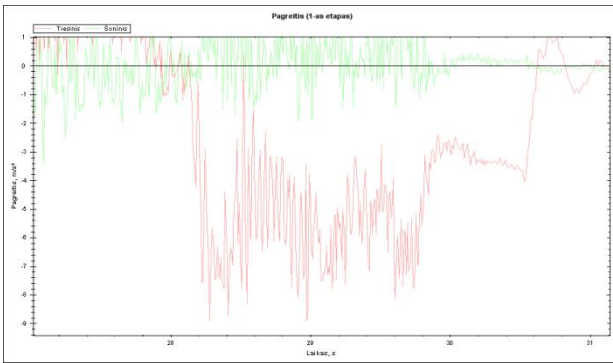
Fig. 12. Car without ABS speed before braking – 40 km/h
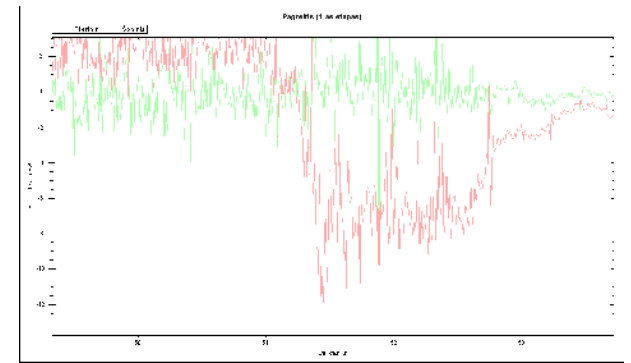
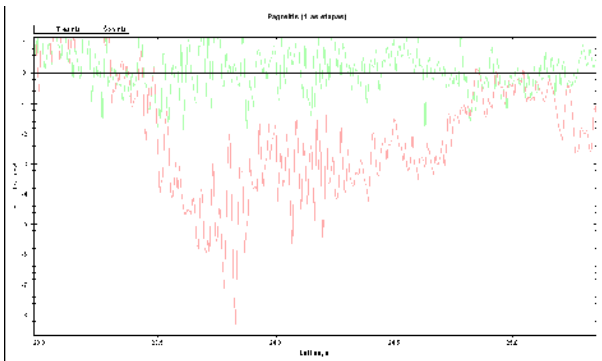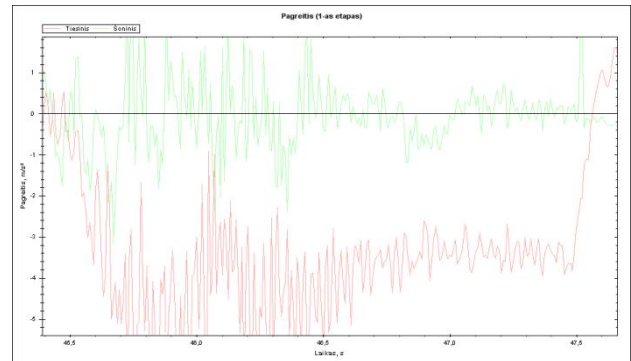Fig. 13. Car without ABS speed before braking – 40 km/h

3.3. Road surface - snow-covered asphalt

The seventh test is carried out when the car is running snow-covered roads, 20 km/h. The test results are seen in Fig. 14 and 15:
- without ABS sopping distance – 5 m, deceleration: max. – 7.62 m/s^2, average – 4 m/s^2;
- with ABS stopping distance – 4.8 m, deceleration: max. – 7.82 m/s^2, average – 4 m/s^2.

We can see that with ABS braking is more effective. The deceleration of the brake test confirms that the data is correct. Test data from the asphalt surface also present in Fig. 22.

The eighth test is carried out when the car is running snow-covered roads, 35 km/h. The test results are seen in Fig. 16 and 17:
- without ABS stopping distance – 14.7 m, deceleration: max. – 8.23 m/s^2, average – 4 m/s^2;
- with ABS stopping distance – 18.7 m, deceleration: max. – 7.88 m/s^2, average – 4 m/s^2.

We can see that with ABS braking is more effective. The deceleration of the brake test confirms that the data is correct. Test data from asphalt surface coating also present in Fig. 22.

The ninth test is carried out when the car is running snow-covered roads, 40 km/h. The test results are seen in Fig. 18 and 19:
- without ABS stopping distance – 25 m, deceleration: max. – 11.28 m/s^2, average – 4 m/s^2;
- with ABS stopping distance – 22.20 m, deceleration: max. – 11.87 m/s^2, average – 4 m/s^2.

We can see that with ABS braking is more effective. The deceleration of the brake test confirms that the data is correct. Test data from asphalt surface coating also present in Fig. 22.

Fig. 14. Car without ABS speed before braking – 20 km/h

Fig. 15. Car without ABS speed before braking – 20 km/h

Fig. 16. Car without ABS speed before braking – 20 km/h

Fig. 17. Car without ABS speed before braking – 20 km/h

Fig. 18. Car without ABS speed before braking – 40 km/h

Fig. 19. Car without ABS speed before braking – 40 km/h

Table 2

The results of the Study

Speed km/h		Stopping distance, m		Max. deceleration, m/s²		Average deceleration, m/s²	
		Without ABS	With ABS	Without ABS	With ABS	Without ABS	With ABS
Dry asphalt	20	1,45	1,35	12,42	15,56	7	8
	35	5,2	4,7	9,3	11,2	7	7
	40	10,0	8,7	9,32	14,79	6	7
Wet asphalt	20	2,6	2,8	9,77	9,21	6	6
	35	5,3	4,9	12,05	12,47	6	7
	40	15,4	13	8.92	12,55	6	7
Snow coved asphalt	20	5	4,8	7,62	7,82	4	4
	35	18,7	14,7	7,88	8,23	4	4
	40	25	22,2	11,28	11,87	4	4

Accelerometer data confirm the study of justice. Comparing stopping distances in the road with the accelerometer data numeric values mismatch was not found.

The test data are presented in the Table 2, and the Figs. 20-22.

On dry asphalt the braking with ABS was more effective in all three tests (Fig. 20).

On dry asphalt the braking with ABS was more effective in two of the three tests (Fig. 21).

On dry asphalt the braking with ABS was more effective in all three tests (Fig. 22).
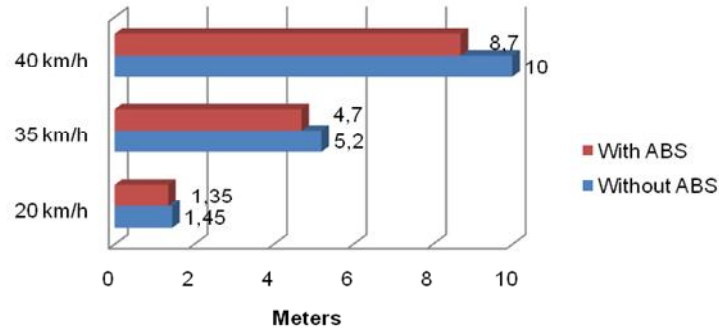
Fig. 20. Stopping distance **-** Dry asphalt
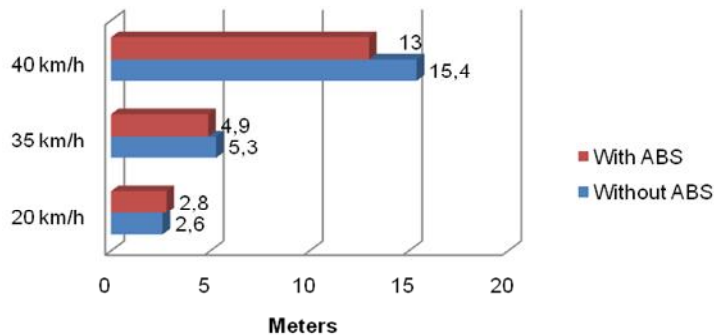
Fig. 21. Stopping distance **-** Wet asphalt
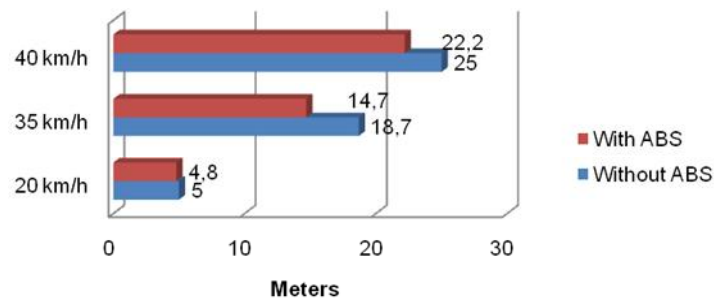
Fig. 22. Stopping distance **-** Snowcoved asphalt

4. Conclusions

1. Going **20 km/h** braking distance (Fig. 3, 4, 5):
   a. on the dry asphalt without ABS - 1.45 m., with ABS - 1.35 m.;   With ABS braking **more effective**
   b. on the wet asphalt without ABS - 2,6 m., with ABS 2.8 m.;   With ABS braking **worse**
   c. on the snow-covered asphalt without ABS - 5m., with ABS - 4.8 m.;   With ABS braking **more effective**
2. Going **35 km/h** braking distance (Fig. 3, 4, 5):
   a. on the dry asphalt without ABS - 5.2 m., with ABS - 4.7 m.;   With ABS braking **more effective**
   b. on the wet asphalt without ABS - 5.3 m., with ABS - 4,9 m.;   With ABS braking **more effective**
   c. on the snow –covered asphalt without ABS - 18.7 m., with ABS - 14.7 m.; With ABS braking **more effective**
3. Going **40 km/h** braking distance (Fig. 3, 4, 5):
   a. on the dry asphalt without ABS - 10m., with ABS - 8.7 m.;   With ABS braking **more effective**
   b. on the wet asphalt without ABS - 15.4 m., ABS-13m.;   With ABS braking **more effective**
   c. on the snow-covered asphalt without ABS - 25m., with ABS - 22.2 m.; With ABS braking **more effective**

4. The braking with ABS was more effective in 17 testings of 18. Braking **with ABS efficiency is 94.4%** of the tests. Braking distance without **ABS efficiency is 5.6 %** of the tests.
5. After the automatic braking system (ABS) performance analysis and the analysis of the data obtained, it can be said that driving a car (data of the study) in the permitted speed, the **stopping distance with ABS is less than without ABS.**
6. When driving in the VW Golf V car with **ABS braking is more efficient.**

Acknowledgements

References

1. **Zeidan Aly E.-S., Hamed A., Salem F.** An antilock-braking systems (ABS) control: A technical review. Intelligent Control and Automation, vol. 2, pp. 186–195, 2011.
2. **Hamzah N., Sam M. Y., Basari A. A.** Enhancement of driving safety feature via sliding mode control approach. In proc. of the 4th International Conference on Computational Intelligence, Robotics and Autonomous Systems, Palmerston North, New Zealand, 2007, pp. 116–120.
3. **Antic D., Nikolic V., Mitic D., Milojkovic M., Peric S.** Sliding mode control of anti-lock braking system: An overview. FACTA UNIVERSITATIS Series: Automatic Control and Robotics, vol. 9, no. 1, pp. 41–58, 2010.
4. **Sandovič V., Bureika G.** Automobilio staigaus stabdymo efektyvumo tyrimas. Transporto inžinerija ir vadyba: 15-osios Lietuvos jaunųjų mokslininkų konferencijos „Mokslas – lietuvos ateitis" straipsnių rinkinys, 2012 m. gegužės 4 d., Vilnius, Lietuva, 28–32 p.

Authors Index